Ground Stress in Mining (Part 2): Calibrating and Verifying Longwall Stress Models

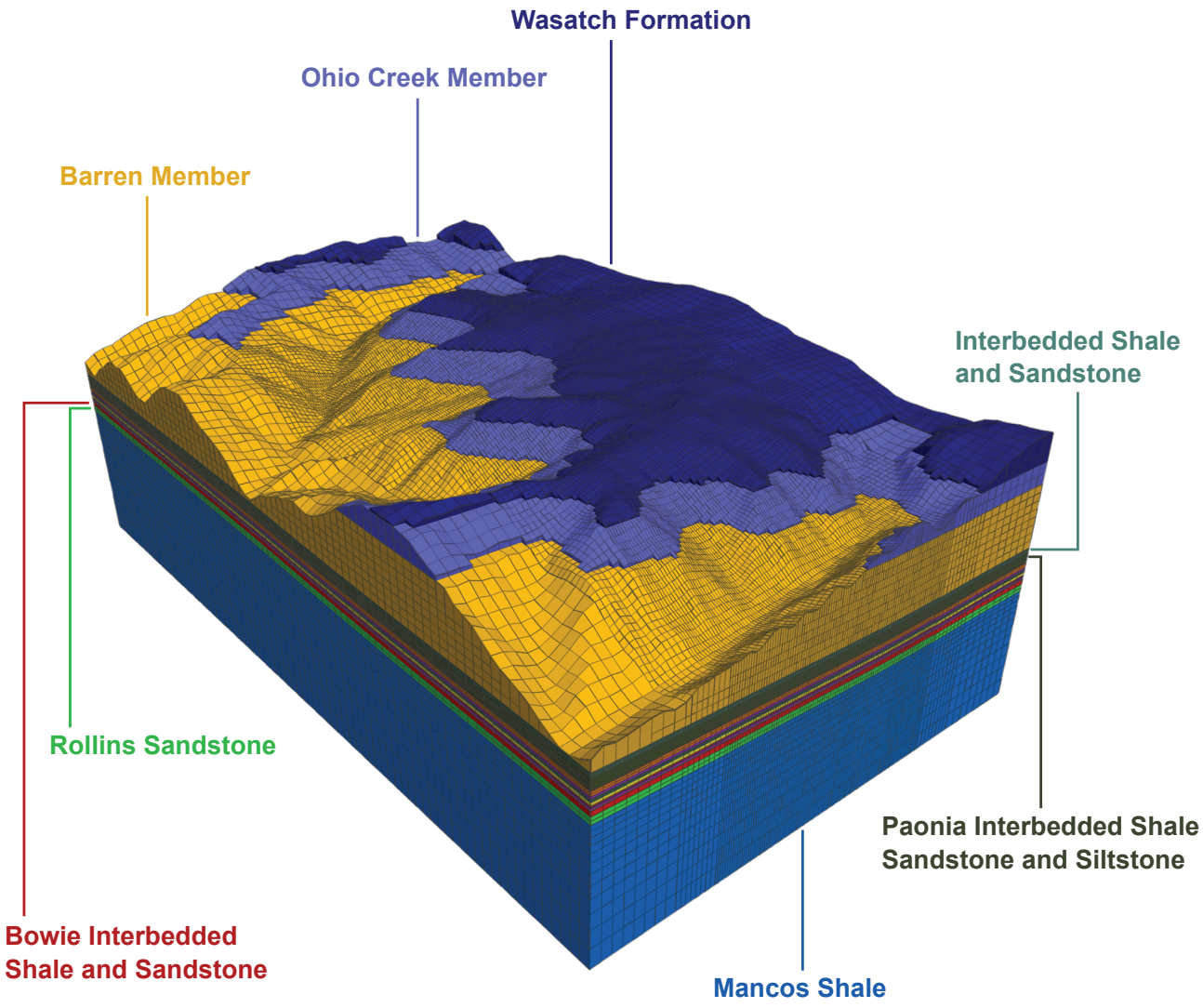

Centers for Disease Control and Prevention
National Institute for Occupational Safety and Health

Report of Investigations 9703

Ground Stress in Mining (Part 2): Calibrating and Verifying Longwall Stress Models

Mark K. Larson, Douglas R. Tesarik, Jeffrey C. Johnson

DEPARTMENT OF HEALTH AND HUMAN SERVICES
Centers for Disease Control and Prevention
National Institute for Occupational Safety and Health
Office of Mine Safety and Health Research
Pittsburgh, PA • Spokane, WA

January 2020

Disclaimer

Get More Information

Find NIOSH products and get answers to workplace safety and health questions:

1-800-CDC-INFO (1-800-232-4636) | TTY: 1-888-232-6348
CDC/NIOSH INFO: cdc.gov/info | cdc.gov/niosh
Monthly NIOSH eNews: cdc.gov/niosh/eNews

Suggested Citation

NIOSH [2020]. Ground stress in mining (part 2): calibrating and verifying longwall stress models. By Larson MK, Tesarik DR, Johnson JC. WA: U.S. Department of Health and Human Services, Centers for Disease Control and Prevention, National Institute for Occupational Safety and Health, DHHS (NIOSH) Publication No. 2020-104. https://doi.org/10.26616/NIOSHPUB2020104.

DOI: https://doi.org/10.26616/NIOSHPUB2020104.

DHHS (NIOSH) Publication No. 2020-104

January 2020

Table of Contents

Figures

Tables

ACRONYMS AND ABBREVIATIONS

ALPS	Analysis of Longwall Pillar Stability
ARMPS	Analysis of Retreat Mining Pillar Stability
BPC	borehole pressure cell
CMRR	Coal Mine Roof Rating
CPC	cylindrical pressure cell
CWFS	cohesion weakening, friction strengthening
FISH	FLACish
FLAC	Fast Lagrangian Analysis of Continua
FLAC^{3D}	Fast Lagrangian Analysis of Continua in Three Dimensions
LTD	load transfer distance
MSHA	Mine Safety and Health Administration
MMT	Mass Mining Technology
NIOSH	National Institute for Occupational Safety and Health
PIB	Program Information Bulletin
Sh	shale
Siltst	siltstone
SS	sandstone
SSMC	strain-softening Mohr Coulomb
UCS	unconfined compressive strength
UDEC	Universal Distinct Element Code

UNIT OF MEASURE ABBREVIATIONS

cm	centimeter or centimeters
°	degree or degrees
ft	foot or feet
GPa	gigapascal or gigapascals
in	inch or inches
kg	kilogram or kilograms
kg/m^3	kilograms per meter cubed
km	kilometer or kilometers
kPa	kilopascal or kilopascals
ksi	kilopounds per square inch
lb	pound force
lb/ft^3	pound force per cubic foot
m	meter or meters
mm	millimeter or millimeters
MPa	megapascal or megapascals
Pa	pascal or pascals
psi	pound per square inch or pounds per square inch
s	second or seconds

Ground Stress in Mining: (Part 2): Calibrating and Verifying Longwall Stress Models

Mark K. Larson[1], Douglas R. Tesarik[2], Jeffrey C. Johnson[3]

Abstract

Researchers from the National Institute for Occupational Safety and Health (NIOSH) have been conducting ground control research with the goal of improving the stability of mine excavations to ensure the safety of mine workers. Numerical models are used to evaluate mine layout design to establish better procedures for predicting ground stress in mining to identify safe and unsafe working areas and escapeways. Current published guidance by the Mine Safety and Health Administration (MSHA) recommends an approach to calibrating models to observations, but it does not include recommendations for using in situ measurements to calibrate such models. A specific goal of this research is to explore and demonstrate procedures for calibrating numerical models to both observations and measurements.

In cooperation with two mining companies in the western United States, NIOSH researchers compiled large data sets of measurements and observations during mining. The purpose of these case studies was to determine ways to calibrate and verify models constructed with various modeling tools to measurements and observations, evaluate pillar strength formulas for applicability, identify deficiencies in the model calibration process, and recommend procedures for calibrating models so that longwall gate road design is improved and the margin between safe and unsafe designs is more clear. The data sets from these two mines were described in Part 1, Larson et al. [NIOSH 2020] (herein referred to as Ground Stress in Mining Part 1), of this two-part series of reports. Also in Part 1, a procedure was recommended to detect first arrival of mining-induced abutment stress ahead of the face with various instruments and with an observational survey of ground conditions. Taking such measurements is critical in the model calibration process.

In this report (Part 2), observations of floor heave and no floor heave were used to determine the general range of strength properties of the floors of the mine's gate roads. Measurements of first arrival of mining-induced abutment stress were converted to equivalent side load transfer distances for use in calibrating models. Load transfer distance at Mine A was four times the result calculated with the empirical Peng and Chiang equation. The load transfer distance at Mine B could not be determined with the same precision, but its probable range is consistent with the load transfer distance measured at Mine A.

Calibration of rock mass stiffness or of stratigraphic moduli of elasticity was possible in these case studies using equivalent load transfer distance. However, for the boundary element code LaModel, a displacement-discontinuity program used in this analysis, the rock mass stiffness was so great that it was impossible to calibrate final gob stiffness and achieve reasonable gob loading.

[1] Mining Engineer, Spokane Mining Research Division, NIOSH, Spokane, Washington.
[2] Mechanical Engineer, Spokane Mining Research Division, NIOSH, Spokane, Washington (retired).
[3] Mining Engineer, Spokane Mining Research Division, NIOSH, Spokane, Washington (retired).

The boundary element code MULSIM/NL was modified to accommodate a larger number of elements in the mesh, and a stress-versus-strain material model defined by a piecewise linear function, called the five-point material model, was added and verified. This updated version of MULSIM/NL is named MulsimNL/Large. MulsimNL/Large and FLAC^{3D}, the latter using an unverified and uncalibrated caving model, calculated gob loading that was in a reasonable range. However, better estimates of gob loading are necessary to proceed further with full model calibration.

Detailed pillar models using FLAC^{3D} suggested that alternatives to the Mark-Bieniawski pillar strength model should be considered, especially for pillars with a width-to-height ratio greater than eight. A Holland-Gaddy equation fit to data from FLAC^{3D} models consisting of average pillar strength versus pillar width-to-height ratio showed better ability to describe model results than did the Mark-Bieniawski strength equation. Experience with the detailed pillar models also suggests that stratigraphy should be modeled, wherever possible.

Borehole pressure cell (BPC) trends and comparison of model-calculated load transfer distance with equivalent load transfer distance determined from measurements of first arrival of mining-induced abutment stress strongly suggest that commonly used yield models were inadequate to describe seam material behavior near the ribs at Mine A. A MulsimNL/Large elastic model with the coal modulus reduced in the outer two rings to 60% and 80% of full value, respectively, provided the best match of "measured" versus model-calculated load transfer distance derived from stress increase at each BPC site. In considering appropriate strength models that might sufficiently simulate this behavior, measurements indicate that ribs are sometimes able to take much more stress than that calculated using most common yield strengths models, suggesting that strain-hardening might be an important part of the coal pillar behavior near pillar ribs.

Observations in these two case studies (Mines A and B) suggest that geologic structure changes, not represented in the models, were important for predicting stress and instability of ground. Observations suggest that prior knowledge of structure change and individual structure properties would be necessary to adequately simulate its effect on stresses and failures with a particular mining layout.

Introduction

In any design task, engineers usually follow a process that helps to determine and implement an optimized solution that meets the design objective. Mine layout design is no exception. Peck [1969, Figure 3a] discussed the observational method used by Terzaghi [1961] in soil mechanics and stated that, although it has pitfalls and limitations, it has great advantages in savings of time and money without sacrificing safety. However, he was clear that this method should not be used unless the designer has a plan of action for every unfavorable situation that is discovered. McMahon [1988] estimated a 36% risk of encountering serious geotechnical problems in construction or mining projects. He said that roughly two-thirds of these problems are the result of inadequate recognition of uncertainty in the geotechnical design analyses and around one-third are due to unknown geological conditions, use of the wrong geotechnical criteria, post-investigation design changes, or human errors.

Bieniawski [1992] outlined design principles for rock mechanics and illustrated those principles with a flow chart. Stacey [2009] took Bieniawski's flow chart of principles and illustrated them as a "wheel of design," shown here as Figure 1. Besides illustrating the progression of steps in the design process, the relationship between each step and the last step of "implementation" is emphasized. These relationships mean that the process of design is very dynamic, with the necessity of rethinking each step as problems arise.

Defining the problem, determining requirements and constraints, minimizing the unknowns, and determining a conceptual model are very important. Solving the wrong problem, having inadequate requirements, not considering necessary constraints, or exerting insufficient effort to determine unknowns can result in a poor conceptual model. Models play an important part of this process, playing roles in steps 4 through 7 of Stacey's wheel of design. Various modeling tools are based on different conceptual models, and the availability of specific modeling tools may also affect the choice of conceptual model.

Models may be used to evaluate designs, but only if the model adequately represents important mechanics and if the model is calibrated. Models not properly calibrated are useless in the design evaluation process.

Figure 1. Engineering wheel of design that illustrates the relationship between each step of the design process and the implementation and reevaluation that must take place after each step. After Stacey [2009].

In the aftermath of the Crandall Canyon Mine Disaster [MSHA 2008], MSHA issued Program Information Bulletin (PIB) 09–03 [MSHA 2009] to provide guidance on how to calibrate models used to evaluate underground mine layout designs when analysis beyond simple empirical and analytical methods is warranted or desired. The steps outlined in the PIB were based on earlier work of Karabin and Evanto [1994]. The short descriptions of these steps are:

1. Observe underground areas.
2. Estimate model parameters.
3. Model observed areas.

4. Verify model accuracy.
5. Establish threshold limits.
6. Model new configurations.
7. Evaluate new configurations.
8. Implement best alternative.

In the first of these steps, the modeler categorizes deterioration indexes with differing pillar sizes, panel configurations, and overburden heights to establish patterns. In the second step, model parameters are estimated from laboratory measurements and appropriately scaled. In the absence of measurements and site-specific information, general coal and rock properties (meaning published values from the literature or other reliable sources) may be used. In the third step, these estimated parameters are input to a model and results obtained. The fourth step is, perhaps, the most critical. Skiles and Stricklin [MSHA 2009] state that "each of the areas modeled must be closely examined to ensure that the results correlate with observed conditions." While this statement is good counsel, the PIB does not mention correlation of model results with measurements of stress, load, displacement, or other possible quantities that shed light on the mechanics involved. Measurements and observations together better tell the story of important mechanisms and improve the calibration and verification of numerical models. Interestingly, in six and a half years since this PIB was published, not one mine layout plan has been submitted to MSHA where these steps were followed to calibrate and verify a numerical model that justifies the proposed design [Mark 2015].

The purpose of this report is to describe the research findings of a project entitled, "Calibration and Verification of Longwall Stress Models," conducted over a 3.5-year period that outlines procedures to calibrate and verify numerical models to not only observations, but to selected kinds of measurements, principally stress or load change measurements that provide estimates of load transfer distance (LTD). The LTD is the distance to the side of the mined panel at which load increase resulting from mining is first detected. More information on LTD and its meaning is found later in this report. The results of this report and its companion report, including consequential guidelines, are intended to be applicable, at minimum, to calibrating models used to evaluate mine layout in any tabular deposit.

Although the calibration procedure of numerical models is extremely important, another important step precedes the use of a numerical model. The user needs to evaluate the mechanics of a site and decide which are important and then choose the appropriate tool that is capable of simulating those important mechanisms. For example, although finite element methods or finite difference methods might be more time-consuming, they might be capable of following an important failure mechanism in the roof or floor of a mine that cannot be captured by an elastic representation of the rock mass found in boundary element methods. Joints and faults may play such an important role that they cannot be well represented by a scaled continuum but must be more appropriately modeled directly. Such evaluation of important mechanics must take place before calibration proceeds. It has been shown that choice of modeling tool can limit the solution space available [Larson and Whyatt 2009b; 2010]. While all numerical models are simplified simulations of reality, critical mistakes can be made by not selecting the appropriate tool with important mechanisms. For example, Heasley found in his back analysis of the Crandall Canyon collapse with LaModel that one of the likely triggers of the seismic event was slip along a vertical fault soon after pillars started to be mined in retreat [Heasley 2008a, 2009a].

In Part 1 of this two-part report, measurements and observations were reported of maximum distance from the face at which first arrival of mining-induced stress increase is detected at two

mine sites in the western United States. These data were obtained with various instruments and techniques, and subsequently, were analyzed. However, the distance from the face or gob to where first arrival of mining stress was detected is almost always in a direction outby the face and does not meet the definition of LTD by Peng and Chiang [1984]—i.e., the distance to the side of an excavated panel to the location where mining-induced stress is first detected. This definition also assumes that the measurement location is far from both the face and the start-up room. Therefore, these distances of first arrival reported in Part 1 still needed to be converted to an equivalent side-of-panel LTD.

In this report (Part 2), these distances at first arrival of abutment stress were converted to equivalent LTD at the side of the panels. The LTDs then were used to calibrate several models as much as was possible. A full calibration was not possible because of the lack of measurements on distribution of overpanel weight between the gob and the unmined coal. The results of several numerical modeling tools are compared, and these results are, in turn, compared to results from the empirical approach. Reference to the design process as illustrated in Figure 1 is repeated in this report as the results of the Mine A and Mine B case studies are presented. Because of lacking measured material properties that match observations of ground behavior, two alternative methods for calibrating numerical models are demonstrated. Research needed to facilitate or improve calibrations is recommended in the Conclusions and Recommendations section.

The subject of coal bumps or mining-induced seismic events and how to design and evaluate the risk of such events is an exhaustive subject in itself. Although such mining-induced events did occur at the mines studied, ranging from very small events to damaging events such that they are very much of concern, calibration of models that evaluate such risk depend on better understanding of post-peak-strength behavior. Such behavior was not measured and making such measurements was beyond the scope of this study. Instead, this study concentrates on general calibration of models that include elastic parameters, yielding, and peak strength. Proper evaluation of mining-induced seismic risk would require much more specific properties study, identification of probable mechanisms, and calibration of post-peak-strength behavior. Although some work has been done in determining likely mechanisms of mining-induced seismic events, such as mining-induced fault slip [Mark et al. 2012], the authors of this report have not dismissed other mechanisms as possible candidates. Such subject matter deserves careful and extensive treatment elsewhere.

In mine layout design, the engineer should start simply, with approaches such as using empirical methods. When such methods have historically indicated designs that have had success, these methods should be sufficient, except in cases where conditions significantly depart from standard conditions. If conditions warrant more investigation, modeling tools can assist with evaluation of conditions and mechanisms. Empirical tools are quick and provide a statistical approach with comparison against an extensive database. In cases where local conditions are highly variable or where they depart from assumptions of the empirical method, using techniques that more closely simulate the effects of stratigraphy or specific failure mechanisms are likely necessary to improve understanding to increase the chance of success and minimize risk. One example might be the work on pillar strength and design by Wilson [1972] and Wilson and Ashwin [1972] in which they describe the mechanics of pillars, including the concept of an inner core and confining failed material.

Before proceeding with the details of this study, a review of the literature on the calibration of numerical models is appropriate. Such a review will provide the reader with an understanding of successful numerical modeling calibration practices over the last 35 years.

Literature Survey on Model Calibration

Various modeling methods and modeling software might be used to evaluate mine layout design. For various reasons, boundary element methods, finite element methods, finite difference methods, discrete element methods, particle methods, or displacement discontinuity analysis methods might be used. Each method has its limitations, including the mechanisms that each can simulate. Moreover, each has limitations or ranges of solution space that can be accessed [Larson and Whyatt 2009a, 2009b; Larson and Whyatt 2010]. If an appropriate model is used for a specific case, the input parameters, such as the elastic and strength properties, need to be calibrated so that the model calculations output have relevance.

Models might be calibrated in several ways, including scaling properties between laboratory and field, scaling model calculations to empirical results, and scaling to experimental results or observations among others. The following sections detail the different methods.

Calibration Using Scale Factors

The material properties used for initial numerical models can be based on measured laboratory values of elastic parameters and strengths. However, these values need to be scaled to reflect the larger-scale behavior of the rock mass, which may have several joints, flaws, or other imperfections that weaken the rock mass [Heuze 1980]. Heuze stated that the majority of cases have a ratio between field and laboratory scale for modulus from 0.20 to 0.60.

One well-founded method is used and described by Pariseau et al. [1984], Pariseau et al. [1986], and by Pariseau et al. [USBM 1992d]. These authors describe using measurements with extensometers over a large scale, which are monitored as mining progresses. By comparing relative displacements between anchor locations as calculated by the model with those measured displacements, an average slope, determined by regression analysis, represents a reduction factor needed to adjust from laboratory-scale moduli to rock mass scale moduli and is represented by the equation:

$$slope\ or\ strength\ reduction\ factor = \frac{rock\ mass\ moduli}{laboratory\ moduli} \quad (1)$$

assuming only small variation in conditions that affect scaling. As long as the anchor positions are in ground that remains linear or only slightly nonlinear, then this slope represents an average reduction factor for the elastic moduli in the model. In their case, Pariseau et al. [USBM 1992d] reported an elastic reduction factor of 14% to 17%. The correlation coefficient, r^2, in the reduction of elastic properties in this case was 0.75, which the authors deemed satisfactory.

By preference, strength should be reduced independently of the elastic moduli. Pariseau et al. [USBM 1992d] stated that this should be done by determining extent of yield zones through measurement and observation and comparing with yield zones calculated by the model. They stated that "the usual indication of yielding is a relatively large increase in measured displacements compared with previous displacement changes and earlier stope cuts." They also noted that some yielding may take the form of violent rock bursts. Models having strengths that are too high will not be able to produce the displacements that are associated with yielding.

However, these authors reported that none of the extensometers in their case were placed in a way to define the yield zones. Yielding took place elsewhere. Instead, they outlined two

empirical rules or approaches that allow the user to estimate the strength reduction factor compared to the elastic moduli reduction factor:

First, the strain to failure is maintained constant under uniaxial compression. Then

$$\varepsilon_f = \left(\frac{C_0}{E}\right) \tag{2}$$

is a constant, where ε_f = strain at failure, C_0 = unconfined compressive strength, and E = Young's modulus. Thus, the strength scaling factor is equal to the elastic modulus scaling factor.

Second, the strain energy is constant at failure under uniaxial compression. According to this rule,

$$U_{strain} = \frac{(C_0)^2}{2E} \tag{3}$$

is a constant, where U_{strain} = strain energy density at failure. In their case, Pariseau et al. [USBM 1992d] selected an elastic scaling factor range of 0.14 to 0.17 but found that using the same reduction factor for strength and modulus provided too much yielding. Therefore, they used the second rule, so that if the elastic modulus reduction factor were 0.16, the strength reduction factor would be 0.40 (= $\sqrt{0.16}$). Thus, the range of the strength reduction factor was 0.37 to 0.41.

Using the same rule in a later study, Pariseau et al. [USBM 1996] adjusted the elastic modulus and strength reduction factors to 0.25 and 0.50, respectively. They also justified this strength factor because of the amount of yielding inferred from a calibrated two-dimensional model done by Pariseau et al. [USBM 1995] and a simple analytical relationship between two- and three-dimensional back analyses of long cylindrical and spherical excavations. Later, Pariseau et al. [2012] maintained these reduction factor amounts for a study associated with the Deep Underground Science and Engineering Laboratory (DUSEL) project.

Zipf [2006] started with laboratory point-load tests for strength, then reduced to rock-mass scale for model by applying a 0.56 fraction, per Gale and Tarrant [1997]. He made major, but reasonable assumptions for input parameters for the strain-softening model in FLAC.

Gale et al. [2004] used laboratory tests, scaled by 0.58. This scaling factor was obtained by extrapolating to a 1-m diameter specimen using an equation fitted to compiled data by Hoek and Brown [1980] for relating strength of specimens having diameters between 10 mm and 200 mm [Gale 2016]. The 1-m size was considered representative of the rock mass scale. Esterhuizen et al. [2010b] justified using the 0.58 scaling factor in the same way. Gale et al. [2004] inferred modulus from stress measurement strains obtained by Dolinar [2003]. The focus of Gale et al. [2004] was the study of interaction between roof rock and bolts on a small scale, as opposed to a mine-wide scale.

Calibration to Empirical Results

Esterhuizen et al. [2010b] used FLAC^{3D}. They took pillar stress measurements from field studies in the U.S., with peak stress about 5 m into the pillar. They numerically tested the sensitivity of interface properties and considered the experience of other researchers with interface properties. They calibrated Hoek-Brown strength parameters to match the Bieniawski strength equation. The results for cases with pillar width-to-height ratios between 3 and 8 fit reasonably with the final input parameter set. They represented gob using [Salamon's1990] equation for caved material:

$$\sigma = \frac{a\,\varepsilon}{b - \varepsilon}, \tag{4}$$

where σ = vertical stress on the gob,
ε = vertical strain, and
a and b are empirically derived parameters.

This equation was fit to tests of Pappas and Mark [USBM 1993] on scaled gob material of shale, weak sandstone, and strong sandstone.

In modeling 670 cases of the influence of support, Esterhuizen and Tulu [2015] calibrated their models against the results of empirically based Analysis of Roof Bolt Stability (ARBS) [Mark et al. 2001], which is based on cases in 37 mines in the eastern U.S.

Calibration to Both Empirical and Experimental Results

Ozbay and Badr [2010] used strain softening to predict the behavior of chain pillars in a longwall gate road with a FLAC^{3D} model. They calibrated a model of a pillar loaded against empirical assumptions. They adjusted parameters to fit their model to three in-situ pillar-deformation tests by Wagner [1974], including fitting to post-peak behavior. Afterward, they applied these results to a deep, two-entry longwall mine using yielding chain pillars. In examining verification of their model, they compared model results with BPC measurements in the pillars. Stress relief in the pillars as indicated with the BPCs was much earlier than that predicted by the model; however, the longwall face position at the onset of maximum stress was within a few meters of that predicted by the model. Although rates of stress reduction compared well, amounts of stress reduction differed, which fact is not surprising, given the experience at Mine A by NIOSH. Ozbay and Badr [2010] recommended further studies, such as looking at dynamic failures with discrete element models to analyze failure mechanisms. In other words, their present model might be useful in predicting risk, but more detailed models that can simulate bump mechanisms are needed.

Calibration to Other Measurements and Observations

Wiles [2007] advocated model calibration by using back analysis of consistent mine behavior and correlating model results with mine results. Figure 2 (Wiles' Figure 6) illustrates the process of considering inputs to the model and comparing the model's predictions with consistent observations and measurements in the mine and then using coefficient of variation for estimating the reliability of the model to predict observed behavior. In this process Wiles gave specific examples of using pillar failure, microseismicity, and structurally controlled overbreak to calibrate and refine models.

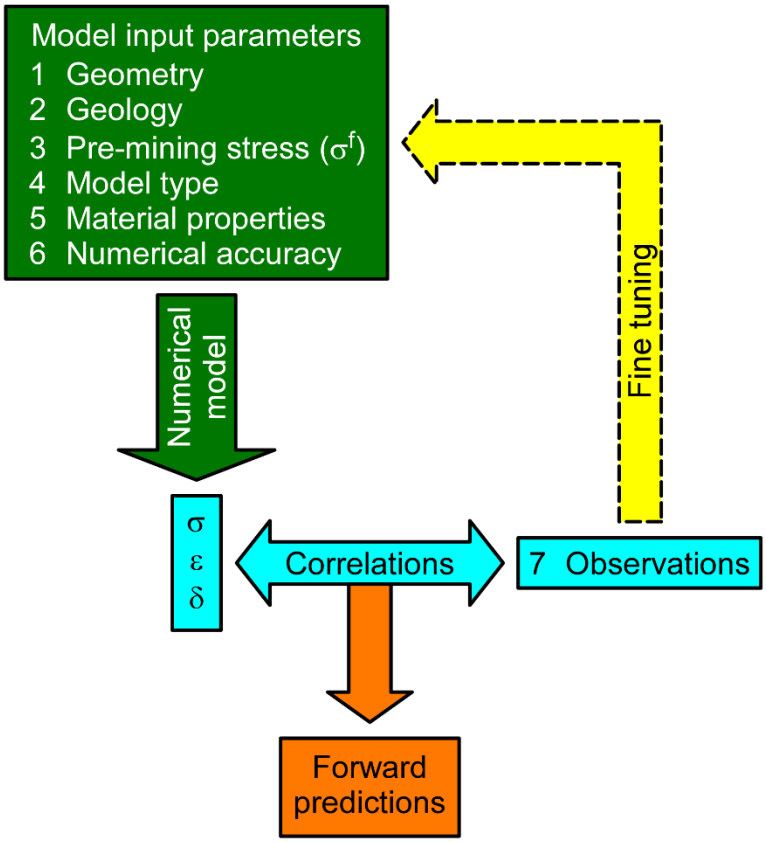

Figure 2. Diagram of the model input and calibration process as described by Wiles. After Wiles [2007].

Andrieux et al. [2008] advocated using microseismicity to calibrate strength of materials in a model, especially the post-peak softening part of a strength-strain curve. In their approach, they advocated: (1) carefully selecting seismic events that are the result of stress increase from mining to be part of a comparison database, (2) including relevant geologic horizons in the model, and (3) identifying mining steps that have caused the largest and clearest seismic reactions. When this was performed in their case study, they compared extent of zone yielding with location of these seismic events. After several iterations, they were able to determine the strength curve, including the softening portion of the curve so that extent of yielding matched location of seismic events.

Crockford et al. [2015] determined depth of yielding from a seismic array, drilling cores, and observations from site visits. They tested several models: Hoek-Brown, strong strain-softening Mohr Coulomb (SSMC), and cohesion weakening, friction strengthening (CWFS). The SSMC model fit results the best. In order to optimize the parameter fit, three more models were run: A stronger SSMC model, a strong brittle SSMC model, and a CWFS model with a higher initial friction. The stronger SSMC model provided the best fit to the field data.

General Procedure of Calibration of Models

Displacement discontinuity codes require a different procedure for calibration because of their simpler framework. However, the same fundamental procedure can be used to calibrate

codes based on other modeling methods, such as finite element method, finite difference method, or even discrete element method. Referring to his code, LaModel [Heasley 2007; 2010 for later version], Heasley [2008b] identified that the following items are interrelated and need to be calibrated in the following order:

1. Rock mass stiffness
2. Gob stiffness
3. Coal strength

Heasley noted that the interrelationship between these items usually requires that multiple iterations of these steps be performed before the model is adequately calibrated. In the absence of measurements and observations, Heasley [2008b] recommended calibrating to the empirical database criterion established by Mark [1987; USBM 1990; Mark 1992] for the Analysis for Longwall Pillar Stability (ALPS) program, and later, the Analysis for Retreat Mining Pillar Stability (ARMPS) program [Mark and Chase 1997]. The empirical criterion relies on the equation for the distance from the mined panel that the load is transferred to the abutment as determined by Peng and Chiang [1984], based on cases in the eastern United States:

$$D_{1.0} = 9.3\sqrt{H} \tag{5}$$

where $D_{1.0}$ = distance from the gob in ft within which is found 100% of the portion of the overpanel weight that is transferred to the abutment as a result of mining, and
H = height in ft of the overburden.

Calibrating to $D_{1.0}$ is impossible for this class of codes because the load transferred in the model solution is approaching zero but is theoretically still nonzero at an infinite distance from the gob. Heasley recommended calibrating to $D_{0.9}$, which is the distance from the gob within which 90% of the transferred overpanel weight is located. Using Mark's abutment loading inverse function [USBM 1990], $D_{0.9}$ is approximately:

$$D_{0.9} = 5\sqrt{H} \tag{6}$$

The procedure for calibrating gob stiffness is less straightforward due, in part, to there being few cases where actual gob loading has been measured or can be accurately estimated. In LaModel's input software LamPre [Heasley 2010], the final gob stiffness is determined in an iterative two-dimensional scheme based on the empirically assumed amount of gob loading. To the knowledge of the authors of this report, only Maleki et al. [1984] have successively measured gob pressures in one case, which was accomplished with Gloetzl cells and is described later in this report. Others' attempts to measure gob loading are discounted for reasons given later.

Measuring gob load is very difficult in today's longwall panels. However, opportunities to measure gob load arise if cross-panel entries are developed well in advance of the longwall face [Seymour et al. 1998]. A possible alternative would require expensive drilling in the floor across the panel and installation of an instrument in these boreholes. Currently, the authors of this report are not aware of a proven set of instruments that could be inserted in such long boreholes.

Coal strength calibration is an area of study with much room for advancement. The empirical method of ALPS and ARMPS assumes a uniaxial compressive strength for coal of 6.21 MPa (900 psi). Strength increases with depth into the pillar because of confinement, depending on the pillar strength formula used—the Mark-Bieniawski formula in the case of ALPS and ARMPS [Mark 1999]. Improvement upon this assumption of coal strength might be made by

measurements, observations, and using some of the techniques of authors previously mentioned [USBM 1992d; Wiles 2007; Andrieux et al. 2008].

Calibration to Post-peak Strength Behavior

It is beyond the scope of this paper to address calibration of post-peak behavior. Even so, such calibration is very important to predicting risk of mining-induced seismic events and, therefore, the literature is reviewed here. Such calibration can only happen indirectly—such as by comparing model results of deformation or yielding obtained with a set of post-peak parameters to measurements or observations of deformation or yielding—or by measuring such behavior in the laboratory and making assumptions about post-peak strength behavior on a larger scale. There have been many attempts to simulate it in the laboratory, but the attempts to calibrate models of field sites involving post-peak behavior are not extensive. Instead, here is only a very small sampling of papers about post-peak behavior and calibrating to it.

Several factors affect post-peak-strength behavior. Width-to-height ratio of samples has been shown to drastically affect residual strength levels, probably even more so than it affects peak strength (see Figure 3) [Das 1986] [Özbay 1989]. At low ratios of 0.5 or 1.0, a rock sample may be extremely brittle, losing all strength immediately. With increasing width-to-height ratio, the stress-strain curves of uniaxial tests begin to show residual strength, followed by ductile and strain hardening behavior. The degree of hardening may increase with increasing width-to-height ratio [Das 1986]. Özbay [1989] showed with several rock types that post-peak modulus is dependent on width-to-height ratio, also. Esterhuizen et al. [2010a] conducted numerical experiments on pillars calibrated to the Bieniawski pillar strength formula. The pillars began to strain harden if their width-to-height ratios were above 8.0. Small width-to-height pillar ratio has been associated with several massive pillar collapses that occurred in the U.S. [Chase et al. 1994].

Confining pressure also has a similar effect in changing a rock sample's behavior that might be brittle with no lateral confinement to ductile [Cook 1965; Wawersik and Fairhurst 1970; Price 1979; Hakami 1988; Kumar et al. 2010] or even strain hardening [Bawden 2010] (see Figure 4). Class II behavior can be present for brittle material with unconfined testing [Wawersik and Fairhurst 1970] (see Figure 5). Confining pressure changes class II to class I behavior. Zhao [1994] conducted tests on Carmenellis granite with a geothermal testing system. The triaxial tests showed typical variation of post-peak behavior with confining pressure—that is, the elastic modulus remained constant, but the peak stress and associated strain increased with confining pressure as did the residual strength. They found that peak strength was decreased significantly by increased temperature. Mishra and Nie [2013] conducted unconfined testing using lateral strains as feedback for a closed-loop servo-hydraulic system. With such a system, they were able to follow class II behavior with no confinement. Coal samples from the Hiawatha seam showed class II behavior with no confinement and exhibited class I behavior with confinement. When confinement was 1,000 psi, this coal showed strain-hardening behavior. Tesarik et al. [2003] measured stress change and dilation of pillars confined by backfill, with pillars mined sequentially. They calibrated a UTAH3 model to extensometer readings using the elastic-perfectly plastic Drucker-Prager constitutive material model. The calibrated model showed post-peak hardening if there was confinement.

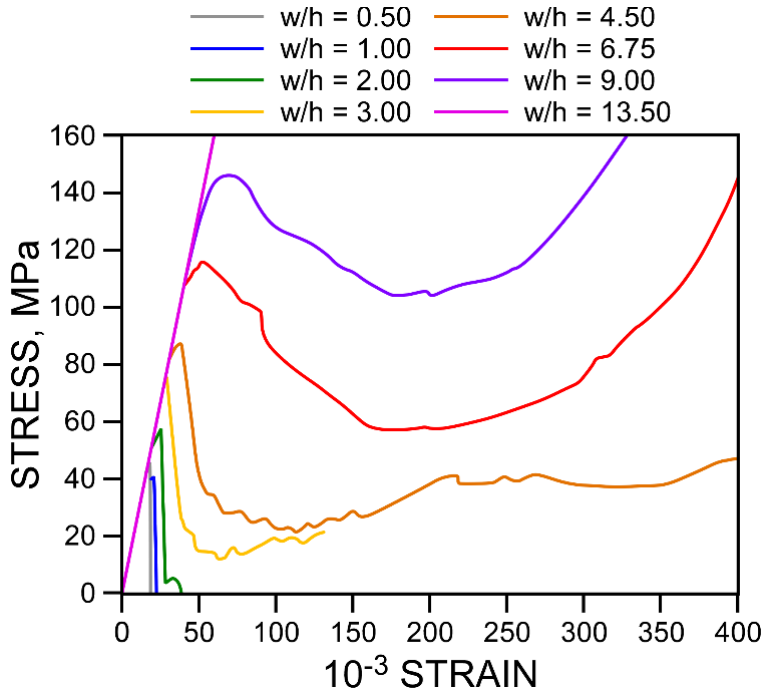

Figure 3. Plots of experimental results of stress versus strain on coal according to various width-to-height ratios. After Das [1986, Figure 3a].

Lan et al. [2010] performed numerical tests with Universal Distinct Element Code (UDEC) [Itasca Consulting Group 2012] on simulated samples with grain-line structure. This type of model was used to simulate the microheterogeneity caused by elastic variation and contact stiffness anisotropy. The results showed that the compressive stress required to initiate the formation of macroscale dilation and strain localization is controlled by crack density.

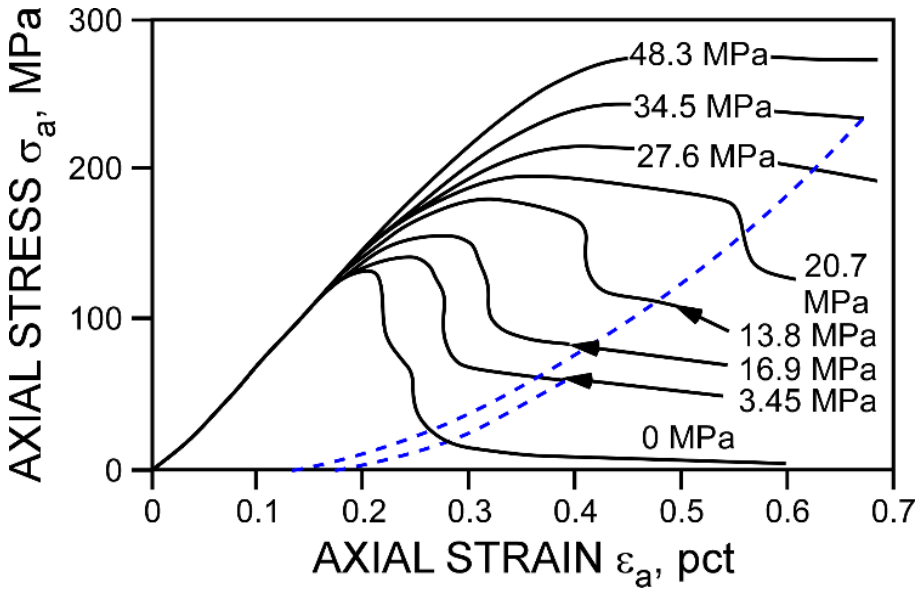

Figure 4. Complete axial stress-strain curves obtained in triaxial compression tests on Tennessee Marble at various confining pressures. After Wawersik and Fairhurst [1970].

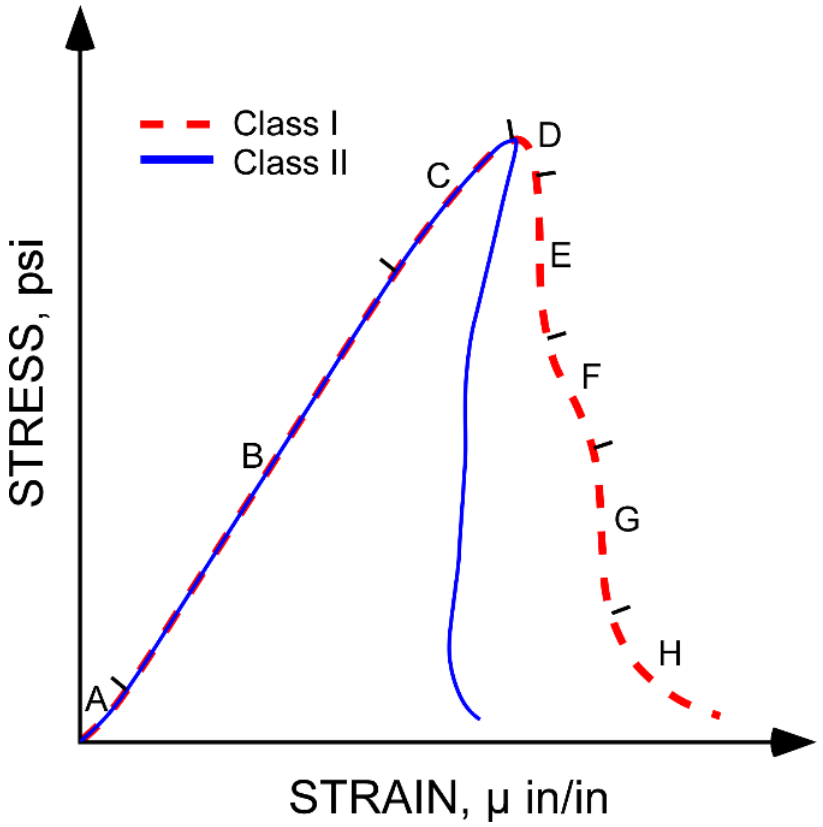

Figure 5. Class I and class II post-peak strength behavior of rock illustrated in general plot of stress with strain. After Wawersik and Fairhurst [1970].

Zhang et al. [2015] conducted numerical experiments on a synthetic rock mass specimen of particles. Various characteristics of joint sets were inserted into the specimen. Peak strength was dependent on orientation of the joints, with highest strength at orientations of 0° and 90°, and minimum strength at 45°. The peak strength also decreased with increasing joint size. Brittle post-peak behavior was observed in specimens having low persistence of joints. The post-peak behavior became more ductile when the joint sets were inclined or more persistent.

As mentioned earlier, Andrieux et al. [2008] were able to determine the strength curve, including the softening portion of the curve so that extent of yielding in the rock mass matched location of seismic events.

Jaiswal and Shrivastva [2009] developed a model for coal pillars, based on deterioration of some Hoek-Brown parameters and the dilatancy model of Alejano and Alonso [2005]. They calibrated their model to fit several cases of coal pillars in Indian mines, determining initial and residual values of the Hoek-Brown parameters among other material constants.

Li and Heasley [2015] used the concept of local mine stiffness [Salamon 1970] to calibrate post-peak behavior of coal that caused extensive bump damage in the Crandall Canyon Mine disaster [MSHA 2008].

Summary

Calibration of models can best be accomplished by adjusting key model inputs so that model calculations match measurements and observed behavior as much as possible. Laboratory measurements of elastic modulus and strength properties are a good start, with appropriate

scaling applied. However, measurements and observations provide justification for further refinement of elastic properties, strength properties, gob properties, and possibly can be used to infer post-peak-strength behavior. In the cases with measurements described in Part 1 of this series of reports, these principles of calibration, with particular reference to the steps outlined by Heasley [2008b], will be followed to determine possible ways forward to calibrate numerical models.

Case Studies Description

Sites

Both case studies (Mines A and B) were conducted in western U.S. coal mines located close to each other and in an area of dramatic variability in topographic relief. They had similar geology, but were in different seams, and the range of overburden thickness for each mine was significantly different. For Mine A, the cover depth ranged from 405 m to 735 m (1,330 ft to 2,410 ft) in the study area. For Mine B, the overburden ranged from 204 m to 354 m (670 ft to 1,160 ft) in the area where the study was conducted. At Mine A, the 1 North outby instrumentation site had an average overburden of about 682.3 m (2,239 ft), while the 2 North outby instrumentation site averaged about 691.4 m (2,268 ft). The average overburden between these sites was 686.9 m (2,253.5 ft). At Mine B, the instrumentation sites had overburden ranging from 229 m (750 ft) to 337 m (1,105 ft).

Ground Stress in Mining Part 1 described the geology of both Mine A and Mine B that will not be repeated here. However, a description of the geometry of the gate roads is important to this discussion. Figure 6 shows a map of the area of Mine A where the study was conducted, including the mining of Panel 1 and Panel 2. Panel 1 is the longwall panel between the 1 North and 2 North gate roads. Panel 2 is the panel between the 2 North and 3 North gate roads. The red boxes indicate the location of most of the installed instruments. The sites in each set of gate roads were differentiated with the names inby and outby. Thus, the instrumented sites were named the 1 North inby, 1 North outby, 2 North inby, and 2 North outby. The 3 North gate roads were under development during early mining of Panel 1. The 4 North gate roads and 5 North gate roads had not been developed at the time of this study.

Faulting intersected the gate roads in several locations, as shown in Figure 6. The location of these faults influenced the selection of the test sites, although the 2 North outby site was placed close to the fault intersecting the south pillar for practical reasons.

Table 1 lists geometric information of the pillars and entries in the 1 North and 2 North gate roads. Table 2 lists the dimensions of Panels 1 and 2. The width of the 2 North pillars was increased as a result of the development of a local, deep-cover Analysis of Longwall Pillar Stability [Mark 1987] database, determining a critical stability factor for the mine. Subsequent negotiations with MSHA resulted in approval of a pillar width about 14% larger than that required by the locally determined critical stability factor.

In fact, this increased pillar size did not prevent a mining-induced seismic event of magnitude 3.1 on the Richter scale that occurred on February 17, 2011, at 17:47 local time in the 2 North gate roads. The location was somewhere between crosscuts 11 and 15.

Subsequently, the Panel 2 longwall face was advanced a short distance to approximately crosscut 15, and a new startup room was developed at crosscut 10. The longwall mining

equipment was moved between March 25, 2011, and April 6, 2011, when longwall mining resumed and continued until Panel 2 was completed.

For modeling purposes, the description of stratigraphy by Robeck [2005], whose graphical column is reproduced here as Figure 7, was adapted and idealized to that shown in Figure 8. Material properties from laboratory tests of core samples taken from the area were not available for these stratigraphic members. Therefore, best estimates of material properties listed in Tables 3 and 4 were chosen on the following basis:

- Experience modeling generic cases that represent a typical Utah coal field stratigraphic column [Larson and Whyatt 2009b].
- General knowledge that the strata of western Colorado was less stiff and not as strong as the Utah strata.
- Experience of a contractor drilling in various seams in these mines that suggested the DU Seam, where Panels 1 and 2 were located, was weaker and slightly less stiff than the other seams.
- The values chosen were within the wide range of values suggested in the literature for the basic member types [Farmer 1968; Pariseau 2012; Goodman 1989; Blyth and de Freitas 1984; Sheorey 1997; Maleki et al. 2007; Vutukuri et al. 1974; Lama and Vutukuri 1978c, 1978b, 1978a].

No scaling of these initial estimates was performed to more closely represent rock mass scale other than to include ubiquitous joints in the FLAC^{3D} [Itasca Consulting Group 2009] model. It was assumed that field scale was, at least in part, built in to these estimated amounts.

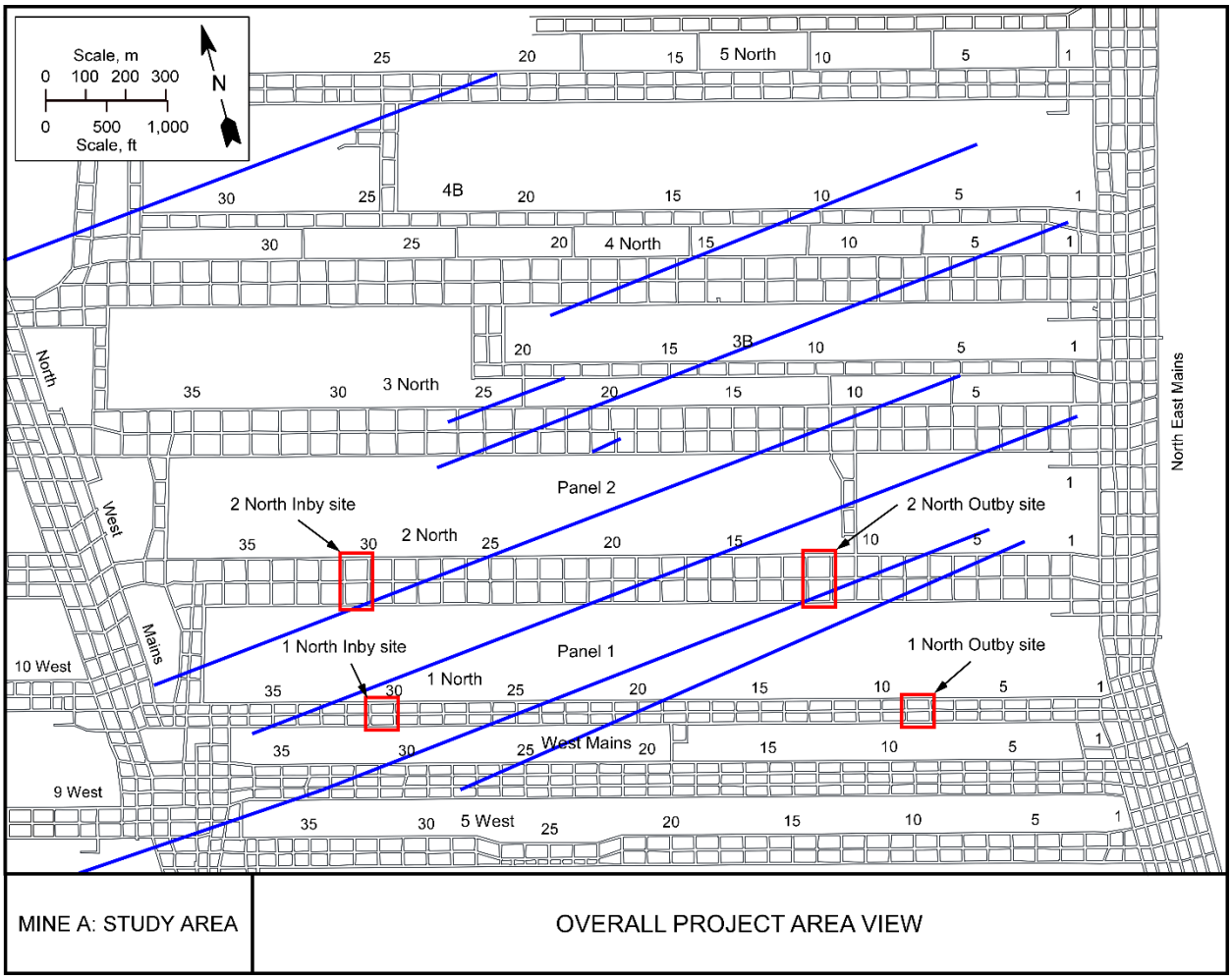

Figure 6. A map of Mine A with overlain mapped and projected faulting. After Larson et al. [NIOSH 2019]. Blue lines indicate both mapped and projected faults. Red boxes indicate location of main instrument sites in this study.

Table 1. Gate road geometry at Mine A

Item	1 North, m	1 North, ft	2 North, m*	2 North, ft*
Entry width	6.1	20	6.1	20
Crosscut width	6.1	20	6.1	20
Pillar width	22.3	73	51.8	170
Pillar length	54.9	180	54.9	180
Mining height used for models	3.4	11	3.4	11

*3 North geometry is the same as 2 North geometry.

Table 2. Panel geometry at Mine A

Item	Panel 1, m	Panel 1, ft	Panel 2, m	Panel 2, ft
Width*	245.4	805	257.7	845.6
Length*	2,128	6,980	2,225	7,300

*Panel width and length include half of adjacent entries.

The conceptual model of the stratigraphic column was developed for the code FLAC^{3D} because the idealized stratigraphy could be preserved. The idealized column was further simplified to optimize the FLAC^{3D} model in the discussion that follows. The initial properties for the boundary element codes were determined from the column developed for FLAC^{3D}.

Several strata members had thicknesses that were too small to model efficiently in a volume-element code like FLAC^{3D}. For that reason, these thin members were combined with adjacent thicker strata. Table 5 lists five groups of strata that were combined. All of these groups included thin coal seams that were lumped with thicker strata members. Material properties for the equivalent strata member were determined by thickness-weighted averaging. No interfaces were placed between or within strata members in FLAC^{3D} models of this scale.

Initial Young's modulus and Poisson's ratio of the rock mass at Mine A for boundary element tools, described later, were determined by thickness-weighted averaging of Young's moduli and Poisson's ratios of the strata above the DU Seam using the average thickness of the overburden at the outby instrumentation sites. These same values were used as a starting point at Mine B because the weighted average of elastic parameters at that mine above the B Seam is not significantly different from that determined for Mine A.

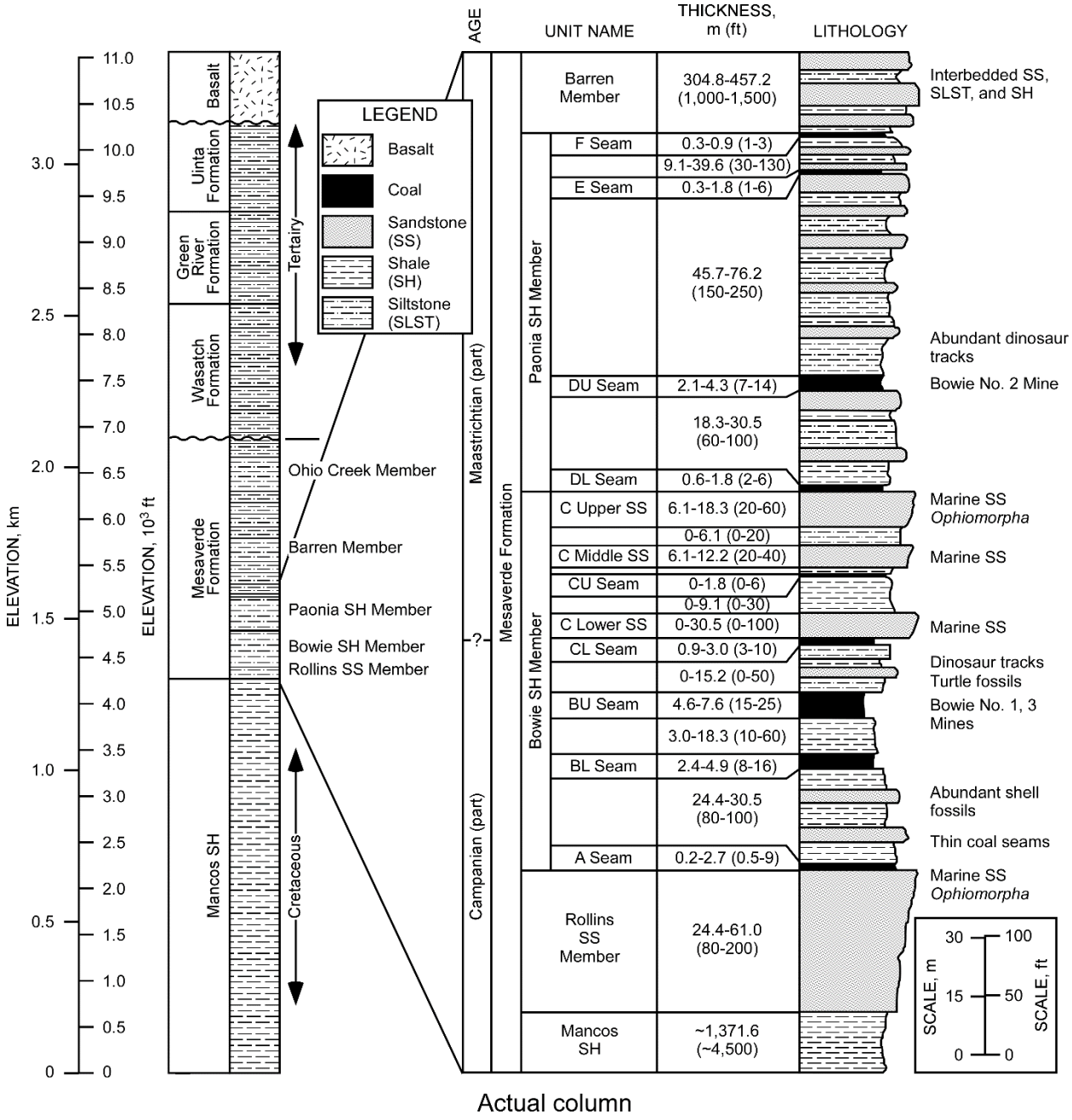

Figure 7. Lithology of the area around Mine A and Mine B. Adapted from Robeck [2005].

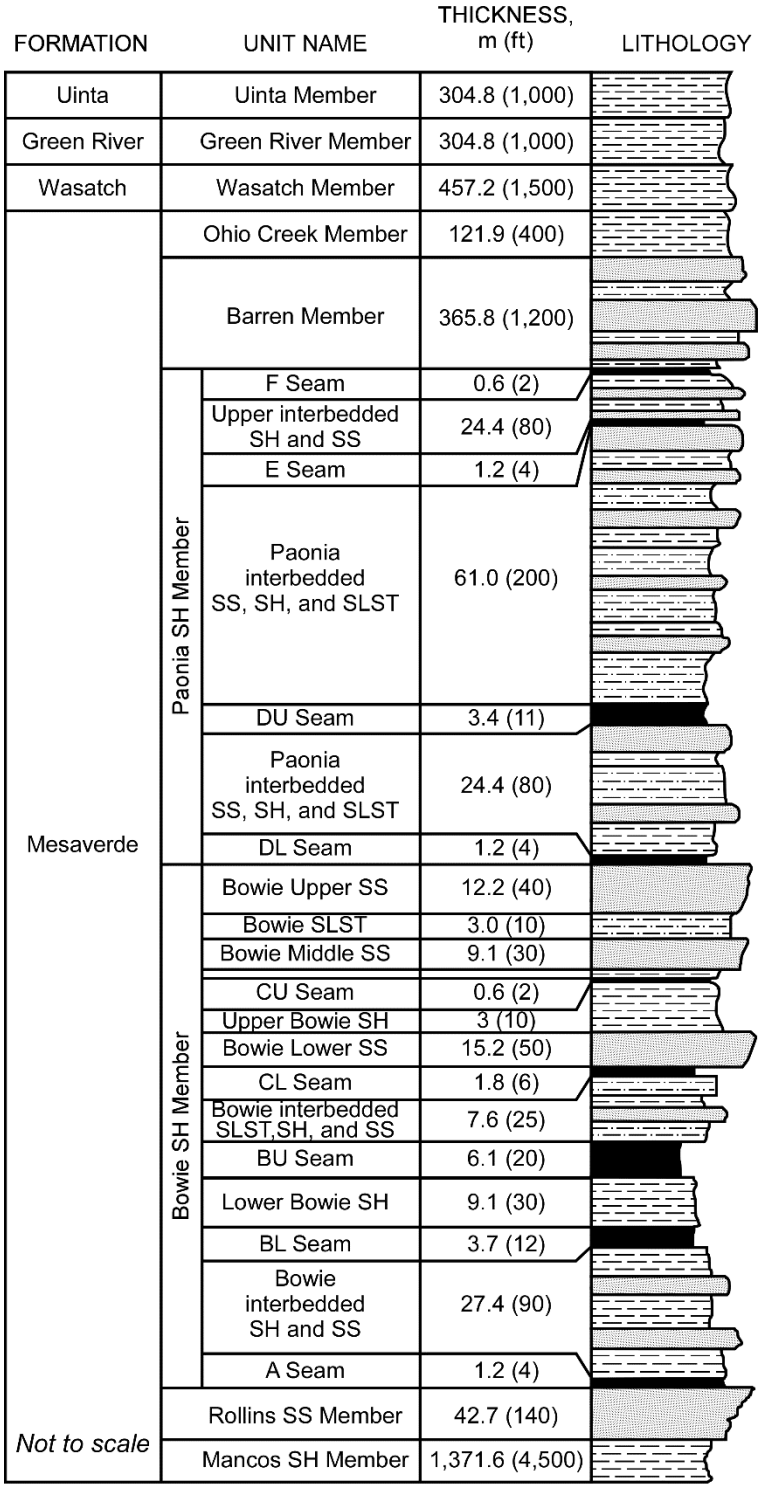

Figure 8. Idealized stratigraphic column adapted from Robeck [2005] (full lithology shown in Figure 7) and used for modeling in this report.

Table 3. Strata members of idealized stratigraphic column with thickness, density, and elastic properties

Strata	Thickness, m	Thickness, ft	Young's modulus, GPa	Young's modulus, 10^3 psi	Poisson's ratio	Density, kg/m^3	Density, lb/ft^3
Wasatch Formation	152	500	16.2	2.350	0.291	2,595	162
Ohio Creek Member	122	400	16.2	2.350	0.291	2,595	162
Barren Member	366	1,200	16.9	2.450	0.277	2,595	162
F Seam	0.610	2	2.76	0.400	0.330	1,362	85
Upper Interbedded Sh*, SS†	24.4	80	13.8	2.000	0.326	2,595	162
E Seam	1.22	4	2.76	0.400	0.330	1,362	85
Paonia Interbedded Sh, SS, Siltst‡	61.0	200	13.1	1.900	0.323	2,595	162
DU Seam	3.35	11	2.55	0.370	0.350	1,362	85
Paonia Interbedded SS, Sh, Siltst	24.4	80	20.2	2.930	0.293	2,595	162
DL Seam	1.22	4	2.55	0.370	0.350	1,362	85
Bowie Upper SS	12.2	40	27.6	4.000	0.230	2,595	162
Bowie Siltst	3.05	10	13.8	2.000	0.250	2,595	162
Bowie Middle SS	9.14	30	27.6	4.000	0.230	2,595	162
CU Seam	0.610	2	2.76	0.400	0.330	1,362	85
Upper Bowie Shale	3.05	10	10.3	1.500	0.350	2,595	162
Bowie Lower SS	15.2	50	27.6	4.000	0.230	2,595	162
CL_Seam	1.83	6	2.76	0.400	0.330	1,362	85
Bowie Interbedded Siltst, SS, Sh	7.62	25	14.9	2.160	0.269	2,595	162
BU Seam	6.10	20	2.76	0.400	0.330	1,362	85
Lower Bowie Shale	9.14	30	10.3	1.500	0.350	2,595	162
BL Seam	3.66	12	2.76	0.400	0.330	1,362	85
Bowie Interbedded Sh, SS	27.4	90	12.8	1.850	0.333	2,595	162
A Seam	1.22	4	2.76	0.400	0.330	1,362	85
Rollins Sandstone	42.7	140	27.6	4.000	0.230	2,595	162
Mancos Shale	1,370	4,500	10.3	1.500	0.350	2,595	162

*Sh = shale
†SS = sandstone
‡Siltst = siltstone

Table 4. Strata members of idealized stratigraphic column with strength properties

Strata	UCS*, MPa	UCS, psi	Friction angle, °	Tensile strength, MPa	Tensile strength, psi
Wasatch Formation	1.42	9,800	32.5	0.142	980
Ohio Creek Member	1.42	9,800	32.5	0.142	980
Barren Member	1.48	10,200	32.5	0.148	1,020
F Seam	0.174	1,200	35	0.0174	120
Upper Interbedded Sh, SS	1.16	8,000	32	0.116	800
E Seam	0.174	1,200	35	0.0174	120
Paonia Interbedded Sh, SS, Siltst	1.07	7,400	31.5	0.107	740
DU Seam	0.131	900	35	0.0131	90.0
Paonia Interbedded SS†, Sh‡, Siltst§	1.13	7,800	26	0.113	780
DL Seam	0.131	900	35	0.0131	90.0
Bowie Upper SS	2.03	14,000	35	0.203	1,400
Bowie Siltst	1.16	8,000	30	0.116	800
Bowie Middle SS	2.03	14,000	35	0.203	1,400
CU Seam	0.174	1,200	35	0.0174	120
Upper Bowie Shale	0.580	4,000	30	0.0580	400
Bowie Lower SS	2.03	14,000	35	0.203	1,400
CL Seam	0.174	1,200	35	0.0174	120
Bowie Interbedded Siltst, SS, Sh	1.29	8,900	31.25	0.129	890
BU Seam	0.174	1,200	35	0.0174	120
Lower Bowie Shale	0.580	4,000	30	0.0580	400
BL Seam	0.174	1,200	35	0.0174	120
Bowie Interbedded Sh, SS	1.02	7,000	31.5	0.102	700
A Seam	0.174	1,200	35	0.0174	120
Rollins Sandstone	2.03	14,000	35	0.203	1,400
Mancos Shale	0.580	4,000	30	0.0580	400

*UCS = Unconfined compressive strength
†Sandstone
‡Shale
§Siltstone

Table 5. Groups of strata that were combined in FLAC^{3D} models because a member or members had thickness that was too small for modeling purposes

Group 1 strata	Group 2 strata	Group 3 strata	Group 4 strata	Group 5 strata
1. F Seam	**1. Paonia Interbedded SS, Sh, Siltst**	1. CU Seam	**1. Bowie Lower SS**	**1. Bowie Interbedded Sh, SS**
2. Upper Interbedded Sh, SS	2. DL Seam	**2. Upper Bowie Shale**	2. CL Seam	2. A Seam
3. E Seam				

The name of the dominating stratigraphic member that was used as a name for the group in a modified stratigraphic column is bolded.

Figure 9 shows a plan view of the gate roads at Mine B in the vicinity of the instrumentation sites. In Ground Stress in Mining Part 1, Larson et al. [NIOSH 2020] described the instruments installed and measurements at the locations indicated. In most cases, the gate roads consisted of two yield pillars (between entries 1 and 2) alongside an abutment pillar (between entries 2 and 3). Table 6 lists the dimensions of the pillars and gate roads in the area. Table 7 lists the panel block widths and lengths, without any entry space in the dimensions.

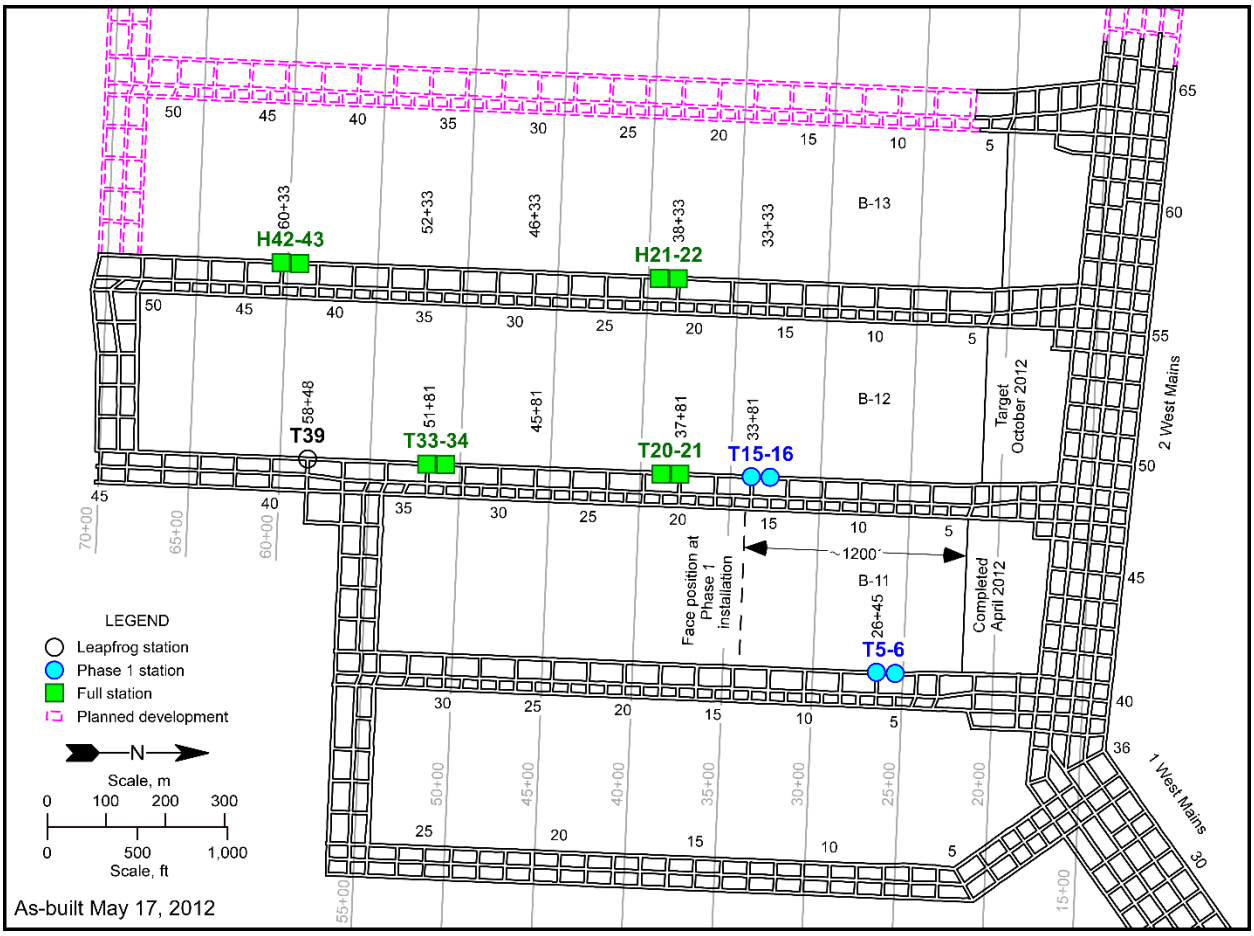

Figure 9. Mine B gate roads in the vicinity of the study site. Numbers along gate roads identify crosscuts.

Table 6. Gate road geometry at Mine B

Item	B10 TG*, m	B10 TG, ft	B10 HG†, m	B10 HG, ft	B11 HG, m	B11 HG, ft	B12 HG, m	B12 HG, ft	B13 HG, m	B13 HG, ft
Entry width	5.5	18	5.5	18	5.5	18	5.5	18	5.5	18
Crosscut width	5.5	18	5.5	18	5.5	18	5.5	18	5.5	18
Pillar width‡	20.4 and 20.4	67 and 67	14.6 and 31.1	48 and 102	14.6 and 28.0	48 and 92	14.6 and 34.1	48 and 112	14.6 and 38.7	48 and 127
Pillar length‡	40.2 and 40.2	132 and 132	25.0 and 55.5	82 and 182	25.0 and 55.5	82 and 182	25.0 and 55.5	82 and 182	25.0 and 55.5	82 and 182
Mining height used for models	2.7	9	2.7	9	2.7	9	2.7	9	2.7	9

*TG = Tailgate
†HG = Headgate
‡For pillar width and length, the first number is the dimension of the pillar between entries 1 and 2, and the second number is the dimension of the pillar between entries 2 and 3.

Table 7. Panel geometry at Mine B

Item	B10 Panel, m	B10 Panel, ft	B11 Panel, m	B11 Panel, ft	B12 Panel, m	B12 Panel, ft	B13 Panel, m	B13 Panel, ft
Width*	263	862	263	862	266	872	266	872
Length	941.8	3,090	989.1	3,245	1,530	5,020	1,457	4,780

*Panel width only includes the panel block and is not center-to-center of entries.

Observations and Measurements

In Ground Stress in Mining Part 1, Larson et al. [NIOSH 2020] described observations and measurements made at Mine A and Mine B. Important points concerning calibration and verification of numerical models are as follows:

- Floor heave was present in 2 North as the longwall face approached. Floor heave in 1 North was insignificant, except for minor heave in anomalous areas associated with faults. Not all locations where faults intersected the gate roads in 1 North experienced floor heave. Calibrated models should have properties and/or structure features with properties that explain this phenomenon.
- Borehole pressure cells (BPCs), instrumented support Cans, ground condition surveys, and floor-to-roof closures, particularly when not right next to a support Can, gave some measure of first arrival of abutment stress resulting from mining. The distance from gob to first arrival of abutment stress was much higher than that calculated by the empirical equation [see Equation 5], even before conversion to an equivalent side load transfer distance (LTD). The LTD is very important for calibrating material properties of the strata. BPCs had the most sensitivity to first arrival of abutment stress. Instrumented support Cans that measure load on the Can were almost as sensitive as BPCs in detecting first arrival. Ground condition surveys and entry closure were significantly less sensitive and may be approximately the same insensitivity.

- Measurements of BPC cell pressure indicate that the coal behavior varied significantly. Trends indicate a variable capacity to take load near the ribs (cells at 2.3 m (7.5 ft) of depth). Usually peak stress was reached at these BPCs during mining of the panel, but peak stresses varied greatly. Many BPCs became damaged or a steady, lower stress after passage of the face was not often reached; therefore, residual load usually was not possible to determine, assuming the cell pressure to be indicative of rock stress. The largest stress was located deeper into the pillar; for example, the highest measured cell pressures were located at 5.33 m (17.5 ft) from the rib. The center of the pillar carried less stress than cells located at 5.33 m (17.5 ft) from the rib. These trends in the pillar profile are useful when considering the coal strength model that might be most suitable.
- Because BPCs were not installed in the panel being mined, it is impossible to accurately estimate the front abutment stress profile and, in turn, estimate the side abutment stress profile. Such estimation, if made, would infer the proportion of overpanel weight transferred through the gob. Therefore, it is not possible to calibrate gob stiffness with measurements made in these case studies. It is only possible to assess whether or not the gob loading indicated by a model output is reasonable.

Converting the Measurement of Distance to First Arrival of Abutment Stress to Equivalent Load Transfer Distance

Several reported load transfer distances are reported in the literature [Larson et al. 2015], but such reported data were measured in various ways and most were detected ahead of the face. Such a reported location does not adhere to load transfer distance as defined by Peng and Chiang [1984].

Larson et al. [NIOSH 2019] reported on measuring of the distance to the first arrival of abutment stress by several instrument types and methods. Comparing these first arrivals of mining-induced abutment stress with the empirically calculated load transfer distance (LTD) is only possible if the measured distances to first arrival are converted to an equivalent side distance, or LTD. Recall that LTD was defined by Peng and Chiang [1984] to be at the side of a panel at about midlength, as illustrated in Figure 10. This is possible through use of an appropriate model that compares ratios of the distances from gob to a contour line of stress increase—i.e., the distance from the corner of the gob to the contour line in the direction of the instrument at first arrival of abutment stress compared to the distance from the side of the gob at mid-panel to the same contour line in the direction perpendicular to the side edge of the panel. This ratio varies because the instruments are located to the sides of the panel in the pillar, barrier pillar, or next panel. The ratio has to be determined for a given angle from the panel where the instrument is located at the first arrival of abutment stress, detected by a stress increase equivalent to that represented by the contour line.

Mine A

Larson and Whyatt [2012] used the model calculations from a LaModel simulation of panel mining at Mine A to determine conversion or equivalency factors from these ratios (see Figure

11). Lines at various angles from the panel were drawn and marked for determining ratios of distance to contour line in a particular direction with respect to that on the side at midpanel. The model's rock mass stiffness was calibrated, but it was great enough that the influence of the gate roads on the contours was negligible. Also, the ratios were determined from the 69-kPa (10-psi) contour line instead of the 138-kPa (20-psi) line, in which the increase served as the threshold indicating arrival of abutment stress. Presumably, the ratios determined from any contour line near the 69-kPa (10-psi) contour should be at least nearly equal. The ratios were determined at 5° intervals, and a fifth-order polynomial equation was fitted to the ratios for interpolating between sampled ratios. In this case, fitted parameters for polynomial equations for higher than second order were not significant. However, the fitted fifth-order polynomial produced the least maximum error and the highest r-squared statistic, it was only slightly higher than that of the lower-order fitted polynomial equations. Fitting such a function to equivalency ratios at this interval was justifiable because of the negligible influence of the gate roads. Figure 12 shows the sample ratios and fitted equations for both headgate and tailgate. Larson and Whyatt [2012] used these equivalency factors to determine equivalent side LTD by subtracting an assumed yield distance of 9.1 m (30 ft) from the net distance to gob and dividing that quantity by the equivalency factor for the particular direction to the instrument at detection of first arrival of abutment stress. The 9.1-m (30-ft) distance of assumed yield was an estimated result from the LaModel pre-processor.

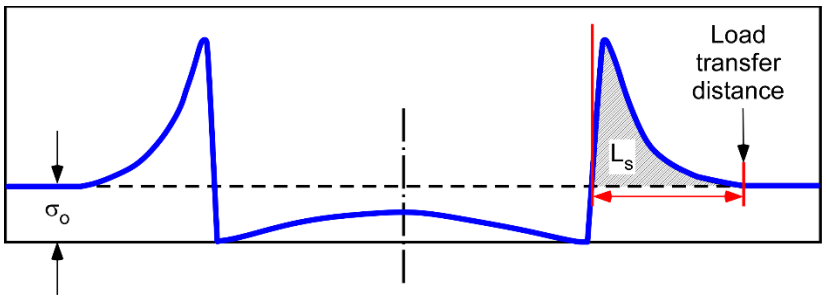

Figure 10. Loading profile in a vertical section at mid-panel of a conceptual model of loading as a result of longwall mining. Load transfer distance is shown. σ_0= premining stress, or stress on the seam before mining of the panel.

However, Larson et al. [NIOSH 2019] reported a technical audit of face positions with shift reports, which caused adjustment of some face positions with time. This adjustment affected the detection of distance to first arrival of abutment stress and net distance compared to those distances reported previously by Larson and Whyatt [2012]. Moreover, Larson and Whyatt [2013] found that MulsimNL/Large (also referred to as Mulsim in this report) was a better alternative to LaModel for the stratigraphy around these mines because the rock mass stiffness in the LaModel simulation had to be increased to unrealistic values to achieve measured LTD. The high rock mass stiffness prevented almost all loading of the gob in LaModel, and calibration of gob stiffness became impossible. In addition, as explained later in this report, the best model for matching first arrival of abutment stress as calculated by Mulsim was the model with coal represented as an elastic material. However, yielding was represented in the model by reducing the coal modulus in the outer ring of 3.0-m (10-ft) wide elements in pillars and panels to 60% of the full value and reducing it in the second ring of elements to 80% of the full value. The gate roads were present in this model (see Figure 13). The conversion ratios were determined for a smaller range of angles (0° to 30°), with ratio samples taken at 1° intervals or smaller as needed

to capture changing trends in the contour line. In addition, all ratios were calculated with respect to the side distance on the right of the panel because of the interference of workings to the left of the panel. No continuous function could adequately describe the trends. Therefore, interpolation for converting first arrival distance to equivalent LTD was done on a piecewise linear basis, based on the result shown in Figure 14. The presence of the gate roads caused minimal disturbance in the trend of the contours, but they did cause some contours to form complete rings inside the pillars of the headgate, tailgate, and West Mains.

In the absence of measurements or observations indicating LTD, Heasley [2008b, 2009b] recommended calibrating to the empirical representation (Equation 6) of the distance at which 90% of the abutment load is transferred to each of the abutments. The abutment load is determined from the overpanel weight using the abutment angle, β. The empirical curve does not have a yield zone naturally incorporated into its stress profile. In Heasley's [2010] preprocessor to the LaModel program, LamPre, the abutment load within the estimated yield zone depth is neglected, and the amount of load within distance $D_{0.9}$ of the extent of the laminated yield zone is matched to the empirical abutment load that occurs within distance $D_{0.9}$ of the rib. Accordingly, before converting to equivalent LTD, the yield distance assumed in this model (two rings of elements) of 6.1 m (20 ft) was assumed to have negligible stress and, therefore, was subtracted from the net distance from gob determined by Larson et al. [NIOSH 2020] (Ground Stress in Mining Part 1) at which abutment stress was first detected.

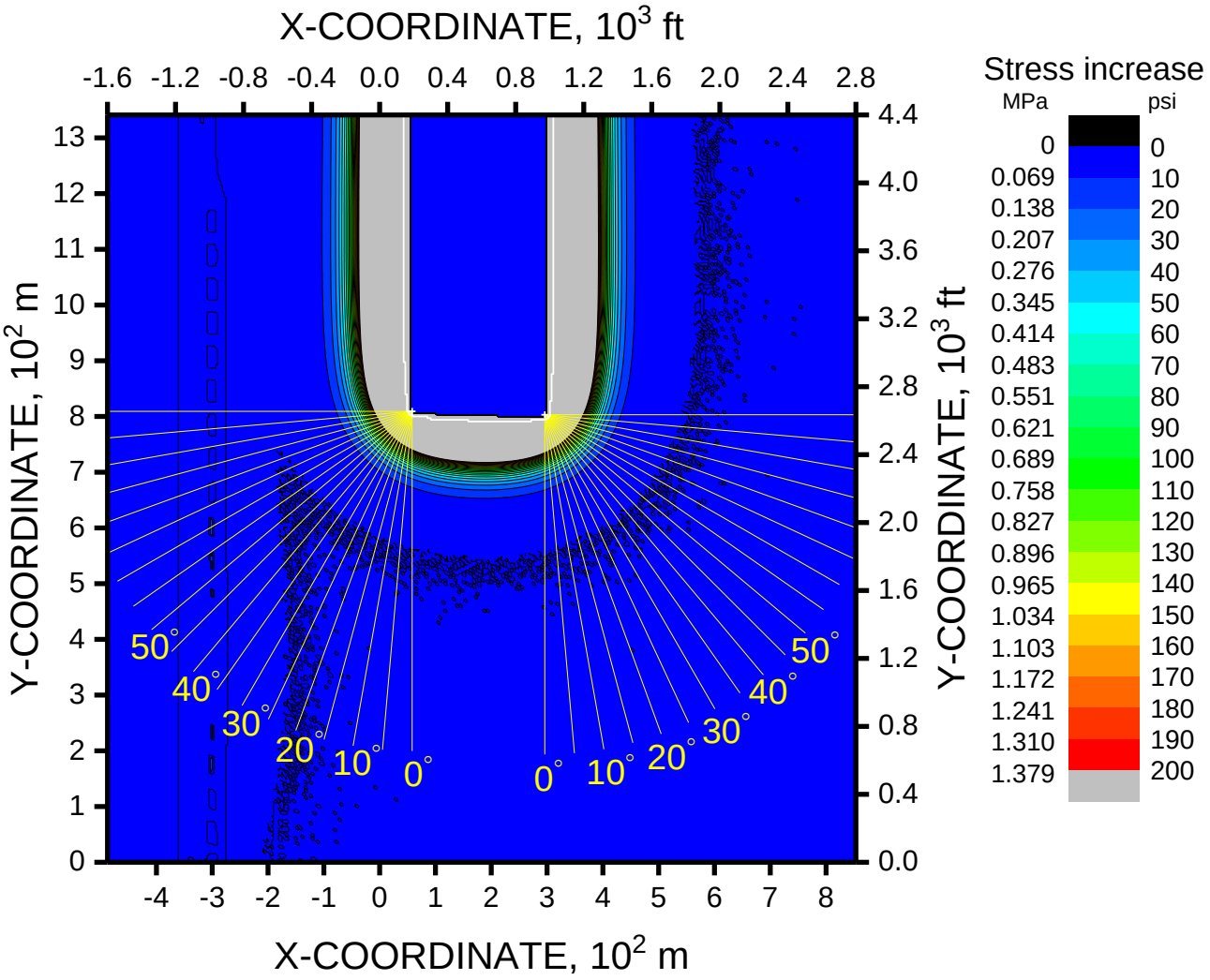

Figure 11. LaModel contours of stress increase resulting from panel mining. Coordinate system was chosen for convenience in modeling. Also shown are lines at various angles from the gate roads. These lines were used to help in determining equivalency factors.

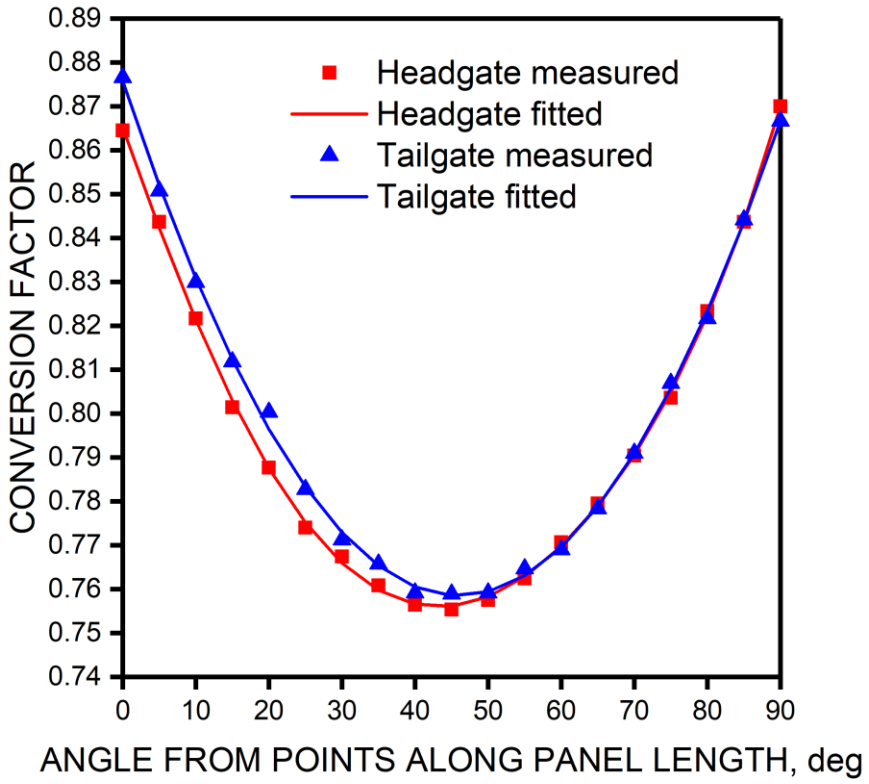

Figure 12. Conversion factors determined from LaModel's calculated result.

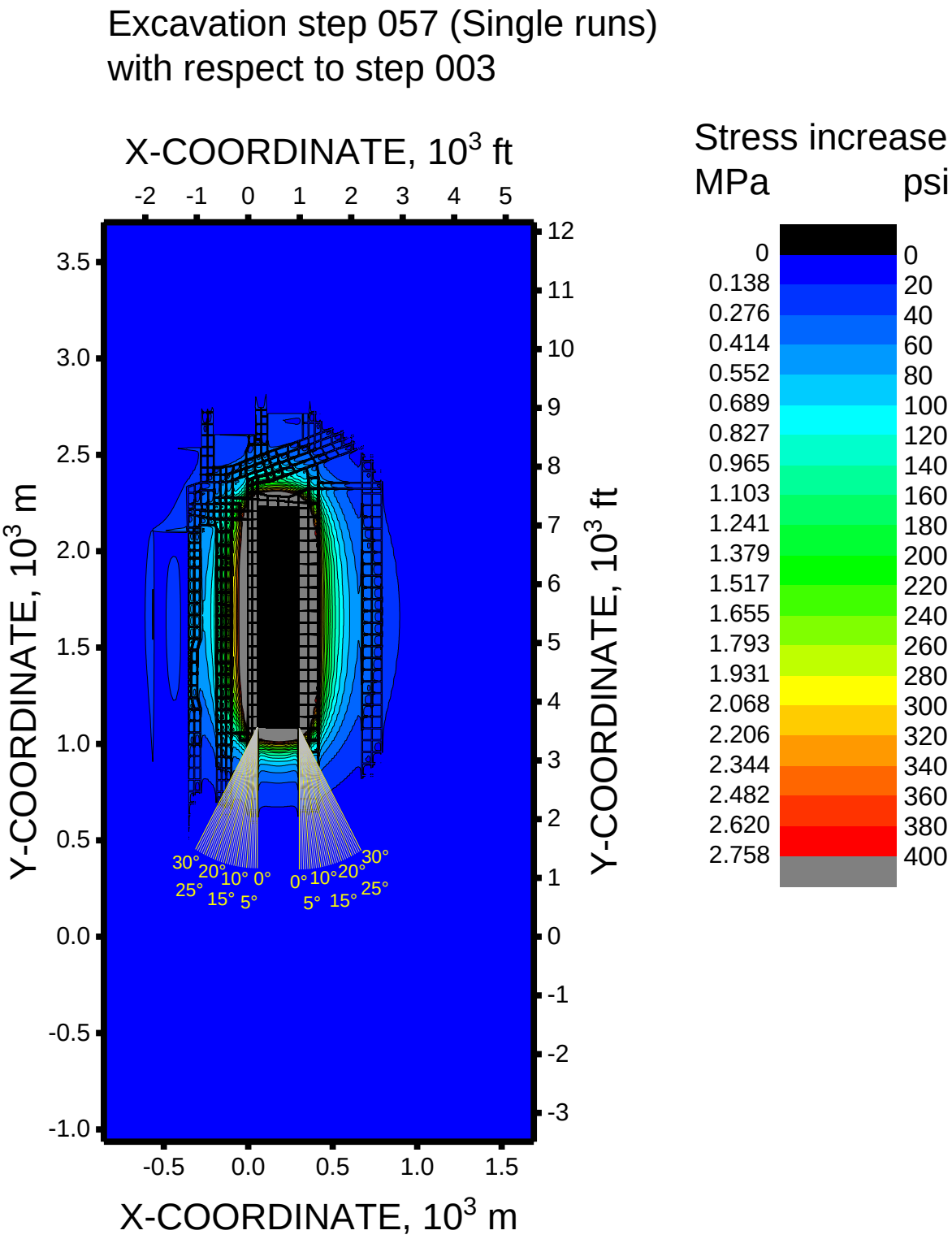

Figure 13. A Mulsim elastic model with reduced coal modulus near rib. This model was used to determine conversion factors for equivalent LTD on the side of the panel.

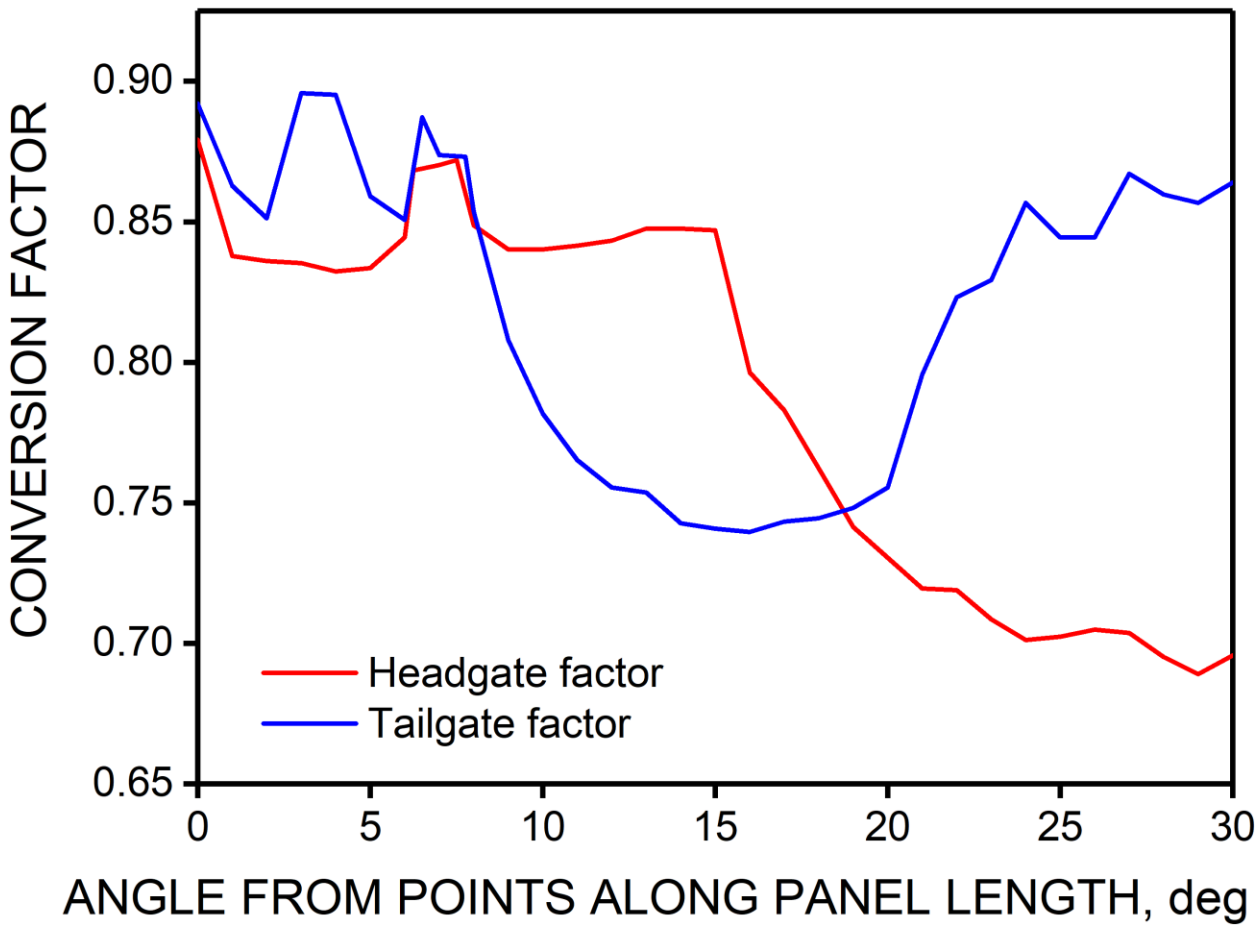

Figure 14. Piecewise linear conversion factor functions derived from the Mulsim model for determining equivalent LTD at Mine A.

Table 8 lists the net distance to first arrival of mining-induced stress for BPCs at the 1 North outby instrument site, as reported by Larson et al. [NIOSH 2020] in Ground Stress in Mining Part 1, along with the angle from the panel, corresponding conversion factor from Figure 14, and equivalent LTD. Table 9 presents the same data for BPCs at the 2 North outby station. The standard deviation of the average site LTD at both of these sites was surprisingly low—8.4% and 4.4% for the 1 North outby and 2 North outby sites, respectively. Table 10 summarizes the average distances for each site and lists the average for the two sites. This average LTD is 3.98 times that calculated with the empirical Peng and Chiang Equation 5, using an average depth of 686.9 m (2,253.5 ft).

Table 8. BPC data from the 1 North outby site

Instrument	Net distance from gob minus yield distance, m	Net distance from gob minus yield distance, ft	Angle from entry along panel when threshold reached, °	Conversion factor	Equivalent LTD, m	Equivalent LTD, ft
BP2	445.5	1,461.5	11.13	0.7640	583.1	1,913.0
BP3	511.5	1,678.3	12.96	0.7537	678.7	2,226.7
SP1	436.4	1,431.8	3.97	0.8951	487.6	1,599.6
SP2	462.4	1,517.0	4.12	0.8907	519.1	1,703.1
SP3	464.8	1,525.0	4.81	0.8661	536.7	1,760.9
SP4	500.6	1,642.4	5.12	0.8581	583.4	1,914.0
SP5	481.3	1,579.1	5.69	0.8533	564.1	1,850.6
NP1	476.0	1,561.8	2.37	0.8678	548.5	1,799.7
NP2	489.5	1,605.9	1.95	0.8517	574.7	1,885.5
NP3	467.0	1,532.2	1.35	0.8588	543.8	1,784.1
NP4	465.8	1,528.1	0.65	0.8731	533.4	1,750.1
NP5	479.9	1,574.6	0.27	0.8842	542.8	1,780.8
Average					**558.0**	**1,830.7**
St. Dev.					**46.9**	**153.9**

Table 9. BPC data from the 2 North outby site

Instrument	Net distance from gob minus yield distance, m	Net distance from gob minus yield distance, ft	Angle from entry along panel when threshold reached, °	Conversion factor	Equivalent LTD, m	Equivalent LTD, ft
NP3	457.6	1501.4	8.60	0.8437	542.4	1779.7
NP4	425.4	1395.8	11.20	0.8418	505.4	1658.1
NP5	412.2	1352.5	13.59	0.8476	486.4	1595.8
NP6	448.3	1470.9	13.28	0.8476	529.0	1735.4
NP7	423.0	1387.9	14.50	0.8473	499.3	1638.1
Average					**512.5**	**1681.4**
St. Dev.					**22.8**	**74.7**

Table 10. List of equivalent LTDs determined from BPCs for 1 North and 2 North outby sites and the average LTD for both sites

Location	Average equivalent LTD, m	Average equivalent LTD, ft	St. dev. of equivalent LTD, m	St. dev. of equivalent LTD, ft
1 North outby	558.0	1,830.7	46.9	153.9
2 North outby	512.5	1,681.4	22.8	74.7
Average	**535.2**	**1,756**		

The conversion factors were applied to the net distances at first detection of abutment stress determined from instrumented support Cans, as reported by Larson et al. [NIOSH 2020] in Ground Stress in Mining Part 1. The net distances minus assumed yield distance, angle from along the gate roads, conversion factors, and equivalent LTD for the 2 North outby site are listed in Table 11 for those instrumented Cans whose trends to determine first arrival of abutment stress met a quality criteria (set forth in Ground Stress in Mining Part 1). The average equivalent LTD was 502.0 m (1,647 ft), which is 3.73 times the empirical LTD. This LTD is 6.2% less than that indicated by the BPCs.

Table 11. Support Can data from the 2 North outby site

Support Can	Net distance from gob minus yield distance, m	Net distance from gob minus yield distance, ft	Angle from entry along panel when threshold reached, °	Conversion factor	Equivalent LTD, m	Equivalent LTD, ft
A	384.5	1,345.4	15.43	0.8254	504.2	1,654.3
C	405.6	1,330.7	15.60	0.8167	504.1	1,653.9
F	410.1	1,261.5	16.85	0.7849	497.6	1,632.6
Average					**502.0**	**1,647.0**
St. Dev.					**3.78**	**12.40**

Table 12 lists similar data determined from closure measurements with string potentiometers located in the entries near support Cans and mounted on a support Can. In Ground Stress in Mining Part 1, Larson et al. [NIOSH 2020] found entry closure measurements to have greater success in detecting first arrival of abutment stress than those measurements from sensors mounted on a Can assembly. The average equivalent LTD was 381.1 m (1250 ft), which is 2.83 times the empirical LTD, or 28.8% lower than that determined with the BPCs.

Table 12. Closure instrument data from entry 3 of 2 North of Mine A

Instrument	Net distance to gob minus yield distance, m	Net distance to gob minus yield distance, ft	Angle from entry along panel when threshold reached, °	Conversion factor	Equivalent LTD, m	Equivalent LTD, ft
Int-RF9	234.5	769.3	27.33	0.7008	334.6	1,097.7
Int-RF10	2,551.2	824.3	26.13	0.7047	356.5	1,169.6
Can A	275.7	904.6	23.13	0.7076	389.7	1,278.4
MP-RF7	285.9	938.0	22.77	0.7110	402.2	1,319.4
MP-RF8	318.2	1044.1	20.36	0.7265	438.0	1,437.1
MP-RF10	257.2	843.9	25.40	0.7034	365.7	1,199.7
Average					381.1	1,250.3
St. Dev.*					36.8	120.7

*St. Dev. = Standard Deviation

Table 13 lists ranges of net distances from the yield extent around the gob, angle from along the gate roads when the first arrival threshold was met, conversion factors, and equivalent LTD ranges. Because the ground condition surveys were not conducted with more frequency, the ranges are large. Even so, it appears that sensitivity of ground condition surveys to determining LTD may be close to and probably slightly less than that of the closure measurements.

If the average LTD of each method is used as an indicator of sensitivity of the determining method, and the BPC method is used as the standards, the relative sentivities as a fraction of the BPC-determined LTD are calculated. These distances and ratios are found in Table 14.

Table 13. Data from instrument sites where ground condition surveys were conducted

Site	Net distance to gob minus yield distance, m	Net distance to gob minus yield distance, ft	Angle from entry along panel when threshold reached, °	Conversion factor	Equivalent LTD, m	Equivalent LTD, ft
1 North outby	286.1 to 515.1	938.6 to 1,690.0	4.97 and 2.78	0.8603 and 0.8860	332.5 to 581.4	1,091.0 to 1907.4
2 North outby	61.2 to 261.1	200.9 to 856.7	54.58 and 11.85	0.6259 and 0.8430	97.8 to 309.7	320.9 to 1016.2
***Average of 1 North minimum and 2 North maximum**					**321.1**	**1053.6**

*This average provided for approximate determination of relative sensitivity factor between methods.

Table 14. Summary of LTD and relative sensitivity factors by method

Method	LTD, m	LTD, ft	Sensitivity ratio
BPCs	535.2	1756	1
Instrumented Cans	502.0	1647	0.938
Closures	381.1	1250.3	0.712
Ground condition surveys	321.1	1053.6	0.6

Mine B

The process used to determine the conversion factors for the equivalent load transfer distance (LTD) at Mine A was also applied at Mine B. Figure 15 shows stress increase contours of the B-13 Panel at approximately the location when BPCs at the H22 site detected first arrival of mining-induced abutment load. As at Mine A, the coal within a distance of 6.1 m (20 ft) from the gob was assumed to have yielded. The shortest distance from this yield perimeter to the threshold contour was determined at regular angular intervals from the direction of the gate roads. In addition, such distances were determined at angles between these intervals where directional changes in the threshold contour line warranted the additional data. The distance from the headgate gob to the same contour at midpanel was also determined, so that ratios representing conversion factors could be established between the various directions and the side direction at midpanel. A similar contour plot was made for the B-12 Panel and conversion factors determined in the same manner. Figure 16 shows the piecewise linear conversion factors determined for each gate road of the two panels mined. Differences between panels are mostly the result of changes in gate road geometry, although previous mining of the B-11 Panel may have played a role. Mining of the B-10 Panel was assumed to have a negligible effect and is not represented in this model.

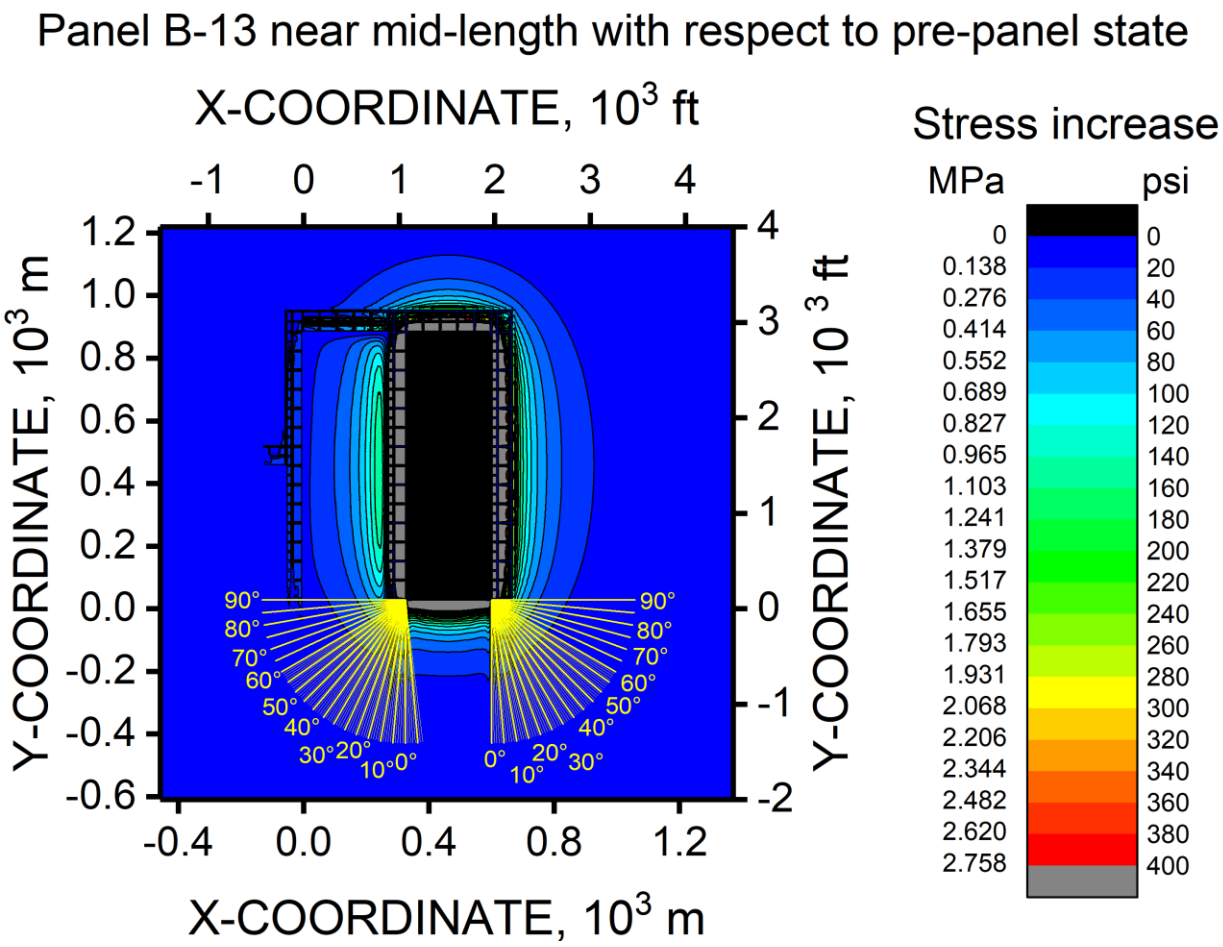

Figure 15. Contours of stress increase resulting from mining the B-13 Panel. Lines at various angles from the gob corners are superimposed.

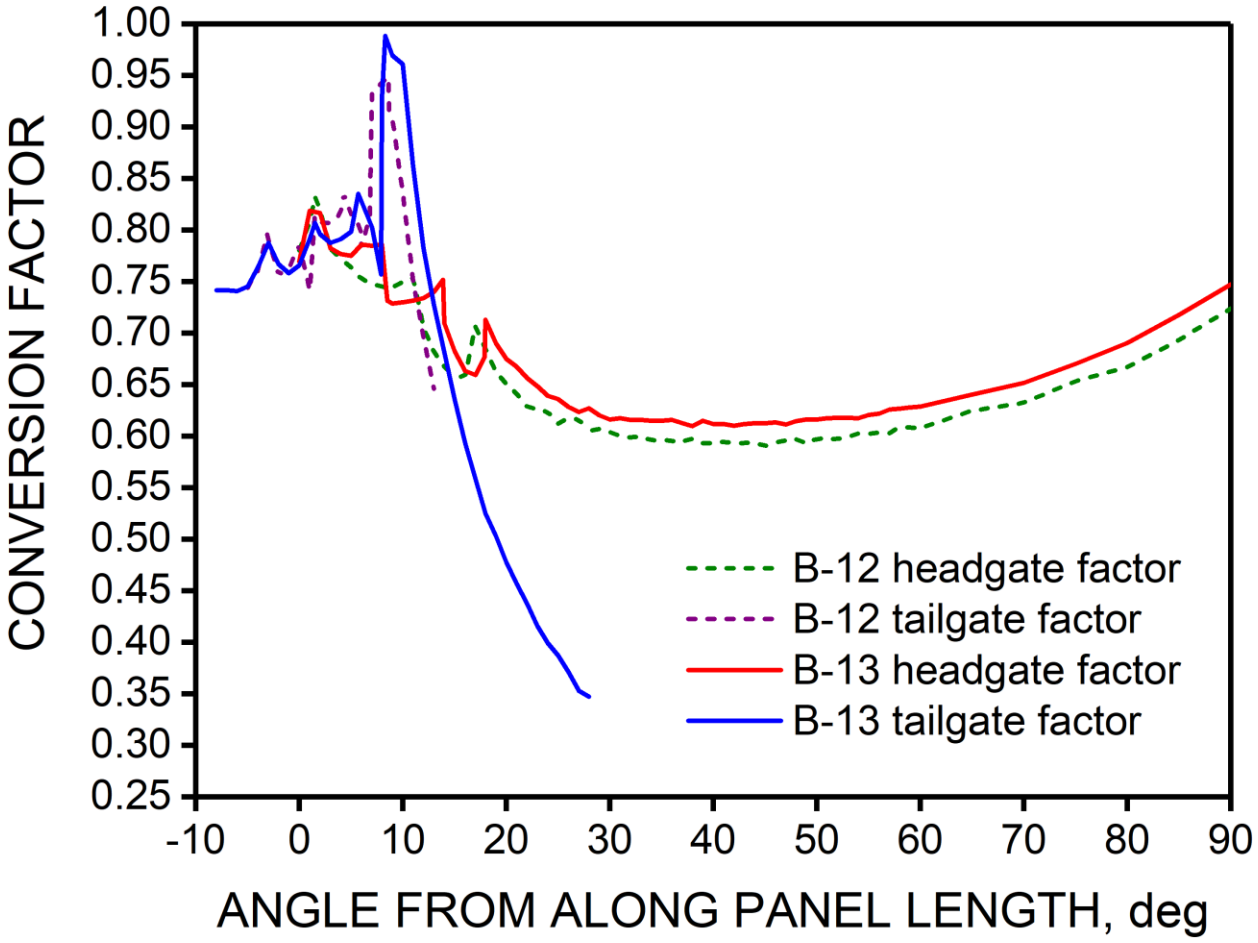

Figure 16. Piecewise linear conversion factor functions derived from Mulsim model for determining equivalent LTD at Mine B.

For ease of comparing results to empirical LTD, Table 15 lists the overburden depth at each site.

Table 15. Overburden depth at each instrument site

Site	Overburden depth, m	Overburden depth, ft
T5	228.6	750
T6	231.6	760
T15	297.2	975
T16	304.8	1,000
T39	263.7	865
T34	254.5	835
T33	253	830
T21	277.4	910
T20	286.5	940
H43	323.1	1,060
H42	329.2	1,080
H22	335.3	1,100
H21	336.8	1,105

Larson et al. [NIOSH 2019] analyzed measurements taken with various instruments at Mine B. None of these measurements passed the quality tests used at Mine A to continue as candidates for determining LTD. Larson et al. described the causes of the quality deterioration, which are not enumerated here. In spite of the quality of the measurements, they characterized cell pressure trends and were used to determine ranges of distance from the face at which the cell pressure trends departed from pre-abutment stress trends, indicating first arrival of mining-induced abutment stress. In the case of closure measurements, better precision of the Midas datalogger permitted consideration of a much smaller threshold to indicate arrival of abutment stress. In this case, the two thresholds were used as the lower and upper bounds of a range of distance to the gob at first arrival. In either case, ranges were generally reported (Ground Stress in Mining Part 1). The bounds of these ranges were also converted to equivalent LTD.

Table 16 lists data used to determine equivalent LTD for BPCs at sites H22 in the B-12 headgate and T21 in the B-12 tailgate. The range of confidence in the determinations varies, as does the range equivalent LTD. The large upper bound reported, 748.5 m (2,456 ft), seems extremely high, and therefore, it is considered to be an outlier and discounted. The remaining range of equivalent LTD ranges from 227.8 m to 472.6 m (747.2 ft to 1,551 ft), which corresponds to a range of ratios with respect to the empirical LTD of 2.66 to 5.53.

Table 16. List of BPCs at Mine B from which measurements of distance could be determined from the gob at first arrival of abutment stress

BPC	Net distance to gob minus yield distance, m	Net distance to gob minus yield distance, ft	Confidence in measurement	Angle from entry along panel when threshold reached, °	Conversion factor	Equivalent LTD, m	Equivalent LTD, ft	Ratio to empirical LTD
T21-P46	187.9*	616.5*	Low	4.14	0.8250	227.8	747.2	2.66
T21-P12	272.5 to 393.0	894.0 to 1289	Fair to good for range	0.752 to 0.525	0.7524 to 0.7624	362.2 to 748.5	1,188 to 2456†	4.24 to 8.75†
T21-L12	254.5 to 360.7	835.0 to 1,183	Fair to good for range	-1.41 to -1.00	0.7605 to 0.7632	334.7 to 472.6	1,098 to 1551	3.91 to 5.53
H22-P48	177.4	581.9	Good	12.47	0.6942	255.5	838.2	2.72
H22-P12	177.8 to 298.1	583.2 to 977.9	Low	15.97 to 9.58	0.6572 to 0.7476	270.5 to 398.7	887.4 to 1,308	2.88 to 4.24

*In Ground Stress in Mining Part 1, Larson et al. [2020] argued that this net distance could have ranged as high as 253 m (830 ft) by different selection of initial points to characterize the trend before first arrival.
† Upper range is considered to be too high and an outlier.

Table 17 lists results from one Can that was used to determine equivalent LTD. The data was very noisy, but the departure from initial trend was very pronounced. Therefore, it is difficult to assume this LTD is an outlier. To justify the result, we might look to local variation in the geology that might have caused additional closure at this site, but such information is not available.

Table 17. List of results from the H21 outby instrumented support Can with determined equivalent LTD

Support Can	Net distance to gob minus yield distance, m	Net distance to gob minus yield distance, ft	Angle from entry along panel when threshold reached, °	Conversion factor	Equivalent LTD, m	Equivalent LTD, ft	Ratio to empirical LTD
H21-outby	523.9	1,719	6.17	0.7518	696.9	2,286	7.41

Table 18 lists results from two closure-measurement histories from the T34 site. The equivalent LTD ranges are reasonable.

Table 18. List of results from the T34 closure data with determined equivalent LTD

Instrument	Net distance to gob minus yield distance, m	Net distance to gob minus yield distance, ft	Angle from entry along panel when threshold reached, °	Conversion factor	Equivalent LTD, m	Equivalent LTD, ft	Ratio to empirical LTD
T34 inby entry	203.8 to 283.7	668.7 to 930.7	0.374 to 0.271	0.7906 to 0.7878	257.8 to 360.1	845.8 to 1181	3.15 to 4.40
T34 inby Can	201.2 to 281.0	660.0 to 922.0	0.379 to 0.274	0.7908 to 0.7879	254.4 to 356.7	834.6 to 1,170	3.11 to 4.35

Summary

The equivalent LTD for Mine A was derived from measurement trends that provide more confidence in the results, as compared to Mine B. Therefore, they give some measure of sensitivity between the methods. Given similar stratigraphy, the difference in overburden depth would suggest that the equivalent LTD at Mine B would be less than that at Mine A. The range of ratio of measured-equivalent-to-empirical LTD at Mine B (2.7 to 5.5) does not permit confirmation of this expectation. However, the best quality determinations (derived from the BPC at H22-P48 and the two closure measurements at T34) may indicate such ratios of 2.7 and approximately 3.1 to 4.4. The finer threshold associated with these upper bounds may have been smaller than the accuracy of the sensor hardware, suggesting that the lower portion of these ranges is more realistic. Therefore, the more likely ratio of measured-equivalent-to-empirical LTD is likely in the range of 2.7 and 3.8. This range would be consistent with measured LTD at Mine A. The results of measurements at Mine B do not support that LTD at that mine is comparable to the empirical LTD.

Later in this report, the best loading model at Mine A is shown to be an elastic model in Mulsim with the outer two rings of elements having elastic modulus reduced to 60% and 80% of the full amount. If the same rock mass stiffness is used as the value calibrated for LTD at Mine A, then this model suggests that Mine B has an LTD of 326 m (1,068 ft) when the overburden depth is 335 m (1,100 ft) and a ratio of measured-equivalent-to-empirical LTD of 3.5 at Mine B.

Modeling Tools

Several modeling tools are commonly used to evaluate coal mine layout design. These are the empirical method (ALPS), displacement discontinuity codes such as LaModel and MulsimNL/Large, and FLAC^{3D}. Each has advantages and disadvantages when used for evaluation of coal mine layout. In this section, each tool is described in order to inform the reader of their backgrounds and capabilities. Also, some of the challenging issues in using FLAC^{3D} are described.

Empirical Method

The empirical approach forms the basis of two research publications that describe mine layout software tools: Analysis of Longwall Pillar Stability [Mark 1987, 1992] and Analysis of Retreat Mining Pillar Stability [Mark and Chase 1997]. The empirical method uses three equations as its basis to describe stress distribution resulting from mining. The first equation is used to determine overpanel weight transferred to the abutment. Mark [1987] used the conceptual loading model suggested by King and Whittaker [1970], shown here as Figure 17. For his empirical database, Mark noted field measurements from which he calculated β ranging from 10.7° to 25.2° and concluded that β = 21° was sufficiently conservative for longwall pillar design.

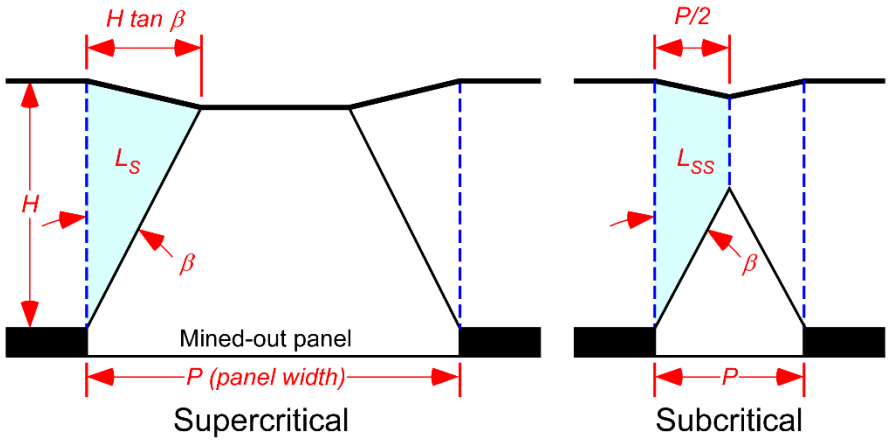

Figure 17. Conceptualizations of the side abutment load, patterned after King and Whittaker [1970].

The weight per unit length of gate road is represented in Figure 17 as L_s and L_{ss} for supercritical and subcritical cases, respectively. They are calculated as

$$L_s = H^2(\tan\beta)\left(\frac{\gamma}{2}\right), \text{ and} \tag{7}$$

$$L_{ss} = \left[\frac{HP}{2} - \frac{P^2}{8\tan\beta}\right]\gamma, \tag{8}$$

where L_s = weight per unit length of gate road, shown in the shaded region in the left part of Figure 17, that is transferred to the abutment for the case of a critical or supercritical panel;

L_{ss} = weight per unit length of gate road, also shown as a shaded region on the right in Figure 17, that is transferred to the abutment for the case of a subcritical panel;

H = height of the overburden;

P = width of the panel;

β = the angle that defines the portion of the overpanel volume whose weight is transferred to the abutment; and

γ = density of the overburden.

If $P \geq 2H\tan\beta$, then Equation 7 is used; otherwise, Equation 8 is used. Also, L_s (or L_{ss} for the subcritical case) is that area under the abutment stress curve in Figure 10.

The second equation, proposed by Peng and Chiang [1984], defines load transfer distance (LTD) as a function of overburden depth (H) based on a small number of observations. This equation was mentioned earlier as Equation 5 and shown graphically in Figure 10. It is repeated here, using LTD instead of $D_{1.0}$ to emphasize that it is load transfer distance,

$$LTD = 9.3\sqrt{H}. \tag{9}$$

Equation 10 describes the decay of mining-induced stress, σ, as a function of distance from the abutment rib, x, until $x = LTD$. This rule, proposed by Mark [USBM 1990], is based on a curve fit of a small group of pressure measurements. The magnitude of mining-induced stress transferred to the abutment, L, depends on the angle, β, which represents partitioning of undermined overburden loading between abutments and gob. (See Figure 17, where L is represented by L_s or L_{ss}.)

$$\sigma = \frac{3L(\beta)}{(LTD)^3}[(LTD) - x]^2, \tag{10}$$

where σ = stress transferred to the coal seam from mining the panel,

$L(\beta) = L_s$ or L_{ss}, and

x = distance from the edge of the gob.

Loading of pillars is based on tributary load under this curve for a specific pillar, as shown by Mark [USBM 1990]. The load divided by the total strength capacity of the pillar determines the stability factor. The Analysis of Longwall Pillar Stability uses the Mark-Bieniawski pillar equation [Mark 1999] for that purpose:

$$S_p = S_1 \left(0.64 + 0.54\frac{w}{h} - 0.18\frac{w^2}{lh}\right), \quad (11)$$

where S_p = pillar strength,
S_1 = in situ coal strength,
w = pillar width,
h = pillar height, and
l = pillar length.

Mark et al. [1994] found that Coal Mine Roof Rating (CMRR), developed by Molinda and Mark [USBM 1994], could be used to determine a critical stability factor that discriminated correctly between successful and unsuccessful gate road pillar designs in 84% of case histories that they compiled by using the equation

$$ALPS\ SF_R = 1.76 - 0.014\,CMRR, \quad (12)$$

where $ALPS\ SF_R$ = ALPS stability factor suggested for design, and
$CMRR$ = Coal Mine Roof Rating.

Advantages of this method are that it is simple to execute and is founded in the results of many case histories. However, it does not account for local variability caused by geology and structure. For example, Lawson et al. [2013] found significant sensitivity of loading factors to β and measured LTD, instead of that calculated with Equation 9. In reality, structure and properties of the overburden can vary the amount of overpanel weight that transfers through the gob versus that transferred to the abutment. Measurements described by Larson and Whyatt [2012], which were updated earlier in this report, attest to large departures from the empirical LTD in some mines, particularly those in the western United States having massive, strong strata above or below the seam being mined.

The LaModel Code

Based on work of Salamon [1963], Crouch and Fairhurst [1973] developed a code for representing a tabular deposit in an elastic medium with a series of squares, each having a closure and stress centered at its midpoint. This was a displacement-discontinuity-type boundary element code. Others have developed versions of this type of code, but one code has been used prevalently in evaluating coal mining layouts for the last 16 or 17 years.

Heasley [1998] developed a displacement discontinuity modeling code, LaModel, that is based on the solution described by Salamon [1991] of a crack in a continuous medium consisting of a series of frictionless laminated plates, based on thin plate theory. Heasley [2010] developed this software into a very convenient tool, with pre- and post-processors (LamPre and LamPlt, respectively). LamPre is equipped with tools (called wizards) for determining lamination thickness, coal properties, and gob properties that approximately calibrate to the empirical solution (for example, calibrating rock mass stiffness so that 90% of the load falls with the calculated result of Equation 6). With a laminated rock mass, the LaModel software can reasonably simulate subsidence [Heasley and Barton 1998; Heasley and Barton 1999].

Some of the capabilities of the current version (3.0) of LaModel are:

- 2,000 by 2,000 seam grid;
- Simulation of topography by adding compression and tensile stresses at a datum above the coal seam;

- Grid determination from an AutoCAD map;
- Three coal models: elastic, Mark-Bieniawski coal with post-peak modulus (usually zero for elastic-perfectly-plastic material), and strain-softening to a residual stress;
- Three gob models, including linear, bilinear, and linearly increasing tangent modulus;
- Ability to calculate stress and displacement on an off-seam plane;
- Ability to define an off-seam fault plane;
- Ability to do energy calculations;
- Ability to calculate safety factors;
- Ability to calculate roof bending stresses; and
- Ability to accommodate 200 mining steps, although LamPre is hardwired to allow a maximum of only 20.

One of the tremendous advantages of LaModel is the speed of calculations. Because it only calculates vertical stress and vertical displacements (closure of the seam and off-seam displacements), calculation time is usually much less than using other numerical modeling tools. This advantage allows the user to complete calculations of over 100 mining steps overnight or in just a few hours.

A caution is appropriate for using the topographic feature. Whyatt et al. [2011] found that highly variable terrain can introduce some errors in the propagation of stresses onto the seam, but generally, reasonable results are obtained by using a datum representing the average height of the overburden above the coal seam over the entire model.

The main disadvantage of LaModel or any boundary element code is that the rock mass is represented as an elastic medium. Therefore, no roof or floor failure mechanics can be simulated.

Grids for the current problem were not constructed directly from AutoCAD because the stage represented in existing drawings did not coincide with the gate road workings. Instead, a grid was superimposed on the AutoCAD map having the closest gate road state to what was needed for representing development in the model. A grid was set up in an Excel spreadsheet, and gate roads were constructed by assigning the character "1" if the greatest area of an element were mined and "A" if the greatest area of an element were unmined. Subsequent mining steps such as longwall mining were accomplished on other pages of the spreadsheet with the copy and paste function, with only minor changes made to represent the mining for that step. Yield elements were determined by copying the grid into an input file for one cut and letting LamPre assign the yield materials. This grid was then copied to a text file, and tab characters were deleted. Final input files were then constructed using DOS copy functions to combine initial inputs and subsequent mining step material codes. In this fashion, for example, a 185-step model was constructed to simulate mining of Panel 1 and Panel 2 at Mine A.

MulsimNL/Large

Mulsim is another displacement-discontinuity code that was developed to model tabular deposits. Sinha [1979] developed the original version to analyze multiple, parallel coal seams. He included the ability to subdivide coarse blocks into finer mesh so that the scheme was computationally more efficient. Beckett and Madrid [1986]; [USBM 1988] developed additional features for Mulsim (their version was called MULSIM/BM), such as additional seam materials like gob, pack walls, and cribs; graphical development of grids; and an increase in the number of coarse blocks and the number of blocks that could be subdivided into finer mesh. Donato [USBM 1992c] converted MULSIM/BM to a PC environment. Itasca Consulting Group added

the ability to consider multiple mining steps [USBM 1992b]. Zipf [USBM 1992b, 1992a] added nonlinear seam materials such as strain-softening, elastic-plastic, bilinear hardening gob, and strain-hardening—the same materials mentioned for LaModel. Zipf's version, called MULSIM/NL, ran from DOS. Its use has decreased over the years because LaModel was better supported, faster, and easier to use.

Mulsim differs from LaModel in that the rock mass is represented by an elastic medium with no laminations. As such, it does not simulate surface subsidence very well. Mulsim handles four seams, the same as LaModel, but these seams only have to be parallel, and not horizontal. The version of Mulsim in the public domain does not handle topography yet, but energy equations are part of the analysis. The code divides the seam into course blocks. The user designates a rectangular area of interior blocks that are divided into five-by-five fine elements. The outside boundary of the coarse blocks is not allowed to displace, whereas the outside boundaries of a LaModel grid can be rigid like Mulsim boundaries or they can be symmetrical.

Larson and Whyatt [2013] took Zipf's MULSIM/NL and expanded it to examine problems described in this report and called it MulsimNL/Large. The current version runs in DOS and has not been released by NIOSH. Appendix A describes the format of this updated version. The code's input precision and output precision were increased to allow better comparison with results from other modeling tools. Additionally, Zipf's three example problems [USBM 1992a] were run with MulsimNL/Large (see Appendix A) for purposes of verification. Results compare very well.

Construction of the input file for modeling Mine A, particularly the fine and coarse codes, was a daunting task, with room for many potential mistakes, if done manually. Most of this difficulty was the result of the decision to convert a certain perimeter of LaModel fine element codes into the closest equivalent coarse code to reduce the size of the MulsimNL/Large model. This was necessary because of the significantly increased time required to run a Mulsim problem. This process was automated with a Visual Basic macro. The steps required to construct both LaModel and Mulsim grids are described in Appendix B. This appendix also lists the Visual Basic functions used to accomplish this task. The macros can be adjusted easily to be used on any size grid, with an interior grid that contains fine-element blocks converted to zeroes, as needed by the Mulsim coarse grid input.

The Finite Difference Code FLAC^{3D}

If failure mechanics of the roof or floor are important, or more thorough mechanics of the coal seam is important, then a volume-element type of modeling code is necessary. Possible code types might include finite element, finite difference, or distinct element codes. In this study, the finite difference code FLAC^{3D}, both versions 4.0 and 5.0, was used to model Mine A only. Such models may not be used extensively by most engineers who perform analysis and modeling of mining layout because of the time, cost, and detail required. Volume element codes require many more inputs than boundary element codes, including determination of appropriate constitutive laws and material parameters, determining geometry for purposes of construction of a model grid, and including irregularities that might be important, such as nonplanar stratigraphy and variable topography.

For purposes of this study, the idealized stratigraphy shown in Figure 8 was used along with properties listed in Tables 3 and 4 for basic rock types, as described earlier. Thin coal seams were combined with the thickest member for those groups listed in Table 5. Presence of faults

was ignored, but elevations of the top of seam and surface were obtained using the AutoCAD Civil 3D for the purposes of constructing a model. The model was built with FISH (short for FLACish, a computer language embedded in Itasca Consulting Group codes) functions, using elevations of the top of the DU Seam and all other stratigraphy having constant thickness and being parallel with that seam. The lowest member, the Mancos Shale, had a constant elevation at the bottom of the model. The FISH functions built the model one plan-view section at a time. Section division was necessary to accommodate geometries of the panels and graduation of zone sizes. Within each section, the zones were constructed one strata member at a time, with columns of zones with the x and y coordinates being constant for a column of grid points. No interfaces were used between strata. A view of the constructed model grid is shown in Figure 18. Overcoring stress measurements taken in the area showed variable results, but generally were not much different from that induced by gravity loading.[4] For that reason, bottom and side boundaries were fixed for normal displacement and loading was by gravity before any excavations were introduced to the model.

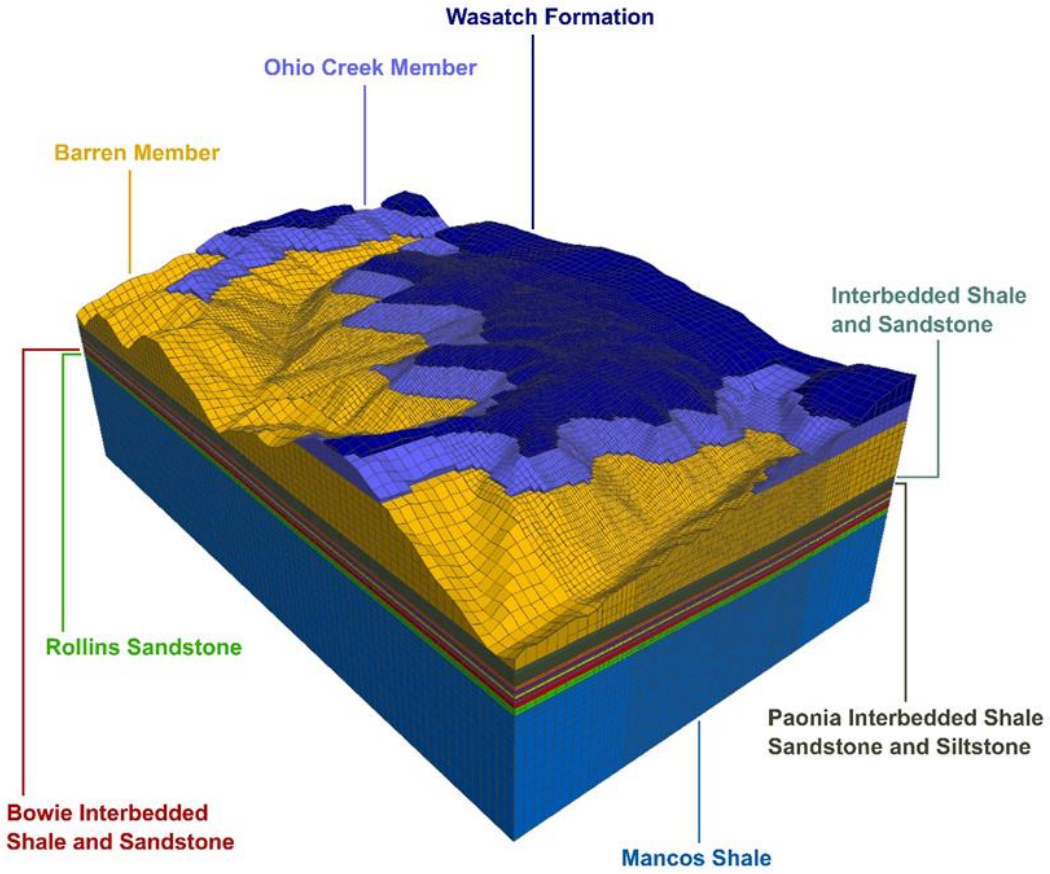

Figure 18. FLAC^{3D} model showing topography.
Each color represents a different member of the strata.

[4] Measurements from private communication with mine operator. Statement is the judgment of the authors.

To use FLAC^{3D} to model longwall mining, there are two significant challenges. These are:

- Simulation of caving or gob loading; and
- Simulation of local effects, particularly of the coal seam—simulating such effects would require building a model with such fine zones that the model would be too large for available workstation memory and also require long computational times to complete the task, even if such memory were available.

Gob Simulation

The problem of how to reasonably and accurately model gob loading has never been solved well. In longwall coal mining, it is not currently possible to measure loading of the gob. Maleki et al. [1984] measured pressure at the floor of gob at various points in a retreat pillar section that was mined in similar fashion to a longwall panel. That is, a longwall-like panel was mined by developing two rows of pillars at the face end of the panel. One row of pillars closest to the gob was mined, leaving one row of pillars. The next row of pillars was then developed, and the cycle repeated. This sequence allowed placement of Gloetzl cells (a brand of earth pressure cells) on the floor of the cross-panel entries. The cells were buried in 0.3 m (1 ft) of gravel and covered with a conveyer belt for protection. The hydraulic lines led to the gate roads, and these were protected with slotted wooden 2 by 4 pieces, overlapped and fastened together around the lines. These measurements showed that initial panel mining resulted in almost all load being transferred to the abutments and gate roads. Caving was largely controlled by the presence of periodic faults (that is, when a fault was undermined). Others have installed instrumentation to measure gob loading, but either critical details of the instrument and installation were missing to permit critical review [Ramírez Oyanguren 1972; Wade and Conroy 1980] or the nonlinear behavior resulting from the absence of full contact between the rigid cylinder and the borehole wall does not inspire full confidence in the results [Wade and Conroy 1980].

Point measurements, even over time, do not create a full picture of gob loading, but gob loading should vary according to stratigraphy and structural features. Thus, the empirical standard of $\beta = 21°$ is not likely to hold true for cases having massive, strong strata in the overburden.

This report describes three approaches to modeling gob loading. In using any of the three approaches, the model still must be calibrated and verified.

Gob Stiffness Increases Linearly with Increasing Stress

Modeling the nonlinear nature of gob loading took a significant step when Zipf [USBM 1992a, 1992b] included a gob hardening material in Mulsim/NL. Previously, the gob had been represented as an inserted linear-elastic material that could be adjusted because of changing cave heights [Beckett and Madrid 1986; USBM 1988, 1992c]. The basic equation for the gob modulus was

$$E_{gob} = \left(\frac{E_F - E_I}{n\,\sigma_F}\right)\sigma + \frac{E_I}{n}, \tag{13}$$

where E_{gob} = gob modulus,
σ_F = final or ultimate gob stress,
E_I = initial gob modulus,
E_F = final or ultimate gob modulus (the modulus at σ_F),
σ = gob vertical stress, and
n = gob height factor—the ratio of gob height to seam height. This factor is needed to reduce the gob stiffness if the gob height is larger than the seam height.

As Zipf [USBM 1992b] showed, an expression for gob stress as a function of strain or closure can be obtained by solving the differential relation between stress and strain,

$$d\sigma = E_{gob}\,d\varepsilon, \tag{14}$$

where ε = seam closure strain.

The solution produces

$$\sigma = \frac{E_I}{n}\left(\frac{n\,\sigma_F}{E_F - E_I}\right)\left\{e^{\left[\left(\frac{E_F - E_I}{n\,\sigma_F}\right)\left(\frac{D}{h}\right)\right]} - 1\right\}, \tag{15}$$

where D = seam closure, and
h = seam height.

Heasley [1998] implemented this same equation in LaModel. In LamPre, the gob wizard assumes an initial modulus of 0.689 MPa (100 psi) and an ultimate stress of 27.58 MPa (4,000 psi) [Heasley 2010]. It uses a built-in version of the LaM2D (two-dimensional LaModel program) to solve for the final modulus so that gob loading matches that suggested by the empirical method.

The Pappas and Mark Gob

Pappas and Mark [USBM 1993] conducted several tests on three materials to determine how to characterize gob stiffness for numerical models. From photographs of gob material, they developed a method to determine three-dimensional particle-size distribution from two-dimensional photographs and to scale these distributions down to laboratory size. Three materials were then used to construct 20 samples total of shale, weak sandstone, and strong sandstone. The specimens were tested in a chamber with an inner diameter of 36.36 cm (14.314 in) and a height of 30.48 cm (12 in). The samples were filled to about 2.54 cm (1 in) of the top, and a top platen was used to apply load. Initial weight with initial volume was used to determine initial void ratio.

Results showed nonlinear stiffness for each material. Salamon's equation for compressive behavior of backfill [1990] was fitted to the experimental data very well. His equation is

$$\sigma = \frac{E_0\,\varepsilon}{1-\frac{\varepsilon}{\varepsilon_m}}, \tag{16}$$

where σ = gob stress
E_0 = initial secant modulus,
ε = strain, and
ε_m = maximum strain.

This equation can be differentiated ($^{d\sigma}/_{d\varepsilon}$) to determine the current tangent modulus,

$$E_t = E_0 = \frac{2\sigma}{\varepsilon_m} + \frac{\sigma^2}{\varepsilon_m^2\,E_0}, \tag{17}$$

where E_t = tangent modulus.

Parameters were fitted for each of the three materials. For shale, weak sandstone, and strong sandstone, the fitted equations are (with stress in units of psi), respectively,

$$\sigma = \frac{1110\,\varepsilon}{1-\frac{\varepsilon}{(1/2.26)}}, \tag{18}$$

$$\sigma = \frac{1340\,\varepsilon}{1-\frac{\varepsilon}{(1/2.49)}}, \text{ and} \tag{19}$$

$$\sigma = \frac{1890\,\varepsilon}{1-\frac{\varepsilon}{(1/2.34)}}. \tag{20}$$

These equations might be used easily in numerical models to calculate stresses in gob material following excavation of a cut in a panel or mining a pillar in a retreat section.

Alternatively, Pierce [2010a] fit a general equation for the instantaneous gob modulus that conforms to the Pappas and Mark results [USBM 1993]. That equation is described further in the next section.

Longwall Caving Model

Itasca Consulting Group developed a model for block caving for two mining-industry-funded projects, the International Caving Study (ICS) and the Mass Mining Technology Project (MMT). The conceptual model, shown in Figure 19, shows a mobilized or caved volume or zone, below a volume of yielded material that has developed much fracturing, but has not displaced much. An air gap is usually between these zones. Above the yielded zone, microseismic events have occurred as a result of joint slip and fracture extension in the seismogenic zone. Elastic material is, of course, above the seismogenic zone.

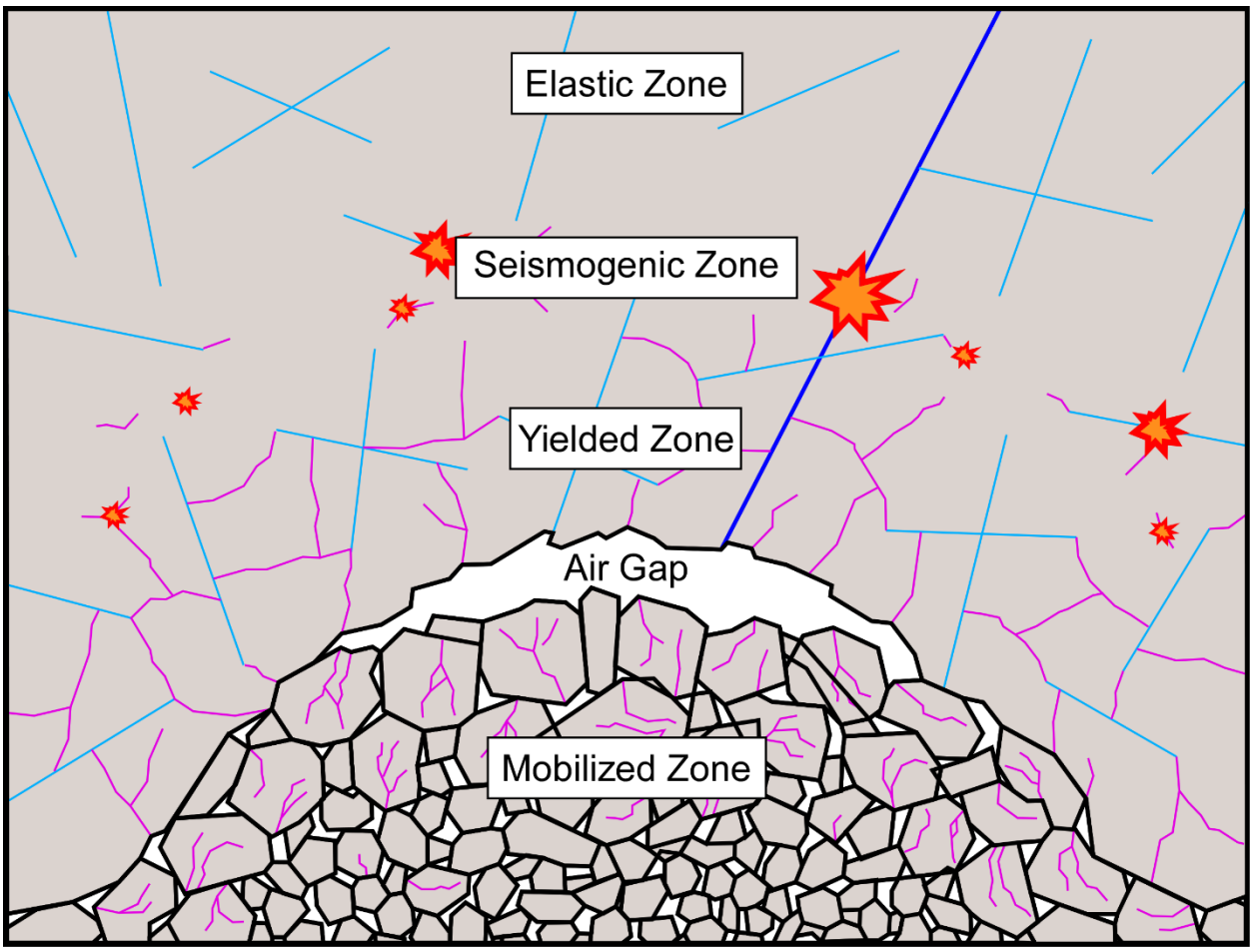

Figure 19. Conceptual model of caving. After Pierce and Board [2010a], who adapted this figure from Duplancic and Brady [1999].

The model uses the strain-softening ubiquitous joint model to represent cohesion weakening, tensile strength weakening, friction strengthening, and dilation in zones having a continuum matrix and embedded ubiquitous joints. Clark [2006] first developed the ubiquitous joint rock mass model for FLAC, but it was later adapted to use with FLAC^{3D} [Sainsbury et al. 2008; Board and Pierce 2009].

During caving, the rock mass increases in volume because of dilation under shear or volumetric expansion under tension. This increase in volume decreases the stiffness of the caving material.

Pierce and Board [2010a] adapted this model for sedimentary deposits. This adaptation is described here and briefly in Appendix C. Their conceptual model for sedimentary deposits is shown in Figure 20. In this case, the mobilized zone is the same as the indicated cave zone, and the fractured zone is the same as the yielded zone. However, the equivalent of the seismogenic zone is absent from the figure. Pierce and Board [2010a] state that this model "is likely to be more complex in longwalling, involving slip and tensile failure on large-scale persistent bedding planes and brittle failure of massive, thick, brittle units (e.g. sandstone) as well as slip on open joints, opening of new fractures in tension and slip on major faults."

Poeck et al. [2008] conducted a study using the Universal Distinct Element Code (UDEC) and compared caving with random blocks formed by Voronoi tessellation, a method derived

from the work of Voronoi [1908], with blocks characteristic of stratified ground. The results showed that stratified ground exhibits less bulking and more surface subsidence, suggesting that a lower dilation angle and lower maximum porosity are appropriate in stratified ground compared to porphyries, where the block caving mining method is used.

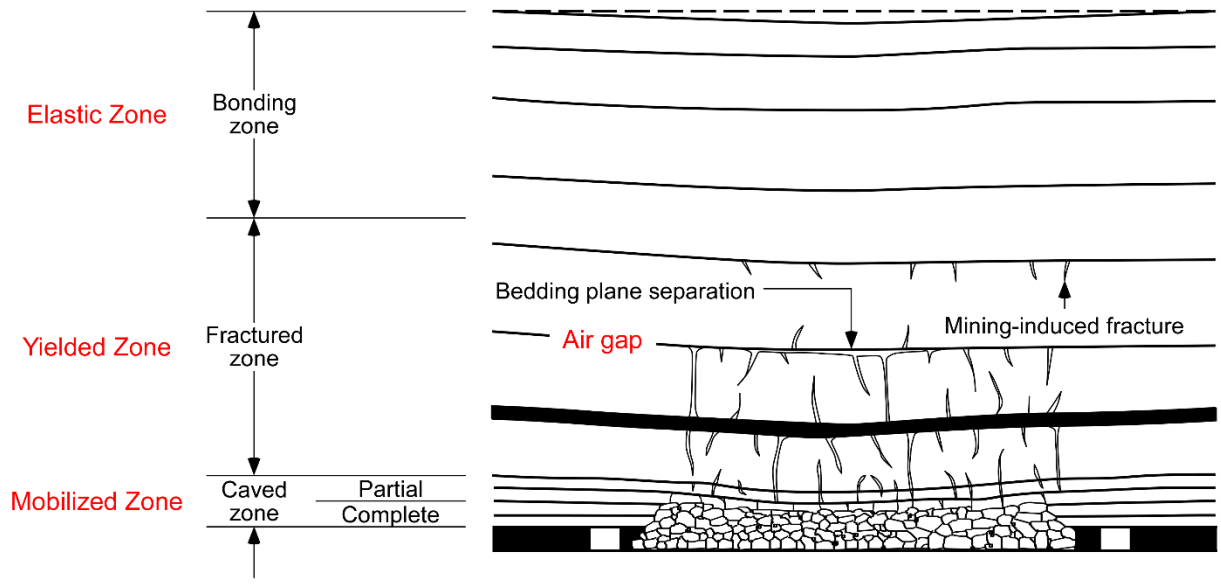

Figure 20. Conceptual model of caving in longwall mining. After Pierce and Board [2010a]. Modified from Singh and Kendorski [1981].

In their tests on scaled gob materials, Pappas and Mark [USBM 1993] reported equations relating tangent modulus of the material with unconfined compressive strength (UCS) of the material and the average shape factor (thickness to width ratio) of the materials. The equations took the form:

$$E_t = a\ (UCS)\ +\ b\ (shape\ factor)\ -\ c, \tag{21}$$

where a, b, and c are constants that vary with bulking factor. Pierce [2010b] fit an equation to each of these constants, because they were related to bulking factor. By using volumetric strain (ε_{vsi}) (bulking factor = $1 + \varepsilon_{vsi}$) as the dependent variable, he fitted the following equations to represent the constants:

$$a = 0.1316(\varepsilon_{vsi})^{-2.145}, \tag{22}$$

$$b = 1110.5(\varepsilon_{vsi})^{-2.574}, \text{ and} \tag{23}$$

$$c = 981.14(\varepsilon_{vsi})^{-2.318}, \tag{24}$$

where a is dimensionless, and b and c have units of psi.

Pierce [2010b] noted that these equations were valid only in the volumetric strain range of 0.25 to 0.50. The upper limit of bulking is manually set to be within this range. For caving material having a value of ε_{vsi} between 0 and 0.25, the tangent elastic modulus is interpolated linearly between the intact modulus and that calculated by Equation 21 with ε_{vsi} = 0.25.

In the original caving algorithm, much of the microseismicity occurred before peak strength. In the case of longwall mining, there can be massive failure of units or slip along faults, both of which can cause release of very large amounts of energy. Because of the potential for massive amounts of energy release, energy tracking was set up to keep track of dissipated and stored elastic energy of each zone. The tracking also included separating the volumetric and deviatoric components of both dissipated and stored elastic energy, along with the totals of both [Pierce and Board 2010a].

The original Longwall Modeling Environment [Pierce and Board 2010b] had FISH (FISHish) functions that read strata information and properties from a text file. These functions set up a uniform and horizontal grid for each stratum, with a radially constructed surrounding grid that extends to some far-field boundary. A driver file called the functions to execute construction of the grid, assignment of properties, setting up of panel mining, and panel mining. The authors modified these functions to exclude the radial zones out to a far-field boundary. Instead, the area of interest formed its own boundary, and sides and bottom boundaries were fixed in the normal direction. The topographic model generator described earlier was incorporated.

Detailed Pillar Models and Equivalent Element Method

The size of a panel-scale model would require more zones than is possible or practical for either Mine A or Mine B panels. However, coarse elements do not allow for direct simulation of gate roads and the complexities of pillar loading in the gate roads of a longwall panel. Board and Damjanac [2003] (see also [Board et al. 2007]) developed a method to capture the detailed pillar and rib behavior to include in a panel scale model with coarser zones. This is done by constructing and loading fine-zoned pillar models that include detailed strata and structural features of and near the seam that are representative of actual geometry, material behavior, and conditions. An example for a half pillar is shown in Figure 21. A different model is required for each pillar (or half- or quarter-pillar), barrier, and solid-coal geometry in the panel model. A detailed model is loaded by applying a small, downward, even, constant velocity at the top boundary of the model such that the model maintains quasi-equilibrium. Two models of each case, one with plasticity and one that is purely elastic, are required so that macro-seam plastic behavior can be separated from elastic behavior.

Esterhuizen and Mark [2009] developed a procedure for implementing the Board and Damjanac approach to capture the detailed pillar behavior as a one-dimensional equivalent element that could be implemented into the panel model. The equivalent element has for dimensions the height of the seam and the width and length of the outer boundaries of the detailed model. The equivalent element addresses are set up in a memory chain in a FISH function. This allows the program to set all stress components except the vertical stress to zero at each calculation step, thus keeping the equivalent element one-dimensional.

The strain determination in this report differs from the one implemented Esterhuizen and Mark. Esterhuizen and Mark used strain at one set of grid points at the center of the pillar. Here the authors, instead, computed a strain that was averaged over the entire plan view of the detailed pillar model. An average stress was calculated from those zones whose centroids were within one zone height of the midpillar plane. Arrays of these grid points were established before loading the model.

The objective of modeling the detailed pillar was to obtain a cohesion-versus-strain curve that represented the nonlinear plastic behavior of the pillar, floor, and roof near the pillar,

combined and represented as if all such plastic behavior is in the horizon of the excavation height (height of the pillar). The details of determining this curve for a particular equivalent element are found in the section Equivalent Elements and Detailed Pillar Models of Appendix C.

In the case of Mine A, for which a large multipanel model was constructed, the entire DU Seam was replaced with equivalent elements, with each set of equivalent elements having the same dimensions. Upon converting to equivalent elements after establishing equilibrium of the unmined panel model, the stress of each equivalent element having entry excavations was adjusted according to the extraction ratio.

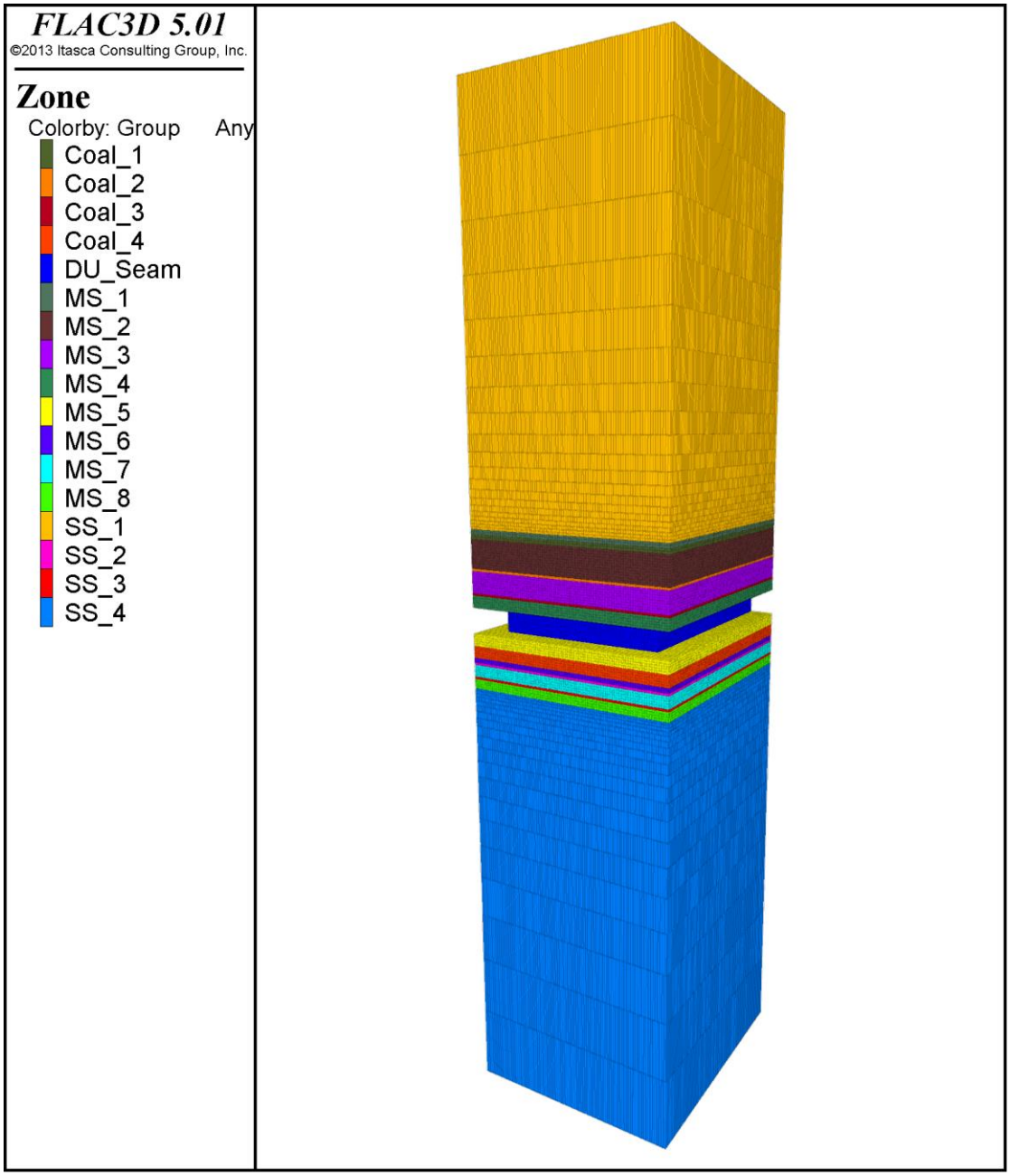

Figure 21. Example of a detailed model of half of a pillar showing strata as FLAC^{3D} groups.

After the model was executed to simulate mining the longwall panels, the displacement history of the elements representing locations of instrument sites was obtained. This information was used to determine stress state at instrument sites (for example BPC locations) within the detailed pillar model, most often by interpolation between saved states. These calculated stresses at instrument locations might be referred to as synthetic instrument stresses.

This method had the disadvantage that, while the detailed pillar model was loaded evenly, the equivalent element was loaded unevenly, especially near the mined panel. This caused nonuniform closure across the equivalent elements. Therefore, the synthetic instrument stresses were just estimates, and with some error, particularly when the face was near the equivalent element. The authors' arsenal of detailed pillar model script functions has the capability of adding a tilt in the loading surface with initial linear variation in velocity of the top boundary. However, that capability was never used because the "tilt" of an equivalent element changes with the progress of mining, making it nearly impossible to load the detailed model in the same way for every single equivalent element. Instead, presence of error is acknowledged, but the user can estimate location of the largest errors in the detailed pillar models, as panel mining effects on instruments are estimated.

Interchanging Tools for Various Modeling Steps

In the process of modeling tool testing and analysis, the advantages and disadvantages of each tool came to light. The various scales necessary for modeling the problem accurately caused examination of which tool might be optimum for a particular part of the problem, and whether an interface between results and inputs might be possible. Appendix C describes the different parts of a modeling problem—in situ stress distribution, pillar-scale modeling, and panel-scale modeling—and how they might optimally be accomplished with more than one tool, with the output of one tool used as input to another tool. For example, for highly variable topography, FLAC^{3D} might provide the most accurate result of topographic loading. Such results, if grids match that of LaModel, for example, can be input directly to LaModel, thanks to a slight modification made by Heasley, mentioned briefly by Whyatt et al. [2011], and described more fully in Appendix C.

The same can be said of other tools. Simple spreadsheet calculations of pillar behavior, including calculations of synthetic instrument readings, according to various pillar models can be compared to actual measurements to infer the best pillar model. The best pillar model might then be optimally used in a boundary element code.

Complicated failure mechanisms involving floor and/or roof require investigations with detailed pillar models using a volume-element tool, such as FLAC^{3D}. An analysis of important mechanisms is required in evaluating the optimum tool for any phase of modeling.

Calibration Procedures

The two sites were not conducive to installation of many extensometers, which would be required to do the kind of calibrations suggested by Pariseau et al. [1984], Pariseau et al. [1986], and Pariseau et al. [USBM 1992d]. Microseismic activity is troublesome in sedimentary deposits because elevation of events cannot be located accurately unless a good vertical velocity model is determined. Therefore, the methods of Andrieux et al. [2008] to calibrate strength and post-peak

behavior cannot be used in this study. The principles of the approach of [Wiles 2007] can be used for these two sites, but the three focuses or steps in the approach of [Heasley 2008b] seems appropriate for all evaluation tools, and not just displacement discontinuity codes. Those steps will be restated later in this section. Model calibration procedures are part of the evaluation process of design.

Although the mine layout designs at both Mines A and B were determined before this study, it is useful to discuss the process of mine layout design with reference to Stacey's engineering wheel of design (Figure 1). Probably the original problem statement used by mine engineers was to determine the size of gate road pillars to maintain safe openings and reduce the risk of mining-induced seismic events. Likely requirements and constraints were that: (1) pillars needed to safely bear the load transferred from the overpanel weight—i.e., the weight of the overburden over the mined panel; and (2) other hazards should not be introduced or increased. In the design wheel process, efforts were made to determine several unknowns, but that information was not significantly used in the initial gate road design process.

For example, as previously mentioned, at Mine A the empirical method, Analysis of Longwall Pillar Stability, was used. Because ALPS does not have a critical stability factor associated with depth of cover, Mine A developed its own local ALPS database for deep cover. A local critical stability factor was determined, but MSHA agreed to a critical stability factor that was 14% larger, resulting in the large pillar size for two rows of chain pillars. In effect, efforts in step 3 of the wheel of design process were put into developing the local ALPS database and developing a critical stability factor. The conceptual model was decided upon, and then pertinent unknowns were gathered. The result raised other concerns, such as ventilation. A similar story at Mine B resulted in a gate road system of yield pillars alongside larger pillars.

In what follows, attempts were made to improve upon the results by using modeling tools and applying the MSHA [2009] PIB09–03, which outlines steps to calibrate models to observations. However, an attempt at improvement to this process was also made, so that a working modification was made to the PIB steps. The modified list would be, with additions italicized:

1. Observe *and make measurements in* underground areas,
2. *Evaluate which modeling tool is appropriate,*
3. Estimate model parameters,
4. Model observed *and measured* areas,
5. Verify model accuracy,
6. Establish threshold limits,
7. Model new configurations,
8. Evaluate new configurations, and
9. Implement best alternative.

The challenge is in making good measurements with accurate and reliable instruments. What should be measured and with what? Some of those questions have been answered by Larson et al. [NIOSH 2019] and work presented earlier in this report. The most sensitive instrument was the borehole pressure cell (BPC), with which the load transfer distance (LTD) was measured to be 535 m (1,756 ft) at Mine A and probably between 256 m and 354 m (840 ft and 1160 ft) at Mine B for 335 m (1,100 ft) of overburden depth.

But more attention is needed to lacking information. Heasley [2008b] summarized it concisely in the steps he recommended for calibrating a model with LaModel. Those steps were to calibrate, in this order:

1. Rock mass stiffness,
2. Gob stiffness, and
3. Coal strength.

The process is slightly more complicated than this simplistic list, but it captures the essence of the process. First, the stiffness of the overburden in any tool has to be calibrated to distribute the overpanel load over the abutment accurately. Heasley [2008b] recommended, in the absence of measurements and observations, to calibrate to the empirical standard. For rock mass stiffness, he calibrated to distance from the gob within which 90% of the distributed overpanel weight was transferred. This was necessary instead of using LTD because the LaModel solution theoretically never goes to zero, except for approximating it at an infinite distance from the mined panel.

This is a data-limited problem [Starfield and Cundall 1988], in that nothing is known about loading of the gob—i.e., how much of the overpanel weight is transferred through the gob. In the cases described in this report, no measurements of gob loading were made, nor could the amount of gob loading be inferred by approximating the abutment loading curve. If gob loading could be estimated reasonably, then gob stiffness (presumed nonlinear) must be adjusted to meet that gob loading target. That adjustment in turn affects LTD so that rock mass stiffness must be adjusted again. This iterative process is necessary until both rock mass stiffness and gob stiffness are calibrated.

Floor and roof strata properties can be calibrated and verified by observations and measurements. For example, at Mine A significant floor heave was encountered in the 2 North gate roads, but almost no floor heave was found in the 1 North gate roads. This difference might be caused by the larger pillar, but differences in strata column and properties might also need to be considered.

Finally, pillar strength and behavior are unknowns. Perhaps a more accurate description is needed for the coal strength model. This term emphasizes that selection of an appropriate coal strength model is required, in addition to calibrating strength amounts within that model. Perhaps the best way to evaluate a pillar strength model is to compare synthetic instrument readings calculated from various models to actual measurements at various locations in a pillar. Once a reasonable pillar model is selected and calibrated, it may be necessary to make slight adjustments to the rock mass stiffness and gob stiffness, followed by calibration adjustments to the coal model until all three parts of Heasley's recommended calibration process are satisfied.

In the case of Mine A and Mine B, no measurement or reasonable estimate of gob loading was available. The best scenario possible was to estimate gob stiffness and to see if it provided gob loading in a reasonable range.

Empirical Method Calibration

The empirical method fixes the loading, stress profile, and coal strength according to the overburden height and panel width for all three calibration steps outlined by Heasley [2008b]. However, this loading profile does not reflect the long LTDs measured at Mine A and Mine B. The stress profile could be adjusted to a measured LTD of 535.2 m (1,756 ft), adjusted simply in Equation 10.

Figure 22 shows the empirical stress profile using standard equations and the stress profile calibrated to measured LTD. Locations of gob, headgate pillars, and the next panel of coal are shown to give an indication of the contrast in pillar loading in each case. Larson and Whyatt [2013] found the area under the calibrated empirical curve to be low compared to a Mulsim

profile and adjusted the calibrated curve proportionally to have equal area compared to the Mulsim profile. Even so, the pillar loading next to the mined panel was low compared to the loading calculated with the Mulsim model.

Using such a calibrated empirical approach is not recommended, because it deviates from the standard approach. Another conceptual model is necessary.

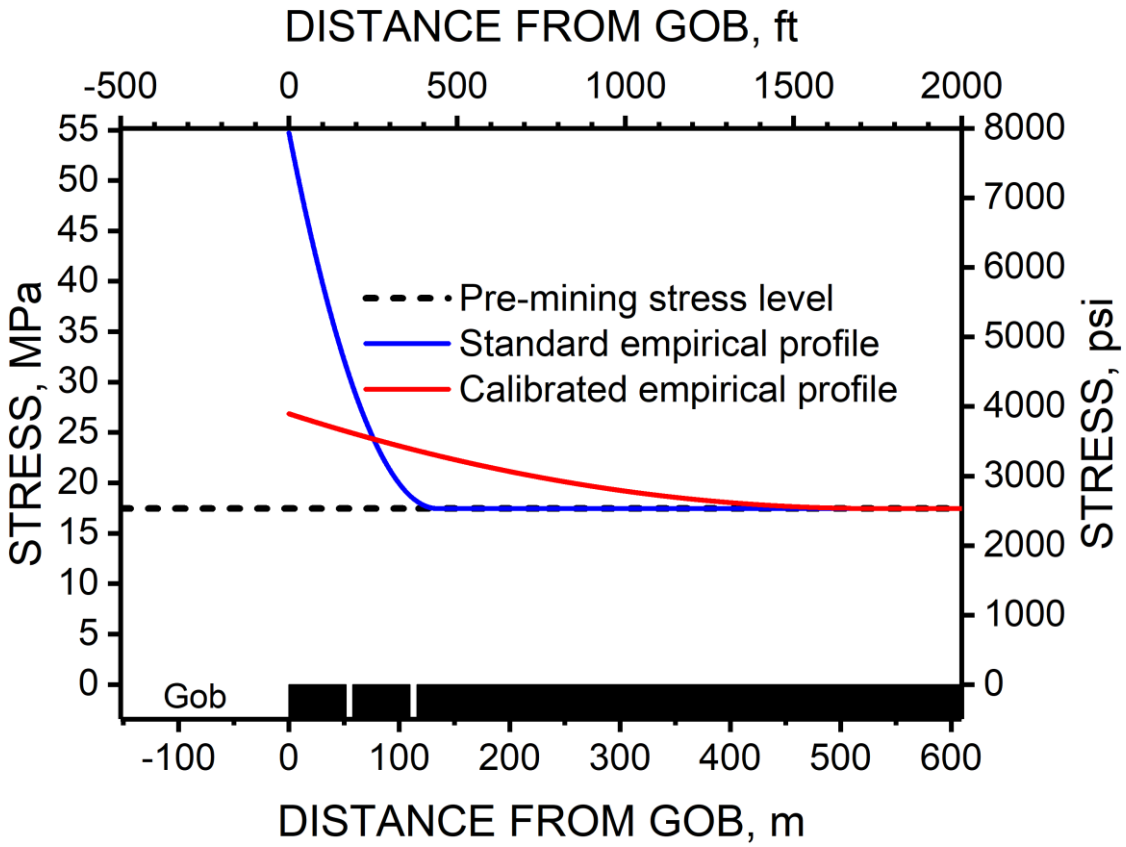

Figure 22. Standard empirical stress profile for Mine A headgate geometry and empirical stress profile calibrated to measured load transfer distance (LTD).

LaModel Calibration

LaModel is based on another conceptual model—a nonlinear material model for the seam surrounded above and below by a series of plates having no friction or cohesion between them—and deserves consideration in calibration toward design analysis because of its widespread use. Calibration of a model using LaModel could only be accomplished for the rock mass stiffness, given that no measurements were taken that could be used to reasonably estimate gob loading.

As a starting point, elastic modulus of the rock mass was calculated as a thickness-weighted average of the elastic moduli of the overburden listed in Table 3. Lamination thickness was then calculated with the LamPre numerical modeling wizard, using Equation 25:

$$t = \frac{2\,E_s\sqrt{12\,(1-\nu^2)}}{E\,h}\left(\frac{5\sqrt{H}-d}{\ln(0.1)}\right)^2, \tag{25}$$

where E = elastic modulus of overburden,
ν = Poisson's Ratio of overburden,
E_s = elastic modulus of the seam,
h = seam thickness,
d = extent of coal yielding at the edge of the gob, and
H = seam depth.

Values from Table 3 were used as much as possible, but the default coal strength of 6.21 MPa (900 psi) was used to conform to the empirical standard. The gob wizard in LamPre was used to determine final gob modulus associated with 27.58 MPa (4,000 psi)—the default ultimate stress.

In calibrating LaModel when there are no measurements or observations to indicate LTD, Heasley [2008b] recommends calibrating to the empirical standard. This is done by requiring that the distance from the gob at which 90% of the abutment loading be the same for LaModel as it is for the empirical method. From this equivalency, Heasley derived this equation by rearranging Equation 25:

$$Et = \frac{2\,E_s\sqrt{12\,(1-\nu^2)}}{h}\left(\frac{5\sqrt{H}-d}{\ln(0.1)}\right)^2. \tag{26}$$

Recall that the term $5\sqrt{H}$ is the empirical distance within which 90% of the abutment load is found. The single seam solution is invariant with the product, Et, making it the actual rock mass stiffness property.

It is not clear how to identify the $D_{0.9}$ boundary in a mine. However, the LTD has been demonstrated as measurable by Peng and Chiang [1984] and shown again recently by Larson and Whyatt [2012] (see also NIOSH [2020] and earlier in this report). As reported by Larson and Whyatt [2012], the procedure to calibrate to LTD with LaModel is to reorder Equation 5 to find an effective H corresponding to the LTD, and substituting the effective H into Equation 26.

Figure 23 shows contours of stress increase with respect to prepanel conditions at one longwall face position with the face approaching the 2 North outby station. The locations of instruments along the entries when first arrival of mining-induced stress increase was detected are superimposed for this face position. The 138-kPa (20-psi) contour in the model results is far from the locations of the instruments when a 20-psi increase in the cells was detected. The figure highlights the need for calibration of rock mass stiffness to better approximate LTD.

The calibration procedure outlined above, using effective H in Equation 26 was carried out. Figure 24 shows contours of model-calculated stress increase with respect to prepanel mining conditions, but with calibrated Et. The locations of the instruments when they detected first arrival of mining-induced stress increase was detected are superimposed for this face position—the average position when the BPCs detected that stress increase. The 138-kPa (20-psi) stress-increase contour is much closer to where the BPCs detected a 138-kPa (20-psi) change. However, Larson and Whyatt [2013] found that the rock mass was so stiff that only 0.28% of the overpanel weight was transferred through the gob. By comparison, the empirical method and LaModel, calibrated to the empirical standard, transferred 23% and 47%, respectively, of the overpanel weight through the gob. The total overpanel weight is different for LaModel than for the empirical method because LaModel accounts for topography. Even so, the small amount of

gob loading with calibrated Et strongly suggests that a laminated model is inappropriate for this stratigraphy.

Because of this result, no attempts were made to model the Mine B mine layout with LaModel. Instead, another conceptual model—a nonlinear material model for the seam in an elastic continuum—and its associated modeling tool (MulsimNL/Large) was considered.

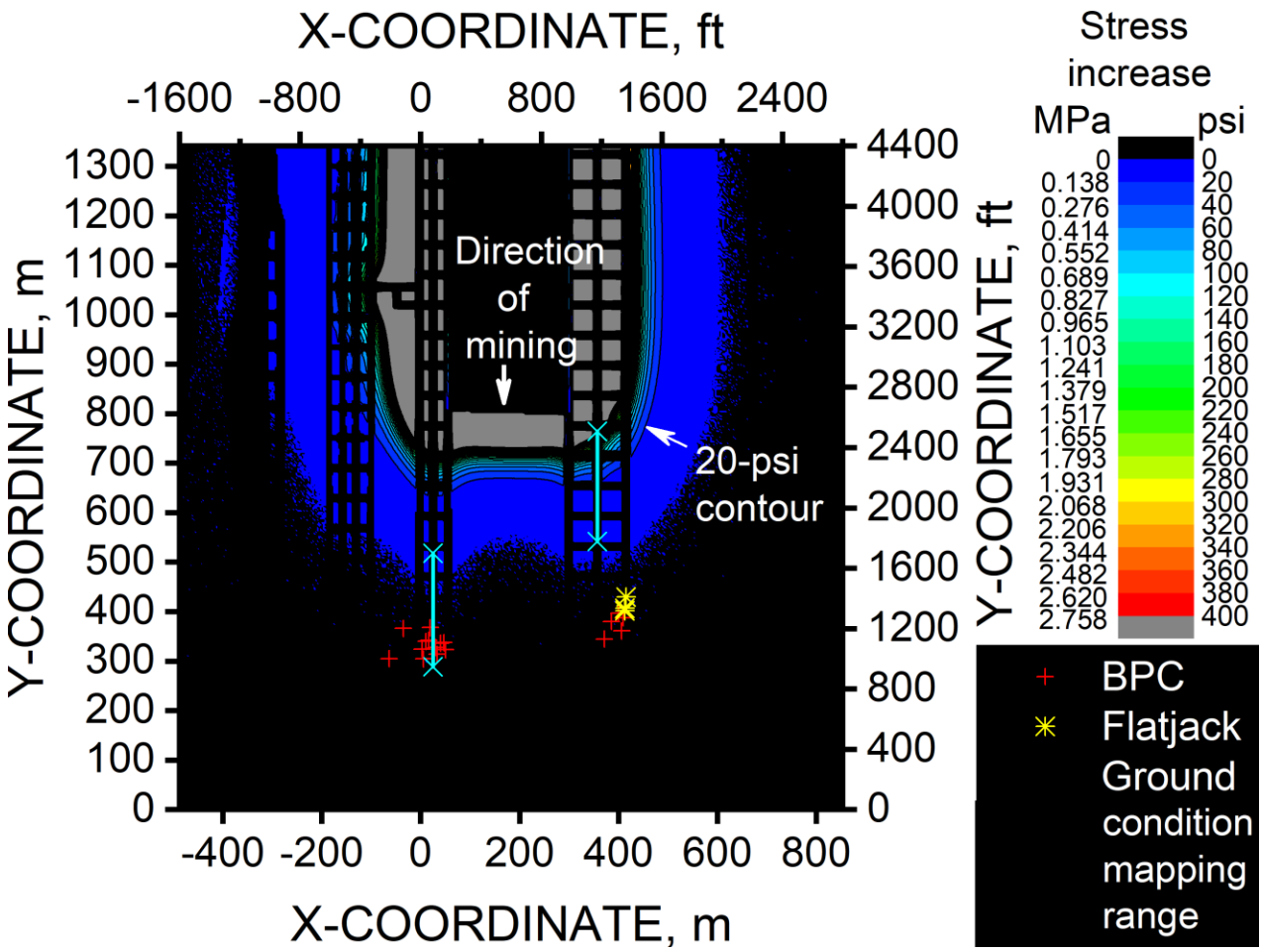

Figure 23. Contours of stress increase over prepanel-mining stress for case of Et calibrated to the empirical standard.

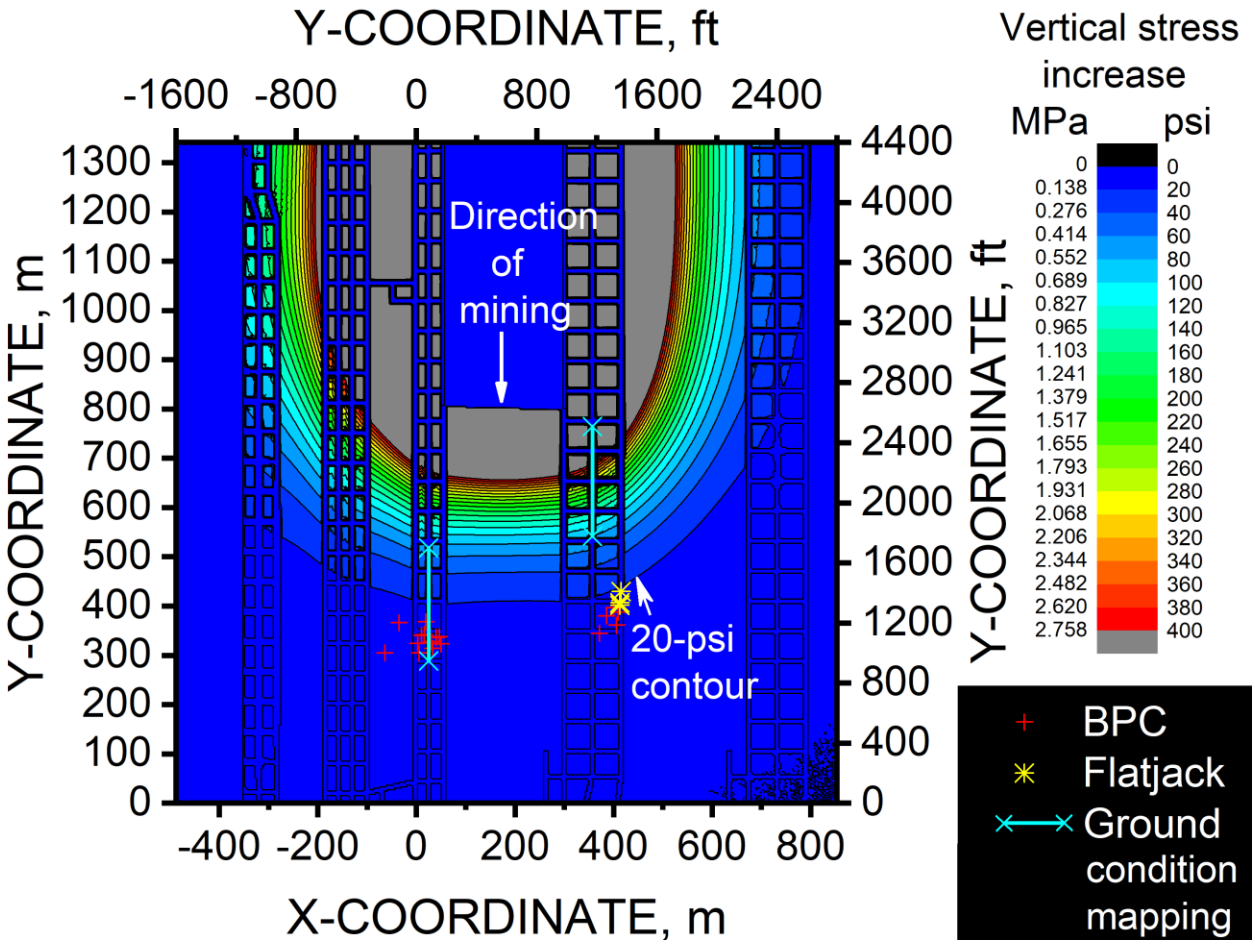

Figure 24. Contours of stress increase over prepanel-mining stress for the case of Et calibrated to LTD.

MulsimNL/Large Calibration

Calibration steps for MulsimNL/Large are the same as outlined by Heasley [2008b]—that is, in order, rock mass stiffness, gob stiffness, and coal strength. As with LaModel, we cannot determine gob stiffness with measurement with the current data set. Therefore, the authors proceeded with the same initial rock mass elastic modulus determined for LaModel from values listed in Table 3. Final gob stiffness was determined with the LamPre utility of the LaModel software using appropriate geometry, the coal modulus from Table 3, and a coal strength of 6.21 MPa (900 psi)—the standard for the empirical method. This combination of rock mass stiffness and gob stiffness was the starting point for models that were investigated for purposes of calibration.

Mulsim has elastic, elastic-perfectly plastic (or elastic followed by hardening), and elastic-softening models, as does LaModel. These calibration exercises began with elastic, perfectly-plastic yield models because it is the most common strength model in use. However, several possible strength models might be implemented. For example, the Mark-Bieniawski formula [Mark and Chase 1997], Holland-Gaddy formula [Holland 1964], the Maleki confinement formula, and the Maleki structural formula [1992] all calculate various pillar strengths according to various criteria (for example, pillar width-to-height ratio). Appendix D contains a discussion

of pillar formulas by one of the authors of this report, Dr. Jeffrey C. Johnson. He shows how these formulas can be integrated to provide mathematical representation of yield strength by location in the pillar. Such representations permit calculation of strengths necessary for MulsimNL/Large input files.

Yield Models

Larson and Whyatt [2012] previously demonstrated that rock mass stiffness could be calibrated using LaModel with a Mark-Bieniawski material yield model to measured LTD at Mine A. However, they found that the rock mass had to be excessively stiff so that it was impossible to determine a gob stiffness that would provide reasonable distribution of overpanel weight between the gob and the abutment [Larson and Whyatt 2013] for such large LTD with respect to the empirical LTD. For that reason, LaModel was not used in further analysis in this study.

LaModel's LamPre has material wizards that calculate Mark-Bieniawski strength for various element locations. The coal material wizard's default uniaxial strength is 6.21 MPa (900 psi). Other input parameters such as lamination interval and final gob stiffness are also calibrated with wizards to the empirical assumptions. The case of 6.21-MPa (900-psi) coal with default wizard-determined final gob stiffness was the first case that was modeled with MulsimNL/Large. Figure 25 shows contours of stress increase over the prepanel stress state when the face was approximately at the location when BPCs detected the threshold increase in cell pressure. The location of the line of BPCs in the headgate is indicated. The figure also shows that contours are affected by yielding of coal near the ribs—this effect bends the contour significantly outby as it nears the gate roads. This bending aside, the base trend of the contour appears to have overshot the instrument line slightly.

Figure 26 shows pillar strength calculated with various common pillar strength formulas with width-to-height ratio. For the Bieniawski and Holland-Gaddy strength models, the coal strength was 6.21 MPa (900 psi). The width-to-height ratios of 1 North and 2 North pillars were 6.64 and 15.45, respectively. Figure 27 shows how these same formulas, integrated to show strength by distance from the rib, vary from one another with distance from the rib for a seam height of 3.4 m (11 ft). Post-yield softening would only cause greater bending of the threshold contour outby as it approaches the gate roads. Examination of other pillar strength equations compared to the Bieniawski formula reveals less capacity to load near ribs, even for large pillars such as those found in 2 North. The Bieniawski formula (and by extension, the Mark-Bieniawski equation) seems to be the upper limit of strength for those big pillars. Therefore, the Mark-Bieniawski strength equations were used for another MulsimNL/Large model, but with a 9.65-MPa (1,400-psi) strength coal. It was thought that this value was beyond the upper bound of coal strength possible at Mine A.

Figure 28 shows contours of stress increase with respect to the prepanel stress state when the face was approximately at the location when the BPCs first detected mining-induced abutment stress. As with the lower strength Mark-Bieniawski model, the contours curve outby as they approach the gate roads, which is inconsistent with measurements. However, the trend of the threshold contour line when it is not close to the gate roads suggests that rock mass stiffness would be calibrated for this strength model aside from the effect of yielding at and near the gate roads. This result says something about the coal strength model, suggesting that hardening must be involved in the seam material behavior, even near the ribs. The yield models, with elastic-perfectly-plastic behavior are inadequate to model the stress distribution accurately.

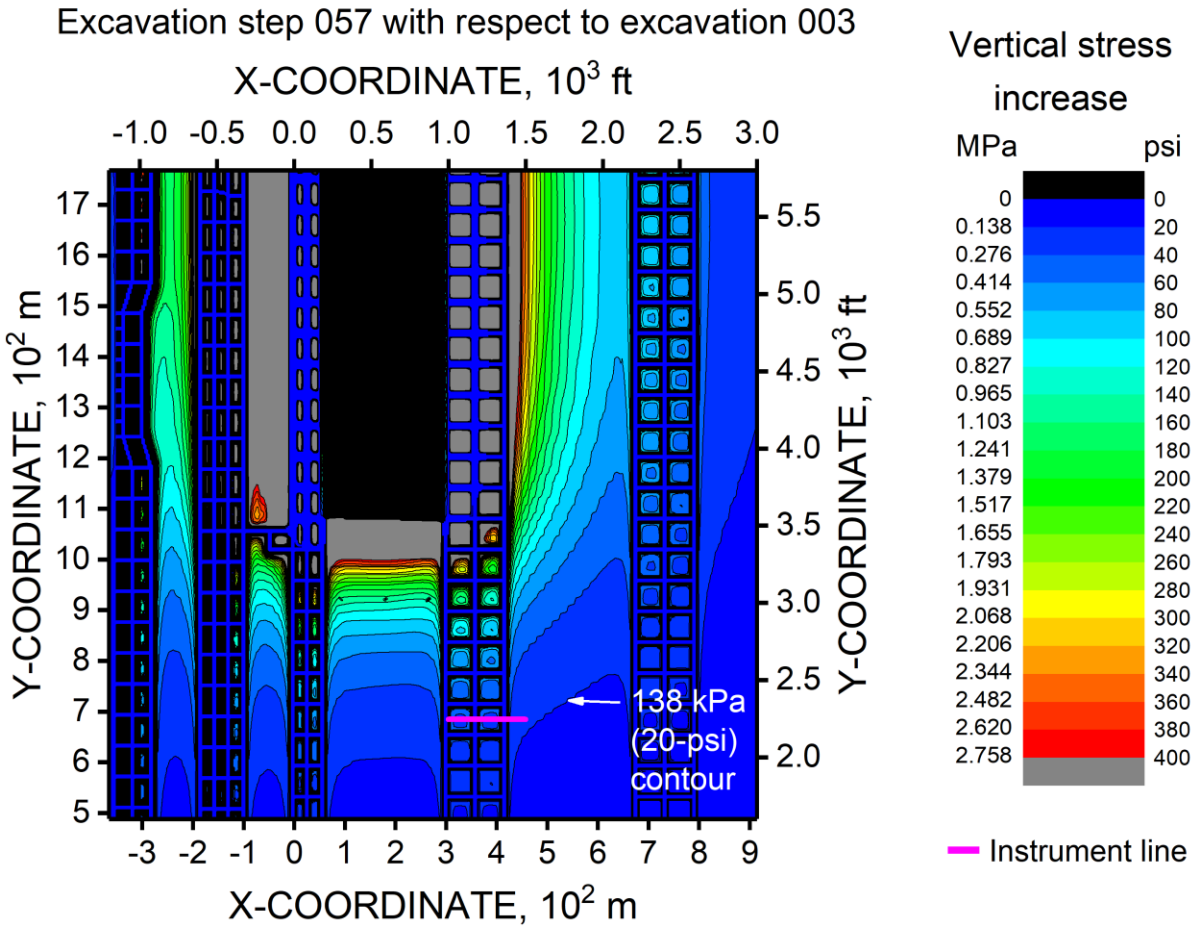

Figure 25. Stress increase contour graph for MulsimNL/Large model of Panel 1 of Mine A using Mark-Bieniawski [Mark and Chase 1997] 6.21-MPa (900-psi) strength model.

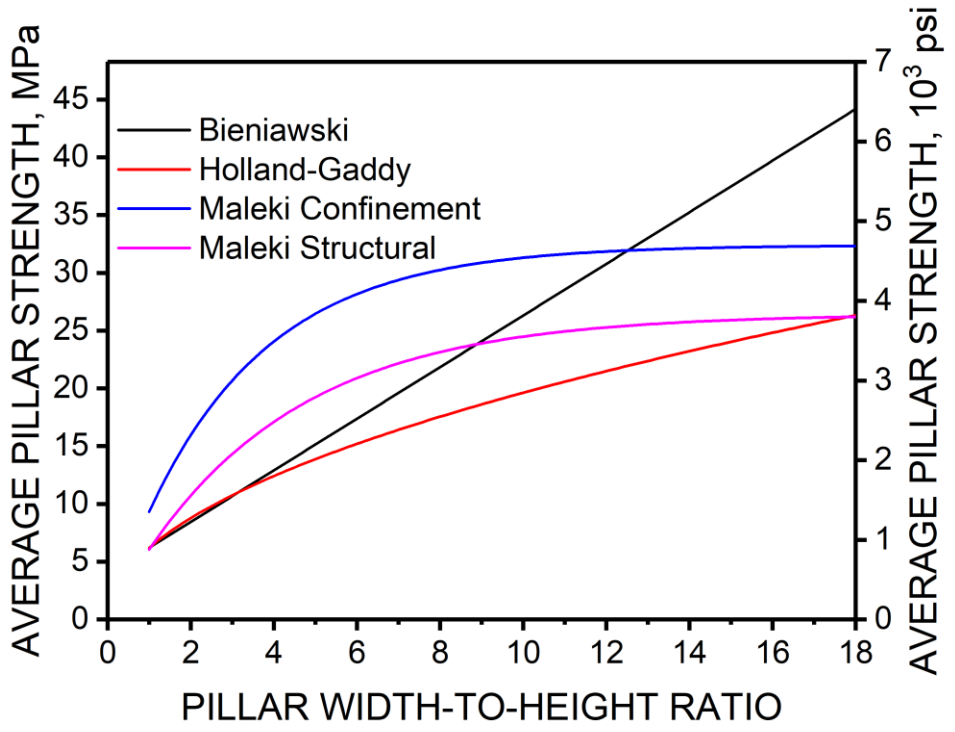

Figure 26. Pillar strengths versus pillar width-to-height ratio. Coal strength is set at 6.21 MPa (900 psi) where applicable.

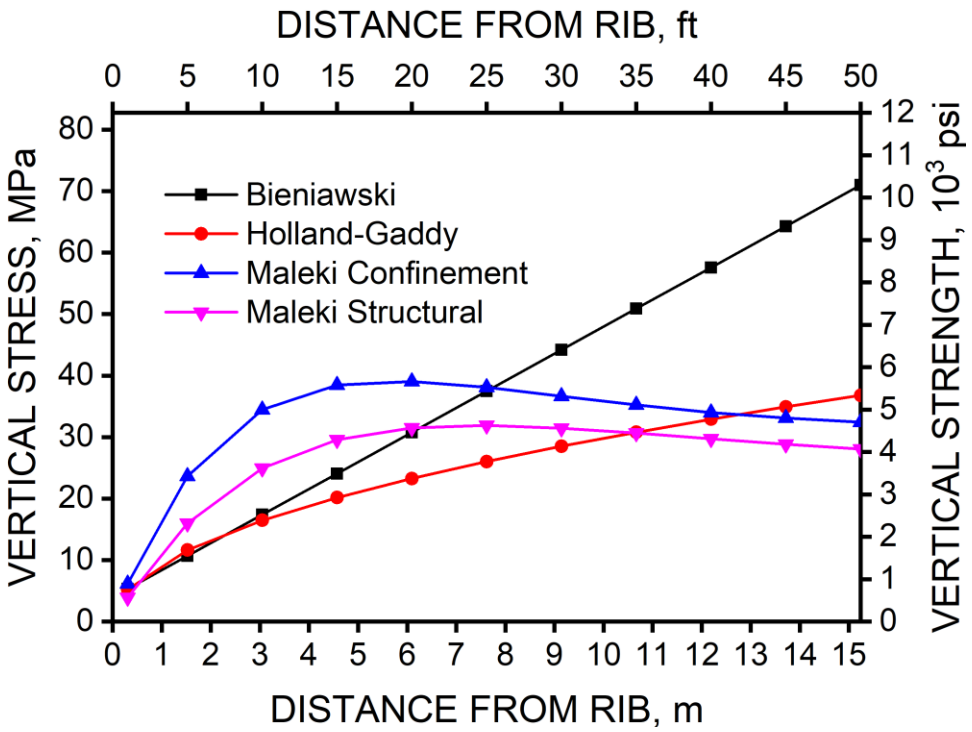

Figure 27. Strength by distance from the rib in a coal pillar for various pillar strength criteria shown in Figure 26.

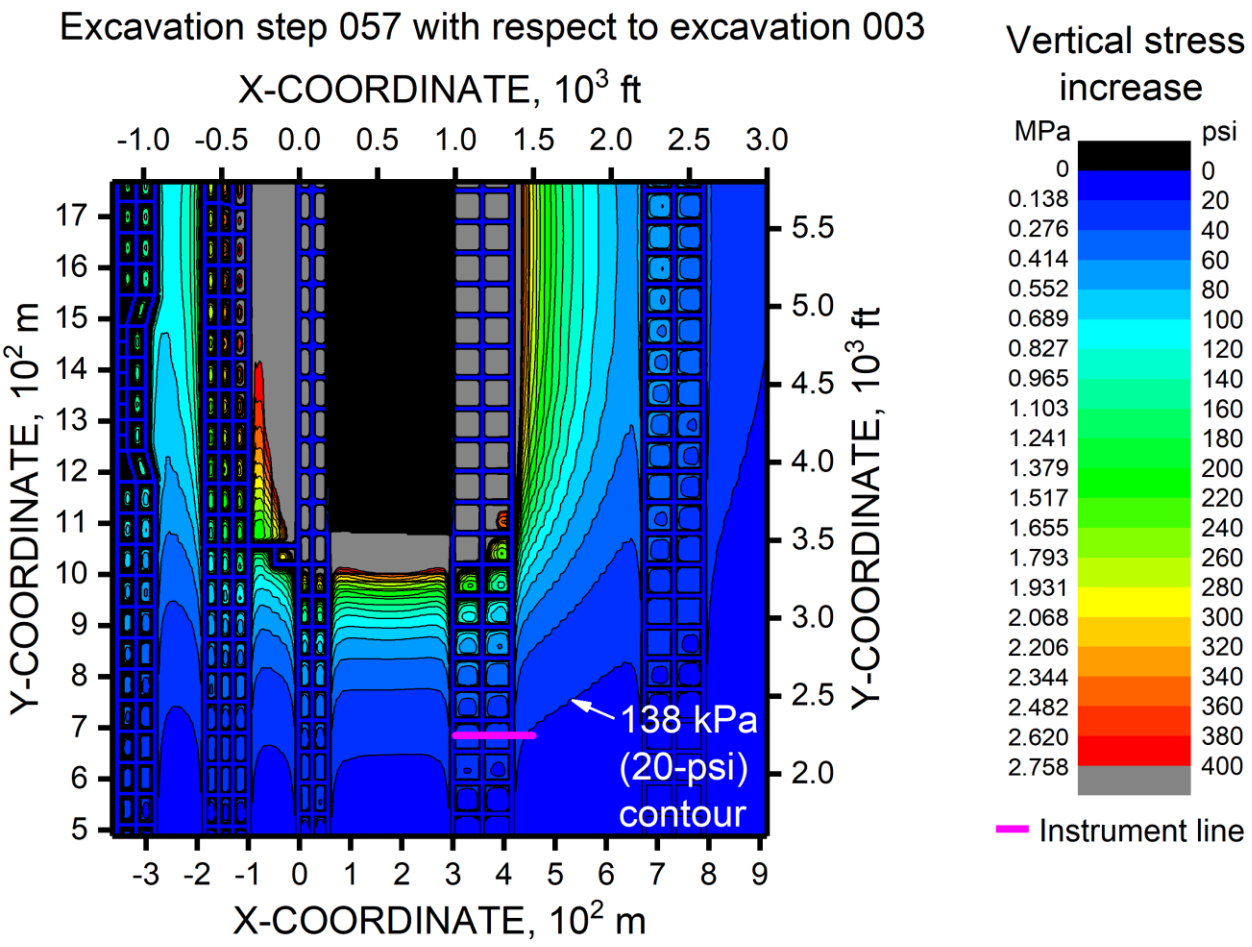

Figure 28. Stress increase contour graph for MulsimNL/Large model of Panel 1 of Mine A using Mark-Bieniawski 9.65-MPa (1,400-psi) strength model [Mark and Chase 1997].

Elastic Models

Because common yield models were inadequate, an elastic model was applied. However, loading of the ribs was too high. To compensate for some minor yielding of the rib, the elastic modulus of the first and second rings of "yield" elements were reduced to 60% and 80% of the full amount. Figure 29 shows contours of stress increase over the prepanel state when the face was approximately located when the BPCs detected a 138-kPa (20-psi) increase in cell pressure. In the figure, the contours are only perturbed slightly near the gate roads. Moreover, the threshold contour appears to run very close to the instrument line. Surprisingly, the rock mass elastic properties for this model were determined by thickness-weighted averaging of the properties chosen for each member above the DU Seam in the idealized stratigraphic column. Figure 29 shows that the initial set of elastic properties was close enough to achieve initial calibration to LTD.

The result says something more about the seam material model. The behavior at the ribs is softened compared to that of the interior of the pillar. However, if a strength material model is to be used, then the secant stiffness of the combined elastic and hardening portions of the strength-strain model must show similar reduction compared to the full amount of elastic modulus.

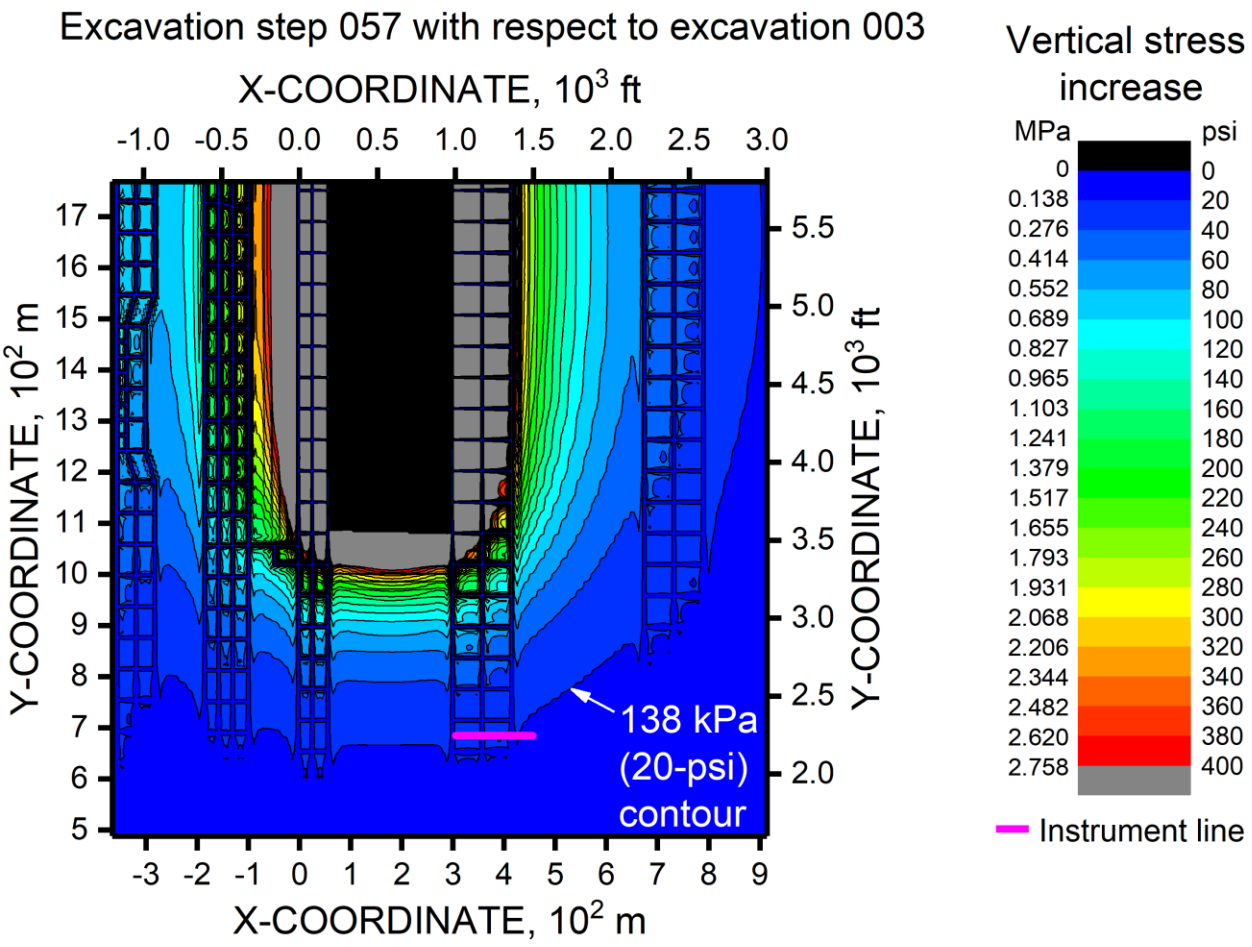

Figure 29. Stress increase contour graph for MulsimNL/Large model using elastic seam material with the elastic modulus in the first and second rings of elements reduced to 60% and 80% of the full amount to simulate the effect of some yielding near the ribs.

Another way of illustrating the necessity of this softening effect is to compare measured LTD with "synthetic" LTD—that is, LTD as calculated from various models. Figure 30 shows measured LTD by BPC location along with LTD calculated at these locations from various models. Also shown is the average LTD of the two sites. The models having yielded coal near the ribs could not calculate a load transfer distance. For synthetic LTDs calculated by interpolation from two elements, one having yielded, the results were low, causing the synthetic LTDs at more interior locations to be too high compared to the measured LTDs. Only the elastic model with less stiff outer rings of elements provided a reasonable match between synthetic and measured LTDs.

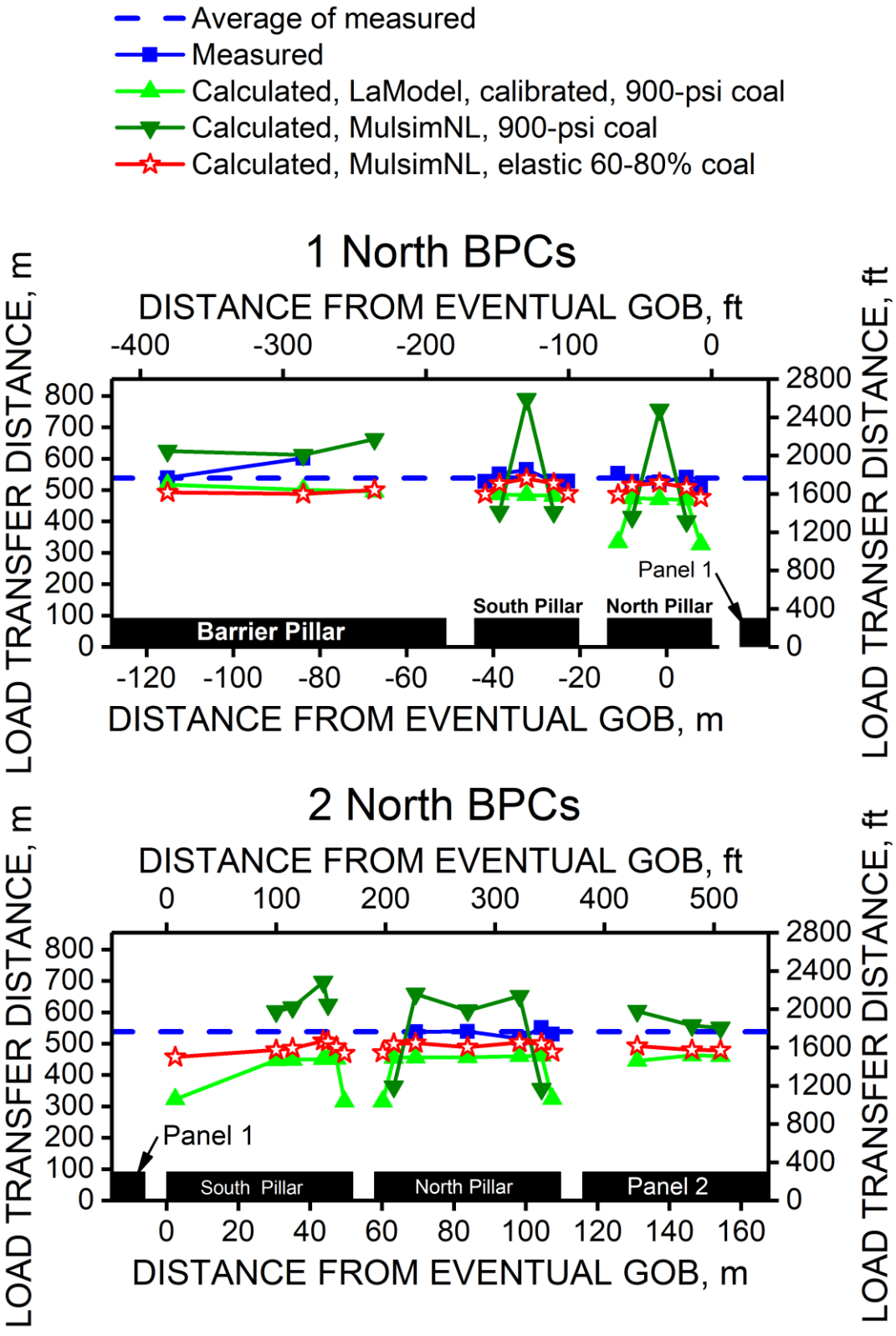

Figure 30. Measured and synthetic load transfer distance by borehole pressure cell location.

At Mine B, the measured LTD was not definitive. However, for modeling calibration, LTD is necessary information. For the purpose of testing model calibration, site H22 was selected as the reference point from which to locate a longwall face in the model that should produce the threshold stress increase resulting from mining of the panel at the H22 site. The longwall face location was determined by averaging data from Table 16. For ranges of distance, the midpoint of each range was used as a site measurement. Weights were assigned: 1 for low confidence, 2 for fair to good confidence of being within the range, and 10 for good confidence. The resulting average distance to the face along the entry was 219.4 m (719.8 ft). Using MulsimNL/Large, a model was constructed in which a face position was 217.9 m (715 ft) inby the H22 instrument site.

Figure 31 shows contours of stress increase calculated by MulsimNL/Large at a face location when the B-12 Panel was being mined. The stress increase is with respect to the stress state just before that panel was mined. The seam material was elastic with the moduli of the outer two rings of elements reduced, as described before. The rock mass material properties used are the same as those used at Mine A. The 138-kPa (20-psi) contour line appears to run approximately through the H22 instrument line, thus indicating that the best-guess properties that calibrated to LTD at Mine A appear to calibrate to LTD at Mine B as well. The uncertainty of the Mine B LTD makes this a weak conclusion, but the result appears to be consistent with that at Mine A.

Because gob stiffness could not be calibrated, two other final gob stiffnesses were used to examine the effect on calibration. The final gob stiffnesses used were 3.134 GPa (454,500 psi), 5.114 GPa (741,700 psi), and 8.343 GPa (1,210,000 psi), and labeled soft gob, default gob, and stiff gob. These stiffnesses are significantly different from each other. Choice of final gob stiffness caused a change in the load transfer distance. However, it was found that rock mass stiffness could be easily recalibrated by adjusting it linearly according to the ratio of the distance from the yield depth around the corner of the gob to the instrument line over the distance along the same path to the threshold contour line.

At this point in the design process, MulsimNL/Large, with the elastic rock mass, appears to provide the closest match to measured LTD, but an elastic seam does not permit calculation of safety factors, and therefore, a simple evaluation of safety or adequacy of the design. The results suggest the need for a material model having strain hardening. This issue is discussed later in this report.

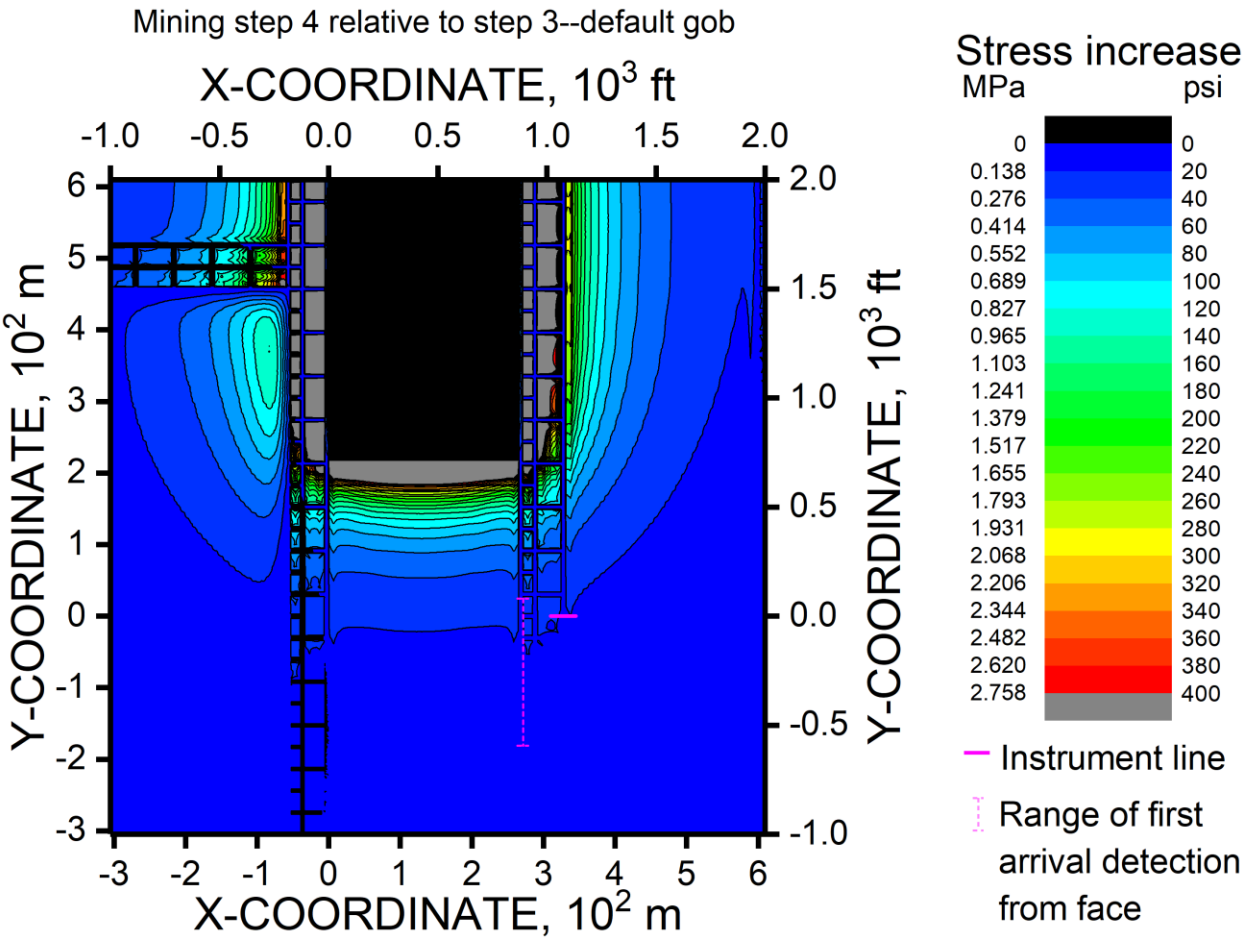

Figure 31. Contours of stress increase with respect to prepanel mining stress of the B-12-Panel at Mine B.

Correlation of Model Results with Ground Condition Survey Data

Results of LaModel and MulsimNL/Large model calculations of entry closure versus ground condition ratings are described and shown in Appendix E. Ground condition ratings had no correlation to model-calculated closures. The difference in ground condition ratings is likely the result of variation in local structure and conditions that could not be represented in the numerical models.

BPC Calibration Issues Identified with MulsimNL/Large Model

Data from borehole pressure cells (BPCs) have been reduced under specific assumptions of horizontal to vertical loading by one of two methods: the Lu method [1984] or the Babcock method [1986]. Appendix F describes these methods. Because the Babcock method is nonlinear, it was preferred in this report for representing stress from BPCs. However, as detailed in Appendix F, neither calibration method provides reasonable stress values, at least at higher cell pressure. This is likely the result of the coal not behaving elastically. The BPC appears to act as a hard inclusion, so that stresses determined from raw BPC data were higher than were possible as estimated with the MulsimNL/Large elastic model with the modulus reduced in the outer two rings to simulate some yielding effect near the ribs.

Therefore, the reader must be aware that the amount of stress calculated from raw BPC data is not accurate, particularly at higher stress. Even so, trends of BPC curves still provide information about the seam material behavior and are useful in evaluating potential strength models for coal.

The results of this study indicate that it would be useful to develop a softer inclusion instrument having the stable characteristics of the BPC. Such an instrument must be rugged, but not depend on elastic behavior of host material to be accurate.

FLAC^{3D} Method Calibration

Larson et al. [NIOSH 2020] described various caving conditions in Panel 1 at Mine A ranging from immediate initial caving with gradual caving behind the longwall shields to intact roof sagging until it contacted the floor. In addition, they reported different roof, rib, and floor conditions in the gate roads; most notably, significant floor heave was observed in the headgate of Panel 1, but no significant floor heave was observed in that panel's tailgate. For these reasons, another conceptual model that allowed failure in the roof and floor was desired. FLAC^{3D} was used because it is capable of following the mechanics of failure in the roof, floor, and coal, and it was thought that the elastic rock mass of the displacement discontinuity codes may not be sufficient to follow significant failure mechanisms. Moreover, the authors of this report wanted to try a new caving simulation capability that was available in FLAC^{3D} and was described earlier, even though caving calibration had not yet been investigated and was not performed in this study.

Calibration of a FLAC^{3D} Panel Model using Stress and Strain from a FLAC^{3D} Pillar Model

A FLAC^{3D} pillar model, using half symmetry, comprised of the mine roof, coal seam, and mine floor with 6.1-m (20-ft) entries and crosscuts, was used to produce average stress-versus-strain relationships for sections of the pillar. These relationships, and those for locations in the pillar at which BPCs were located, as shown in Figures 32 and 33, were used to calibrate a FLAC^{3D} panel model. Mine strata were included in the model for thicknesses as small as one foot, and for this reason, it was called a "detailed pillar model."

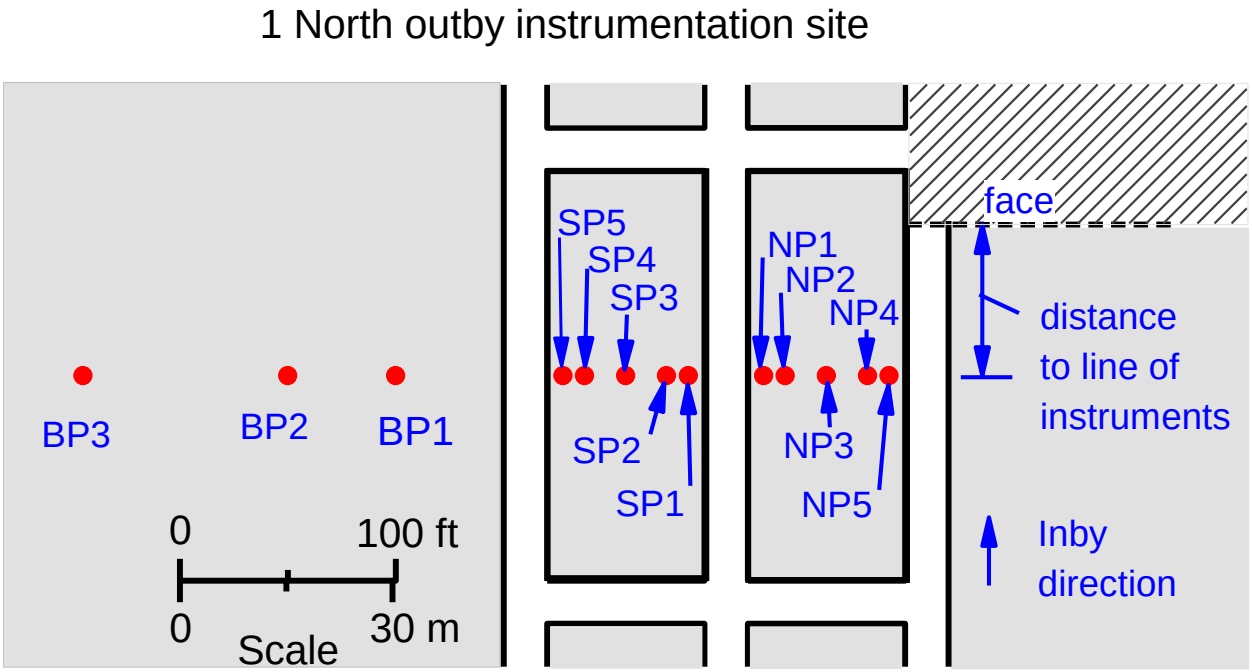

Figure 32. Plan view of 1 North pillars and barrier pillar at outby site with locations of borehole pressure cells.

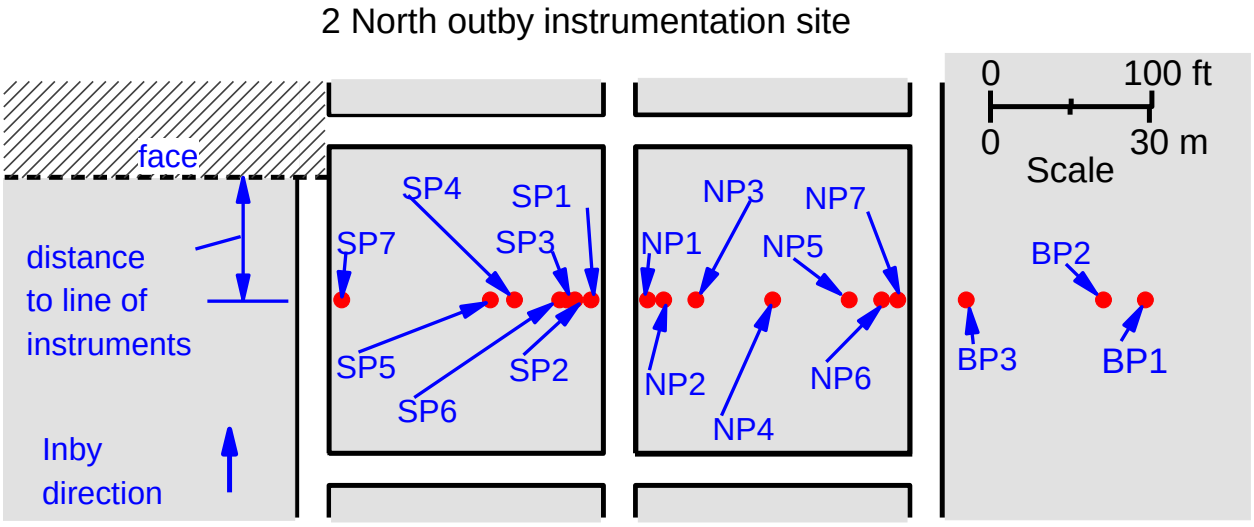

Figure 33. Plan view of 2 North pillars and barrier pillar at outby site with locations of borehole pressure cells.

Hoek-Brown parameters used for the DU Coal Seam and the other remaining coal seams are listed in Table 19. These properties were determined by [Esterhuizen et al. 2010b]. Rock properties used in the models, listed in Table 20, were based on modeling experience of Utah stratigraphy, and a small reduction of those properties was estimated as appropriate for western Colorado. A survey of material properties in the literature [Farmer 1968; Pariseau 2012; Goodman 1989; Blyth and de Freitas 1984; Sheorey 1997; Maleki et al. 2007] found these

properties within reasonable range, even if high for field scale. Cohesion, tension, and dilation angle were strain softened over a plastic shear strain of 0.04. Residual cohesion for each rock type was 10% of its initial value. The initial and residual dilation angles for the three rock types were 5° and 0°, respectively.

Table 19. Elastic properties and Hoek-Brown constitutive equation parameters for all coal used in detailed pillar models

Parameter	Amount
UCS (laboratory scale)	20.00 MPa (2901 psi)
Young's modulus	3.00 GPa (435 ksi)
Poisson's ratio	0.25
a	0.65
m	1.47
m, residual	1.00
s	0.07
s, residual	0.001
Peak-to-residual strain	0.04

Strain-softening ubiquitous joints (subiquitous joints is the abbreviated term used by Itasca Consulting Group, Inc. to refer to this strength model), with their properties listed in Table 21, were used to reduce rock properties from laboratory-scale to field-scale. Peak-to-residual plastic shear strain was 0.005 for those properties that were softened. Interfaces between strata were not applied.

Table 20. Material properties used in FLAC^{3D} detailed pillar and panel models

Material	Young's Modulus, GPa (ksi)	Poisson's ratio	Angle of internal friction,°	Cohesion, MPa (psi)	Unconfined compressive strength, MPa (psi)	Tensile strength, MPa (psi)	Specific density, kg/m^3 (lb/ft^3)
Sandstone	34.47 (5,000)	0.2	40	13.05 (1,893)	56.0 (8,120)	5.6 (812)	2,595 (162)
Mudstone	27.6 (4,000)	0.25	30	16.26 (2,344)	56.0 (8,120)	5.6 (812)	2,595 (162)
Shale	20.68 (3,000)	0.35	20	19.6 (2,843)	56.0 (8,120)	5.6 (812)	2,595 (162)

Table 21. Subiquitous joint properties

Rock type	Cohesion, MPa (psi)	Residual cohesion, MPa	Angle of internal friction, °	Residual angle of internal friction, °	Tension, MPa (psi)	Residual tension, MPa	Dilation angle,°	Residual dilation angle,°
Sandstone	13.05 (1,893)	0	35	35	5.6 (812)	0	5	0
Mudstone	0.16 (23.4)	0	25	25	0	0	5	0
Shale	0.07 (10.0)	0	15	15	0	0	5	0

The mine roof was meshed with 0.3 m (1-ft) thick cubes to a height of 9.8 m (32 ft) above the seam and 10.4 m (34 ft) below the seam. For zones located greater than 9.8 m (32 ft) above the seam, the vertical dimension of each successive zone increased by a ratio of 1.9. Zones located greater than 10.4 m (34 ft) below the seam increased in the vertical dimension by a ratio of 1.9.

The zone side-length in the horizontal direction was 0.3 m (1 ft) for all zones. Load was applied with a constant boundary velocity at the top of the mesh of 2.54×10^{-6} m/s (0.0001 in/s), where the time unit is not actual, but used in the static calculation process toward equilibrium.

The average vertical stress-versus-strain relationship produced from the detailed pillar model was used to describe the stress-versus-strain relationship for selected zones that comprised pillars in a FLAC^{3D} panel model, called "equivalent elements." Stress in the DU Seam of the pillar model was monitored at midheight, and strain was measured from 7.6 m (26 ft) below the seam to 7.9 m (25 ft) above the seam. Substituting the stress-versus-strain relationship of the multistrata pillar model into equivalent elements in the panel model provided a means of incorporating the effect of complex stratigraphy in a coarsely discretized panel model.

Figure 34 illustrates the use of this method for a 1 North pillar. In this case, a FLAC^{3D} zone that represents one pillar and one-half of the adjacent entries in the panel model is indicated by the outer red perimeter line. This pillar is subdivided into four equivalent elements. The stress-versus-strain relationship produced from section A of the detailed pillar model is used to describe the pillar behavior for the four detailed cases as shown in Figure 34. For the larger 2 North pillars, two stress-versus-strain relationships are developed from the detailed pillar model, indicated by "A" and "B" in Figure 35.

When the panel model is executed, corner node displacements of each equivalent element are monitored. These displacements for adjacent equivalent elements that represent half of a pillar, including half of a crosscut, are used to determine strain for half of a pillar (e.g., equivalent elements "A" on the upper side of the equivalent element in Figure 34). This strain can be related to calculated strain of the underlying detailed pillar model. Average stress is calculated by averaging the stress of the equivalent elements that compose the same half-pillar. This stress can be related also to the stress calculated by the underlying detailed pillar model. The resulting stress-versus-strain relationship is then used to extract stresses from the detailed pillar model for borehole pressure cells (BPCs) as described in the next section.

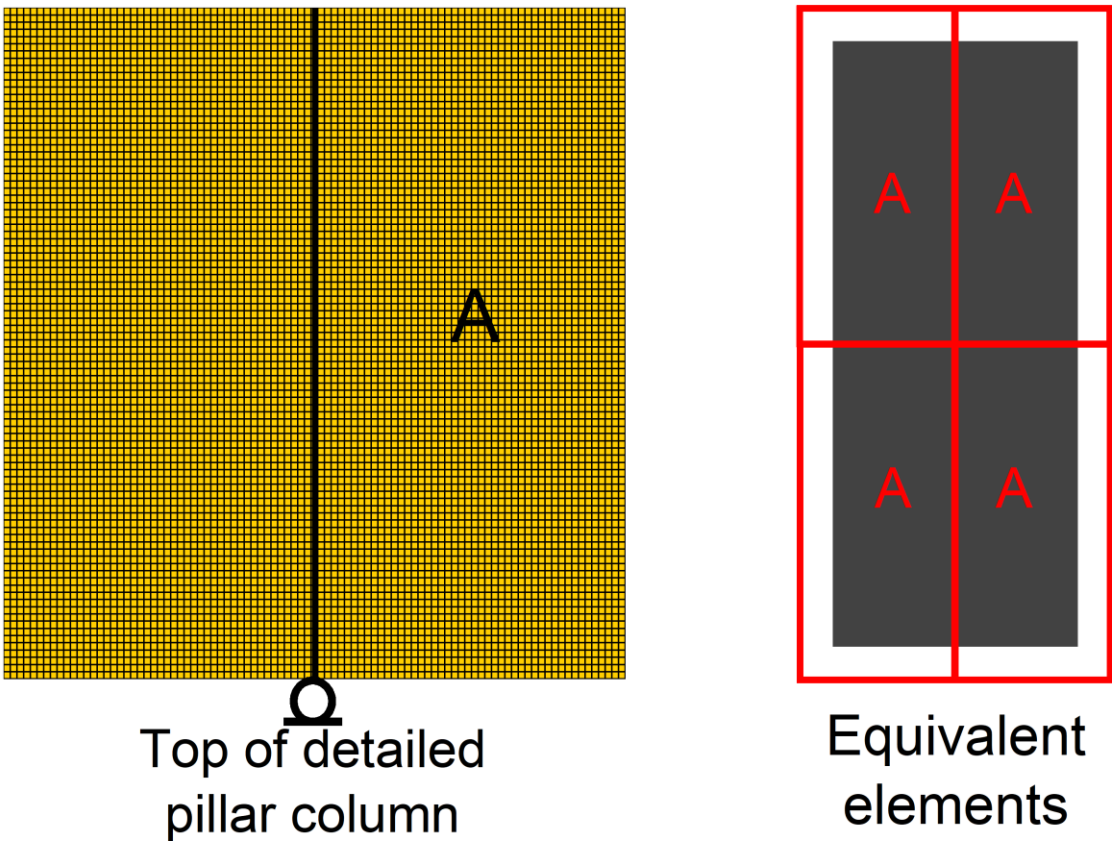

Figure 34. Plan view of 1 North detailed pillar model with monitored section "A" used in FLAC^{3D} panel model equivalent element.

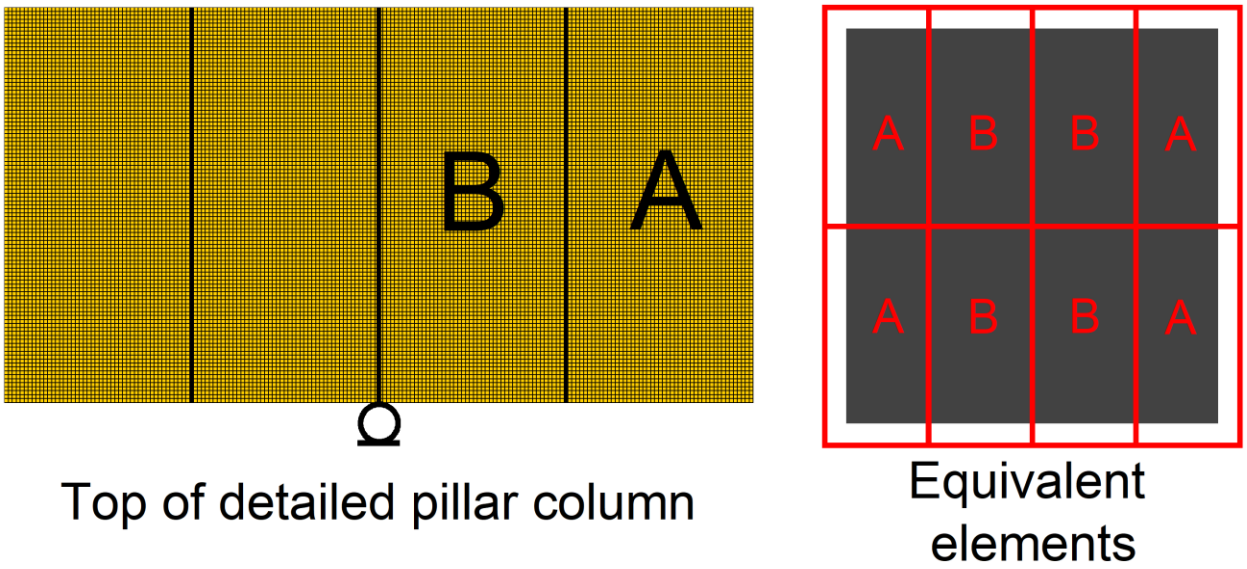

Figure 35. Plan view of 2 North detailed pillar model with monitored sections "A" and "B" used in FLAC^{3D} panel model equivalent element.

Procedure for Comparing Modeled-to-Measured Stress Changes

Stress changes from the FLAC^{3D} panel model with equivalent elements were compared to measured stress changes by implementing the steps listed below. The term "face distance" refers to the distance between an instrument location and longwall face along the entry adjacent to the panel. "Prepanel mining vertical stress" in a pillar refers to average vertical stress in a pillar at a face distance large enough such that mining-induced stress has not yet occurred. For example, 1,790 m (5,900 ft) was a sufficient distance for the 1 North panel model. The steps for comparison are:

1. A FLAC^{3D} detailed pillar model was run. The average vertical stress for section "A" and vertical stress for BPC locations (interpolated from adjacent zones) were plotted as a function of the average closure strain of section "A" as shown in Figure 36.
2. A FLAC^{3D} panel model containing equivalent elements was run, and the resulting average vertical stresses and strains for equivalent elements that contained BPCs were paired in a spreadsheet with face distance.
3. The prepanel-mining vertical stress on an equivalent element containing instruments was used to calculate average pillar force on this pillar, and in turn, this force was used to calculate average vertical stress when applied to the detailed pillar. The resulting stress on the detailed pillar was larger than that of the equivalent element because of the smaller horizontal cross-sectional area of the detailed pillar.
4. The closure strain corresponding to the premining detailed pillar stress was located on the stress-versus-strain plot as shown in Figure 36. For this example, the average vertical stress is 21.1 MPa (2,909 psi), and the corresponding closure strain is 0.009.
5. The vertical BPC strain changes corresponding to longwall face advance as recorded in the spreadsheet were located along the BPC curves in Figure 36, and the associated stresses were obtained for each BPC. For example, the strain change from prepanel mining, i.e., a face distance of -1790 m (-5900 ft), to a face distance of -30.5 m (-100 ft) is 0.007. The corresponding stress at this strain increment for the BPC labeled NP1 is 6.89 MPa (1,000 psi).
6. Step 5 was repeated for various face distances, and the resulting stresses were plotted along with measured stresses as a function of face distance as illustrated in Figure 37, and with results of several other models. The comparison between measured and numerically calculated stresses served as a guideline for altering the parameters in the Hoek-Brown failure equation and improving the match between calculated and measured BPC stresses.

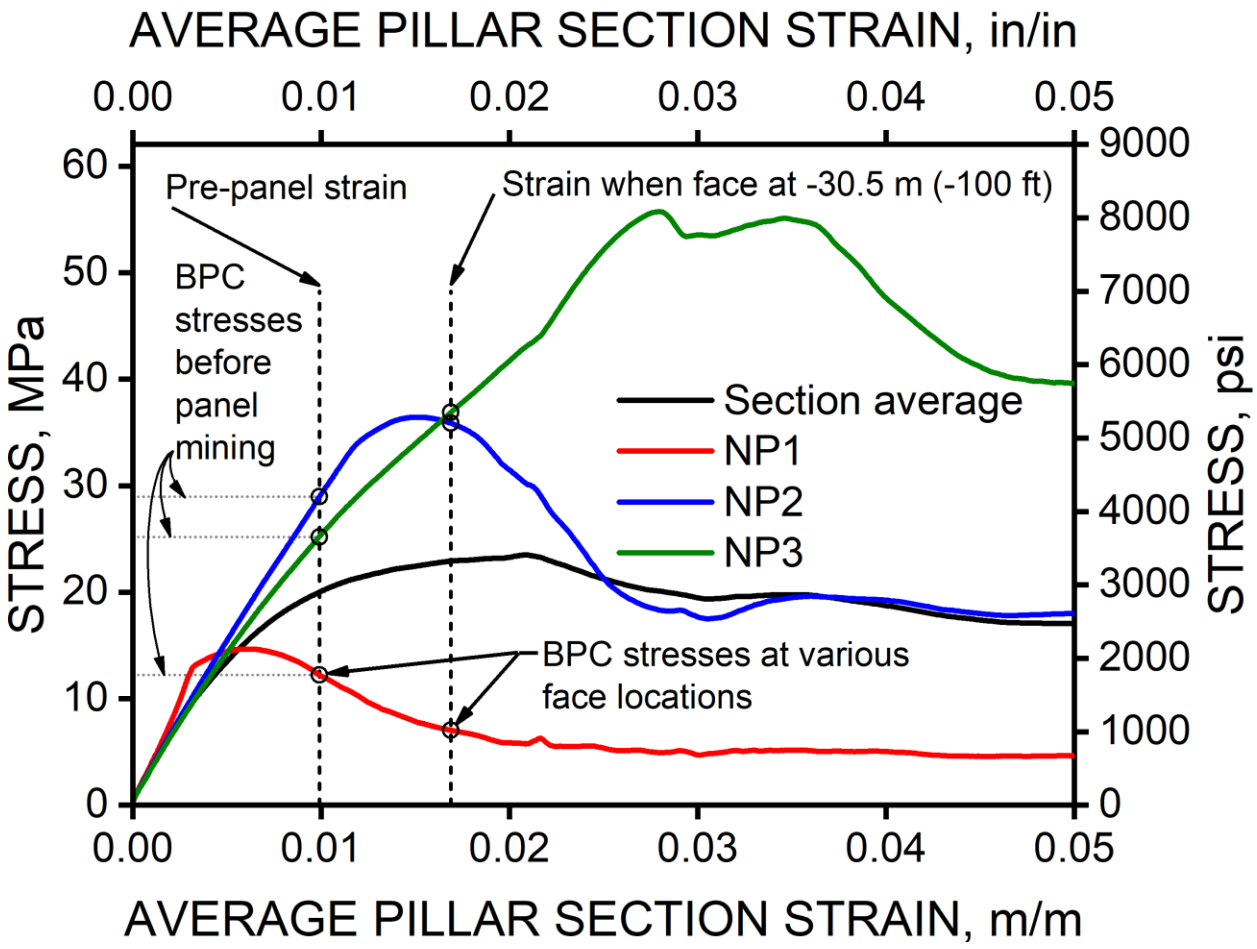

Figure 36. Stress-versus-strain for a quarter section "A" of a 1 North coal pillar model and calculated BPCs labeled NP1-3.

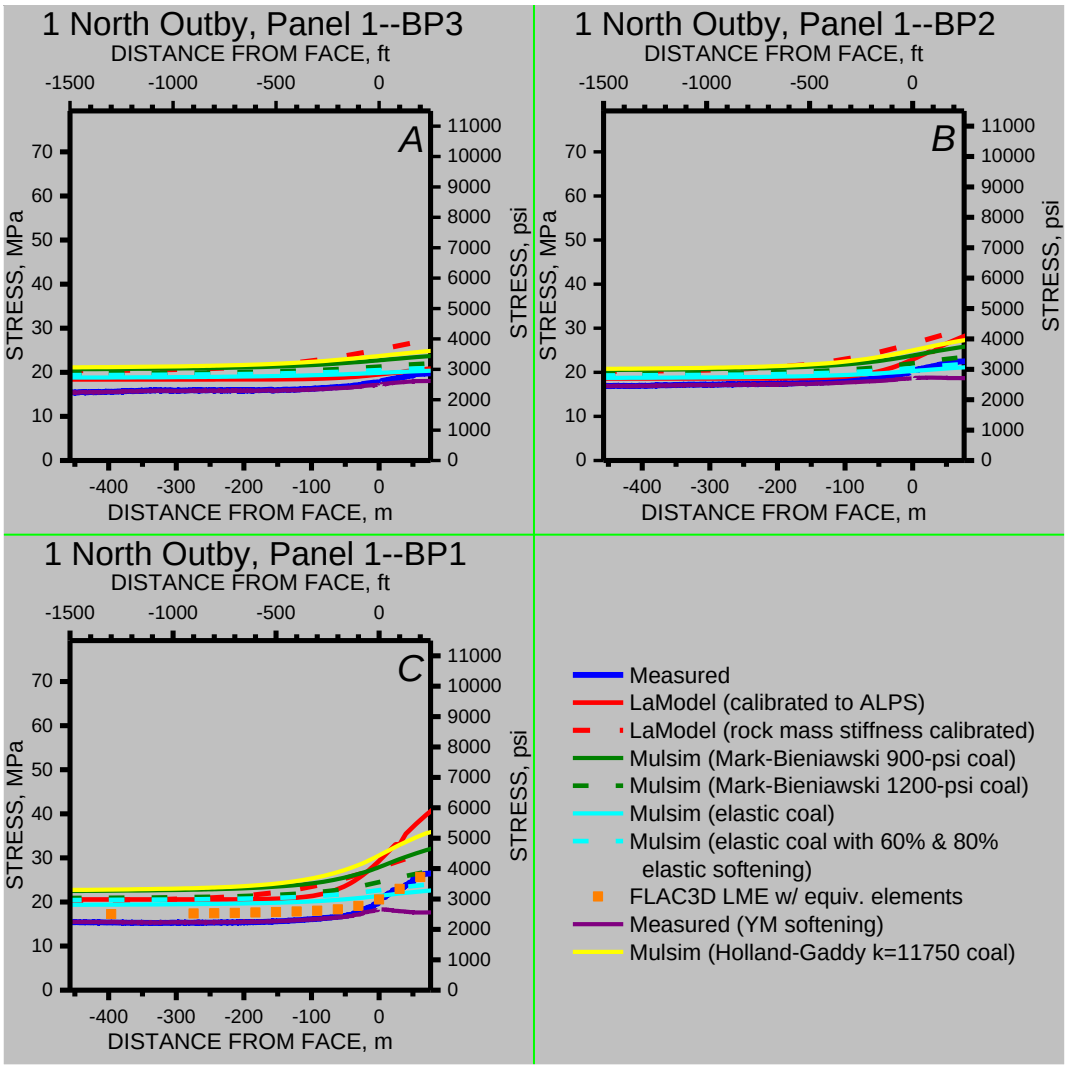

Figure 37. Vertical stress calculated from measurements and models for BPC locations at the 1 North outby site, barrier pillar. *A*, Instrument BP3; *B*, BP2; and *C*, BP1.

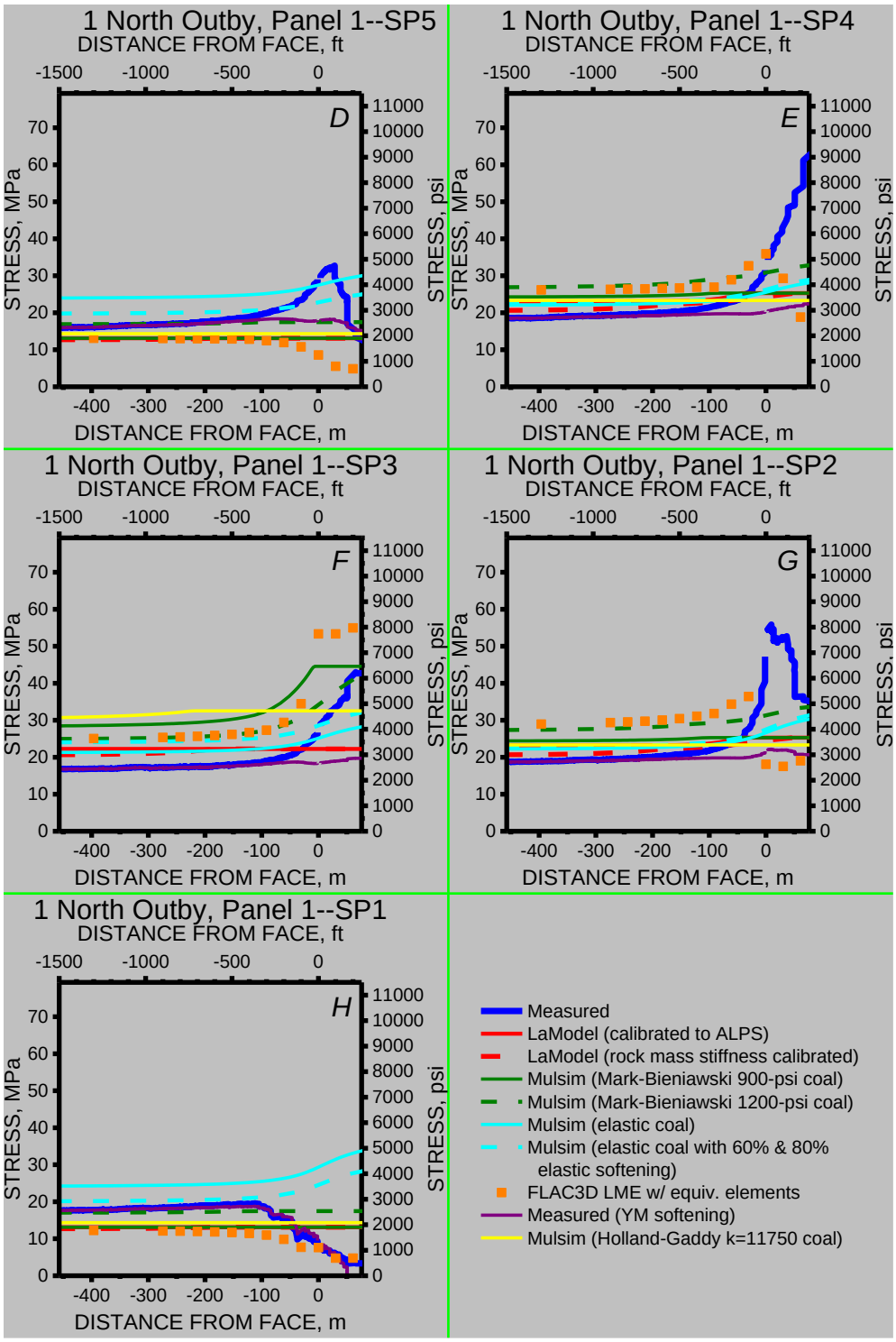

Figure 37 (continued). Vertical stress calculated from measurements and models for BPC locations at the 1 North outby site, south pillar. *D*, Instrument SP5; *E*, SP4; *F*, SP3; *G*, SP2; and *H*, SP1.

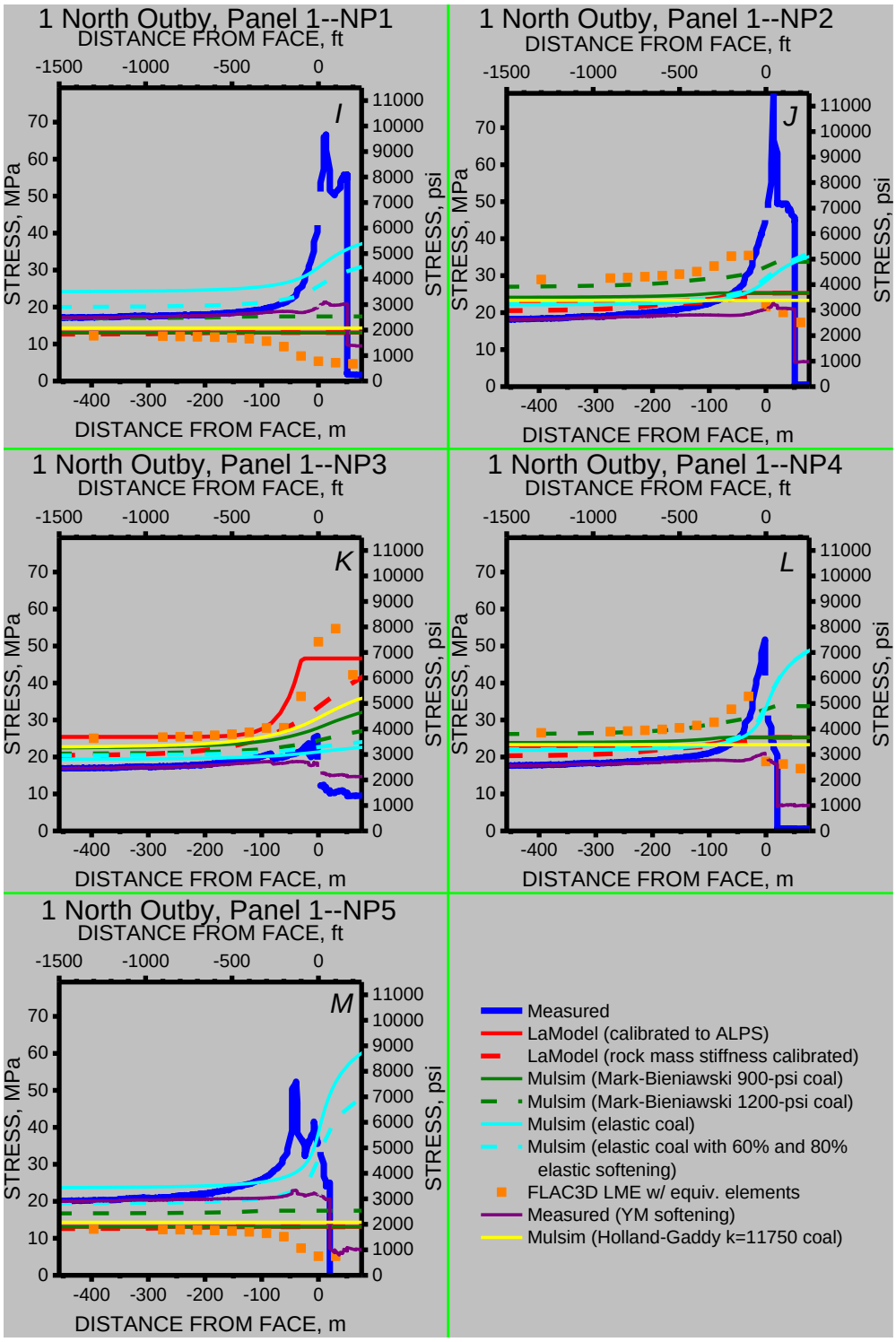

Figure 37 (continued). Vertical stress calculated from measurements and models for BPC locations at the 1 North outby site, north pillar. *I*, Instrument NP1; *J*, NP2; *K*, NP3; *L*, NP4; and *M*, NP5.

A comparison between trend lines of measured and numerically calculated stresses in 1 North pillars and the barrier pillar follows.

Instruments located in the barrier pillar (BP1):

- Plots of measured and numerically calculated stresses for BP1 are nearly identical. (Stress and strain were not monitored in the detailed model for BP2 and BP3.)

Instruments located 2.3 m (7.5 ft) from the pillar rib (SP1, SP5, NP1, and NP5):

- Stresses measured by SP5, NP1, and NP5 peaked near the instrument line. Numerically calculated stresses were at their post-failure values at -457.2 m (-1,500 ft) from the instrument line and decreased near the instrument line.
- Both measured and numerically calculated stresses for SP1 were at their post-failure values at a face distance of -457.2 m (-1500 ft), and their trend lines have similar shapes.

Instruments located 5.3 m (17.5 ft) from the pillar rib (SP2, SP4, NP2, and NP4):

- Numerically calculated peak stresses occur before measured peak stresses with respect to face distance.

Instrument location near the pillar center (SP3 and NP3):

- Plots of measured and numerically calculated stresses for SP3 have similar shapes. Numerically calculated stresses peak before measured stresses.
- Measured peak stress for NP3 is about 60% of the stress measured by SP3, which suggests that NP3 did not function correctly, or there is an anomalous weak zone in the pillar at this location.

The same procedure that was used to compare measured to numerically calculated stress changes for pillars in 1 North pillars was used to compare these stresses in 2 North pillars. Vertical stresses at BPC locations in the 2 North detailed pillar model shown in Figure 33 and average vertical stresses for sections “A” and “B” pictured in Figure 35 were calculated. Numerically calculated and measured stress changes are plotted as a function of face distance in Figure 38, along with results of several other models.

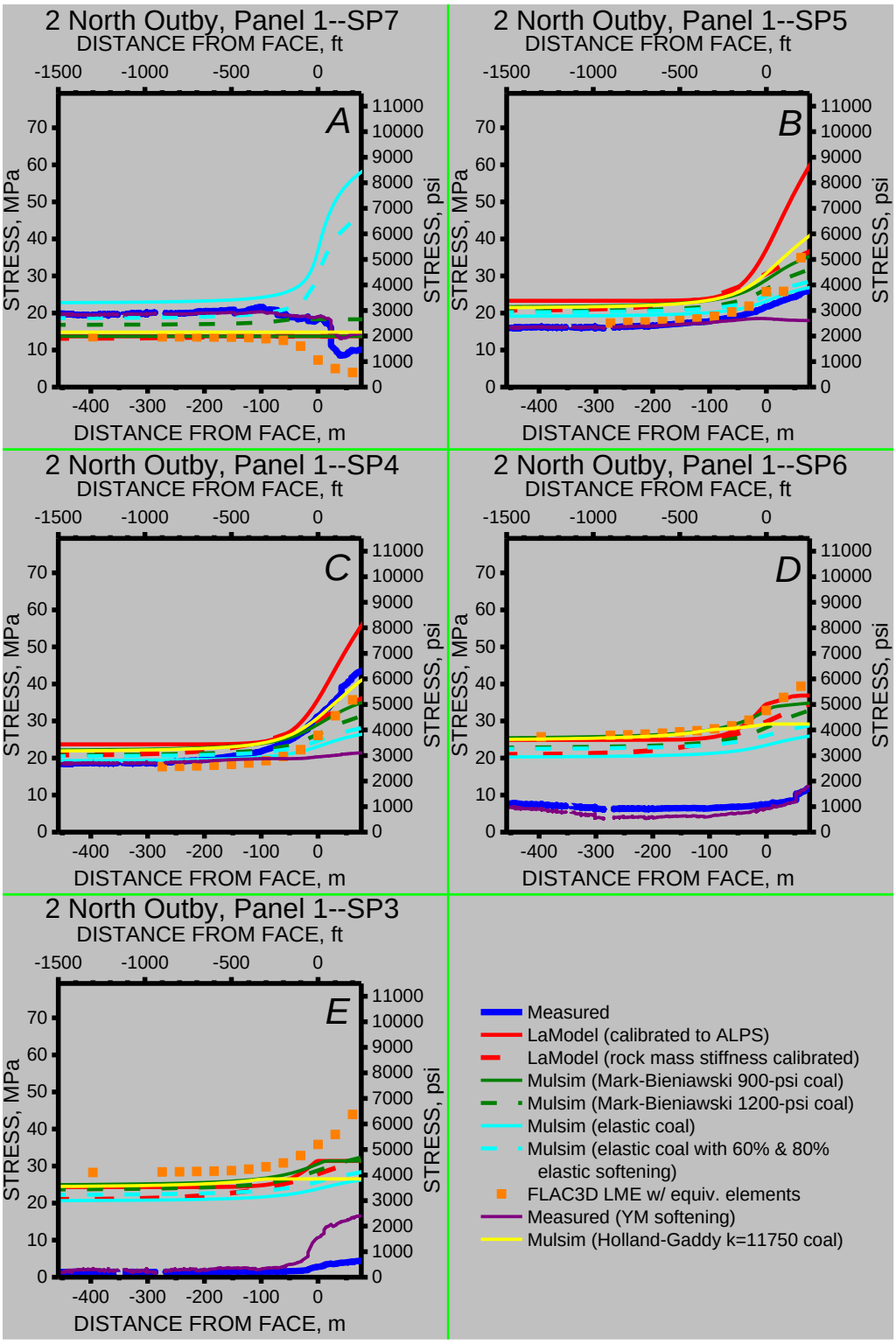

Figure 38. Vertical stress calculated from measurements and models for BPCs in 2 North, south pillar, north pillar, and next panel. *A*, Instrument SP7; *B*, SP5; *C*, SP4; *D*, SP6; and *E*, SP3.

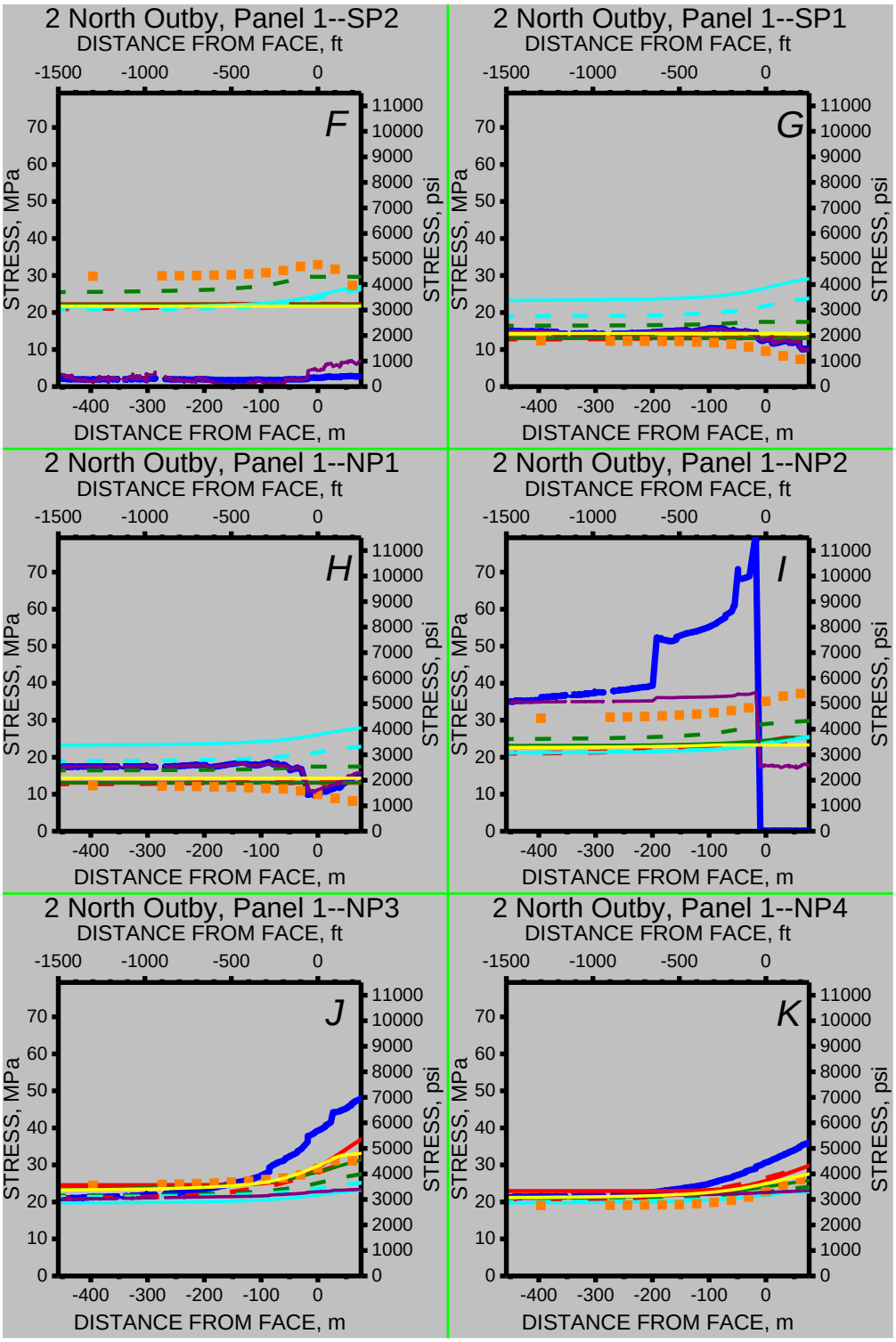

Figure 38 (continued). Vertical stress calculated from measurements and models for BPCs in 2 North, south pillar, north pillar, and next panel. *F*, Instrument SP2; *G*, SP1; *H*, NP1; *I*, NP2; *J*, NP3; and *K*, NP4.

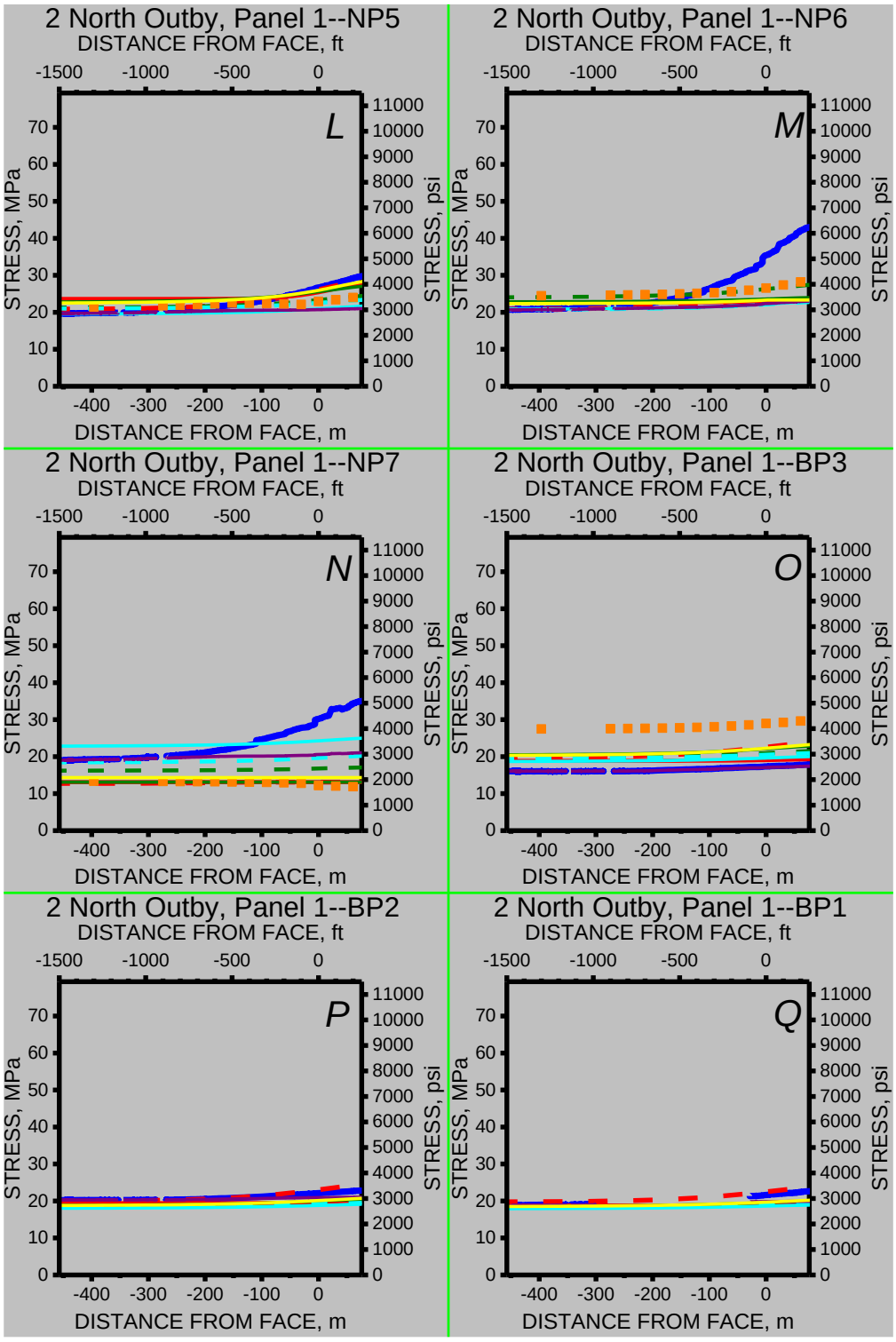

Figure 38 (continued). Vertical stress calculated from measurements and models for BPCs in 2 North, south pillar, north pillar, and next panel. *L*, Instrument NP5; *M*, NP6; *N*, NP7; *O*, BP3; *P*, BP2; and *Q*, BP1.

A comparison between measured and model-calculated stresses in 2 North pillars and Panel 2 follows.

Instruments located in Panel 2 (BP3):

- Plots of measured and numerically calculated stresses for BP3 are similar in shape. (Stress and strain were not monitored in the detailed model for BP2 and BP1.)

Instruments located 2.3 m (7.5 ft) from the pillar rib (SP1, SP7, NP1, and NP7):

- Both measured and numerically calculated stresses for SP1, SP7, and NP1 were at their post-failure values at a face distance of -457.2 m (-1,500 ft).
- Measured stresses remain relatively unchanged for NP7, up to a face distance of -274.4 m (-900 ft), and then increase, whereas numerically calculated stresses were at their post-failure values at a face distance of -457.2 m (-1,500 ft) and decrease at a face distance of about -91.4m (-300 ft).

Instruments located 4.6 to 11.4 m (15 to 37.5 ft) from the pillar rib (SP2, SP3, SP6, NP2, NP3, NP5, and NP6):

- The low magnitude of instrument readings from SP2, SP, and SP6 at a face distance of -457.2 m (-1,500 ft) indicates these instruments probably malfunctioned.
- Measured stresses for NP2 and NP3 increased more rapidly than numerically calculated stresses at face distances near the instrument line.
- Plots of measured and numerically calculated stresses from NP5 are nearly identical.

Instrument locations near the pillar center (SP4, SP5, and NP4):

- Plots of measured and numerically calculated stresses are similar in shape.

The most prominent difference between modeled and in situ pillar behavior indicated by comparing plots of measured and numerically calculated vertical stresses is that modeled pillar ribs fail before in situ pillar ribs as the longwall approaches the instrument line. An increase in pillar strength achieved by increasing σ_c in the initial Hoek-Brown yield envelope could possibly address this discrepancy.

A comparison between measured and numerically calculated stress changes was made to determine if a modification of the elastic modulus of the coal pillar could improve the match between modeled and in situ pillar behavior. Calculated-versus-measured vertical stress changes at instrument locations were plotted as shown in Figures 39 and 40. Only prefailure stress changes, as indicated by the instrument readings, were used. The small r^2 values of 0.54 and 0.32 for 1 North and 2 North, respectively, indicate that measured and numerically calculated stress changes are not well correlated and, thus, the slope of the regression line cannot be used to provide a factor to modify the elastic modulus of the coal pillar.

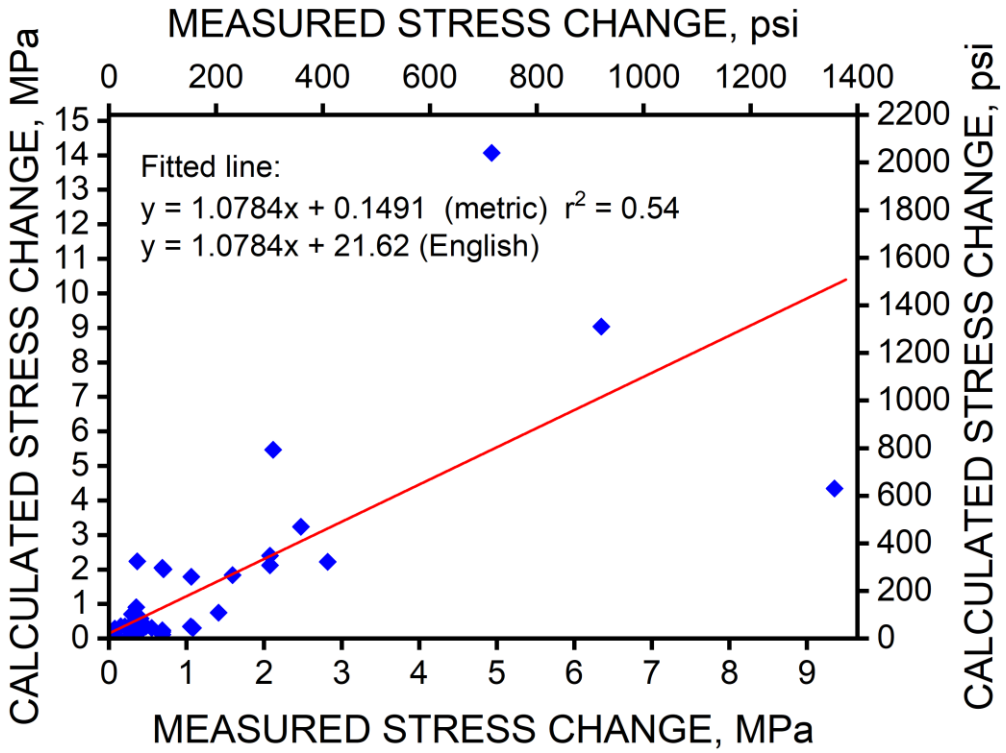

Figure 39. Calculated vertical stress with FLAC^{3D} versus measured vertical stress (reduced with Babcock method) for 1 North pillars and barrier pillar.

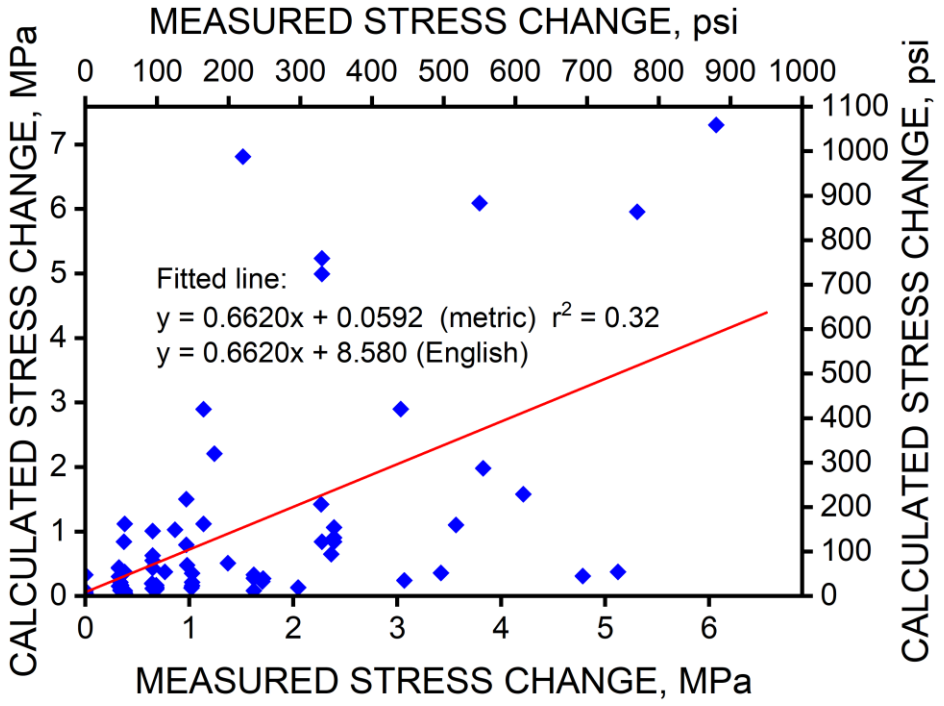

Figure 40. Calculated vertical stress with FLAC^{3D} versus measured vertical stress (reduced with Babcock method) for 2 North pillars and Panel 2.

MulsimNL/Large with Coal and Floor Properties from FLAC^{3D} Pillar Model Calibration

Calibration of Hoek-Brown Properties for Coal

The first step in the calibration of the MulsimNL/Large panel model was to determine the parameters for the Hoek-Brown equation [Hoek et al. 2002] for coal. This equation was selected as the strength criterion because it has been used to successfully model the in situ behavior of coal pillars [Duncan Fama et al. 1995; Esterhuizen et al. 2010b; Jaiswal and Shrivastva 2009, 2012], and is written as follows:

$$\sigma_1 = \sigma_3 + \sigma_c \left(m \frac{\sigma_3}{\sigma_c} + s \right)^a, \tag{27}$$

where σ_1 = maximum principal strength,

σ_3 = least confining stress,
σ_c = uniaxial compressive strength of intact rock, and
m, s, and a = empirically derived parameters.

Hoek-Brown parameters were first calibrated to a scaled stress-versus-strain curve from one of Bieniawski's in situ unconfined compression tests of a pillar with a width-to-height ratio of 2.78 [Bieniawski and Van Heerden 1975] by using FLAC^{3D}. Experimental stresses and strains were halved to adjust to the U.S. empirical coal strength of 6.2 MPa (900 psi) [Mark and Barton 1996] as shown in Figure 41. The 20.6 MPa (2,985 psi) capacity of Bieniawski's in situ pillar was reduced to 10.2 MPa (1475 psi) for the target curve and is consistent with Bieniawski's equation, represented by Equation 28, when 6.2 MPa (900 psi) is used for strength. The specific weight of the coal was 1,281 kg/m^3 (80 lb/ft^3).

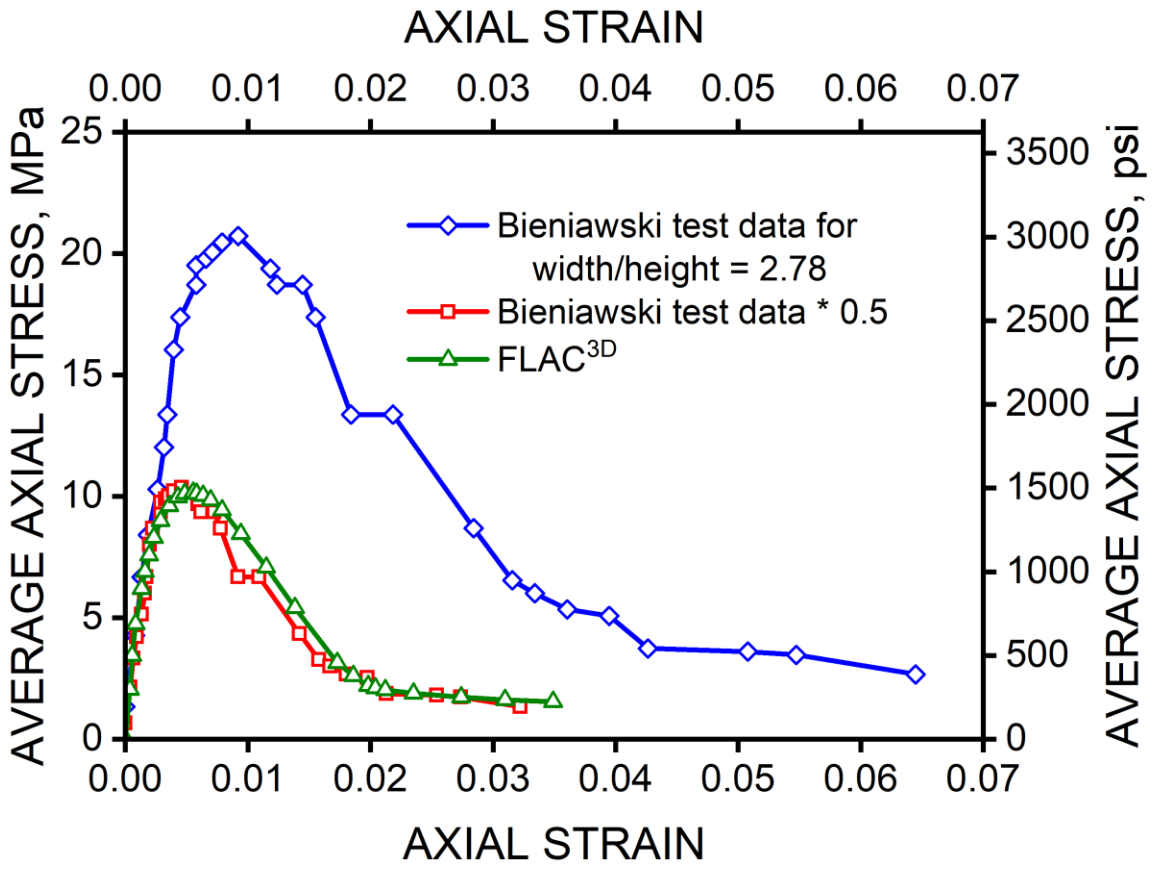

Figure 41. Experimental, re-referenced, and model curves showing average pillar stress versus strain for width-to-height of 2.78.

Bieniawski's pillar equation is

$$\sigma_P = UCS_{cube}\left(0.64 + 0.36\frac{w}{h}\right), \tag{28}$$

where σ_P = average pillar capacity,

UCS_{cube} = unconfined compressive strength of a coal cube with side length = 1.5 m (5 ft),

w = width of a square pillar, and

h = height of a square pillar

A FLAC^{3D} model was constructed of the mine roof, coal pillar, and mine floor at Mine A using quarter symmetry, as shown in Figure 42. The model did not include detail of stratigraphy but simulated one average material for the roof and another for the floor. It was then exercised to calibrate the Hoek-Brown parameters. The strata above the seam was constructed of mesh layers having thicknesses, from bottom to top, of 3, 3.7, 14.6, and 26.8 m (10, 12, 48, and 88 ft) and side lengths of 0.3, 0.6, 1.2, and 2.4 m (1, 2, 4, and 8 ft), respectively. The mine floor was symmetrical with respect to the roof, except that the thickness of the 2.4-m (8-ft) zone layer was increased to 78 m (256 ft) to decrease the influence of boundary conditions. Load was applied by a constant velocity boundary condition at the top of the mesh of 2.54×10^{-6} m/s (0.0001 in/s).

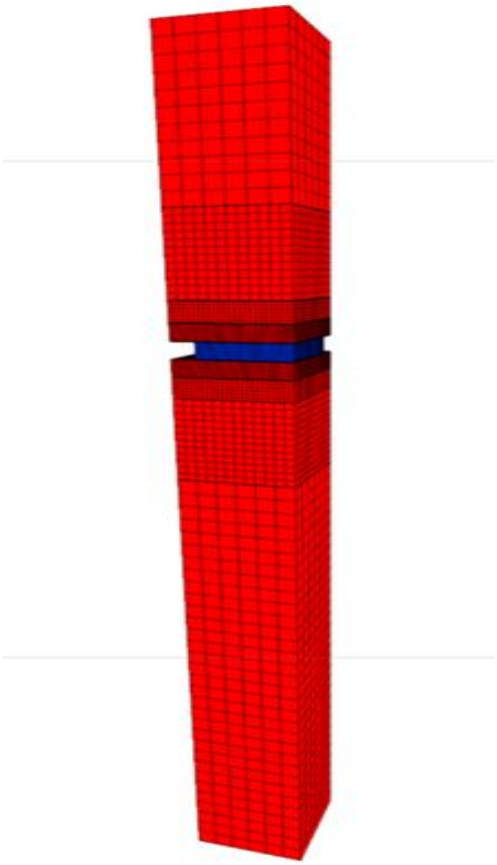

Figure 42. FLAC^{3D} zones for mine floor, coal seam, and mine roof.

The roof and floor in the numerical model were kept elastic with typical sandstone properties of 20.68 GPa ($3x10^6$ psi) for the modulus [Pariseau 2012], 2,595 kg/m^3 (162 lb/ft^3) for specific density, and 0.25 for Poisson's ratio. Initial Hoek-Brown parameters developed by Esterhuizen et al. [2010b], who used parameter softening, were adjusted in the FLAC^{3D} model until a stress-versus-strain plot for the coal pillar produced by FLAC^{3D} matched Bieniawski's experimental curve as shown in Figure 41 [Tesarik et al. 2013].

These calibrated parameters, listed in Table 22, were then used in FLAC^{3D} pillar models with various width-to-height ratios to ensure that modeled strengths were acceptably close to pillar strengths produced by Bieniawski's empirical strength equation. The match between the two sets of strength data was acceptable up to a width-to-height ratio of 8 as shown in Figure 43. The maximum pillar width-to-height ratio used in Bieniawski's tests was 3.4, which indicates that the use of these calibrated Hoek-Brown parameters in FLAC^{3D} produce realistic pillar behavior.

Table 22. Elastic properties and Hoek-Brown constitutive equation parameters used in models

Parameter	Amount
UCS (laboratory scale)	20.3 MPa (2950 psi)
Young's modulus	3.79 GPa (550 ksi)
Poisson's ratio	0.25
a	0.65
m	1.47
m, residual	0.36
s	0.07
s, residual	0.001
Peak-to-residual strain	0.051

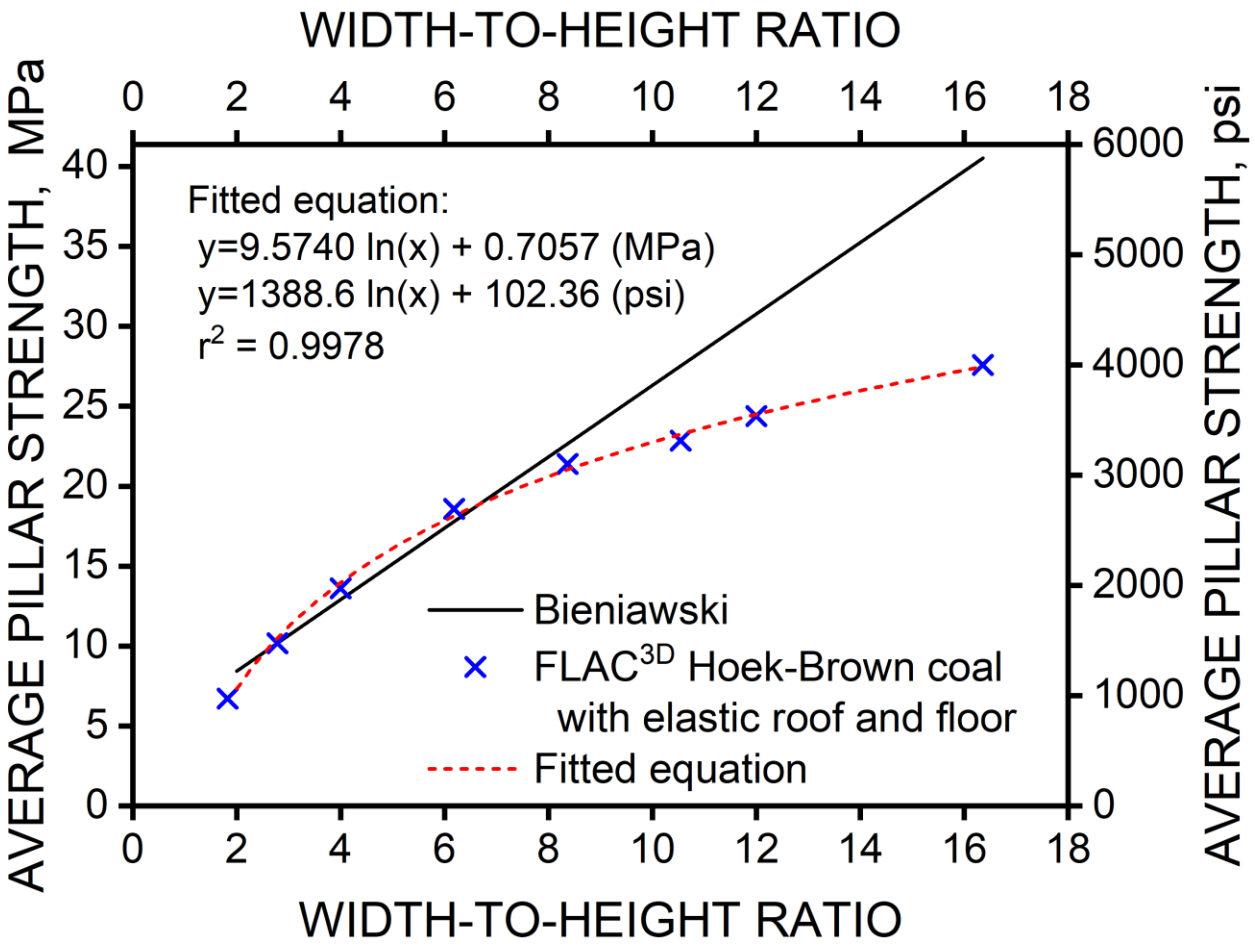

Figure 43. Average pillar strengths from numerical pillar model compared to Bieniawski's pillar strength equation.

Calibration of Floor Properties

The next step in the calibration of the FLAC^{3D} model of the mine floor, coal seam, and mine roof was to calibrate the mine floor to underground observations at Mine A. It was observed that the floor heaved near 51.8-m (170-ft) wide pillars and was absent around 22.3-m (73-ft) wide pillars. Modeled pillar widths of 52.4 m (172 ft) and 23 m (76 ft) were used to simplify mesh construction. These dimensions were considered close enough for purposes of this exercise.

The elastic modulus of the mine roof in the numerical model was reduced to 9.79 GPa (1.42 × 10^6 psi), which is in the lower range of modulus values for shale [Farmer 1968]. Specific density in the mine roof was 2,195 kg/m^3 (137 lb/ft^3) and Poisson's ratio was 0.25.

The floor stratigraphy was represented as a continuum using the Mohr-Coulomb failure criterion [Jaeger and Cook 1976]. This assumption implies that there were no structures in the floor that dominated its response to load. It was also assumed that the stratigraphy of the floor beneath the two pillar sizes was the same. Young's modulus, specific density, and Poisson's ratio for the floor were the same as that of the roof.

Floor strength parameters were varied systematically in a number of models [Tesarik et al. 2013]. The goal was to define a floor strength parameter region that would replicate floor deformation observations for both the 52.4-m (172-ft) wide and 23-m (76-ft) wide pillars. Floor heave was defined as a distortion of the floor where vertical displacement at one point exceeded another by 3.8 cm (1.5 in). Any model whose calculations continued until the pillar at the rib had shortened to 0.9 m (3 ft) (roughly 30% strain) and the relative floor displacement did not exceed 3.8 cm (1.5 in) was designated as having no floor heave. Boundary lines that separate floor heave from no floor heave are plotted in Figure 44 for the two pillar sizes. The property set that results in no floor heave for the 23-m (76-ft) wide pillars is above the red line in the figure and the property set that results in floor heave for the 52.4-m (172-ft) wide pillars is below the blue line. The property set between the two lines produces numerical model results that satisfy observed underground heave or no-heave conditions of the floor for both pillar sizes.

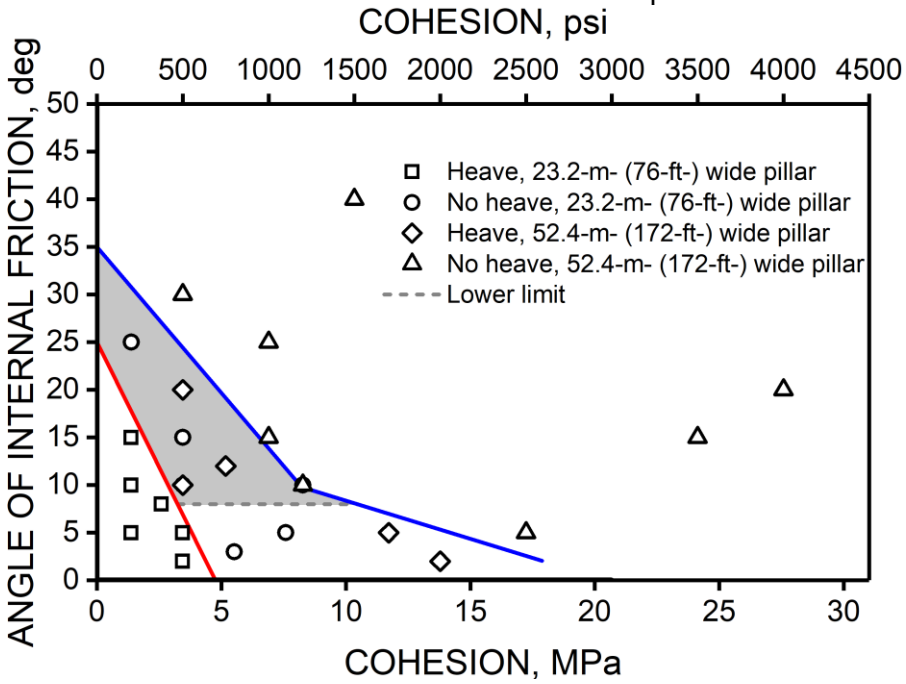

Figure 44. Mine floor property set domain based on floor heave observations.

A lower, horizontal boundary of 8° was added to the material property set based on FLAC^{3D} results and the observed location of floor heave. It was observed that floor heave occurred at the center of the entry and was produced at this location by FLAC^{3D} when the angle of internal friction was greater than 8°.

Application of Floor Properties in a Boundary Element Panel Model

A method of calculating the strength distribution in a pillar as a function of distance from the pillar's rib was developed by Johnson et al. [2014]. They assumed that pillar strength as a function of distance from the pillar's rib has the same shape as average pillar strength expressed as a function of pillar width-to-height ratio. This method was used to establish strength distributions for pillars in a panel-scale boundary element model of a section of Mine A.

The function used in this study that relates average pillar strength to pillar width-to-height ratio was developed using the FLAC^{3D} model as described above. A point near the center of the property set domain in Figure 44, having a cohesion of 3.4 MPa (500 psi) and an angle of internal friction of 15°, was selected for floor properties in the pillar model. The FLAC^{3D} model was run for various width-to-height ratios, and average pillar strength was plotted against pillar width-to-height ratio, as shown in Figure 45. The empirical Holland-Gaddy equation [Holland 1964] was then fit to these data by setting parameter k to 9,700 lb/in$^{3/2}$ in Equation 29. Parameters in the Holland-Gaddy equation are expressed in English units for comparison with other values reported in the literature [Holland 1964; Lawall and Holland 1937]. The Holland-Gaddy equation and their material parameter k are:

$$\sigma_P = \frac{k\sqrt{w}}{h}, \tag{29}$$

where k = Gaddy constant [Gaddy 1956] (lb/in$^{3/2}$) defined in Equation 30

w = pillar width (in),

h = pillar height (in),

σ_P = pillar strength (lb/in^2), and

$$k = S_c\sqrt{d}, \tag{30}$$

where S_c = coal specimen strength, (lb/in^2), and

d = side length of specimen cube (in).

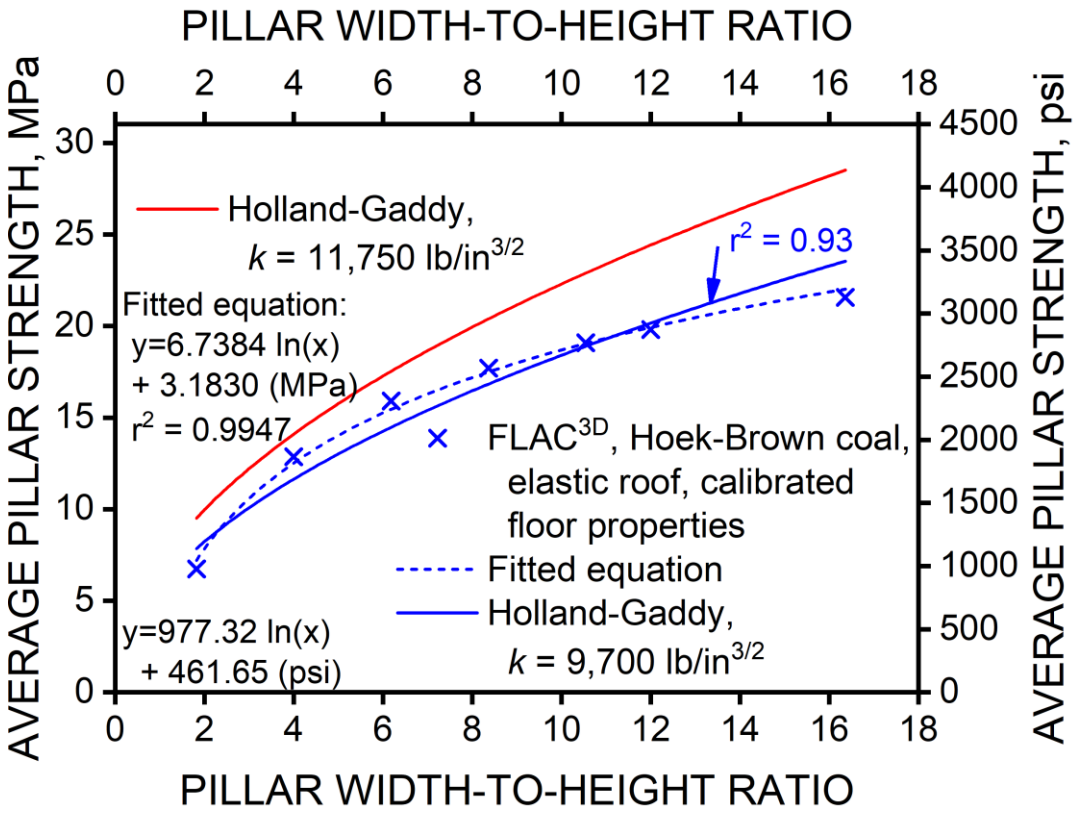

Figure 45. Average pillar strengths from FLAC^{3D} pillar models and Holland-Gaddy equation.

Equation 29 served as the basis for defining the vertical strength distribution as a function of distance from a pillar's rib, using the method developed by Johnson et al. [2014]. This strength distribution, in turn, was used to assign strengths to "cells" or pillar subdivisions in the numerical model MulsimNL/Large [Larson and Whyatt 2013], which is an enlarged version of Zipf's Mulsim/NL [USBM 1992a, 1992b]. Post-yield strength for each cell in the model was assigned the value of yield stress of that cell, and remained constant as a function of strain, i.e. the stress-versus-strain functions for the cells were elastic, perfectly plastic. MulsimNL/Large, herein referred to as just Mulsim, was then used to simulate mining of the longwall panels at Mine A.

The comparison of measured (reduced using the Babcock method [1986]) and numerically calculated vertical stresses for 1 North, shown in Figure 46, indicates that:

- In general, calculated vertical stresses peak before measured stresses with respect to face distance. The term "face distance" refers to the distance along the entry between the location of the line of instruments and the longwall face.
- In most cases, calculated vertical stresses peaked when the longwall face was greater than 457 m (1,500 ft) inby the instruments' locations. This is indicated by the horizontal lines on the graphs, such as is shown in Figure 46, graph D. The line is the residual section of the elastic, perfectly plastic, stress-versus-strain function for the Mulsim cell at an instrument's location.
- The trends of the measured and calculated vertical stress-versus-distance plots for instruments located in the 1 North longwall gate roads were similar, but calculated vertical stresses exceeded measured vertical stresses as shown in Figure 46, graphs A-C.

Comparison of measured (reduced using the Babcock method [1986]) and numerically calculated vertical stresses for 2 North shown in Figure 46 indicates that:

- Calculated vertical stresses peaked before measured vertical stresses at locations near pillar ribs.
- The trends of vertical stress versus face distance were similar in shape for those instruments located near the center of pillars such as instruments SP5, SP4, and NP4 as shown in Figure 47.

Based on the above results, an increase in pillar strength as a function of distance from the rib was needed in the Mulsim model in order to achieve a closer match between calculated and measured vertical stress trend lines. The value of "k" in the Holland-Gaddy equation was increased to 11,750 lb/ft$^{3/2}$ as a first step, then the vertical stress distribution as a function of distance from the rib was calculated using the method developed by Johnson et al. [2014], and the panel-wide model was run again using Mulsim.

In general, increasing k in the Holland-Gaddy equation to 11,750 lb/ft$^{3/2}$ did not significantly improve the match between measured and numerically calculated vertical stress trend lines. Numerically calculated peak stresses still occurred before measured peak stresses with regard to the longwall panel face location. Exceptions to this generality are instrument BP1, located in 1 North as shown in Figure 46, and instruments SP4 and SP5, located in 2 North near the middle of the south pillar as shown in Figure 47. These results emphasize again the need for a material model having strain hardening.

To summarize this candidate procedure, detailed pillar models were calibrated to determine the range of material properties which produced observed floor behavior. A pillar equation was matched to the results. This pillar equation was integrated (see Appendix D for the details of the integration) to determine equations for calculating Mulsim cell strength parameters. Although this method did not work as well as hoped because of the element yielding near the ribs, it might well work for conditions of shallower cover, where strain hardening may not be required. Safety factors could then be determined, and the mine layout design evaluated. Calculation of safety factors is not currently incorporated into MulsimNL/Large but could be easily added.

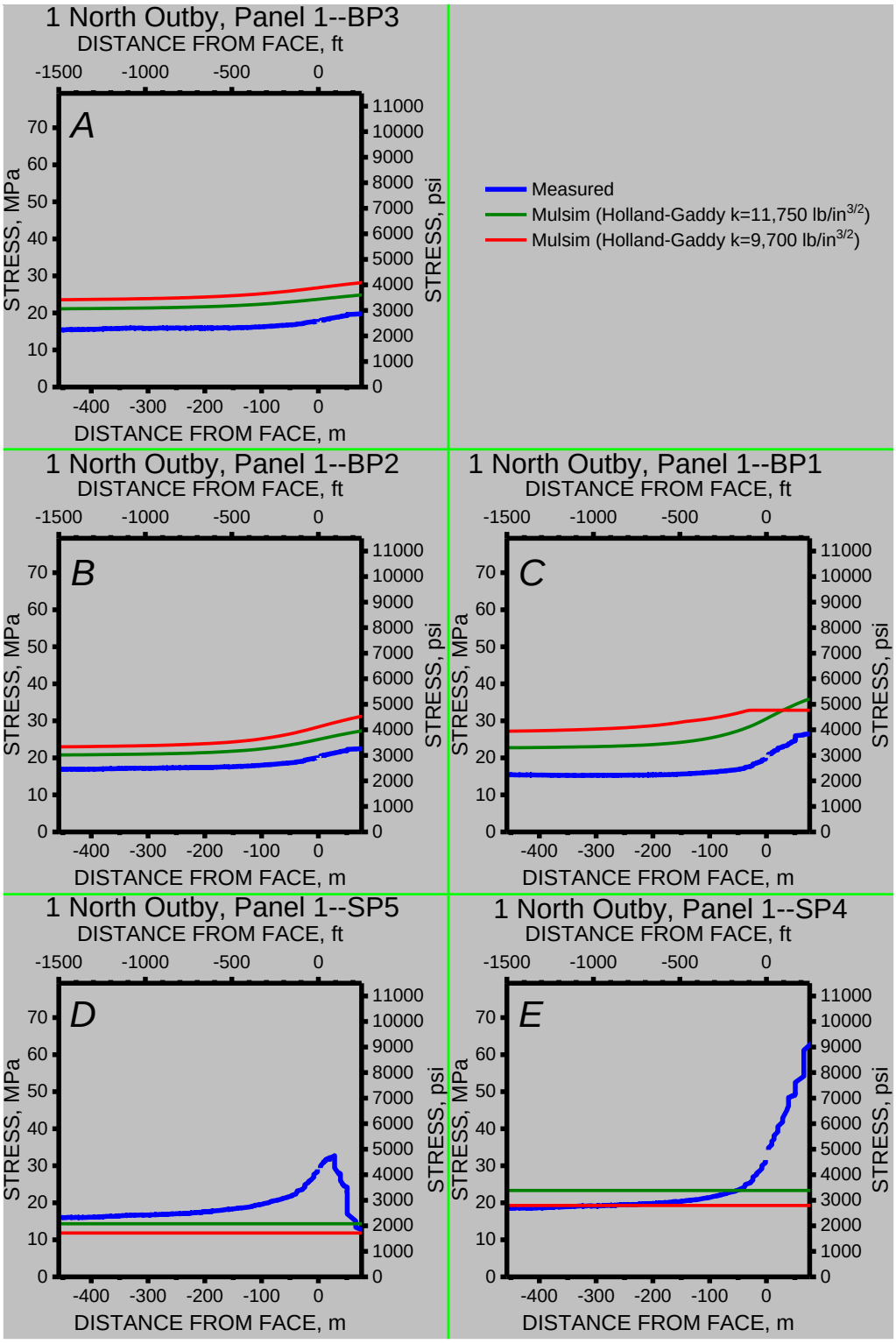

Figure 46. Measured and Mulsim-calculated vertical stress in 1 North section. A, Instrument BP3; B, BP2; C, BP1; D, SP5; and E, SP4.

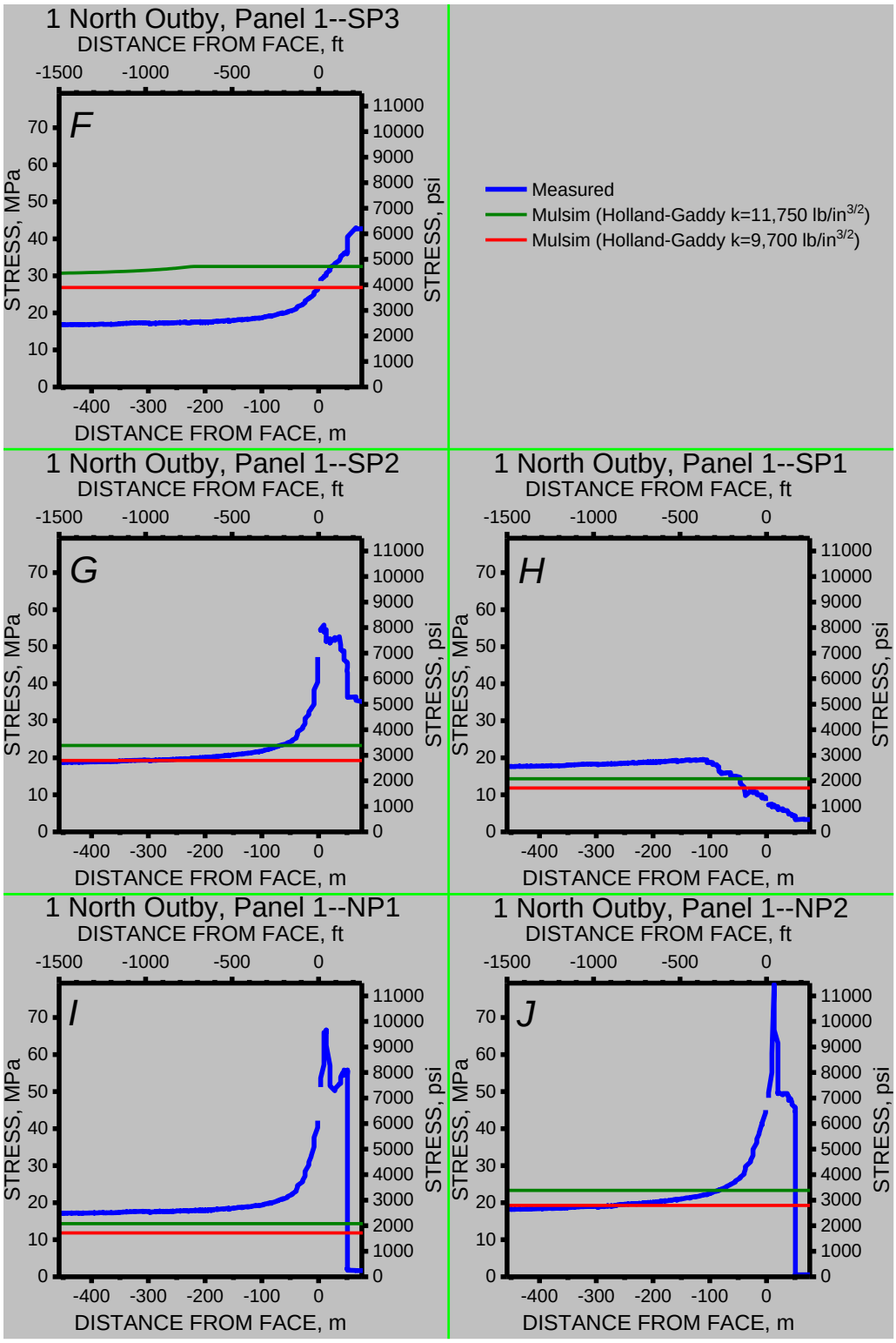

Figure 46 (continued). Measured and Mulsim-calculated vertical stress in 1 North section. F, Instrument SP3; G, SP2; H, SP1; I, NP1; and J, NP2.

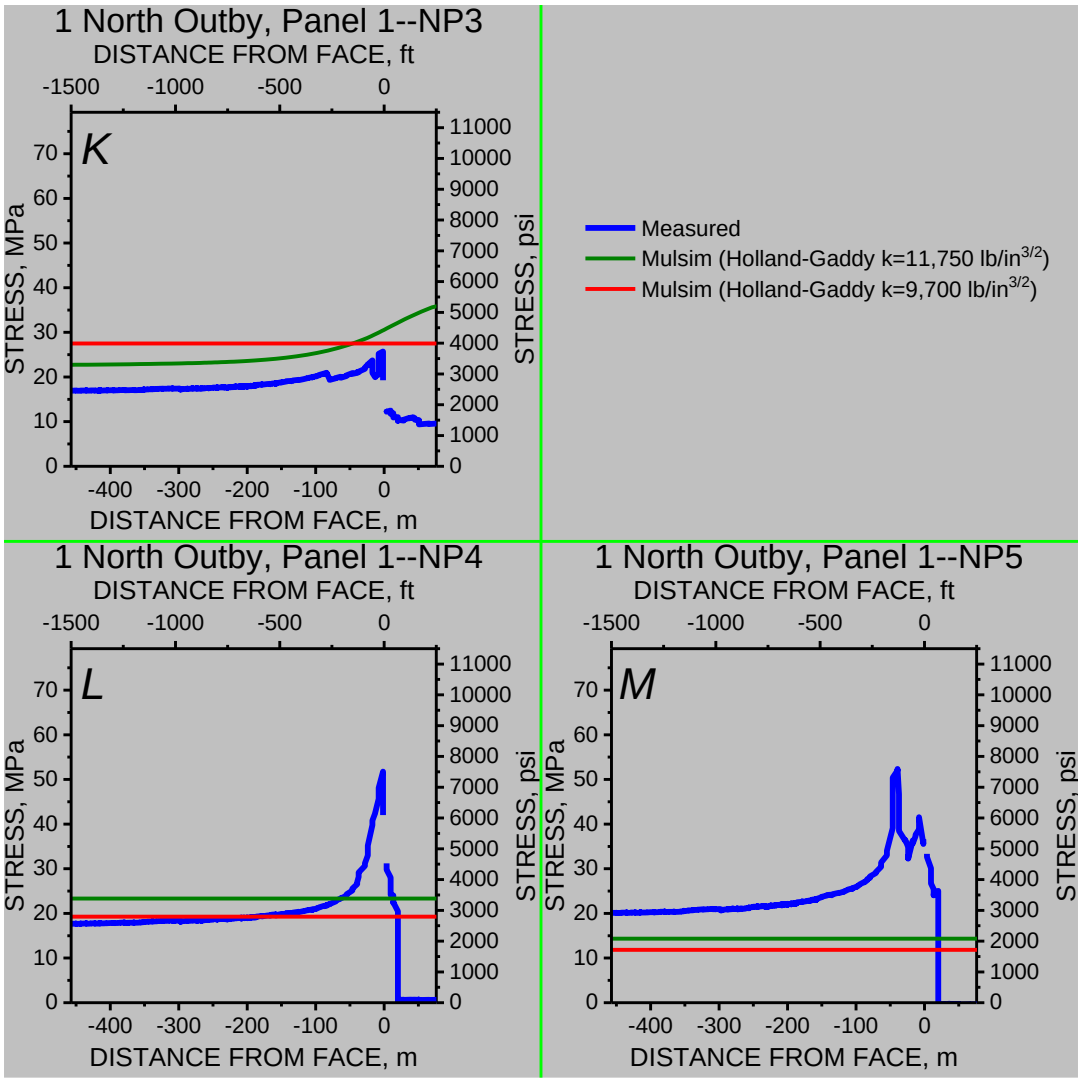

Figure 46 (continued). Measured and Mulsim-calculated vertical stress in 1 North section. *K*, Instrument NP3; *L*, NP4; and *M*, NP5.

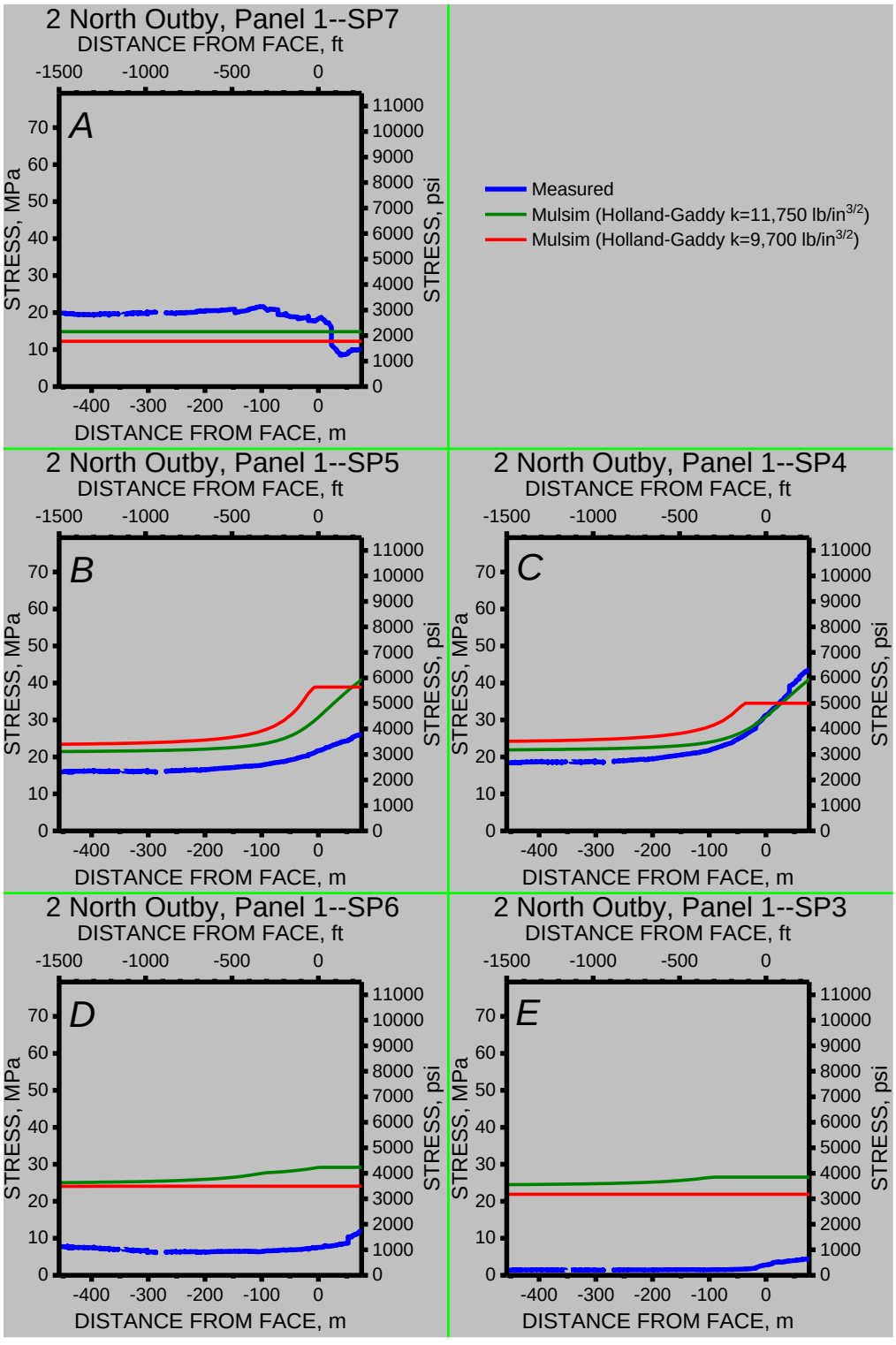

Figure 47. Measured and Mulsim-calculated vertical stress in 2 North section. A, Instrument SP7; B,SP5; C, SP4; D, SP6; and E, SP3.

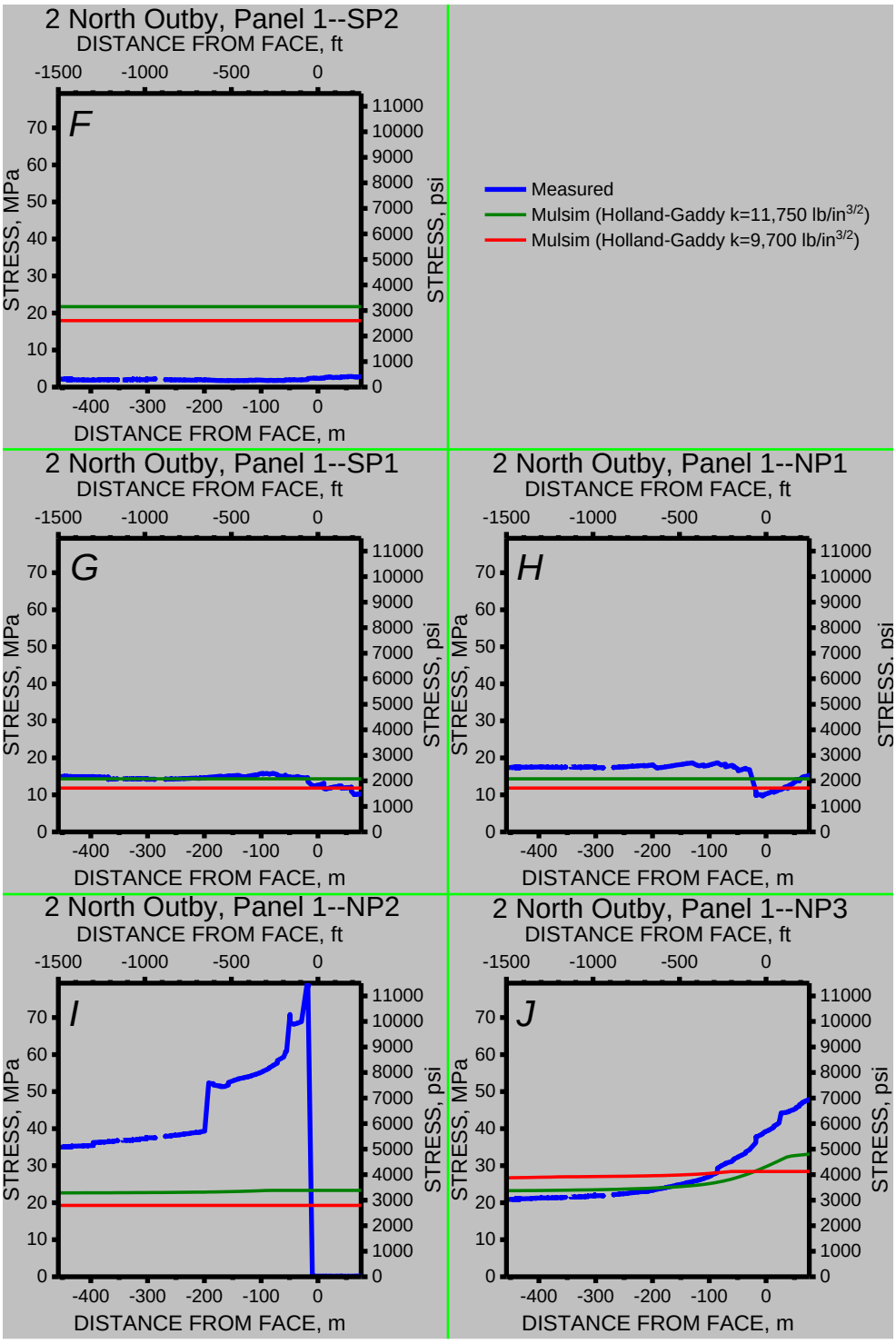

Figure 47 (continued). Measured and Mulsim-calculated vertical stress in 2 North section. *F*, Instrument SP2; *G*, SP1; *H*, NP1; *I*, NP2; and *J*, NP3.

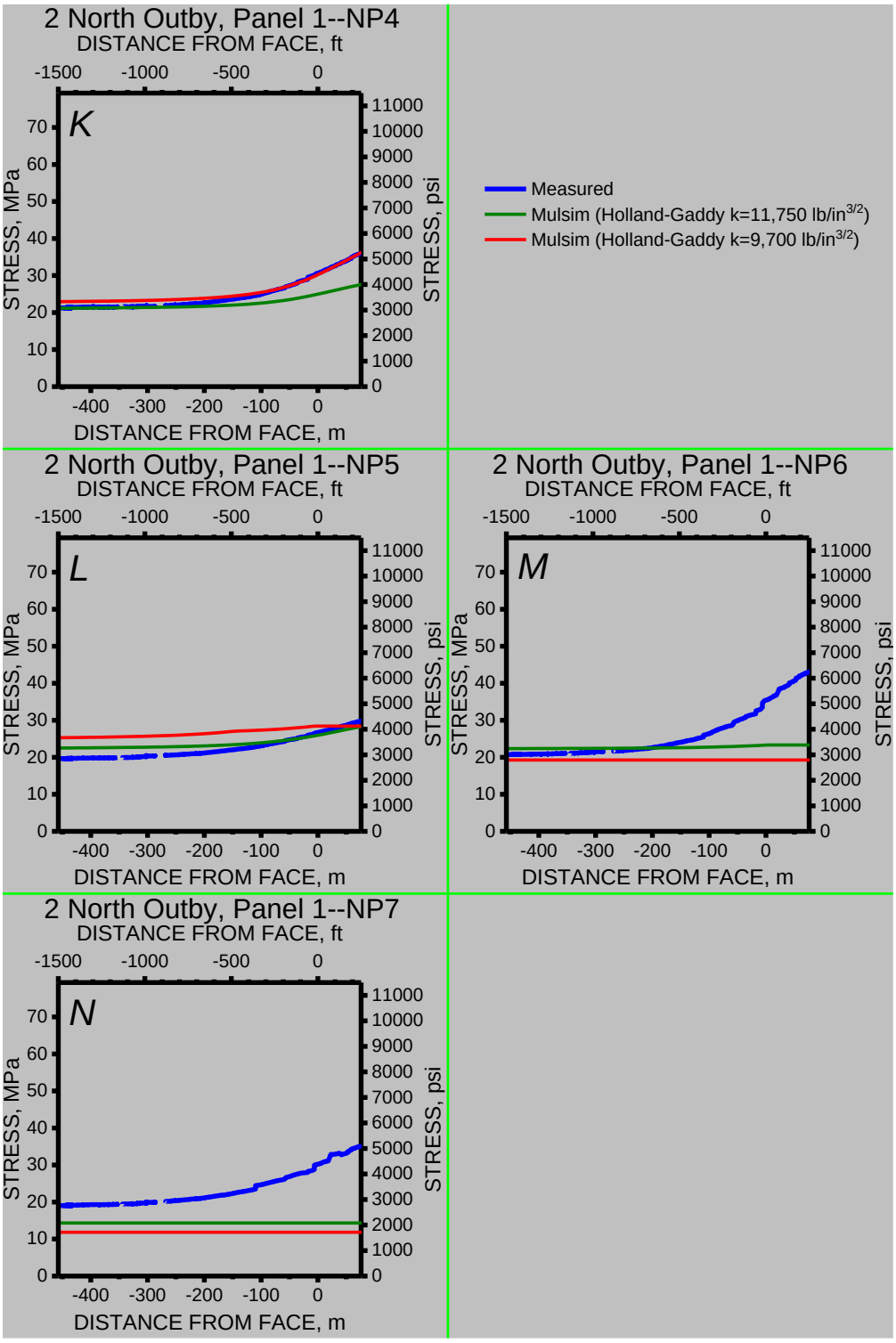

Figure 47 (continued). Measured and Mulsim-calculated vertical stress in 2 North section. *K*, Instrument NP4; *L*, NP5; *M*, NP6; and *N*, NP7.

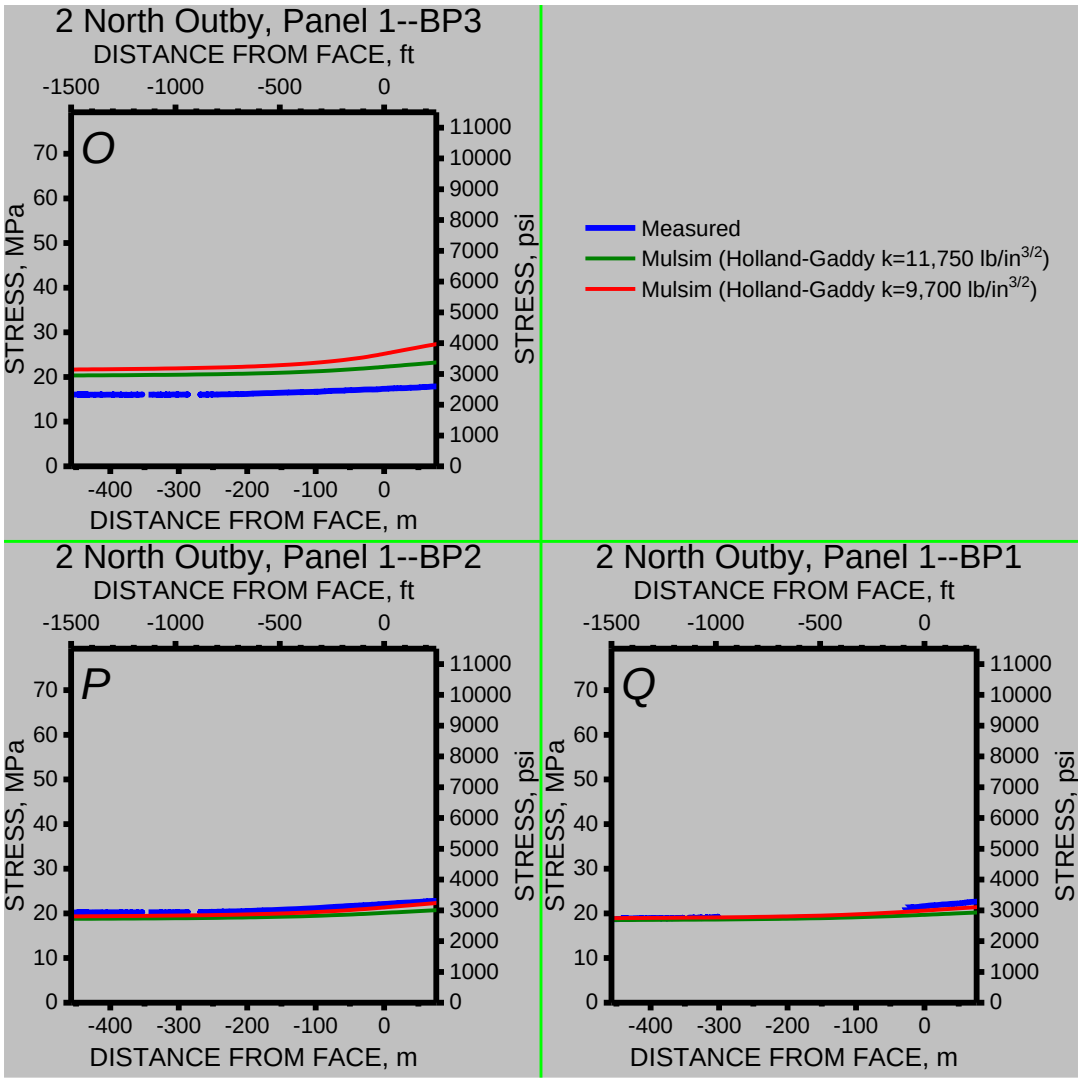

Figure 47 (continued). Measured and Mulsim-calculated vertical stress in 2 North section. *O*, Instrument BP3; *P*, BP2; and *Q*, BP1.

Calibration Using Scaled Stratigraphy

The method just described did not use all information available about stratigraphy. Near-seam stratigraphy was determined from drilling reports. Cores were drilled in the roof and floor near both outby instrumentation sites by a contractor. For example, cores were taken from the roof to a depth of 9.3 m (31.5 ft) and from the floor to a depth of 9.3 m (30.5 ft) in crosscut 11 of 2 North. In 1 North, cores were taken from the roof to a depth of 9.8 m (32 ft) at crosscut 5. A hole was cored in the floor to a depth of 8.7 m (28.4 ft) in entry #2 of 1 North, but its location along that entry is unknown.

Mine stratigraphy was used in the detailed FLAC^{3D} pillar model in a second calibration of the coal strength for MulsimNL/Large. Strata type and thickness are shown in Tables 23 and 24. Laboratory-scale material properties for sandstone and shale were selected from published values as listed in Table 25 [Farmer 1968; Pariseau 2012; Goodman 1989; Blyth and de Freitas 1984; Sheorey 1997; Maleki et al. 2007] because measured values from core were not available. A value of 0.25 was assumed for Poisson's ratio for sandstone, shale, and mudstone. Tensile

strength was assumed to be 10% of the unconfined compressive strength (UCS). Strength values were chosen for mudstone with the assumption that the failure envelope for mudstone was between shale and sandstone. Laboratory properties were then reduced as shown in Tables 25 and 26, as described below.

Table 23. Strata type and thickness for 1 North, listed in order of strata member from top to bottom

Material	Thickness, m (ft)
Sandstone	51.2 (168)
Mudstone	0.61 (2)
Coal	0.61 (2)
Mudstone	3.66 (12)
Coal	0.30 (1)
Mudstone	2.74 (9)
Coal	0.30 (1)
Mudstone	1.52 (5)
DU seam	3.35 (11)
Mudstone	1.52 (5)
Coal	1.52 (5)
Mudstone	0.61 (2)
Sandstone	0.30 (1)
Mudstone	1.52 (5)
Sandstone	0.30 (1)
Mudstone	1.22 (4)
Sandstone	53.95 (177)

Table 24. Strata type and thickness for 2 North, listed in order of strata member from top to bottom

Material	Thickness, m (ft)
Sandstone	51.21 (168)
Coal	1.22 (4)
Sandstone	0.91 (3)
Mudstone	0.91 (3)
Sandstone	3.04 (10)
Mudstone	3.66 (12)
DU seam	3.35 (11)
Mudstone	1.22 (4)
Sandstone	0.3 (1)
Mudstone	0.61 (2)
Sandstone	0.91 (3)
Mudstone	0.91 (3)
Sandstone	1.52(5)
Coal	0.61 (2)
Shale	0.91 (3)
Coal	0.91 (3)
Shale	0.61 (2)
Sandstone	0.61 (2)
Sandstone	53.34 (175)

Table 25. Laboratory-scale material properties

Material	Young's Modulus, GPa (ksi)	Poisson's ratio, m/m (in/in)	Angle of internal friction, °	Cohesion, MPa (psi)	Unconfined compressive strength, MPa (psi)	Tensile strength, MPa (psi)	Specific density, kg/m^3 (lb/ft^3)
Sandstone	34.47 (5,000)[a,b]	0.25	34[c,d]	15.33 (2,224)[c,d]	57.67 (8,365)[a,b]	5.77 (837)	2,307 (144)[a]
Mudstone	27.6 (4,000)	0.25	30	16.26 (2,344)	56.0 (8,120)	5.6 (812)	2,275 (142)
Shale	20.68 (3,000)[a,b]	0.25	23[c,d,e]	15.15 (2,197)[c,d,e]	45.78 (6,640)[a,b,f]	4.58 (664)	2,275 (142)[a]

[a][Farmer 1968]
[b][Pariseau 2012]
[c][Goodman 1989]
[d][Blyth and de Freitas 1984]
[e][Sheorey 1997]
[f][Maleki et al. 2007]

The target elastic modulus for the composite mine floor was 9.65 GPa (1.4×10^6 psi). This was the floor modulus used in the FLAC^{3D} models that satisfied field observations for floor heave. The reduction factor for 1 North was calculated by dividing 9.65 GPa (1.4×10^6 psi) by the thickness-weighted laboratory modulus, yielding 0.42. The reduction factor for 2 North was obtained by the same method, which yielded 0.39. The average reduction factor of 0.4 was then used to multiply the laboratory value of Young's modulus of each stratigraphic rock layer in 1

North and 2 North to obtain field-scale moduli. This value is midrange of moduli reduction factors produced from a collection of test data [Heuze 1980].

The laboratory-scale strength properties for the angle of internal friction and UCS were reduced using the same method used to reduce Young's moduli and are listed in Table 26. The cohesion was calculated from the reduced angle of internal friction and reduced UCS. The average laboratory material properties for each major rock type are shown in Figure 48. The scaled properties, also shown in the figure, are all found in the region that produces the observed heave or no heave condition.

An interface was introduced between the mined coal seam and each of the adjacent layers above and below it. Each interface was given a relatively large friction angle and tensile strength to provide confinement near the pillar's rib and to help prevent heave at its location. Another interface was inserted between the two strata below and adjacent to the coal seam being mined. Weak properties were assigned to this interface in the 2 North pillar model to allow horizontal movement and induce floor heave near the center of the floor. Cohesion and angle of internal friction for this interface in the 1 North model were assigned larger values than those in the 2 North model to help prevent floor heave. This difference in interface properties was necessary because, if stratigraphy was included in the model, the heave/no-heave observation was not simulated. The interface properties are listed in Tables 27 and 28.

Table 26. Field-scale material properties for each major rock type

Material	Young's Modulus, GPa (ksi)	Poisson's ratio, m/m (in/in)	Angle of internal friction, °	Cohesion, MPa (psi)	Unconfined compressive strength, MPa (psi)	Tensile strength, MPa (psi)	Specific density, kg/m^3 (lb/ft^3)
Sandstone	13.79 (2,000)	0.25	18	4.15 (602)	11.41 (1,655)	1.14 (166)	2,307 (144)
Mudstone	11.03 (1,600)	0.25	16	4.19 (608)	11.07 (1,606)	1.11 (161)	2,275 (142)
Shale	8.27 (1,200)	0.25	12	3.66 (531)	9.06 (1,314)	0.90 (131)	2,275 (142)

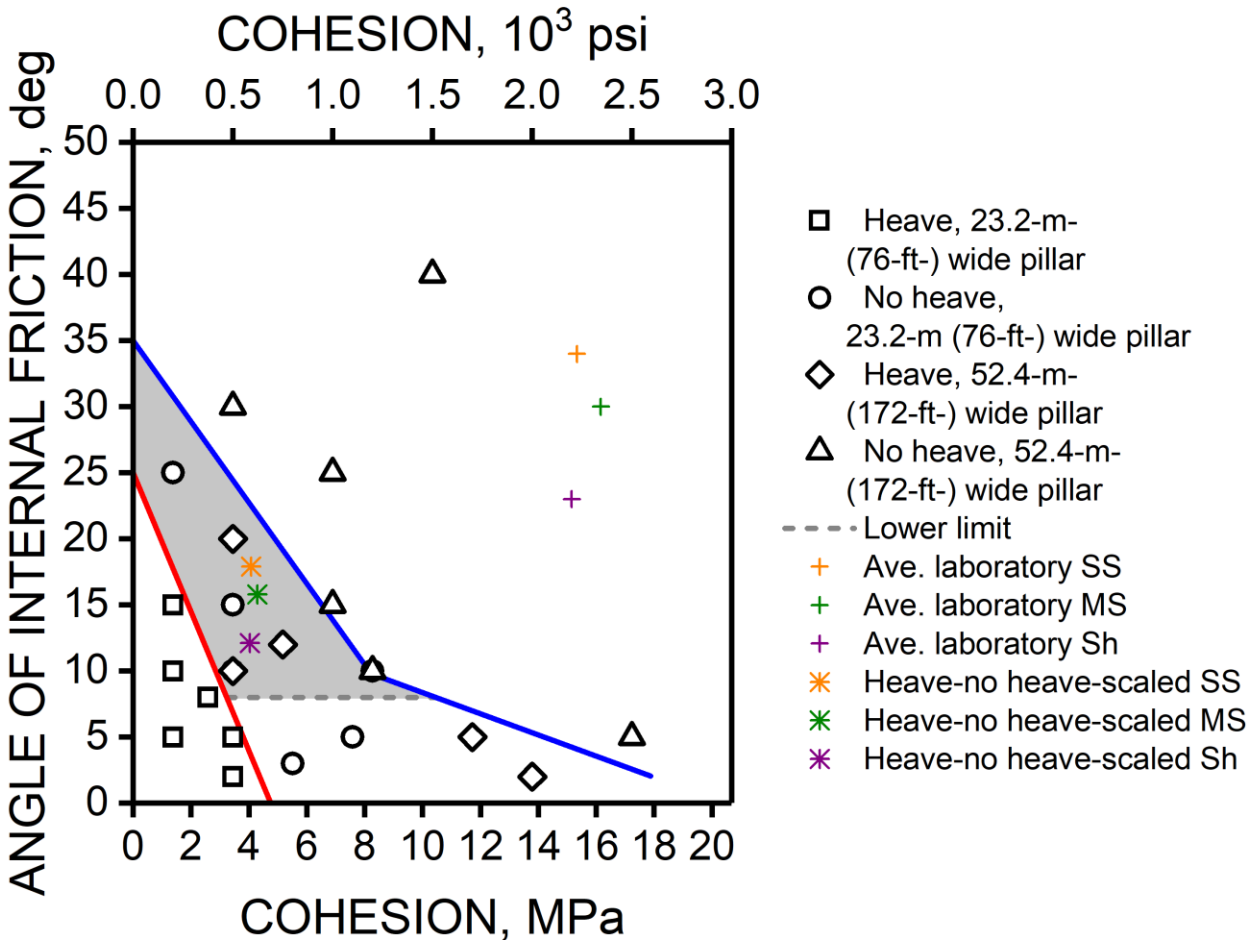

Figure 48. Average laboratory properties for sandstone, mudstone, and shale are shown with reference to the region of properties, producing observed heave or no heave of the floor, along with scaled values to be used in detailed pillar models.

Table 27. Interface properties for 1 North pillar model

Interface	Normal stiffness, MPa/m (psi/in)	Shear stiffness, MPa/m (psi/in)	Cohesion, kPa (psi)	Friction angle, °	Tensile strength, MPa (psi)
1*	7,329,072 (27,000,000)	7,329,072 (27,000,000)	103 (15)	25	150
2†	7,329,072 (27,000,000)	7,329,072 (27,000,000)	103 (15)	25	150
3‡c	7,329,072 (27,000,000)	7,329,072 (27,000,000)	103 (15)	5	0

*Interface between coal seam and roof
†Interface between coal seam and floor
‡Interface between the two strata beneath and adjacent to coal seam

Table 28. Interface properties for 2 North pillar model

Interface	Normal stiffness, MPa/m (psi/in)	Shear stiffness, MPa/m (psi/in)	Cohesion, kPa (psi)	Friction angle, °	Tensile strength, MPa (psi)
1[a]	7,329,072 (27,000,000)	7,329,072 (27,000,000)	103 (15)	25	150
2[b]	7,329,072 (27,000,000)	7,329,072 (27,000,000)	103 (15)	25	150
3[c]	7,329,072 (27,000,000)	7,329,072 (27,000,000)	34 (5)	2	0

[a]Interface between coal seam and roof
[b]Interface between coal seam and floor
[c]Interface between two strata beneath and adjacent to coal seam

Using the properties listed in Tables 27 and 28 produced about 22.9 cm (9 in) of heave in the center of the floor next to the 2 North pillar and limited heave to less than 2.5 cm (1 in) in the floor next to the 1 North pillar, which was not considered visually perceptible in the field [Tesarik et al. 2013]. These results confirmed that this material property set satisfied visual observations. Vertical stress-versus-strain relationships from 3 m x 3 m (10 ft × 10 ft) sections of the FLAC^{3D} pillar model were then used as input to the Mulsim panel-scale model. These sections are shown graphically in Figure 49.

Figure 50 shows stress-versus-strain curves extracted from various cells of the 2 North detailed pillar model. Because of symmetry, only one quarter of the pillar was considered. Similar results were obtained from the 1 North detailed pillar model that was 24 m (80 ft) in width. The curves for the 1 North detailed pillar model that was 21 m (70 ft) in width were very close to those of the 24-m (80-ft) wide pillar model, such that fitting of 5-point approximation curves was based solely on the 24-m (80-ft) wide pillar model. In LaModel and Mulsim, each yield ring normally has two types of strengths, the corner cell and the side cell. From these results, it was determined that the cells immediately adjacent to the corner cells were significantly different from the other side cells, so that a different material model was warranted. Therefore, three types of cells per yield ring were determined—corner, adjacent to side, and side. There was some degree of variational trend from the corner cell to the middle side cell in any given ring. However, aside from the cells adjacent to the corner cell, the rest of the side cells were not significantly different from each other, so that they were considered together for the purposes of fitting a five-point, piecewise linear model to the extracted strength-versus-strain curves. Figure 50 shows graphs by those distinctions (i.e., corner, adjacent to corner, and rest of side) for each ring of elements. Included in these graphs of curves extracted from the FLAC^{3D} models are the five-point, piecewise linear models that were fitted visually.

Figure 51 shows the fitted five-point models from the 1-North pillar model, and Figure 52 shows the same from the 2 North pillar model. All detailed model calculations were stopped where the curves end because a zone had deformed excessively and triggered FLAC^{3D}'s "illegal geometry" error that stops the calculations. Because of those stoppages, no evidence of yielding was present in ring 4. Therefore, for purposes of implementation in MulsimNL/Large, ring 4 was considered elastic, and only three yield rings were used.

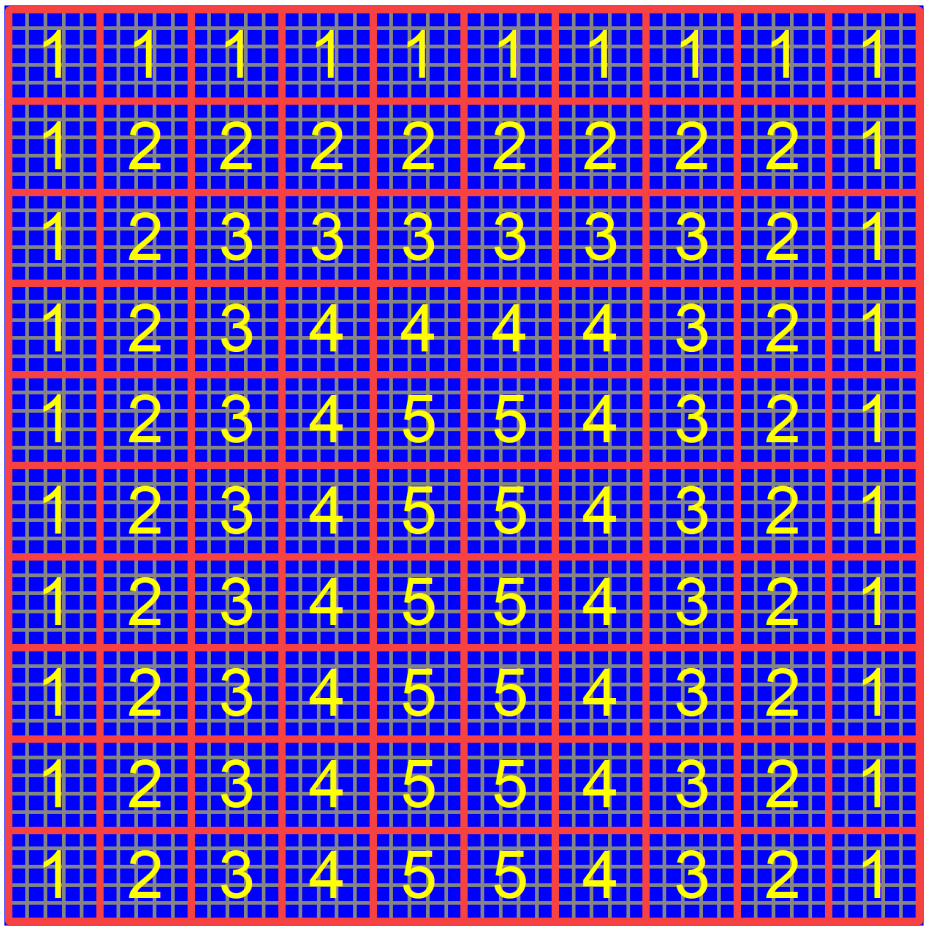

Figure 49. Horizontal cross section of FLAC^{3D} model at seam midheight showing how finite difference zones are grouped into "Mulsim cells." Strength versus strain is then extracted for each cell. The numbers represent the "yield ring" number.

Figure 53 shows the fitted five-point model for the three types of elements of each of the three yield rings for 1 North. For comparison, the equivalent elastic-plastic yield rings for Mark-Bieniawski strength models for the 1 North case are shown. The first ring models compare very well. The second and third rings show notable differences in the amount of final strength. The FLAC^{3D}-extracted second ring models show significantly higher ultimate elastic-plastic strength than do the Mark-Bieniawski models. The FLAC^{3D}-extracted third ring elastic-plastic strengths are higher than the Mark-Bieniawski strengths, but the differences are not as high as in the second ring.

The FLAC^{3D}-extracted material models were organized as input to a MulsimNL/Large model of the two panels in Mine A. As a comparison to earlier stress increase contour graphs, Figure 54 shows stress increase with respect to the stress state before mining Panel 1 at the average face location when 2 North instruments detected the threshold stress increase of 138 kPa (20-psi). As with the other strength models, this model also shows a bending of the model-calculated threshold contour as it approaches and encounters the gate roads, which is incompatible with measurements.

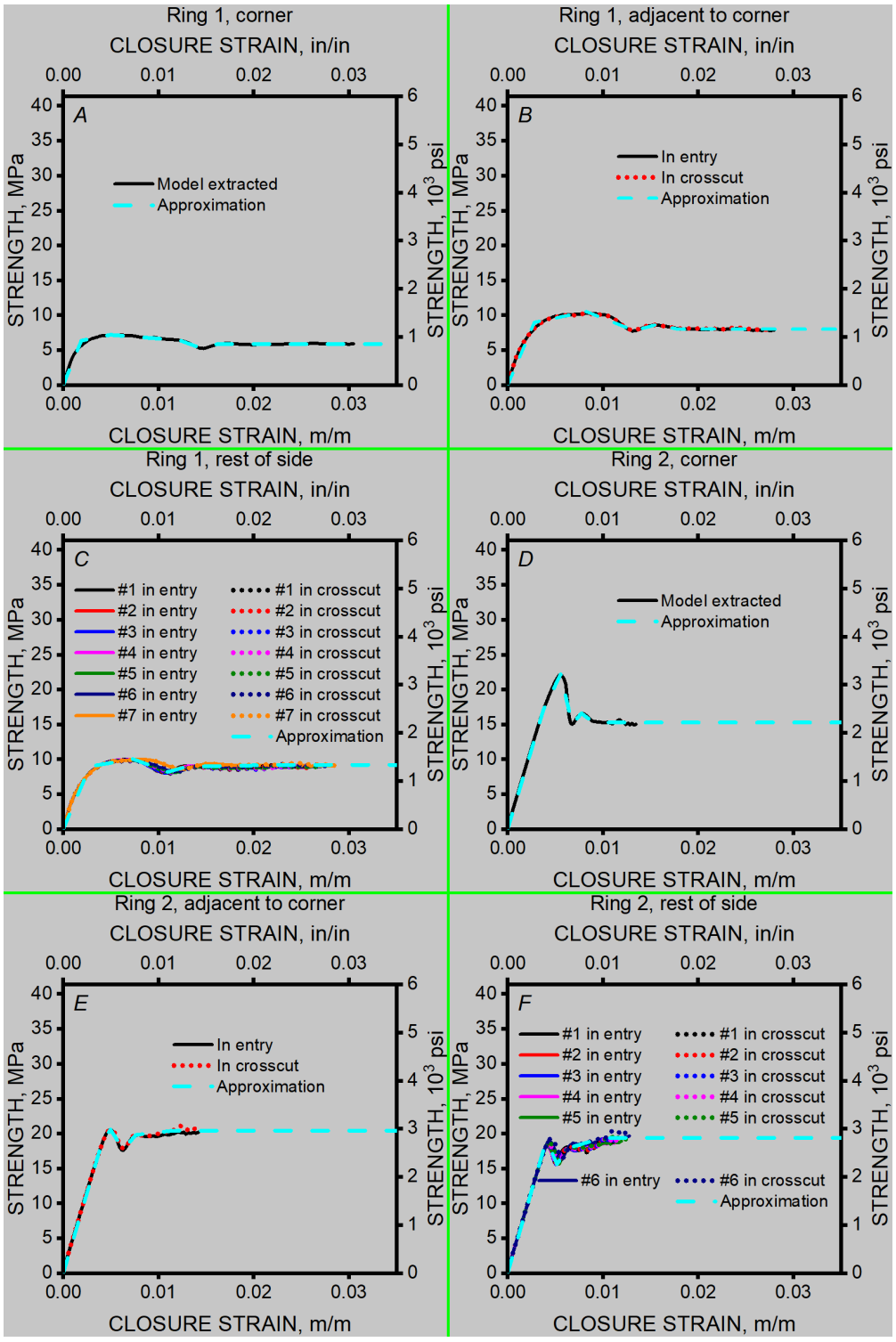

Figure 50. Stress versus strain extracted from cells representing Rings 1, 2, 3, and 4 of the 2 North detailed pillar model. Also shown is the approximation of the curve or curves with a five-point representation that can be input as a model in MulsimNL/Large. *A*, Ring 1 corner cell; *B*, Ring 1 cells adjacent to corner; *C*, Ring 1 remaining side cells; *D*, Ring 2 corner cell; *E*, Ring 2 cells adjacent to corner; *F*, Ring 2 remaining side cells.

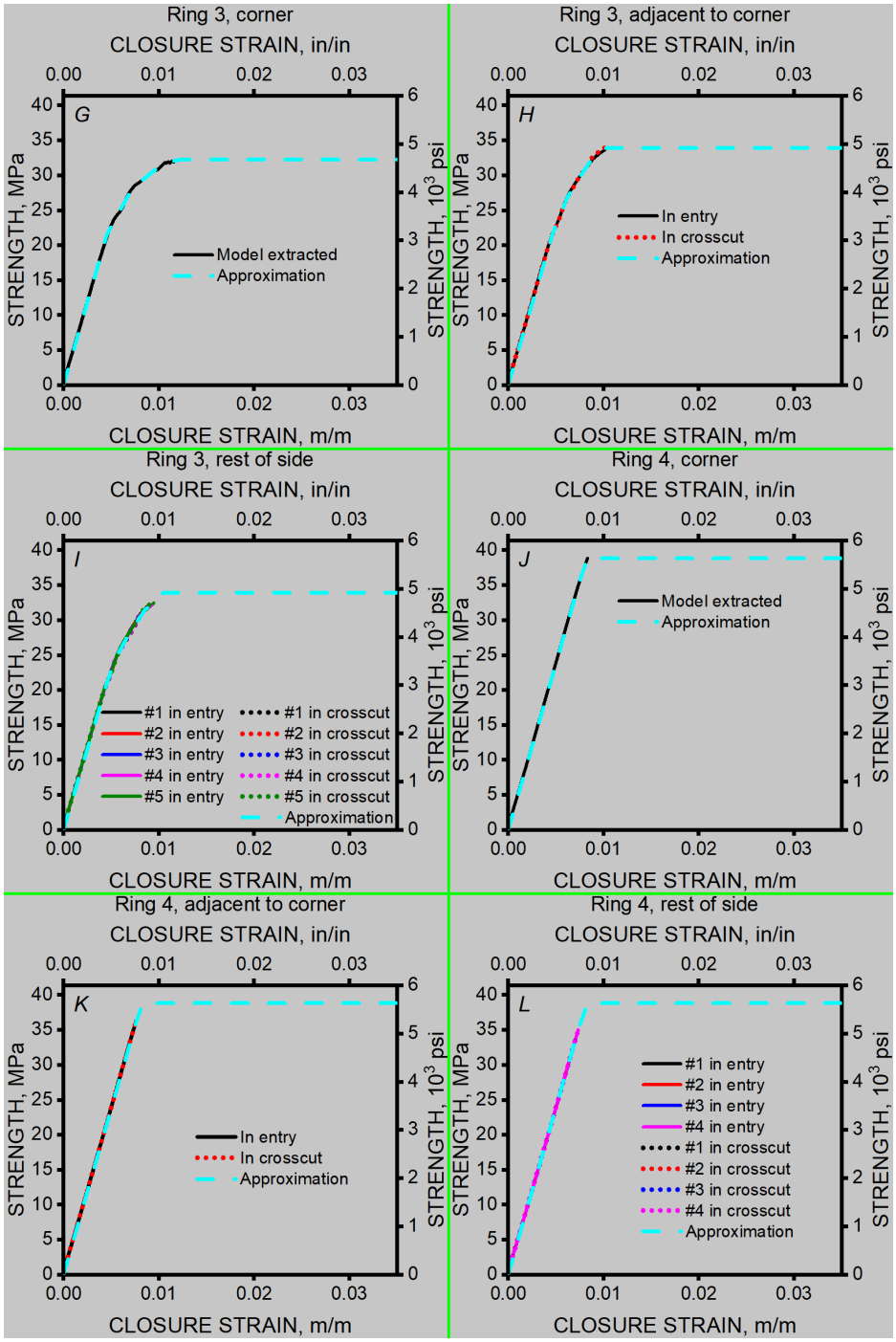

Figure 50 (continued). Stress versus strain extracted from cells representing Rings 1, 2, 3, and 4 of the 2 North detailed pillar model. Also shown is the approximation of the curve or curves with a five-point representation that can be input as a model in MulsimNL/Large. *G*, Ring 3 corner cell; *H*, Ring 3 cells adjacent to corner; *I*, Ring 3 remaining side cells; *J*, Ring 4 corner cell; *K*, Ring 4 cells adjacent to corner; *L*, Ring 4 remaining side cells.

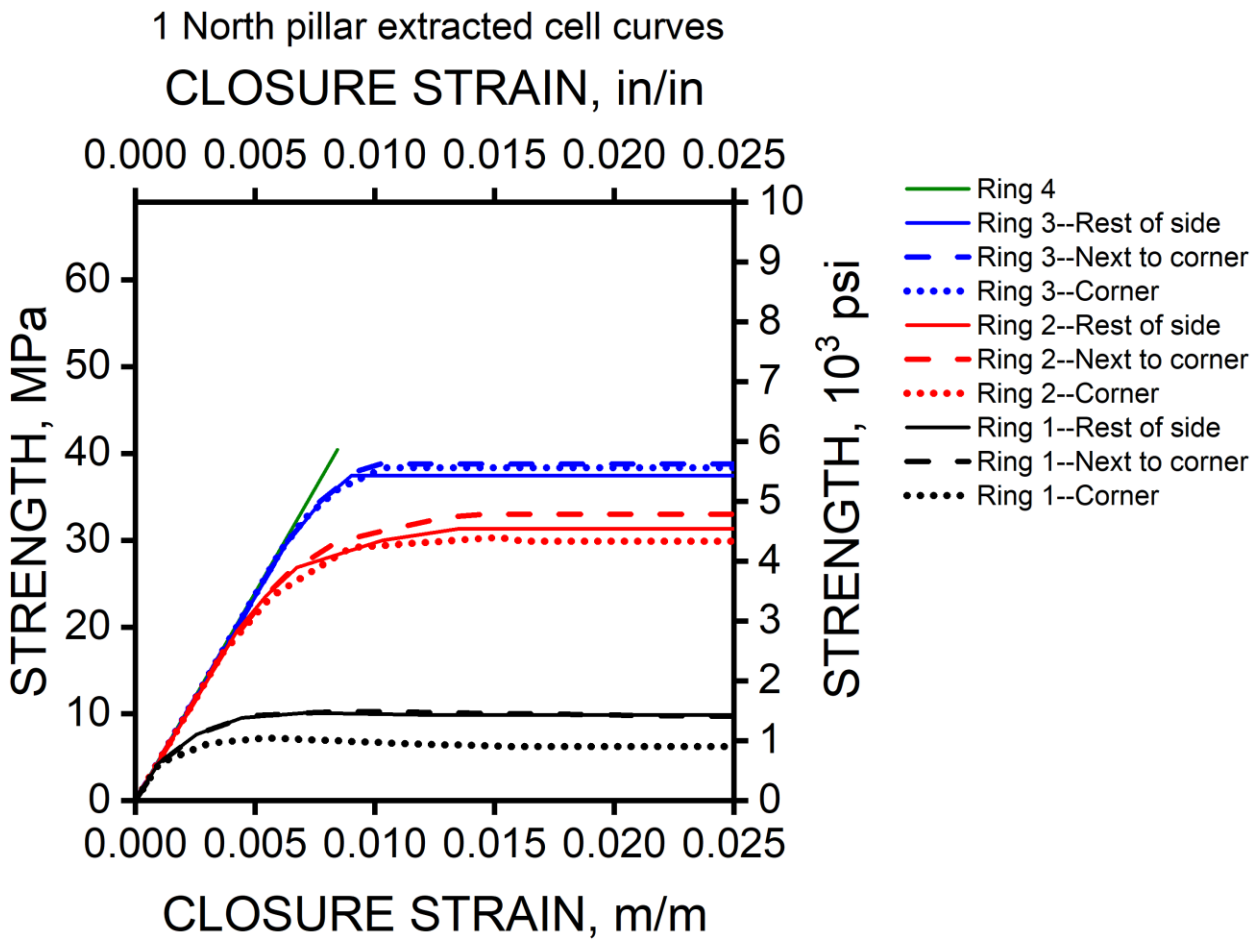

Figure 51. Five-point strength versus strain curves used to represent such curves extracted from detailed pillar model of 1 North pillars.

Comparison of contours in Figure 54 with the contours of the elastic model with reduced modulus in the outer rings (Figure 31)—the model that best matches model-calculated LTD with measured LTD at the BPC sites—suggests that the FLAC^{3D} model needs improvement. The comparison of side stress profiles at midpanel shown in Figure 55 demonstrates that the FLAC^{3D}-extracted material models cause the peak stress to be higher and further into the pillar than the Mark-Bieniawski 6.21-MPa (900-psi) material model, which may be an improvement. However, in this case, the Hoek-Brown coal model needs to reflect higher strength. When compared with a higher-strength Mark-Bieniawski model (Figure 28), higher strength alone seems insufficient, making strain-hardening near the ribs necessary. Therefore, the Hoek-Brown model may not be adequate to simulate the coal behavior measured at Mine A.

Even though the MulsimNL/Large model results using FLAC^{3D}-extracted curves did not produce a good enough result to simulate coal behavior, particularly near the ribs, the method of using FLAC^{3D}-extracted curves is demonstrated. This tool can be used with better FLAC^{3D} models to produce material curves that more closely match measured behavior.

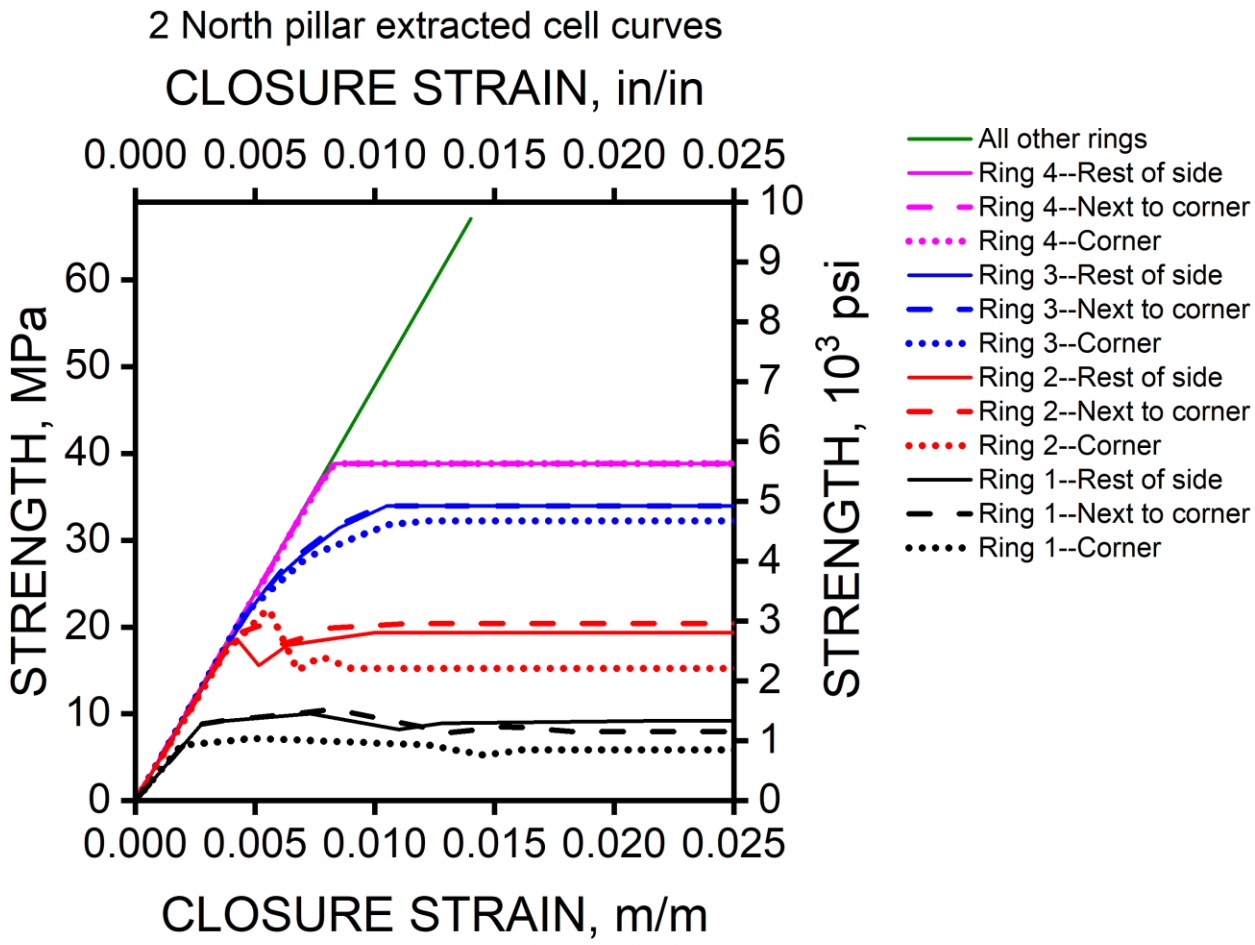

Figure 52. Five-point strength versus strain curves used to represent such curves extracted from detailed pillar model of 2 North pillars.

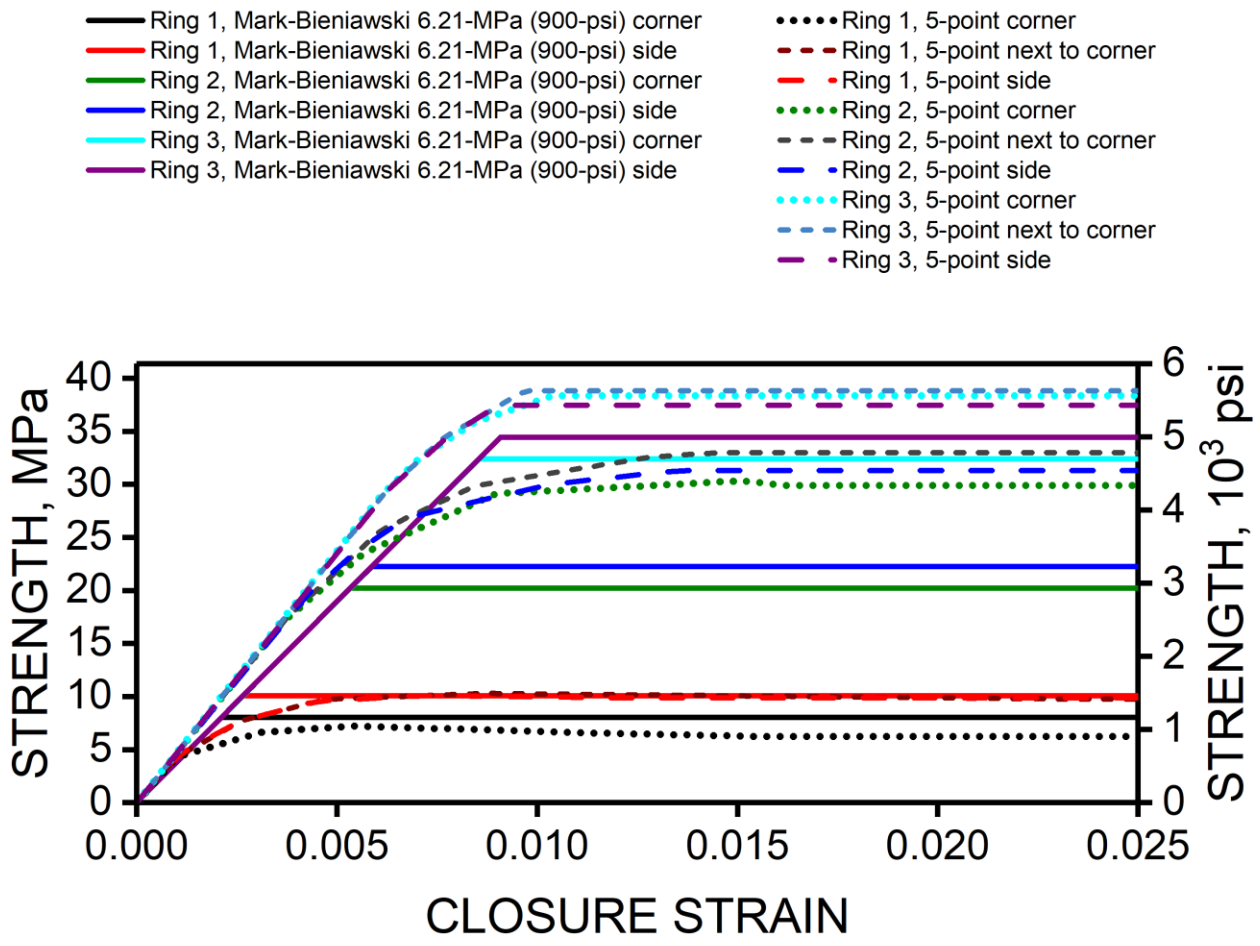

Figure 53. Five-point strength-versus-strain curves for three rings representing 1 North pillar behavior shown for comparison with Mark-Bieniawski curves for a 6.21 MPa (900 psi) coal.

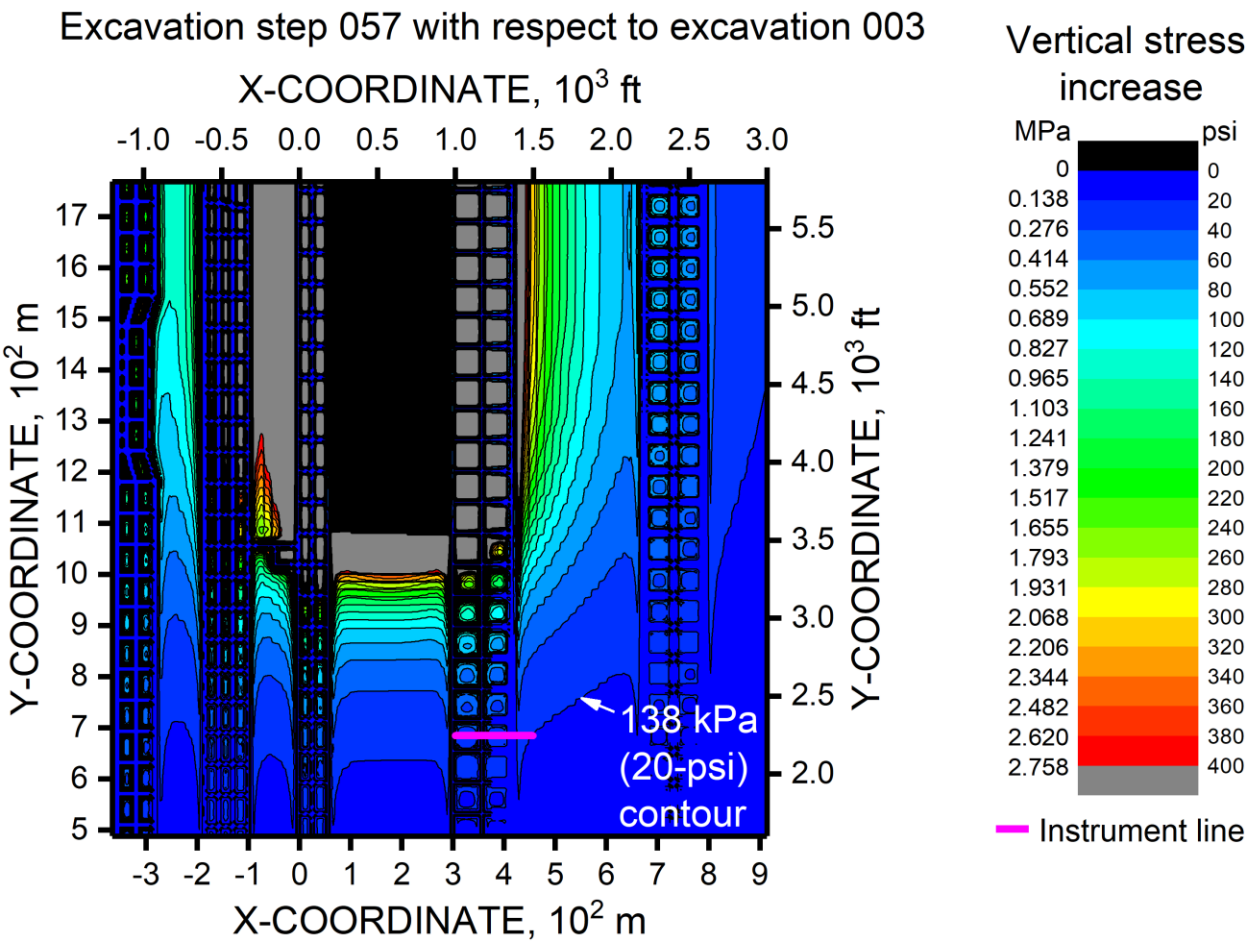

Figure 54. Contours of stress increase with respect to prepanel state with MulsimNL/Large model using FLAC^{3D}-extracted cell curves.

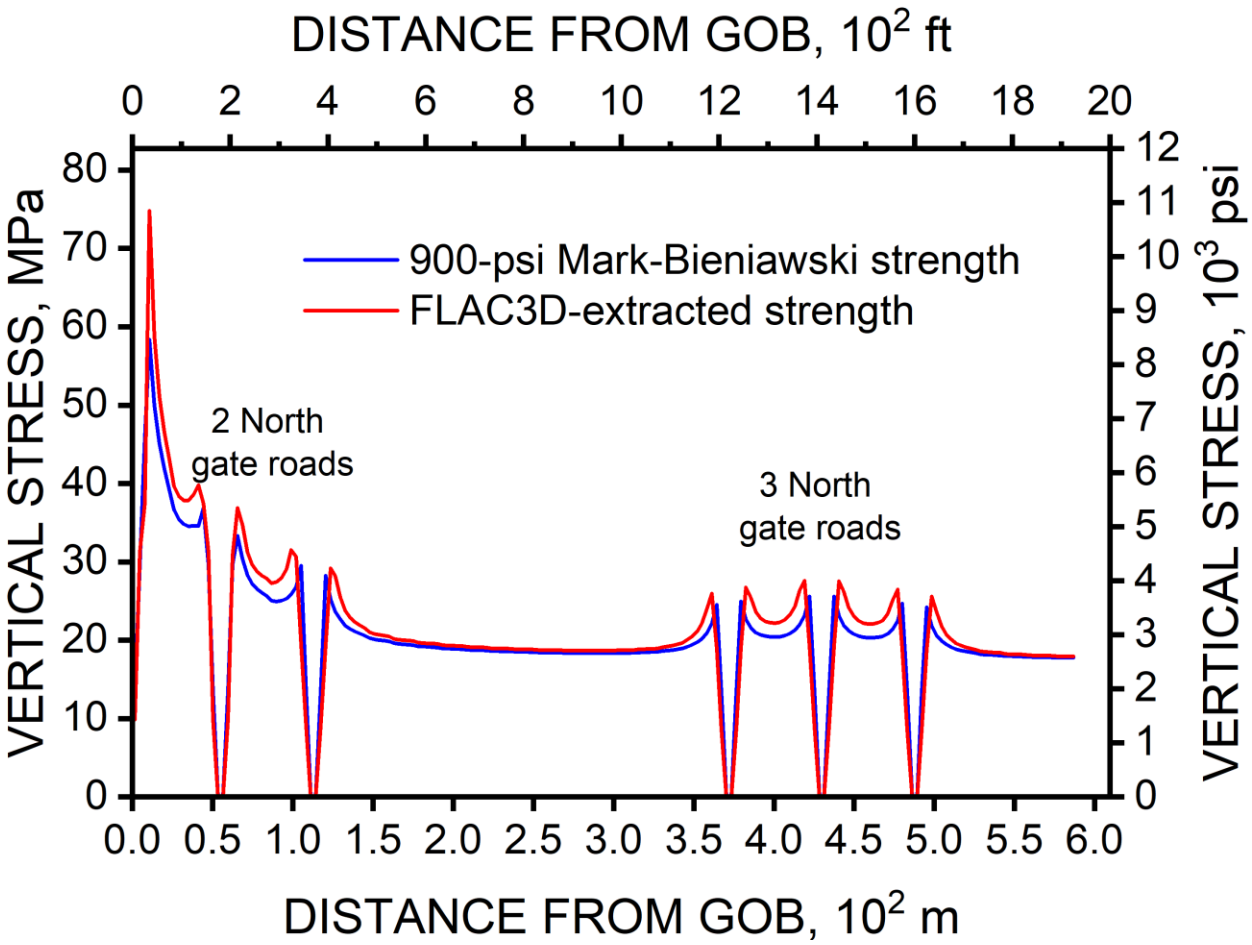

Figure 55. Vertical seam stress profile calculated at midpanel of Panel 1 from gob at headgate, through the next panel to be mined, and passing through the next headgate and beyond. Mining of Panel 1 is complete, and Panel 2 remains unmined. For comparison, the stress profile for a 6.21-MPa (900-psi) coal is also shown.

Summary of Calibration

The model calibration procedures demonstrated in this report provide multiple ways to determine a reasonable model. There are various ways to measure LTD, each with varying sensitivities. The BPCs do not provide accurate measurements of stress change when cell pressures are in their upper range, presumably because the elastic condition upon which calibration equations are based is violated. But the BPC cell pressure histories are still very useful in evaluating material strength models and providing the best measure of first arrival of mining-induced abutment stress and LTD.

Larson et al. [NIOSH 2020] demonstrated that the entry closure and support-Can closure did not produce enough high-quality measurements to make determinations of LTD; however, with recommended adjustments in procedure, measured support Can loads might be used to determine a more consistent LTD that is nearly as sensitive as LTD measured with BPCs. Ground condition surveys, though less sensitive than BPCs, can provide useful information about changes in LTD and possible changes in structure along gate roads.

The Mulsim/NL model has been revived as MulsimNL/Large, and a five-point seam material model has been successfully added. Using alternative material models and extracting such material models from a FLAC^{3D} detailed pillar model have been demonstrated. MulsimNL/Large demonstrated the ability to show reasonable behavior for a large range of final gob stiffness while maintaining calibration to LTD. With LaModel, the final gob stiffness could not be adjusted to provide reasonable gob loading while maintaining measured LTD.

In the calibration sequence, the ways to make measurements or estimations of gob-versus-abutment loading by overpanel weight are lacking. Measurement methods for longwall situations are either not developed or not proven. Gob-loading estimation methods need to be developed for the purpose of calibration of gob simulation models. One way to estimate the gob loading fraction might be by using a calibrated caving model [Pierce and Board 2010a, 2010b], but the model still needs verification, and calibration procedures still need to be developed.

In Ground Stress in Mining Part 1, Larson et al. [NIOSH 2020] reported that ground condition surveys reveal that conditions were variable along the gate roads, and that differences in caving indicate that structure significantly affects behavior. This behavior deviates from calibrated model predictions, which are based on constant geology. Implementation of the guidance provided by MSHA for calibration of models would be improved by the addition of measurements to observations and ground condition mapping in calibrating and verifying a model.

In the progress toward predicting risk of seismic events with models, it is important to have a well calibrated model, but it is also important to simulate the geologic features that might contribute to risk of seismic events. Models used might better be used to study indicators of seismic risk if better information about geologic structure, gob loading, and material properties were available. Inclusion of these features in models, along with better information on coal and other strata peak strength and post-peak strength properties, must be implemented because multiple mechanisms are known to cause seismic events (see papers from the 1958 Coal Bump Symposium [Brown 1958; Campbell 1958; Holland 1958; Mauck 1958; Peperakis 1958; Talman and Schroder 1958; Thomas 1958] and [Newman 2008; Iannacchione and Tadolini 2016; Maleki 2017].

Referring to the wheel of design in Figure 1, the ability of the numerical models as calibrated in this report to indicate elevated seismic hazard was not evaluated. In fact, various pillar sizes were used throughout the mine (see Figure 6), and none of them prevented mining-induced seismic events. Pillar sizing is not the only factor to consider when designing a safe mine layout. Although the calibration process outlined here must be completed, other unknown factors that might increase the risk of such events need to be evaluated and understood.

Conclusions and Recommendations

The following conclusions can be drawn from this research:

- The 138-kPa (20-psi) cell pressure increase with BPCs served well as a way to determine load transfer distance and calibrate rock mass stiffness or stiffnesses. The cells must, however, be installed in clean boreholes and fully encapsulated in grout if not pre-encapsulated.
- Load transfer distance at Mine A was determined to be about four times that calculated by the Peng and Chiang empirical equation. The range of load transfer

distance determined at Mine B was large compared to that calculated with the empirical equation.

- In addition to instrument data, observations of ground behavior were found to be very important in determining appropriate material properties and possibly material models. For example, drilling observations provided the basis for making the seam being mined less stiff and slightly weaker than other seams in the model.
- Calibration of LaModel rock mass stiffness to large load transfer distance was possible, but such calibrated rock mass stiffness did not allow any significant gob loading and, as a result, final gob stiffness could not be calibrated.
- MulsimNL/Large easily calibrated to large load transfer distance, and a wide range of final gob stiffness was possible for calibrating overpanel weight distribution between abutment and gob.
- The added MulsimNL/Large five-point material model provided additional capability to model strain-hardening seam behavior. This piecewise linear function is also capable of characterizing softening.
- Borehole pressure cell data reduction procedures in the literature do not hold true in the case of Mine A at higher cell pressures.
- Local variability in conditions and structure made it difficult to incorporate these variations in a panel-scale numerical model, which made it difficult to match observations to model outputs, as suggested by Skiles and Stricklin [MSHA 2009]. In such case, a recommendation follows.
- Observations of caving and ground condition surveys suggest that knowledge of geologic structure is very important to be able to calibrate models. Prediction of hazards cannot be accomplished unless significant structure is known, along with its significant characteristics, and then represented in a calibrated model.

As a result of this study, the following recommendations are offered:

- In case of much local variation in conditions, multiple local models or even panel scale models with properties representing various local behavior is recommended to assess the effect of local variation of conditions on the mine layout design.
- The calibration of BPCs should be re-examined with careful laboratory testing in blocks of coal to determine how the cells behave at high cell pressure when the state of the coal has surpassed elasticity.
- A soft-inclusion pressure cell should be developed to minimize the effect of instruments acting as hard inclusions.
- More studies should be conducted on coal strength behavior, especially with regard to appropriate material models that describe the full stress-strain curve.
- Procedures for calibration of the longwall caving model should be developed.
- Procedures for calibration of material models using microseismic data, particularly peak and post-peak strength behavior, should be developed and tested.
- Research should be conducted in characterizing peak and post-peak strength behavior of various coal-measure rocks found in regions prone to mining-induced seismic events. Modeling studies should be conducted to determine conditions likely to produce such events (e.g., location with respect to the mined seam and thickness of brittle strata).

- Mine design evaluation should include characterization of the full stress-versus-strain curve for near-seam strata and characterization of structure that might cause the risk of unstable failure in gate road systems to increase significantly.

Acknowledgments

The authors are greatly indebted to the mining companies that operate Mine A and Mine B for allowing NIOSH personnel to come on site and install instruments. Engineers and personnel at these mines participated in installation of the instruments and subsequent monitoring. They made this project possible. Agapito and Associates installed the BPCs at Mine A. Their drilling expertise, careful notes, and subsequent discussion of measurements and providing information are very much appreciated. NIOSH Mining co-workers, Brad Seymour, Craig Compton, David Oyler, Tristan Jones, and Dennis Dolinar participated in various parts of the field installations. Their efforts are very much appreciated. Co-worker Eric Zahl was on site at the mines numerous times to lead installation efforts, troubleshoot problems, make equipment moves, and extract datalogger readings. His efforts and dedication made possible the results of this project.

Helpful discussions with Dr. R. Karl Zipf (retired, NIOSH) about the Fortran source code for MULSIM/NL are gratefully acknowledged. Dr. Marc Loken (former Senior Research Fellow, NIOSH) assisted by examining the source code and changing Fortran compilers to successfully compile an early version of MulsimNL/Large.

Dr. Matthew Pierce, of Itasca Consulting Group, contributed to Appendix C by adding to the description of the Longwall Modeling Environment. The authors gratefully acknowledge his help and wonderful cooperation. The authors also thank Dr. Jeffrey K. Whyatt (retired, NIOSH), for his useful ideas on content, technical issues, and structure of that appendix.

Finally, the help, discussions, and encouragement of Dr. Jeffrey K. Whyatt over the life of this research project and writing of both reports, Part 1 and Part 2, have been invaluable.

References

Alejano LR, Alonso E [2005]. Considerations of the dilatancy angle in rocks and rock masses. Int. J. Rock Mech. Min. Sci., Vol. 42, No. 4, pp. 481–507.

Andrieux PP, Hudyma MR, O'Connor CP, Li H, Cotesta L, Brummer RK [2008]. Calibration of large-scale three-dimensional non-linear numerical models of underground mines using microseismic data. In: Hart R et al. eds. Continuum and Distinct Element Numerical Modeling in Geo-Engineering – 2008, Proceedings of the 1st International FLAC/DEM Symposium. (Minneapolis, MN: August 25-27, 2008) Minneapolis, MN: Itasca Consulting Group, Inc., pp. 343–350 pp.

Babcock CO [1986]. Equations for the analysis of borehole pressure cell data. In: Hartman HL ed., Rock Mechanics: Key to Energy Production, Proceedings of the 27th U.S. Symposium on Rock Mechanics. (Tuscaloosa, AL: June 23–25, 1986) Littleton, CO: Society of Mining Engineers, pp. 233–240.

Bawden WF [2010]. Thoughts on quantitative field scale characterization of post-failure rock mass conditions and their influence on underground mine design. In: McLennan J et al. eds. Proceedings: 44th U.S. Rock Mechanics Symposium and 5th U.S./Canada Rock Mechanics Symposium. Invited presentation, (Salt Lake City, UT: June 27–30, 2010) Alexandria, VA: American Rock Mechanics Association, 18 pp.

Beckett LA, Madrid RS [1986]. Practical application of MULSIM/BM for improved mine design. In: Proceedings: 3rd Conference on the Use of Computers in the Coal Industry. (Morgantown, WV: July 28–30, 1986), pp. 209–219.

Bieniawski ZT [1992]. Invited paper: Principles of engineering design for rock mechanics. In: Tillerson JR, Wawersik WR eds. Rock Mechanics: Proceedings of the 33rd U.S. Symposium. (Santa Fe, NM: June 3–5, 1992) Rotterdam: A. A. Balkema, pp. 1031–1040.

Bieniawski ZT, Van Heerden WL [1975]. The significance of in situ tests on large rock specimens. Int. J. Rock Mech. Min. Sci. & Geomech. Abstr., Vol. 12, No. 4, pp. 101–113.

Blyth FGH, de Freitas MH [1984]. A geology for engineers. 7th ed., New York: Elsevier, 336 pp.

Board M, Damjanac B [2003]. Development of a methodology for analysis of instability in room and pillar mines. In: Stephansson O ed., Proceedings of the 2003 Swedish Rock Mechanics Day Conference.2003) Stockholm: SvebeFo, pp. 1–22 pp.

Board M, Damjanac B, Pierce M [2007]. Development of a methodology for analysis of instability in room and pillar mines. In: Potvin Y ed., Deep Mine 07: Proceedings of the Fourth International Seminar on Deep and High Stress Mining. (Perth, Australia: November 7–9, 2007) Perth: Australian Centre for Geomechanics, pp. 273–282.

Board M, Pierce ME [2009]. A review of recent experience in modeling of caving. In: Esterhuizen GS et al. eds. NIOSH Information Circular 9512, Proceedings of the International Workshop on Numerical Modeling for Underground Mine Excavation Design. (Asheville, NC: June 28, 2009) Pittsburgh, PA: U.S. Department of Health and Human Services, pp. 19–28.

Brown A [1958]. Ground stress investigations in Canadian coal mines. Mining Eng., Vol. 10, No. 8, 1958, pp. 879–887.

Campbell WF [1958]. Deep coal mining in Springhill No. 2 Mine. Mining Eng., Vol. 10, No. 9, 1958, pp. 987–982.

Chase FE, Zipf J, R. Karl, Mark C [1994]. The massive collapse of coal pillars—case histories from the United States. In: Peng SS ed., Proceedings of 13th International Conference on Ground Control in Mining. (Morgantown, WV: August 2–4, 1994) Morgantown, WV: West Virginia University, pp. 69–80.

Clark IH [2006]. Simulation of rockmass strength using ubiquitous joints. In: Hart R, Varona P eds. Proceedings of the 4th International FLAC Symposium on Numerical Modeling in Geomechanics. (Madrid, Spain: May 29–31, 2006) Minneapolis, MN: Itasca Consulting Group, Inc., Paper 08-07, 04 pp. pp.

Cook NGW [1965]. The failure of rock. Int. J. Rock Mech. Min. Sci., Vol. 2, pp. 389–403.

Crockford AM, Kalenchuk KS, Bawden WF [2015]. Calibration of inelastic constitutive behaviour at a late stage mine and the challenges associated with data limited calibration. In: Chan A et al. eds. 49th U.S. Rock Mechanics/Geomechanics Symposium. Paper 15–552, (San Francisco: June 28–July 1, 2015) Alexandria, VA: American Rock Mechanics Symposium (ARMA), 8 pp.

Crouch SL, Fairhurst C [1973]. The mechanics of coal mine bumps and the interaction between coal pillars mine roof and floor. U.S.B.M. Contract No. H0101778, Open File Report 53-73, 1973, Washington, D.C., Department of the Interior, Bureau of Mines, 99 pp.

Das MN [1986]. Influence of width/height ratio on post-failure behaviour of coal. Int. J. Min. Geol. Eng., Vol. 4, No. 1, pp. 79–87.

Dolinar D [2003]. Variation of horizontal stresses and strains in mines in bedded deposits in the eastern and midwestern United States. In: Peng SS et al. eds. Proceedings: 22nd International Conference on Ground Control in Mining. (Morgantown, WV: August 5–7, 2003) Morgantown, WV: West Virginia University, pp. 178–185.

Duncan Fama ME, Trueman R, Craig MS [1995]. Two- and three-dimensional elasto-plastic analysis for coal pillar design and its application to highwall mining. Int. J. Rock Mech. Min. Sci. & Geomech. Abstr., Vol. 32, No. 3, pp. 215-225.

Duplancic P, Brady BH [1999]. Characterisation of caving mechanisms by analysis of seismicity and rock stress. In: Vouille G, Berest P eds. Proceedings: 9th International Congress on Rock Mechanics. (Paris, France: August 25–28, 1999) Rotterdam: A.A. Balkema, pp. 1049–1053 pp.

Esterhuizen E, Mark C, Murphy MM [2010a]. The ground response curve, pillar loading and pillar failure in coal mines. In: Barczak T et al. eds. Proceedings: 29th International Conference on Ground Control in Mining. (Morgantown, WV: July 27–29, 2010) Morgantown, WV: West Virginia University, pp. 19–27.

Esterhuizen E, Mark C, Murphy MM [2010b]. Numerical model calibration for simulating coal pillars, gob and overburden response. In: Barczak T et al. eds. Proceedings: 29th International Conference on Ground Control in Mining. (Morgantown, WV: July 27–29, 2010) Morgantown, WV: West Virginia University, pp. 46–57.

Esterhuizen GS, Mark C [2009]. Three-dimensional modeling of large arrays of pillars for coal mine design. In: Esterhuizen GS et al. eds. NIOSH Information Circular 9512, Proceedings of the International Workshop on Numerical Modeling for Underground Mine Excavation Design. (Asheville, NC: June 28, 2009) Pittsburgh, PA: U.S. Department of Health and Human Services, pp. 37–46.

Esterhuizen GS, Tulu IB [2015]. Rapid assessment of roof stability in coal mine entries based on the outcome of validated numerical models. In: Chan A et al. eds. 49th U.S. Rock Mechanics/Geomechanics Symposium. Paper 15–138, (San Francisco: June 28–July 1, 2015) Alexandria, VA: American Rock Mechanics Symposium (ARMA), 7 pp.

Farmer IW [1968]. Engineering properties of rocks, London: E. & F. N. Spon, 180 pp.

Gaddy FL [1956]. A study of the ultimate strength of coal as related to the absolute size of the cubical specimens tested. Bulletin of the Virginia Polytechnic Institute, Engineering Experiment Station Series No. 112. Vol. 49, No. 10, Blacksburg, VA: Virginia Polytechnic Institute, 27 pp.

Gale W, Mark C, Oyler D, Chen J [2004]. Computer simulation of ground behaviour and rock bolt interaction at Emerald Mine. In: Peng SS et al. eds. Proceedings: 23rd International Conference on Ground Control in Mining. (Morgantown, WV: August 3–5, 2004) Morgantown, WV: West Virginia University, pp. 27–34.

Gale WJ [2016]. E-mail, Personal communication to Larson MK, May 24, 2 pp.

Goodman RE [1989]. Introduction to rock mechanics. 2nd ed., New York: John Wiley & Sons, 576 pp.

Hakami MH [1988]. Post-failure behaviour of brittle rock. Ph.D. thesis. Luleå, Sweden: Luleå University of Technology, 150 pp.

Heasley KA [1998]. Numerical modeling of coal mines with a laminated displacement-discontinuity code. Ph.D. Dissertation. Golden, Colorado: Colorado School of Mines, 205 pp.

Heasley KA [2007]. LaModel, ver. 2.1, Morgantown, WV: West Virginia University.

Heasley KA [2008a]. Back-analysis of the Crandall Canyon Mine using the LaModel program. Appendix S in Gates, Richard A. et al. Mine Safety and Health Administration, Report of Investigation, Underground Coal Mine, Fatal Underground Coal Burst Accidents, August 6 and 16, 2007, Crandall Canyon Mine. ID No. 42–01715, Arlington, VA. Department of Labor, Mine Safety and Health Administration, 54 pp.

Heasley KA [2008b]. Some thoughts on calibrating LaModel. In: Peng SS et al. eds. Proceedings: 27th International Conference on Ground Control in Mining. (Morgantown, WV: July 29–31, 2008) Morgantown, WV: West Virginia University, pp. 7–13.

Heasley KA [2009a]. A back analysis of the Crandall Canyon Mine collapse. In: 2009 SME Annual Meeting & Exhibit and CMA's 111th National Western Mining Conference. Preprint 09-154, (Denver, CO: February 22–25, 2009) Littleton, CO: Society for Mining, Metallurgy, and Exploration, Inc., 9 pp.

Heasley KA [2009b]. An overview of calibrating and using the LaModel program for coal mine design. In: Esterhuizen GS et al. eds. NIOSH Information Circular 9512, Proceedings of the International Workshop on Numerical Modeling for Underground Mine Excavation Design.

(Asheville, NC: June 28, 2009) Pittsburgh, PA: U.S. Department of Health and Human Services, pp. 63–74.

Heasley KA [2010]. LaModel, ver. 3.0, Morgantown, WV: West Virginia University.

Heasley KA, Barton TM [1998]. Subsidence prediction using a laminated boundary-element program. In: Vol. 35, Nos. 4-5, NARMS'98—3rd North American Rock Mechanics Symposium, International Journal of Rock Mechanics and Mining Sciences. (Cancún, Mexico: June 3–5, 1998), pp. 381–390.

Heasley KA, Barton TM [1999]. Coal mine subsidence prediction using a boundary-element program. In: SME Annual Meeting. Preprint 99-181, (Orlando, FL: March 9–11, 1999) Littleton, CO: Society for Mining, Metallurgy, and Exploration, Inc., 6 pp.

Heuze FE [1980]. Scale effects in the determination of rock mass strength and deformability. Rock Mech., Vol. 12, No. 3–4, pp. 167-192.

Hoek E, Brown ET [1980]. Underground excavations in rock. London: The Institution of Mining and Metallurgy, 532 pp.

Hoek E, Carranza-Torres C, Corkum B [2002]. Hoek-Brown failure criterion—2002 edition. In: Hammah R et al. eds. 1, Proceedings of the 5th North American Rock Mechanics Symposium and the 17th Tunnelling Association of Canada Conference: NARMS-TAC 2002—Mining and Tunnelling Innovation and Opportunity. (Toronto, Ontario, Canada: July 7-10, 2002) Toronto, Ontario, Canada: University of Toronto, pp. 267–273.

Holland CT [1958]. Cause and occurrence of coal mine bumps. Mining Eng., Vol. 10, No. 9, 1958, pp. 994–1004B.

Holland CT [1964]. The strength of coal in mine pillars. In: Spokes EM, Christiansen CR eds. Proceedings of the Sixth Symposium on Rock Mechanics. (Rolla, MO: October 1964) Rolla, MO: University of Missouri at Rolla, pp. 450–466.

Iannacchione AT, Tadolini SC [2016]. Occurrence, predication, and control of coal burst events in the U.S. Int. J. Min. Sci. Technol., Vol. 26, No. 1, pp. 39–46.

Itasca Consulting Group [2009]. FLAC3D: Fast Lagrangian analysis of continua in 3 dimensions—user's guide (version 4.0). 274 pp.

Itasca Consulting Group [2012]. UDECTM version 6.0, Distinct-element modeling of jointed and blocky material in 2D: User's guide. Minneapolis, MN: Itasca Consulting Group, 268 pp.

Jaeger JC, Cook NGW [1976]. Fundamentals of rock mechanics. 2nd ed., New York: John Wiley & Sons, Inc., 604 pp.

Jaiswal A, Shrivastva BK [2009]. Numerical simulation of coal pillar strength. Int. J. Rock Mech. Min. Sci., Vol. 46, No. 4, pp. 779–788.

Jaiswal A, Shrivastva BK [2012]. Stability analysis of the proposed hybrid method of partial extraction for underground coal mining. Int. J. Rock Mech. Min. Sci., Vol. 52, pp. 103–111.

Johnson JC, Whyatt JK, Loken MC [2014]. A generalized method for calculating pillar cell capacities for boundary element modeling of coal mines. In: Preprints 2014: 2014 SME Annual Meeting & Exhibit. (Salt Lake City, UT: February 23–26, 2014) Denver, CO: Society for Mining, Metallurgy, and Exploration, Inc., pp. Preprint 14-162, 122 pp.

Karabin G, J., Evanto MA [1994]. Experience with the boundary element method of numerical modeling as a tool to resolve complex ground control problems. In: Peng SS ed., Proceedings of 13th International Conference on Ground Control in Mining. (Morgantown, WV: August 2–4, 1994) Morgantown, WV: West Virginia University, pp. 201–213.

King HJ, Whittaker BN [1970]. A review of current knowledge on roadway behaviour, especially the problems on which further information is required. In: Proceedings of the Symposium on Roadway Strata Control in Roadways. (Nottingham, U.K.: April 16, 1970) London: The Institution of Mining Engineers, pp. 73–87.

Kumar R, Sharma KG, Varadarajan A [2010]. Post-peak response of some metamorphic rocks of India under high confining pressures. Int. J. Rock Mech. Min. Sci., Vol. 47, No. 8, pp. 1357–1362.

Lama RD, Vutukuri VS [1978a]. Handbook on mechanical properties of rocks—testing techniques and results, 4 vols, Vol. IV, Clausthal, Germany: Trans Tech Publications, 534 pp.

Lama RD, Vutukuri VS [1978b]. Handbook on mechanical properties of rocks—testing techniques and results, 4 vols, Vol. III, Clausthal, Germany: Trans Tech Publications, 416 pp.

Lama RD, Vutukuri VS [1978c]. Handbook on mechanical properties of rocks—testing techniques and results, 4 vols, Vol. II, Clausthal, Germany: Trans Tech Publications, 495 pp.

Lan H, Martin CD, Hu B [2010]. Effect of heterogeneity of brittle rock on micromechanical extensile behaviour during compression loading. J. Geophys. Res., Vol. 115, No. B01202, pp. 1–14.

Larson MK, Lawson HE, Tesarik DR [2015]. Load transfer distance measurements at two mines in the western U.S. In: Barczak TM et al. eds. Proceedings of the 34th International Conference on Ground Control in Mining. (Morgantown: July 28–30, 2015) Morgantown, WV: West Virginia University, pp. 54–64.

Larson MK, Whyatt JK [2009a]. Critical review of numerical stress analysis tools for deep coal longwall panels under strong strata. In: Miller H et al. eds. 2009 SME Annual Meeting & Exhibit and Colorado Mining Association's 111th National Western Mining Conference. Preprint 09-011, (Denver, CO: February 22–25, 2009) Denver, CO: Society for Mining, Metallurgy, and Exploration, Inc., 12 pp.

Larson MK, Whyatt JK [2009b]. Deep coal longwall panel design for strong strata: The influence of software choice on results. In: Esterhuizen GS et al. eds. NIOSH Information Circular 9512, Proceedings of the International Workshop on Numerical Modeling for Underground Mine Excavation Design. (Asheville, NC: June 28, 2009) Pittsburgh, PA: U.S. Department of Health and Human Services, pp. 75–87.

Larson MK, Whyatt JK [2010]. Critical comparison of numerical stress analysis tools for deep coal longwall panels under strong strata. 2009 Transactions, Vol. 326, pp. 49–60.

Larson MK, Whyatt JK [2012]. Load transfer distance calibration of a coal panel scale model: A case study. In: Barczak T et al. eds. Proceedings of the 31st International Conference on Ground Control in Mining. (Morgantown, WV: July 31–August 2, 2012) Morgantown, WV: West Virginia University, pp. 195–205.

Larson MK, Whyatt JK [2013]. Panel-scale modeling of a deep longwall panel: The Mulsim alternative. In: Barczak T et al. eds. Proceedings: 32nd International Conference on Ground Control in Mining. (Morgantown, WV: July 30–August 1, 2013) Morgantown, WV: West Virginia University, pp. 181–188.

Lawall CE, Holland CT [1937]. Some physical characteristics of West Virginia coals. Research Bulletin No. 17, Engineering Experiment Station, Morgantown, WV: West Virginia University, 50 pp.

Lawson HE, Whyatt J, Larson M [2013]. Investigation of pillar loading considerations in determination of pillar stability factors for longwall gateroad design. In: Barczak T et al. eds. Proceedings, 32nd International Conference on Ground Control in Mining. (Morgantown, WV: July 30–August 1, 2013) Morgantown, WV: West Virginia University, pp. 28–37.

Li K, Heasley KA [2015]. Calculating the potential for coal pillar bumps using a local mine stiffness criterion. In: Chan A et al. eds. 49th U.S. Rock Mechanics/Geomechanics Symposium. Paper 15–241, (San Francisco: June 28–July 1, 2015) Alexandria, VA: American Rock Mechanics Symposium (ARMA), 8 pp.

Lu PH [1984]. Mining-induced stress measurement with hydraulic borehole pressure cells. In: Dowding CH, Singh MM eds. Rock Mechanics in Productivity and Protection, Proceedings: Twenty-Fifth Symposium on Rock Mechanics. (Evanston, IL: June 25–27, 1984) New York, NY: Society of Mining Engineers, pp. 204–211.

Maleki H [1992]. In situ pillar strength and failure mechanisms for U.S. coal seams. In: Iannacchione AT et al. eds. Bureau of Mines Information Circular 9315, Proceedings of the Workshop on Coal Pillar Mechanics and Design. (Santa Fe, NM: June 7, 1992) U.S. Department of the Interior, pp. 73–77.

Maleki H [2017]. Coal pillar mechanics of violent failure in U.S. mines. Int. J. Min. Sci. Technol., Vol. 27, No. 3, pp. 387–392.

Maleki H, Hustrulid W, Johnson D [1984]. Pressure measurements in the gob. In: Dowding CH, Singh MM eds. Rock Mechanics in Productivity and Protection—Proceedings: 25th U.S. Symposium on Rock Mechanics. (Evanston, Illinois: June 25–27, 1984) New York: Society of Mining Engineers, pp. 533–545.

Maleki H, Stewart C, Stone R [2007]. Three-seam stress analyses at Bowie Mines, Colorado. In: Peng SS et al. eds. Proceedings: 26th International Conference on Ground Control in Mining. (Morgantown, WV: July 31–August 2, 2007) Morgantown, WV: West Virginia University, pp. 29–37.

Mark C [1987]. Analysis of longwall pillar stability. Ph.D. Thesis. University Park, PA: The Pennsylvania State University, 441 pp.

Mark C [1992]. Analysis of Longwall Pillar Stability (ALPS): An update. In: Iannacchione AT et al. eds. Proceedings of the Workshop on Coal Pillar Mechanics and Design. Pittsburgh, PA: U.S. Department of the Interior, Bureau of Mines Information Circular 9315, pp. 238–249.

Mark C [1999]. Empirical methods for coal pillar design. In: Christopher M et al. eds. Information Circular 9448, Proceedings of the Second International Workshop on Coal Pillar Mechanics and Design. Pittsburgh, PA: U.S. Department of Health and Human Services, Centers

for Disease Control and Prevention, National Institute for Occupational Safety and Health, DHHS (NIOSH), pp. 145–154.

Mark C [2015]. E-mail, Personal communication to Larson MK, November 10, 3 pp.

Mark C, Barton T [1996]. The uniaxial compressive strength of coal: Should it be used to design pillars? In: Ozdemir L et al. eds. Proceedings: 15th International Conference on Ground Control in Mining. (Golden, CO: August 13-15, 1996) Golden, CO: Colorado School of Mines, pp. 61–78.

Mark C, Chase FE [1997]. Analysis of Retreat Mining Pillar Stability (ARMPS). In: Mark C, Tuchman RJ eds. Proceedings: New Technology for Ground Control in Retreat Mining, DHHS (NIOSH) Publication No. 97-133, IC 9446. Pittsburgh, PA: National Institute for Occupational Safety and Health (NIOSH), pp. 17–34.

Mark C, Chase FE, Molinda GM [1994]. Design of longwall gate entry systems using roof classification. In: Special Publication 01–94, Proceedings of the U.S. Bureau of Mines Technology Transfer Seminar. New Technology For Longwall Ground Control. U.S. Department of the Interior, Bureau of Mines, pp. 5–17.

Mark C, Molinda G, Dolinar D [2001]. Analysis of roof bolt systems. In: Peng SS et al. eds. Proceedings: 20th International Conference on Ground Control in Mining. (Morgantown, WV: August 7–9, 2001) Morgantown, WV: West Virginia University, pp. 218–225.

Mark C, Phillipson S, Tyrna P, Gauna M [2012]. Characteristics of coal bursts in the North Fork Valley of the Gunnison River Valley, Colorado. In: Barczak T et al. eds. Proceedings: 31st International Conference on Ground Control in Mining. (Morgantown, WV: July 31–August 2, 2012) Morgantown, WV: West Virginia University, pp. 1–13.

Mauck HE [1958]. Coal mine bumps can be eliminated. Mining Eng., Vol. 10, No. 9, 1958, p. 923.

McMahon BK [1988]. Australian Geomechanics Society E.H. Davis Memorial Lecture: Geotechnical design in the face of uncertainty. Austr. Civil Eng. Trans., pp. 93–106.

Mishra B, Nie D [2013]. Experimental investigation of the effect of change in control modes on the post-failure behavior of coal and coal measures rock. Int. J. Rock Mech. Min. Sci., Vol. 60, pp. 363–369.

MSHA [2008]. Report of investigation—Fatal underground coal burst accidents, August 6 and 16, 2007, Crandall Canyon Mine, Genwal Resources Inc, Huntington, Emery County, Utah. By Gates RA, Gauna M, Morley TA, O'Donnell JR, Smith GE, Watkins TR, Weaver CA, and Zelanko JC. CAI-2007-15-17, 19-24 U.S. Department of Labor, Mine Safety and Health Administration (MSHA), 472 pp.

MSHA [2009]. General guidelines for the use of numerical modeling to evaluate ground control aspects of proposed coal mining plans. By Skiles ME, and Stricklin KG. Program Information Bulletin No. P09-03, March 16, 2009, Arlington, VA: U.S. Department of Labor, Mine Safety and Health Administration (MSHA), 7 pp.

Newman D [2008]. Coal mine bumps: Case histories of analysis and avoidance. In: Peng SS et al. eds. Proceedings: 27th International Conference on Ground Control in Mining. (Morgantown, WV: July 29-31, 2008) Morgantown, WV: West Virginia University, pp. 1-6.

NIOSH [2020]. Ground stress in mining (part 1): Measurements and observations at two western U.S. longwall mines. By Larson MK, Lawson HE, Zahl EG, Jones TH. U.S. Department of Health and Human Services, Centers for Disease Control and Prevention, National Institute for Occupational Safety and Health, DHHS (NIOSH) Publication No. 2019-175, RI 9702.

Özbay MU [1989]. The stability and design of yield pillars located at shallow and moderate depths. Journal of the South African Institute of Mining and Metallurgy, Vol. 89, No. 3, pp. 73–79.

Ozbay U, Badr S [2010]. Numerical modeling of yielding chain pillars in deep longwall coal mines. In: Mark C et al. eds. Proceedings: 3rd International Workshop on Coal Pillar Mechanics and Design. (Morgantown, WV: July 26, 2010) Morgantown, WV: West Virginia University, pp. 64–71.

Pariseau WG [2012]. Design analysis in rock mechanics. 2nd ed., London: Taylor and Francis, 698 pp.

Pariseau WG, Fowler ME, Johnson JC, Poad M, Corp EL [1984]. Geomechanics of the Carr Fork Mine test stope, Ch. 1, In: Geomechanics applications in underground hardrock mining, ed. by Pariseau WG, New York: Society of Mining Engineers of the American Institute of Mining, Metallurgical, and Petroleum Engineers, Inc., pp. 3–38.

Pariseau WG, Poad M, Corp EL, Schmuck CH [1986]. Rock mechanics of a deep VCR stope at the Homestake Mine. In: Karmis M ed., International Symposium on Application of Rock Characterization Techniques in Mine Design. (New Orleans, LA: March 1986) Society of Mining Engineers, Inc., pp. 56–70.

Pariseau WG, Tesarik DR, Trancynger TC [2013]. Rock mechanics of the Davis Detector Cavern. Transactions of the Society for Mining, Metallurgy, and Exploration, Vol. 332, pp. 370–388.

Peck RB [1969]. Advantages and limitations of the observational method in applied soil mechanics. Géotechnique, Vol. 19, No. 2, pp. 171–187.

Peng SS, Chiang HS [1984]. Longwall mining, New York: John Wiley & Sons, 720 pp.

Peperakis J [1958]. Mountain bumps at the Sunnyside Mines. Mining Eng., Vol. 10, No. 9, 1958, pp. 982–986.

Pierce M, Board M [2010a]. Development of a three-dimensional numerical modeling environment for caving and stress analysis of longwall mining. Report 2552-05, Prepared for NIOSH, Spokane Research Laboratory, August 31, 2010, Minneapolis, MN, Itasca Consulting Group, Inc., 43 pp.

Pierce M, Board M [2010b]. FLAC3D Longwall Modeling Environment, ver. 1.0, Minneapolis, MN: Itasca Consulting Group.

Pierce ME [2010a]. Equations in FISH function of LME for influence of UCS and shape factor. Verbal, Personal communication to Larson MK, September 15.

Pierce ME [2010b]. Fish function equations to account for bulking in LME. Verbal, Personal communication to Larson MK, September 16.

Poeck E, Corkum A, Board M [2008]. Two-dimensional discontinuum model of longwall collapse. Report #HCI-1866, September 5, 2008, Minneapolis, MN: Itasca Consulting Group Inc., 42 pp.

Price AM [1979]. The effects of confining pressure on the post-yield deformation characteristics of rocks. Ph.D. thesis. University of Newcastle upon Tyne.

Ramírez Oyanguren P [1972]. Simultaneous extraction of two potash beds in close proximity. In: Proceedings, Fifth International Strata Control Conference. (London: 1972) London: National Coal Board, 5 pp.

Robeck ED [2005]. The effects of fault-induced stress anisotropy on fracturing, folding and sill emplacement: Insights from the Bowie Coal Mines, Southern Piceance Basin, western Colorado. M.S. thesis. Provo, UT: Brigham Young University, Department of Geology, 106 pp.

Sainsbury B, Pierce ME, Mas Ivars D [2008]. Analysis of caving behaviour using a synthetic rock mass—ubiquitous joint rock mass modelling technique. In: Potvin Y et al. eds. 1, Proceedings of the 1st Southern Hemisphere International Rock Mechanics Symposium SHIRMS 2012. (Perth, Australia: September 16–19, 2008) Perth, Australia: The Australian Centre for Geomechanics, pp. 243–255.

Salamon MDG [1963]. Elastic analysis of displacements and stresses induced by the mining of seam or reef deposits. Part I. Fundamental principles and basic solutions as derived from idealized models. J. S. Afr. Inst. Min. Metall., Vol. 64, pp. 128–149.

Salamon MDG [1970]. Stability, instability and design of pillar workings. Int. J. Rock Mech. Min. Sci., Vol. 7, No. 1, 1970, pp. 613–631.

Salamon MDG [1990]. Mechanism of caving in longwall coal mining. In: Hustrulid WA, Johnson GA eds. Rock Mechanics Contributions and Challenges: Proceedings of the 31st U.S. Symposium. (Golden, CO: June 18–20, 1990) A.A. Balkema, pp. 161–168 pp.

Salamon MDG [1991]. Deformation of stratified rock masses: A laminated model. J. S. Afr. Inst. Min. Metall., Vol. 91, No. 1, 1991, pp. 9–26.

Seymour B, Tesarik D, Larson M, Shoemaker J [1998]. Stability of backfilled cross-panel entries during longwall mining. In: Peng SS ed., Proceedings: 17th International Conference on Ground Control in Mining. (Morgantown, WV: August 4–6, 1998) Morgantown, WV: Department of Mining Engineering, West Virginia University, pp. 11–20 pp.

Sheorey PR [1997]. Empirical rock failure criteria, Rotterdam: A.A. Balkema, 176 pp.

Singh MM, Kendorski FS [1981]. Strata disturbance prediction forming beneath surface water and waste impoundments. In: Peng SS ed., Proceedings of the 1st Annual Conference on Ground Control in Mining. (Morgantown, WV: July 27–29, 1981) West Virginia University, pp. 76–89.

Sinha KP [1979]. Displacement discontinuity technique for analyzing stress and displacements due to mining in seam deposits. Ph.D. Thesis. University of Minnesota, 325 pp.

Stacey TR [2009]. Design—a strategy issue. J. South. Afr. Inst. Min. Metall., Vol. 109, pp. 157–162.

Starfield AM, Cundall PA [1988]. Towards a methodology for rock mechanics modelling. Int. J. Rock Mech. Min. Sci., Vol. 25, No. 3, pp. 99–106.

Talman WG, Schroder JL, Jr. [1958]. Control of mountain bumps in the Pocahontas No. 4 Seam. Mining Eng., Vol. 10, No. 8, pp. 888–891.

Terzaghi K [1961]. Past and future of applied soil mechanics. J. Boston Soc. Civ. Engrs., Vol. 68, pp. 110–139.

Tesarik DR, Seymour JB, Yanske TR [2003]. Post-failure behavior of two mine pillars confined with backfill. Int. J. Rock Mech. Min. Sci., Vol. 40, No. 2, pp. 221–232.

Tesarik DR, Whyatt JK, Larson MK [2013]. Inferring mine floor properties from pillar size and floor heave. In: Pyrak-Nolte LJ et al. eds. Proceedings of the 47th U.S. Rock Mechanics/Geomechanics Symposium. (San Francisco, CA: June 23–26, 2013) Alexandria, VA: American Rock Mechanics Association, pp. 438–450.

Thomas E [1958]. U. S. Bureau of Mines investigations and research on bumps. Mining Eng., Vol. 10, No. 8, 1958, pp. 878–879.

USBM [1988]. MULSIM/BM—A structural analysis computer program for mine design. Beckett LA, Madrid RS. Information Circular 9168, Pittsburgh, PA: U.S. Department of the Interior, Bureau of Mines (USBM), 306 pp.

USBM [1990]. Pillar design methods for longwall mining. By Mark C. Information Circular 9247, Pittsburgh, PA: U.S. Department of the Interior, Bureau of Mines (USBM), 55 pp.

USBM [1992a]. MULSIM/NL application and practitioner's manual. By Zipf RK, Jr. Information Circular 9322, Pittsburgh, PA: U.S. Department of the Interior, Bureau of Mines (USBM), 44 pp.

USBM [1992b]. MULSIM/NL theoretical and programmer's manual. By Zipf, RK, Jr. Information Circular 9321, Pittsburgh, PA: U.S. Department of the Interior, Bureau of Mines (USBM), 52 pp.

USBM [1992c]. MULSIM/PC—a personal-computer-based structural analysis program for mine design in deep tabular deposits. By Donato DA. Information Circular 9325, Pittsburgh, PA: U.S. Department of the Interior, Bureau of Mines (USBM), 60 pp.

USBM [1992d]. Rock mechanics investigations at the Lucky Friday Mine (in three parts): 3. Calibration and validation of a stope-scale finite-element model. By Pariseau WG, Whyatt JK, and McMahon TJ. Report of Investigations 9434, Pittsburgh, PA: U.S. Department of the Interior, Bureau of Mines (USBM), 20 pp.

USBM [1993]. Behavior of simulated longwall gob material. By Pappas DM, and Mark C. Report of Investigations 9458, Pittsburgh, PA: U.S. Department of the Interior, Bureau of Mines (USBM), 42 pp.

USBM [1994]. Coal Mine Roof Rating (CMRR): A practical rock mass classification for coal mines. By Molinda GM, and Mark C. Information Circular 9387, Pittsburgh, PA: U.S. Department of the Interior, Bureau of Mines (USBM), 83 pp.

USBM [1995]. Rock mechanics study of shaft stability and pillar mining, Homestake Mine, Lead, SD (in three parts) 2. Mine measurements and confirmation of premining results. By Pariseau WG, Johnson JC, McDonald MM, Poad ME. Report of Investigations 9576, Pittsburgh, PA: U.S. Department of the Interior, Bureau of Mines (USBM), 22 pp.

USBM [1996]. Rock mechanics study of shaft stability and pillar mining, Homestake Mine, Lead, SD (in three parts) 3. Geomechanical monitoring and modeling using UTAH3. By Pariseau WG, Johnson JC, McDonald MM, and Poad ME. Report of Investigations 9618, Pittsburgh, PA: U.S. Department of the Interior, Bureau of Mines (USBM), 36 pp.

Voronoi G [1908]. Nouvelles applications des paramètres continus à; a théorie des formes quadratiques. Premier mémoire. Sur quelques propriétés des formes quadratiques positives parfaites. J Reine Angew. Math., Vol. 1908, No. 133, pp. 97–102.

Vutukuri VS, Lama RD, Saluja SS [1974]. Handbook on mechanical properties of rocks—testing techniques and results. 1st ed., 4 vols, Vol. I, Clausthal, Germany: Trans Tech Publications, 300 pp.

Wade LV, Conroy PJ [1980]. Rock mechanics study of a longwall panel. Mining Eng., Vol. 32, No. 12, pp. 1728–1735.

Wagner H [1974]. Determination of the complete load-deformation characteristics of coal pillars. In: II, Part B, Themes 3-5, Advances in Rock Mechanics: Reports of Current Research: Proceedings of the Third Congress of the International Society for Rock Mechanics. (Denver, CO: September 1–3, 1974) Washington, D.C.: National Academy of Sciences, pp. 1076–1081 pp.

Wawersik WR, Fairhurst C [1970]. A study of brittle rock fracture in laboratory compression experiments. Int. J. Rock Mech. Min. Sci. & Geomech. Abstr., Vol. 7, No. 5, pp. 561–575.

Whyatt JK, Larson MK, Heasley KA [2011]. Topography and coal seam initial stress estimation: A sensitivity study. In: Barczak T et al. eds. Proceedings: 30th International Conference on Ground Control in Mining. (Morgantown, WV: July 26–28, 2011) Morgantown, WV: West Virginia University, pp. 58–66.

Wiles T [2007]. Evidence based model calibration for reliable predictions. In: Potvin Y ed., Deep Mine 07, Proceedings of the Fourth International Seminar on Deep and High Stress Mining. (Perth, Australia: November 7–9, 2007) Perth: Australian Centre for Geomechanics, pp. 3–20 pp.

Wilson AH [1972]. A hypothesis concerning pillar stability. Part 1 of research into the determination of pillar size. The Mining Engineer, Vol. 131, Part 9, 1972, pp. 409–417.

Wilson AH, Ashwin DP [1972]. Research into the determination of pillar size. The Mining Engineer, Vol. 131, No. 141, Part 9, pp. 409–430.

Zhang Y, Stead D, Elmo D [2015]. Characterization of strength and damage of hard rock pillars using a synthetic rock mass method. Comput. Geotech., Vol. 65, pp. 56–72.

Zhao J [1994]. Geothermal testing and measurements of rock and rock fractures. Geothermics, Vol. 23, No. 3, pp. 215–231.

Zipf RK, Jr. [2006]. Numerical modeling procedures for practical coal mine design. In: Yale D et al. eds. Golden Rocks 2006—50 Years of Rock Mechanics—Landmarks and Future Challenges: Proceedings of the 41st U.S. Rock Mechanics Symposium (USRMS). (Golden, CO: June 17–21, 2006) Alexandria, VA: American Rock Mechanics Association, pp. 1–11 pp.

Appendix A: MulsimNL/Large File Format and Verification Problems

Summary

Because of difficulties encountered in calibrating a panel-scale model using LaModel [Heasley 2010] to a large load transfer distance (LTD) and finding final gob stiffness that produced reasonable gob loading, the Zipf version of MULSIM/NL [USBM 1992b, 1992a] was enlarged, and other enhancements were added for ease of use. This appendix describes the changes that were made and the format needed for the input file for this enlarged and enhanced version, called MulsimNL/Large. Three example problems from the work of R. K. Zipf, Jr. [USBM 1992a] were run, and the results verified that MulsimNL/Large is working properly. Additionally, a five-point constitutive law was added to MulsimNL/Large. This addition is described in Appendix G but is mentioned here for the purpose of providing information on the input file format.

Background

The last public version of Mulsim was developed by Zipf [USBM 1992b, 1992a]. Zipf's version of Mulsim has largely been supplanted by LaModel [Heasley 2010] as a tool for evaluating coal mine design, largely because of the further development of LaModel and the shorter time to complete model calculations. However, Larson and Whyatt [2013] recently demonstrated that it is difficult to calibrate LaModel to a large LTD and maintain reasonable gob loading. The authors of this report took Zipf's copy of the source code and enlarged the arrays so that it handles problems of a size comparable to that of LaModel. This was necessary because the maximum number of coarse blocks in both x- and y-directions in the original source code was 70—too small to handle today's panel-scale models. The maximum number of coarse blocks in the x or y-direction that could be converted to 5 × 5 fine elements was 50, making the maximum fine mesh size 250 × 250. In addition, the maximum number of material codes was 26, which was insufficient to handle the number of yield rings around larger pillars for the case study examined by Larson and Whyatt [2012, 2013]. The number of material codes was increased to 52, all of which were identified by using both capital and small letters of the alphabet.

As upgrades to the code began, other needed improvements became apparent. Output files from any problem were given the same name, necessitating first that problems be run in separate folders, and second that filename changes be made so that results from different models were not mixed inadvertently after completion. Filename maintenance became cumbersome, even with the use of DOS batch files to effect the name changes.

In addition, some Fortran syntax was out of date and needed correction. Initially, a Lahey-Fujitsu compiler [Lahey Computer Systems 2011] was used in an attempt to compile the code but was abandoned without success. Intel Visual Fortran Studio XE for Windows with Microsoft Visual Studio provided a successful development environment.[5]

[5] Mention of specific products does not imply endorsement by the National Institute for Occupational Safety and Health.

Changes in Features

The current compiled version of MulsimNL/Large is version 1.2. The following features were changed from the Zipf version:

- The number of coarse block elements was increased from 70 by 70 to 450 by 450.
- The number of these coarse block elements that could convert to 5 by 5 fine elements was increased to 400 by 400 from 50 by 50, thus making it possible to have 2,000 by 2,000 fine elements instead of only 250 by 250 fine elements.
- The number of material codes was increased to 52 (denoted by letters A through Z and a through z) from 26 material codes (A through Z).
- The number of significant digits of variables in all output files was increased. Stresses output in the Zipf version of the code were rounded to the nearest 10 units (usually psi). Although such rounding may be practical, it did not lend itself to code verification nor to close comparison to outputs from LaModel. In the current version, both stresses and closure displacements are output with seven decimal places. The responsibility belongs to the user to report specific results that are rounded appropriately.
- The program asks for keyboard input of the variable "rootname." This string forms the first part of all input and output filenames. For example, if the root filename is entered as "Model1", then the input file must be named Model1.inp, the output files will be named Model1_for11.dat, Model1_for21.dat, Model1_for31.dat, and Model1_for41.dat, and the log file will be named Model1_log.dat. In addition, two files are created at the start and end of a model and are named, for example, Model1_start.txt and Model1_end.txt. These two files only contain a date and time stamp so that the user can determine the time duration of the model calculations.
- A five-point strength law (constitutive model #7) was added. The last point represents a residual strain that remains constant for strains greater than that at the fifth point. Figure A1 shows an example of such a law. Details of this constitutive law and its verification are found in Appendix G.
- Energy calculations were updated to be in accordance with the equations described by Sears [2009].

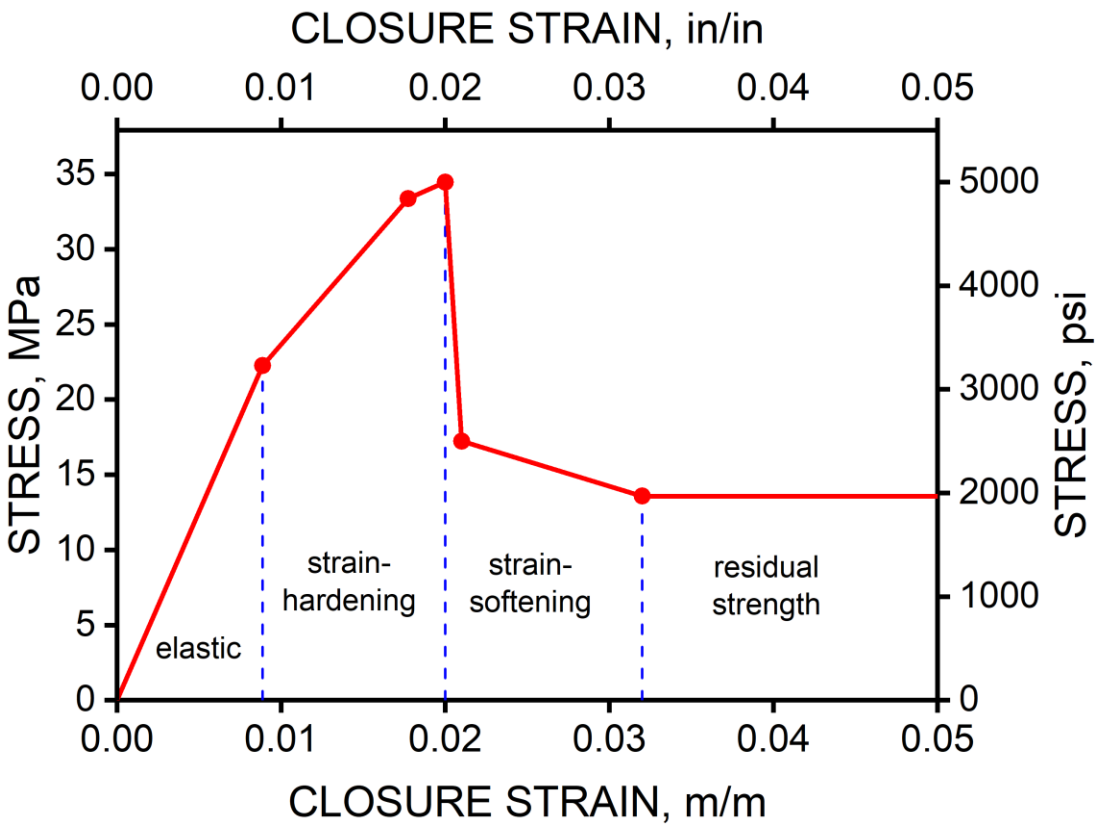

Figure A1. Example of five-point strength law.

Possible Future Capabilities

Two capabilities found in LaModel have not yet been implemented in the MulsimNL/Large software, but are future possibilities:

- Border symmetry (currently, only fixed borders are possible).
- Topography, implemented the same as by Heasley [1998], with forces applied and propagated from a datum at average depth above the seam.

In addition, it might be advantageous, as Heasley [2010] has done, to implement pre- and post-processing capabilities.

Input File Format

The input file variables and formats are listed in Table A1. Table A2 lists the parameters needed for each constitutive model. Table A3 lists additional varaibles needed for constitutive model 7, the five-point strength law.

Table A1. Records, variables, and formats for MulsimNL/Large input files

Record	Variables	Description	Format
1	Title	Descriptive title of model	20a4
2	v, e, nseam	Poisson's ratio and Young's modulus of rock mass, number of parallel seams at depth	f8.6, e12.5, i8
3	Nmats	Number of in-seam materials (up to 52)	i8
4	(eprop(n,i), i=1,12)*	Properties for nth material (need nmats lines for this record)†	f8.0, 11e16.7
5	a11, b11, a12, b12, a13, b13, a22, b22, a23, b23, a33, b33	Primitive stress parameters (σ_{xx}, $\Delta\sigma_{xx}$, τ_{xy}, $\Delta\tau_{xy}$, τ_{xz}, $\Delta\tau_{xz}$, σ_{yy}, $\Delta\sigma_{yy}$, τ_{yz}, $\Delta\tau_{yz}$, σ_{zz}, $\Delta\sigma_{zz}$	6(f12.5, f12.8)
6	bw, nbxx, nbyy, nosp, ifxs, ifxe, ifys, ifye	Block width, number of blocks in x-direction, number of blocks in y-direction, number of off-seam planes, fine-mesh starting block in x-direction, fine-mesh ending block in x-direction, fine-mesh starting block in y-direction, fine-mesh ending block in y-direction	f8.2, 2i8, 8x, 5i8
7	(xo(n), yo(n), zo(n), sthick(n), n = 1, nseam)	Global coordinates, xo, yo, & zo of the centroid of the lower, left block of seam n, thickness of seam n	4f8.1
8	((en(i,j),i = 1, 3),j = 1, 3)	Direction cosines of local coordinate system axes	9f8.6
9	orf, sigacc, itmax, nstep, mxstep	Over-relaxation factor, stress convergence criterion, maximum number of iterations, beginning mining step number, number of new mining steps	f8.6,f12.10,i8,24x,2i8
10	(fmptmp(ltmp,k),k=1,nexx)	Fine material property codes for seam 1 for first mining step	2000a1
	(fmptmp(ltmp,k),k=1,nexx)	Fine material property codes for seam 2† for first mining step	2000a1
	(fmptmp(ltmp,k),k=1,nexx)	Fine material property codes for seam 3† for first mining step	2000a1
	(fmptmp(ltmp,k),k=1,nexx)	Fine material property codes for seam 4† for first mining step	2000a1
11	(mtsblc(jb,ib,ns),ib=1,nbxx)	Coarse material property codes for seam 1 for first mining step	2000a1
	(mtsblc(jb,ib,ns),ib=1,nbxx)	Coarse material property codes for seam 2† for first mining step	2000a1
	(mtsblc(jb,ib,ns),ib=1,nbxx)	Coarse material property codes for seam 3† for first mining step	2000a1
	(mtsblc(jb,ib,ns),ib=1,nbxx)	Coarse material property codes for seam 4† for first mining step	2000a1
12	(fmptmp(ltmp,k),k=1,nexx)	Fine material property codes for seam 1 for second mining step§	2000a1
	(fmptmp(ltmp,k),k=1,nexx)	Fine material property codes for seam 2† for second mining step§	2000a1
	(fmptmp(ltmp,k),k=1,nexx)	Fine material property codes for seam 3† for second mining step§	2000a1
	(fmptmp(ltmp,k),k=1,nexx)	Fine material property codes for seam 4† for second mining step§	2000a1

Record	Variables	Description	Format
13	(mtsblc(jb,ib,ns),ib=1,nbxx)	Coarse material property codes for seam 1 for second mining step§	2000a1
	(mtsblc(jb,ib,ns),ib=1,nbxx)	Coarse material property codes for seam 2† for second mining step§	2000a1
	(mtsblc(jb,ib,ns),ib=1,nbxx)	Coarse material property codes for seam 3† for second mining step§	2000a1
	(mtsblc(jb,ib,ns),ib=1,nbxx)	Coarse material property codes for seam 4† for second mining step§	2000a1
Repeat records 12 and 13 for additional mining steps			

*Not all fields are used, depending on the material type selected. See Table A2 and Table A3 for the list of material types and inputs needed.
†Material code inputs for seams 2 through 4 are only if those seams exist in the model.
‡For gravitational stresses, one would enter the absolute stresses as zero, and the changes in stress per unit of depth as nonzero. Changes in shear stresses per unit of depth are zero if the initial principal stresses line up with the model axes.
§Material code inputs for mining steps greater than the first mining step are only if those mining steps are designated by variable mxstep in record 9.

Table A2. Material model parameters and material properties for array EPROP in record 4 (after Zipf [USBM 1992a], except model 7)

Model	Parameter 1	Parameter 2	Parameter 3	Parameter 4	Parameter 5	Paramater 6
1	Linear elastic coal (1)	Young's modulus	Shear modulus	NA*	NA	NA
2	Strain-softening coal (2)	Peak stress	Peak strain	Residual stress	Residual strain	Poisson's ratio
3	Elastic-plastic coal (3)	Peak stress	Peak strain	Plastic modulus	Poisson's ratio	NA
4	Bilinear-hardening gob (4)	Offset stress	Offset strain	Hardening modulus	Poisson's ratio	Gob height factor
5	Strain-hardening gob (5)	Initial modulus	Final modulus	Final stress	Gob height factor	Poisson's ratio
6	Linear elastic gob (6)	Young's modulus	Shear modulus	Gob height factor	NA	NA
7	Five-point stress-strain coal (7)	Stress 1	Strain 1	Stress 2	Strain 2	Stress 3

*NA = Not applicable

Table A3. Material model parameters and material properties for parameters 7 to 12 for model 7 for array EPROP in record 4

Model	Parameter 7	Parameter 8	Parameter 9	Parameter 10	Parameter 11	Parameter 12
7	Strain 3	Stress 4	Strain 4	Residual stress	Residual strain	Poisson's ratio

Verification Problems

Zipf [USBM 1992a] listed three verification problems: (1) longwall example, (2) multiple-seam example, and (3) random pillar example. The contents of the input files are located at the end of this appendix, but the font is reduced in size to minimize the number of lines that are continued as multiple lines. These problems, whose inputs are listed in the format presently required, were run with version 1.2 of MulsimNL/Large. As the post-processing code that Zipf used for Mulsim was not available, the authors used OriginPro v. 9.0 to generate contour plots for comparison with those shown by Zipf.

The longwall example simulates the progression of a longwall retreat from mining step 1 to mining step 2. The area of mesh refinement includes part of the gob and one of the gate roads. Figure A2 shows plots of stress and seam closure calculated by MulsimNL/Large at mining step 2. It is difficult to discern the location of grayscale contours in Zipf's plots, but this figure seems to correspond well to Zipf's Figure 24, shown here as Figure A3. A more detailed comparison is possible by comparing the same stress and closure profiles calculated with those provided by Zipf [USBM 1992a]. The corresponding profiles calculated by MulsimNL/Large are shown here in Figure A4. Zipf's comparable figures are shown here as Figures A5 and A6. It should be noted that Zipf's results were calculated with much less precision than does MulsimNL/Large. For example, his stress output was rounded to the nearest 10 stress units (for example, psi) in the version received by the authors. Therefore, slight differences in output are inevitable, and may be evident in the output plots. Even so, it appears that the profiles of Figure A4 and the contours of Figue A2 reasonably match those corresponding contours and profiles in the figures of Zipf [USBM 1992a].

The multiple-seam example includes an upper seam with room and pillar mining and a lower seam with longwall development. The metric system is used, with the two seams at 560 m and 600 m from the surface. Only one mining step is calculated. Three material property types are used: (1) linear elastic with no extraction of material, (2) linear elastic with 50% extraction, and (3) linear elastic gob. The simulated extraction of the second material was done by using half of the elastic modulus used in the first material. Contours of vertical stress of each seam as calculated with MulsimNL/Large are shown in Figure A7. Zipf's matching Figure 32 is shown here as Figure A8. Contours of closure of each seam are shown in Figure A9. Zipf's matching Figure 33 is shown here as Figure A10. Again, these results seem to correspond very well to those of Zipf [USBM 1992a].

The random pillar example is a seam at a 20° dip. Four linear-elastic materials are used, with properties representing extraction ratios of 0%, 75%, 50%, and 25%, named A, B, C, and D, respectively. A high vertical stress gradient is used to simulate the effect of a hillside. Although this problem had three mining steps, only the first two steps were simulated for verification purposes, because Zipf [USBM 1992a] only showed contours of stress and closure for mining step 2. Figure A11 shows contours of stress and closure calculated with MulsimNL/Large for mining step 2. These contours also seem to correspond well to those shown by Zipf in his Figure 41, shown here as Figure A12.

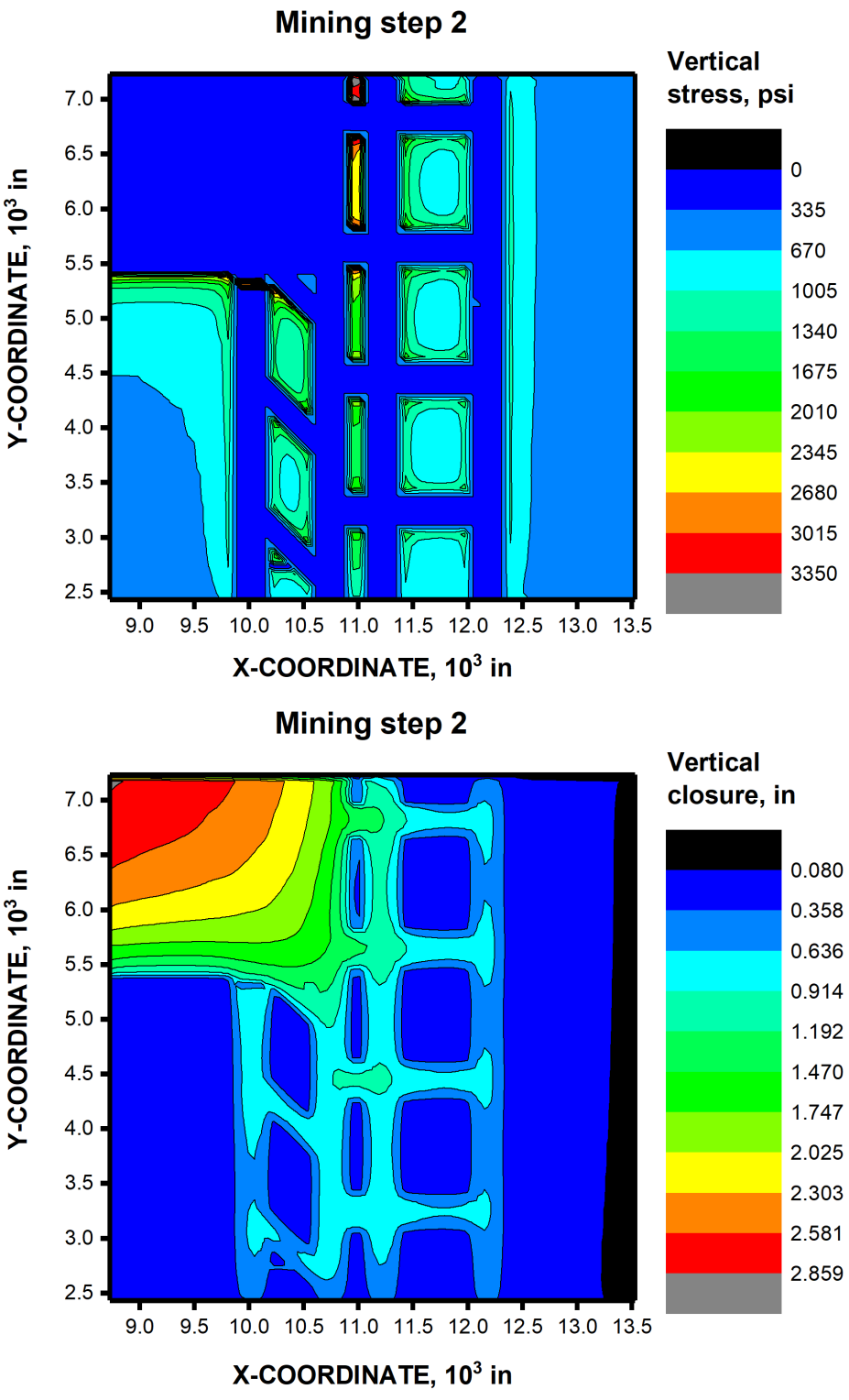

Figure A2. Contours of vertical stress (upper) and closure (lower) of results calculated with MulsimNL/Large for longwall example from Zipf [USBM 1992a].

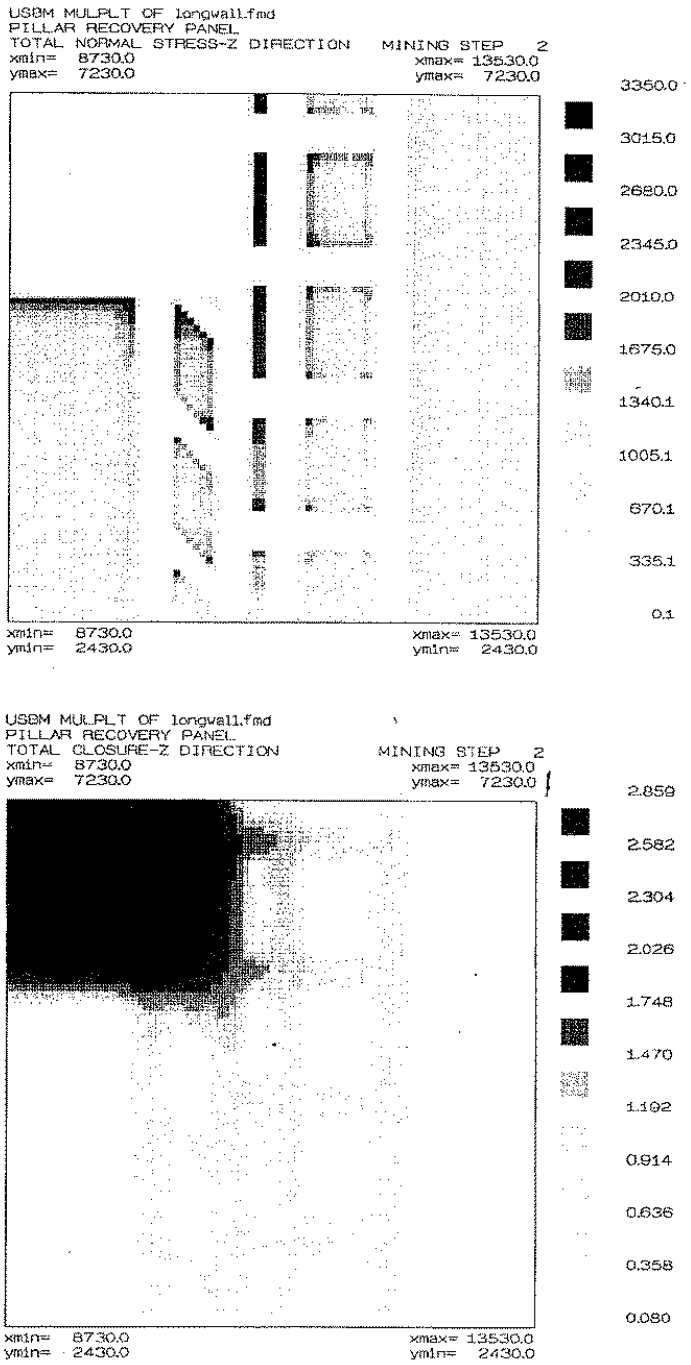

Figure A3. Longwall example—results of vertical stresses (top) and closure displacements (bottom) around headgate during mining step 2. Stresses are in units of psi, and displacements are in units of inches. After Zipf [USBM 1992a], Figure 24.

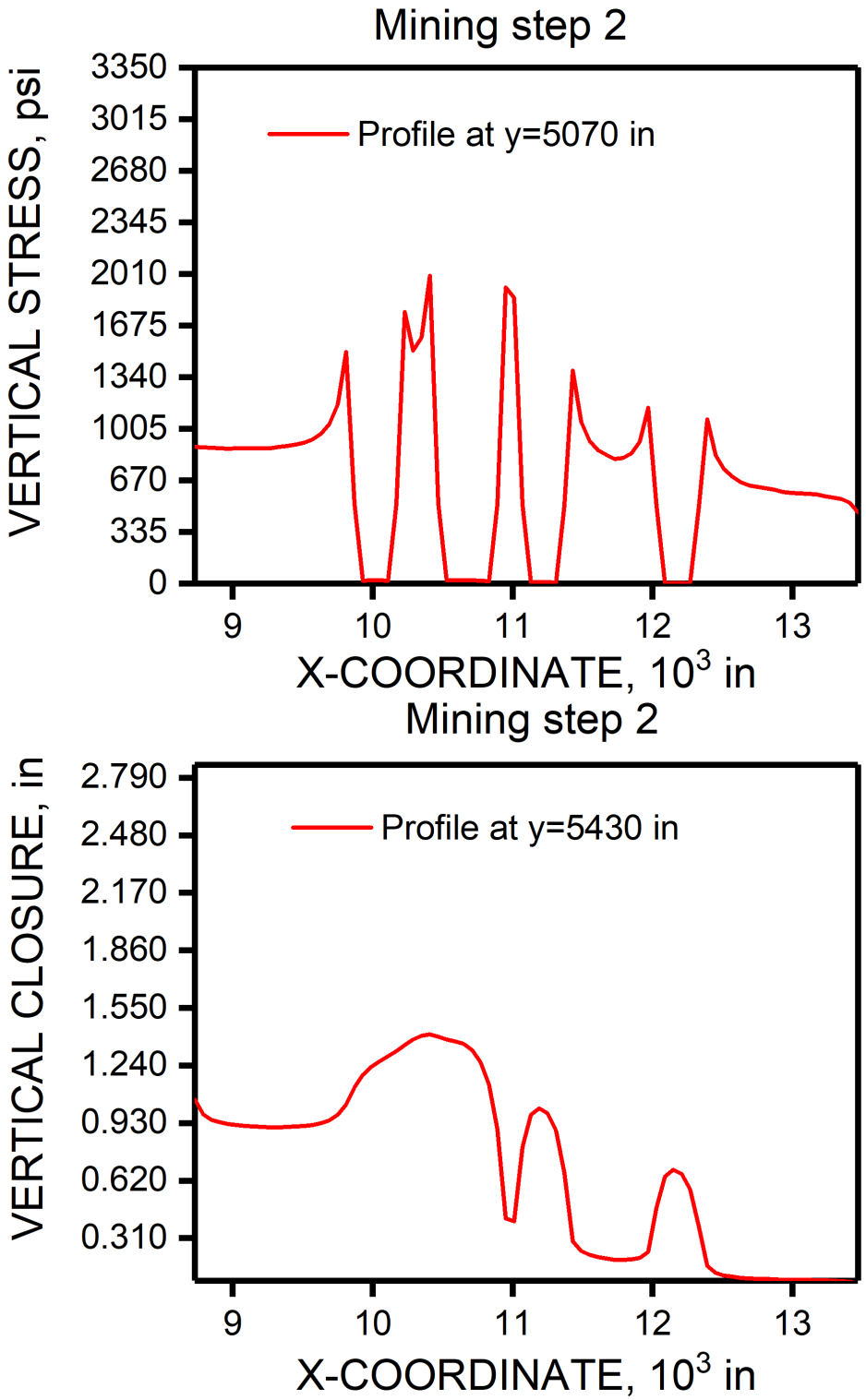

Figure A4. Cross-sectional profiles of stresses (upper) and closures (lower) calculated with MulsimNL/Large for longwall example from Zipf [USBM 1992a].

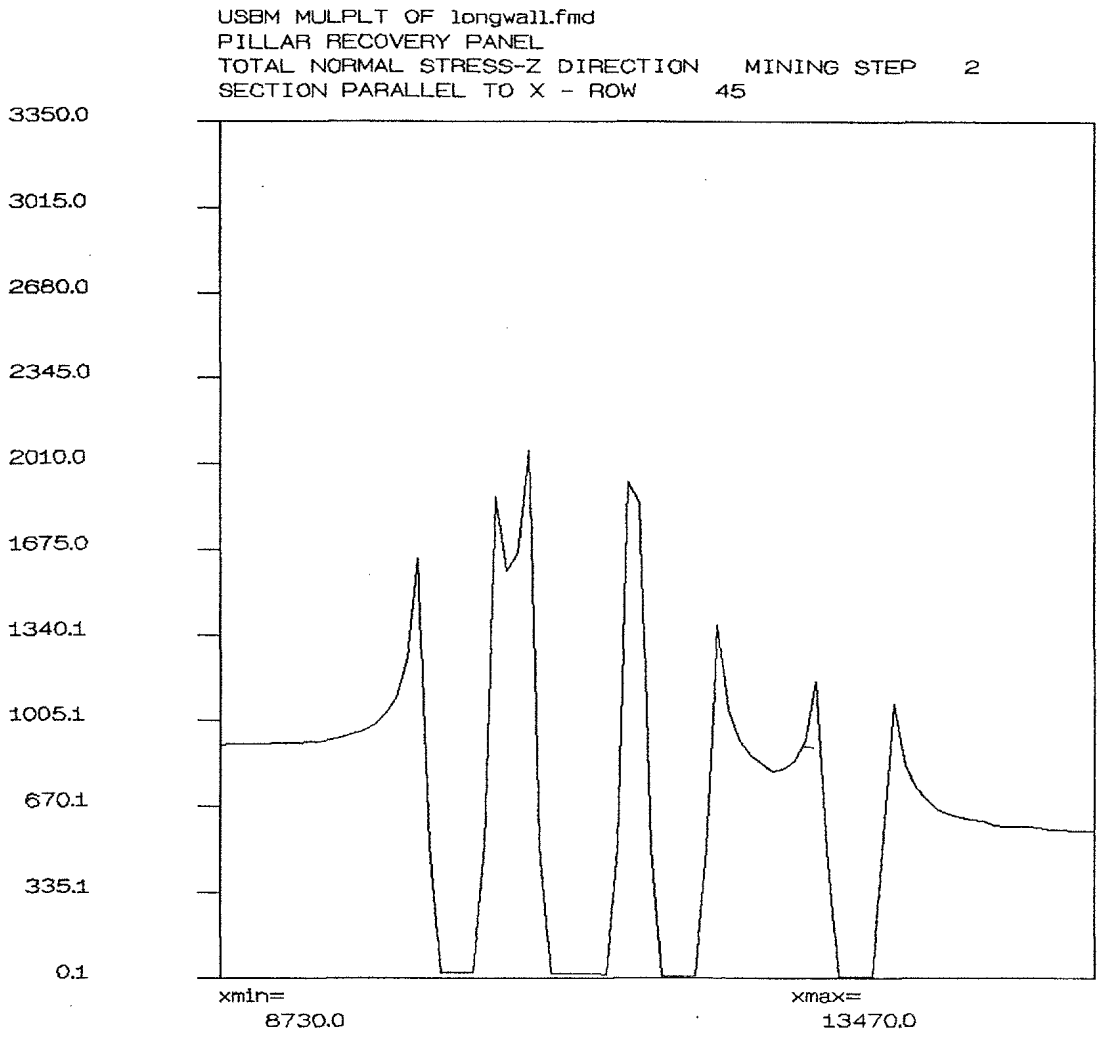

Figure A5. Longwall example—normal stresses along cross section just ahead of face during mining step 2. Stresses are in psi. After Zipf [USBM 1992a, Figure 25].

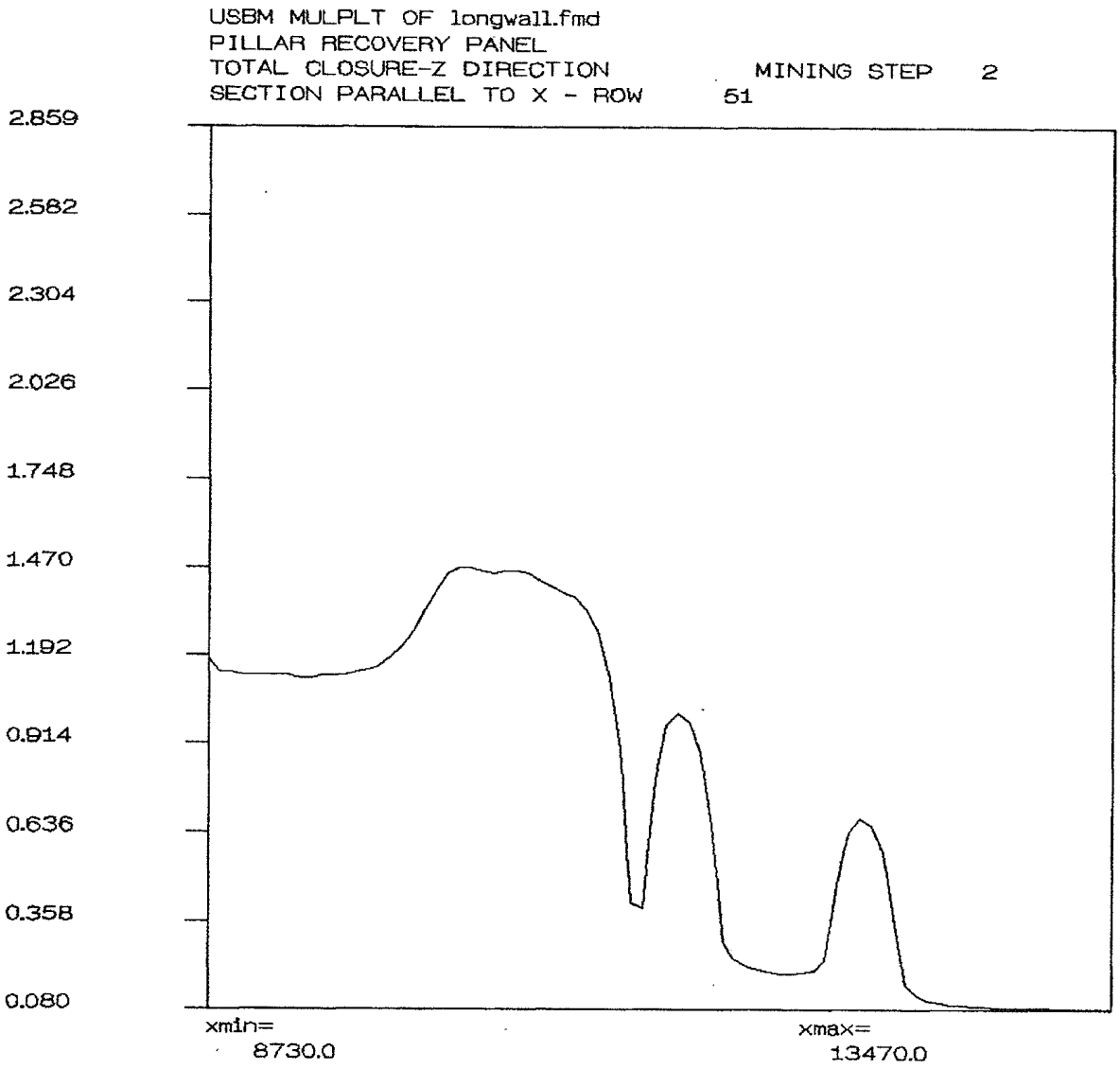

Figure A6. Longwall example—normal closures along cross section just behind face during mining step 2. Displacements are in inches. After Zipf [USBM 1992a, Figure 26].

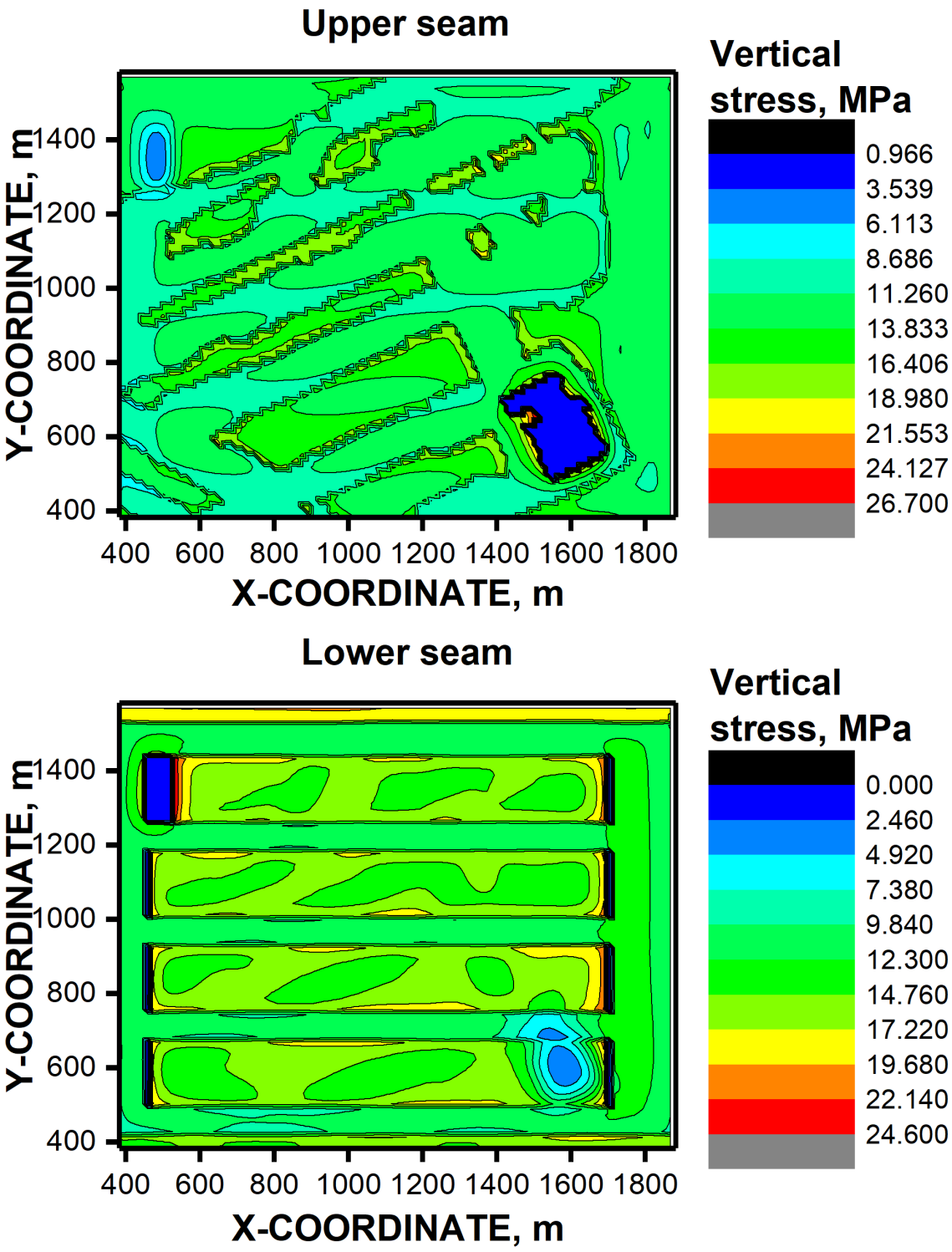

Figure A7. Contours of normal stresses as calculated by MulsimNL/Large for multiple-seam example in Zipf [USBM 1992a].

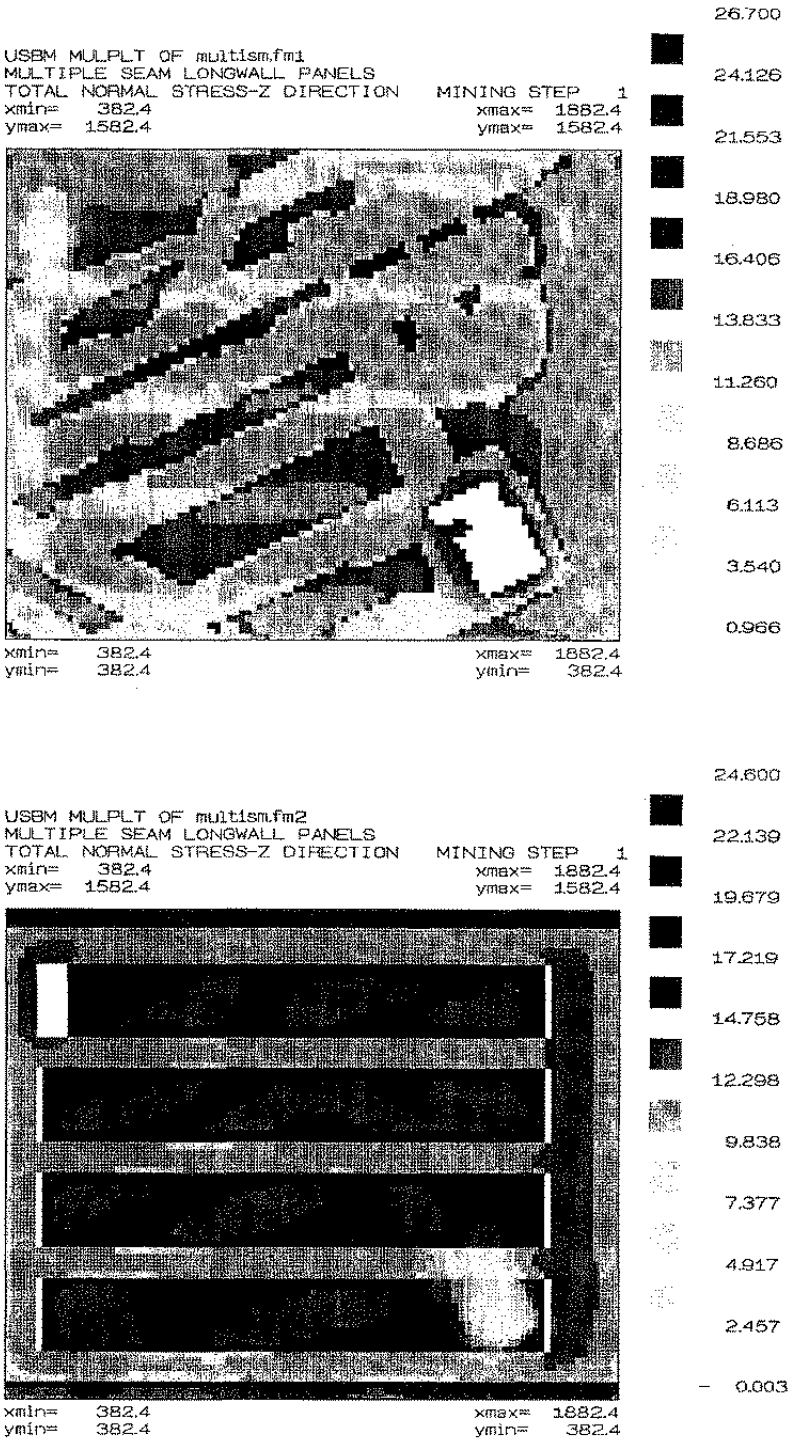

Figure A8. Multiple-seam mining example—normal stresses. Top, Upper seam; bottom, lower seam. Stresses are in MPa. After Zipf [USBM 1992a, Figure 32].

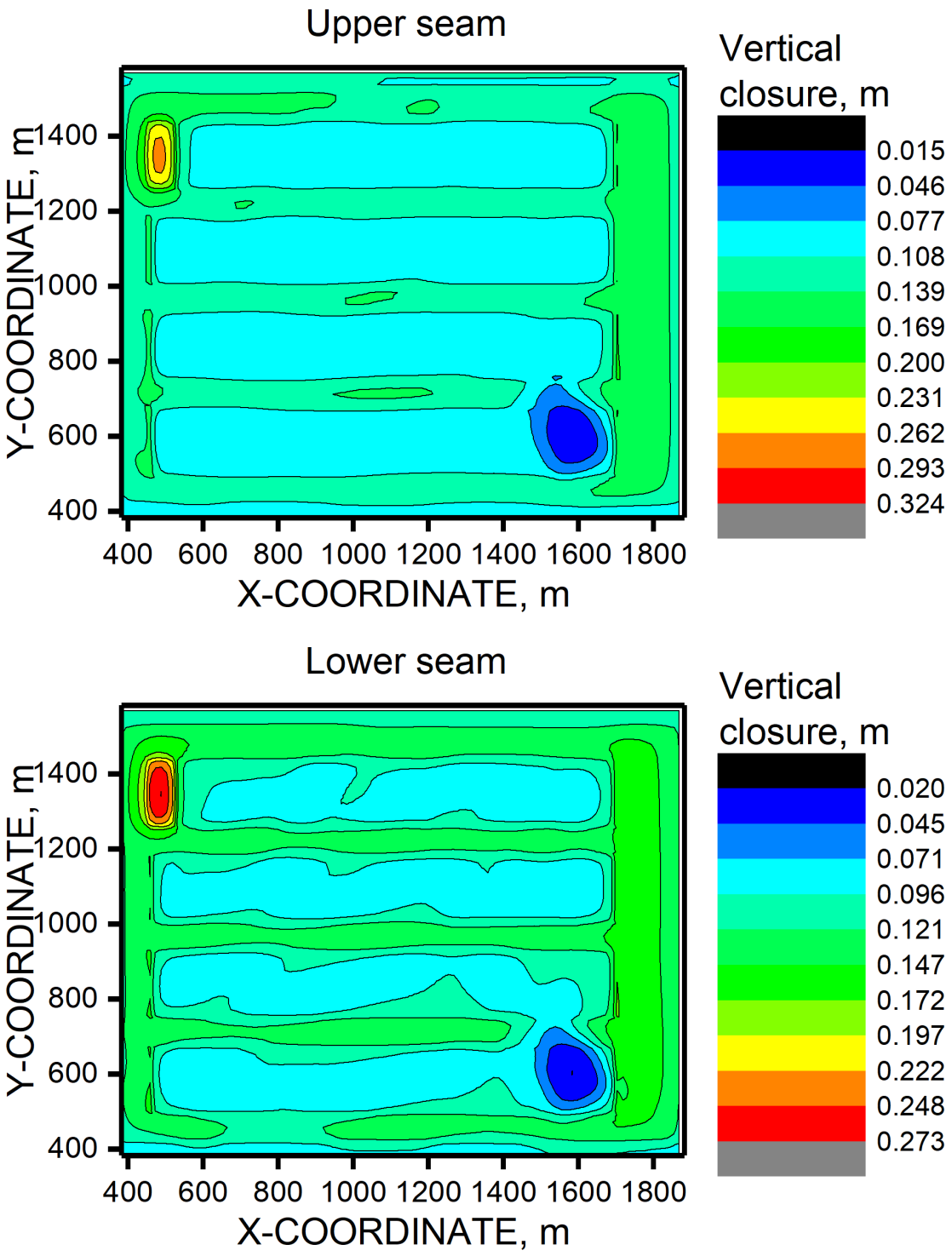

Figure A9. Contours of normal closures as calculated by MulsimNL/Large for multiple-seam example in Zipf [USBM 1992a].

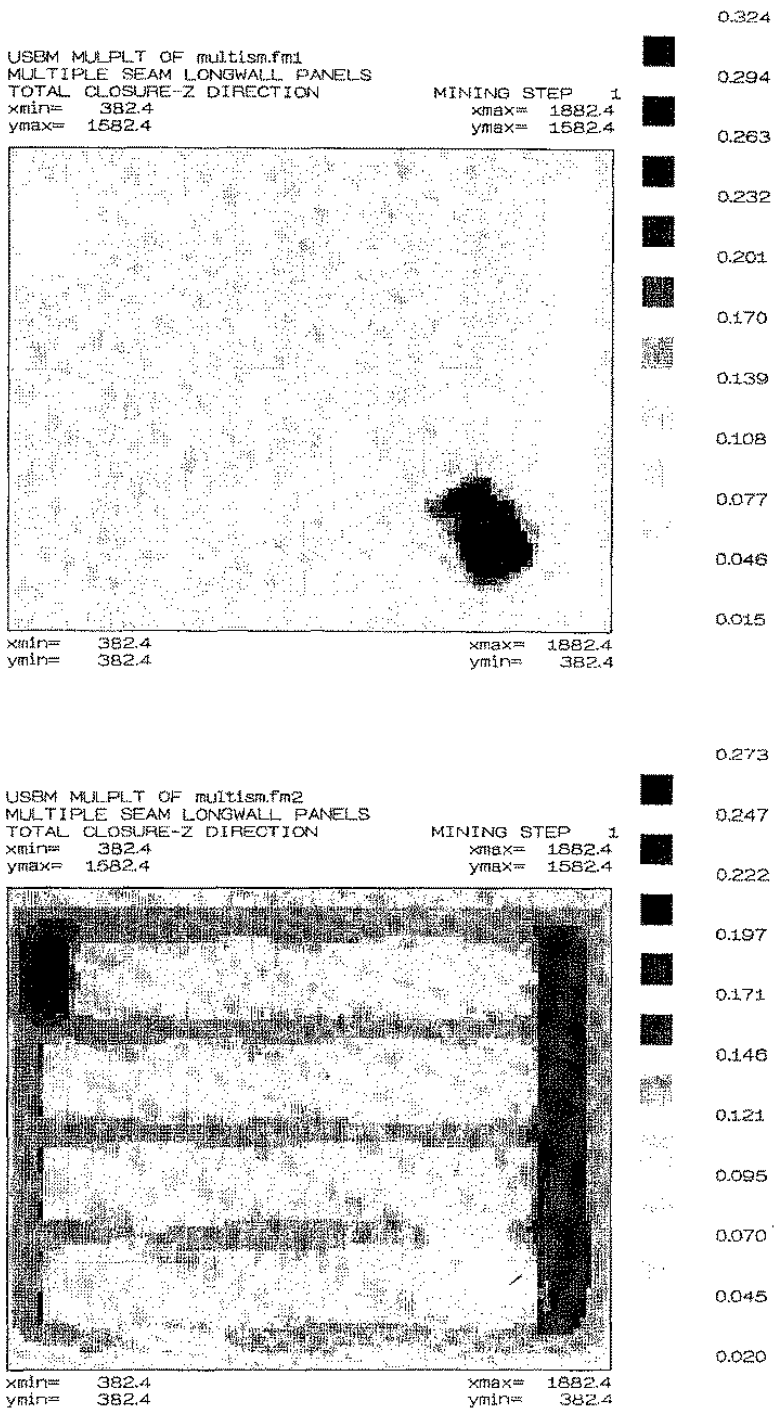

Figure A10. Multiple-seam mining example—normal closures. Top, Upper seam; bottom, lower seam. Displacements are in meters. After Zipf [USBM 1992a, Figure 33].

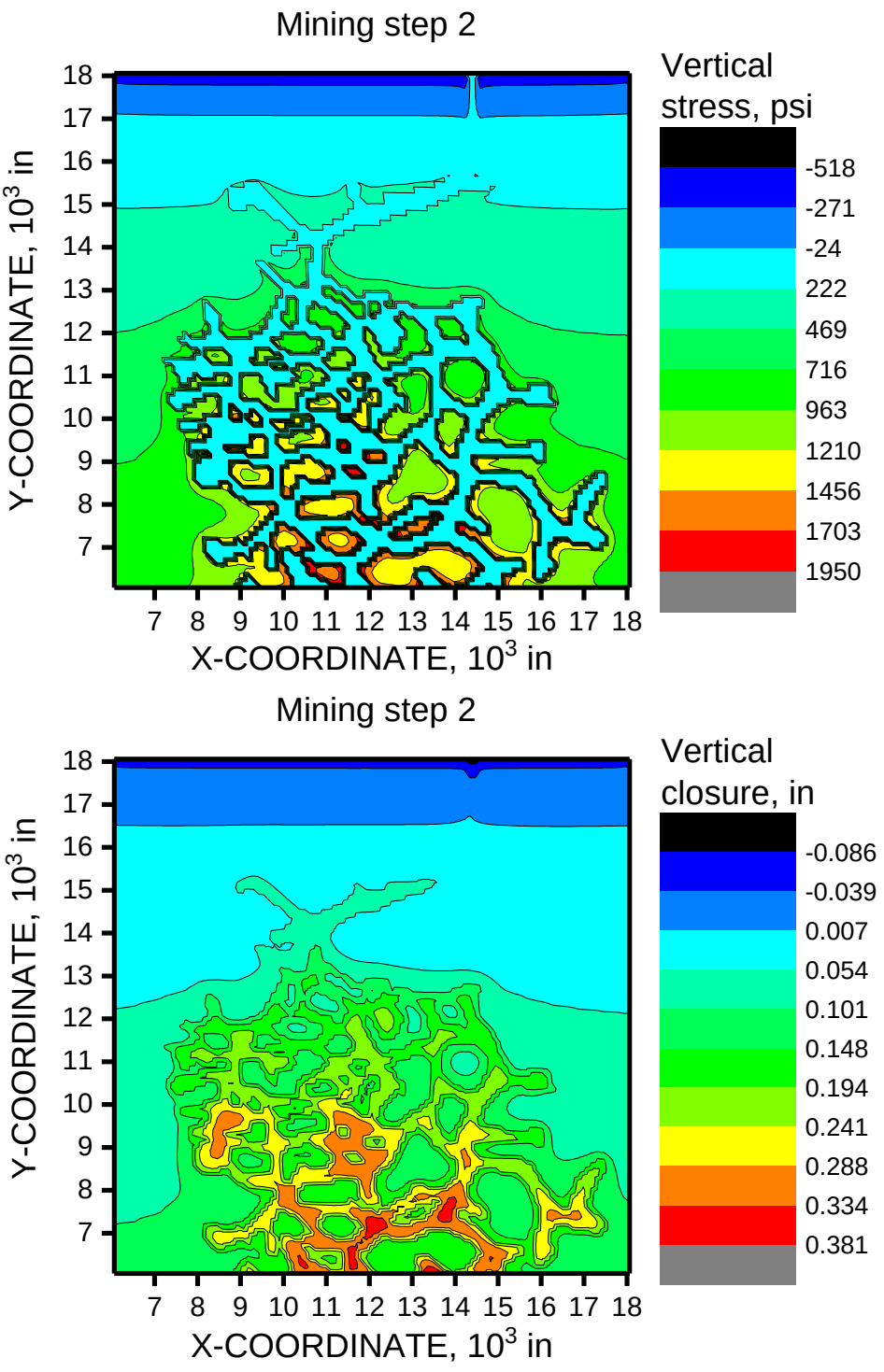

Figure A11. Contours of normal stress (upper) and normal closure as calculated by MulsimNL/Large for the random pillar example in Zipf [USBM 1992a].

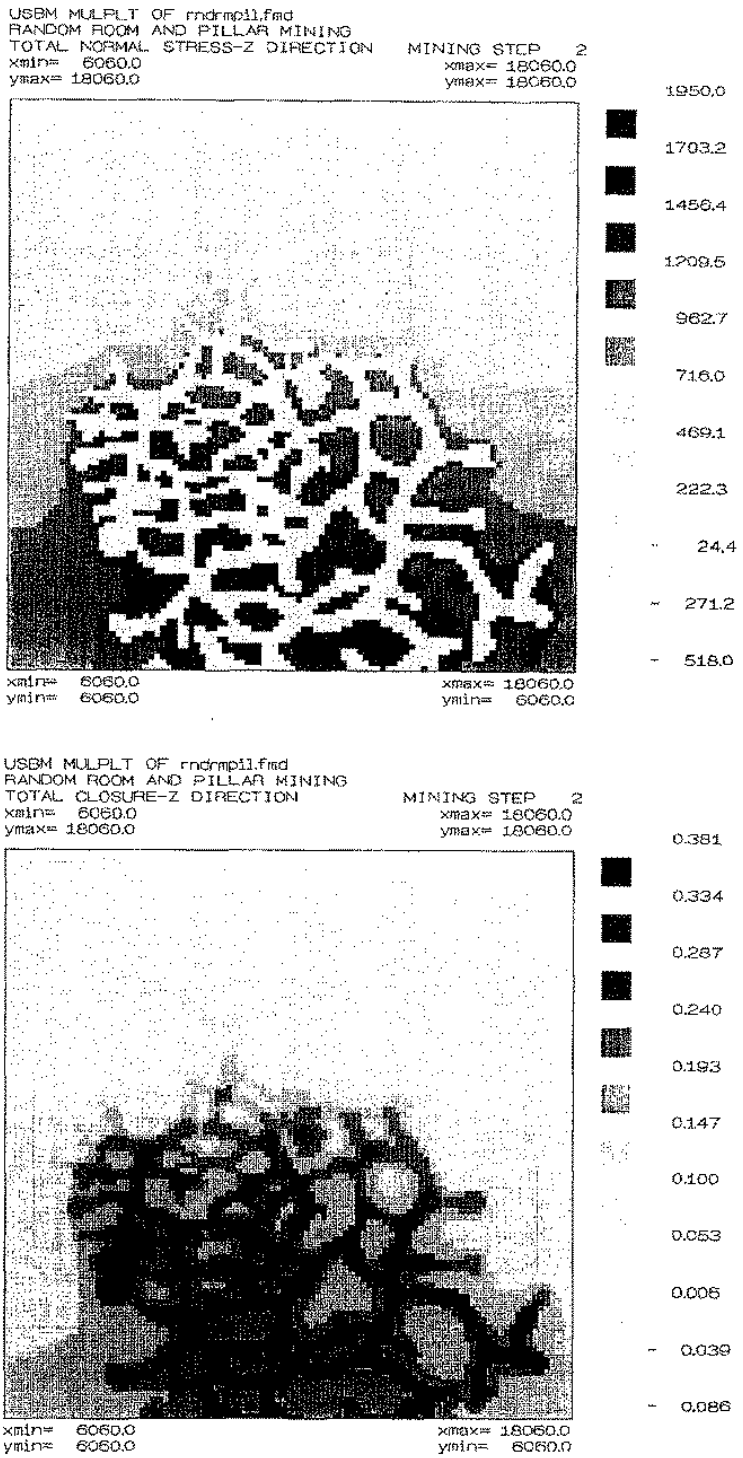

Figure A12. Random room-and-pillar mining example—normal stresses (top) and normal closures (bottom) during mining step 2. Stresses are in psi. After Zipf [USBM 1992a, Figure 41].

Conclusion

MulsimNL/Large version 1.2 has been verified by running the example problems provided by Zipf [USBM 1992a] and showing similar results. Any slight differences can be attributed to the greater precision used in MulsimNL/Large and slight differences between Zipf's post processor and OriginPro v. 9.0 in calculating contour placement.

References for Appendix A

Heasley KA [1998]. Numerical modeling of coal mines with a laminated displacement-discontinuity code. Ph.D. Dissertation. Golden, Colorado: Colorado School of Mines, 205 pp.

Heasley KA [2010]. LaModel, ver. 3.0, Morgantown, WV: West Virginia University.

Lahey Computer Systems I [2011]. Lahey/Fujitsu Fortran, ver. 7.3.

Larson MK, Whyatt JK [2012]. Load transfer distance calibration of a coal panel scale model: A case study. In: Barczak T et al. eds. Proceedings of the 31st International Conference on Ground Control in Mining. (Morgantown, WV: July 31–August 2, 2012) Morgantown, WV: West Virginia University, pp. 195–205.

Larson MK, Whyatt JK [2013]. Panel-scale modeling of a deep longwall panel: The MULSIM alternative. In: Barczak T et al. eds. Proceedings: 32nd International Conference on Ground Control in Mining. (Morgantown, WV: July 30–August 1, 2013) Morgantown, WV: West Virginia University, pp. 181–188.

Sears MM [2009]. Implementing energy release rate calculations into the LaModel program. M.S. thesis. Morgantown, WV: West Virginia University, 95 pp.

USBM [1992a]. MULSIM/NL application and practitioner's manual. By Zipf RK, Jr. Information Circular 9322, Pittsburgh, PA: U.S. Department of the Interior, Bureau of Mines (USBM), 44 pp.

USBM [1992b]. MULSIM/NL theoretical and programmer's manual. By Zipf, RK, Jr. Information Circular 9321, Pittsburgh, PA: U.S. Department of the Interior, Bureau of Mines (USBM), 52 pp.

Listing of Verification Problem Input File Contents

In this appendix, the demonstration problems used by Zipf verified that the present version of Mulsim produces output that is equivalent to that obtained by Dr. Zipf. However, because the format of the input has since changed to permit more precision, the input files are listed here by problem. For example, the input file listings are found under subheadings that identify the test problem—longwall example, multiple-seam example, and random room-and-pillar example.

Longwall Example

```
LONGWALL EXAMPLE
0.150000 9.00000E+05       1
       8
      1.  5.0000000E+005  2.1700000E+005  0.0000000E+000  0.0000000E+000  0.0000000E+000
      6.  5.0000000E+003  1.7900000E+003  1.0000000E+000  0.0000000E+000  0.0000000E+000
      1.  2.7500000E+005  1.1900000E+005  0.0000000E+000  0.0000000E+000  0.0000000E+000
      3.  5.0000000E+002  0.2500000E-002  0.0000000E+000  0.3000000E+000  0.0000000E+000
      1.  4.0000000E+005  1.7400000E+005  0.0000000E+000  0.0000000E+000  0.0000000E+000
      1.  3.0000000E+005  1.3000000E+005  0.0000000E+000  0.0000000E+000  0.0000000E+000
      1.  2.0000000E+005  8.7000000E+004  0.0000000E+000  0.0000000E+000  0.0000000E+000
      1.  1.0000000E+005  4.3000000E+004  0.0000000E+000  0.0000000E+000  0.0000000E+000
     0.00000  0.04580000     0.00000  0.00000000     0.00000  0.00000000     0.00000  0.04580000     0.00000
0.00000000     0.00000  0.09170000   //This line is a continuation of the previous line.
  300.00      50      32                0      30      45       9      24
     0.0     0.0 -6000.0    72.0
1.000000 0.00000 0.00000 0.00000 1.00000 0.00000 0.00000 0.00000 1.00000
1.350000 50.00000000     100                                  1       2
AAAAAAAAAAAAAAAAAAAAAAAAAAAAAAAAD1111DAAD1111DAAAAAAAAAAD1111DAAAAAAAAAAAAAAAAAA
AAAAAAAAAAAAAAAAAAAAAAAAAAAAAAAAD1111DAAD1111DAAAAAAAAAAD1111DAAAAAAAAAAAAAAAAAA
AAAAAAAAAAAAAAAAAAAAAAAAAAAAAAAAD1111DAAD1111DAAAAAAAAAAD1111DAAAAAAAAAAAAAAAAAA
AAAAAAAAAAAAAAAAAAAAAAAAAAAAAAAAD1111DAAD1111DAAAAAAAAAAD1111DAAAAAAAAAAAAAAAAAA
AAAAAAAAAAAAAAAAAAAAAAAAAAAAAAAAD1111111111111111111111111111111DAAAAAAAAAAAAAAAAAA
AAAAAAAAAAAAAAAAAAAAAAAAAAAAAAAAD1111111111111111111111111111111DAAAAAAAAAAAAAAAAAA
AAAAAAAAAAAAAAAAAAAAAAAAAAAAAAAAD1111111111111111111111111111111DAAAAAAAAAAAAAAAAAA
AAAAAAAAAAAAAAAAAAAAAAAAAAAAAAAAD1111111111111111111111111111111DAAAAAAAAAAAAAAAAAA
AAAAAAAAAAAAAAAAAAAAAAAAAAAAAAAAD1111DDDD1111DDDDDDDDDDDD1111DAAAAAAAAAAAAAAAAAA
AAAAAAAAAAAAAAAAAAAAAAAAAAAAAAAAD1111DAAD1111DAAAAAAAAAAD1111DAAAAAAAAAAAAAAAAAA
AAAAAAAAAAAAAAAAAAAAAAAAAAAAAAAAD1111DAAD1111DAAAAAAAAAAD1111DAAAAAAAAAAAAAAAAAA
AAAAAAAAAAAAAAAAAAAAAAAAAAAAAAAAD1111DAAD1111DAAAAAAAAAAD1111DAAAAAAAAAAAAAAAAAA
AAAAAAAAAAAAAAAAAAAAAAAAAAAAAAAAD1111DAAD1111DAAAAAAAAAAD1111DAAAAAAAAAAAAAAAAAA
AAAAAAAAAAAAAAAAAAAAAAAAAAAAAAAAD1111DAAD1111DAAAAAAAAAAD1111DAAAAAAAAAAAAAAAAAA
AAAAAAAAAAAAAAAAAAAAAAAAAAAAAAAAD1111DAAD1111DAAAAAAAAAAD1111DAAAAAAAAAAAAAAAAAA
AAAAAAAAAAAAAAAAAAAAAAAAAAAAAAAAD1111DAAD1111DAAAAAAAAAAD1111DAAAAAAAAAAAAAAAAAA
AAAAAAAAAAAAAAAAAAAAAAAAAAAAAAAAD1111DAAD1111DAAAAAAAAAAD1111DAAAAAAAAAAAAAAAAAA
AAAAAAAAAAAAAAAAAAAAAAAAAAAAAAAAD1111DAAD1111DAAAAAAAAAAD1111DAAAAAAAAAAAAAAAAAA
AAAAAAAAAAAAAAAAAAAAAAAAAAAAAAAAD1111DAAD1111DAAAAAAAAAAD1111DAAAAAAAAAAAAAAAAAA
AAAAAAAAAAAAAAAAAAAAAAAAAAAAAAAAD1111DAAD1111DAAAAAAAAAAD1111DAAAAAAAAAAAAAAAAAA
AAAAAAAAAAAAAAAAAAAAAAAAAAAAAAAAD1111DDDD1111DDDDDDDDDDDD1111DAAAAAAAAAAAAAAAAAA
AAAAAAAAAAAAAAAAAAAAAAAAAAAAAAAAD1111111111111111111111111111111DAAAAAAAAAAAAAAAAAA
AAAAAAAAAAAAAAAAAAAAAAAAAAAAAAAAD1111111111111111111111111111111DAAAAAAAAAAAAAAAAAA
AAAAAAAAAAAAAAAAAAAAAAAAAAAAAAAAD1111111111111111111111111111111DAAAAAAAAAAAAAAAAAA
AAAAAAAAAAAAAAAAAAAAAAAAAAAAAAAAD1111DDDD1111DDDDDDDDDDDD1111DAAAAAAAAAAAAAAAAAA
AAAAAAAAAAAAAAAAAAAADDDDDDDDDDAAD1111DAAD1111DAAAAAAAAAAD1111DAAAAAAAAAAAAAAAAAA
AAAAAAAAAAAAAAAAAAAD1111D1111DDD1111DAAD1111DAAAAAAAAAAD1111DAAAAAAAAAAAAAAAAAA
AAAAAAAAAAAAAAAAAADAAAADD1111DD1111DAAD1111DAAAAAAAAAAD1111DAAAAAAAAAAAAAAAAAA
AAAAAAAAAAAAAAAAAAD1111DAD1111D1111DAAD1111DAAAAAAAAAAD1111DAAAAAAAAAAAAAAAAAA
AAAAAAAAAAAAAAAAAAD1111DAAD11111111DAAD1111DAAAAAAAAAAD1111DAAAAAAAAAAAAAAAAAA
AAAAAAAAAAAAAAAAAAD1111DAAAAD1111111DAAD1111DAAAAAAAAAAD1111DAAAAAAAAAAAAAAAAAA
AAAAAAAAAAAAAAAAAAD1111DAAAAAD11111DAAD1111DAAAAAAAAAAD1111DAAAAAAAAAAAAAAAAAA
AAAAAAAAAAAAAAAAAAD1111DAAAAAD1111DAAD1111DAAAAAAAAAAD1111DAAAAAAAAAAAAAAAAAA
AAAAAAAAAAAAAAAAAAD1111DAAAAAD1111DAAD1111DAAAAAAAAAAD1111DAAAAAAAAAAAAAAAAAA
AAAAAAAAAAAAAAAAAAD1111DAAAAAD1111DAAD1111DAAAAAAAAAAD1111DAAAAAAAAAAAAAAAAAA
AAAAAAAAAAAAAAAAAAD1111DAAAAAD1111DDDD1111DDDDDDDDDDDD1111DAAAAAAAAAAAAAAAAAA
AAAAAAAAAAAAAAAAAAD1111DAAAAAD11111111111111111111111111DAAAAAAAAAAAAAAAAAA
AAAAAAAAAAAAAAAAAAD1111DAAAAAD11111111111111111111111111DAAAAAAAAAAAAAAAAAA
AAAAAAAAAAAAAAAAAAD11111DAAAAAD11111111111111111111111111DAAAAAAAAAAAAAAAAAA
AAAAAAAAAAAAAAAAAAD111111DAAAAD11111111111111111111111111DAAAAAAAAAAAAAAAAAA
AAAAAAAAAAAAAAAAAAD1111111DAAD1111DDDD1111DDDDDDDDDDDD1111DAAAAAAAAAAAAAAAAAA
AAAAAAAAAAAAAAAAAAD11111111DAAD1111DAAD1111DAAAAAAAAAAD1111DAAAAAAAAAAAAAAAAAA
AAAAAAAAAAAAAAAAAAD1111D1111DAD1111DAAD1111DAAAAAAAAAAD1111DAAAAAAAAAAAAAAAAAA
AAAAAAAAAAAAAAAAAAD1111DD1111DD1111DAAD1111DAAAAAAAAAAD1111DAAAAAAAAAAAAAAAAAA
AAAAAAAAAAAAAAAAAAD1111DAD1111D1111DAAD1111DAAAAAAAAAAD1111DAAAAAAAAAAAAAAAAAA
AAAAAAAAAAAAAAAAAAD1111DAAD11111111DAAD1111DAAAAAAAAAAD1111DAAAAAAAAAAAAAAAAAA
AAAAAAAAAAAAAAAAAAD1111DAAAAD111111DAAD1111DAAAAAAAAAAD1111DAAAAAAAAAAAAAAAAAA
AAAAAAAAAAAAAAAAAAD1111DAAAAAD1111DAAD1111DAAAAAAAAAAD1111DAAAAAAAAAAAAAAAAAA
AAAAAAAAAAAAAAAAAAD1111DAAAAAD1111DAAD1111DAAAAAAAAAAD1111DAAAAAAAAAAAAAAAAAA
AAAAAAAAAAAAAAAAAAD1111DAAAAAD1111DAAD1111DAAAAAAAAAAD1111DAAAAAAAAAAAAAAAAAA
AAAAAAAAAAAAAAAAAAD1111DAAAAAD1111DDDD1111DDDDDDDDDDDD1111DAAAAAAAAAAAAAAAAAA
AAAAAAAAAAAAAAAAAAD1111DAAAAAD11111111111111111111111111DAAAAAAAAAAAAAAAAAA
AAAAAAAAAAAAAAAAAAD1111DAAAAAD11111111111111111111111111DAAAAAAAAAAAAAAAAAA
AAAAAAAAAAAAAAAAAAD11111DAAAAAD11111111111111111111111111DAAAAAAAAAAAAAAAAAA
AAAAAAAAAAAAAAAAAAD111111DAAAAD11111111111111111111111111DAAAAAAAAAAAAAAAAAA
AAAAAAAAAAAAAAAAAAD1111111DAAD1111DDDD1111DDDDDDDDDDDD1111DAAAAAAAAAAAAAAAAAA
AAAAAAAAAAAAAAAAAAD11111111DAAD1111DAAD1111DAAAAAAAAAAD1111DAAAAAAAAAAAAAAAAAA
AAAAAAAAAAAAAAAAAAD1111D1111DAD1111DAAD1111DAAAAAAAAAAD1111DAAAAAAAAAAAAAAAAAA
AAAAAAAAAAAAAAAAAAD1111DD1111DD1111DAAD1111DAAAAAAAAAAD1111DAAAAAAAAAAAAAAAAAA
AAAAAAAAAAAAAAAAAAD1111DAD1111D1111DAAD1111DAAAAAAAAAAD1111DAAAAAAAAAAAAAAAAAA
AAAAAAAAAAAAAAAAAAD1111DAAD11111111DAAD1111DAAAAAAAAAAD1111DAAAAAAAAAAAAAAAAAA
AAAAAAAAAAAAAAAAAAD1111DAAAAD111111DAAD1111DAAAAAAAAAAD1111DAAAAAAAAAAAAAAAAAA
AAAAAAAAAAAAAAAAAAD1111DAAAAAD11111DAAD1111DAAAAAAAAAAD1111DAAAAAAAAAAAAAAAAAA
AAAAAAAAAAAAAAAAAAD1111DAAAAAD1111DAAD1111DAAAAAAAAAAD1111DAAAAAAAAAAAAAAAAAA
AAAAAAAAAAAAAAAAAAD1111DAAAAAD1111DAAD1111DAAAAAAAAAAD1111DAAAAAAAAAAAAAAAAAA
AAAAAAAAAAAAAAAAAAD1111DAAAAAD1111DDDD1111DDDDDDDDDDDD1111DAAAAAAAAAAAAAAAAAA
AAAAAAAAAAAAAAAAAAD1111DAAAAAD11111111111111111111111111DAAAAAAAAAAAAAAAAAA
AAAAAAAAAAAAAAAAAAD1111DAAAAAD11111111111111111111111111DAAAAAAAAAAAAAAAAAA
AAAAAAAAAAAAAAAAAAD11111DAAAAAD11111111111111111111111111DAAAAAAAAAAAAAAAAAA
AAAAAAAAAAAAAAAAAAD111111DAAAAD11111111111111111111111111DAAAAAAAAAAAAAAAAAA
AAAAAAAAAAAAAAAAAAD1111111DAAD1111DDDD1111DDDDDDDDDDDD1111DAAAAAAAAAAAAAAAAAA
AAAAAAAAAAAAAAAAAAD11111111DAAD1111DAAD1111DAAAAAAAAAAD1111DAAAAAAAAAAAAAAAAAA
AAAAAAAAAAAAAAAAAAD1111D1111DAD1111DAAD1111DAAAAAAAAAAD1111DAAAAAAAAAAAAAAAAAA
AAAAAAAAAAAAAAAAAAD1111DD1111DD1111DAAD1111DAAAAAAAAAAD1111DAAAAAAAAAAAAAAAAAA
```

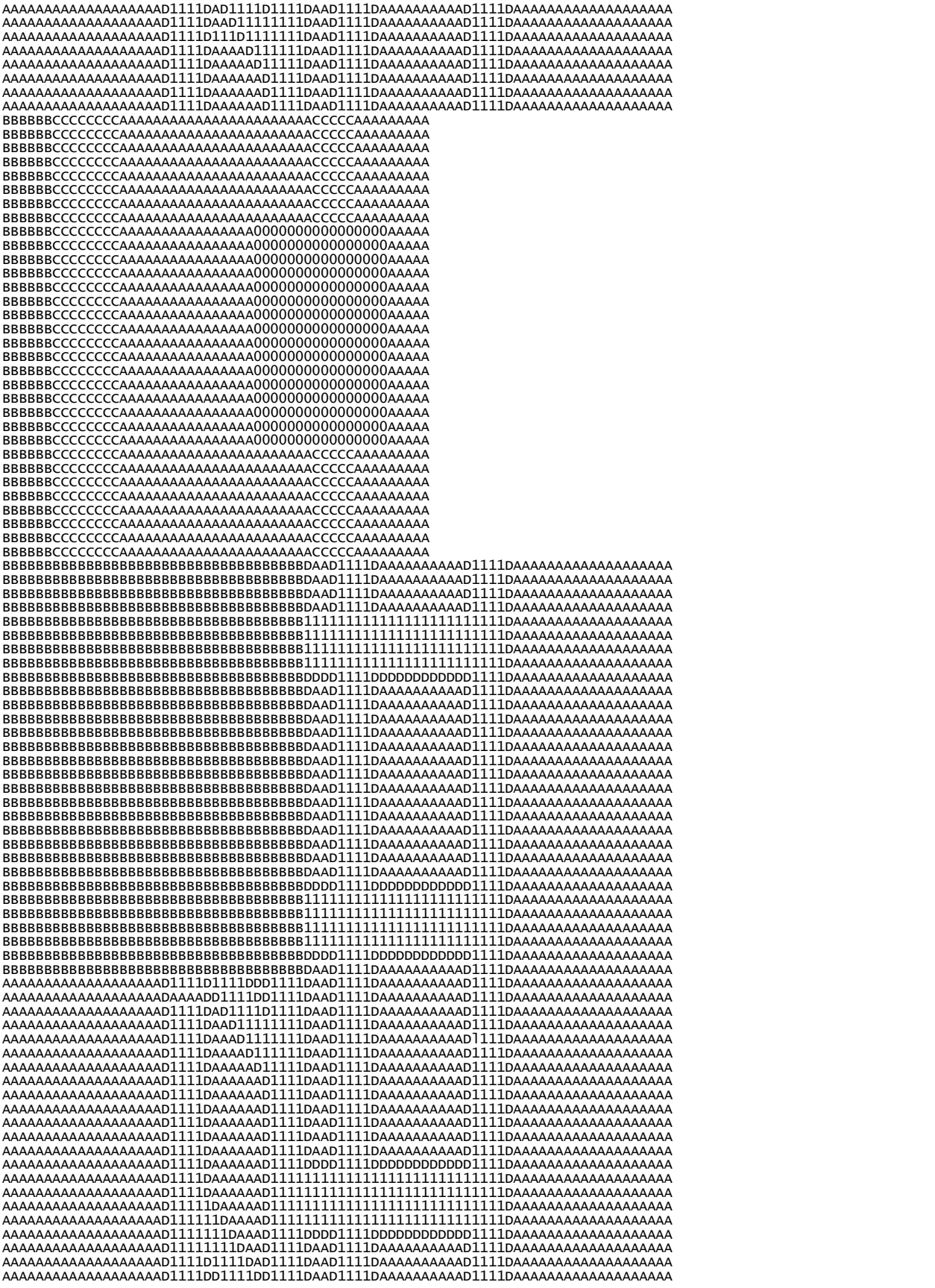

AAAAAAAAAAAAAAAAAAAD1111DAD1111D1111DAAD1111DAAAAAAAAAAD1111DAAAAAAAAAAAAAAAAAA
AAAAAAAAAAAAAAAAAAAD1111DAAD11111111DAAD1111DAAAAAAAAAAD1111DAAAAAAAAAAAAAAAAAA
AAAAAAAAAAAAAAAAAAAD1111DAAAD1111111DAAD1111DAAAAAAAAAAD1111DAAAAAAAAAAAAAAAAAA
AAAAAAAAAAAAAAAAAAAD1111DAAAAD111111DAAD1111DAAAAAAAAAAD1111DAAAAAAAAAAAAAAAAAA
AAAAAAAAAAAAAAAAAAAD1111DAAAAAD11111DAAD1111DAAAAAAAAAAD1111DAAAAAAAAAAAAAAAAAA
AAAAAAAAAAAAAAAAAAAD1111DAAAAAD1111DAAD1111DAAAAAAAAAAD1111DAAAAAAAAAAAAAAAAAA
AAAAAAAAAAAAAAAAAAAD1111DAAAAAD1111DAAD1111DAAAAAAAAAAD1111DAAAAAAAAAAAAAAAAAA
AAAAAAAAAAAAAAAAAAAD1111DAAAAAD1111DAAD1111DAAAAAAAAAAD1111DAAAAAAAAAAAAAAAAAA
AAAAAAAAAAAAAAAAAAAD1111DAAAAAD1111DAAD1111DAAAAAAAAAAD1111DAAAAAAAAAAAAAAAAAA
AAAAAAAAAAAAAAAAAAAD1111DAAAAAD1111DAAD1111DAAAAAAAAAAD1111DAAAAAAAAAAAAAAAAAA
AAAAAAAAAAAAAAAAAAAD1111DAAAAAD1111DDDD1111DDDDDDDDDDDD1111DAAAAAAAAAAAAAAAAAA
AAAAAAAAAAAAAAAAAAAD1111DAAAAAD11111111111111111111111111DAAAAAAAAAAAAAAAAAA
AAAAAAAAAAAAAAAAAAAD1111DAAAAAD11111111111111111111111111DAAAAAAAAAAAAAAAAAA
AAAAAAAAAAAAAAAAAAAD11111DAAAAD11111111111111111111111111DAAAAAAAAAAAAAAAAAA
AAAAAAAAAAAAAAAAAAAD111111DAAAD11111111111111111111111111DAAAAAAAAAAAAAAAAAA
AAAAAAAAAAAAAAAAAAAD1111111DAAD1111DDDD1111DDDDDDDDDDDD1111DAAAAAAAAAAAAAAAAAA
AAAAAAAAAAAAAAAAAAAD11111111DAAD1111DAAD1111DAAAAAAAAAAD1111DAAAAAAAAAAAAAAAAAA
AAAAAAAAAAAAAAAAAAAD1111D1111DAD1111DAAD1111DAAAAAAAAAAD1111DAAAAAAAAAAAAAAAAAA
AAAAAAAAAAAAAAAAAAAD1111DD1111DD1111DAAD1111DAAAAAAAAAAD1111DAAAAAAAAAAAAAAAAAA
AAAAAAAAAAAAAAAAAAAD1111DAD1111D1111DAAD1111DAAAAAAAAAAD1111DAAAAAAAAAAAAAAAAAA
AAAAAAAAAAAAAAAAAAAD1111DAAD11111111DAAD1111DAAAAAAAAAAD1111DAAAAAAAAAAAAAAAAAA
AAAAAAAAAAAAAAAAAAAD1111D111D1111111DAAD1111DAAAAAAAAAAD1111DAAAAAAAAAAAAAAAAAA
AAAAAAAAAAAAAAAAAAAD1111DAAAAD111111DAAD1111DAAAAAAAAAAD1111DAAAAAAAAAAAAAAAAAA
AAAAAAAAAAAAAAAAAAAD1111DAAAAAD11111DAAD1111DAAAAAAAAAAD1111DAAAAAAAAAAAAAAAAAA
AAAAAAAAAAAAAAAAAAAD1111DAAAAAD1111DAAD1111DAAAAAAAAAAD1111DAAAAAAAAAAAAAAAAAA
AAAAAAAAAAAAAAAAAAAD1111DAAAAAD1111DAAD1111DAAAAAAAAAAD1111DAAAAAAAAAAAAAAAAAA
AAAAAAAAAAAAAAAAAAAD1111DAAAAAD1111DAAD1111DAAAAAAAAAAD1111DAAAAAAAAAAAAAAAAAA
BBBBBBCCCCCCCCCBBBBBBBBBBBBBBBBBBBBBBBCCCCCAAAAAAAAAA
BBBBBBCCCCCCCCCBBBBBBBBBBBBBBBBBBBBBBBCCCCCAAAAAAAAAA
BBBBBBCCCCCCCCCBBBBBBBBBBBBBBBBBBBBBBBCCCCCAAAAAAAAAA
BBBBBBCCCCCCCCCBBBBBBBBBBBBBBBBBBBBBBBCCCCCAAAAAAAAAA
BBBBBBCCCCCCCCCBBBBBBBBBBBBBBBBBBBBBBBCCCCCAAAAAAAAAA
BBBBBBCCCCCCCCCBBBBBBBBBBBBBBBBBBBBBBBCCCCCAAAAAAAAAA
BBBBBBCCCCCCCCCBBBBBBBBBBBBBBBBBBBBBBBCCCCCAAAAAAAAAA
BBBBBBCCCCCCCCCBBBBBBBBBBBBBBBBBBBBBBBCCCCCAAAAAAAAAA
BBBBBBCCCCCCCCCBBBBBBBBBBBBBBB000000000000000AAAAA
BBBBBBCCCCCCCCCBBBBBBBBBBBBBBB000000000000000AAAAA
BBBBBBCCCCCCCCCBBBBBBBBBBBBBBB000000000000000AAAAA
BBBBBBCCCCCCCCCBBBBBBBBBBBBBBB000000000000000AAAAA
BBBBBBCCCCCCCCCBBBBBBBBBBBBBBB000000000000000AAAAA
BBBBBBCCCCCCCCCBBBBBBBBBBBBBBB000000000000000AAAAA
BBBBBBCCCCCCCCCAAAAAAAAAAAAAAAA000000000000000AAAAA
BBBBBBCCCCCCCCCAAAAAAAAAAAAAAAA000000000000000AAAAA
BBBBBBCCCCCCCCCAAAAAAAAAAAAAAAA000000000000000AAAAA
BBBBBBCCCCCCCCCAAAAAAAAAAAAAAAA000000000000000AAAAA
BBBBBBCCCCCCCCCAAAAAAAAAAAAAAAA000000000000000AAAAA
BBBBBBCCCCCCCCCAAAAAAAAAAAAAAAA000000000000000AAAAA
BBBBBBCCCCCCCCCAAAAAAAAAAAAAAAA000000000000000AAAAA
BBBBBBCCCCCCCCCAAAAAAAAAAAAAAAA000000000000000AAAAA
BBBBBBCCCCCCCCCAAAAAAAAAAAAAAAA000000000000000AAAAA
BBBBBBCCCCCCCCCAAAAAAAAAAAAAAAAAAAAAAAACCCCCAAAAAAAAAA
BBBBBBCCCCCCCCCAAAAAAAAAAAAAAAAAAAAAAAACCCCCAAAAAAAAAA
BBBBBBCCCCCCCCCAAAAAAAAAAAAAAAAAAAAAAAACCCCCAAAAAAAAAA
BBBBBBCCCCCCCCCAAAAAAAAAAAAAAAAAAAAAAAACCCCCAAAAAAAAAA
BBBBBBCCCCCCCCCAAAAAAAAAAAAAAAAAAAAAAAACCCCCAAAAAAAAAA
BBBBBBCCCCCCCCCAAAAAAAAAAAAAAAAAAAAAAAACCCCCAAAAAAAAAA
BBBBBBCCCCCCCCCAAAAAAAAAAAAAAAAAAAAAAAACCCCCAAAAAAAAAA

Multiple Seam Example

```
MULTIPLE SEAM MINING EXAMPLE
0.250000 2.00000E+04       2
       3
      1.  5.0000000E+002  2.0000000E+002  0.0000000E+000  0.0000000E+000  0.0000000E+000
      1.  2.5000000E+002  1.0000000E+002  0.0000000E+000  0.0000000E+000  0.0000000E+000
      6.  5.0000000E+001  2.0000000E+001  4.0000000E+000  0.0000000E+000  0.0000000E+000
     0.00000  0.00000000      0.00000  0.00000000      0.00000  0.00000000      0.00000  0.00000000      0.00000
0.00000000      0.00000  0.02500000   //This line is a continuation of the previous line.
   75.00      30      26              0       6      25       6      21
     0.0      0.0  -560.0      2.0
     0.0      0.0  -600.0      3.0
1.00000 0.00000 0.00000 0.00000 1.00000 0.00000 0.00000 0.00000 1.00000
1.35    0.200000000      100                                   1       1
AAAAAAAAAAAAAAAAAAAAAAAAAAAAAAAAAAAAAAAAAAAAAAAABBBBBBBBBBBBBBBBBBBBBBBBBBBBBBBBBBBBBBBBBBAAAAAAAAAA
AAAAAAAAAAAAAAAAAAAAAAAAAAAAAAAAAAAAAAAAAAAAAABBBBBBBBBBBBBBBBBBBBBBBBBBBBBBBBBBBBBBBBBBBAAAAAAAAAAA
AAAAAAAAAAAAAAAAAAAAAAAAAAAAAAAAAAAAAAAAAAAABBBBBBBBBBBBBBBBBBBBBBBBBBBBBBBBBBBBBBBBBBBBAAAAAAAAAAAA
AAAAAAAAAAAAAAAAAAAAAAAAAAAAAAAAAAAAAAAAAABBBBBBBBBBBBBBBBBBBBBBBBBBBBBBBBBBBBBBBBBBBBBAAAAAAAAAAAAA
AAAAAAAAAAAAAAAAAAAAAAAAAAAAAAAAAAAAAAAABBBBBBBBBBBBBBBBBBBBBBBBBBBBBBBBBBBBBBBBBBBBBBAAAAAAAAAAAAAA
AAAAAAAAAAAAAAAAAAAAAAAAAAAAAAAAAAAAAABBBBBBBBBBBBAAABBBBBBBBBBBBBBBBBBBBBBBBBBBBBBBBAAAAAAAAAAAAAAA
AAAAAAAAAAAAAAAAAAAAAAAAAAAAAAAAAAAAAABBBBBBBBBBBBBAAAAABBBBBBBBBBBBBBBBBBBBBBBBBBAAAAAAAAAAAAAAAAAA
AAAAAAAAAAAAAAAAAAAAAAAAAAAAAAAAABBBAABBBBBBBBBBBAAAAAAAABBBBBBBBBBBBBBBBBBBBBBAAAAAAAAAAAAAAAAAAAAA
AAAAAAAAAAAAAAAAAAAAAAAAAAAAAAAABBBBBBBBBBBBBBBBAAAAAAAAAABBBBBBBBBBBBBBBBBBBAAAAAAAAAAAAAAAAAAAAAAA
AAAAAAAAAAAAAAAAAAAAAAAAAAAAAAAABBBBBBBBBBBBBBAAAAAAAAAABBBBBBBBBBBBBBBBBBBBAAAAAAAAAAAAAAAAAAAAAAAA
AAAAAAAAAAAAAAAAAAAAAAAAAAAAAAAABBBBBBBBBBBBAAAAAAABBBABBBBBBBBBBBBBBBBBBBBAAAAABAAAAAAAAAAAAAAAAAAA
AAAAAAAAAAAAAAAAAAAAAAAAAAAAAAABBBBBBBBBBAAAAAAABBBBBBBBBBBBBBBBBBBBBBBBBABBBABBBBBBBAAAAAAAAAAAAAAA
AAAAAAAAAAAAAAAAAAAAAAAAAAAAAAABBBBBBBAAAAAAABBBBBBBBBBBBBBBBBBBBBBBBBBAAAABBBBBBBBBBAAAAAAAAAAAAAAA
AAAAAAAAAAAAAAAAAAAAAAAAAAAAAAABBBBBBAAAAAAAABBBBBBBBBBBBBBBBBBBBBBBBBAAAAAABBBBBBBBBAAAAAAAAAAAAAAA
AAAAAAAAAAAAAAAAAAAAAAAAAABBBBBBBBBBBBAAAAAAAABBBBBBBBBBBBBBBBBBBBBAAAAABBBBBBBBBBBBBAAAAAAAAAAAAAAA
AAAAAAAAAAAAAAAAAAAAAAAABBBBBBBBBBBBBAAAAAAAAABBBBBBBBBBBBBBBBBABBBAABBBBBBBBBBBBBBBBAAAAAAAAAAAAAAA
AAAAAAAAAAAAAAAAAAAAAABBBBBBBBBBBBBBBAAAAAAAAABBBBBBBBBBBBBBBBBAAABBBABBBBBBBBBBBBBBBAAAAAAAAAAAAAA
AAAAAAAAAAAAAAAAAABBBBBBBBBBBBBBBBBBBBAAAAAABBBBBBBBBBBBBBBBBBAAAAAABBBBBBBBBBBBBBBBBBAAAAAAAAAAAAAA
AAAAAAAAAAAAAAAABBBBBBBBBBBAABBBBBBAAAAAABBBBBBBBBBBBBBBBBBAAAAAAABBBBBBBBBBBBBBBBBBBBAAAAAAAAAAAAAA
AAAAAAAAAAAABBBBBBBBBBAAAABBBBBBBAABBBBBBBBBBBBBBBBBBBAAAAAABBBBBBBBBBBBBBBBBBBBBBBBBBAAAAAAAAAAAAAA
AAAAAAAAABBBBBBBBBBBBBAAAAAABBBBBBBBBBBBBBBBBBBBBBBBBBBAAAABBBBBBBBBBBBBBBBBBBBBBBBBBBAAAAAAAAAAAAAA
AAABBBBBBBBBBBBBBBBBAAAAABBBBBBBBBBBBBBBBBBBBBBBABBBBBBBBBBBBBBBBBBBBBBBBBBBBBBBBBBBBBBBAAAAAAAAAAAA
ABBBBBBBBBBBBBBBBBBBAAAAAABBBBBBBBBBBBBBBBBBBBBBBBBBAAAABBBBBBBBBBBBBBBBBBBBBBBABBBBBBBBAAAAAAAAAAAA
BBBBBBBBBBBBBBBBBBAAAAAAAABBBBBBBBBBBBBBBBBBBBBBBAAAAAABBBBBBBBBBBBBBBBBBBBAAABBBBBBBBBBAAAAAAAAAAAA
BBBBBBBBBBBBBBAAAAAAAAAABBBBBBBBBBBBBBBBBBBAAAAABBBBBBBBBBBBBBBBBBBBBBBBBBAAABBBBBBBBBBBAAAAAAAAAAAA
BBBBBBBBBBBBBAAAAAAAAAAAABBBBBBBBBBBBBBBBBAAAAAABBBBBBBBBBBBBBBBBBBBBBBBBBBAABBBBBBBBBBBBAAAAAAAAAAA
BBBBBBBBBBBAAAAAAAAAAAAAABBBBBBBBBBBBBBBAAAAAABBBBBBBBBBBBBBBBBBBBBBBBBBBBBBABBBBBBBBBBBBAAAAAAAAAAA
BBBBBBBBBBBAAAAAAAAAAAAABBBBBBBBBBBBBBAAAAAAABBBBBBBBBBBBBBBBBBBBBBBBBBABBBBBBBBBBBBBBBBAAAAAAAAAAA
BBBBBBBBBAAAAAAAAAAAAAAAABBBBBBBBBBBBAAAAAAABBBBBBBBBBBBBBBBBBAAAABBBBBBBBBBBBBBBBBBBBBBAAAAAAAAAAAA
BBBBBBBBBBAAAAAAAAAAAABBBBBBBBBBBBAAAAAAAAABBBBBBBBBBBBBBBBBBBBAAAABBBBBBBBBBBBBBBBBBBBBAAAAAAAAAAAA
BBBBBBBBBAAAAAAABBAABBBBBBBBBBBBBBBAAAAAAAAAABBBBBBBBBBBBBBBBBBBAAAABBBBBBBBBBBBBBBBBBBBAAAAAAAAAAAA
BBBBBBBBBAAABBBBBBBBBBBBBBBBBBBBBBAAAAAAAAABBBBBBBBBBBBBBBBBBBAAABBBBBBBBBBBBBBBBBBBBBBBAAAAAAAAAAAA
BBBBBBBBBABBBBBBBBBBBBBBBBBBBBAAAAAAABBBBBBBBBBBBBBBBBBBBBBBBBBBBAABBBBBBBBBBBBBBBBBBBBBBAAAAAAAAAAA
BBBBBBBBBBBBBBBBBBBBBBBBBBAAAAAAABAABBBBBBBBBBBBBBBBBBAABBBBBBBBBBBBBBBBBBBBBBBBBBBBBBBBBAAAAAAAAAAA
BBBBBBBBBBBBBBBBBBBBBBBBBAAAAAABBBBBBBBBBBBBBBBBBBBBBAAAAABBBBBBBBBBBBBBBBBBBBBBBBBBBBBBBAAAAAAAAAAA
BBBBBBBBBBBBBBBBBBBBBBAAAAAABBBBBBBBBBBBBBBBBBBBBAAAAAAABBBBBBBBBBBBBBBBBBBBBBBBBBBBBBBBBAAAAAAAAAAA
BBBBBBBBBBBBBBBBBBBAAAAAAABBBBBBBBBBBBBBBBBBBBAAAAAAAAAABBBBBBBBBBBBBBBBBBBBBBBBBBBBBBBBBAAAAAAAAAAA
BBBBBBBBBBBBBBBBAAAAAAABBBBBBBBBBBBBBBBBBBBBBAAAAAAAAAAAABBBBBBBBBBBBBBBBBBBBBBBBBBBBBBBAAAAAAAAAAAA
BBBBBBBBBBBBBBAAAAAAAABBBBBBBBBBBBBBBBBBBBBBAAAAAAAAAAABBBBBBBBBBBBBBBBBBBBBBBBBBBBBBBBAAAAAAAAAAAAA
BBBBBBBBBBBBAAAAAAAABBBBBBBBBBBBBBBBBBBBBBBAAAAAAAAAAAABBBBBBBBBBBBBBBBBBBBBBBBBBBBBBBBAAAAAAAAAAAAA
BBBBBBBBBBAAAAAAABBBBBBBBBBBBBBBBBBBBBAAAAAAAAAAAAAABBBBBBBBBBBBBBBBBBBBBBBBBBBBBBBAAAAAAAAAAAAAAAAA
BBBBBBBBAAAAAABBBBBBBBBBBBBBBBBBBBBBBBBAAAAAAAAAAABBBBBBBBBBBBBBBBBBBBBBBBBBAAABBAAAAAAAAAAAAAAAAAAA
BBBBBAAAAAABBBBBBBBBBBBBBBBBBBBBBBAAAAAAAAAAAABBBBBBBBBBBBBBBBBBBBBBBBBAAAAAAAAAAAAAAAAAAAAAAAAAAAAA
BBBAAAAABBBBBBBBBBBBBBBBBBBBBBBBBAAAAAAAAAAAAAABBBBBBBBBBBBBBBBBBBBBBBBAAAAAAAAAAAAAAAAAAAAAAAAAAAAA
BBBAAABBBBBBBBBBBBBBBBBBBBBBBBAAAAAAAAAAAAABBBBBBBBBBBBBBBBBBBBBBBBBBBBAAAAAAAAAAAAAAAAAAAAAAAAAAAAA
BBBBBBBBBBBBBBBBBBBBBBBBBBBBBAAAAAAAAAAABBBBBBBBBBBBBBBBBBAAABBBBBBBBBBBAAAAAAAAAAAAAAAAAAAAAAAAAAAA
BBBBBBBBBBBBBBBBBBBBBBBBBAAAAAAAAAAAAABBBBBBBBBBBBBBBBBBBBAAAAABBBBBBBBBAAAAAAAAAAAAAAAAAAAAAAAAAAAA
BBBBBBBBBBBBBBBBBBBABBBBAAAAAAAAAAAABBBBBBBBBBBBBBBBAAAAAAAAABBBBBBBBBBAAAAAAAAAAAAAAAAAAAAAAAAAAAAA
BBBBBBBBBBBBBBBBAAAAAAAAAAAAAAAABBBBBBBBBBBBBBBBBBBAAAAAAAAAABBBBBBBBBBAAAAABAAAAAAAAAAAAAAAAAAAAAAA
BBBBBBBBBBBBBBAAAAAAAAAAAAAAAAABBBBBBBBBBBBBBBBBBBAAAAAAAAAAAAABBBBBBBBBBAAABBBBBAAAAAAAAAAAAAAAAAAA
BBBBBBBBBBBBBBAAAAAAAAAAAAABBBBBBBBBBBBBBBBBBAAAAAAAAAAAAAAAAABBBBBBBBBBBABBBBBBBAAAAAAAAAAAAAAAAAAA
BBBBBBBBBBBBAAAAAAAAAAAAAABBBBBBBBBBBBBBBBBBAAAAAAAAAAAAAAAAAAAABBBBBBBBBBBBBBBBBAAAAAAAAAAAAAAAAAAA
BBBBBBBBBBBAAAAAAAAAAABBBBBBBBBBBBBBBBBBBBAAAAAAAAAAAAAAAAAAAAAABBBBBBBBBBBBBBBBBBAAAAAAAAAAAAAAAAAA
BBBBBBBBAAAAAAAAAAAABBBBBBBBBBBBBBBBBBBBAAAAAAAAAAAAAAAAAAAAAAABBBBBBBBBBBBBBBBBBBBAAAAAAAAAAAAAAAAA
BBBBBAAAAAAAAABBBBBBBBBBBBBBBBBBBBBBBBBAAAAAAAAAAAAAAAAAAAAAAAAAAAABBBBBBBBBBBBCCCBBBBBAAAAAAAAAAAAA
BBBAAAAAAAAAABBBBBBBBBBBBBBBBBBBBBBBBBAAAAAAAAAAAAAAAAAAAAAAAAAAAABBBBBBBBBBBBCCCCBBBBBBAAAAAAAAAAAA
BAAAAAAAAAABBBBBBBBBBBBBBBBBBBBBBBBBAAAAAAAAAAAAAAAAAAAAAAAAABBBBBBBBBBBBBCCCCCCBBBBBBAAAAAAAAAAAAAA
BAAAAAAABBBBBBBBBBBBBBBBBBBBBBBBBBAAAAAAAAAAAAAAAAAAAAAAAAAABBBBBBBBBBBBCCCCCCCCCBBBBBAAAAAAAAAAAAAA
BBBAAAAABBBBBBBBBBBBBBBBBBBBBBAAAAAAAAAAAAAAAAAAAAAAAAAABBBBBBBBBBBBBBCCCCCCCCCCCCCCBBBAAAAAAAAAAAAA
BBBBBAABBBBBBBBBBBBBBBBBBBBBBBAAAAAAAAAAAAAAAAAAAAAAAAAABBBBBBBBBBBBBBCCCCCCCCCCCCCBBBAAAAAAAAAAAAAA
BBBBBBBBBBBBBBBBBBBBBBBBBBAAAAAAAAAAAAAAAAAAAAAAAAAABBBBBBBBBBBBBBBBBCCBBCCCCCCCCCCBBBBAAAAAAAAAAAAA
BBBBBBBBBBBBBBBBBBBBBBBBAAAAAAAAAAAAAAAAAAAAAAAAAABBBBBBBBBBBBBBBBBBBBBBBBBCCCCCCCCBBBAAAAAAAAAAAAAA
BBBBBBBBBBBBBBBBBBBBBBAAAAAAAAAAAAAAAAAAAAAAAAAABBBBBBBBBBBBBBBBBBBBBBBBBBCCCCCCCCBBBBAAAAAAAAAAAAAA
BBBBBBBBBBBBBBBBBBBBBAAAAAAAAAAAAAAAAAAAAAAAABBBBBBBBBBBBBBBBBBBBBBBBBBBBCCCCCCCCCCCBBBBAAAAAAAAAAAA
BBBBBBBBBBBBBBBBBBBAAAAAAAAAAAAAAAAAAAAAAAABBBBBBBBBBBBBBBBBBBBBAABBBBBBCCCCCCCCCCCCBBBBAAAAAAAAAAAA
ABBBBBBBBBBBBBBBBAAAAAAAAAAAAAAAAAAAAAAAABBBBBBBBBBBBBBBBBBBBBAAAABBBBBBCCCCCCCCCCCCBBBBAAAAAAAAAAAA
AABBBBBBBBBBBBBBBBABBAAAAAAAAAAAAAAAAAAABBBBBBBBBBBBBBBBBBBBBAAAAAABBBBBBCCCCCCCCCCCCBBBAAAAAAAAAAAA
AAAABBBBBBBBBBBBBBBBBBBBBAAAAAAAAAAAABBBBBBBBBBBBBBBBBBABBBBAAAAAAAAAABBBBBBCCCCCCCCCCCCBBBAAAAAAAAA
AAAAABBBBBBBBBBBBBBBBBBBBAAAAAAAAAABBBBBBBBBBBBBBBBBBAAAAAAAAAAAAAAAAABBBBBCCCCCCCCCCCBBBBBBAAAAAAAA
AAAAAABBBBBBBBBBBBBBBBBBBAAAAAAAABBBBBBBBBBBBBBBBBAAAAAAAAAAAAAAAAAAAABBBBBCCCCCCCCCBBBBBBBAAAAAAAAA
AAAAAAAABBBBBBBBBBBBBBBAAABBBBBBBBBBBBBBBBBBAAAAAAAAAAAAAAAAAAAAAAABBBBBBCCCCCBBBBBBBAAAAAAAAAAAAAAA
BAAAAAAAAAABBBBBBBBBBBBBBBBBBBBBBBBBBBBBBBBBBAAAAAAAAAAAAAAAAAAAAAAABBBBBBCCCBBBBBBBAAAAAAAAAAAAAAAA
BBBAAAAAAAAAAABBBBBBBBBBBBBBBBBBBBBBBBBBBBBBAAAAAAAAAAAAAAAAAAAABBBBBBBBBBBBCBBBBBBBAAAAAAAAAAAAAAAA
BBBBBAAAAAAAAABBBBBBBBBBBBBBBBBBBBBBBBBBBBBAAAAAAAAAAAAAAAAAAABBBBBBBBBBBBBBBBBBBBBAAAAAAAAAAAAAAAAA
BBBBBBBAAAAAAAAABBBBBBBBBBBBBBBBBBBBBBBBAAAAAAAAAAAAAAAAAAAABBBBBBBBBBBBBBBBBBBBBAAAAAAAAAAAAAAAAAAA
BBBBBBBAAAAAAAAAAABBBBBBBBBBBBBBBBBBBBAAAAAAAAAAAAAAAAAAAABBBBBBBBBBBBBBBBBBBBBBAAAAAAAAAAAAAAAAAAAA
```

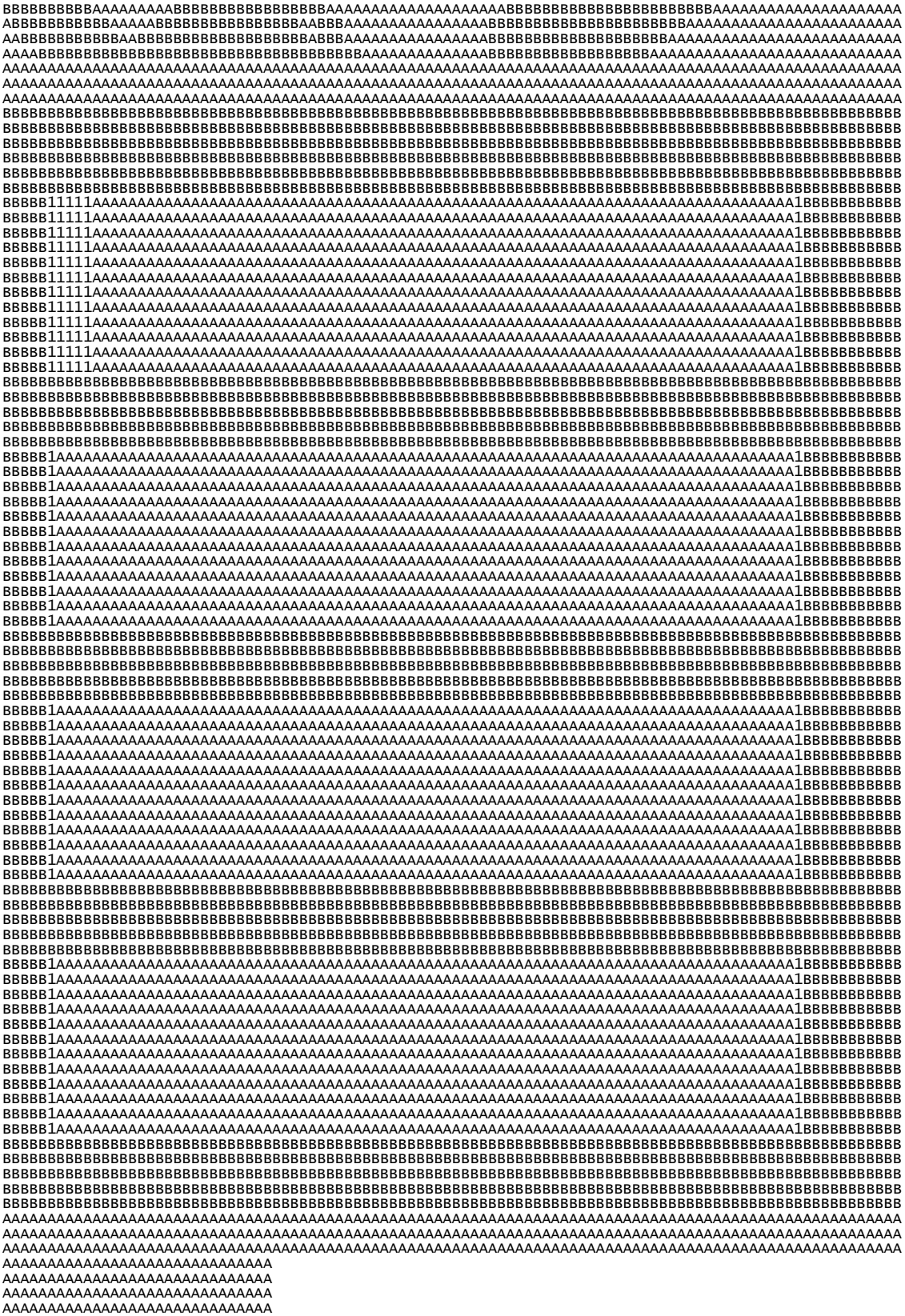

AAAAA00000000000000000000AAAAA
AAAAA00000000000000000000AAAAA
AAAAA00000000000000000000AAAAA
AAAAA00000000000000000000AAAAA
AAAAA00000000000000000000AAAAA
AAAAA00000000000000000000AAAAA
AAAAA00000000000000000000AAAAA
AAAAA00000000000000000000AAAAA
AAAAA00000000000000000000AAAAA
AAAAA00000000000000000000AAAAA
AAAAA00000000000000000000AAAAA
AAAAA00000000000000000000AAAAA
AAAAA00000000000000000000AAAAA
AAAAAAAAAAAAAAAAAAAAAAAAAAAAA
AAAAAAAAAAAAAAAAAAAAAAAAAAAAA
AAAAAAAAAAAAAAAAAAAAAAAAAAAAA
AAAAAAAAAAAAAAAAAAAAAAAAAAAAA
AAAAAAAAAAAAAAAAAAAAAAAAAAAAA
BBBBBBBBBBBBBBBBBBBBBBBBBBBBB
BBBBBBBBBBBBBBBBBBBBBBBBBBBBB
BBBBBBBBBBBBBBBBBBBBBBBBBBBBB
BBBBBBBBBBBBBBBBBBBBBBBBBBBBB
BBBBBBBBBBBBBBBBBBBBBBBBBBBBB
AAAAA00000000000000000000AAAAA
AAAAA00000000000000000000AAAAA
AAAAA00000000000000000000AAAAA
AAAAA00000000000000000000AAAAA
AAAAA00000000000000000000AAAAA
AAAAA00000000000000000000AAAAA
AAAAA00000000000000000000AAAAA
AAAAA00000000000000000000AAAAA
AAAAA00000000000000000000AAAAA
AAAAA00000000000000000000AAAAA
AAAAA00000000000000000000AAAAA
AAAAA00000000000000000000AAAAA
AAAAA00000000000000000000AAAAA
AAAAAAAAAAAAAAAAAAAAAAAAAAAAA
AAAAAAAAAAAAAAAAAAAAAAAAAAAAA
AAAAAAAAAAAAAAAAAAAAAAAAAAAAA
AAAAAAAAAAAAAAAAAAAAAAAAAAAAA

Random Room and Pillar Example

```
RANDOM ROOM AND PILLAR MINING EXAMPLE
0.25000 6.00000E+006       1
      4
     1.  2.0000000E+006  8.0000000E+005  0.0000000E+000  0.0000000E+000  0.0000000E+000
     1.  5.0000000E+005  2.0000000E+005  0.0000000E+000  0.0000000E+000  0.0000000E+000
     1.  1.0000000E+006  4.0000000E+005  0.0000000E+000  0.0000000E+000  0.0000000E+000
     1.  1.5000000E+006  6.0000000E+005  0.0000000E+000  0.0000000E+000  0.0000000E+000
    0.00000  0.05830000     0.00000  0.00000000     0.00000  0.00000000     0.00000  0.05830000     0.00000
0.00000000     0.00000  0.23420000   //This line is a continuation of the previous line.
  600.00      40      40              0      11      30      11      30
    0.0     0.0 -6744.0   240.0
-1.00000 0.00000 0.00000 0.00000-0.92718 0.37461 0.00000 0.37461 0.92718
1.350000 50.00000000     100                             1       3
AAAAAAAAAAAAAAAAAAAAAAAAAAAAAAAAAAAAAAAAAAAAAAAAAAAAAAAAAAAAAAAAAAAAAAAAAAAAAAAAAAAAAAAAAAAAAAAAAAAA
AAAAAAAAAAAAAAAAAAAAAAAAAAAAAAAAAAAAAAAAAAAAAAAAAAAAAAAAAAAAAAAAAAAAAAAAAAAAAAAAAAAAAAAAAAAAAAAAAAAA
AAAAAAAAAAAAAAAAAAAAAAAAAAAAAAAAAAAAAAAAAAAAAAAAAAAAAAAAAAAAAAAAAAAAAAAAAAAAAAAAAAAAAAAAAAAAAAAAAAAA
AAAAAAAAAAAAAAAAAAAAAAAAAAAAAAAAAAAAAAAAAAAAAAAAAAAAAAAAAAAAAAAAAAAAAAAAAAAAAAAAAAAAAAAAAAAAAAAAAAAA
AAAAAAAAAAAAAAAAAAAAAAAAAAAAAAAAAAAAAAAAAAAAAAAAAAAAAAAAAAAAAAAAAAAAAAAAAAAAAAAAAAAAAAAAAAAAAAAAAAAA
AAAAAAAAAAAAAAAAAAAAAAAAAAAAAAAAAAAAAAAAAAAAAAAAAAAAAAAAAAAAAAAAAAAAAAAAAAAAAAAAAAAAAAAAAAAAAAAAAAAA
AAAAAAAAAAAAAAAAAAAAAAAAAAAAAAAAAAAAAAAAAAAAAAAAAAAAAAAAAAAAAAAAAAAAAAAAAAAAAAAAAAAAAAAAAAAAAAAAAAAA
AAAAAAAAAAAAAAAAAAAAAAAAAAAAAAAAAAAAAAAAAAAAAAAAAAAAAAAAAAAAAAAAAAAAAAAAAAAAAAAAAAAAAAAAAAAAAAAAAAAA
AAAAAAAAAAAAAAAAAAAAAAAAAAAAAAAAAAAAAAAAAAAAAAAAAAAAAAAAAAAAAAAAAAAAAAAAAAAAAAAAAAAAAAAAAAAAAAAAAAAA
AAAAAAAAAAAAAAAAAAAAAAAAAAAAAAAAAAAAAAAAAAAAAAAAAAAAAAAAAAAAAAAAAAAAAAAAAAAAAAAAAAAAAAAAAAAAAAAAAAAA
AAAAAAAAAAAAAAAAAAAAAAAAAAAAAAAAAAAAAAAAAAAAAAAAAAAAAAAAAAAAAAAAAAAAAAAAAAAAAAAAAAAAAAAAAAAAAAAAAAAA
AAAAAAAAAAAAAAAAAAAAAAAAAAAAAAAAAAAAAAAAAAAAAAAAAAAAAAAAAAAAAAAAAAAAAAAAAAAAAAAAAAAAAAAAAAAAAAAAAAAA
AAAAAAAAAAAAAAAAAAAAAAAAAAAAAAAAAAAAAAAAAAAAAAAAAAAAAAAAAAAAAAAAAAAAAAAAAAAAAAAAAAAAAAAAAAAAAAAAAAAA
AAAAAAAAAAAAAAAAAAAAAAAAAAAAAAAAAAAAAAAAAAAAAAAAAAAAAAAAAAAAAAAAAAAAAAAAAAAAAAAAAAAAAAAAAAAAAAAAAAAA
AAAAAAAAAAAAAAAAAAAAAAAAAAAAAAAAAAAAAAAAAAAAAAAAAAAAAAAAAAAAAAAAAAAAAAAAAAAAAAAAAAAAAAAAAAAAAAAAAAAA
AAAAAAAAAAAAAAAAAAAAAAAAAAAAAAAAAAAAAAAAAAAAAAAAAAAAAAAAAAAAAAAAAAAAAAAAAAAAAAAAAAAAAAAAAAAAAAAAAAAA
AAAAAAAAAAAAAAAAAAAAAAAAAAAAAAAAAAAAAAAAAAAAAAAAAAAAAAAAAAAAAAAAAAAAAAAAAAAAAAAAAAAAAAAAAAAAAAAAAAAA
AAAAAAAAAAAAAAAAAAAAAAAAAAAAAAAAAAAAAAAAAAAAAAAAAAAAAAAAAAAAAAAAAAAAAAAAAAAAAAAAAAAAAAAAAAAAAAAAAAAA
AAAAAAAAAAAAAAAAAAAAAAAAAAAAAAAAAAAAAAAAAAAAAAAAAAAAAAAAAAAAAAAAAAAAAAAAAAAAAAAAAAAAAAAAAAAAAAAAAAAA
AAAAAAAAAAAAAAAAAAAAAAAAAAAAAAAAAAAAAAAAAAAAAAAAAAAAAAAAAAAAAAAAAAAAAAAAAAAAAAAAAAAAAAAAAAAAAAAAAAAA
AAAAAAAAAAAAAAAAAAAAAAAAAAAAAAAAAAAAAAAAAAAAAAAAAAAAAAAAAAAAAAAAAAAAAAAAAAAAAAAAAAAAAAAAAAAAAAAAAAAA
AAAAAAAAAAAAAAAAAAAAAAAAAAAAAAAAAAAAAAAAAAAAAAAAAAAAAAAAAAAAAAAAAAAAAAAAAAAAAAAAAAAAAAAAAAAAAAAAAAAA
AAAAAAAAAAAAAAAAAAAAAAAAAAAAAAAAAAAAAAAAAAAAAAAAAAAAAAAAAAAAAAAAAAAAAAAAAAAAAAAAAAAAAAAAAAAAAAAAAAAA
AAAAAAAAAAAAAAAAAAAAAAAAAAAAAAAAAAAAAAAAAAAAAAAAAAAAAAAAAAAAAAAAAAAAAAAAAAAAAAAAAAAAAAAAAAAAAAAAAAAA
AAAAAAAAAAAAAAAAAAAAAAAAAAAAAAAAAAAAAAAAAAAAAAAAAAAAAAAAAAAAAAAAAAAAAAAAAAAAAAAAAAAAAAAAAAAAAAAAAAAA
AAAAAAAAAAAAAAAAAAAAAAAAAAAAAAAAAAAAAAAAAAAAAAAAAAAAAAAAAAAAAAAAAAAAAAAAAAAAAAAAAAAAAAAAAAAAAAAAAAAA
AAAAAAAAAAAAAAAAAAAAAAAAAAAAAAAAAAAAAAAAAAAAAAAAAAAAAAAAAAAAAAAAAAAAAAAAAAAAAAAAAAAAAAAAAAAAAAAAAAAA
AAAAAAAAAAAAAAAAAAAAAAAAAAAAAAAAAAAAAAAAAAAAAAAAAAAAAAAAAAAAAAAAAAAAAAAAAAAAAAAAAAAAAAAAAAAAAAAAAAAA
AAAAAAAAAAAAAAAAAAAAAAAAAAAAAAAAAAAAAAAAAAAAAAAAAAAAAAAAAAAAAAAAAAAAAAAAAAAAAAAAAAAAAAAAAAAAAAAAAAAA
AAAAAAAAAAAAAAAAAAAAAAAAAAAAAAAAAAAAAAAAAAAAAAAAAAAAAAAAAAAAAAAAAAAAAAAAAAAAAAAAAAAAAAAAAAAAAAAAAAAA
AAAAAAAAAAAAAAAAAAAAAAAAAAAAAAAAAAAAAAAAAAAAAAAAAAAAAAAAAAAAAAAAAAAAAAAAAAAAAAAAAAAAAAAAAAAAAAAAAAAA
AAAAAAAAAAAAAAAAAAAAAAAAAAAAAAAAAAAAAAAAAAAAAAAAAAAAAAAAAAAAAAAAAAAAAAAAAAAAAAAAAAAAAAAAAAAAAAAAAAAA
AAAAAAAAAAAAAAAAAAAAAAAAAAAAAAAAAAAAAAAAAAAAAAAAAAAAAAAAAAAAAAAAAAAAAAAAAAAAAAAAAAAAAAAAAAAAAAAAAAAA
AAAAAAAAAAAAAAAAAAAAAAAAAAAAAAAAAAAAAAAAAAAAAAAAAAAAAAAAAAAAAAAAAAAAAAAAAAAAAAAAAAAAAAAAAAAAAAAAAAAA
AAAAAAAAAAAAAAAAAAAAAAAAAAAAAAAAAAAAAAAAAAAAAAAAAAAAAAAAAAAAAAAAAAAAAAAAAAAAAAAAAAAAAAAAAAAAAAAAAAAA
AAAAAAAAAAAAAAAAAAAAAAAAAAAAAAAAAAAAAAAAAAAAAAAAAAAAAAAAAAAAAAAAAAAAAAAAAAAAAAAAAAAAAAAAAAAAAAAAAAAA
AAAAAAAAAAAAAAAAAAAAAAAAAAAAAAAAAAAAAAAAAAAAAAAAAAAAAAAAAAAAAAAAAAAAAAAAAAAAAAAAAAAAAAAAAAAAAAAAAAAA
AAAAAAAAAAAAAAAAAAAAAAAAAAAAAAAAAAAAAAAAAAAAAAAAAAAAAAAAAAAAAAAAAAAAAAAAAAAAAAAAAAAAAAAAAAAAAAAAAAAA
AAAAAAAAAAAAAAAAAAAAAAAAAAAAAAAAAAAAAAAAAAAAAAAAAAAAAAAAAAAAAAAAAAAAAAAAAAAAAAAAAAAAAAAAAAAAAAAAAAAA
AAAAAAAAAAAAAAAAAAAAAAAAAAAAAAAAAAAAAAAAAAAAAAAAAAAAAAAAAAAAAAAAAAAAAAAAAAAAAAAAAAAAAAAAAAAAAAAAAAAA
AAAAAAAAAAAAAAAAAAAAAAAAAAAAAAAAAAAAAAAAAAAAAAAAAAAAAAAAAAAAAAAAAAAAAAAAAAAAAAAAAAAAAAAAAAAAAAAAAAAA
AAAAAAAAAAAAAAAAAAAAAAAAAAAAAAAAAAAAAAAAAAAAAAAAAAAAAAAAAAAAAAAAAAAAAAAAAAAAAAAAAAAAAAAAAAAAAAAAAAAA
AAAAAAAAAAAAAAAAAAAAAAAAAAAAAAAAAAAAAAAAAAAAAAAAAAAAAAAAAAAAAAAAAAAAAAAAAAAAAAAAAAAAAAAAAAAAAAAAAAAA
AAAAAAAAAAAAAAAAAAAAAAAAAAAAAAAAAAAAAAAAAAAAAAAAAAAAAAAAAAAAAAAAAAAAAAAAAAAAAAAAAAAAAAAAAAAAAAAAAAAA
AAAAAAAAAAAAAAAAAAAAAAAAAAAAAAAAAAAAAAAAAAAAAAAAAAAAAAAAAAAAAAAAAAAAAAAAAAAAAAAAAAAAAAAAAAAAAAAAAAAA
AAAAAAAAAAAAAAAAAAAAAAAAAAAAAAAAAAAAAAAAAAAAAAAAAAAAAAAAAAAAAAAAAAAAAAAAAAAAAAAAAAAAAAAAAAAAAAAAAAAA
AAAAAAAAAAAAAAAAAAAAAAAAAAAAAAAAAAAAAAAAAAAAAAAAAAAAAAAAAAAAAAAAAAAAAAAAAAAAAAAAAAAAAAAAAAAAAAAAAAAA
AAAAAAAAAAAAAAAAAAAAAAAAAAAAAAAAAAAAAAAAAAAAAAAAAAAAAAAAAAAAAAAAAAAAAAAAAAAAAAAAAAAAAAAAAAAAAAAAAAAA
AAAAAAAAAAAAAAAAAAAAAAAAAAAAAAAAAAAAAAAAAAAAAAAAAAAAAAAAAAAAAAAAAAAAAAAAAAAAAAAAAAAAAAAAAAAAAAAAAAAA
AAAAAAAAAAAAAAAAAAAAAAAAAAAAAAAAAAAAAAAAAAAAAAAAAAAAAAAAAAAAAAAAAAAAAAAAAAAAAAAAAAAAAAAAAAAAAAAAAAAA
AAAAAAAAAAAAAAAAAAAAAAAAAAAAAAAAAAAAAAAAAAAAAAAAAAAAAAAAAAAAAAAAAAAAAAAAAAAAAAAAAAAAAAAAAAAAAAAAAAAA
AAAAAAAAAAAAAAAAAAAAAAAAAAAAAAAAAAAAAAAAAAAAAAAAAAAAAAAAAAAAAAAAAAAAAAAAAAAAAAAAAAAAAAAAAAAAAAAAAAAA
AAAAAAAAAAAAAAAAAAAAAAAAAAAAAAAAAAAAAAAAAAAAAAAAAAAAAAAAAAAAAAAAAAAAAAAAAAAAAAAAAAAAAAAAAAAAAAAAAAAA
AAAAAAAAAAAAAAAAAAAAAAAAAAAAAAAAAAAAAAAAAAAAAAAAAAAAAAAAAAAAAAAAAAAAAAAAAAAAAAAAAAAAAAAAAAAAAAAAAAAA
AAAAAAAAAAAAAAAAAAAAAAAAAAAAAAAAAAAAAAAAAAAAAAAAAAAAAAAAAAAAAAAAAAAAAAAAAAAAAAAAAAAAAAAAAAAAAAAAAAAA
AAAAAAAAAAAAAAAAAAAAAAAAAAAAAAAAAAAAAAAAAAAAAAAAAAAAAAAAAAAAAAAAAAAAAAAAAAAAAAAAAAAAAAAAAAAAAAAAAAAA
AAAAAAAAAAAAAAAAAAAAAAAAAAAAAAAAAAAAAAAAAAAAAAAAAAAAAAAAAAAAAAAAAAAAAAAAAAAAAAAAAAAAAAAAAAAAAAAAAAAA
AAAAAAAAAAAAAAAAAAAAAAAAAAAAAAAAAAAAAAAAAAAAAAAAAAAAAAAAAAAAAAAAAAAAAAAAAAAAAAAAAAAAAAAAAAAAAAAAAAAA
AAAAAAAAAAAAAAAAAAAAAAAAAAAAAAAAAAAAAAAAAAAAAAAAAAAAAAAAAAAAAAAAAAAAAAAAAAAAAAAAAAAAAAAAAAAAAAAAAAAA
AAAAAAAAAAAAAAAAAAAAAAAAAAAAAAAAAAAAAAAAAAAAAAAAAAAAAAAAAAAAAAAAAAAAAAAAAAAAAAAAAAAAAAAAAAAAAAAAAAAA
AAAAAAAAAAAAAAAAAAAAAAAAAAAAAAAAAAAAAAAAAAAAAAAAAAAAAAAAAAAAAAAAAAAAAAAAAAAAAAAAAAAAAAAAAAAAAAAAAAAA
AAAAAAAAAAAAAAAAAAAAAAAAAAAAAAAAAAAAAAAAAAAAAAAAAAAAAAAAAAAAAAAAAAAAAAAAAAAAAAAAAAAAAAAAAAAAAAAAAAAA
AAAAAAAAAAAAAAAAAAAAAAAAAAAAAAAAAAAAAAAAAAAAAAAAAAAAAAAAAAAAAAAAAAAAAAAAAAAAAAAAAAAAAAAAAAAAAAAAAAAA
AAAAAAAAAAAAAAAAAAAAAAAAAAAAAAAAAAAAAAAAAAAAAAAAAAAAAAAAAAAAAAAAAAAAAAAAAAAAAAAAAAAAAAAAAAAAAAAAAAAA
AAAAAAAAAAAAAAAAAAAAAAAAAAAAAAAAAAAAAAAAAAAAAAAAAAAAAAAAAAAAAAAAAAAAAAAAAAAAAAAAAAAAAAAAAAAAAAAAAAAA
AAAAAAAAAAAAAAAAAAAAAAAAAAAAAAAAAAAAAAAAAAAAAAAAAAAAAAAAAAAAAAAAAAAAAAAAAAAAAAAAAAAAAAAAAAAAAAAAAAAA
AAAAAAAAAAAAAAAAAAAAAAAAAAAAAAAAAAAAAAAAAAAAAAAAAAAAAAAAAAAAAAAAAAAAAAAAAAAAAAAAAAAAAAAAAAAAAAAAAAAA
AAAAAAAAAAAAAAAAAAAAAAAAAAAAAAAAAAAAAAAAAAAAAAAAAAAAAAAAAAAAAAAAAAAAAAAAAAAAAAAAAAAAAAAAAAAAAAAAAAAA
AAAAAAAAAAAAAAAAAAAAAAAAAAAAAAAAAAAAAAAAAAAAAAAAAAAAAAAAAAAAAAAAAAAAAAAAAAAAAAAAAAAAAAAAAAAAAAAAAAAA
AAAAAAAAAAAAAAAAAAAAAAAAAAAAAAAAAAAAAAAAAAAAAAAAAAAAAAAAAAAAAAAAAAAAAAAAAAAAAAAAAAAAAAAAAAAAAAAAAAAA
AAAAAAAAAAAAAAAAAAAAAAAAAAAAAAAAAAAAAAAAAAAAAAAAAAAAAAAAAAAAAAAAAAAAAAAAAAAAAAAAAAAAAAAAAAAAAAAAAAAA
AAAAAAAAAAAAAAAAAAAAAAAAAAAAAAAAAAAAAAAAAAAAAAAAAAAAAAAAAAAAAAAAAAAAAAAAAAAAAAAAAAAAAAAAAAAAAAAAAAAA
AAAAAAAAAAAAAAAAAAAAAAAAAAAAAAAAAAAAAAAAAAAAAAAAAAAAAAAAAAAAAAAAAAAAAAAAAAAAAAAAAAAAAAAAAAAAAAAAAAAA
AAAAAAAAAAAAAAAAAAAAAAAAAAAAAAAAAAAAAAAAAAAAAAAAAAAAAAAAAAAAAAAAAAAAAAAAAAAAAAAAAAAAAAAAAAAAAAAAAAAA
AAAAAAAAAAAAAAAAAAAAAAAAAAAAAAAAAAAAAAAAAAAAAAAAAAAAAAAAAAAAAAAAAAAAAAAAAAAAAAAAAAAAAAAAAAAAAAAAAAAA
AAAAAAAAAAAAAAAAAAAAAAAAAAAAAAAAAAAAAAAAAAAAAAAAAAAAAAAAAAAAAAAAAAAAAAAAAAAAAAAAAAAAAAAAAAAAAAAAAAAA
AAAAAAAAAAAAAAAAAAAAAAAAAAAAAAAAAAAAAAAAAAAAAAAAAAAAAAAAAAAAAAAAAAAAAAAAAAAAAAAAAAAAAAAAAAAAAAAAAAAA
AAAAAAAAAAAAAAAAAAAAAAAAAAAAAAAAAAAAAAAAAAAAAAAAAAAAAAAAAAAAAAAAAAAAAAAAAAAAAAAAAAAAAAAAAAAAAAAAAAAA
```

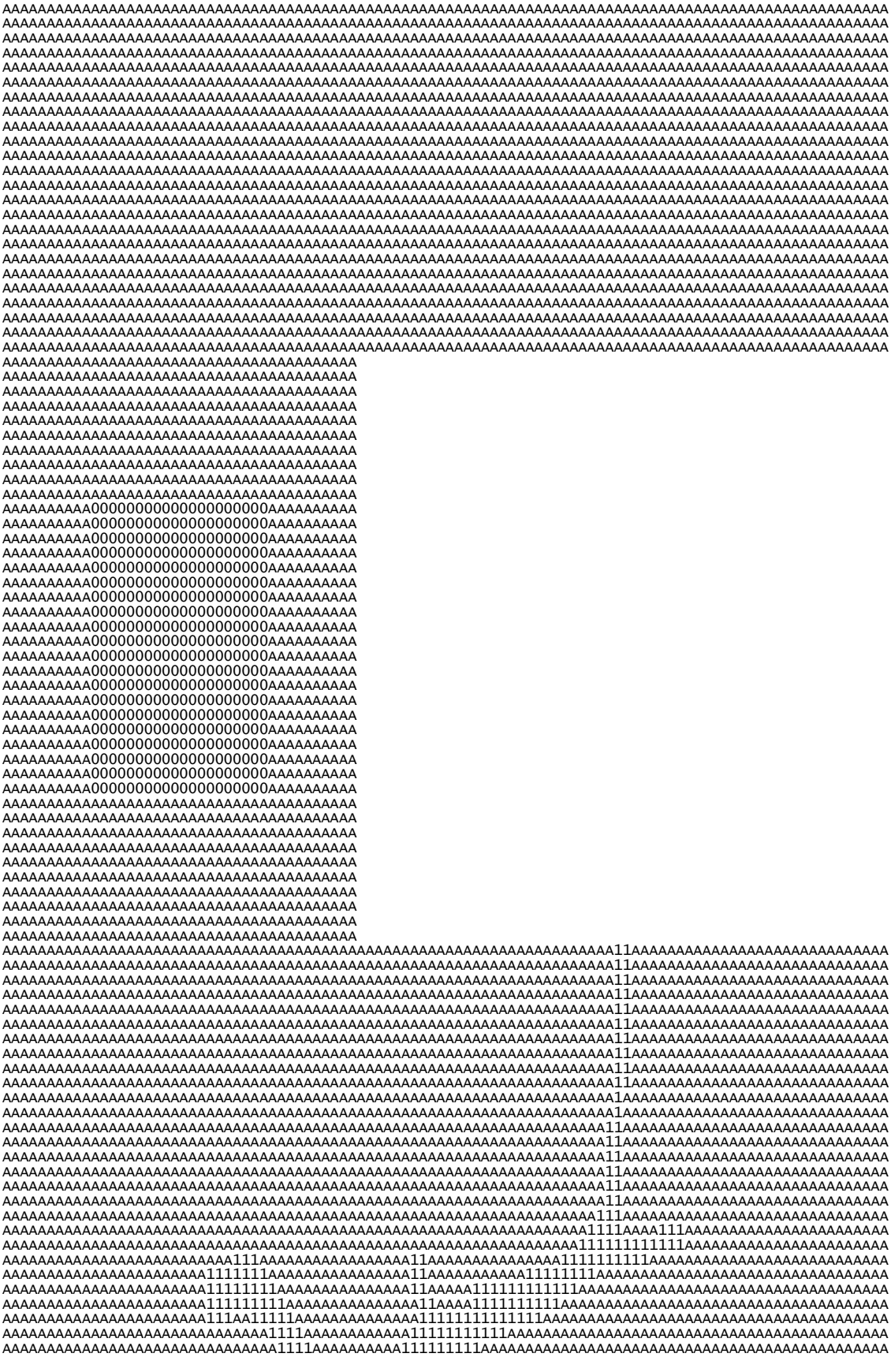

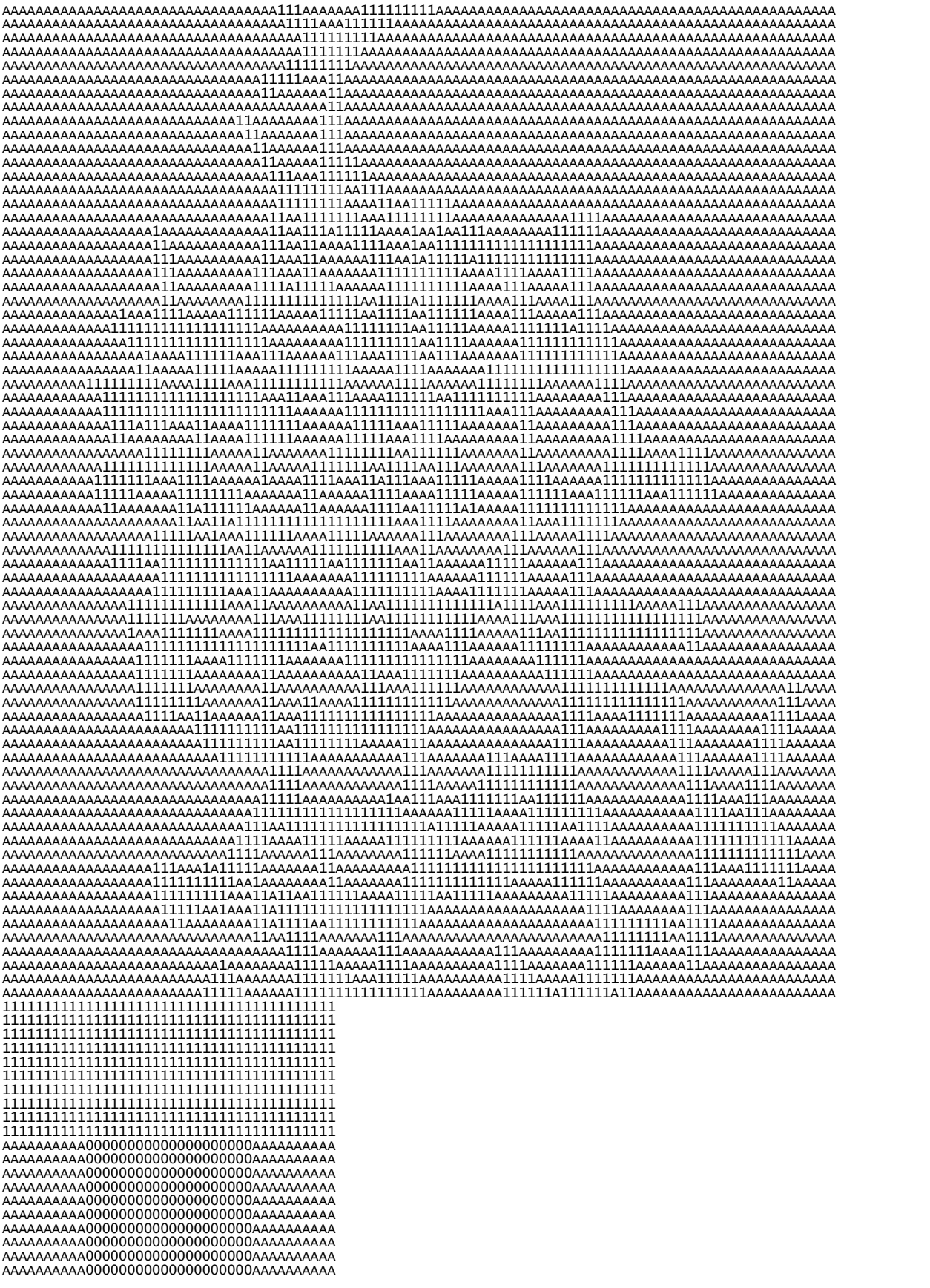

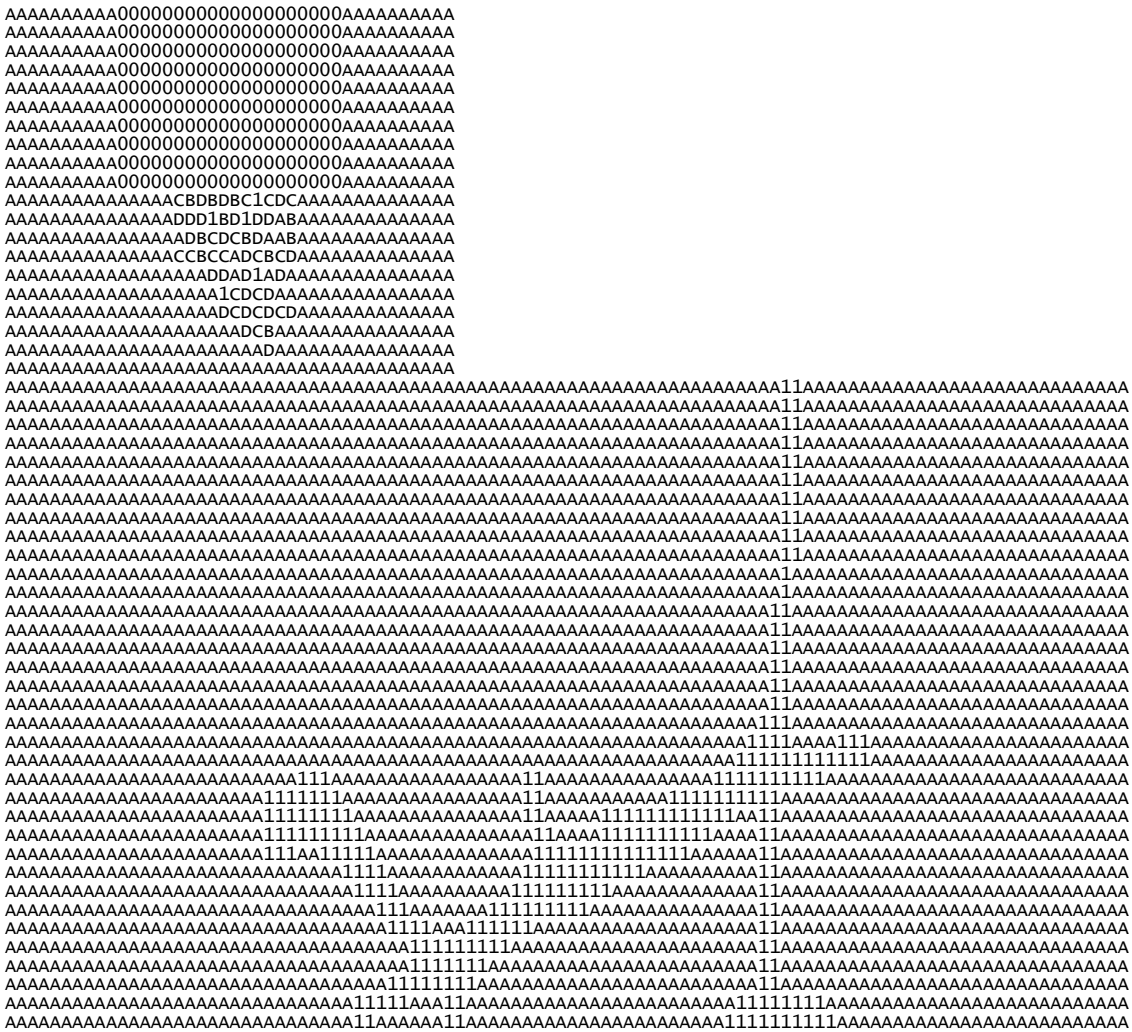

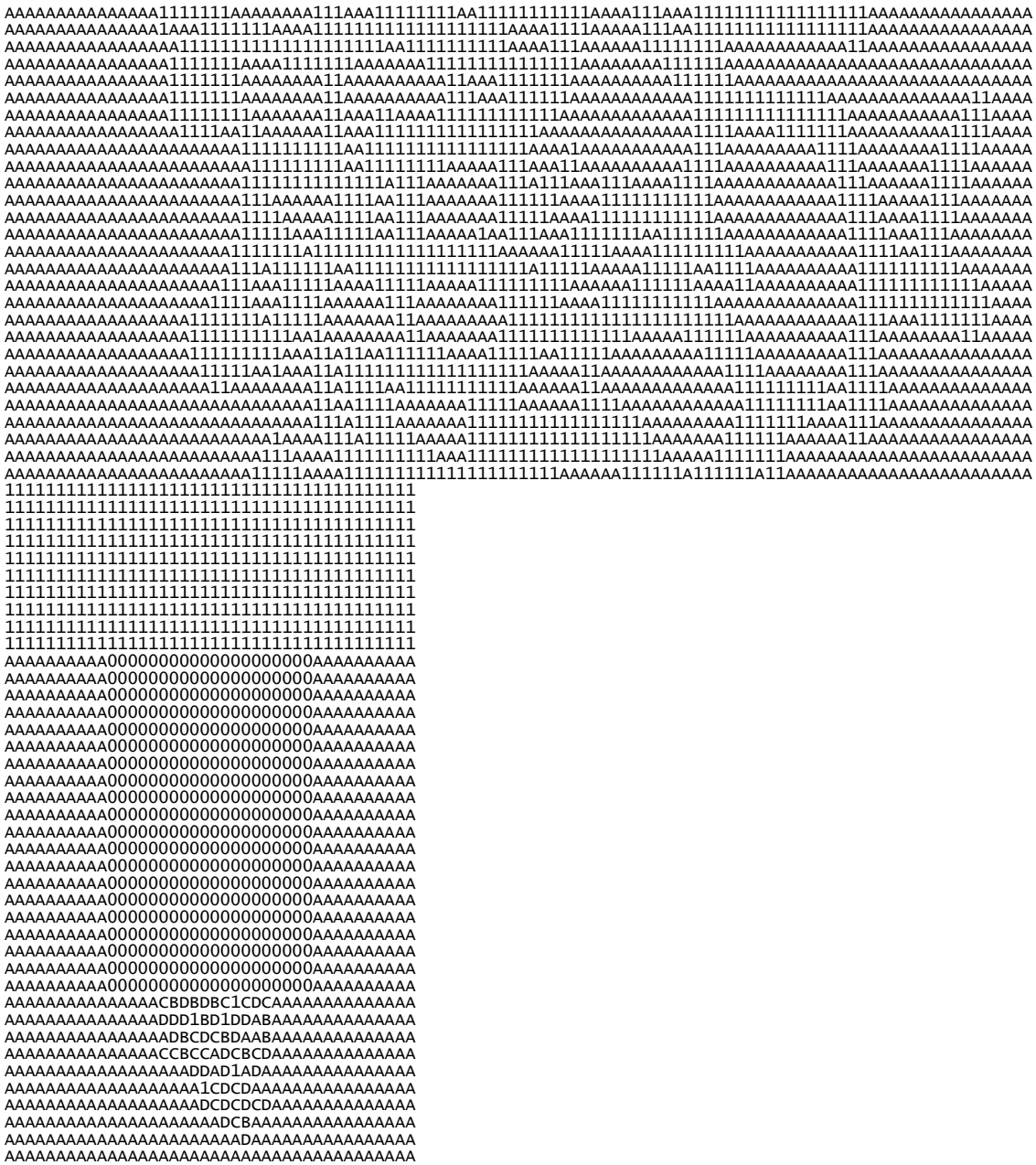

Appendix B: Visual Basic Macros for Microsoft Excel to Convert Fine Element Material Codes to Block Material Codes

Summary

An automated process via Visual Basic macros in Microsoft Excel is described to convert some of the fine element material codes from a grid for LaModel to equivalent coarse block material codes for MulsimNL/Large. The macros used are listed.

Background

None of the Mulsim codes, including MulsimNL/Large, has had symmetrical boundary conditions. They are fixed—meaning that no closure is allowed in the seam at the outer x- and y-boundaries of the model. To minimize boundary effects in the area of mining, boundaries must be far away. Placing the boundaries far away increases the size of the model substantially. However, the structure of a Mulsim grid is a rectangular array of even, square, coarse blocks. In the area of interest, the coarse blocks are further subdivided into five by five fine elements. In this way, the size of the problem may be kept to a minimum by minimizing the rectangular area of coarse blocks that is converted to fine elements.

A grid in LaModel is comprised of only fine elements. However, if symmetry is designated on the boundaries, then the necessity of locating outer boundaries far from the area of interest is minimized. In this study, an LaModel grid with a series of excavations was constructed before any Mulsim grid. Mulsim models of comparable size take much longer to run than do those in LaModel. For that reason it is desirable, when converting a grid from LaModel to Mulsim, to further reduce the size of the inner grid of fine elements by converting several five-by-five fine elements to equivalent coarse blocks. This process is done on and near the boundary of the inner grid of fine elements that is initially formed by the LaModel grid. The choice to convert fine elements to coarse blocks is made judiciously where the elements are still a reasonable distance from the area of mining interest. Equivalency is approximate by choosing a coarse block material code that best represents the average behavior of the composite of fine elements that it replaces.

This appendix reviews the procedure used in constructing LaModel grids in this study and the conversion of these grids to be appropriate for MulsimNL/Large. The conversion process was tedious and prone to mistakes, if done manually. The need was great for the process to be automated.

Construction of Material Codes for LaModel

In preparing material codes for LaModel [Heasley 2010], an AutoCad map was available, but it was not the size of the model grid planned, and the map did not show the exact excavation state. Therefore, LaModel's interface [Heasley et al. 2003; Wang and Heasley 2005] for AutoCad was not used to assign material property codes to cells. Instead, a grid was superimposed on the map and codes were chosen, fine element by fine element, and placed in a spreadsheet. The panel excavations and progression of panel mining were then easy to add to the initial gate roads model. These initial codes were comprised only of the characters, "A", "1", "Z", and "a", which represented the elastic material, excavated cell, Panel 1 gob and previous

gob, and Panel 2 gob, respectively. However, Heasley's [2010] pre-processing tool in LamPre 3.0 was used for preparing input for LaModel 3.0 [Heasley 2010]. This tool was used to individually assign yield codes for each mining step. These codes were then assembled into one input file for the 185 excavations used in the model.

Each mining step was placed on a different sheet, with first row and column having index numbers and the next row and column being blank or having x- or y-coordinates. The sheet with the gate roads was then copied to the next sheet, and panel mining was able to proceed with easy copy and paste exercises. Thus, all 185 mining cuts were easily constructed after the initial gate road layout was completed.

Construction of Material Codes for MulsimNL/Large

When converting the same mining steps for use with MulsimNL/Large, the size of the fine mesh in LaModel was too large for efficient running of Mulsim models. It was decided to narrow down the dimensions of the fine-element area by converting some of the 5-by-5 fine element codes outside of that narrowed fine-element area to average block codes. Therefore, the 640 columns by 1,370 rows of fine-element material codes used with LaModel were modified to convert some of the fine-element material codes to average block material codes. Material codes found in the block defined by columns 66 to 475 and rows 170 to 1,150 (counting from bottom to top) were kept the same. However, 5-by-5 fine-element material codes outside that area were converted to block material codes by averaging the peak strengths of the fine-element material codes within that block and selecting a block code whose peak strength was closest to that average value. To that end, the Mark-Bieniawski strengths [Mark and Iannacchione 1992] calculated for 10-ft elements and 12 yield rings were used in that determination because that system is linear. To the outside of these converted block codes in each sheet of the spreadsheet, 20 block rows and columns were added to form additional border distance. Thus, the left coarse-block border consisted of 20 added columns plus 13 converted columns, and the right coarse-block border consisted of 33 converted columns and 20 added columns. The bottom coarse-block border consisted of 20 added rows plus 34 converted rows, and the top coarse-block border consisted of 44 converted rows and 20 added rows. These added rows and columns served to distance the area of interest from the rigid boundaries of the model because MulsimNL/Large does not yet have implemented symmetrical boundary conditions.

A procedure was developed for automating the conversion of 5-by-5 fine-element material codes to an average code for block elements. The procedure was completed using Excel functions. Figure B1 shows an area of the spreadsheet, where column XT, in this case, is two columns to the right of the last column where the LaModel material codes were located on each sheet. In the area with the light green background, the material codes are listed along with their corresponding strength (in this case, 900-psi Mark-Bieniawski coal [Mark and Barton 1996]). For an excavated cell, zero strength is given. For the two gob materials, "Z" and "a", some strength was needed that was higher than zero. The authors elected to use the first yield ring side element strength as the strength for both gobs for the purposes of average block strength estimation.

The procedure was to copy a 5-by-5 set of fine codes from the spreadsheet, corresponding to a coarse block, and paste them in the area with light blue background, beginning at row 3, as shown in Figure B1. Rows 9 through 13 below that, in the light orange, contain the corresponding peak strengths obtained with Excel's VLOOKUP function on columns XT and

XU. Cell XX15, with cyan background, has the result of the average of the strengths listed in the light orange cells. Column XV, with light red background, contains the absolute value of the difference between the code strength in column XU and the average block strength (in cyan). The yellow highlighted area shows the minimum from column XV, the row number where that minimum appears (via the MATCH function), and the corresponding material code (via the INDIRECT function). That letter code is then copied and pasted to the centroid cell of the block being converted from fine-element material codes to an equivalent block code.

Even with the use of Excel functions, the risk of error is very high. Therefore, the authors wrote Visual Basic macros to automate this process after first copying the contents of the cells shown in Figure B1 to the same cells in all sheets. These macros are found later in this appendix. The first macro, AllSheetsToCoarse(), loops through the sheets. The second macro, MakeCoarseElements(), performs the automatic looping through the various sets of 5-by-5 fine elements that correspond to a block, copies it to the cells XX3:YB7 and replaces the fine elements with blanks in all cells of the block except the center cell, where it places the average coarse block material code determined in cell XX19. The macro puts "0" in the center cell of blocks that will retain the fine-element codes. A copy of the original spreadsheet with fine element codes was retained so that a record was maintained of the fine-element codes.

After the code conversion macros were executed, the coarse-block material codes of each mining step were copied to an ASCII text file editor, such as Notepad. Tab codes were removed by the Search and Replace utility, and then saved with a name reflecting that the file has coarse material codes and the number of the mining step. The fine element codes were copied from the fine-element area to another text file, the tab codes removed, and the file saved, with the name reflecting that the file contains fine-element material codes and the number of the mining step.

The control block of the series of mining steps was constructed in another ASCII text file. This control block includes the first few lines of the input file that define the model parameters but does not include the material codes. The authors chose to run each mining step in parallel instead of in series in order to save time. Running each mining step in parallel means that the solution is arrived at from the premining state instead of from the previous mining step. The question arose on how this shortcut might affect the final output of each step; however, it was determined that the only likely problem was an increase in seam closure with each sequential mining step and that the differences would be minimal. Therefore, a model was run with 10 successive mining steps. The same mining steps were run individually from the premining state. Results from the parallel and series models were compared and found to produce very small differences. Therefore, all subsequent models with several mining steps were run in parallel. An input file for each mining step was produced by using a Disk Operating System (DOS) batch file to combine three files into one input file for each mining step: a control file, a fine-element material codes file, and a block material codes file.

	A	B	XS	XT	XU	XV	XW	XX	XY	XZ	YA	YB
1												
2				Code	Strength	Abs(Strength - average block strength)		**Current block fine element material codes**				
3	**1370**	11180		A	22666.9	906.676		1	A	A	A	A
4	**1369**	11170		B	20899.6	860.624		A	A	A	A	A
5	**1368**	11160		C	20605.1	1155.124		A	A	A	A	A
6	**1367**	11150		D	19132.4	2627.824		A	A	A	A	A
7	**1366**	11140		E	18837.8	2922.424		A	A	A	A	A
8	**1365**	11130		F	17365.1	4395.124		**Current block fine element peak strengths**				
9	**1364**	11120		G	17070.5	4689.724		0	22666.9	22666.9	22666.9	22666.9
10	**1363**	11110		H	15597.8	6162.424		22666.9	22666.9	22666.9	22666.9	22666.9
11	**1362**	11100		I	15303.3	6456.924		22666.9	22666.9	22666.9	22666.9	22666.9
12	**1361**	11090		J	13830.5	7929.724		22666.9	22666.9	22666.9	22666.9	22666.9
13	**1360**	11080		K	13536	8224.224		22666.9	22666.9	22666.9	22666.9	22666.9
14	**1359**	11070		L	12063.3	9696.924						
15	**1358**	11060		M	11768.7	9991.524		21760.2	<== Average block strength			
16	**1357**	11050		N	10296	11464.224						
17	**1356**	11040		O	10001.5	11758.724		860.624	<== Minimum difference			
18	**1355**	11030		P	8528.73	13231.494		4	<== Row # of minimum difference			
19	**1354**	11020		Q	8234.18	13526.044		B	<== Corresponding material code			
20	**1353**	11010		R	6761.45	14998.774						
21	**1352**	11000		S	6466.91	15293.314						
22	**1351**	###		T	4994.18	16766.044						
23	**1350**	###		U	4699.64	17060.584						
24	**1349**	###		V	3226.91	18533.314						
25	**1348**	###		W	2932.36	18827.864						
26	**1347**	###		X	1459.64	20300.584						
27	**1346**	###		Y	1165.09	20595.134						
28	**1345**	###		1	0	21760.224						
29	**1344**	###		Z	1459.64	20300.584						
30	**1343**	10310		a	1459.64							
31	**1342**	###										

1 2 3 4 5 6 7 8 9 10 11 12 13 14 15 16 17 18 19 20

Figure B1. Portion of spreadsheet where conversion to average coarse material code was calculated.

```
————————————————————————————————————————————————————————————
Sub AllSheetsToCoarse()
   Dim k As Integer
   k = 1
   Do While k < 36     ' 36 represents the number of sheets, each sheet representing a mining step with fine material codes before
' execution of this macro.  This subroutine loops down the sheets.  The 185 mining steps of this model had to be broken up into multiple
' spreadsheet files to reduce the size of the file.
     Sheets(k).Select
     Range("C3").Select
     MakeCoarseElements
     Range("C3").Select
     k = k + 1
   Loop
End Sub
————————————————————————————————————————————————————————————
Sub MakeCoarseElements()
'
' MakeCoarseElements Macro
'
'
   Dim i As Integer, j As Integer, NumZ As Integer, NumA As Integer
   Dim fineilower As Integer, fineiupper As Integer
   Dim finejlower As Integer, finejupper As Integer
   Dim MyRef1 As String, MyRef2 As String, MyRef As String, Cont1 As String
   Dim CC11 As String, CC12 As String, CC13 As String, CC14 As String, CC15 As String
   Dim CC21 As String, CC22 As String, CC23 As String, CC24 As String, CC25 As String
   Dim CC31 As String, CC32 As String, CC33 As String, CC34 As String, CC35 As String
   Dim CC41 As String, CC42 As String, CC43 As String, CC44 As String, CC45 As String
   Dim CC51 As String, CC52 As String, CC53 As String, CC54 As String, CC55 As String
   Application.Goto Reference:="R3C3"
   i = 3                          ' 3 means row 3 of the spreadsheet, or the first row of codes, since the codes begin on row 3
' of the spreadsheet.
   finejlower = 66 + 2            ' 66 is the beginning column of fine-element material codes that will not be converted to
' coarse-block material codes.
   finejupper = 475 + 2           ' 475 is the last column of fine-element material codes that will not be converted to coarse-
' block material codes.
   fineilower = 1370 - 1150 + 3   ' 1370 is the last row of fine-element material codes; 1150 is the last row, counting backward
' from the last row, where fine element codes will not be converted to coarse-block material codes.
   fineiupper = 1370 - 171 + 3    ' 171 is the first row, counting backward from the last row, where fine-element material
' codes will not be converted to coarse-block material codes.
   Do While i < 1372              ' 1372 is 2 greater than the number of rows in the material codes of the model; in the
' spreadsheet, the 1370-row-by-640-column material codes are placed in spreadsheet rows 3 to 1372 and columns 3 to 642.
     j = 3                        ' 3 means column 3 of the spreadsheet, or the first column of codes, since the codes begin on
' column 3 of the spreadsheet.
     Do While j < 642             ' 642 is 2 greater than the number of columns in the material codes of the model; in the
```

```
'spreadsheet, the 1370-row-by-640-column material codes are place in spreadsheet rows 3 to 1372 and columns 3 to 642.
    MyRef1 = "R" & i
     MyRef2 = "C" & j
     MyRef = MyRef1 & MyRef2
     Application.Goto Reference:=MyRef
     If i >= fineilower Then      'Test if within fine mesh area
      If i <= fineiupper Then
       If j >= finejlower Then
        If j <= finejupper Then
         CC11 = ActiveCell.Range("A1").Value
         If CC11 = "" Then
          GoTo Line1
         End If
         PutInZero      'Within fine mesh area; Put in zero
         GoTo Line1
        End If
       End If
      End If
     End If
     NumZ = 0
     NumA = 0
     ActiveCell.Range("A1").Select
     CC11 = ActiveCell.Range("A1").Value
     If CC11 = "" Then
      GoTo Line1
     End If
'
     If CC11 = "Z" Then NumZ = NumZ + 1
     If CC11 = "A" Then NumA = NumA + 1
     ActiveCell.Offset(0, 1).Range("A1").Select
     CC12 = ActiveCell.Range("A1").Value
     If CC12 = "Z" Then NumZ = NumZ + 1
     If CC12 = "A" Then NumA = NumA + 1
     ActiveCell.Offset(0, 1).Range("A1").Select
     CC13 = ActiveCell.Range("A1").Value
     If CC13 = "Z" Then NumZ = NumZ + 1
     If CC13 = "A" Then NumA = NumA + 1
     ActiveCell.Offset(0, 1).Range("A1").Select
     CC14 = ActiveCell.Range("A1").Value
     If CC14 = "Z" Then NumZ = NumZ + 1
     If CC14 = "A" Then NumA = NumA + 1
     ActiveCell.Offset(0, 1).Range("A1").Select
     CC15 = ActiveCell.Range("A1").Value
     If CC15 = "Z" Then NumZ = NumZ + 1
     If CC15 = "A" Then NumA = NumA + 1
     ActiveCell.Offset(1, -4).Range("A1").Select
```

```
CC21 = ActiveCell.Range("A1").Value
If CC21 = "Z" Then NumZ = NumZ + 1
If CC21 = "A" Then NumA = NumA + 1
ActiveCell.Offset(0, 1).Range("A1").Select
CC22 = ActiveCell.Range("A1").Value
If CC22 = "Z" Then NumZ = NumZ + 1
If CC22 = "A" Then NumA = NumA + 1
ActiveCell.Offset(0, 1).Range("A1").Select
CC23 = ActiveCell.Range("A1").Value
If CC23 = "Z" Then NumZ = NumZ + 1
If CC23 = "A" Then NumA = NumA + 1
ActiveCell.Offset(0, 1).Range("A1").Select
CC24 = ActiveCell.Range("A1").Value
If CC24 = "Z" Then NumZ = NumZ + 1
If CC24 = "A" Then NumA = NumA + 1
ActiveCell.Offset(0, 1).Range("A1").Select
CC25 = ActiveCell.Range("A1").Value
If CC25 = "Z" Then NumZ = NumZ + 1
If CC25 = "A" Then NumA = NumA + 1
ActiveCell.Offset(1, -4).Range("A1").Select
CC31 = ActiveCell.Range("A1").Value
If CC31 = "Z" Then NumZ = NumZ + 1
If CC31 = "A" Then NumA = NumA + 1
ActiveCell.Offset(0, 1).Range("A1").Select
CC32 = ActiveCell.Range("A1").Value
If CC32 = "Z" Then NumZ = NumZ + 1
If CC32 = "A" Then NumA = NumA + 1
ActiveCell.Offset(0, 1).Range("A1").Select
CC33 = ActiveCell.Range("A1").Value
If CC33 = "Z" Then NumZ = NumZ + 1
If CC33 = "A" Then NumA = NumA + 1
ActiveCell.Offset(0, 1).Range("A1").Select
CC34 = ActiveCell.Range("A1").Value
If CC34 = "Z" Then NumZ = NumZ + 1
If CC34 = "A" Then NumA = NumA + 1
ActiveCell.Offset(0, 1).Range("A1").Select
CC35 = ActiveCell.Range("A1").Value
If CC35 = "Z" Then NumZ = NumZ + 1
If CC35 = "A" Then NumA = NumA + 1
ActiveCell.Offset(1, -4).Range("A1").Select
CC41 = ActiveCell.Range("A1").Value
If CC41 = "Z" Then NumZ = NumZ + 1
If CC41 = "A" Then NumA = NumA + 1
ActiveCell.Offset(0, 1).Range("A1").Select
CC42 = ActiveCell.Range("A1").Value
If CC42 = "Z" Then NumZ = NumZ + 1
```

```
    If CC42 = "A" Then NumA = NumA + 1
    ActiveCell.Offset(0, 1).Range("A1").Select
    CC43 = ActiveCell.Range("A1").Value
    If CC43 = "Z" Then NumZ = NumZ + 1
    If CC43 = "A" Then NumA = NumA + 1
    ActiveCell.Offset(0, 1).Range("A1").Select
    CC44 = ActiveCell.Range("A1").Value
    If CC44 = "Z" Then NumZ = NumZ + 1
    If CC44 = "A" Then NumA = NumA + 1
    ActiveCell.Offset(0, 1).Range("A1").Select
    CC45 = ActiveCell.Range("A1").Value
    If CC45 = "Z" Then NumZ = NumZ + 1
    If CC45 = "A" Then NumA = NumA + 1
    ActiveCell.Offset(1, -4).Range("A1").Select
    CC51 = ActiveCell.Range("A1").Value
    If CC51 = "Z" Then NumZ = NumZ + 1
    If CC51 = "A" Then NumA = NumA + 1
    ActiveCell.Offset(0, 1).Range("A1").Select
    CC52 = ActiveCell.Range("A1").Value
    If CC52 = "Z" Then NumZ = NumZ + 1
    If CC52 = "A" Then NumA = NumA + 1
    ActiveCell.Offset(0, 1).Range("A1").Select
    CC53 = ActiveCell.Range("A1").Value
    If CC53 = "Z" Then NumZ = NumZ + 1
    If CC53 = "A" Then NumA = NumA + 1
    ActiveCell.Offset(0, 1).Range("A1").Select
    CC54 = ActiveCell.Range("A1").Value
    If CC54 = "Z" Then NumZ = NumZ + 1
    If CC54 = "A" Then NumA = NumA + 1
    ActiveCell.Offset(0, 1).Range("A1").Select
    CC55 = ActiveCell.Range("A1").Value
    If CC55 = "Z" Then NumZ = NumZ + 1
    If CC55 = "A" Then NumA = NumA + 1
    ActiveCell.Offset(-4, -4).Range("A1").Select
    If NumZ >= 13 Then
      PutInZ
      GoTo Line1
    End If
    If NumA = 25 Then
      PutInA
      GoTo Line1
    End If

' Determine replacement letter and copy into appropriate cell
    ActiveCell.Range("A1:E5").Select
    Selection.Copy
```

```
        Application.Goto Reference:="R3C648"  ' This is the location of where the 5 by 5 fine-element codes belong to a
' block are copied for analysis of average strength.  The 3 and the 648 are absolute spreadsheet row and column.
        ActiveSheet.Paste
        Application.Goto Reference:=MyRef
        ActiveCell.Range("A1:E5").Select
        Selection.ClearContents
        Application.Goto Reference:="R19C648"   ' This cell in the spreadsheet provides, via the match function, the row
' number where the closest matching strength is located.  R20C648 is the cell providing the corresponding code which will be copied to the
'middle cell of the 5-by-5 fine-element cells as the average coarse-block material code.  All other cells in the 5-by-5 cells will be made blank.
        Application.CutCopyMode = False
        Selection.Copy
        Application.Goto Reference:=MyRef
        ActiveCell.Offset(2, 2).Range("A1").Select
        Selection.PasteSpecial Paste:=xlPasteValues, Operation:=xlNone, SkipBlanks _
        :=False, Transpose:=False
        ActiveCell.Offset(-2, -2).Range("A1").Select

Line1:
        j = j + 5     ' Go to next row of 5-by-5 fine-element material codes.
      Loop
      i = i + 5       ' Go to the next column of 5-by-5 fine-element material codes.
    Loop
End Sub
————————————————————————————————————————————————————————
Sub PutInZero()
'
' PutInZero Macro
'
'
    ActiveCell.Range("A1:E5").Select
    Selection.ClearContents
    ActiveCell.Offset(2, 2).Range("A1").Select
    ActiveCell.Range("A1").Value = "0"
    ActiveCell.Offset(-2, -2).Range("A1").Select
End Sub
————————————————————————————————————————————————————————
Sub PutInZ()
'
' PutInZ Macro
'
'
    ActiveCell.Range("A1:E5").Select
    Selection.ClearContents
    ActiveCell.Offset(2, 2).Range("A1").Select
    ActiveCell.Range("A1").Value = "Z"
    ActiveCell.Offset(-2, -2).Range("A1").Select
```

```
End Sub
```

```
Sub PutInA()
'
' PutInA Macro
'
'
    ActiveCell.Range("A1:E5").Select
    Selection.ClearContents
    ActiveCell.Offset(2, 2).Range("A1").Select
    ActiveCell.Range("A1").Value = "A"
    ActiveCell.Offset(-2, -2).Range("A1").Select
End Sub
```

References for Appendix B

Heasley KA [2010]. LaModel, ver. 3.0, Morgantown, WV: West Virginia University.

Heasley KA, Agioutantis Z, Wang Q [2003]. Automatic grid generation allows faster analysis of coal mines. Trans. Soc. Min. Metall. Explor. Inc., Vol. 314, pp. 75–80.

Mark C, Barton T [1996]. The uniaxial compressive strength of coal: Should it be used to design pillars? In: Ozdemir L et al. eds. Proceedings: 15th International Conference on Ground Control in Mining. (Golden, CO: August 13-15, 1996) Golden, CO: Colorado School of Mines, pp. 61–78.

Mark C, Iannacchione AT [1992]. Coal pillar mechanics: Theoretical models and field measurements compared. In: Iannacchione AT et al. eds. Bureau of Mines Information Circular 9135, Proceedings of the Workshop on Coal Pillar Mechanics and Design. Washington, DC: U.S. Department of the Interior, pp. 78–93.

Wang Q, Heasley K [2005]. Stability mapping system. In: Peng SS et al. eds. Proceedings: 24th International Conference on Ground Control in Mining. (Morgantown, WV: August 2–4, 2005) Morgantown, WV: West Virginia University, pp. 243–249.

Appendix C: Distributed Modeling of Longwall Panels: Expanding Option[6]

Summary

Modeling the ground response to mining of deep coal panels has long been complicated by the wide range of scales pertinent to design. These scales range from man-sized structures (entries and pillars) to individual panels to mine-wide structures (topography and barrier pillars). While models are readily constructed at each of these scales with a variety of modeling programs, comprehensive modeling has been problematic. In part, this is because different modeling programs often are well suited for modeling only particular parts of the problem. Some modeling programs also have difficulties with large contrasts in element or block sizes. In addition, the large computational requirements of comprehensive modeling can be prohibitive. However, recent progress in constructing links between modeling methods and scales promises to expand options available to modelers. These links allow separation of analyses into pieces that are both appropriate, and most efficient. That is, modeling is "distributed" into smaller, more optimal parts. This appendix describes a distributed approach to modeling longwall panels in a deep coal mine. It describes software that has been created for linking various pillar- and panel-scale models. These models range in sophistication from spreadsheet calculations to LaModel and FLAC^{3D} panel-scale models. In this case, these links allow division of the problem into three parts—in situ stress estimation, pillar behavior, and panel behavior. These capabilities are demonstrated by modeling gate road pillar response to mining of a longwall panel in a deep coal mine.

Background

This appendix grew out of an effort to verify and calibrate a stress model of deep longwall coal panels under mountainous topography. The project was designed to implement recent MSHA guidance on verification of numerical stress models to ground condition observations [MSHA 2009], and then expand this process to incorporate a variety of other observations and measurements. The project draws from a field investigation that included rating of ground deterioration with face advance [Lawson et al. 2012] in accord with this guidance. The field investigation also included observation of ground deformation mechanisms, instrumentation of gate roads and pillars, and deployment of a seismic monitoring system. Further complications were provided by mountainous overburden and geologic structures, including a set of shear zones striking at low angles to the gate roads. This appendix presents a strategy for developing a stress model of this site. The strategy is based on decoupling of modeling into a number of steps and scales and tackling each with the most appropriate (and efficient) modeling tools. While this approach is not entirely novel, it is one of the most extensive efforts aimed at modeling of a deep coal panel. As such, it required modification of mainstream modeling tools, and a number of new software tools and utilities.

[6] This appendix was coauthored by Mark K. Larson, author of this RI, and Jeffrey K. Whyatt, formerly Acting Director, NIOSH Spokane Mining Research Division, Spokane, WA.

Strategy

The essential strategy for this modeling effort revolved around breaking the problem into coordinated parts that could be optimized for particular objectives, while retaining links to other portions of the model. These parts were organized on three basic scales. The largest scale was essentially the mountain overlying the mine, and the distribution of previous mining in several coal seams. The intermediate scale incorporated mining of the first two panels of a new district. Fortunately, the seam mined in this district was the first to be mined. The smallest scale was a number of pillar and gate road sections where observations of ground conditions and ground deformation mechanisms, as well as point measurements of closure and pillar stress, were modeled. The resulting scheme, illustrated in Figure C1, revolved around establishing appropriate links in boundary conditions and load response curves to effectively link models at these various scales.

For example, LaModel, a displacement-discontinuity boundary-element code, might adequately estimate initial stress if the relief is not highly variable. Otherwise, a volume-element code, such as FLAC^{3D} might be required to more accurately determine the effect of high topographical relief on seam-level initial stress. Initial stresses may be imported from other tools, as long as the format of the information matches that of the receiving tool. Seam-level stresses from LaModel may be imposed at the same horizon in FLAC^{3D}, but some assumptions may then be necessary to determine stresses throughout the rest of the body. The Itasca Longwall Modeling Environment is an additional capability in FLAC^{3D} that allows for mechanistic simulation of longwall caving. At the pillar scale, the Mark-Bieniawski formula is a common formula used in displacement discontinuity codes, but other material models might be substituted in the input file of such codes. FLAC^{3D} has multiple constitutive laws that might be necessary if pillar failure is largely dependent on confinement or structural failure in the floor or the roof.

The scheme is similar to sub-modeling efforts employed in a number of programs, most notably for this application, the pre-defined response of pillars typically found in boundary element programs [Crouch 1976; Sinha 1979; Karabin and Evanto 1999]. The scheme also uses the typical boundary element approach of defining an initial stress field as a starting point for mining-induced stress calculations, although some further equilibrating may be required when volume element methods are used to model panel scale stresses with this approach.

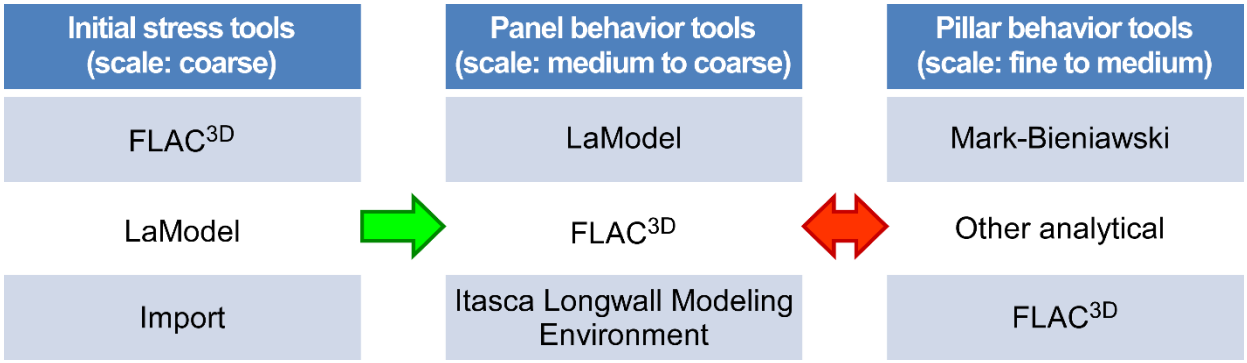

Figure C1. Diagram showing relationship between tools, categories of their use and their scales.

Pillars and Panels

Wizard and Spreadsheet Pillar Models

LaModel [Heasley 1998, 2010c], like many boundary element programs, abstracts pillar behavior as a one-dimensional response to loading that may include hardening or softening after an elastic limit is reached. This response can be based on a more detailed model but is most commonly generated by a simple program or spreadsheet using simplifying assumptions. LaModel, for instance, includes a wizard application for defining these curves consistent with the Mark-Bieniawski pillar capacity formula [Mark and Chase 1997; Mark and Iannacchione 1992]. Typically, the program is used to generate an elastic-perfectly-plastic curve for cells making up various portions of a pillar, as shown in Figure C2.

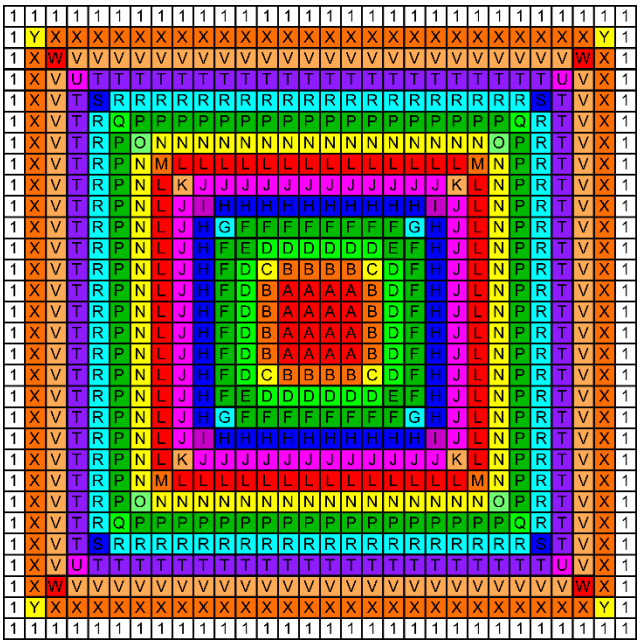

Figure C2. Plan view of LaModel pillar showing cells.

The wizard can also generate softening curves, based on the work by Karabin and Evanto [1999]. One such cell curve—the LamPre 3.0 default for softening—is shown in Figure C3. Heasley proposed more severe softening curves in his Crandall Canyon analysis. One important result of softening is that it causes pillar capacity to undershoot the Mark-Bieniawski capacity as various parts of the pillar fail at different stages in the pillar deformation process. A simple spreadsheet routine, assuming a rigid roof and floor, was used to produce the capacities for a pillar having a width-to-height ratio of 8:1 for various softening assumptions in Table C1. The formulae are vastly different, as can be seen by the results in the table. For example, the Wilson equation [1972, 1981; 1982] evaluates certain loading conditions of a pillar, whereas the Bieniawski, Mark-Bieniawski, and Maleki formulae give general strength capacities.

Table C1. Average pillar maximum stress for a pillar with width-to-height of 8, calculated by various methods. PIllar parameters are listed below the table

Method	Pillar capacity, MPa	Pillar capacity, psi
Bieniawski	21.84	3168
Mark-Bieniawski	21.84	3168
Maleki (structurally controlled)	23.15	3357
Maleki (confining controlled)	30.27	4390
Gaddy-Holland	17.55	2546
Wilson	18.63	2702
Vesić	21.59	3131

Parameters used:

Pillar width/height = 8.
Pillar length = pillar width = 24.4 m (80 ft)

Bieniawski:

Coal unconfined comp. strength = 6.20 MPa (900 psi)

Wilson:

$\phi = 30°$
$\gamma = 25.4$ kN/m^3 (162 pcf)
H = 609.6 m (2000 ft)
In situ coal strength = 6.20 MPa (900 psi)
Uniaxial strength of fractured coal = 96.5 kPa (14 psi)

Vesić:

cohesion = 3.52 MPa (510 psi)
$N_c = 5.142$
$N_q/N_c = 0.194$
Coal was saturated

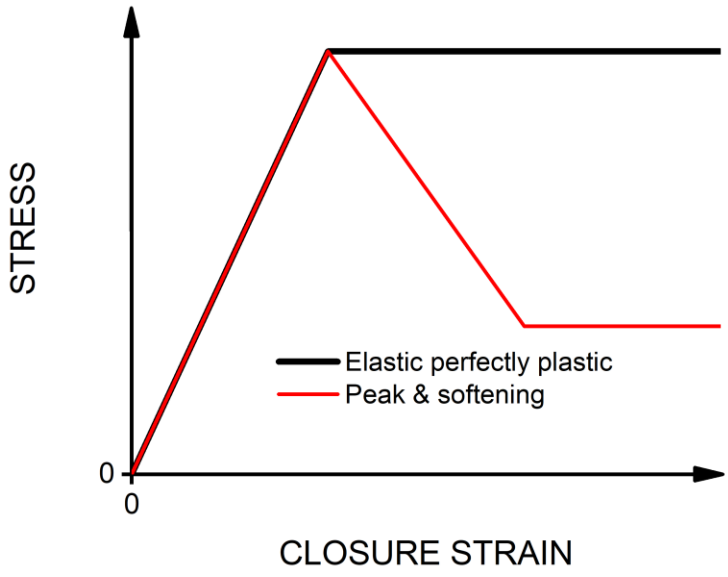

Figure C3. Typical load deformation curve defined for a pillar cell in LaModel.

LaModel can also import any similar three-segment curves defined by the user, allowing for further modification of both pillar capacity and deformation. This is important, because while the LaModel wizard employs Mark-Bieniawski's formula to estimate the peak load in each cell, assignment of the curve shape—its initial modulus, softening modulus and post-peak capacity is independent of this criterion. The wizard defaults to the Karabin and Evanto [1999] criterion—a log function fitting residual stress to distance from the pillar rib. However, this function has two flaws. First, the stress goes to negative infinity at the pillar rib (i.e. depth of zero), and it is unbounded for large pillars—meaning that there is a pillar size where softening becomes hardening, or strengthening, of the pillar.

Fortunately, it is rather simple to construct spreadsheets that employ alternative rules for generating pillar response curves and simple to introduce these curves into LaModel. Empirical capacity rules can be manipulated to provide stress gradients which can, in turn, be integrated into cell peak capacities. The process is even more straightforward for analytical criteria, as they provide a stress function directly. A number of spreadsheets were generated, including four additional empirical criteria [Bieniawski and Van Heerden 1975; Mark and Chase 1997; Maleki 1992] and two analytical criteria [Wilson 1972; Vesić 1975] (Table C2). In addition, alternative softening schemes were implemented—including a modified log function and a constant strength loss—and these schemes provide a wide variety of options for adapting the model to a specific site. They also provide a means for examining competing failure criteria. For example, the Bieniawski pillar and Vesić floor strength equations might both apply to the pillar and floor at a site – one of which will limit capacity of a particular pillar size. Use of both of these formulations might be used to limit the strength of a pillar, as illustrated in Figure C5.

Table C2. Strength capacity in pillar by location

Method	Equations for strength by location in the pillar
Bieniawski See Figure C4 A core element exists only when the centroid of an element coincides with the pillar centroid.	For side elements: $\sigma_v = S_1\left(0.64 + 2.16\frac{x}{h}\right)$ For corner elements: $\sigma_v = S_1\left(0.64 + 2.16\frac{\left(x-\frac{w}{6}\right)}{h}\right)$ For core elements: $\sigma_v = S_1\left(0.64 + 2.16\frac{\left(x-\frac{w}{3}\right)}{h}\right)$
Mark-Bieniawski See Figure C4	For side elements: $\sigma_v = S_1\left(0.64 + 2.16\frac{x}{h}\right)$ For corner elements: $\sigma_v = S_1\left(0.64 + 2.16\frac{\left(x-\frac{w}{6}\right)}{h}\right)$ For core elements: $\sigma_v = S_1\left(0.64 + 2.16\frac{\left(x-\frac{w}{3}\right)}{h}\right)$
Maleki (structural control strength)	$\sigma_v = 3836\left[1 - e^{\frac{-2(0.260)x}{h}}\left\{1 - \frac{4(0.260)}{h}x + \frac{2(0.260)^2}{h^2}x^2\right\}\right]$
Maleki (confinement control strength)	$\sigma_v = 4700\left[1 - e^{\frac{-2(0.339)x}{h}}\left\{1 - \frac{4(0.339)}{h}x + \frac{2(0.339)^2}{h^2}x^2\right\}\right]$
Wilson	$\sigma_v = k\,p'\left(\frac{2x}{h} + 1\right)^{k-1}$
Vesić	$\sigma_v = c\,N_c\left(1 + \frac{N_q}{N_c}\right)$ for saturated condition

Variable definitions:
σ_v = Average vertical strength of coal pillar
x = distance from rib
h = extraction height of coal pillar
S_1 = unconfined compressive strength of ≥ 1.5-m sided cube of coal
k = triaxial stress factor = $\left[\frac{1+\sin\phi}{1-\sin\phi}\right]$, where ϕ= 30° to 37°
p' = unconfined compressive strength of failed coal at pillar edge (14 psi)
c = cohesion
N_q and N_c = foundation factors = 0.9975 and 5.142, respectively, for saturated condition (ϕ = 0°)

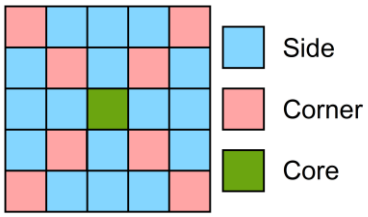

Figure C4. Type of element by location in plan view.

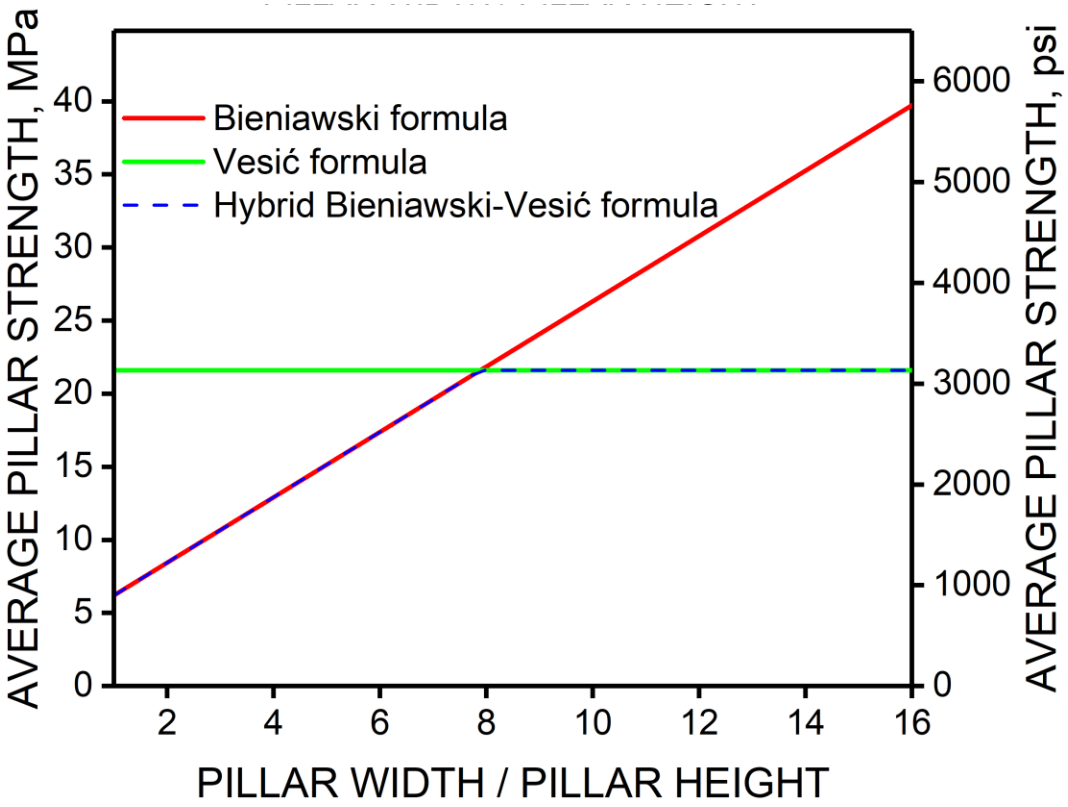

Figure C5. Average pillar strength according to the Bieniawski and Vesić formulas, showing how both might be used together to limit pillar strength. For the Vesić formula, internal friction angle = 0° and cohesion = 510 psi.

FLAC^{3D} Pillar Models

Abstracting of pillar response to loading also can be based on more detailed models. These can be used as a basis for cell curves introduced to LaModel runs. Alternatively, they can be linked to volume element models of panel-scale behavior in FLAC^{3D}. Board and Damjanac [2003; Board et al. 2007] developed a method to capture the local behavior effects of pillar loading and represent that behavior as "equivalent zones" or "equivalent elements" in a panel-scale FLAC^{3D} model of a room-and-pillar trona operation. Esterhuizen and Mark [2009] used this approach when modeling a room-and-pillar coal panel using a softening Hoek-Brown strength criteria for coal that was calibrated to Bieniawski's empirical pillar strength equation. Esterhuizen, Mark, and Murphy [2010] showed that the "equivalent-element" approach compared very well with detailed models. Models constructed for typical lithology of Western and Eastern U.S. coal performed well, and were compared to loading at various stages of mining predicted by NIOSH's ARMPS (Analysis of Retreat Mining Pillar Systems) program [Mark and Chase 1997]. Their comparison showed that stress models can depart significantly from ARMPS estimates, especially for stiffer overburden, as is often found in western U.S. coal mines.

Models can be used to approximate and expand on other pillar capacity equations, most notably the Wilson approach to incorporating the effect of weak partings and the Vesić equation for estimating pillar foundation strength. Generation of yielding in multiple regions—floor, pillar, and parting planes, for instance—allows for a more complete model of pillar behavior that

may depart from a "weakest link" criterion based on individual capacity equations [Lawson et al. 2012]. It also provides a physical basis for the deformations and residual stresses that are largely based on simple assumptions in the spreadsheet approach.

Pillar and Panel Linkage—One Step Further

In our application, we need to take this linkage one step further, by developing expected or synthetic readings for instruments placed in the gate roads. That is, our linkages need to go both ways so that pillar deformations at the panel scale can be translated into synthetic readings of instruments at particular points (Figure C6). A pillar model is used to generate stress-strain curves that are used in cells or elements in the panel model. These elements are much coarser than cells or elements in the pillar model. The panel model outputs displacements and/or closure strains, which are used as linkages to state(s) in the pillar model, which is used to generate synthetic instrument readings (e.g., borehole pressure cells), which can be compared directly to actual measurements with installed instruments. Table C3 distinguishes between the types of linkages between pillar and panel models. Those linkage types are described separately.

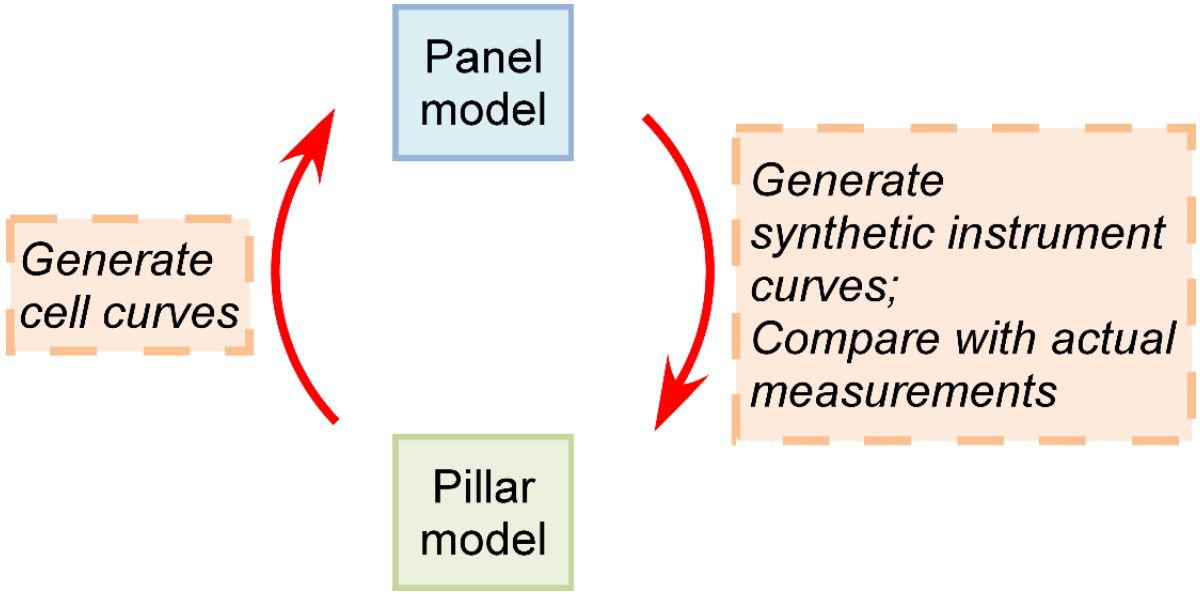

Figure C6. Diagram illustrating linkages between the pillar model and the panel model.

Table C3. Various linkages between pillar and panel models

		Panel model tool	Panel model tool	Panel model tool
		LaModel	FLAC^{3D}	FLAC^{3D} with Longwall Modeling Environment
Pillar model tool	Spreadsheet	Linkage type 1	Linkage type 3	Linkage type 5
Pillar model tool	FLAC^{3D}	Linkage type 2	Linkage type 4	Linkage type 6

Linkage type 1—Spreadsheet Pillar Model and LaModel Panel Model

This linkage is very trivial. A spreadsheet-type pillar model is imposed on cells in LaModel, assuming that the spreadsheet model is simple enough to be represented by three stress-strain line segments, the last being at constant stress. For example, Heasley [2010c] has a coal softening wizard in LamPre version 3.0 that generates such curves based on the integrated Mark-Bieniawski pillar formula [Mark and Chase 1997; Mark and Iannacchione 1992] and the Karabin and Evanto [1999] residual stress. Such linkage could easily be established for LaModel 3.0 with other models that can be described in three such line segments.

Linkage type 2—FLAC^{3D} Pillar Model and LaModel Panel Model

In this case, a detailed pillar model generated with FLAC^{3D} is used to average stress-strain calculation results for various sections, which correspond to the various grid cells of the pillar in LaModel. The stress-strain behavior is approximated with three line segments for each cell. Such material behavior is input to LaModel and a panel model is run. The closure strain in cells that encompass instrument sites are extracted, and these strains form a link to the FLAC^{3D} pillar model. Synthetic instrument readings are generated at corresponding specific locations in the FLAC^{3D} pillar model by linking cell closure strains output from LaModel to the same average section closure strain in the pillar model.

Linkage type 3—Spreadsheet Pillar Model and FLAC^{3D} Panel Model

By using equivalent elements as developed and used by Board and Damjanac [2003] and Esterhuizen and Mark [2009], various spreadsheet models can define a pillar or barrier pillar stress-strain response that can be input to FLAC^{3D} panel models. The closure strain of equivalent elements in the panel model is used to indicate the approximate stresses in the spreadsheet pillar model at locations of instruments. Here, care must be taken, because constant closure across many cells of a spreadsheet model may not be a good assumption. In such cases, the linkage to generate synthetic measurements can only be obtained by imposing a reasonable model of the distribution of closure strain across the pillar. The average of these closure strains must equal the strain output from the FLAC^{3D} panel model.

Linkage type 4—FLAC^{3D} Pillar Model and FLAC^{3D} Panel Model

Using this linkage, a more complicated stress-strain curve might be developed for equivalent elements used in the panel model. Assuming that the pillar model has several saved states along the process of its loading, the closure strain of an equivalent element from the panel model can be used as a link to the closure strain of an equivalent horizon in the detailed pillar model. The seam-lumped strain (plastic displacement of the roof and floor are included as seam strain) of the equivalent element must be modified to reflect equivalent-horizon strain. This strain can then be used to match or interpolate column strain of the equivalent horizon from a couple of saved states in the detailed pillar model. Synthetic instrument readings can then be extracted from the detailed pillar models.

Linkage types 5 and 6—Various Pillar Models with Longwall Modeling Environment

If linkage types 3 and 4 are established, then linkage types 5 and 6 can be established. Using the Longwall Modeling Environment [Pierce and Board 2010] for the panel model is no more complicated than using the FLAC^{3D} with standard features for the panel model.

Calibration Using Specific Measurements vs. Synthetic Measurements

Whatever modeling tool is used for the panel scale, synthetic measurements at the same coordinates as real instruments can be extracted from the model. By comparing real measurements with synthetic measurements, fine-tuning of models can proceed. Figure C7 shows an example how real borehole pressure cell measurements might be compared to synthetic borehole pressure cell measurements. The important comparison here is the difference in stress resulting from mining. These cells were spaced from the left rib of a pillar in order (BPC1, BPC2, BPC3, and BPC4) until BPC 4 was in the center of the pillar, as shown in the figure. BPC 5 was placed near the right rib, which was next to the panel being mined, at the same distance from the rib as BPC1 was from the left rib. A model was built and run with LaModel and synthetic BPC measurements were extracted from the results. The in-seam model was an elastic-perfectly plastic coal. The actual measurements indicate a yielding of the pillar near the right rib, and highest load change at BPC2. In this case, the instruments indicate that a softening model should be used for in-seam material before further calibration.

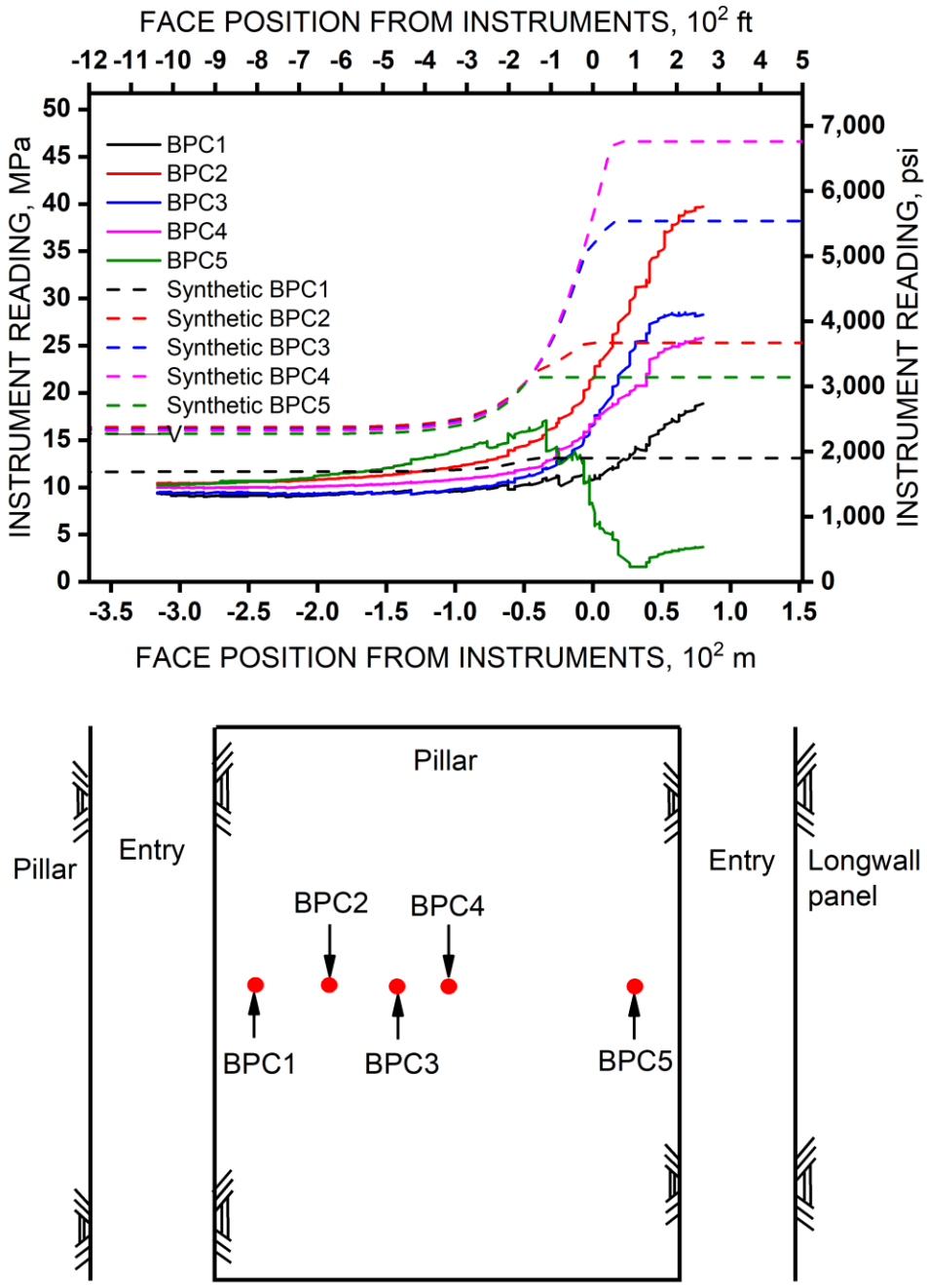

Figure C7. Example showing how synthetic borehole pressure cell measurements generated by a model might be compared to actual measurements. Layout of the instruments within the pillar is also shown.

Synthetic Measurements

Synthetic measurements at instrument sites can also be generated from FLAC^{3D} models, but with an additional step. For a given longwall face position in the panel model, the closure strain of the equivalent element containing the measuring instrument is extracted. The two saved states of the detailed pillar model having seam-lumped closure strain above and below that amount are examined. The seam stresses in a pillar at instrumentation sites can be retrieved from save states and interpolated according to the seam-lumped nonlinear closure strain. Closure strain in an entry can be determined in the same way. Synthetic measurements of stress for instruments located between zone centroids can be determined through a second interpolation.

From these measurements, it is possible to display synthetic measurements for a detailed pillar (Figure C8), for a profile along an instrumentation line, or for an instrument with respect to face position, as in Figure C9. These can be compared to actual measurements made with instruments for the purposes of fine-tuning the calibration of the panel and detailed pillar models.

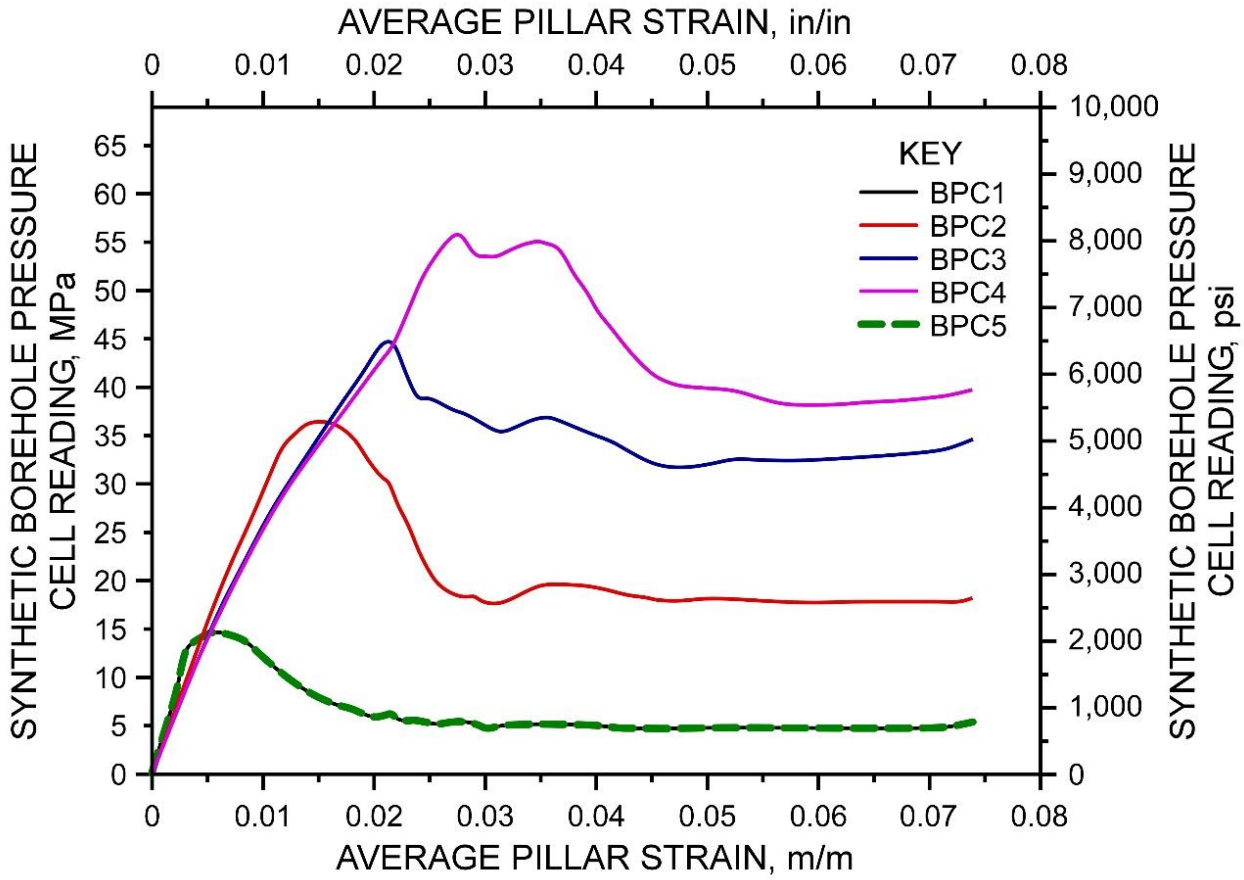

Figure C8. Example of synthetic borehole pressure cell measurements with average pillar strain as extracted from a FLAC^{3D} detailed model of a pillar.

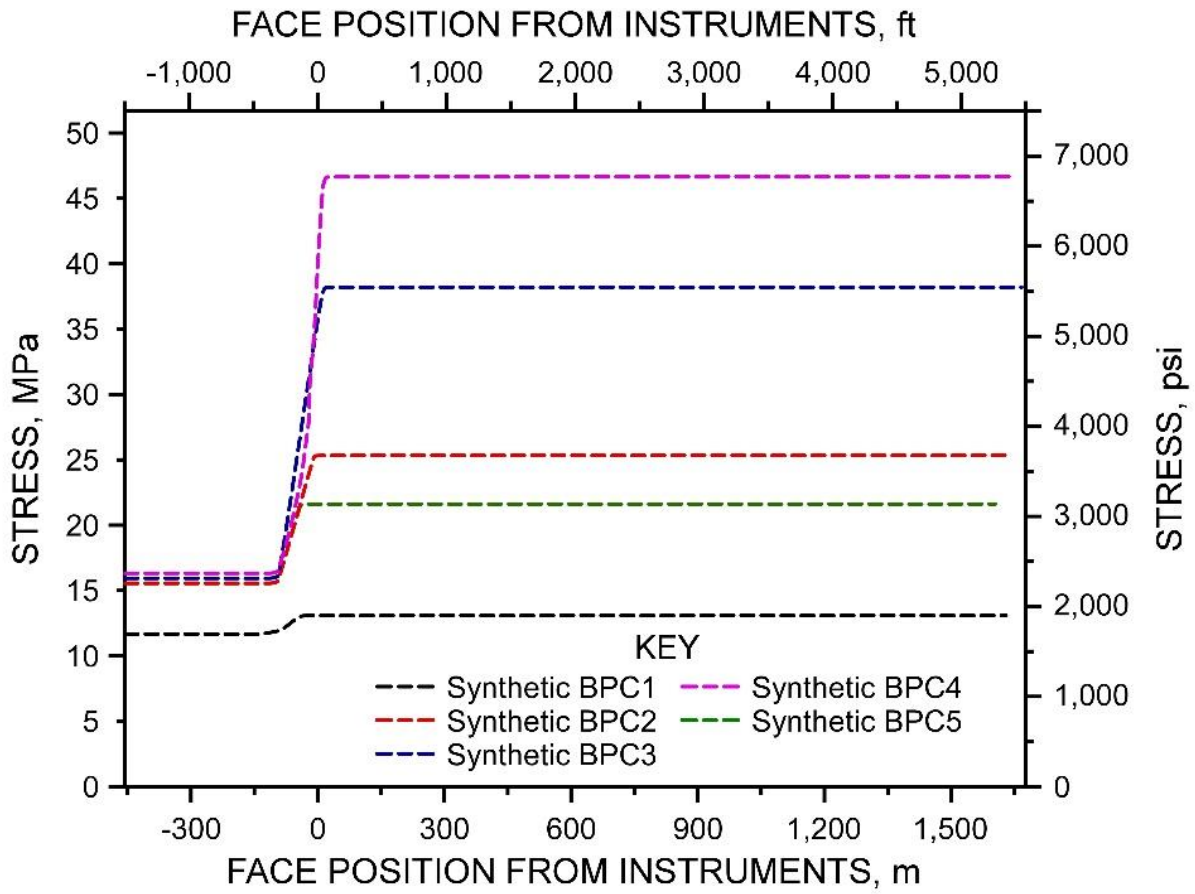

Figure C9. Example showing synthetic borehole pressure cell measurements generated from LaModel calculations.

Application of Overburden Stress

The first step in a large- (panel-) scale model is determining the in situ stress state. For FLAC^{3D}, that means determining the stress state in every zone at equilibrium before any excavations. For LaModel, it means determining the premining stress on each element of in-seam material. In the case of high-relief topographic terrain, Heasley's routine [1997] to account for topographic effects may have some limitations [Whyatt et al. 2011]. In such cases, the user may desire to take advantage of a link to overburden stresses on the seam determined from another source, such as FLAC^{3D}.

To create such a linkage between premining FLAC^{3D} results and LaModel overburden stress input, the user only need arrange the vertical stresses calculated with FLAC^{3D}, which correspond to the exact locations of the LaModel seam grid centroids and arrange them one per line in a text file of the same name as the name of the LaModel run with the .tpo extension. The order of the stresses, where *i* and *j* represent the x and y indices, starting in the lower left-hand corner of the grid, $\sigma_{1,1}$, $\sigma_{1,2}$, …, $\sigma_{1,n}$, $\sigma_{2,1}$, $\sigma_{2,2}$, …, $\sigma_{2,n}$, …, $\sigma_{m,1}$, $\sigma_{m,2}$, …, $\sigma_{m,n}$. Here, *m* and *n* are the maximum indices in the x and y directions, respectively. The first three lines of the .tpo text file are filled with information listed in Table C4, with each item delimited by a comma. A linkage between another source and LaModel can be established in the same manner.

Table C4. Contents and format of the .tpo file or overburden stress file that serves as input to LaModel

Line	Item 1	Item 2	Item 3	Item 4	Item 5	Item 6	Item 7
1	1	Number of grid cells	Distance between cells (in)	Number of grid cells in x direction	Number of grid cells in y direction	X coordinate of origin (in)	Y coordinate of origin (in)
1 format	I3	I8	F13	I4	I4	F13	F13
2	1	Overburden stress	NU	NU	NU	NU	NU
2 format	I3	S17					
3	1	Units (psi)	NU	NU	NU	NU	NU
3 format	I3	S17					
4 and after	Stress	NU	NU	NU	NU	NU	NU
4 and after format	F13						

NU = Not used
Format key:
I = Integer (I3 = Integer of 3 characters)
F = Floating point number or scientific notation (F13 = Floating point number of 13 characters)
S = String (S17 = string of 17 characters)

Another linkage is to provide initial stress for each zone in a FLAC^{3D} model by some other calculation. This might be done in one of two ways:

1. Calculating stress for each zone with some other tool, be it a modeling tool, or a spreadsheet calculation of some initial stress model. Save such calculations an initial stress file in text format. With the aid of a FISH function, read in the initial stress file and assign stresses by matching coordinates.
2. Implement the initial stress model calculations in a FISH function. Calculate the initial stress and assign the stress state for each zone in FLAC^{3D}.

Program Modifications—LaModel

LaModel is one of the most used modeling tools for evaluation of coal and trona mine design. Its advantage is the speed at which a model may be completed, including preprocessing, model calculations, and post-processing. However, it has some limitations that may cause the modeler to choose to use another code. Some of these limitations have been overcome by recent modifications of LaModel.

Decoupling of Initial Stress Routine

Most modeling procedures use an assumed initial stress field or they use the same modeling program to generate an initial stress field. In the case of highly variable topography, volume-element codes, such as FLAC [Itasca Consulting Group 2011], FLAC^{3D} [Itasca Consulting Group 2009], or any finite-element code, might impose an initial tectonic stress field and let mass density of the elements and the gravitational field further load the model. Boundary element codes generate their own initial stress field. In his code LaModel [Heasley 2010c], a

displacement discontinuity code that uses frictionless, cohesionless interfaces in the host elastic rock mass, Heasley [1997], since the code's inception, has accounted for topographic loading by imposing forces at a datum which is usually located above the coal seam at the average depth of the overburden. At the request of his co-authors, Dr. Heasley introduced a capability into the code to decouple the overburden stress from the mining-induced stress calculations [Whyatt et al. 2011]. To do this, the overburden stress is input from a file which is previously calculated by LaModel or some other model.

The capability of introducing initial, or overburden, stress through a file has the advantage of speeding the completion of parameter studies because initial stresses do not have to be calculated for each problem. However, this capability also provides the choice to use initial stress calculated from an external source that may not be subject to limitations of the LaModel topographic routine or those of an elastic continuum [Whyatt et al. 2011]. For example, an external model might have the advantage of simulating the influence of major faults on the initial stress.

Increasing Yield Rings and Number of Materials

Heasley [2010a] increased the maximum number of in-seam materials that can be used in a model to 52 for version 3.0 of LaModel. Because of the large loads that may be applied to large abutment pillars in the western U.S., it is often necessary to use enough yield rings so that there is no elastic core. Otherwise, artificially high and incorrect peak stresses may result. The maximum number of materials of different strengths makes it possible, for example, that a large abutment pillar, such as one of dimensions 51.8 m by 54.9 m (170 ft by 180 ft) might now be modeled with 1.5-m (5-ft) elements instead of 3.0-m (10-ft) elements. This would require 35 materials (one elastic and 34 nonlinear) for 17 yield rings. However, LamPre 3.0 has not been updated to accommodate this many yield rings; it is limited to a maximum of 12. Even so, the input file can be modified with a text editor to include the number of materials required and their properties. When more yield rings are desired than 12, the user must manually input the materials in the grid editor.

Increasing Number of Mining Steps

For panel-scale models, it may be desirable to include more than the past traditional limit of 20 mining steps. In a recent release of LaModel 3.0, Dr. Heasley increased that limit to 200 [2010b]. Such increased limit allows the user to model panel-scale models with small mining steps, which is needed especially as the mining face nears instrumentation sites. Smaller mining increments permit more accurate comparison with measurements of stress and displacement for purposes of model calibration.

Synthetic Measurements of Stress and Closure

For fine-tuning calibrations, the authors found it desirable to compare actual measurements, such as those from closure meters and borehole pressure cells with measurements predicted by LaModel. Such a tool for extracting specific measurements at each mining step is not within the capabilities of LamPlt 3.0 at present. The authors use LabTalk script in the software, OriginPro version 8.5 [OriginLab 2011] to conveniently extract and plot such "synthetic measurements" for comparison with actual measurements. Figure C9 shows an example of "synthetic readings"

output from LaModel at locations where actual borehole pressure cell (BPC) measurements were taken.

Program Modifications—FLAC^{3D}

If storage space, calculation time, and complexity of three-dimensional models were not limitations, modeling codes such as FLAC^{3D} would be used more frequently for panel-scale models because of its ability to simulate failure mechanisms in any part of the model and calculate the full stress tensor in each zone or element. However, recent developments have made it possible to capture localized behavior in panel-scale model with coarse zones using linkages to more detailed submodels [Board and Damjanac 2003; Esterhuizen and Mark 2009]. In addition, several FISH functions have been developed for generating a mesh representing high-relief topography where the idealized stratigraphy may not be planar. More FISH functions have been developed that easily implement gob models, and Itasca has recently developed a Longwall Modeling Environment that follows caving logic. Such capabilities make use of FLAC^{3D} desirable and, at least, worth consideration.

Topographic Mesh Generator

For complicated three-dimensional geometries, mesh generation is a complex task. Itasca Consulting Group, Inc. recommends using KUBRIX [2010] along with the CAD software, Rhino3D, to generate such grids. However, the authors chose to develop their own mesh generator for FLAC^{3D} [Itasca Consulting Group 2009] that forms a three-dimensional grid to the topographic surface. Mesh generation is accomplished with FISH functions and is based on the assumption of a geologic column comprised of members having uniform thickness, but that are not necessarily planar. The elevations of the top and bottom of each stratigraphic member are expressed relative to the elevations of the top of the strata member of interest—in this case, the coal seam being mined. Thus, the coal seam does not have to be planar, and input includes elevations of the top of coal seam and elevations of surface topography in a regular plan-view grid. Elevations are input as tab-delineated text files with grid points at regular x- and y-coordinate intervals. The bottom member is generated from a bottom, horizontal plane up to some offset distance from the top of the coal seam. The zones are generated by section, stratigraphic member by stratigraphic member from bottom to top, one zone column at a time. Therefore, grid generation proceeds slowly. Each member is generated from bottom to top, unless the topographic surface is below the top of the member. In such case, the top surface of the top zone of that column is forced to conform to the topographic surface. Each section can have a different x- and y-interval spacing to allow for different mining geometries. However, care must be taken so that grid points on the boundaries of adjacent sections coincide or so that the intervals between them are multiples of each other. Once each section is built, the "attach" command is used to attach adjacent sections together. Any interfaces are constructed after the sections are attached.

Input files for the topographic mesh generator are shown and general contents listed in Figure C10. Each section requires a section file and an Elevs-section file. For example, a mesh with 20 sections will require 20 section files, 20 Elevs-section files, one strata file, and one driver file, all of which are text files. Section and Elevs-section files are data files that can be generated from a spreadsheet that is saved as a text file. However, care must be taken to delete all blank lines after the last line of data—the last line of the file must be the last line of data.

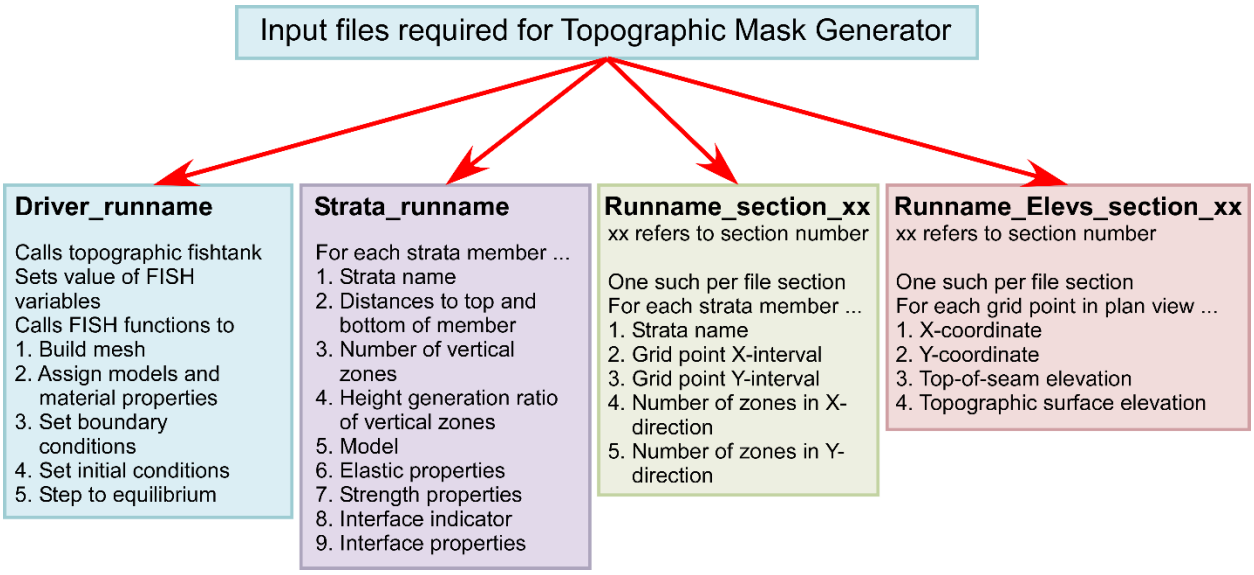

Figure C10. Input files and general content list of each for the topographic mesh generator.

This routine was tested with the case of a high-relief area around a western U.S. coal mine. Elevations of seam and topographic surface were extracted from AutoCAD contours of the seam elevation and contours of topography using AutoCAD Civil 3D [2011]. Thirty-two sections of these elevations were extracted at 15.2-m (50-ft) intervals for an area that was approximately 6.3 km (3.9 miles) in length along the y axis, and 5.8 km (3.6 miles) in length along the x-axis. The FISH routine has the option of skipping a pattern of grid points so that you may chose a coarser grid interval than what was extracted from the elevation contours. Figure C11 shows the resultant grid, where each stratigraphic member is shown in a different color.

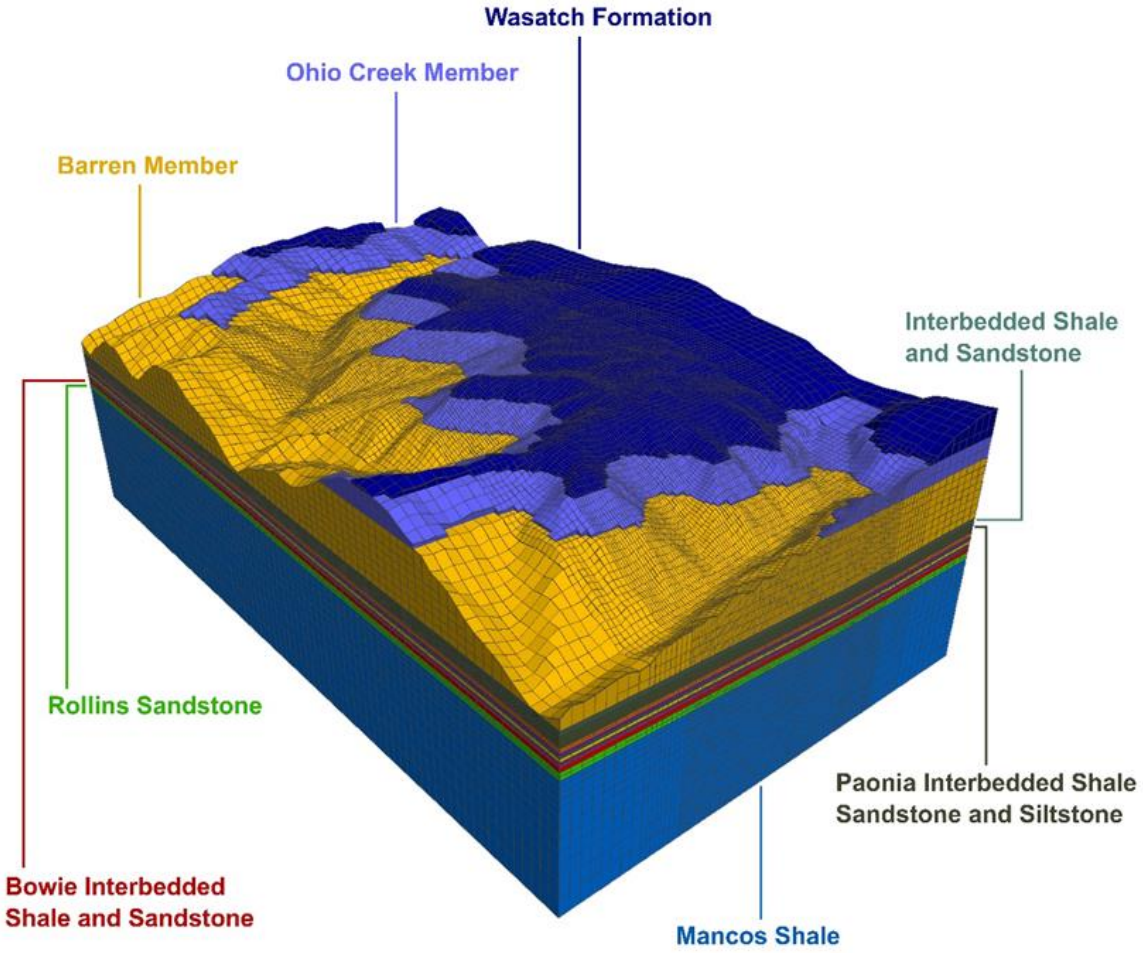

Figure C11. FLAC^{3D} model of area around a western U.S. coal mine as generated by the authors' topographic mesh generator.

Equivalent Elements and Detailed Pillar Models

Esterhuizen and Mark [2009] developed FISH functions to implement the Board-Damjanac method [Board and Damjanac 2003] of equivalent elements to model a pillar or barrier in a detailed way and representing that behavior as a one-dimensional equivalent element. In this method, both sets of authors constructed a detailed model of a pillar or barrier, whose outside dimensions in plan view are the same as those of the equivalent element that will represent the detailed pillar model behavior in the panel-scale model.

The authors took what Esterhuizen and Mark accomplished and made some modifications. First, the Esterhuizen-Mark method of loading a detailed pillar model was based on a servo mechanism controlling applied velocity on the top surface of the model. In the authors' experience, the sudden changes in velocity propagated compression waves through the model, causing premature failure of many zones. To minimize this effect, the authors held the velocity of the top boundary constant. Second, Esterhuizen and Mark calculated the equivalent column strain and the seam strain at the center point of the pillar, only. The authors choose to base these calculated strains of the seam and column on the average of vertical pairs of grid points at the

top and bottom of these horizons from throughout plan-view area of the detailed model. In calculating these strains by section (for example, if the pillar is divided into two or four sections), then only relative displacements of grid point pairs belonging to a particular section were included in the calculation of column and seam strains for that section. For seam stress, we choose average seam stress near the horizontal midplane of the seam, and for column stress, we averaged stress at the bottom row of elements in the equivalent-column horizon, as did Esterhuizen and Mark [2009]. Third, the authors recognized that panel models can load equivalent elements in a nonuniform manner. To account for such response, the detailed pillar model can be loaded nonuniformly in the first few hundred or thousand steps of loading the detailed pillar model. In subsequent steps, the imposed, nonuniform displacement step is kept constant—i.e., all grid points on the top surface of the model are given the same velocity in the vertical direction. Multiple rounds of pillar and panel models must be run until there is little difference between the tilting in the panel model's equivalent elements and that of the detailed pillar model.

In the panel-scale model where the equivalent elements are used, all stresses other than vertical stresses are set to zero at each calculation step—thus preserving the one-dimensional nature of the equivalent element.

From the detailed model, a curve of column stress versus column plastic strain is extracted, but since we only mine the seam, the nonlinear response of the entire column horizon must be lumped into an equivalent element the height of the seam. The equivalent element is forced to follow this strength curve by setting the internal friction angle to 0° and representing the strength curve with a piecewise linear cohesion curve, where cohesion is half of the current uniaxial strength (from the stress-versus-plastic strain curve).

To determine this curve of stress versus plastic (or nonlinear) strain, we need to define some variables, with reference to Figure C12, which represents the equivalent horizon from which we extract the nonlinear response. The variables are as follows:

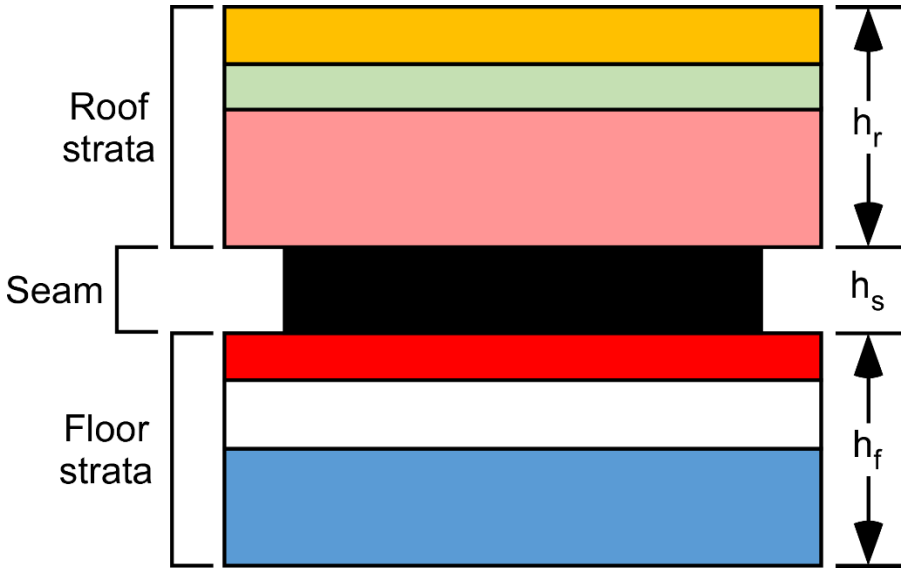

Figure C12. Vertical section of equivalent column horizon, extracted from part of detailed column model.

$\delta_r^e, \delta_r^p, \delta_r$ = elastic, plastic, and total closure displacement (closure displacement is the change in the height of the member) of the roof in the column, respectively.

$\delta_s^e, \delta_s^p, \delta_s$ = elastic, plastic, and total closure displacement of the seam in the column, respectively.

$\delta_f^e, \delta_f^p, \delta_f$ = elastic, plastic, and total closure displacement of the floor in the column, respectively.

$\varepsilon_{col}, \varepsilon_{col}^e$ = total strain of the column and elastic strain of the column (the column refers to the floor, seam, and roof whose responses are considered for the equivalent element), respectively.

h_r, h_s, h_f = heights of roof, seam, and floor, respectively, in the column.

E_{col}, E_s = elastic modulus of column and seam, respectively. Also,

$$\delta_{col} = \delta_r^e + \delta_s^e + \delta_f^e + \delta_r^p + \delta_s^p + \delta_f^p. \quad \text{(C1)}$$

The required data for determination of the column stress-vs.-plastic strain curve (and subsequently, the column cohesion-vs.-plastic strain curve) are the column stress-vs.-total column strain curve from a model that permits element failure, and the stress-vs.-strain curve from a model of the same grid and elastic properties, but with no failure permitted. The latter was accomplished by raising all strength parameters to very high amounts. An example of the relative relationship of such curves is shown in Figure C13.

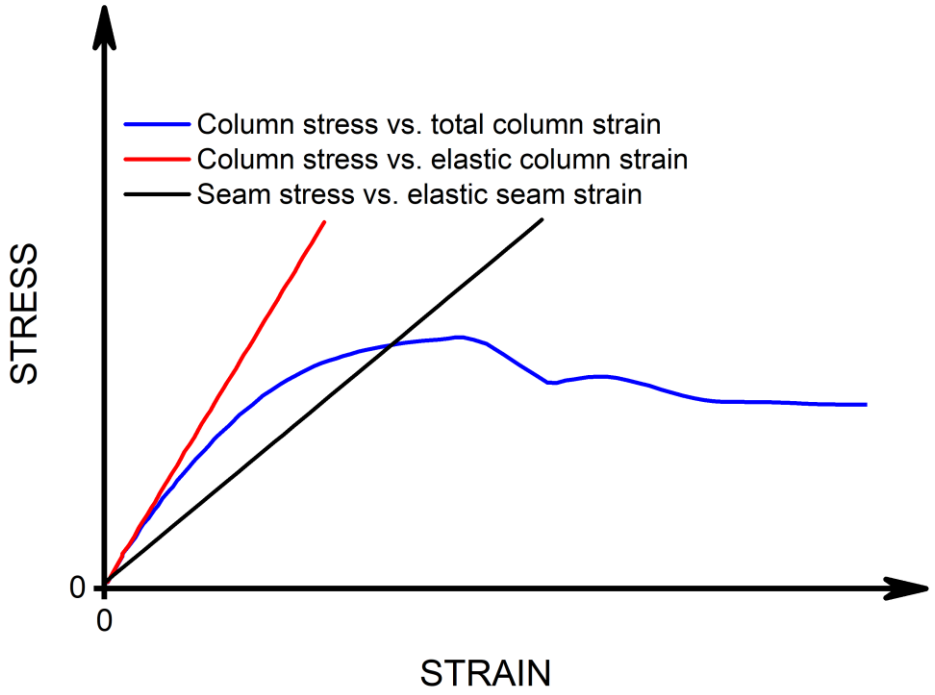

Figure C13. Typical relative curves needed for determination of a detailed response that inputs to an equivalent element. These curves come from two models of the same grid and elastic properties: (1) where zones are permitted to fail, and (2) where zones are not permitted to fail.

Figure C14 shows the same total response curve. That same curve is also shown modified so that the strain is multiplied by the ratio of the column and seam heights. This manipulates the strain so that all of the displacement occurs within the height of the seam.

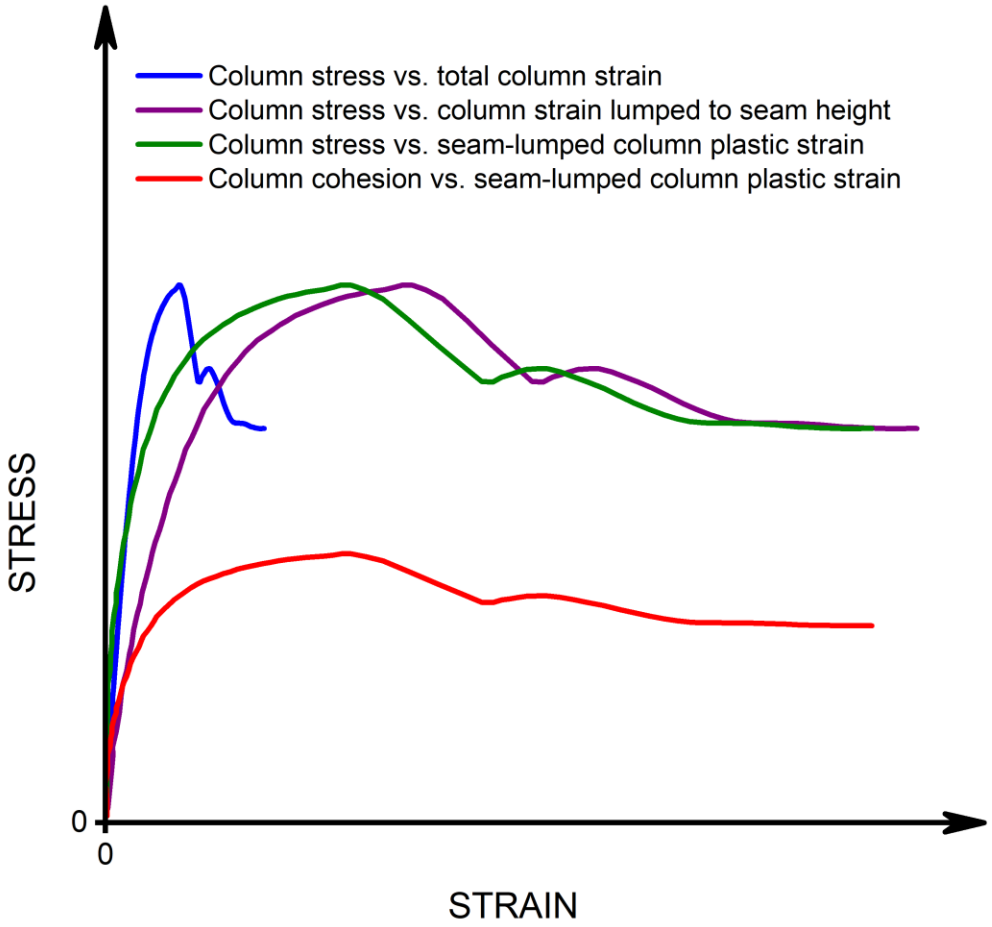

Figure C14. Graph showing the example relative curves obtained in the progression of the determination of cohesion vs. seam-lumped column plastic strain. First, column stress vs. column total strain is extracted, then the total column deformation is lumped into the seam height to obtain seam-lumped column total strain. Next, the seam-lumped plastic strain is extracted. Finally, the curve is expressed as having no friction so that cohesion is half of the total column stress in the final curve for a one-dimensional model.

The elastic strain response of the column is subtracted from the total strain response to obtain the curve of stress vs. plastic strain. Because the command "set large" is used in the FLAC^{3D} models, the plan area of the pillar increases, especially when there is plastic flow. This actually causes a nonlinear elastic response when calculating stress in the seam. However, the purely elastic model does not see much nonlinear elastic behavior because there was no plastic strain. Therefore, the nonlinear-elastic response is actually lumped in with the calculated plastic response.

Finally, the stress is divided by 2 to obtain the cohesion vs. seam-lumped column plastic strain response curve, shown in Figure C14. This can be done because the internal friction of the equivalent element is set to 0°.

To make this approach more clear, the procedure is done in terms of closure displacements, instead of strains. In this approach, we determine plastic column displacements by

$$\delta_{col}^{p} = \delta_{col}^{total} - \delta_{col}^{e}, \tag{C2}$$

where

$$\delta_{col}^{total} = \delta_r + \delta_s + \delta_f \tag{C3}$$

and

$$\delta_{col}^{e} = \delta_r^e + \delta_s^e + \delta_f^e. \tag{C4}$$

The procedure is as follows:

1. From the detailed model with imposed strengths, extract the strain-stress curve of the detailed column (ε_{col} vs. σ_{col}).
2. From the elastic model, extract the strain-stress curves of the detailed column and of the seam alone (ε_{col}^e vs. $\sigma_{col}^e$and ε_s^e vs. σ_s^e).
3. Determine E_{col} and E_s from elastic model. Do this by fitting a line by linear regression to determine slopes (Young's moduli) and intercepts (b_{col}^e, b_s^e).
4. From the stress-strain curve extracted in step 1, convert the strains to displacements and subtract the elastic displacements given the stress, as determined from the elastic model. Ultimately, we want to determine $\frac{\delta_{col}^p}{h_s}$ or $\frac{\left(\delta_r^p + \delta_s^p + \delta_f^p\right)}{h_s}$ at any stress level of the model in step 1. This lumps all of the plastic strain in the seam horizon. Here are the details:
5. From step 1,

$$\delta_r + \delta_s + \delta_f = \varepsilon_{col}\left(h_r + h_s + h_f\right). \tag{C5}$$

From step 2,

$$\left(\delta_r^e + \delta_s^e + \delta_f^e\right) = \left(h_r + h_s + h_f\right)\varepsilon_{col}^e = \left(h_r + h_s + h_f\right)\frac{\sigma_{col}^e}{E_{col}^e}. \tag{C6}$$

Also, Equation C2 is written in more detail as

$$\left(\delta_r^p + \delta_s^p + \delta_f^p\right) = \left(\delta_r + \delta_s + \delta_f\right) - \left(\delta_r^e + \delta_s^e + \delta_f^e\right). \tag{C7}$$

then

$$\frac{\delta_{col}^p}{h_s} = \frac{\left(\delta_r^p + \delta_s^p + \delta_f^p\right)}{h_s} = \frac{\left[\varepsilon_{col}\left(h_r + h_s + h_f\right) - \left(h_r + h_s + h_f\right)\frac{\sigma_{col}^e}{E_{col}^e}\right]}{h_s}. \tag{C8}$$

The plastic strain, as indicated on the left side of Equation C8 is matched to a stress that indicates strength. The cohesion for a one-dimensional problem is half the stress at failure. Thus the curve of cohesion vs. plastic strain is determined. This curve, as a piecewise linear curve is input as the strength envelope for that equivalent element in a panel-scale model.

The FISH functions for using equivalent elements are found in an equivalent element fishtank that may be called in the panel-scale model to convert certain zones to equivalent elements. Cohesion-versus-plastic strain curves are input as text files.

Gob Models

Two commonly-used constitutive models for gob are the linearly-varying elastic modulus, such as that used in Mulsim/NL [USBM 1992] and LaModel [Heasley 1998], and models based on the testing of Pappas and Mark [1993]. For the latter, presently only the equation fit to Pappas and Mark's shale gob have been included in the gob fishtank, but the weak sandstone gob, the strong sandstone gob, or a set of equations that Pierce [2010] fit to all of the Pappas and Mark results could easily be inserted. These equations are

$$E_{current}(psi) = a(UCS) + b(shape\ factor) + c, \quad \text{(C9)}$$

where UCS = unconfined compressive strength of the material (psi),

$shape\ factor$ = the average ratio of maximum and minimum dimensions of the gob particles (a good value in the absence of definitive information is 0.5), and

a, b, c = variable quantities that depend on the volumetric strain (ε_{vol}).

If ε_{vol}>= 0.25, then

$$a = 0.1315(\varepsilon_{vol})^{-2.145}, \quad \text{(C10)}$$

$$b = 1110.5(\varepsilon_{vol})^{-2.574}, \text{ and} \quad \text{(C11)}$$

$$c = 981.14(\varepsilon_{vol})^{-2.3158}. \quad \text{(C12)}$$

If ε_{vol} < 0.25, then the modulus is interpolated between the in situ modulus (i.e. at ε_{vol} = 0) and the modulus that would be estimated with the following coefficients when ε_{vol} = 0.25.:

$$a = 0.1316(0.25)^{-2.145}, \quad \text{(C13)}$$

$$b = 1110.5(0.25)^{-2.574}, \text{ and} \quad \text{(C14)}$$

$$c = 981.14(0.25)^{-2.318}. \quad \text{(C15)}$$

Input values for each stratigraphic layer are assembled as a tab-delimited text file. For these gob files, it is necessary to provide a distance above the coal seam within which all zones whose centroids fall are converted to gob. This procedure is done only above portions of the seam that are converted to gob and is necessary to maintain appropriate gravitational forces (the gob in the coal seam elements cannot have zero density). The density of all gob zones is then adjusted to reflect that the mass of the coal seam was extracted.

Program Modifications—Longwall Modeling Environment

Board and Pierce [2009] described logic that they used to simulate the mechanics of block caving. In said logic, bulking is not imposed, but results from either dilation during shear or volumetric expansion under tensile failure. Such logic seems promising as a way to simulate the caving over a longwall panel. Pierce and Board [2010] modified the caving logic to simulate the caving above a longwall panel. However, longwall caving has some differences compared to block caving of rock masses exhibiting more random jointing. Some of the considerations accommodated by Pierce and Board were:

Because of the persistent, weak, and planar nature of bedding planes, strata are often capable of accommodating shear and tension with less bulking than more randomly jointed rock. As a

result, dilation angle and maximum porosity are likely to be less in stratified ground than in more randomly jointed rock masses.

The associated flow rule for tension tends to over predict bulking in the case of sedimentary rock. The solution by Pierce and Board was to model joints as interfaces or use the ubiquitous joint model or both.

The Longwall Modeling Environment in FLAC^{3D} also tracks volumetric and shear energy, both plastic dissipated energy and elastic stored energy, zone by zone. The model must be run in a quasi-static state because it does not model dynamic events. However, the energy tracking can infer potential for dynamic events or the likelihood of dynamic occurring from one mining step to the next.

The Longwall Modeling Environment capability is compiled in FLAC^{3D} as version 4.01, but implemented fully in version 5.0. However, FISH functions included in a fishtank file are needed to set up the additional calculations. In the initial version of the fishtank, only horizontal strata with a level topography were considered, along with automatic generation of far-field zones away from the panel area. For our purposes, we did away with the far-field mesh generation and incorporated our topographic mesh generator into the Longwall Modeling Environment fishtank. Although the mesh generation is slow, it is a step toward the recommendation of Pierce and Board that the next version of the fishtank include topography [2010].

Conclusions

Each of the modeling tools has advantages and disadvantages, strengths and weaknesses. By understanding these items and the linkages between the tools, the user can effectively break the problem into parts and take advantage of the optimum tool for each task of the modeling exercise. The optimum tool is very problem-dependent, so that there is not a tool that optimally fits all problems.

References for Appendix C

Autodesk Inc. [2011]. AutoCAD Civil 3D. <http://usa.autodesk.com/civil-3d/> [Accessed November 7].

Bieniawski ZT, Van Heerden WL [1975]. The significance of in situ tests on large rock specimens. Int. J. Rock Mech. Min. Sci. & Geomech. Abstr., Vol. 12, No. 4, pp. 101–113.

Board M, Damjanac B [2003]. Development of a methodology for analysis of instability in room and pillar mines. In: Stephansson O ed., Proceedings of the 2003 Swedish Rock Mechanics Day Conference.2003) Stockholm: SvebeFo, pp. 1–22 pp.

Board M, Damjanac B, Pierce M [2007]. Development of a methodology for analysis of instability in room and pillar mines. In: Potvin Y ed., Deep Mine 07: Proceedings of the Fourth International Seminar on Deep and High Stress Mining. (Perth, Australia: November 7–9, 2007) Perth: Australian Centre for Geomechanics, pp. 273–282.

Board M, Pierce ME [2009]. A review of recent experience in modeling of caving. In: Esterhuizen GS et al. eds. NIOSH Information Circular 9512, Proceedings of the International Workshop on Numerical Modeling for Underground Mine Excavation Design. (Asheville, NC: June 28, 2009) Pittsburgh, PA: U.S. Department of Health and Human Services, pp. 19–28.

Crouch SL [1976]. Analysis of stresses and displacements around underground excavations: An application of the displacement discontinuity method. University of Minnesota Geomechanics Report. Minneapolis, MN: University of Minnesota, University of Minnesota, 270 pp.

Esterhuizen E, Mark C, Murphy MM [2010]. Numerical model calibration for simulating coal pillars, gob and overburden response. In: Barczak T et al. eds. Proceedings: 29th International Conference on Ground Control in Mining. (Morgantown, WV: July 27–29, 2010) Morgantown, WV: West Virginia University, pp. 46–57.

Esterhuizen GS, Mark C [2009]. Three-dimensional modeling of large arrays of pillars for coal mine design. In: Esterhuizen GS et al. eds. NIOSH Information Circular 9512, Proceedings of the International Workshop on Numerical Modeling for Underground Mine Excavation Design. (Asheville, NC: June 28, 2009) Pittsburgh, PA: U.S. Department of Health and Human Services, pp. 37–46.

Heasley KA [1997]. A new laminated overburden model for coal mine design. In: Mark C, Tuchman RJe eds. NIOSH Information Circular 9446, Proceedings: New Technology for Ground Control in Retreat Mining. Pittsburgh, PA: U.S. Department of Health and Human Services, pp. 60–73.

Heasley KA [1998]. Numerical modeling of coal mines with a laminated displacement-discontinuity code. Ph.D. Dissertation. Golden, Colorado: Colorado School of Mines, 205 pp.

Heasley KA [2010a]. E-mail from Dr. Heasley, WVU, to, Personal communication to Larson MK, September 12, 1 pp.

Heasley KA [2010b]. E-mail from Dr. Heasley, WVU, to, Personal communication to Larson MK, September 19, 2 pp.

Heasley KA [2010c]. LaModel, ver. 3.0, Morgantown, WV: West Virginia University.

Itasca Consulting Group [2009]. FLAC3D: Fast Lagrangian analysis of continua in 3 dimensions—user's guide (version 4.0). 274 pp.

Itasca Consulting Group [2010]. Kubrix/Rhino users' manual—using KUBRIX and Rhino3D to create grids for FLAC3D, 3DEC, PFC3D & other computer-aided engineering tools. Minneapolis, MN, 124 pp pp.

Itasca Consulting Group [2011]. FLAC: Fast Lagrangian analysis of continua—user's guide (version 7.0), 384 pp.

Karabin GJ, Evanto MA [1999]. Experience with the boundary-element method of numerical modeling to resolve complex ground control problems. In: Mark C et al. eds. NIOSH Information Circular 9448, Proceedings of the Second International Workshop on Coal Pillar Mechanics and Design. Pittsburgh, PA: U.S. Department of Health and Human Services, National Institute for Occupational Safety and Health, pp. 89–113.

Lawson H, Zahl E, Whyatt J [2012]. Ground condition mapping: A case study. In: 2012 SME Annual Meeting, "Mine to Market: Now It's Global" Preprint 12–122, (Seattle, WA: Feb 19–22, 2012) Englewood, CO: Society for Mining, Metallurgy, and Exploration, Inc., 7 pp.

Maleki H [1992]. In situ pillar strength and failure mechanisms for U.S. coal seams. In: Iannacchione AT et al. eds. Bureau of Mines Information Circular 9315, Proceedings of the Workshop on Coal Pillar Mechanics and Design. (Santa Fe, NM: June 7, 1992) U.S. Department of the Interior, pp. 73–77.

Mark C, Chase FE [1997]. Analysis of Retreat Mining Pillar Stability (ARMPS). In: Mark C, Tuchman RJ eds. Proceedings: New Technology for Ground Control in Retreat Mining, DHHS (NIOSH) Publication No. 97-133, IC 9446. Pittsburgh, PA: National Institute for Occupational Safety and Health (NIOSH), pp. 17–34.

Mark C, Iannacchione AT [1992]. Coal pillar mechanics: Theoretical models and field measurements compared. In: Iannacchione AT et al. eds. Bureau of Mines Information Circular 9135, Proceedings of the Workshop on Coal Pillar Mechanics and Design. Washington, DC: U.S. Department of the Interior, pp. 78–93.

MSHA [2009]. General guidelines for the use of numerical modeling to evaluate ground control aspects of proposed coal mining plans. By Skiles ME, and Stricklin KG. Program Information Bulletin No. P09-03, March 16, 2009, Arlington, VA: U.S. Department of Labor, Mine Safety and Health Administration (MSHA), 7 pp.

OriginLab [2011]. Scientific graphing and data analysis software products, Origin and OriginPro. OriginLab, [Accessed November 7].

Pierce M, Board M [2010]. Development of a three-dimensional numerical modeling environment for caving and stress analysis of longwall mining. Report 2552-05, Prepared for NIOSH, Spokane Research Laboratory, August 31, 2010, Minneapolis, MN, Itasca Consulting Group, Inc., 43 pp.

Pierce ME [2010]. Equations in FISH function of LME for influence of UCS and shape factor. Verbal, Personal communication to Larson MK, September 15.

Sinha KP [1979]. Displacement discontinuity technique for analyzing stress and displacements due to mining in seam deposits. Ph.D. Thesis. University of Minnesota, 325 pp.

USBM [1992]. MULSIM/NL application and practitioner's manual. By Zipf RK, Jr. Information Circular 9322, Pittsburgh, PA: U.S. Department of the Interior, Bureau of Mines (USBM), 44 pp.

USBM [1993]. Behavior of simulated longwall gob material. By Pappas DM, and Mark C. Report of Investigations 9458, Pittsburgh, PA: U.S. Department of the Interior, Bureau of Mines (USBM), 42 pp.

Vesić AS [1975]. Bearing capacity of shallow foundations, Ch. 3, In: Foundation engineering handbook, 1st ed., ed. by Winterkorn HF, Fang H-Y, New York: Van Nostrand Reinhold Company, pp. 121–147.

Whyatt JK, Larson MK, Heasley KA [2011]. Topography and coal seam initial stress estimation: A sensitivity study. In: Barczak T et al. eds. Proceedings: 30th International Conference on Ground Control in Mining. (Morgantown, WV: July 26–28, 2011) Morgantown, WV: West Virginia University, pp. 58–66.

Wilson AH [1972]. A hypothesis concerning pillar stability. Part 1 of research into the determination of pillar size. The Mining Engineer, Vol. 131, Part 9, 1972, pp. 409–417.

Wilson AH [1981]. Stress and stability in coal ribsides and pillars. In: Peng SS ed., Proceedings: 1st Conference on Ground Control in Mining. (Morgantown, WV: July 27–29, 1981) Morgantown, WV: West Virginia University, pp. 1–8.

Wilson AH [1982]. Pillar stability in longwall mining, In: State-of-the-art of ground control in longwall mining and mining subsidence, New York: AIME, pp. 85–95.

Appendix D: Pillar Strength Equations

Summary

In this appendix, a mathematical method is given that can be used to calculate pillar strength as a function of distance within a pillar [Johnson et al. 2014]. A description of this method is repeated in this appendix because the equations derived by using this method are used in boundary element programs in this report to model the failure of mine pillars. The method uses a one-dimensional analysis of strength as a function of distance where distance is measured from the rib toward the center of the pillar and is based on a few general principles and assumptions.

Background

Pillar stress yield functions have been investigated by several researchers and their findings are summarized in a seminal paper by Hustrulid [1976]. Mark [2006] normalized many of these equations to have equal strengths for a pillar with a width-to-height (w/h) ratio of 5:1, a shape well-represented in empirical studies, and then compared them. The w/h ratio is an important geometrical property of the pillar that controls its strength and influences failure mechanisms [Mark 1999]. This normalization, which forms the base for Figure D1, illustrates the divergence of different pillar strength estimates for larger pillars with greater w/h ratios.

This divergence is becoming increasingly important, given recent trends towards using larger gate road pillars and similar sized inter-panel barrier pillars. Pillar strength curves published by [Maleki 1992] and Tesarik et al. [2013] have been added to Figure D1 for comparison [after Tesarik et al. 2013]. These curves were of particular interest for studying ground response to mining at a deep western underground coal mine with (roughly) 16:1 w/h gate road pillars.

Johnson et al. [2014] described derivation of the general method of finding the implied pillar stress gradient, given an empirical pillar strength formula. They then described application of this method to estimating pillar cell strengths for boundary element models. This method is demonstrated in the following sections for four types of models.

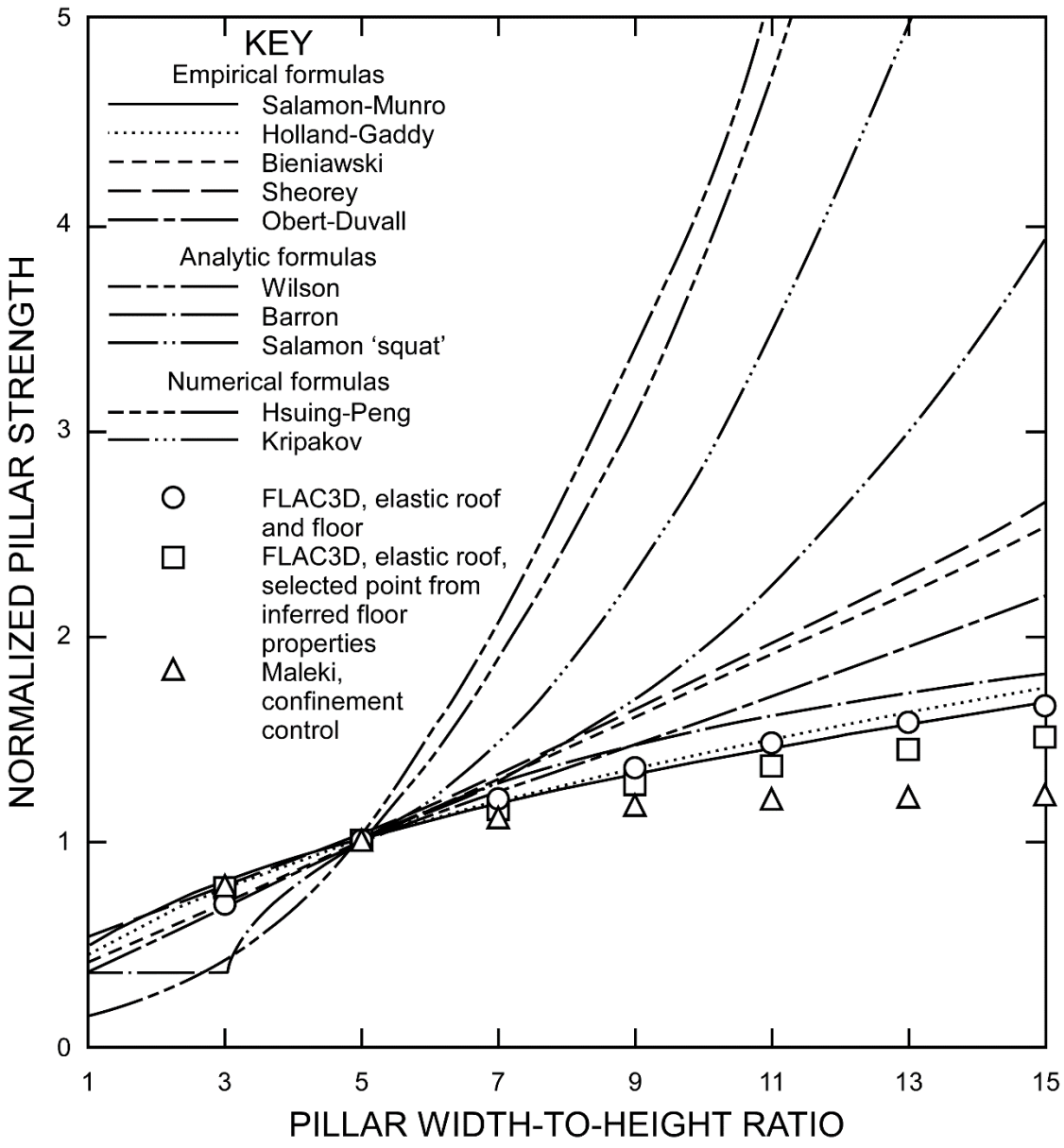

Figure D1. Normalized pillar strength versus pillar width-to-height ratio ([Mark 2006], augmented by Tesarik et al. [2013]).

Models

These pillar yield stress functions include several spatial formulations: (1) constant [Bieniawski 1968], (2) linear [Mark and Iannacchione 1992], (3) square root [Holland and Gaddy 1957], and (4) exponential [Maleki 1992]. The development of these four spatial model types is discussed below.

Constant

Figure D2 shows a square mine pillar at failure at maximum average vertical stress σ_V . This failure stress σ_V is a constant value over the entire pillar. It is calculated from an average pillar strength equation of which the pillar's width, height, and in situ compressive strength are its arguments. The most common of these equations is the Bieniawski equation,

$$\sigma_p = \sigma_c \left(0.64 + 0.36 \frac{w}{h}\right), \quad \text{(D1)}$$

where σ_p = average pillar strength,
σ_c = strength of a cubical specimen tested,
w = width of the pillar, and
h = height of the pillar.

When the average failure stress is integrated over the entire pillar, it is equivalent to the failure force F of the pillar that is equal and opposite to the load capacity R of the pillar.

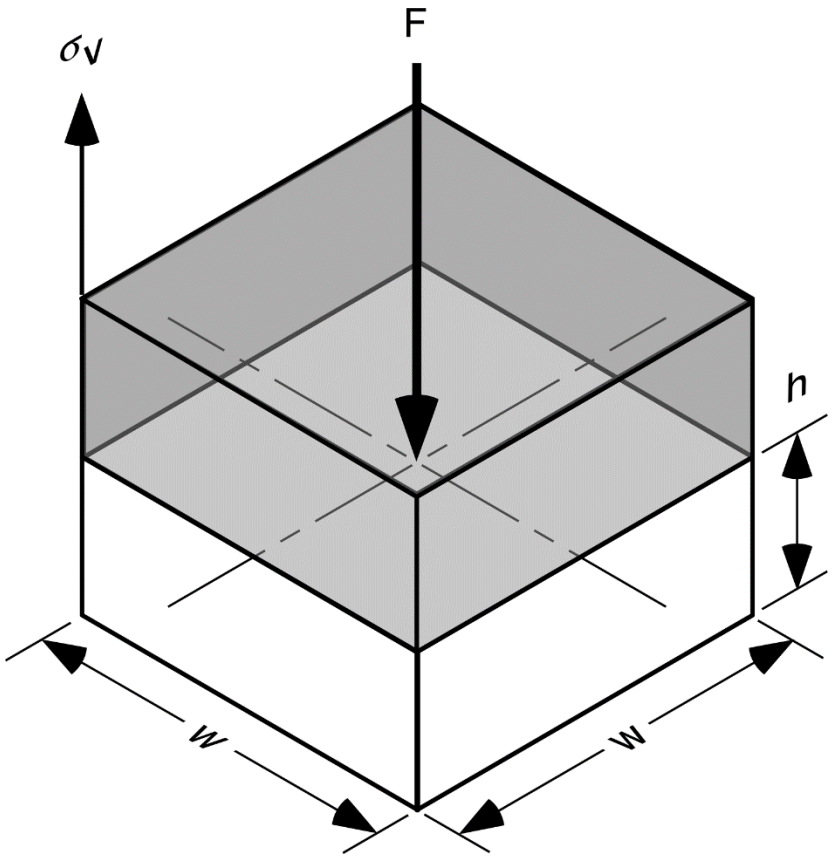

Figure D2. Pillar average vertical failure stress at failure load for constant formulation.

In practice, the vertical stress is not constant but varies throughout the pillar. A practical variation of stress is zero at the edge of the rib that increases toward the core of the pillar. The variation of stress can be obtained from the load capacity of the pillar.

Linear

Mark and Iannacchione [1992] give the variable strength equation for the Bieniawski [1968] average strength equation. The Bieniawski solution gives a linear variation in strength as a function of distance from the pillar rib as shown by the pyramid shape of stress in Figure D3. The Bieniawski solution, as well as a few other equations, were found by a trial-and-error method. These few solutions were used to validate a general mathematical method that has been developed for one-dimensional analyses.

A similar approach may be used for the Obert-Duvall strength equation [Obert and Duvall 1967],

$$\sigma_p = \sigma_c \left(0.778 + 0.222 \frac{w}{h}\right), \tag{D2}$$

which has the same form as the Bieniawski equation, but different constants.

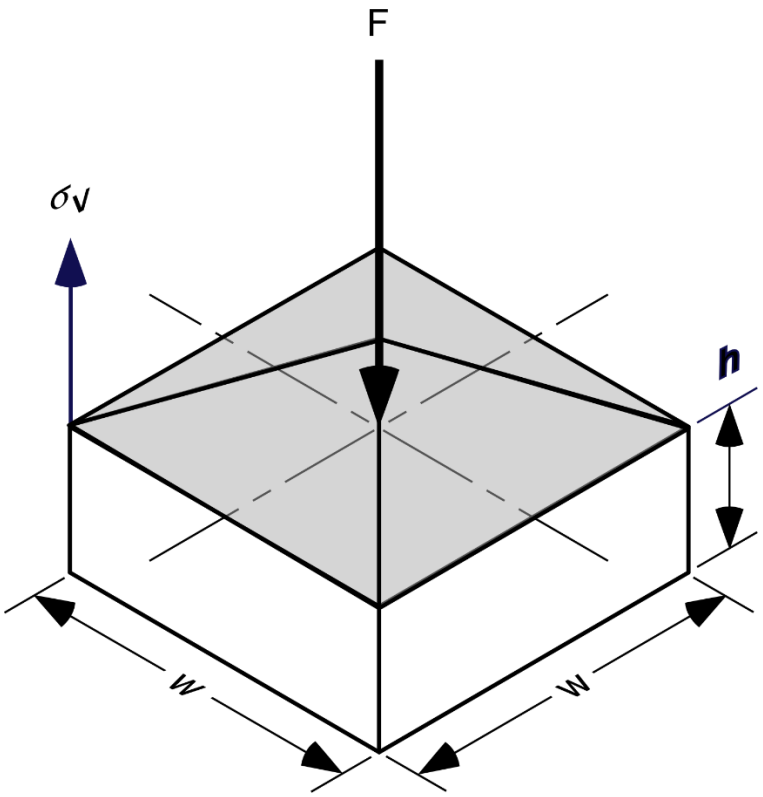

Figure D3. Strength variation over the pillar [Mark and Iannacchione 1992].

Square Root

This class of equations in the literature includes the Holland-Gaddy formula [Holland and Gaddy 1957] (which was based on tests by Gaddy [1956] on large coal specimens). These empirical equations, introduced later in this appendix, also use pillar width and height and unconfined compressive strength (UCS) of the coal to calculate the strength of a mine pillar. These are nonlinear formulations that may be more appropriate for pillars having width-to-height ratios greater than 8. This is of interest because several mines have such ratios approaching 20.

One of the simplest nonlinear average pillar strength equations is the square root model variant of the Holland-Gaddy formula proposed by Holland and Gaddy [1957]; [Holland 1964],

$$\sigma_p = \sigma_c \sqrt{\frac{w}{h}}, \tag{D3}$$

which will be examined later in this appendix. An example shape of that function over a pillar is shown in Figure D4.

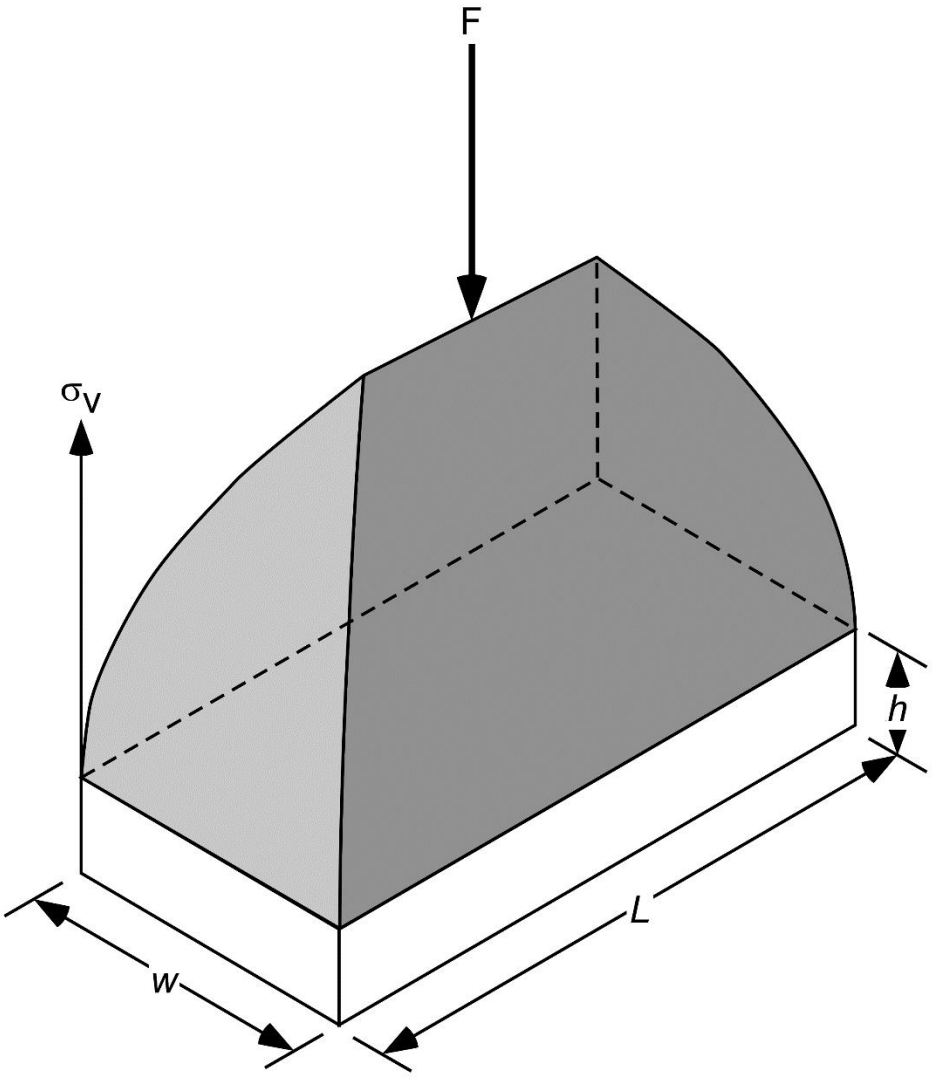

Figure D4. Strength variation over the pillar for the Holland-Gaddy pillar equation.

Exponential

Maleki [1992] proposed two equations of this form for designing coal pillars in western U.S. mines. The equations form an upper limit of coal pillar strength and were based on measurements and observations taken at several western coal mines that showed these coal pillars can sustain maximum average stresses from 26.4 to 32.4 MPa (3,836 to 4,700 psi) depending on the pillars' structure and confinement. Beyond this maximum stress level, the

entire pillar system may incur stability problems. These stability problems can result in failures in the roof, seam, and floor. Two pillar strength equations are given. The first equation describes the failure strength when confinement alone controls the strength. The second equation gives the failure strength when structural flaws decrease the strength of the pillar. The confinement and structural controlled strength equations are, respectively,

$$\sigma_{pC} = 4{,}700\left(1 - e^{\frac{-0.339\,w}{h}}\right) \text{ and} \tag{D4}$$

$$\sigma_{pS} = 3{,}836\left(1 - e^{\frac{-0.260\,w}{h}}\right). \tag{D5}$$

Both equations give the pillar strength in units of psi where distances are measured in feet. The two Maleki equations can be generalized into a single equation:

$$\sigma_p = c_1\left(1 - e^{\frac{c_2 w}{h}}\right), \tag{D6}$$

where c_1 = leading coefficient, and
c_2 = exponential decay constant.

The shape of the confinement equation is shown in Figure D5.

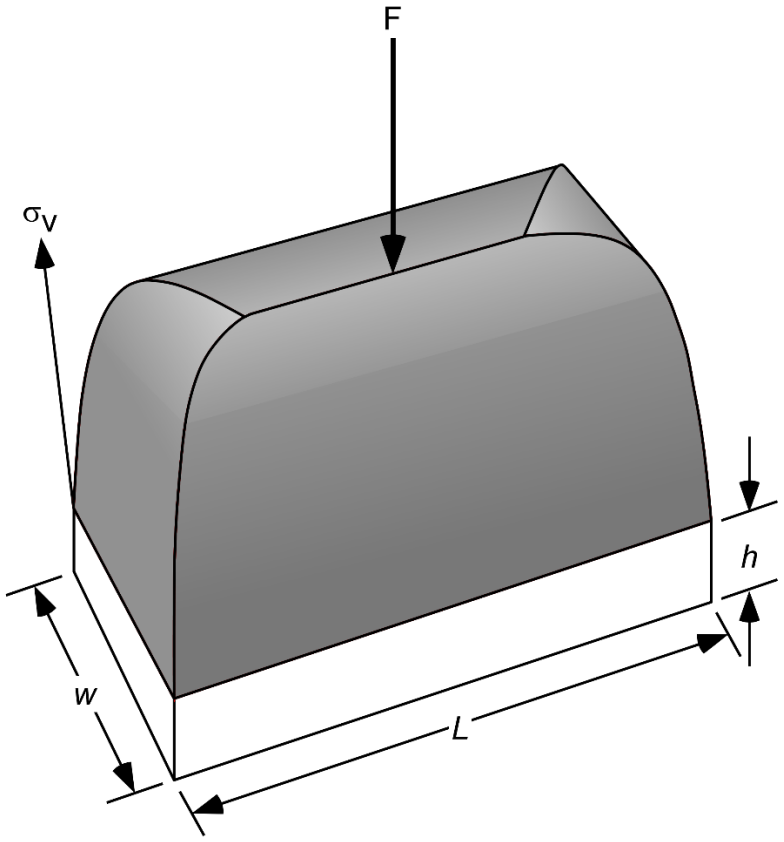

Figure D5. Strength variation over pillar for Maleki [1992] confinement equation. When the pillar is large enough, the strength decreases over the center portion of the pillar from a peak that is closer to the rib.

Assumptions

Given the variety of average pillar strength equations, a generalized method was sought to obtain the corresponding variable strength equations. A few assumptions were necessary in developing a general method to compute a variable from an average pillar strength equation. These assumptions are:

1. The method is for square pillars as most empirical equations were first developed for square pillars.

2. Pillar material is elastic-plastic. This means that all portions of the pillar are at maximum strength at failure.

3. Variation of strength within the pillar is a function of distance from the closest rib. Any other variables such as cleat or structure are ignored.

The square pillar is divided into eight symmetric pieces in order to simplify development of integral equations. These equations link the stress function $\sigma_V(x)$ to failure force of the pillar. The failure force is also a function of its width $F(W)$. Here the stress function is unknown, but the answer $F(W) = R$ (total capacity) is known. This method is illustrated in Figure D6. The integrators defined for the symmetry piece are illustrated on the right side of Figure D6.

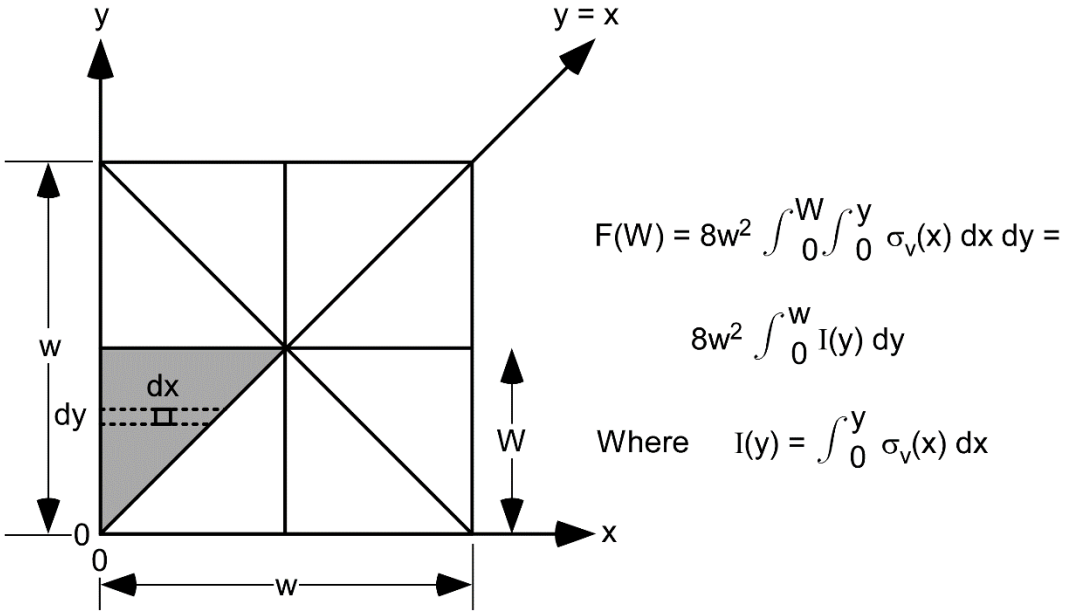

Figure D6. Plan view of the failure stress distribution of a square coal pillar subdivided into eight pieces.

Variables in or associated with Figure D6 are defined as follows:

W = pillar half-width,
$w = 2W$ = pillar width,
F = total vertical force applied to pillar,
R = pillar load capacity,
x = horizontal location within pillar
y = direction perpendicular to x, and

$\sigma_V(x)$ = local strength.

For clarity, the pillar rib is at $x = 0$, and the pillar centerline is at $x = W$.

Numerical Implementation

The total vertical force F is calculated in terms of the vertical pillar stress σ_V where the vertical force is a function of the pillar geometry $F(W)$. Because of symmetry the integration is:

$$F(W) = 8\int_0^W \int_0^y \sigma_V(x)\ dx\ dy = 8\int_0^W I(y)\ dy, \tag{D7}$$

where

$$I(y) = \int_0^y \sigma_V(x)\ dx, \tag{D8}$$

and dy and dx are shown in Figure D6. The w^2 factor in the figure cancels on each side of the equation.

Leibnitz's Rule from elementary calculus is used:

$$\frac{d}{dx}\left(\int_0^x f(t)\ dt\right) = f(x). \tag{D9}$$

This rule is applied twice to the above integral. The variable vertical pillar stress equations are:

$$\frac{dF}{dW} = 8I(W) = 8\int_0^W \sigma_V(x)\ dx, \text{ and} \tag{D10}$$

$$\frac{d^2F}{dW^2} = 8\ \sigma_V(W). \tag{D11}$$

The implementation of this procedure in each of the four spatial models is discussed below.

Constant

The one-dimension method is demonstrated using the Bieniawski average pillar strength equation using a constant variation. Applying the formulas above, the result is linear making it one of the simpler equations. For a square pillar of dimension w , the pillar capacity is

$$F = \sigma_p w^2 = \sigma_c\left(0.64 + 0.36\frac{w}{h}\right)w^2, \tag{D12}$$

where, for ease of implementation, $w = 2W$.

Applying the one-dimension method produces the result that is identical to that reported by Mark and Iannacchione [1992]:

$$\frac{d^2F}{8\ dx^2} = \sigma_V(x) = \sigma_c\left(0.64 + 2.16\frac{x}{h}\right). \tag{D13}$$

Linear

Using a linear variation in the pillar yield stress function, Mark and Iannacchione [1992] conclude that the variable strength equation has the same "shape" as the average pillar strength when average strength is expressed in the pillar's width-to-height ratio. A graph of the linear increase of strength with distance into the pillar is shown in Figure D7. A pillar height of 3.0 m (10 ft) and a UCS of 6.21 MPa (900 psi) from Mark [1992] were assumed.

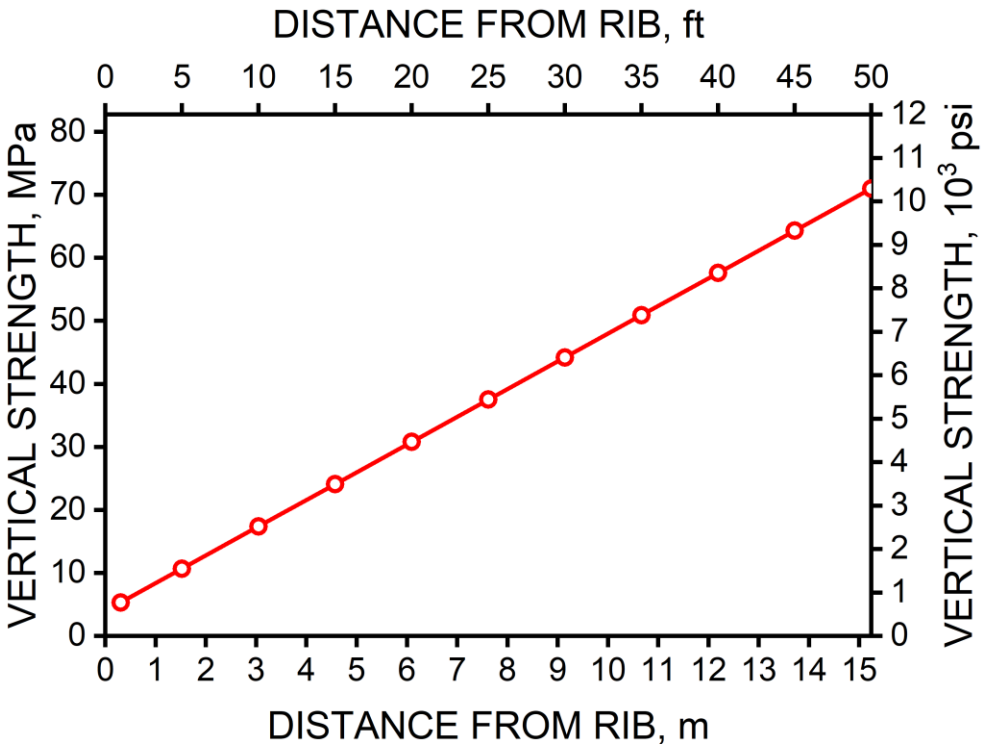

Figure D7. Bieniawski variable strength as a function of distance from the rib.

Square Root

The one-dimension method is applied to the Holland-Gaddy (square root spatial variation) average pillar strength equation. This equation is one of the simpler nonlinear equations where the pillar strength is a square root function of the pillar's width-to-height ratio. Gaddy [1956] found from unconfined compression tests that the UCS of cubical coal specimens from a given coal seam and the side-length of the cubes are related by the following equation.

$$\sigma_c = \frac{k}{\sqrt{d}}, \tag{D14}$$

where σ_c = UCS of the cubical specimen,
d = side-length of cubical specimen, and
k= constant determined by plotting σ_c versus d and is representative of the physical characteristics of the coal bed from which the specimens were obtained [MN/m$^{3/2}$ (lb/in$^{3/2}$)].

Holland and Gaddy [1957] developed the following formula for pillar strength that includes both pillar width and height:

$$\sigma_p = \frac{k\sqrt{w}}{h}, \tag{D15}$$

where σ_p = UCS of the pillar (usually given in psi),
w = pillar width, (usually given as in),
h = pillar height, (usually given as in), and
k = constant determined by plotting σ_c versus h (usually given as lb/in$^{3/2}$).

Solving for k in Gaddy's equation, assuming that d and h are equivalent, and substituting the result into Holland-Gaddy's Equation D15 yields another form of the Holland-Gaddy [Holland and Gaddy 1957] equation:

$$\sigma_p = \sigma_c \sqrt{\frac{w}{h}}. \tag{D16}$$

The pillar capacity is

$$F = \sigma_p w^2 = \sigma_c \sqrt{\frac{w}{h}}\, w^2. \tag{D17}$$

Differentiating the above equation twice with respect to $x = {}^{w}/_{2}$ the result is

$$\frac{d^2F}{8\,dx^2} = \sigma_V(x) = 2.652\,\sigma_c\sqrt{\frac{x}{h}}. \tag{D18}$$

The result using the one-dimension method (Equation D18) is the same variable strength equation as that reported by Mark and Iannacchione [1992], where the shape of this strength variation is graphed in Figure D8. In this figure, the initial pillar strength for a 1-ft cube of coal of 3.037 MPa (440.5 psi) was used. This value was obtained using Gaddy's equation that relates σ_c to k and h (Equation D14) where k is equal to 4,825 lb/in$^{3/2}$ as reported by Holland [1964] for the Clintwood Seam. Assuming a 3.048 m (120-in) seam height gives 3.037 MPa (440.5 psi) for the in situ coal strength.

The form of this equation is such that the pillar strength is zero (with infinite slope) along the rib face and increases to σ_c at the pillar center. Because of the symmetric nature of the assumed variation of the pillar strength, the square root equation is not smooth (differentiable) along the diagonals of the pillar nor at the pillar center.

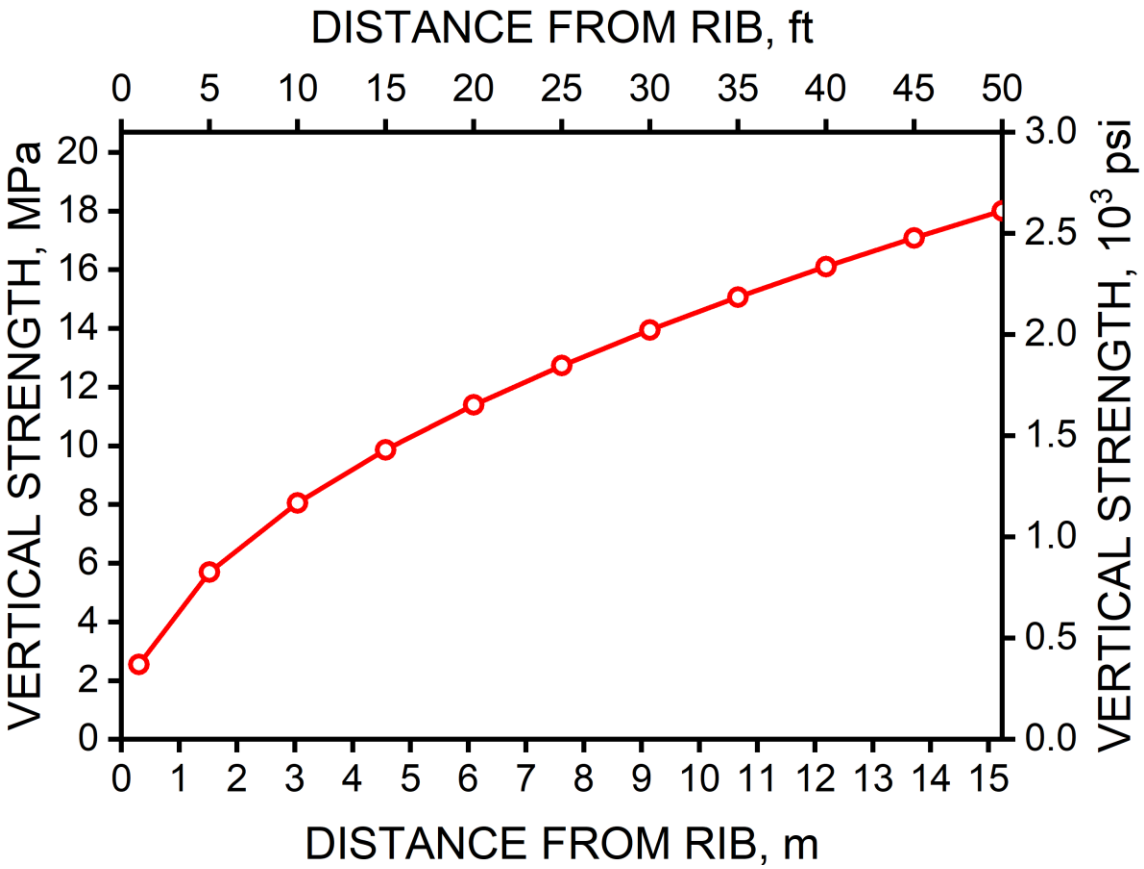

Figure D8. Variable strength as a function of distance from the rib for an example using the Holland-Gaddy pillar strength equation.

Exponential

Taking Equation D6 and applying the one-dimensional method outlined in Equations D7 to D11 results in local pillar strength as

$$\sigma_V = c_1\{1 - e^{ax}[1 + 2ax + 0.5a^2x^2]\}, \quad \text{(D19)}$$

where $a = \frac{2c_2}{h}$. This result is graphed for both of Maleki's equations in Figure D9.

The form of this equation is such that the pillar strength is zero (with finite slope) at the rib face and increases to a maximum at the pillar center. Because of the symmetric nature of the assumed variation of the pillar strength, the exponential model is not smooth (differentiable) along the diagonals of the pillar nor at the pillar center, but it can be made to approximate the Bieniawski (constant) model when $c_2 = \infty$, and the Mark-Bieniawski (linear) model when $c_2 = 0$.

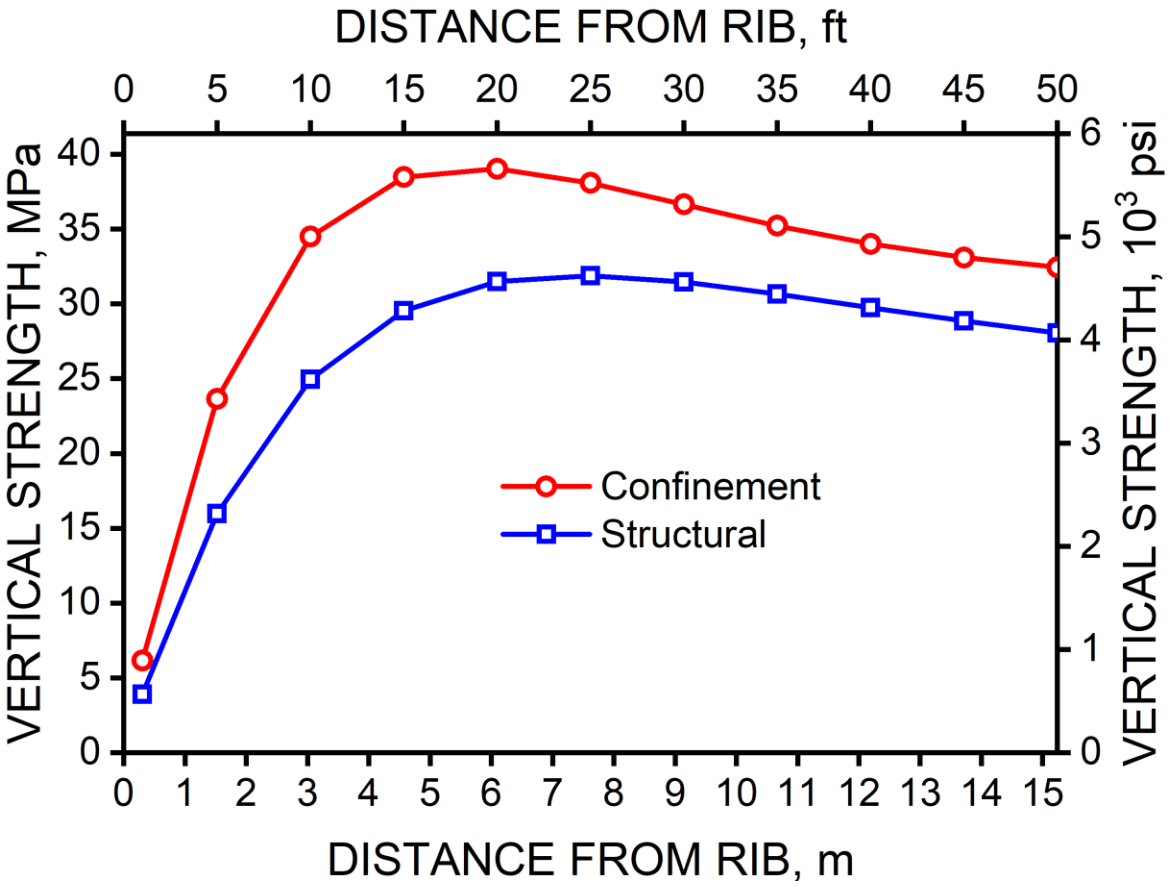

Figure D9. Maleki variable strength as a function of distance from the rib with confined control strength plotted as circles and structure control strength plotted as boxes [Johnson et al. 2014].

Conclusions and Recommendations

This appendix demonstrates a new generalized mathematical method that can be used to calculate the maximum pillar variation of vertical stress or variable strength equation from any average pillar strength equation that is a function of a pillars' width-to-height ratio. The method is demonstrated with formulas in the following classes: constant, linear, square root, and exponential. Once the variable strength equation has been determined, it can then be used to obtain pillar cell strength or load capacity equations that are used to model mine pillars in boundary element programs. The variable strength equation is then used to obtain three pillar cell strength equations that are used to model the mine pillar: the rib, corner, and the core. The core cell is a newly developed addition to the previous pillar cell equations. The results, using the new generalized mathematical method, have been verified with the currently used pillar cell equations as reported in the literature. A benefit of this research to the mining industry is that now the best-suited pillar strength equations, including those developed at any coal field or mine site (based on the width-to-height ratio of the pillar), can be incorporated into boundary element programs. This advance removes a barrier to mining engineers incorporating their full knowledge of local coal and ground characteristics into mine design models.

References for Appendix D

Bieniawski ZT [1968]. The effect of specimen size on compressive strength of coal. Int. J. Rock Mech. Min. Sci., Vol. 5, No. 4, pp. 325–335.

Gaddy FL [1956]. A study of the ultimate strength of coal as related to the absolute size of the cubical specimens tested. Bulletin of the Virginia Polytechnic Institute, Engineering Experiment Station Series No. 112. Vol. 49, No. 10, Blacksburg, VA: Virginia Polytechnic Institute, 27 pp.

Holland CT [1964]. The strength of coal in mine pillars. In: Spokes EM, Christiansen CR eds. Proceedings of the Sixth Symposium on Rock Mechanics. (Rolla, MO: October 1964) Rolla, MO: University of Missouri at Rolla, pp. 450–466.

Holland CT, Gaddy FL [1957]. Some aspects of permanent support of overburden on coal beds. In: 1957 Proceedings of the West Virginia Coal Mining Institute. (Huntington, WV, and White Sulphur Springs, WV: June 22–23, 1956 and November 2–3, 1956), pp. 43–65.

Hustrulid WA [1976]. A review of coal pillar strength formulas. Rock Mech., Vol. 8, No. 2, pp. 115–145.

Johnson JC, Whyatt JK, Loken MC [2014]. A generalized method for calculating pillar cell capacities for boundary element modeling of coal mines. In: 2014 SME Annual Meeting. Preprint 14-162, (Salt Lake City, Utah: February 23–26, 2014) Englewood, CO: Society for Mining, Metallurgy, and Exploration, Inc., 15 pp.

Maleki H [1992]. In situ pillar strength and failure mechanisms for U.S. coal seams. In: Iannacchione AT et al. eds. Bureau of Mines Information Circular 9315, Proceedings of the Workshop on Coal Pillar Mechanics and Design. (Santa Fe, NM: June 7, 1992) U.S. Department of the Interior, pp. 73–77.

Mark C [1992]. Analysis of Longwall Pillar Stability (ALPS): An update. In: Iannacchione AT et al. eds. Proceedings of the Workshop on Coal Pillar Mechanics and Design. Pittsburgh, PA: U.S. Department of the Interior, Bureau of Mines Information Circular 9315, pp. 238–249.

Mark C [1999]. Empirical methods for coal pillar design. In: Christopher M et al. eds. Information Circular 9448, Proceedings of the Second International Workshop on Coal Pillar Mechanics and Design. Pittsburgh, PA: U.S. Department of Health and Human Services, Centers for Disease Control and Prevention, National Institute for Occupational Safety and Health, DHHS (NIOSH), pp. 145–154.

Mark C [2006]. The evolution of intelligent coal pillar design: 1981–2006. In: Peng SS et al. eds. Proceedings: 25th International Conference on Ground Control in Mining. (Morgantown, WV: August 1–3, 2006) Morgantown, WV: West Virginia University, pp. 325–334.

Mark C, Iannacchione AT [1992]. Coal pillar mechanics: Theoretical models and field measurements compared. In: Iannacchione AT et al. eds. Bureau of Mines Information Circular 9135, Proceedings of the Workshop on Coal Pillar Mechanics and Design. Washington, DC: U.S. Department of the Interior, pp. 78–93.

Obert L, Duvall WI [1967]. Rock mechanics and the design of structures in rock, New York: John Wiley & Sons, 650 pp.

Tesarik DR, Whyatt JK, Larson MK [2013]. Inferring mine floor properties from pillar size and floor heave. In: Pyrak-Nolte LJ et al. eds. Proceedings of the 47th U.S. Rock Mechanics/Geomechanics Symposium. (San Francisco, CA: June 23–26, 2013) Alexandria, VA: American Rock Mechanics Association, pp. 438–450.

Appendix E: Ground Condition Ratings versus Model Output

Summary

Ground condition ratings showed no significant correlation with closure calculated with MulsimNL/Large. This lack of correlation suggests that variation in geology over the area of the survey was more significant than correlation of ground conditions with increased stress and closure that result from mining.

Background

Lawson et al. [2012] developed a rating scale for ground conditions of the roof, ribs, and floor of a coal mine. It may require modification for application at any given mine. The specific description for the sites in this study were described by Larson et al. [NIOSH 2020].

The purpose of this appendix is to explore any correlation between ground condition ratings and numerical model output. MulsimNL/Large was used to provide output over the large area of the surveys at Mine A.

Description

Displacement discontinuity codes such as LaModel [Heasley 1998, 2010] and Mulsim [USBM 1992a, 1992b; Larson and Whyatt 2013; Larson 2015] have an advantage of being able to model the mining of a large area in a reasonable amount of time. For calibration and verification purposes, it is useful to explore if some parameter in these codes corresponds well with ground condition ratings. For such a task, because surveys are done in the entries, the logical parameter to compare with ground condition survey data to test correspondence is the entry closure.

To carry out this investigation of correlation, the closure used for comparison was at midpillar, except where the surveys stated the closure was at the intersections. To calculate entry closure, the average of closure of the two elements at the same latitude in an entry was calculated.

Because use of empirical tools is widespread, the first comparison is with ground condition ratings compared to closure as calculated by LaModel, where LaModel has default parameters; that is, parameters that enable calibration criterion to empirical assumptions to be met, as outlined by Heasley [2008]. As seen from Figure E1, there appears to be no correlation between any ground condition rating and model closure.

Because measured load transfer distance (LTD) determined from LaModel was significantly different from that predicted by the Peng and Chiang equation, the comparison was done between ground control ratings and closure output from LaModel when the rock mass stiffness was calibrated to measured LTD. Figure E2 shows that there is no correlation between ground condition rating and calculated closure of the model.

The best Mulsim model for predicting measured LTD was obtained by using a fully elastic seam model, with cells near the rib reduced in modulus to simulate the effect of softer material near ribs that result from yielding or release of gas. Figure E3 shows ground condition ratings versus closure at all sites surveyed at the proper states of mining. Interpolation was necessary

when a survey was done with the face located between face location increments in the model. Again, correlation between any rating and entry closure was poor.

Correlation between the maximum ground condition rating and model-calculated closure was also investigated. However, Figure E4 exhibits extensive data scatter with no discernible correlation.

Examination of results by gate road shows varied results. In 1 North, only one site was sampled, at the outby instrumentation site. Figure E5 shows correlation between rib ratings and model closure and between roof ratings and model closure. However, the number of surveys conducted does not make this correlation certain. Still, Lawson et al. [2012], found ratings at one location over time to be indicative of changing ground conditions. Moreover, Larson and Whyatt found single site ratings useful as an indication of arrival of abutment stress [2012]. Larson et al. [NIOSH 2020] confirmed that use.

In the 2 North gate roads, many more surveys were conducted. However, because areas were identified as being anomalous and nonanomalous in their ground condition, it was necessary to separate these survey results by anomalous and nonanomalous zones for investigating correlation. Figure E6 shows ground condition ratings from nonanomalous zones versus model closure—that is, ground condition ratings were from the zones showing typical behavior for 2 North. The scatter of results appears random. The same result is obtained by examining anomalous zone ground condition ratings versus model closure, shown in Figure E7.

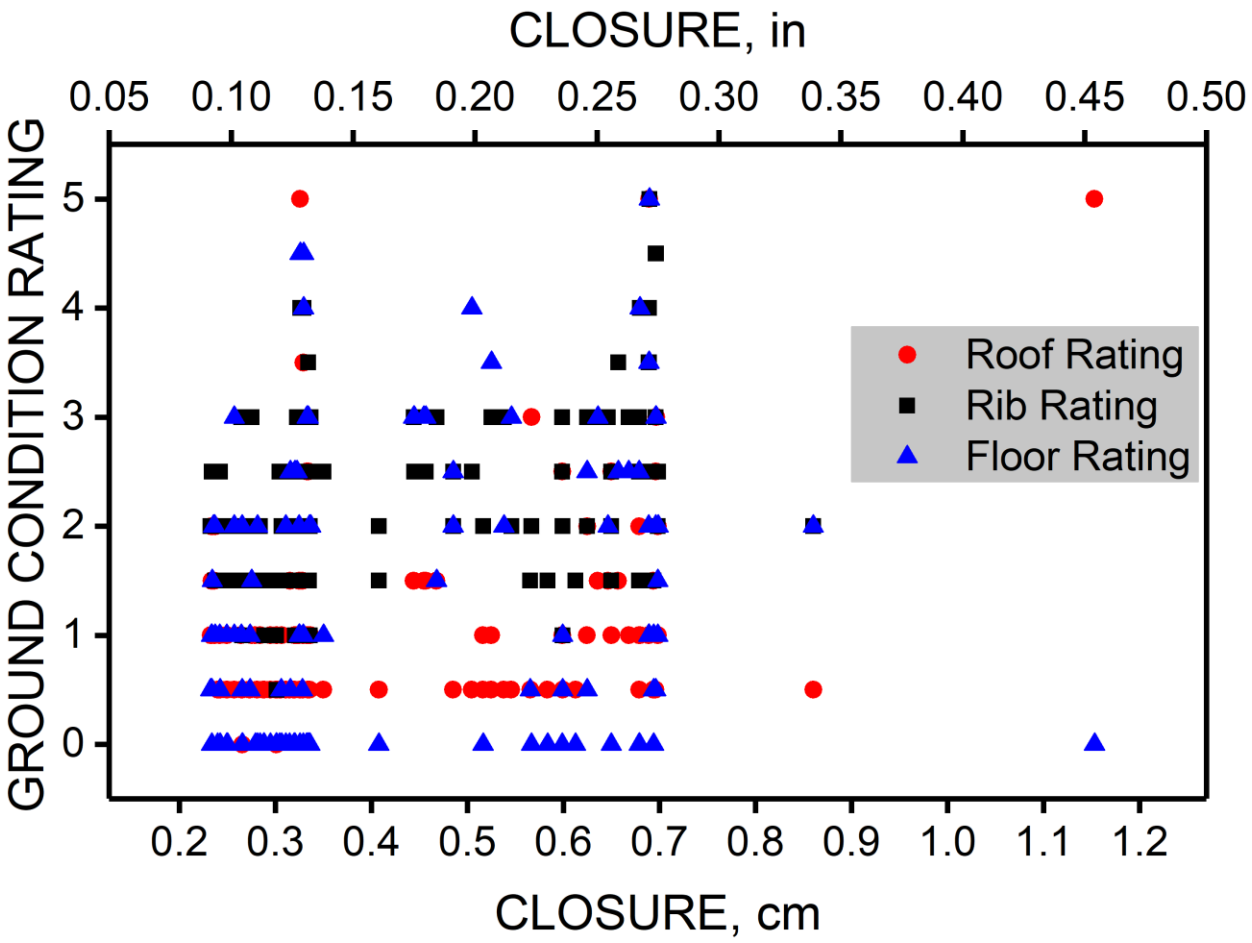

Figure E1. Ground condition ratings vs. closure calculated by LaModel using default parameters for rock mass stiffness and gob stiffness with coal having a uniaxial compressive strength of 6.21 MPa (900 psi) and a distributed strength according to the Mark-Bieniawski criterion [Mark and Chase 1997].

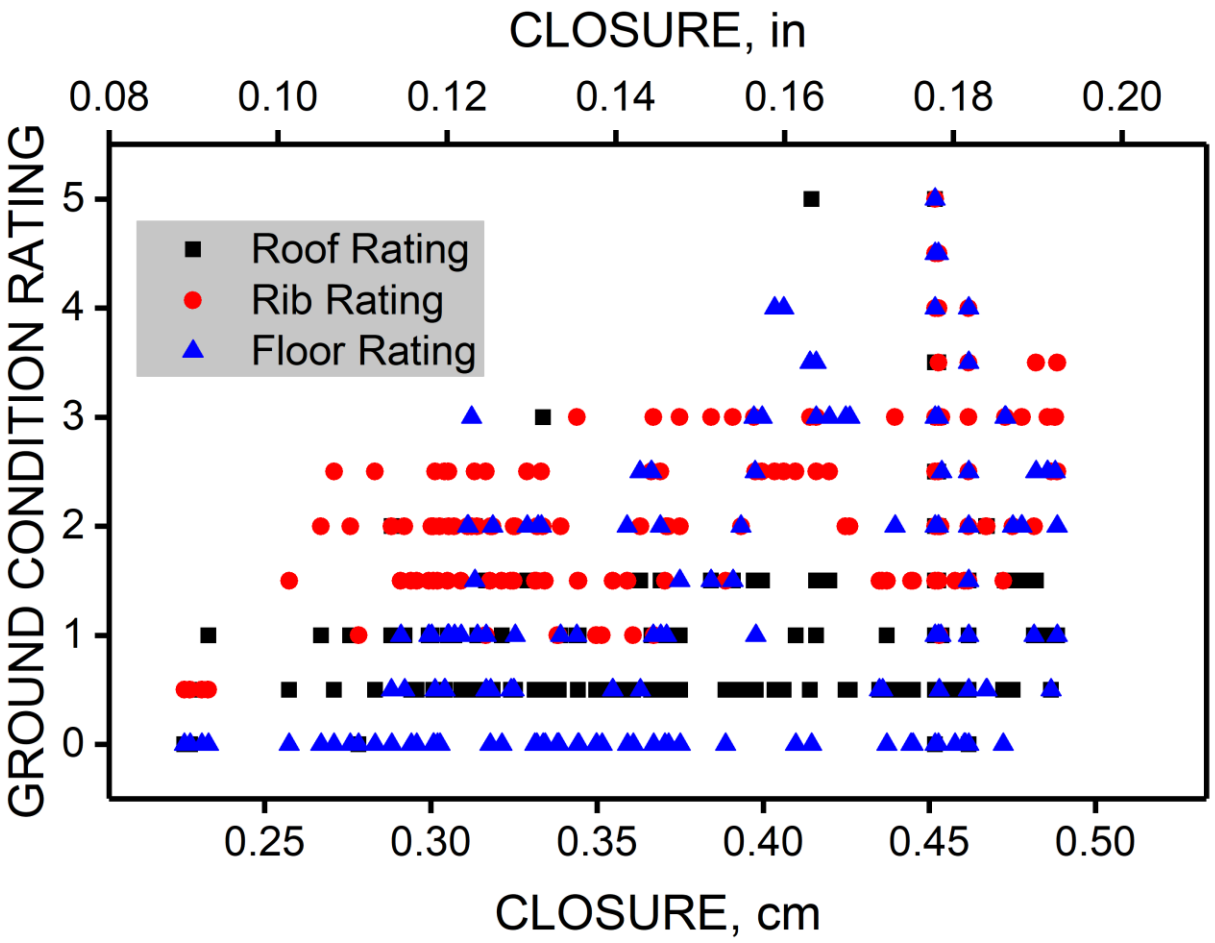

Figure E2. Ground condition ratings versus closure calculated by LaModel using rock mass stiffness calibrated for measured LTD and default gob stiffness with coal having a uniaxial compressive strength of 6.21 MPa (900 psi) and a distributed strength according to the Mark-Bieniawski criterion [Mark and Chase 1997].

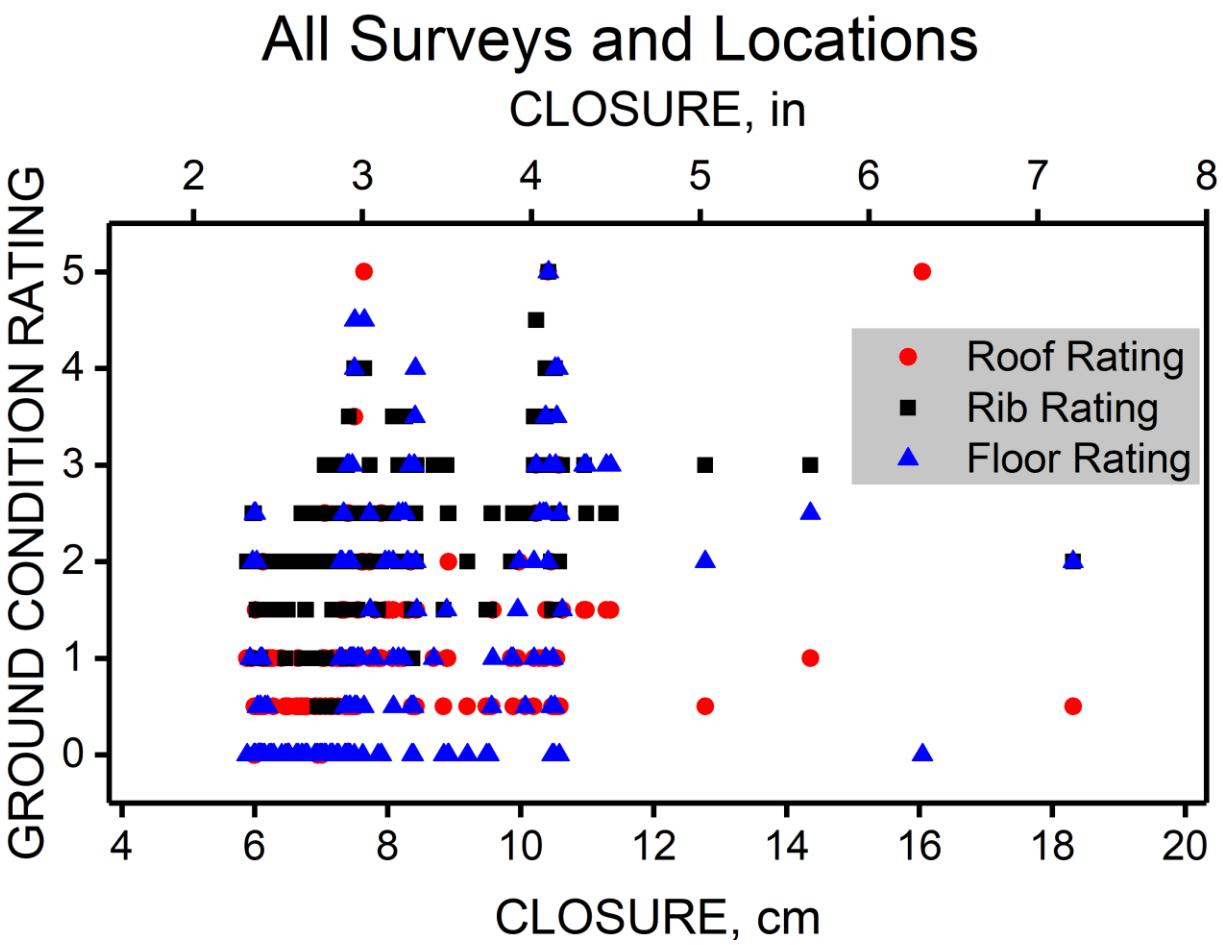

Figure E3. Ground condition ratings versus closure calculated by Mulsim using best-guess parameters for rock mass stiffness and default gob stiffness as calculated by LamPre assuming coal having a uniaxial compressive strength of 6.21 MPa (900 psi) and a distributed strength according to the Mark-Bieniawski criterion [Mark and Chase 1997]. Shown are all ratings for all locations surveyed in both 1 North and 2 North gate roads. Coal was elastic, with modulus of outer two rings reduced to 60% and 80%, respectively, of its full amount.

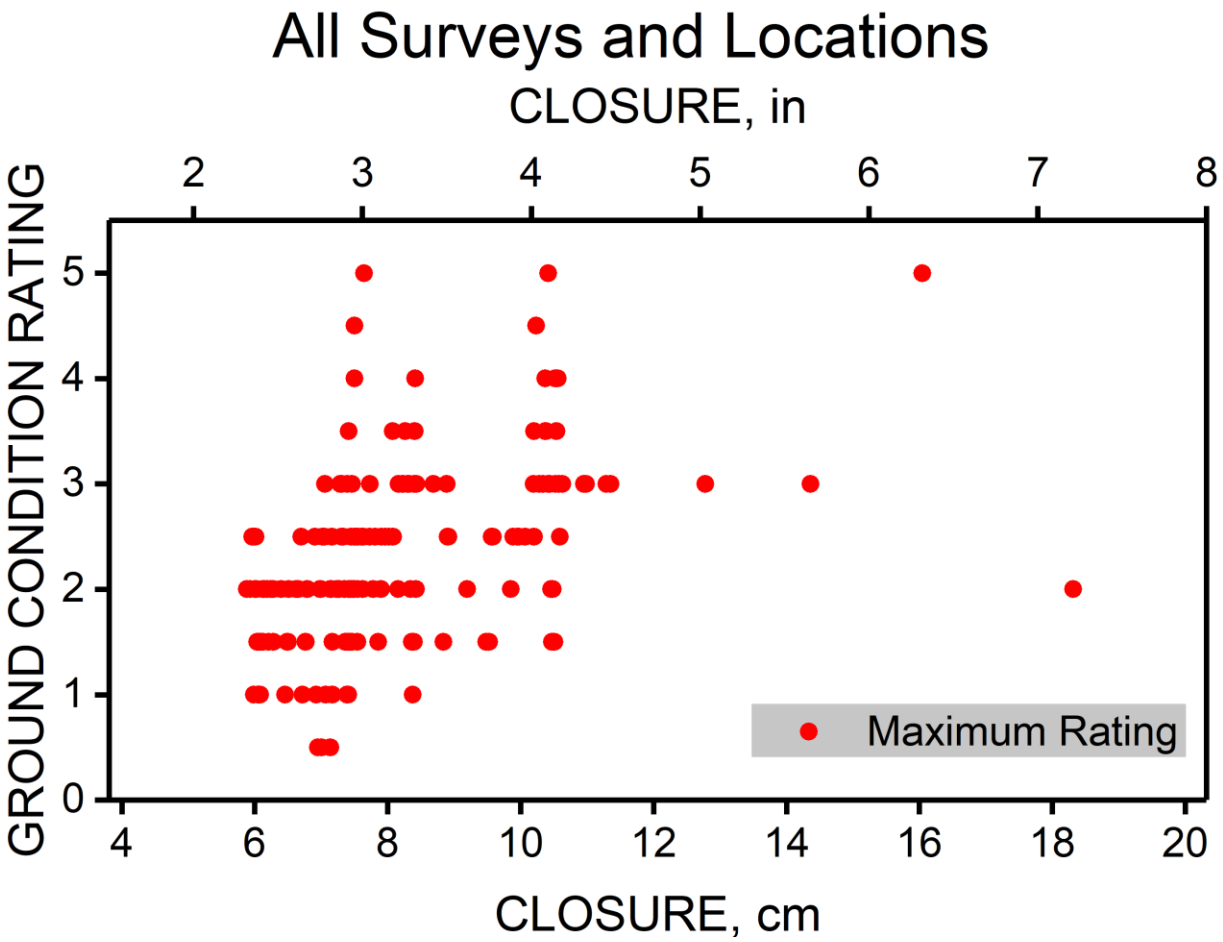

Figure E4. Largest ground condition rating of floor, rib, or roof vs. closure calculated by Mulsim using best-guess parameters for rock mass stiffness and default gob stiffness as calculated by LamPre assuming coal having a uniaxial compressive strength of 6.21 MPa (900 psi) and a distributed strength according to the Mark-Bieniawski criterion [Mark and Chase 1997]. Shown are data from surveys taken at all locations in both 1 North and 2 North gate roads. Coal was elastic, with modulus of outer two rings reduced to 60% and 80%, respectively, of its full amount.

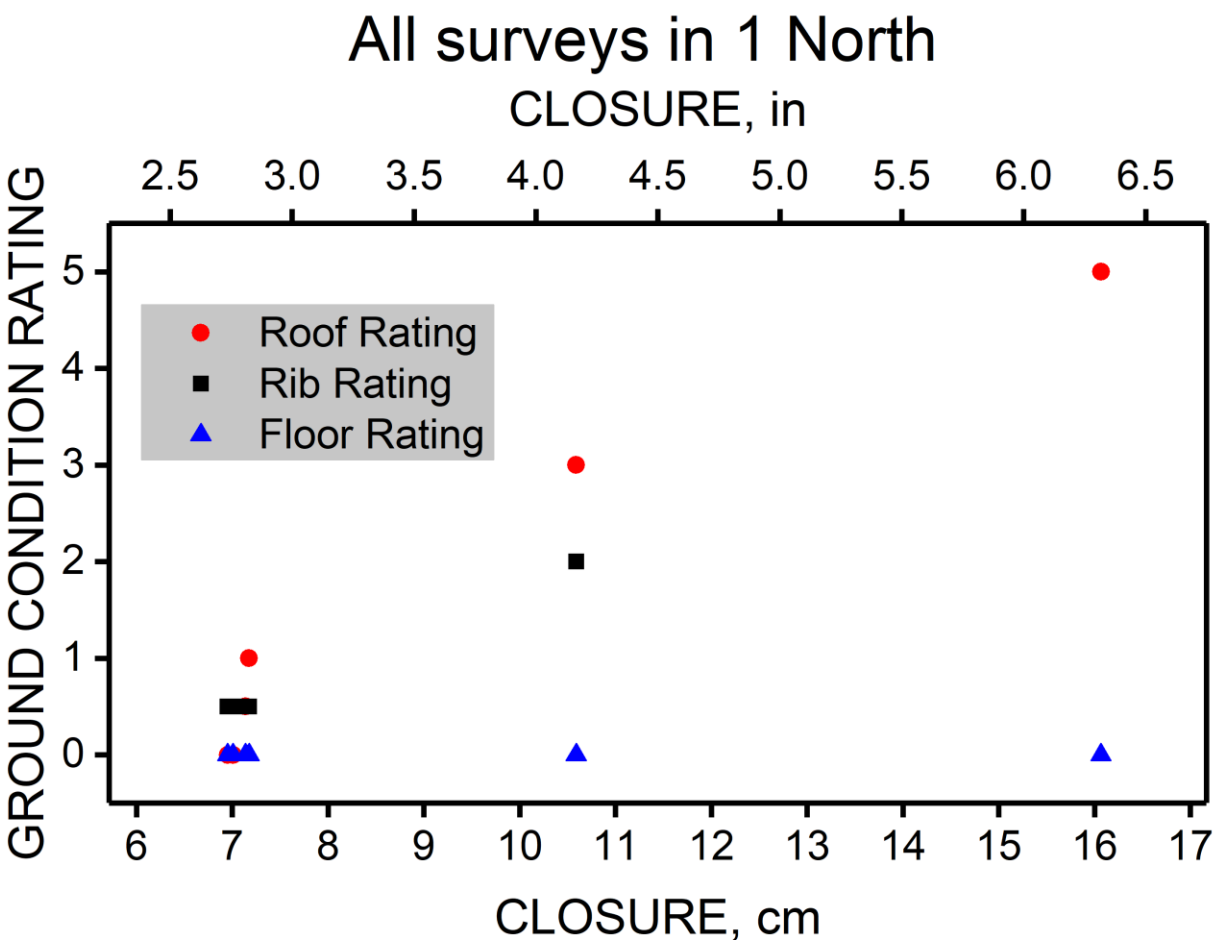

Figure E5. Ground condition ratings versus closure calculated by Mulsim using best-guess parameters for rock mass stiffness and default gob stiffness as calculated by LamPre assuming empirical conditions. Shown are all ratings for one location surveyed in the 1 North gate roads. Coal was elastic, with modulus of outer two rings reduced to 60% and 80%, respectively, of its full amount.

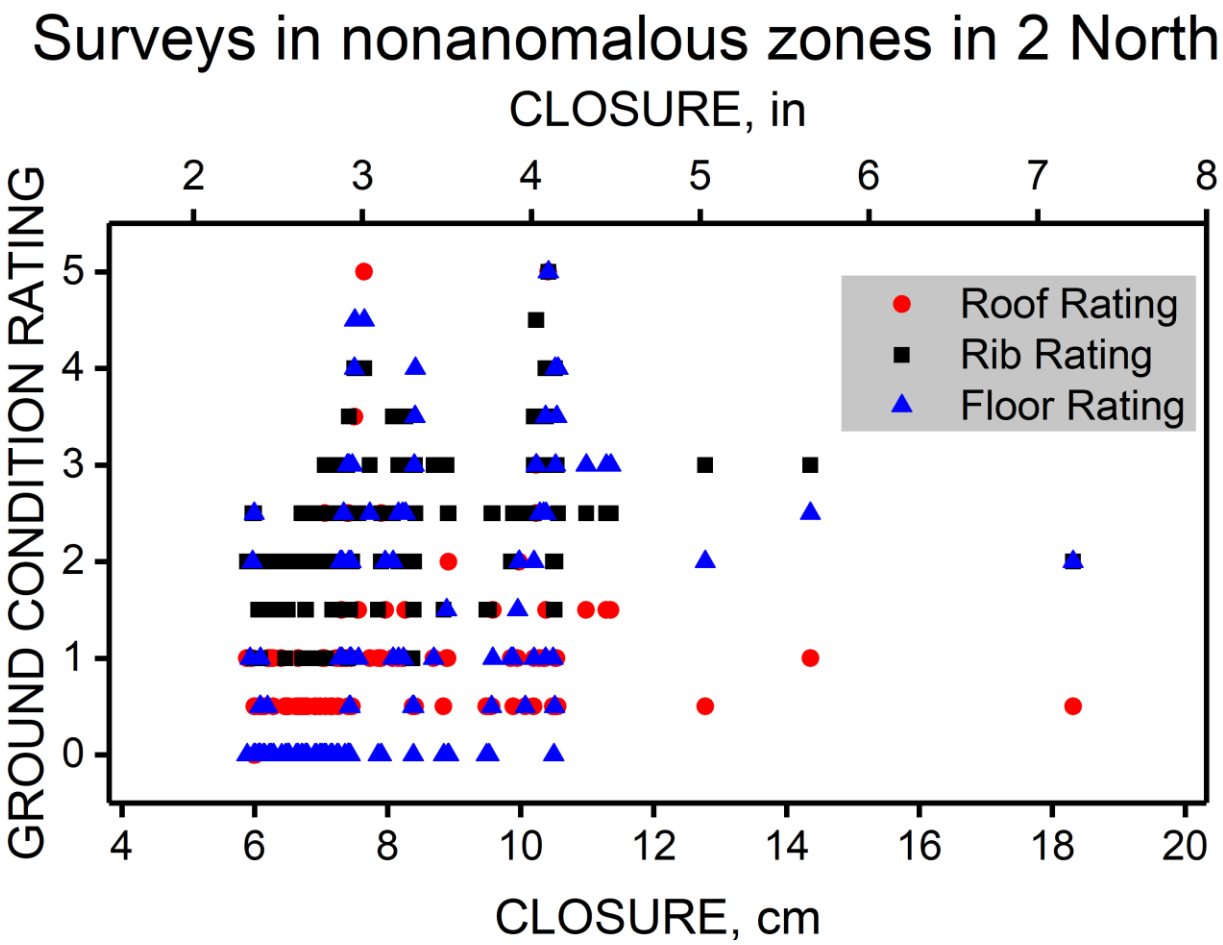

Figure E6. Ground condition ratings versus closure calculated by Mulsim using best-guess parameters for rock mass stiffness and default gob stiffness as calculated by LamPre assuming empirical conditions. Shown are all ratings from all nonanomalous zones surveyed in the 2 North gate roads. Coal was elastic, with modulus of outer two rings reduced to 60% and 80%, respectively, of its full amount.

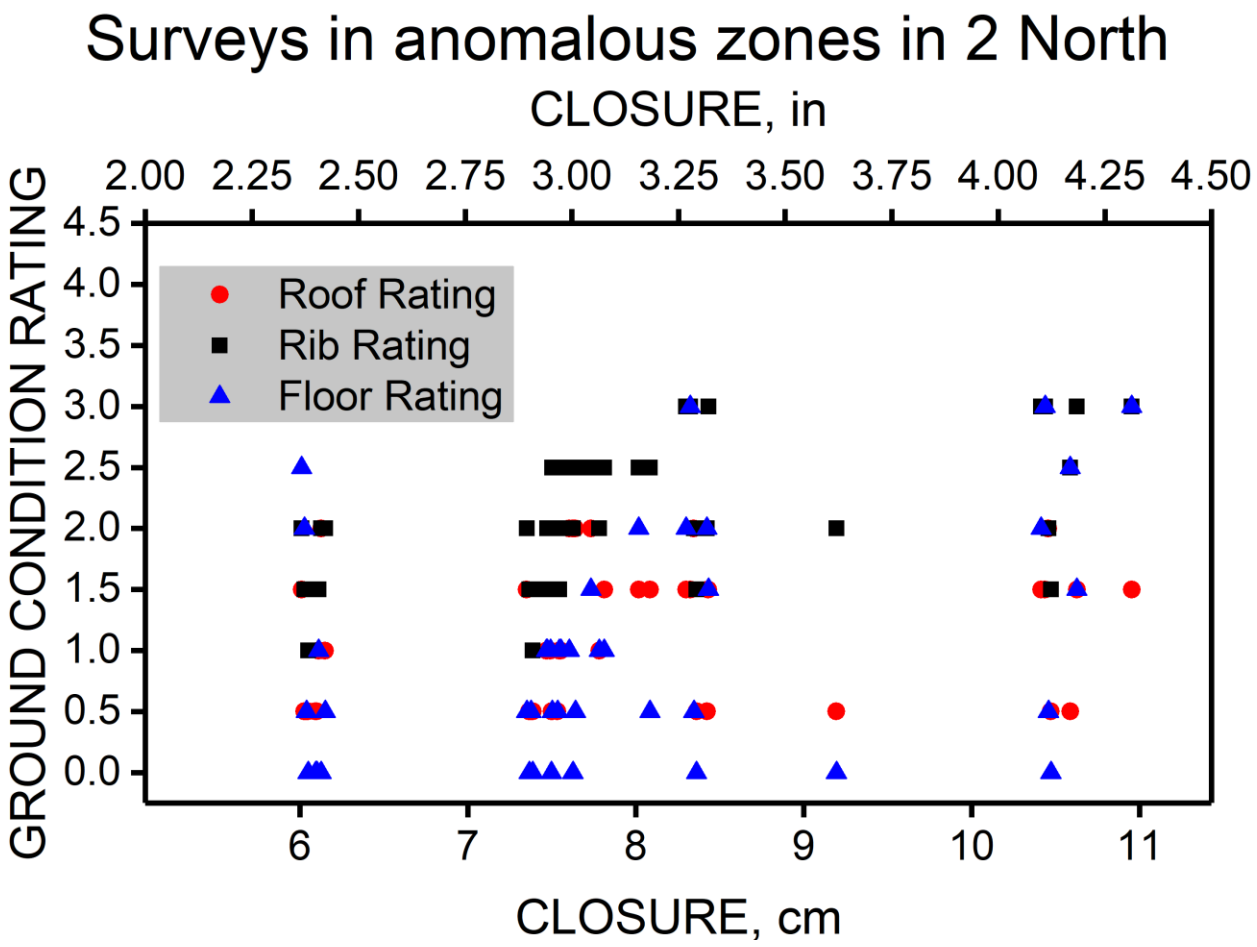

Figure E7. Ground condition ratings versus closure calculated by Mulsim using best-guess parameters for rock mass stiffness and default gob stiffness as calculated by LamPre assuming empirical conditions. Shown are all ratings from all anomalous zones surveyed in the 2 North gate roads. Coal was elastic, with the modulus of outer two rings reduced to 60% and 80%, respectively, of its full amount.

Conclusion

Although ground condition ratings have been found to be useful at a given site to provide some indication of arrival of the abutment stress, no correlation with entry closure as calculated with various models was obtained. The scatter shown in the figures of this appendix are likely indicative of the great variability of ground conditions and possibly stratigraphic variability along the gate roads, particularly in 2 North.

References for Appendix E

Heasley KA [1998]. Numerical modeling of coal mines with a laminated displacement-discontinuity code. Ph.D. Dissertation. Golden, Colorado: Colorado School of Mines, 205 pp.

Heasley KA [2008]. Some thoughts on calibrating LaModel. In: Peng SS et al. eds. Proceedings: 27th International Conference on Ground Control in Mining. (Morgantown, WV: July 29–31, 2008) Morgantown, WV: West Virginia University, pp. 7–13.

Heasley KA [2010]. LaModel, ver. 3.0, Morgantown, WV: West Virginia University.

Larson MK [2015]. MulsimNL/Large: Reviving a USBM tool for modeling coal mines. In: Preprints: 2015 SME Annual Conference & Expo, CMA 117th National Western Mining Conference. Preprint 15-039, (Denver, CO: February 15–18, 2015) Englewood, CO: Society for Mining Metallurgy, and Exploration, Inc., 11 pp.

Larson MK, Whyatt JK [2012]. Load transfer distance calibration of a coal panel scale model: A case study. In: Barczak T et al. eds. Proceedings of the 31st International Conference on Ground Control in Mining. (Morgantown, WV: July 31–August 2, 2012) Morgantown, WV: West Virginia University, pp. 195–205.

Larson MK, Whyatt JK [2013]. Panel-scale modeling of a deep longwall panel: The MULSIM alternative. In: Barczak T et al. eds. Proceedings: 32nd International Conference on Ground Control in Mining. (Morgantown, WV: July 30–August 1, 2013) Morgantown, WV: West Virginia University, pp. 181–188.

Lawson H, Zahl E, Whyatt J [2012]. Ground condition mapping: A case study. In: 2012 SME Annual Meeting, "Mine to Market: Now It's Global" Preprint 12–122, (Seattle, WA: Feb 19–22, 2012) Englewood, CO: Society for Mining, Metallurgy, and Exploration, Inc., 7 pp.

Mark C, Chase FE [1997]. Analysis of Retreat Mining Pillar Stability (ARMPS). In: Mark C, Tuchman RJ eds. Proceedings: New Technology for Ground Control in Retreat Mining, DHHS (NIOSH) Publication No. 97-133, IC 9446. Pittsburgh, PA: National Institute for Occupational Safety and Health (NIOSH), pp. 17–34.

NIOSH [2020]. Ground stress in mining (part 1): Measurements and observations at two western U.S. longwall mines. By Larson MK, Lawson HE, Zahl EG, Jones TH. U.S. Department of Health and Human Services, Centers for Disease Control and Prevention, National Institute for Occupational Safety and Health, DHHS (NIOSH) Publication No. 2019-175, RI 9702.

USBM [1992a]. MULSIM/NL application and practitioner's manual. By Zipf RK, Jr. Information Circular 9322, Pittsburgh, PA: U.S. Department of the Interior, Bureau of Mines (USBM), 44 pp.

USBM [1992b]. MULSIM/NL theoretical and programmer's manual. By Zipf, RK, Jr. Information Circular 9321, Pittsburgh, PA: U.S. Department of the Interior, Bureau of Mines (USBM), 52 pp.

Appendix F: Borehole Pressure Cell Calibration Issues

Summary

Installed in coal, Borehole pressure cell (BPC) internal pressure is shown to depart from the data reduction methods of Lu and Babcock for indicating stress change in the coal. The probable reason is that the instrument becomes a hard inclusion in a nonlinear medium. Small pressure change at close to setting pressure is likely indicative of stress change, and therefore, the instrument is effective for sensing the first arrival of mining-induced abutment stress.

Background

Borehole pressure cells (BPCs) have been used in many coal mines to measure change of stress resulting from mining. It is not always clear how successful or accurate those measurements have been in reflecting change of stress in the coal at the point of installation.

Panek and Stock [1964b] did some experimental work in a limestone mine, developing a technique to measure absolute stress and stress change at the rib with BPCs, large flatjacks, and sensors. In the technique, they set the pressure in a pair of BPCs, and then relieved vertical stress by cutting a slot above the BPCs. The large flatjacks were encapsulated in cement in these slots and pressurized until the fluid pressures in the BPCs were returned to their pre-stress-relief values. The pressure in the large flatjack was then considered to be the earth pressure in the direction perpendicular to the large flatjack.

About the same time, encapsulated BPCs were tested by Miller and Sporcic [1964a] in coal. However, the response of the instruments was not clear, although the instruments did seem to respond in some fashion to mining-induced stress increase, bumps, roof events, and rib falls.

Wright et al. [1979] advocated using response tests to determine the relationship between rock (or coal) pressure and the cell pressure. However, they noted that when the cells were pressurized well over the in situ stress, that fractures formed in line with the cell bladder. Thus, as stress increased, the cell pressure increased substantially more than the stress increase in the surrounding rock because of the area it was supporting. This lesson was learned by the authors and expressed by others in personal communications. As a result, the standard practice of setting installation pressure only slightly above in situ stress—often about 10% above—in the direction perpendicular to the bladder was used. This practice allows the cell to bleed off slightly as seating occurs so that the cell pressure becomes close to the in situ amount of stress.

Several calibration methods have been developed for BPCs and a similar instrument, called the Borehole Platened Flatjack (BPF) [Sellers 1970; Bauer et al. 1985; Heasley 1989], but these methods have relied on linear-elastic theory of the host medium, and it is doubtful that coal behaves linearly.

Two methods of calibration were developed in the 1980s that deserve further consideration, even though neither method considers the possibility of coal loading outside its elastic range. Lu [1984] developed a way to determine absolute stress and stress change using three cells: (1) a cylindrical pressure cell (CPC) placed in a hole of 38.0-mm (1.50-in) diameter (EX hole), which is drilled at the end of a BX hole [60-mm (2.36-in) diameter]; (2) a flat bladder [borehole pressure cell (BPC) made of 1.52-mm (0.060-in) steel that is 20.3 cm (7.99 in) in length, 5.08 cm (2.00 in) wide, and 8.9 mm (0.35 in) high, and encapsulated in a cylinder of Portland cement that is 59.3 mm (2.33 in) in diameter] that is oriented in the BX borehole so that the plane of the

bladder is perpendicular to the vertical direction; and (3) another BPC placed in the BX borehole near the other two instruments and oriented such that its plane is perpendicular to the horizontal direction. This calibration method, which will be described later in this appendix in more detail, relies on a linear relationship between the cell pressure and changes in rock stress, and is, therefore, dependent on linear-elastic behavior of the host coal. Equilibrium pressures of the three gauges at various points in mining history are used to determine absolute stress in the directions perpendicular to the two BPC bladders.

The second method, developed by Babcock [1986] is a nonlinear method that depends on setting pressure and changes relative to that setting pressure. The sensitivity of change in cell pressure to host material stress change is dependent on host material elastic properties, but this sensitivity varies according to setting pressure and subsequent amounts of cell pressure, such that cell pressure changes at higher absolute pressure indicate lower host material pressure changes than does the equivalent cell pressure change at lower absolute pressure. This method is also outlined in more detail later in this appendix. In a laboratory setting, Babcock tested the cell in several elastic materials, covering a wide range of elastic moduli. However, coal was not one of the materials tested, and all tests were conducted at pressures that did not exceed the elastic limit of the host material. Even so, Babcock's tests appear to capture nonlinear behaviors such as that resulting from changing contact area as pressure changes. Caution must be exercised because, again, coal may not behave linearly in its elastic range because of various discontinuities (e.g., cleats and joints) that close with increasing stress. Moreover, the calibration method does not hold if the coal is loaded beyond its elastic range.

Knowing that coal often behaves in a nonlinear fashion and that interaction between the cell, cement, and host material was nonlinear, Su and Hasenfus [1990] conducted a laboratory study and a numerical modeling (finite element) study of what they termed the K-factor—i.e., the ratio of cell pressure change to external pressure change. First, they conducted laboratory experiments with the cell in a nylon block. With a numerical model using gap elements, they were able to reproduce the measured response of the cell versus the loading and unloading of the block very well. In their model, they used elasto-plastic, strain-hardening, plane-stress elements for steel and concrete. A Mohr-Coulomb yield criterion [Jaeger and Cook 1976] was used for the concrete and a von Mises yield criterion [Fung 1965] was used for the steel. After simulating the laboratory experiments, these researchers conducted numerical experiments with their model for coal having a modulus of 1.103 GPa (160,000 psi) and having elastic-perfectly plastic behavior with a Drucker-Prager yield criterion [Drucker and Prager 1952]. Su and Hasenfus [1990] reported the changing contact area between the cement and the borehole wall with increasing stress, adding to the nonlinearity of the K-factor. Figure F1 shows how the K-factor, calculated with model results, varied nonlinearly with setting pressure and increasing external stress. The results of Su and Hasenfus [1990] confirm the nonlinear nature of the geometry, which is also captured in some measure by the Babcock method. However, the representation of elastic coal behavior by Su and Hasenfus [1990] still needs to be confirmed. Moreover, even if their representation is accurate for a particular coal type, more experiments are needed on a wide variety of coal types to develop equations to represent a wider range of response. Validation of post-yield behavior of the coal and its effect on the BPC must also be confirmed and validated.

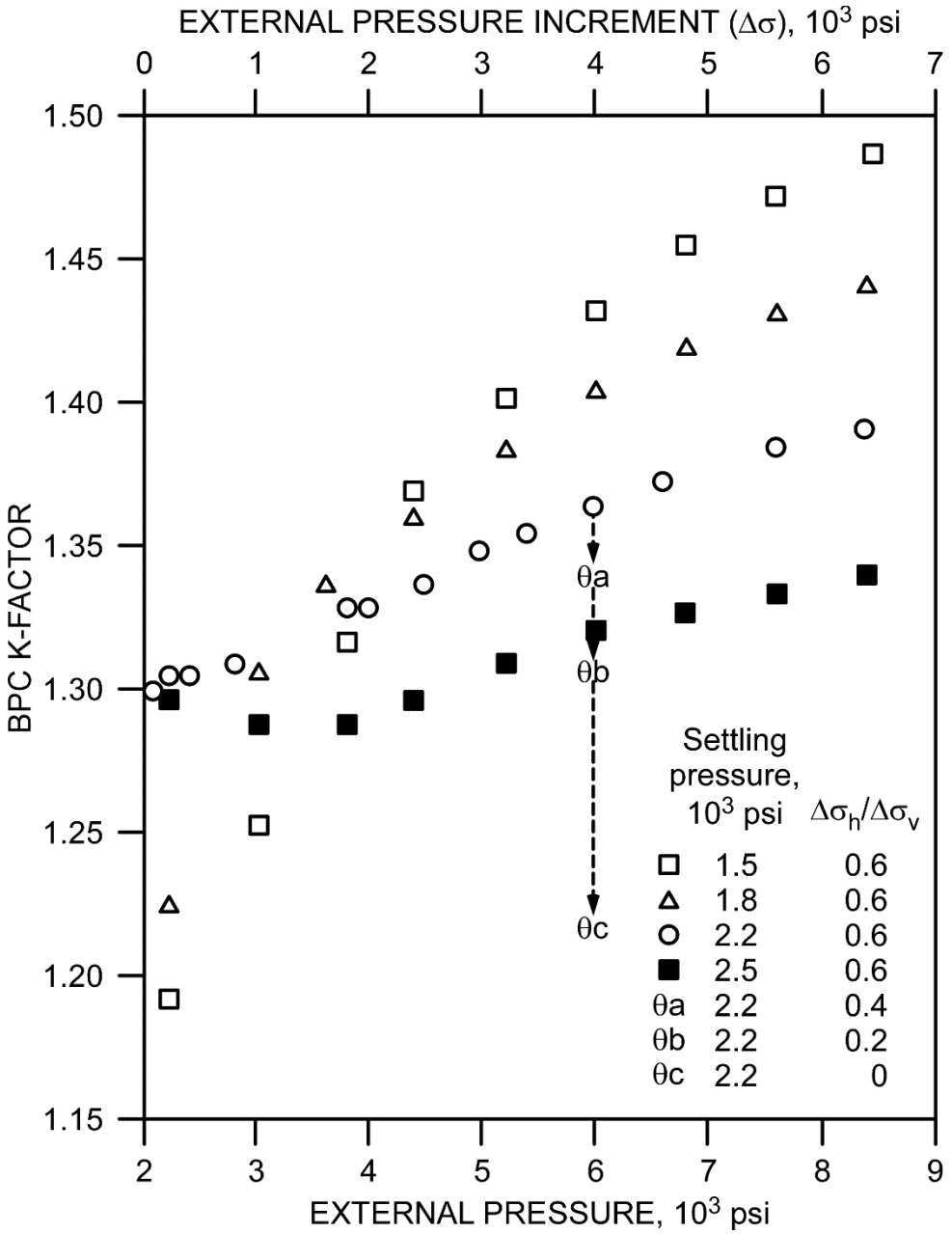

Figure F1. The borehole pressure cell (BPC) K-factor determined with a finite element model of a coal having Young's modulus of 1.103 GPa (160,000 psi). After Su and Hasefus [1990]. $\Delta\sigma_h/\Delta\sigma_v$ is the ratio of externally applied change in horizontal stress to change in vertical stress. The successive positions of θ_a, θ_b, and θ_c, show the effect of reducing the horizontal confinement where setting pressure and applied vertical stress change remain constant.

Examples of BPC use in studies by the Bureau of Mines are DeMarco et al. [1988], Barron [1990], Barron et al. [1994], Barron and DeMarco [1995], and Koehler et al. [1996]. However, in these studies, the raw, relative cell pressure data was used to characterize the timing of loading and relative loads by location [DeMarco 2013]—no data reduction method was used.

Because the Lu and Babcock methods are comprehensive in nature, the theory of each is described in this appendix.

Lu Method

Lu [1984] derived equations for BPC calibration based on elastic theory of plates and thick-walled cylinders, in addition to application of the elastic and viscoelastic correspondence principle. These equations are

$$N_H + N_V = \frac{P_{e-CPC}}{1-\nu}, \text{ and} \tag{F1}$$

$$\frac{N_H}{N_V} = \frac{\left(P_{e-BH}/P_{e-BV} - S\right)}{\left[1-\left(P_{e-BH}/P_{e-BV}\right)S\right]}, \tag{F2}$$

where N_H = horizontal ground pressure,

N_V = vertical ground pressure,

P_{e-CPC} = pressure of the CPC at equilibrium,

ν = Poisson's ratio of the rock mass (or coal),

P_{e-BH} = horizontally oriented (i.e., the normal to its plane is horizontal) BPC pressure at equilibrium,

P_{e-BV} = vertically oriented BPC pressure at equilibrium, and

S = transverse sensitivity of the BPC, which is 0.185, as calculated from the geometry of the BPC that the U.S. Bureau of Mines developed. Transverse sensitivity is a measure of the effect of an increase in stress in the direction perpendicular to the normal direction of the flatjack bladder on the increase in cell pressure.

Changes in pressure are obtained by calculating absolute pressures from the cell readings both before and after mining-induced loading and noting the differences. For each set of cell pressures, the equilibrium must be established during periods when active mining is far enough away so that its effect on load changes of the cells is insignificant.

Other researchers [Vandergrift and Conover 2010], in order to use only vertically oriented BPCs so that more vertical stress measurements can be made (three cells per borehole is the maximum for pre-encapsulated flatjacks), have assumed a relationship between the horizontal and vertical ground stresses. They assumed that

$$\frac{N_H}{N_V} = \frac{\nu}{1-\nu}. \tag{F3}$$

By rearranging Equation F2,

$$P_V = \left(\frac{P_H}{N_H + S\,N_V}\right)(N_V + S\,N_H) \text{ or} \tag{F4}$$

$$P_V = w(N_V + S\,N_H), \tag{F5}$$

where

$$w = \frac{P_H}{N_H + S\,N_V}, \tag{F6}$$

and w is called the response factor, which Vandergrift and Conover [2010] stated is 1.095 for coal. At Poisson's ratio of 0.38 that Vandergrift and Conover used, the ratio of horizontal cell pressure to horizontal ground stress had to be constant at 1.426. Vandergrift and Conover do not cite the source of the response factor that they used. Even so, if their value for w is valid, then the assumption of Equation F3 can be applied so that

$$P_V = w\left[1 + \frac{\nu}{1+\nu}\right] N_V. \quad \text{(F7)}$$

Using the Poisson's ratio of Vandergrift and Conover, the cell pressure would be converted to ground pressure by multiplying it by 0.820, which is $\frac{1}{w}$. In the case of Mine A (the same site), the authors used a Poisson's ratio of 0.33, and the constant for conversion to ground pressure was 0.837.

Although it is advantageous to orient all cells in the vertical direction for stress change profiling, the assumption of Equation F3 must be evaluated in each case. The assumption may not be valid, and therefore introduce error into the stress change calculation. The validity of this assumption may even vary by cell location. For example, confinement near a rib would be different from that in the middle of a pillar.

Babcock Method

Babcock performed laboratory work with BPCs in several materials with wide ranging elastic properties. His experiments showed the transverse sensitivity (N_H/N_V), to be an average of -0.333, which differs from the finding of Sellers [1970] (-0.06) and those of Lu [1984] (-0.185). In his tests of Plexiglas, oil shale, potash, concrete, limestone, sandstone, and granite, Babcock noted the fraction of pressure change of the instrument compared to change of radially applied rock pressure ($\Delta\sigma_{BPC}/\Delta N_R$) and plotted that ratio with setting pressure of the BPC (σ^*_{BPC}). He fit a linear equation to the results for each material:

$$\frac{\Delta\sigma_{BPC}}{\Delta N_R} = m\,\sigma^*_{BPC} + b. \quad \text{(F8)}$$

The slope, m, was also calculated with the intercept, b, set to 0.

Hanna et al. [1991] fit a nonlinear equation to estimate m with dependent variables being Young's modulus and Poisson's ratio. Their equation is

$$m = 4.238\left[\frac{1-\nu^2}{E}\right]^{(2/3)}, \quad \text{(F9)}$$

where E = Young's modulus of the host material, and
ν = Poisson's ratio of the host material.

Vandergrift and Conover [2010] appear to misstate the constant in this equation as 4.348, but both constants give reasonably close approximations to Babcock's data. The authors of this report used the constant listed by Vandergrift and Conover [2010].

Babcock's results fit the equations

$$\Delta N_V - \frac{\Delta N_H}{3} = \frac{1}{m}\, ln\left[\frac{P_V}{P^*_V}\right], \text{ and} \quad \text{(F10)}$$

$$\Delta N_H - \frac{\Delta N_H}{3} = \frac{1}{m}\, ln\left[\frac{P_H}{P^*_H}\right], \quad \text{(F11)}$$

where P^*_V = setting pressure of the vertically oriented cell, and
P^*_H = setting pressure of the horizontally oriented cell.

From these equations, we can determine

$$\Delta N_V = \frac{3}{8m}\, ln\left\{\left[\frac{P_V}{P_V^*}\right]^3 \left[\frac{P_H}{P_H^*}\right]\right\}. \quad \text{(F12)}$$

Equation F12 differs in the constants on the right side of the equation from those in the corresponding Equation 6 of Babcock [1986] and with corresponding equations outlined by Hanna et al. [1991] in their Appendix C. The authors' Equation F12 is confirmed by Vandergrift and Conover [2010].

Using the assumption of Equation F3[7], it follows that the cell pressure ratios would change proportionally in the same way as the rock stresses—that is

$$\frac{P_H}{P_V} = \frac{P_H^*}{P_V^*} = \frac{\nu}{1-\nu} \quad \text{(F13)}$$

Then Equation F12 can be written as

$$\Delta N_V = \frac{3}{8m}\, ln\left\{\left[\frac{P_V}{P_V^*}\right]^4\right\}. \quad \text{(F14)}$$

This equation can then be used to indicate change in vertical stress. In this study, when the Babcock method was used for analysis, the initial stress at a cell location was estimated to be the initial cell pressure—not necessarily the precise setting pressure, but the first logged measurement, which was then treated like a setting pressure for purposes of analysis. Admittedly, the absolute measured stresses calculated in this manner are unlikely to be correct, but this procedure provides reasonable estimation of absolute stress for the purpose of graphical display versus advance of the panel face. Such curves can easily be plotted alongside stress calculated with numerical models at BPC locations as the face advances. However, the objective is to compare changes in stress and not absolute amounts of stress with face advance.

Application of Calibration Methods to BPC Data at Mine A

The earlier survey of the literature in this study underlines the lack of thorough investigation of BPC calibration in various coals. The authors of this report prefer the Babcock method because of its nonlinear nature, but they concede that it has no validity beyond the elastic range of coal and that there is some question about its validity in coal, since it is based entirely on testing other materials only in their elastic range. Results like those of Su and Hasenfus [1990] would likely be preferable, but their study was not comprehensive enough to develop general calibration equations.

For these reasons, Equation F14 was applied as described above to BPC raw pressure measurements. These measurements were correlated to distance from the line of instruments to the face, that distance being negative when the face was inby the instruments and plotted versus face distance. These measurement data are described in detail by Larson et al. [NIOSH 2020]. In this appendix, we also show results of applying the Lu calibration method to the BPC raw pressure measurements for comparison.

[7] Recall the earlier discussion about validity of this assumption and the need to evaluate whether it holds in any particular case and cell location. The same concerns apply here.

Modeled Stress Transfer With and Without Gob

Earlier in the main body of this report, plots show the BPC measurements (reduced by the Babcock method) compared to stress histories at BPC locations interpolated from output stresses of various models. In most cases, unless the instrument failed or the coal yielded, the measured stresses became much higher than what the models predicted as the face approached and passed the line of instruments.

As detailed in the main body of this report, the best Mulsim model for predicting stress appeared to be the elastic case with coal modulus reduced to 60% and 80% of the full amount in the outer first and second rings of elements, respectively. For that reason, this model was used to evaluate the validity of the amounts of stress changes measured with BPCs at Mine A.

The elastic model with reduced moduli in the outer two rings was modified so that no gob was present. In other words, all weight of overburden over the mined panel was transferred to the abutments. This model was used to calculate upper bounds for stress changes at instrument locations resulting from mining of Panel 1. These upper bounds, calculated for various face positions with respect to the instrument lines, were compared with measurements reduced by the Lu and Babcock methods.

Figures F2 and F3 show what stress changes had taken place at the 1 North outby and 2 North outby sites, respectively, when the face was at various distances inby each site's instrument line. Measurements of stress change as determined by Lu [1984] and Babcock [1986] are shown along with the Mulsim results using the reduced coal modulus near the ribs, both with and without gob. The green (or olive) results—without gob—show what should be upper bounds to the BPC measurements. The BPC results, especially as the face approaches each site's instrument line, were well above what is estimated to be physically possible.

Obviously, neither the Lu nor the Babcock calibration methods hold up at higher stress. The trends of stress increase and where those increases occur are not suspect, but the calibration methods of Lu [1984] and Babcock [1986], based on linear-elasticity for the host medium, do not appear to be valid in this case.

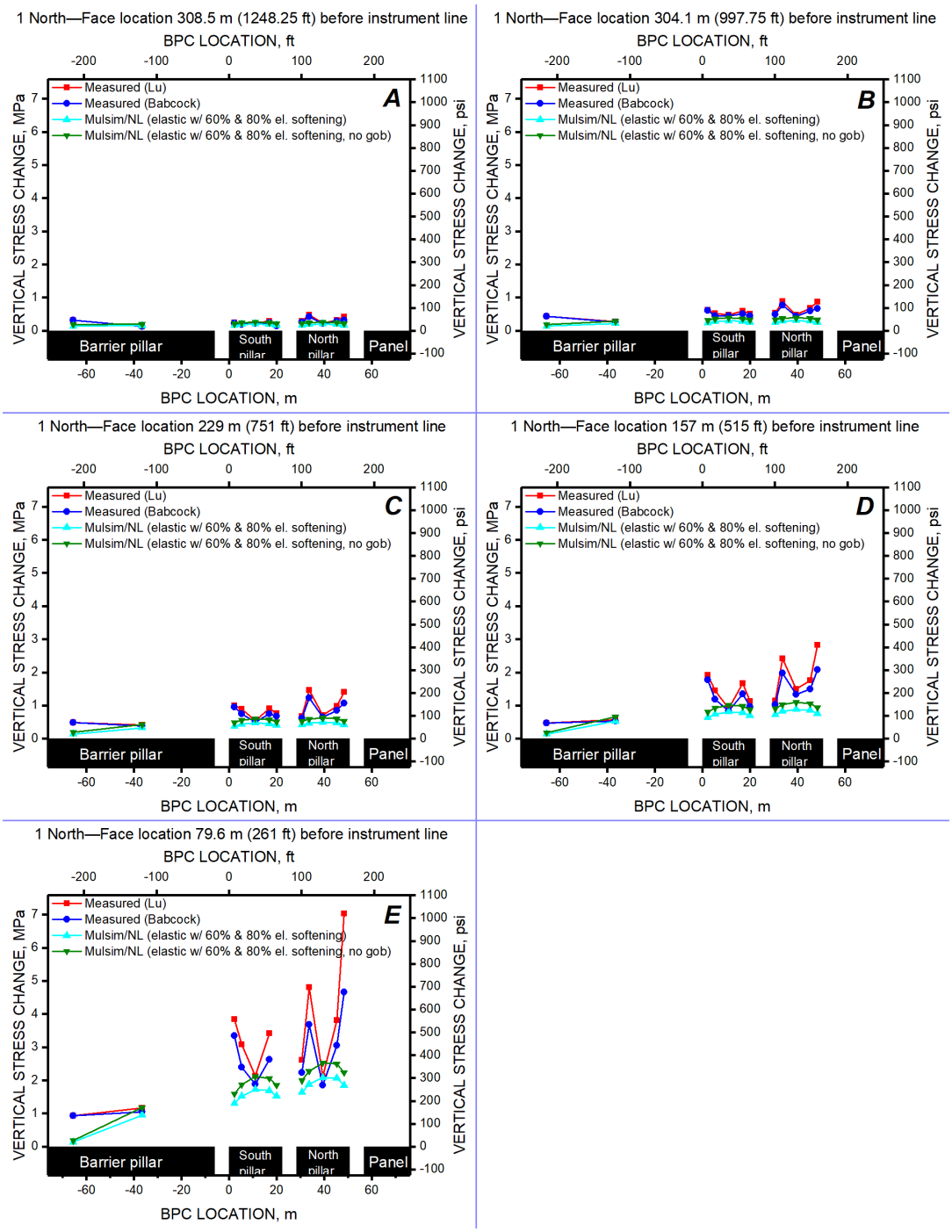

Figure F2. BPC stress change measurements compared to MulsimNL/Large stress change calculations at the 1 North outby site when face was inby the instrument line by several approximate distances: *A*, 381 m (1250 ft); *B*, 305 m (1000 ft); *C*, 229 m (750 ft); *D*, 152 m (500 ft); and *E*, 76 m (250 ft). Only those instruments that met the criteria to be used for LTD measurements [Larson and Whyatt 2012] are shown.

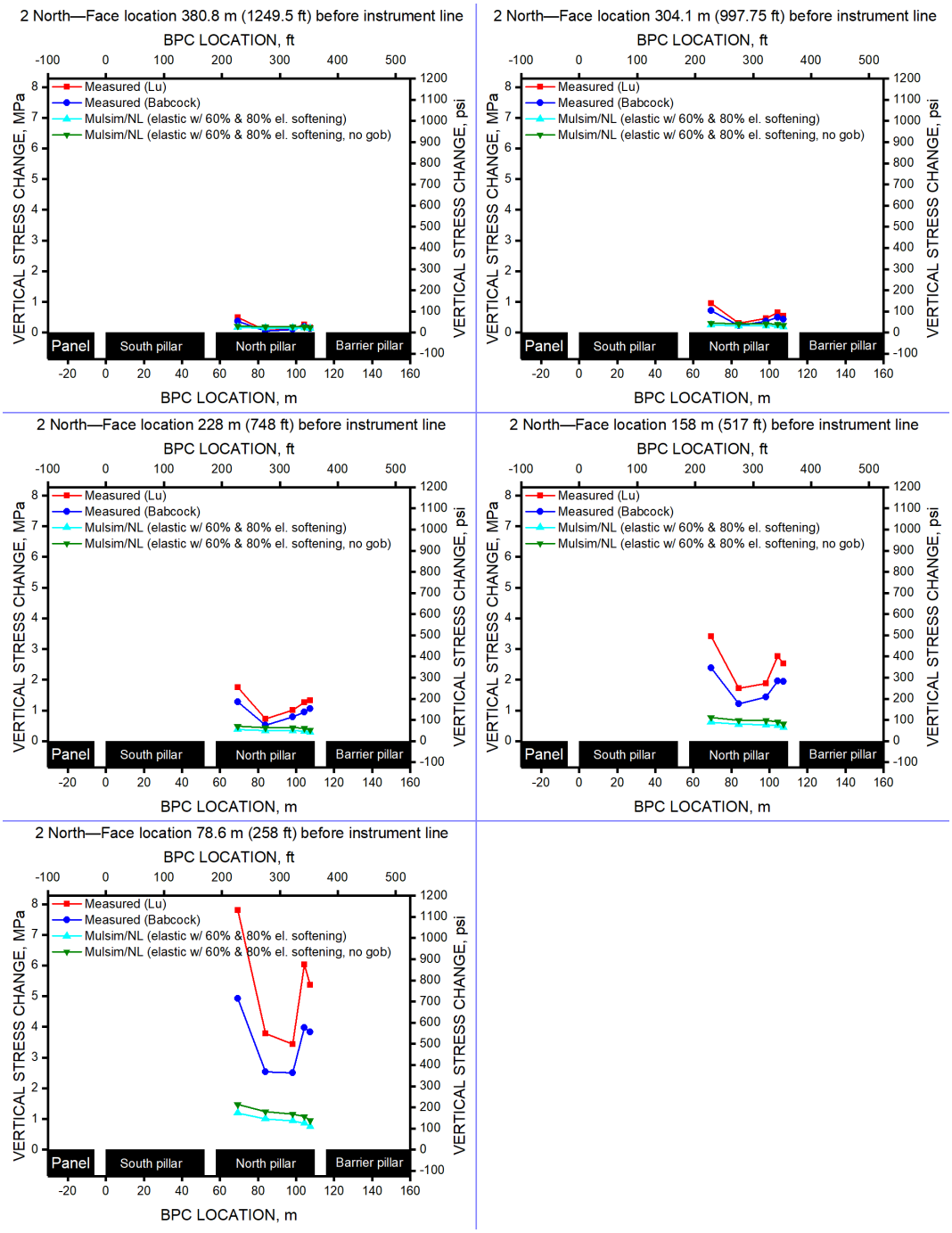

Figure F3. BPC stress change measurements compared to MulsimNL/Large stress change calculations at the 2 North outby site when face was inby the instrument line by several approximate distances: *A*, 381 m (1,250 ft); *B*, 305 m (1,000 ft); *C*, 229 m (750 ft); *D*, 152 m (500 ft); and *E*, 76 m (250 ft). Only those instruments that met the criteria to be used for LTD measurements [Larson and Whyatt 2012] are shown.

Adjustments

Presumably, as stress increases near a BPC, the instrument acts increasingly as a hard inclusion. Rising load, then, increasingly seeks the path of most resistance. Two causes of this phenomenon could be: (1) the failure and deterioration of the coal near the instrument affecting the calibration and (2) the nonlinear-elastic nature of some or most coals.

For the first cause, simulation of coal deterioration might be represented roughly by a decrease in Young's modulus with increasing cell pressure and implemented in Equation F9. For the second cause, the increased nonlinearity might be approximated in some fashion by increasing the constant in Equation F9. These two methods are not good mechanistic representations, but they allow exploration of these concepts and help quantify, in some sense, the degree of change in calibration necessary to account for the effect.

Young's Modulus Adjustment and Results

Figures F2 and F3 show that generally, the nonlinearity of BPC response increases with proximity to the rib and decreases in the center of the pillars. Such response correlates approximately with the degree of confinement and strongly suggests that post-peak strength deterioration of the coal plays a significant role in the increase of nonlinear response.

Trial and error was used to develop a target deterioration of Young's modulus with increasing BPC pressure. The target modulus-versus-BPC-pressure response and a curve from a fitted continuous equation used to represent that response are shown in Figure F4. There is little expectation that Equation F9 holds under such conditions. However, it is used as a vehicle to explore a sense of the yielding involved, as represented by the deterioration of Young's modulus.

Figures F5 and F6 also show the ground stress response recalculated from softening of Young's modulus. In both 1 North and 2 North, these curves were below the curve of upper range of possible responses and were reasonably near the Mulsim result with gob.

The stress-changes determined from the raw cell pressures with these modified Lu and Babcock equations were not only below the upper limits determined with the no-gob model, but they were near the results of the Mulsim model with gob. However, the amount of deterioration in modulus required to bring about these calculated results was, in the opinion of the authors, more than is reasonable, suggesting that more than just coal yielding is responsible for the degree of nonlinearities.

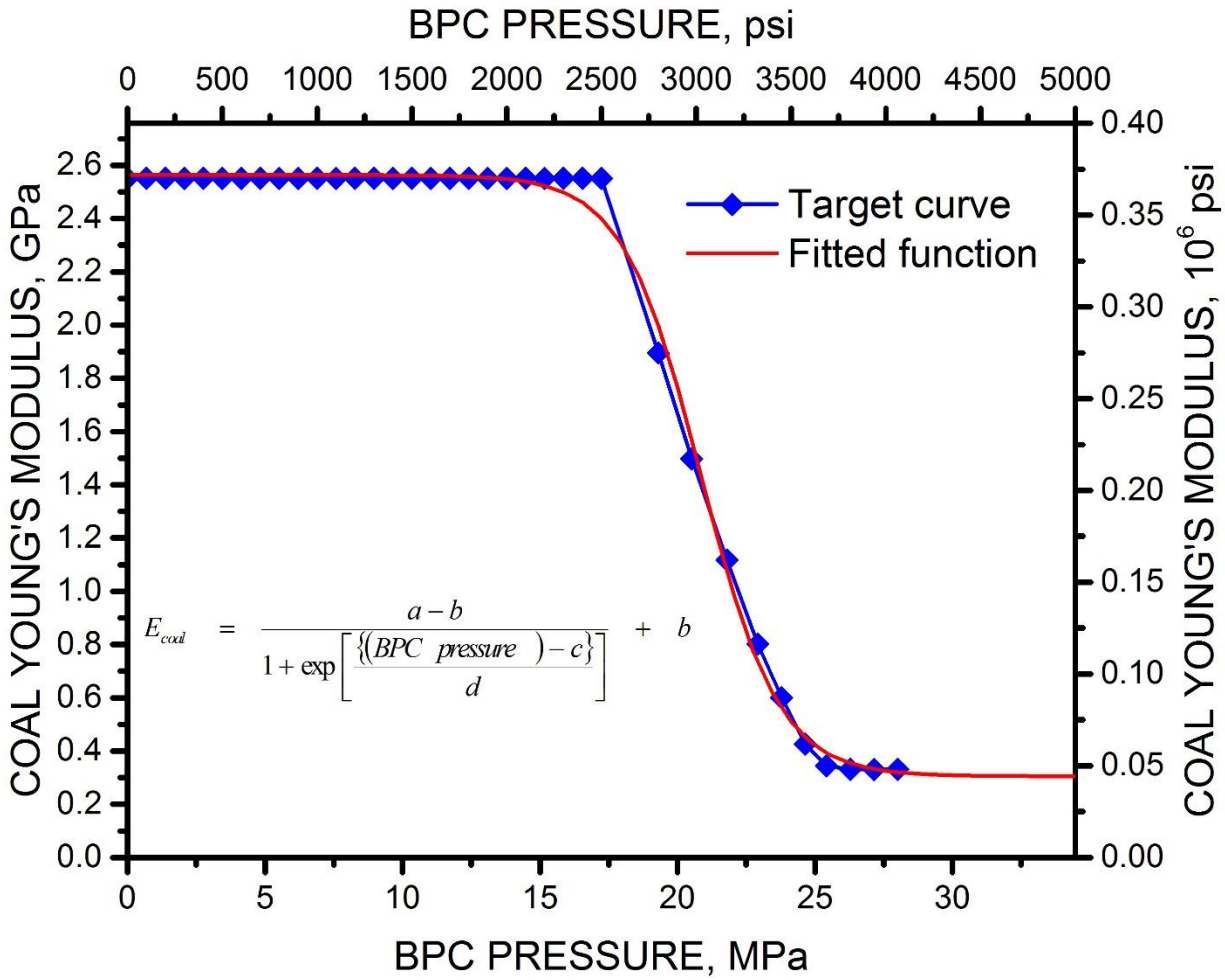

Figure F4. Target and fitted curve for deterioration of Young's modulus of coal to simulate the effect of coal deterioration on the response of the instrument.

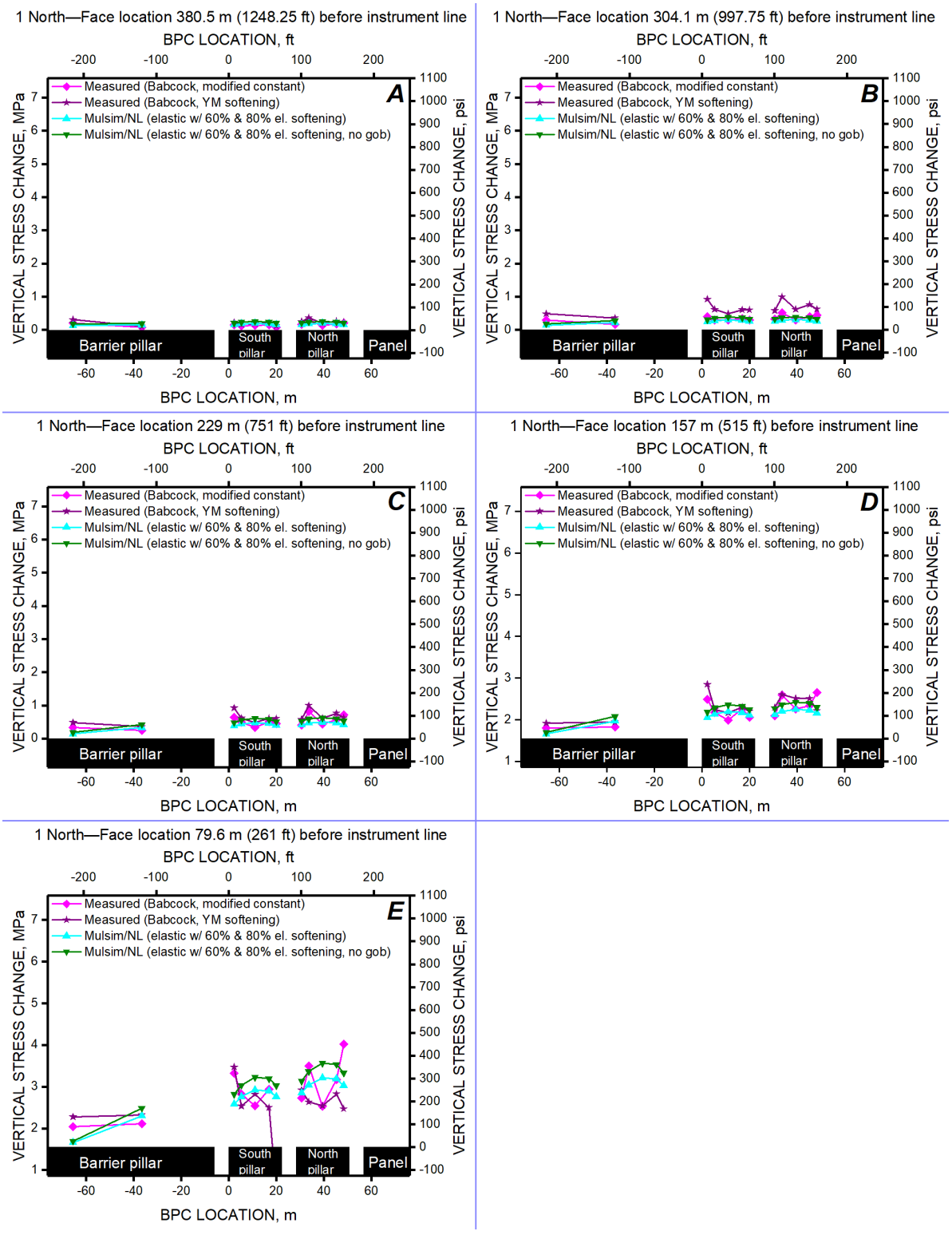

Figure F5. Recalculated BPC stress change measurements (by modifying a nonlinearity constant, and by Young's modulus softening) compared to MulsimNL/Large stress change calculations at the 1 North outby site when face was inby the instrument line by several approximate distances: *A*, 381 m (1,250 ft); *B*, 305 m (1,000 ft); *C*, 229 m (750 ft); *D*, 152 m (500 ft); and *E*, 76 m (250 ft).

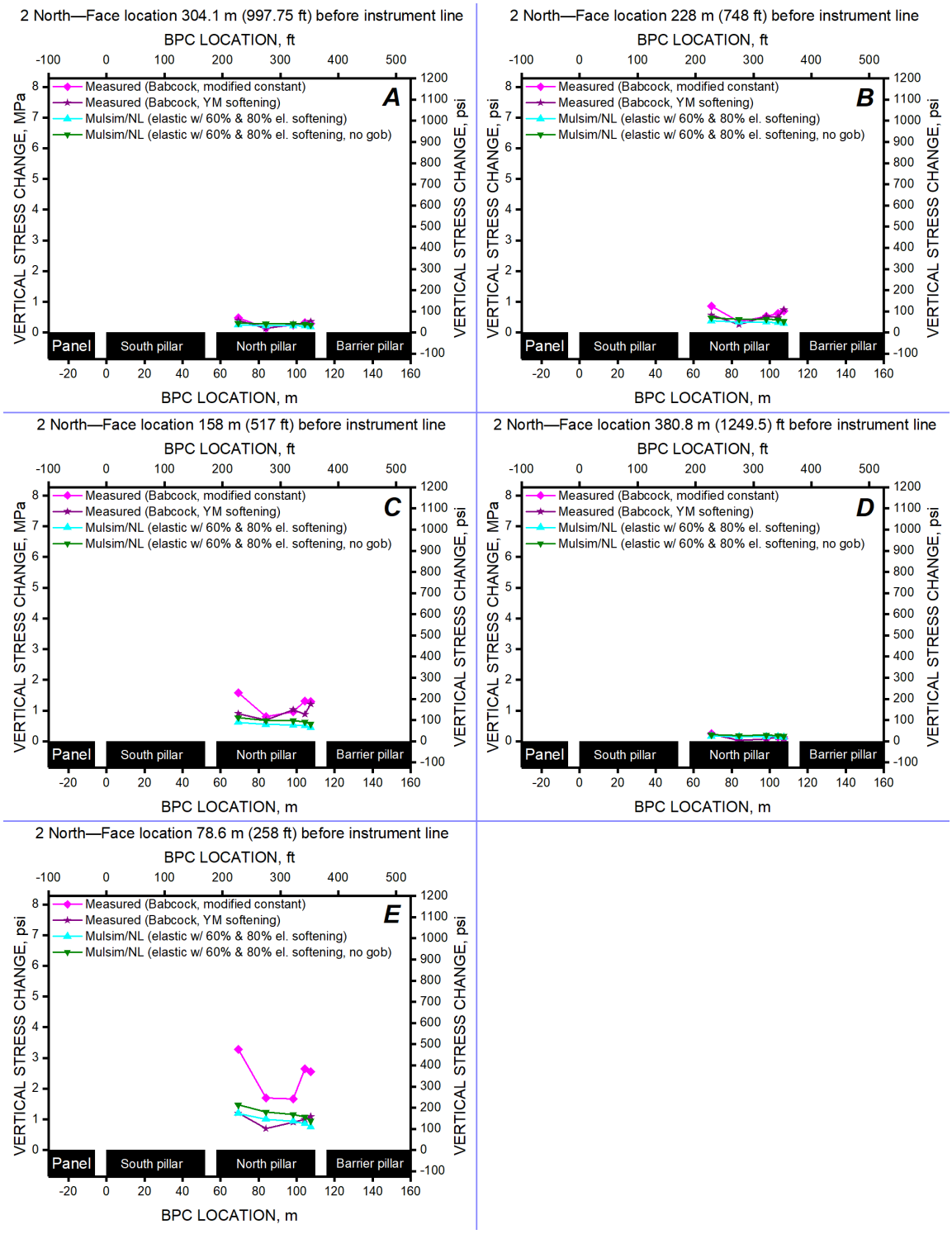

Figure F6. Recalculated BPC stress change measurements (by modifying a nonlinearity constant, and by Young's modulus softening) compared to MulsimNL/Large stress change calculations at the 2 North outby site when face was inby the instrument line by several approximate distances: *A*, 381 m (1,250 ft); *B*, 305 m (1,000 ft); *C*, 229 m (750 ft); *D*, 152 m (500 ft); and *E*, 76 m (250 ft).

Calibration Constant Adjustment and Results

The constant in Equation F9 was changed to 7.538, representing an increase of over 73% above the constant previously used. This increased the calculated nonlinear response considerably. Figures F5 and F6 compare the recalculated ground stress response (labeled "Babcock, modified constant") to the best Mulsim model and the Mulsim model with no gob (the latter representing an upper limit of range of BPC response). The recalculated measured stress was mostly brought within the curve of upper range of possible responses, as calculated by Mulsim, at the 1 North site, but it was still outside that upper range in 2 North. This fact supports drilling observations that coal in 2 North might be weaker than in 1 North.

Conclusions

The Lu [1984] and Babcock [1986] BPC calibration methods, modified for the use of vertically oriented BPCs only, were inadequate for reasonable calculation of stress change in coal at Mine A in this study. The calculated stress changes were higher than was possible, determined by comparing to stress change calculated with a model having no overpanel weight transmitted through the gob, thus representing an upper limit of stress change possible. This comparison was done when the face was at various distances inby the line of BPCs. Among probable causes for the calibrations being inadequate are the nonlinear nature of coal in its elastic range and deterioration of the coal resulting from yielding and post-yield behavior. The cell appeared to act as a hard inclusion in a softening host material such that increased load was concentrated through the instrument. These effects appeared to increase with higher mining-induced stress.

Recommendations

The authors recommend further research to determine the nature of the behavior of various coals, both in the elastic and post-yield ranges. Without that information, calibrations can only be based on assumptions of coal behavior.

Moreover, the authors recommend that the borehole pressure cell and other comparable instruments (e.g., the biaxial stressmeter), be tested under various conditions in both the laboratory and the field. In parallel, the numerical experimental work of Su and Hasenfus [1999] should be expanded to include a wide range of coal behaviors, particularly as more is learned about the behavior of various coals. Improved calibration methods should result from such studies. Subsequently, these methods should be applied and be subject to further evaluation.

References for Appendix F

Babcock CO [1986]. Equations for the analysis of borehole pressure cell data. In: Hartman HL ed., Rock Mechanics: Key to Energy Production, Proceedings of the 27th U.S. Symposium on Rock Mechanics. (Tuscaloosa, AL: June 23–25, 1986) Littleton, CO: Society of Mining Engineers, pp. 233–240.

Barron L, R. [1990]. Longwall stability analysis of a deep, bump-prone western coal mine—case study. In: Peng SS ed., Proceedings: 9th International Conference on Ground Control in Mining. (Morgantown, WV: June 4–6, 1990) Morgantown, WV: University of West Virginia, pp. 142–149 pp.

Bauer ER, Ghekan GJ, Hill JC [1985]. A borehole instrument for measuring mining-induced pressure changes in underground coal mines. In: Ashworth E ed., 2, Research & Engineering Applications in Rock Masses: Proceedings of the 26th U.S. Symposium on Rock Mechanics. (Rapid City, SD: June 26–28, 1985) Rotterdam: A. A. Balkema, pp. 1075–1084.

DeMarco MJ [2013]. BPC data reduction. E-mail, Personal communication to Larson MK, May 25, 2 pp.

DeMarco MJ, Koehler JR, Lu PH [1988]. Characterization of chain pillar stability in a deep western coal mine—a case study. Mining Eng., Vol. 40, No. 12, pp. 1115–1119.

Drucker DC, Prager W [1952]. Soil mechanics and plastic analysis for limit design. Q Appl. Math., Vol. 10, No. 2, pp. 157–165.

Fung YC [1965]. Foundations in solid mechanics, Englewood Cliffs, NJ: Prentice-Hall, Inc., 549 pp.

Heasley KA [1989]. Understanding the hydraulic pressure cell. In: Khair AW ed., Rock Mechanics as a Guide for Efficient Utilization of Natural Resources: Proceedings of the 30th U.S. Symposium. (Morgantown, WV: June 19–22, 1989) Rotterdam: A. A. Balkema, pp. 485–492 pp.

Jaeger JC, Cook NGW [1976]. Fundamentals of rock mechanics. 2nd ed., New York: John Wiley & Sons, Inc., 604 pp.

Koehler JR, DeMarco MJ, Marshall RJ, Fielder J [1996]. Performance evaluation of a cable bolted yield-abutment gate road system at the Crandall Canyon No. 1 Mine, Genwal Resources, Inc., Huntington, Utah. In: Ozdemir L et al. eds. Proceedings: 15th International Conference on Ground Control in Mining. (Golden, Colorado: August 13–15, 1996) Golden, Colorado: Colorado School of Mines, pp. 477–495 pp.

Larson MK, Whyatt JK [2012]. Load transfer distance calibration of a coal panel scale model: A case study. In: Barczak T et al. eds. Proceedings of the 31st International Conference on Ground Control in Mining. (Morgantown, WV: July 31–August 2, 2012) Morgantown, WV: West Virginia University, pp. 195–205.

Lu PH [1984]. Mining-induced stress measurement with hydraulic borehole pressure cells. In: Dowding CH, Singh MM eds. Rock Mechanics in Productivity and Protection, Proceedings: Twenty-Fifth Symposium on Rock Mechanics. (Evanston, IL: June 25–27, 1984) New York, NY: Society of Mining Engineers, pp. 204–211.

NIOSH [2020]. Ground stress in mining (part 1): Measurements and observations at two western U.S. longwall mines. By Larson MK, Lawson HE, Zahl EG, Jones TH. U.S. Department of Health and Human Services, Centers for Disease Control and Prevention, National Institute for Occupational Safety and Health, DHHS (NIOSH) Publication No. 2019-175, RI 9702.

Sellers JB [1970]. The measurement of rock stress changes using hydraulic borehole gages. Int. J. Rock Mech. Min. Sci., Vol. 7, No. 4, pp. 423–435.

Su D, Hasenfus GJ [1990]. Intrinsic response of borehole pressure cells laboratory calibrations and nonlinear fem simulation. In: Peng SS ed., Proceedings: Ninth International Conference on Ground Control in Mining. (Morgantown, WV: June 4–6, 1990) West Virginia University, pp. 260–271.

Su DWH, Hasenfus GJ [1999]. Coal pillar strength and practical coal pillar design considerations. In: Mark C et al. eds. Proceedings of the Second International Workshop on Coal Pillar Mechanics and Design. (Vail, CO: June 6, 1999) Pittsburgh, PA: U.S. Department of Health and Human Services, pp. 155–162.

USBM [1964a]. Development of a hydraulic device for measuring relative pressure changes in coal during mining: A progress report. By Miller TC and Sporcic R. Report of Investigations 6571, Pittsburgh, PA: U.S. Department of the Interior, Bureau of Mines (USBM), 16 pp.

USBM [1964b]. Development of a rock stress monitoring station based on the flat slot method of measuring existing rock stress. By Panek LA and Stock JA. Report of Investigations 6537, Pittsburgh, PA: U.S. Department of the Interior, Bureau of Mines (USBM), 66 pp.

USBM [1991]. Coal mine entry intersection behavior study. By Hanna K, Conover D, Haramy KY. Report of Investigations 9337, Pittsburgh, PA: U.S. Department of the Interior, Bureau of Mines (USBM), 84 pp.

USBM [1994]. Longwall gate road stability in four deep western U.S. coal mines. By Barron LR, DeMarco MJ, Kneisley RO. Information Circular 9406, Pittsburgh, PA: U.S. Department of the Interior, Bureau of Mines (USBM), 94 pp.

USBM [1995]. Longwall gate road stability in a steeply pitching thick coal seam with a weak roof. By Barron LR, DeMarco MJ. Report of Investigations 9580, Pittsburgh, PA: U.S. Department of the Interior, Bureau of Mines (USBM), 37 pp.

Vandergrift T, Conover D [2010]. Assessment of gate road loading under deep western U.S. conditions. In: Mark C et al. eds. Proceedings: 3rd International Conference on Coal Pillar Mechanics and Design. (Morgantown, WV: July 26, 2010) Morgantown, WV: West Virginia University, pp. 38–46.

Wright FD, Howell RC, Dearinger JA [1979]. Rock mechanics study of shortwall mining. Contract No. U.S. D.O.E. ET-73-C-01-9010 (formerly U.S.B.M. H0133039), April 30, 1979, Lexington, KY, University of Kentucky, 288 pp.

Appendix G: Five-Point Stress-Strain Material Model Implemented in MulsimNL/Large

Summary

Borehole pressure cell (BPC) measurement histories, determinations of load transfer distance (LTD), and observations of relative strength during drilling of different seams in the geologic column at Mine A suggested that a more complicated law than was currently available in LaModel or MULSIM/NL was needed. Specifically, it appeared that strain hardening beyond a yield point followed by softening was required to produce the majority of the BPC pressure histories and the LTDs near each rib. As a result, a material strength model with multiple segments defined by five points of stress and strain was implemented in MulsimNL/Large. A verification problem with two mining steps in which a pillar is excavated was run using two existing material models: (1) the elastic coal model with the outer, and next-to-outer, rings of elements having the elastic modulus reduced to 60% and 80%, respectively, of the full elastic modulus; and (2) a Mark-Bieniawski 6.2-MPa (900-psi) coal [Mark and Chase 1997] with softening to a residual stress after the peak stress has been reached. The five-point material model was then used in each case to replicate the original material model. Any differences between the models were very small. Thus, the five-point material model was verified against existing implemented material models.

Background—Need for Five-Point Material Model

Larson and Whyatt [2012] measured LTD with borehole pressure cells (BPCs) at Mine A using, as a threshold for that distance detection, a 0.138-MPa (20-psi) increase in raw pressure of the cell. The measurements showed a fairly tight cluster of LTD distances from the face, even in the cases of BPCs located 2.3 m (7.5 ft) from the rib. Material strength models that implement linear elasticity to a peak, followed by elastic-plastic behavior, could not match this tight cluster of measured distances because the ribs were already yielded during development, so that further increase in stress was not possible. This is illustrated in Figure 30 of this report and is reproduced here as Figure G1 of this appendix. Moreover, some of the BPC histories shown elsewhere in this report suggested eventual softening near the ribs in some cases, but this behavior was not consistent, probably because of the variable nature of the coal. These results, along with drilling observations that this coal was relatively weaker than B-Seam coal, suggested that if yielding were implemented then there must also be significant strain hardening, which would likely be followed by strain softening to a residual stress. Such a strength curve might be implemented most simply with more linear segments on the strength-strain curve of a new constitutive model.

A five-point material strength model (model #7) was added to MulsimNL/Large. It is assumed that the first line segment begins at zero stress and zero closure strain. The last (fifth) point represents a residual stress and strain. For any additional closure strain, the strength remains at the residual stress. Figure G2 shows an example of such a material model. Table A2 and Table A3 in Appendix A indicate the format of input of these five stresses and strains, along with Poisson's ratio.

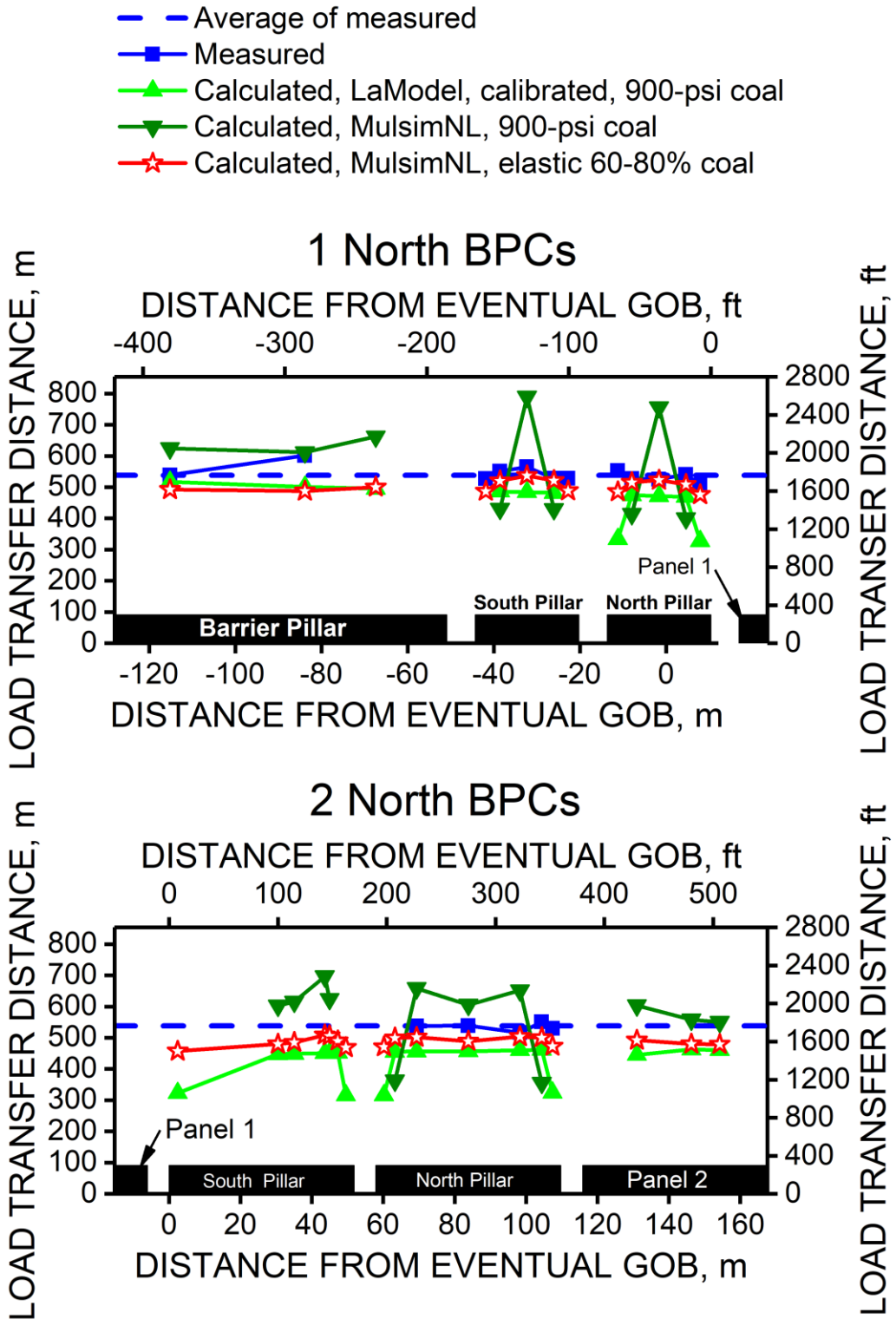

Figure G1. LTD determined from BPC pressure histories (measured) and from interpolation of model results.

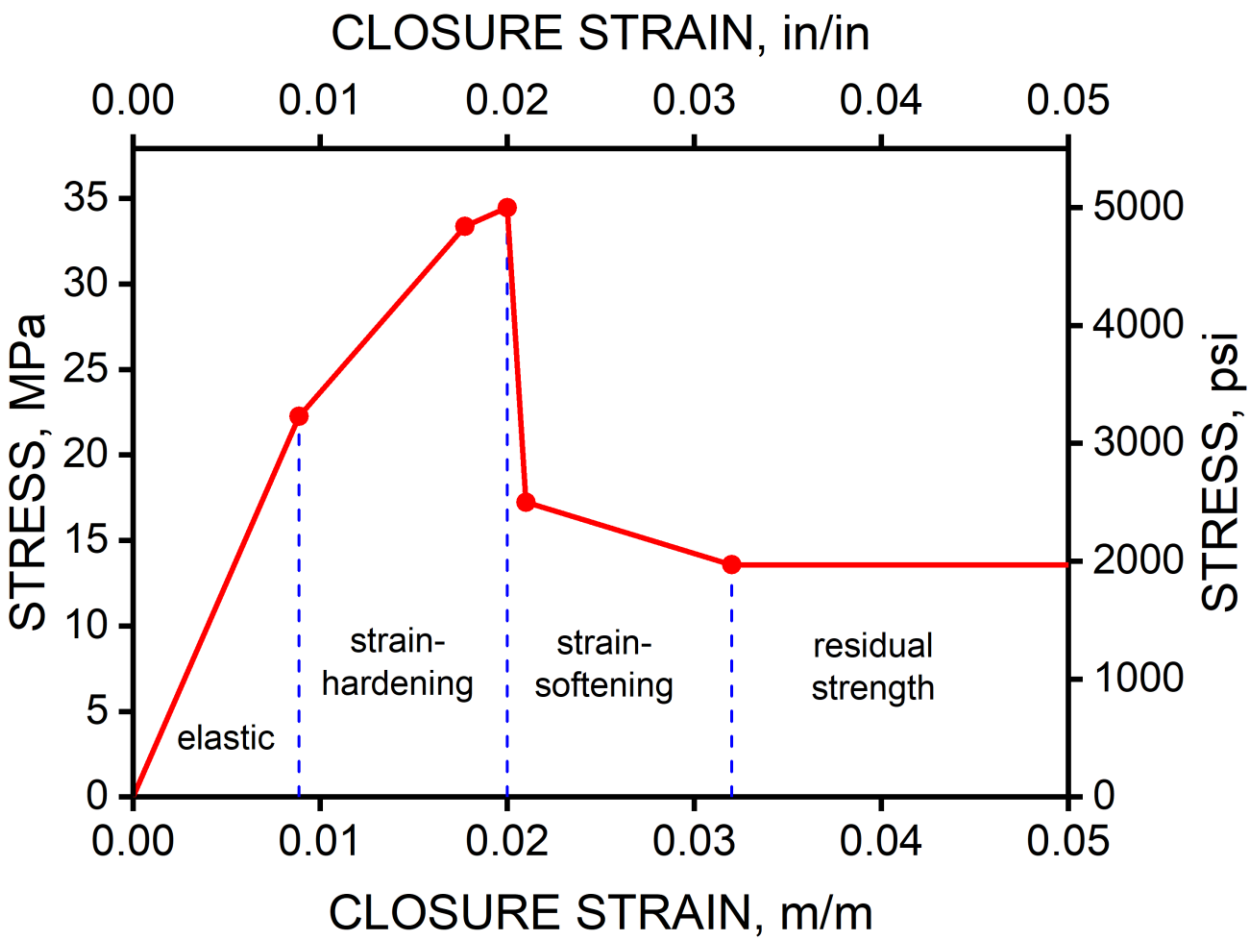

Figure G2. Example of five-point material strength model.

Verification Problems

Two verification problems were run to test the five-point material model against another model. Material models replicated with the five-point material model were the elastic model and the softening model, which has two points.

Figure G3 and Figure G4 show material codes for mining steps 1 and 2, respectively, of the example problem. The fine mesh is seen in the very center of the mesh, with no elastic codes (A). In the first mining step, three pillars are mined, although the upper and lower pillars are partial pillars in that crosscuts are not driven on the upper and lower sides of the fine mesh. Moreover, the lengths of these two partial pillars are shorter than the center pillar. In the second mining step, the center pillar is excavated and converted to gob.

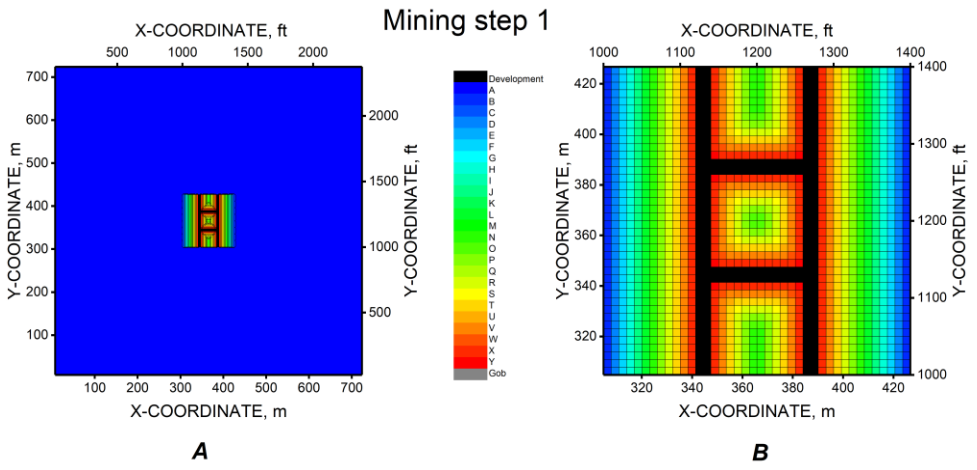

Figure G3. Material codes for mining step 1 of example model. *A*, Entire model; *B*, zoomed in to fine grid.

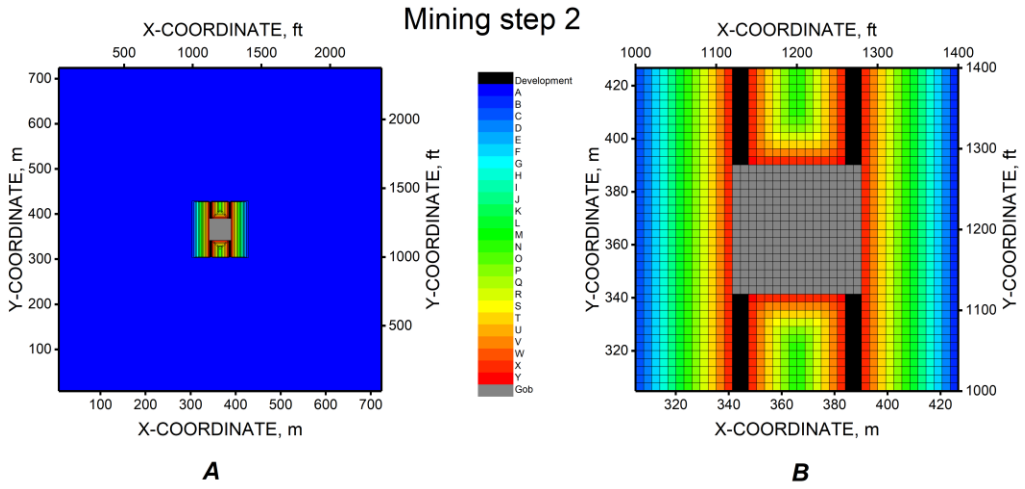

Figure G4. Material codes for mining step 2 of example model. *A*, Entire model; *B*, zoomed in to fine grid.

Elastic Problem

Success was achieved in modeling Mine A by reducing the elastic modulus in the outer ring of elements to 60% of full modulus and to 80% of full modulus in the next-to-outer ring of elements. Accordingly, a model was constructed for a small example, using elastic material for one model and replicating that law with the multipoint material having all five points along the linear-elastic curve for another model. Figures G5 and G6 illustrate the differences in stress output from these models for mining steps 1 and 2, respectively. The maximum difference was ±7 Pa (±0.001 psi), all located within the fine mesh of the models as seen in the legend of the figures. Such difference could be lessened by using a smaller stress tolerance to determine equilibrium. The small differences shown indicate that the five-point material model did, indeed, replicate the elastic model very well.

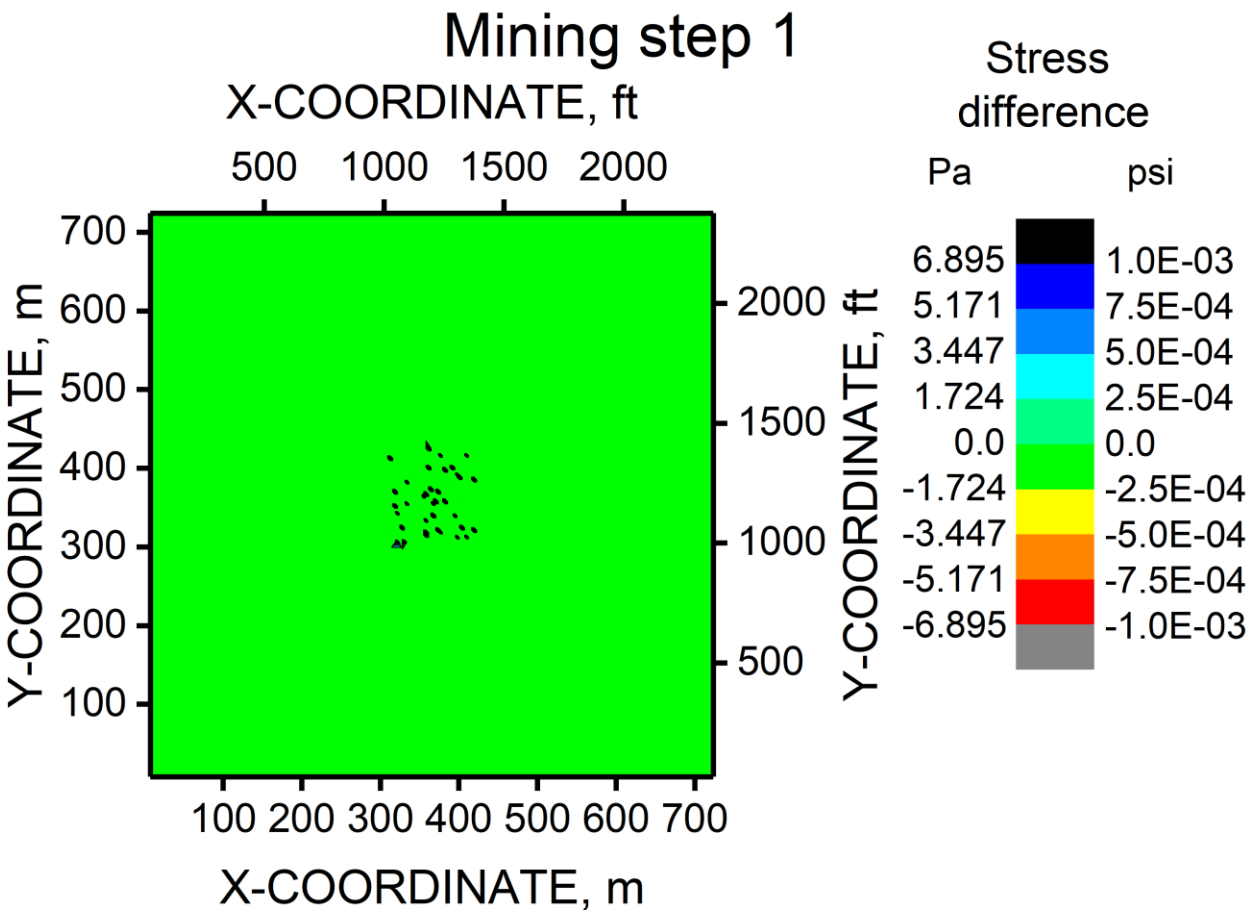

Figure G5. Differences in stress at mining step 1 for elastic problem.

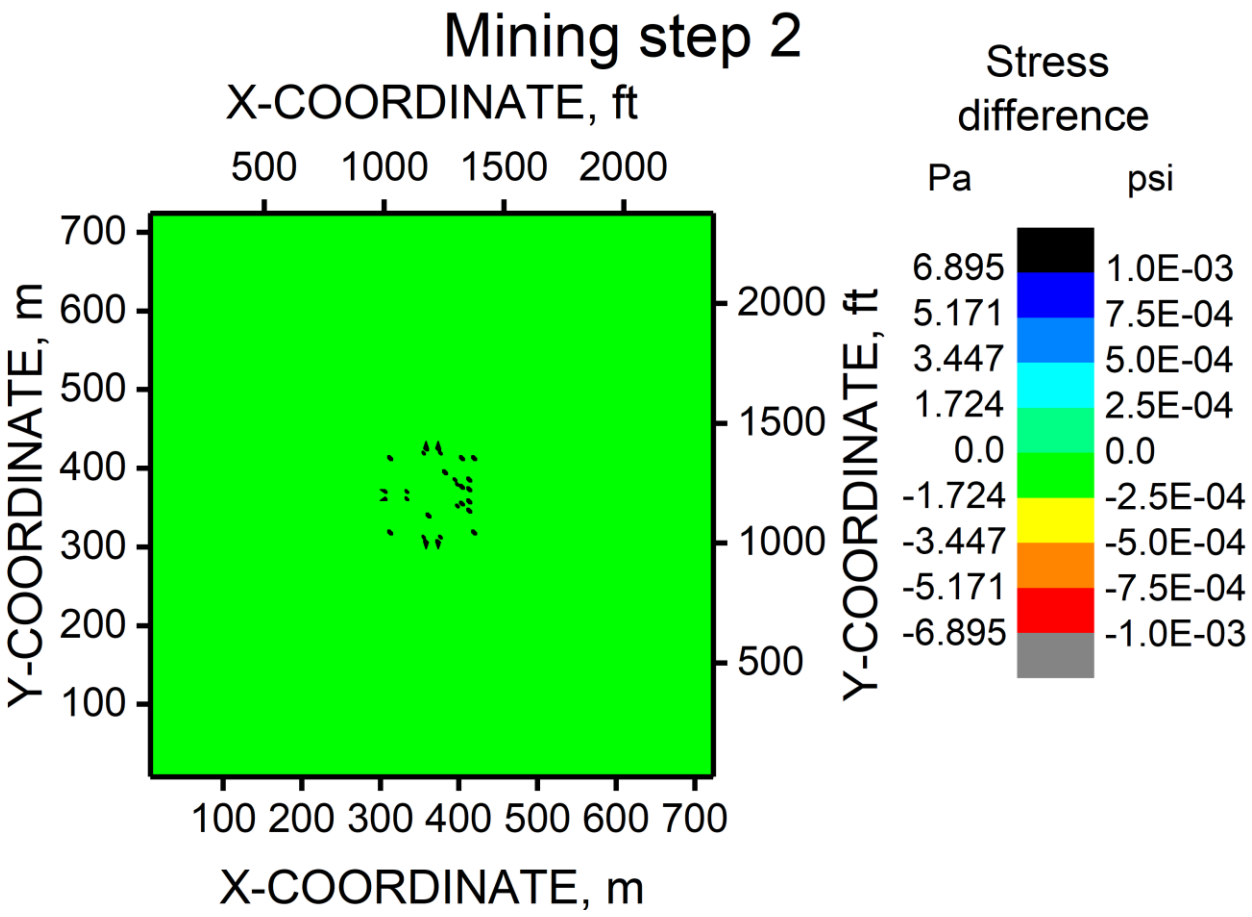

Figure G6. Differences in stress at mining step 2 for elastic problem.

Mark-Bieniawski Softening Problem

The same example as above was modeled, but the Mark-Bieniawski [Mark and Iannacchione 1992] stress-versus-strain formulation with softening and a coal strength of 6.2 MPa (900 psi) was used. Residual stresses were determined by the method of Karabin and Evanto [1994]. Residual strain (strain when residual stress is first reached) was set to twice the peak elastic strain for each yielding material. The five-point model replicated the two-point softening model by placing the third through fifth points further down the residual line. That is, these points had the same residual stress as the last point of the two-point softening model, but increased strain (0.2, 0.3, and 0.4). In mining step 2, the outer corner elements of the partial pillars had closure between points 2 and 3—well past the beginning of residual strain. Output showed no difference in results between the models in both mining steps for both stress and closure to the precision output by the code. For example, maximum closure error was $\pm 1.23 \times 10^{-8}$ mm ($\pm 4.85 \times 10^{-10}$ in). It appears that the five-point material model replicates the strain-softening model very well.

Conclusion

Numerical model results produced using the five-point stress-strain material strength model for coal were compared to results using an elastic coal model and a Mark-Bieniawski coal model with softening. The small differences might be reduced further with tighter equilibrium tolerance, but they indicate that the five-point material model is functioning properly.

References for Appendix G

Karabin G, J., Evanto MA [1994]. Experience with the boundary element method of numerical modeling as a tool to resolve complex ground control problems. In: Peng SS ed., Proceedings of 13th International Conference on Ground Control in Mining. (Morgantown, WV: August 2–4, 1994) Morgantown, WV: West Virginia University, pp. 201–213.

Larson MK, Whyatt JK [2012]. Load transfer distance calibration of a coal panel scale model: A case study. In: Barczak T et al. eds. Proceedings of the 31st International Conference on Ground Control in Mining. (Morgantown, WV: July 31–August 2, 2012) Morgantown, WV: West Virginia University, pp. 195–205.

Mark C, Chase FE [1997]. Analysis of Retreat Mining Pillar Stability (ARMPS). In: Mark C, Tuchman RJ eds. Proceedings: New Technology for Ground Control in Retreat Mining, DHHS (NIOSH) Publication No. 97-133, IC 9446. Pittsburgh, PA: National Institute for Occupational Safety and Health (NIOSH), pp. 17–34.

Mark C, Iannacchione AT [1992]. Coal pillar mechanics: Theoretical models and field measurements compared. In: Iannacchione AT et al. eds. Bureau of Mines Information Circular 9135, Proceedings of the Workshop on Coal Pillar Mechanics and Design. Washington, DC: U.S. Department of the Interior, pp. 78–93.

Input Files Contents Listing for Verification Problems

In this appendix, the two problems were used to verify that the multipoint law resulted in the same output as the elastic or softening law already built in. The input files of each of the two verification problems are listed here in two forms. The first form uses the existing elastic or softening law already in Mulsim. The second lists the implementation of the same using the multipoint law. Thus, there are two input files for each problem in the input file listings that follow.

Filename: test_elastic6080_2step.inp

```
Test Problem, elastic 60%-80% case, 2 step
0.287913 2.34594e+06       1
      27
      1.  0.3700000E+006  1.3909800E+005  0.0000000E+000  0.0000000E+000  0.0000000E+000
      1.  0.3700000E+006  1.3909800E+005  0.0000000E+000  0.0000000E+000  0.0000000E+000
      1.  0.3700000E+006  1.3909800E+005  0.0000000E+000  0.0000000E+000  0.0000000E+000
      1.  0.3700000E+006  1.3909800E+005  0.0000000E+000  0.0000000E+000  0.0000000E+000
      1.  0.3700000E+006  1.3909800E+005  0.0000000E+000  0.0000000E+000  0.0000000E+000
      1.  0.3700000E+006  1.3909800E+005  0.0000000E+000  0.0000000E+000  0.0000000E+000
      1.  0.3700000E+006  1.3909800E+005  0.0000000E+000  0.0000000E+000  0.0000000E+000
      1.  0.3700000E+006  1.3909800E+005  0.0000000E+000  0.0000000E+000  0.0000000E+000
      1.  0.3700000E+006  1.3909800E+005  0.0000000E+000  0.0000000E+000  0.0000000E+000
      1.  0.3700000E+006  1.3909800E+005  0.0000000E+000  0.0000000E+000  0.0000000E+000
      1.  0.3700000E+006  1.3909800E+005  0.0000000E+000  0.0000000E+000  0.0000000E+000
      1.  0.3700000E+006  1.3909800E+005  0.0000000E+000  0.0000000E+000  0.0000000E+000
      1.  0.3700000E+006  1.3909800E+005  0.0000000E+000  0.0000000E+000  0.0000000E+000
      1.  0.3700000E+006  1.3909800E+005  0.0000000E+000  0.0000000E+000  0.0000000E+000
      1.  0.3700000E+006  1.3909800E+005  0.0000000E+000  0.0000000E+000  0.0000000E+000
      1.  0.3700000E+006  1.3909800E+005  0.0000000E+000  0.0000000E+000  0.0000000E+000
      1.  0.3700000E+006  1.3909800E+005  0.0000000E+000  0.0000000E+000  0.0000000E+000
      1.  0.3700000E+006  1.3909800E+005  0.0000000E+000  0.0000000E+000  0.0000000E+000
      1.  0.3700000E+006  1.3909800E+005  0.0000000E+000  0.0000000E+000  0.0000000E+000
      1.  0.3700000E+006  1.3909800E+005  0.0000000E+000  0.0000000E+000  0.0000000E+000
      1.  0.3700000E+006  1.3909800E+005  0.0000000E+000  0.0000000E+000  0.0000000E+000
      1.  0.3700000E+006  1.3909800E+005  0.0000000E+000  0.0000000E+000  0.0000000E+000
      1.  0.2960000E+006  1.1127820E+005  0.0000000E+000  0.0000000E+000  0.0000000E+000
      1.  0.2960000E+006  1.1127820E+005  0.0000000E+000  0.0000000E+000  0.0000000E+000
      1.  0.2220000E+006  8.3458650E+004  0.0000000E+000  0.0000000E+000  0.0000000E+000
      1.  0.2220000E+006  8.3458650E+004  0.0000000E+000  0.0000000E+000  0.0000000E+000
      5.  0.1000000E+003  0.2302920E+006  0.4000000E+004  0.1000000E+001  0.3300000E+000
      5.  0.1000000E+003  0.2158980E+006  0.4000000E+004  0.1000000E+001  0.3300000E+000
     0.00000  0.03786010     0.00000  0.00000000     0.00000  0.00000000     0.00000  0.03786010     0.00000  0.00000000     0.00000
0.09363830
  600.00      48      48               0      21      28      21      28
     0.0     0.0 -27042.   132.0
 1.00000 0.00000 0.00000 0.00000 1.00000 0.00000 0.00000 0.00000 1.00000
1.350000 1.000000000    3000                                1       2
BDFHJLNPRTVX11XVTRPNNPRTVX11XVTRPNLJHFDB
BDFHJLNPRTVX11XVTRPNNPRTVX11XVTRPNLJHFDB
BDFHJLNPRTVX11XVTRPNNPRTVX11XVTRPNLJHFDB
BDFHJLNPRTVX11XVTRPNNPRTVX11XVTRPNLJHFDB
BDFHJLNPRTVX11XVTRPNNPRTVX11XVTRPNLJHFDB
BDFHJLNPRTVX11XVTRPNNPRTVX11XVTRPNLJHFDB
BDFHJLNPRTVX11XVTRPOOPRTVX11XVTRPNLJHFDB
BDFHJLNPRTVX11XVTRQPPQRTVX11XVTRPNLJHFDB
BDFHJLNPRTVX11XVTSRRRRSTVX11XVTRPNLJHFDB
BDFHJLNPRTVX11XVUTTTTTTUVX11XVTRPNLJHFDB
BDFHJLNPRTVX11XWVVVVVVVVVWX11XVTRPNLJHFDB
BDFHJLNPRTVX11YXXXXXXXXXXY11XVTRPNLJHFDB
BDFHJLNPRTVX1111111111111111XVTRPNLJHFDB
BDFHJLNPRTVX1111111111111111XVTRPNLJHFDB
BDFHJLNPRTVX11YXXXXXXXXXXY11XVTRPNLJHFDB
BDFHJLNPRTVX11XWVVVVVVVVVWX11XVTRPNLJHFDB
BDFHJLNPRTVX11XVUTTTTTTUVX11XVTRPNLJHFDB
BDFHJLNPRTVX11XVTSRRRRSTVX11XVTRPNLJHFDB
BDFHJLNPRTVX11XVTRQPPQRTVX11XVTRPNLJHFDB
BDFHJLNPRTVX11XVTRPOOPRTVX11XVTRPNLJHFDB
BDFHJLNPRTVX11XVTRPOOPRTVX11XVTRPNLJHFDB
BDFHJLNPRTVX11XVTRQPPQRTVX11XVTRPNLJHFDB
BDFHJLNPRTVX11XVTSRRRRSTVX11XVTRPNLJHFDB
BDFHJLNPRTVX11XVUTTTTTTUVX11XVTRPNLJHFDB
BDFHJLNPRTVX11XWVVVVVVVVVWX11XVTRPNLJHFDB
BDFHJLNPRTVX11YXXXXXXXXXXY11XVTRPNLJHFDB
BDFHJLNPRTVX1111111111111111XVTRPNLJHFDB
BDFHJLNPRTVX1111111111111111XVTRPNLJHFDB
BDFHJLNPRTVX11YXXXXXXXXXXY11XVTRPNLJHFDB
BDFHJLNPRTVX11XWVVVVVVVVVWX11XVTRPNLJHFDB
BDFHJLNPRTVX11XVUTTTTTTUVX11XVTRPNLJHFDB
BDFHJLNPRTVX11XVTSRRRRSTVX11XVTRPNLJHFDB
BDFHJLNPRTVX11XVTRQPPQRTVX11XVTRPNLJHFDB
BDFHJLNPRTVX11XVTRPOOPRTVX11XVTRPNLJHFDB
BDFHJLNPRTVX11XVTRPNNPRTVX11XVTRPNLJHFDB
BDFHJLNPRTVX11XVTRPNNPRTVX11XVTRPNLJHFDB
BDFHJLNPRTVX11XVTRPNNPRTVX11XVTRPNLJHFDB
BDFHJLNPRTVX11XVTRPNNPRTVX11XVTRPNLJHFDB
BDFHJLNPRTVX11XVTRPNNPRTVX11XVTRPNLJHFDB
BDFHJLNPRTVX11XVTRPNNPRTVX11XVTRPNLJHFDB
AAAAAAAAAAAAAAAAAAAAAAAAAAAAAAAAAAAAAAAAAAAAAAAAAAAAAAAA
AAAAAAAAAAAAAAAAAAAAAAAAAAAAAAAAAAAAAAAAAAAAAAAAAAAAAAAA
AAAAAAAAAAAAAAAAAAAAAAAAAAAAAAAAAAAAAAAAAAAAAAAAAAAAAAAA
AAAAAAAAAAAAAAAAAAAAAAAAAAAAAAAAAAAAAAAAAAAAAAAAAAAAAAAA
AAAAAAAAAAAAAAAAAAAAAAAAAAAAAAAAAAAAAAAAAAAAAAAAAAAAAAAA
AAAAAAAAAAAAAAAAAAAAAAAAAAAAAAAAAAAAAAAAAAAAAAAAAAAAAAAA
AAAAAAAAAAAAAAAAAAAAAAAAAAAAAAAAAAAAAAAAAAAAAAAAAAAAAAAA
AAAAAAAAAAAAAAAAAAAAAAAAAAAAAAAAAAAAAAAAAAAAAAAAAAAAAAAA
AAAAAAAAAAAAAAAAAAAAAAAAAAAAAAAAAAAAAAAAAAAAAAAAAAAAAAAA
AAAAAAAAAAAAAAAAAAAAAAAAAAAAAAAAAAAAAAAAAAAAAAAAAAAAAAAA
```

```
AAAAAAAAAAAAAAAAAAAAAAAAAAAAAAAAAAAAAAAAAAAAAAAA
AAAAAAAAAAAAAAAAAAAAAAAAAAAAAAAAAAAAAAAAAAAAAAAA
AAAAAAAAAAAAAAAAAAAAAAAAAAAAAAAAAAAAAAAAAAAAAAAA
AAAAAAAAAAAAAAAAAAAAAAAAAAAAAAAAAAAAAAAAAAAAAAAA
AAAAAAAAAAAAAAAAAAAAAAAAAAAAAAAAAAAAAAAAAAAAAAAA
AAAAAAAAAAAAAAAAAAAAAAAAAAAAAAAAAAAAAAAAAAAAAAAA
AAAAAAAAAAAAAAAAAAAAAAAAAAAAAAAAAAAAAAAAAAAAAAAA
AAAAAAAAAAAAAAAAAAAAAAAAAAAAAAAAAAAAAAAAAAAAAAAA
AAAAAAAAAAAAAAAAAAAAAAAAAAAAAAAAAAAAAAAAAAAAAAAA
AAAAAAAAAAAAAAAAAAAAAAAAAAAAAAAAAAAAAAAAAAAAAAAA
AAAAAAAAAAAAAAAAAAAA00000000AAAAAAAAAAAAAAAAAAAA
AAAAAAAAAAAAAAAAAAAA00000000AAAAAAAAAAAAAAAAAAAA
AAAAAAAAAAAAAAAAAAAA00000000AAAAAAAAAAAAAAAAAAAA
AAAAAAAAAAAAAAAAAAAA00000000AAAAAAAAAAAAAAAAAAAA
AAAAAAAAAAAAAAAAAAAA00000000AAAAAAAAAAAAAAAAAAAA
AAAAAAAAAAAAAAAAAAAA00000000AAAAAAAAAAAAAAAAAAAA
AAAAAAAAAAAAAAAAAAAA00000000AAAAAAAAAAAAAAAAAAAA
AAAAAAAAAAAAAAAAAAAA00000000AAAAAAAAAAAAAAAAAAAA
AAAAAAAAAAAAAAAAAAAAAAAAAAAAAAAAAAAAAAAAAAAAAAAA
AAAAAAAAAAAAAAAAAAAAAAAAAAAAAAAAAAAAAAAAAAAAAAAA
AAAAAAAAAAAAAAAAAAAAAAAAAAAAAAAAAAAAAAAAAAAAAAAA
AAAAAAAAAAAAAAAAAAAAAAAAAAAAAAAAAAAAAAAAAAAAAAAA
AAAAAAAAAAAAAAAAAAAAAAAAAAAAAAAAAAAAAAAAAAAAAAAA
AAAAAAAAAAAAAAAAAAAAAAAAAAAAAAAAAAAAAAAAAAAAAAAA
AAAAAAAAAAAAAAAAAAAAAAAAAAAAAAAAAAAAAAAAAAAAAAAA
AAAAAAAAAAAAAAAAAAAAAAAAAAAAAAAAAAAAAAAAAAAAAAAA
AAAAAAAAAAAAAAAAAAAAAAAAAAAAAAAAAAAAAAAAAAAAAAAA
AAAAAAAAAAAAAAAAAAAAAAAAAAAAAAAAAAAAAAAAAAAAAAAA
AAAAAAAAAAAAAAAAAAAAAAAAAAAAAAAAAAAAAAAAAAAAAAAA
AAAAAAAAAAAAAAAAAAAAAAAAAAAAAAAAAAAAAAAAAAAAAAAA
AAAAAAAAAAAAAAAAAAAAAAAAAAAAAAAAAAAAAAAAAAAAAAAA
AAAAAAAAAAAAAAAAAAAAAAAAAAAAAAAAAAAAAAAAAAAAAAAA
AAAAAAAAAAAAAAAAAAAAAAAAAAAAAAAAAAAAAAAAAAAAAAAA
AAAAAAAAAAAAAAAAAAAAAAAAAAAAAAAAAAAAAAAAAAAAAAAA
AAAAAAAAAAAAAAAAAAAAAAAAAAAAAAAAAAAAAAAAAAAAAAAA
AAAAAAAAAAAAAAAAAAAAAAAAAAAAAAAAAAAAAAAAAAAAAAAA
AAAAAAAAAAAAAAAAAAAAAAAAAAAAAAAAAAAAAAAAAAAAAAAA
AAAAAAAAAAAAAAAAAAAAAAAAAAAAAAAAAAAAAAAAAAAAAAAA
BDFHJLNPRTVX11XVTRPNNPRTVX11XVTRPNLJHFDB
BDFHJLNPRTVX11XVTRPNNPRTVX11XVTRPNLJHFDB
BDFHJLNPRTVX11XVTRPNNPRTVX11XVTRPNLJHFDB
BDFHJLNPRTVX11XVTRPNNPRTVX11XVTRPNLJHFDB
BDFHJLNPRTVX11XVTRPNNPRTVX11XVTRPNLJHFDB
BDFHJLNPRTVX11XVTRPNNPRTVX11XVTRPNLJHFDB
BDFHJLNPRTVX11XVTRPOOPRTVX11XVTRPNLJHFDB
BDFHJLNPRTVX11XVTRQPPQRTVX11XVTRPNLJHFDB
BDFHJLNPRTVX11XVTSRRRRSTVX11XVTRPNLJHFDB
BDFHJLNPRTVX11XVUTTTTTTUVX11XVTRPNLJHFDB
BDFHJLNPRTVX11XWVVVVVVVVWX11XVTRPNLJHFDB
BDFHJLNPRTVX11YXXXXXXXXXXY11XVTRPNLJHFDB
BDFHJLNPRTVXZZZZZZZZZZZZZZZZXVTRPNLJHFDB
BDFHJLNPRTVXZZZZZZZZZZZZZZZZXVTRPNLJHFDB
BDFHJLNPRTVXZZZZZZZZZZZZZZZZXVTRPNLJHFDB
BDFHJLNPRTVXZZZZZZZZZZZZZZZZXVTRPNLJHFDB
BDFHJLNPRTVXZZZZZZZZZZZZZZZZXVTRPNLJHFDB
BDFHJLNPRTVXZZZZZZZZZZZZZZZZXVTRPNLJHFDB
BDFHJLNPRTVXZZZZZZZZZZZZZZZZXVTRPNLJHFDB
BDFHJLNPRTVXZZZZZZZZZZZZZZZZXVTRPNLJHFDB
BDFHJLNPRTVXZZZZZZZZZZZZZZZZXVTRPNLJHFDB
BDFHJLNPRTVXZZZZZZZZZZZZZZZZXVTRPNLJHFDB
BDFHJLNPRTVXZZZZZZZZZZZZZZZZXVTRPNLJHFDB
BDFHJLNPRTVXZZZZZZZZZZZZZZZZXVTRPNLJHFDB
BDFHJLNPRTVXZZZZZZZZZZZZZZZZXVTRPNLJHFDB
BDFHJLNPRTVXZZZZZZZZZZZZZZZZXVTRPNLJHFDB
BDFHJLNPRTVXZZZZZZZZZZZZZZZZXVTRPNLJHFDB
BDFHJLNPRTVXZZZZZZZZZZZZZZZZXVTRPNLJHFDB
BDFHJLNPRTVX11YXXXXXXXXXXY11XVTRPNLJHFDB
BDFHJLNPRTVX11XWVVVVVVVVWX11XVTRPNLJHFDB
BDFHJLNPRTVX11XVUTTTTTTUVX11XVTRPNLJHFDB
BDFHJLNPRTVX11XVTSRRRRSTVX11XVTRPNLJHFDB
BDFHJLNPRTVX11XVTRQPPQRTVX11XVTRPNLJHFDB
BDFHJLNPRTVX11XVTRPOOPRTVX11XVTRPNLJHFDB
BDFHJLNPRTVX11XVTRPNNPRTVX11XVTRPNLJHFDB
BDFHJLNPRTVX11XVTRPNNPRTVX11XVTRPNLJHFDB
BDFHJLNPRTVX11XVTRPNNPRTVX11XVTRPNLJHFDB
BDFHJLNPRTVX11XVTRPNNPRTVX11XVTRPNLJHFDB
BDFHJLNPRTVX11XVTRPNNPRTVX11XVTRPNLJHFDB
BDFHJLNPRTVX11XVTRPNNPRTVX11XVTRPNLJHFDB
AAAAAAAAAAAAAAAAAAAAAAAAAAAAAAAAAAAAAAAAAAAAAAAA
AAAAAAAAAAAAAAAAAAAAAAAAAAAAAAAAAAAAAAAAAAAAAAAA
AAAAAAAAAAAAAAAAAAAAAAAAAAAAAAAAAAAAAAAAAAAAAAAA
AAAAAAAAAAAAAAAAAAAAAAAAAAAAAAAAAAAAAAAAAAAAAAAA
AAAAAAAAAAAAAAAAAAAAAAAAAAAAAAAAAAAAAAAAAAAAAAAA
AAAAAAAAAAAAAAAAAAAAAAAAAAAAAAAAAAAAAAAAAAAAAAAA
AAAAAAAAAAAAAAAAAAAAAAAAAAAAAAAAAAAAAAAAAAAAAAAA
AAAAAAAAAAAAAAAAAAAAAAAAAAAAAAAAAAAAAAAAAAAAAAAA
AAAAAAAAAAAAAAAAAAAAAAAAAAAAAAAAAAAAAAAAAAAAAAAA
AAAAAAAAAAAAAAAAAAAAAAAAAAAAAAAAAAAAAAAAAAAAAAAA
AAAAAAAAAAAAAAAAAAAAAAAAAAAAAAAAAAAAAAAAAAAAAAAA
AAAAAAAAAAAAAAAAAAAAAAAAAAAAAAAAAAAAAAAAAAAAAAAA
AAAAAAAAAAAAAAAAAAAAAAAAAAAAAAAAAAAAAAAAAAAAAAAA
AAAAAAAAAAAAAAAAAAAAAAAAAAAAAAAAAAAAAAAAAAAAAAAA
```

```
AAAAAAAAAAAAAAAAAAAAAAAAAAAAAAAAAAAAAAAAAAAAAAAA
AAAAAAAAAAAAAAAAAAAAAAAAAAAAAAAAAAAAAAAAAAAAAAAA
AAAAAAAAAAAAAAAAAAAAAAAAAAAAAAAAAAAAAAAAAAAAAAAA
AAAAAAAAAAAAAAAAAAAAAAAAAAAAAAAAAAAAAAAAAAAAAAAA
AAAAAAAAAAAAAAAAAAAAAAAAAAAAAAAAAAAAAAAAAAAAAAAA
AAAAAAAAAAAAAAAAAAAAAAAAAAAAAAAAAAAAAAAAAAAAAAAA
AAAAAAAAAAAAAAAAAAAA00000000AAAAAAAAAAAAAAAAAAAA
AAAAAAAAAAAAAAAAAAAA00000000AAAAAAAAAAAAAAAAAAAA
AAAAAAAAAAAAAAAAAAAA00000000AAAAAAAAAAAAAAAAAAAA
AAAAAAAAAAAAAAAAAAAA00000000AAAAAAAAAAAAAAAAAAAA
AAAAAAAAAAAAAAAAAAAA00000000AAAAAAAAAAAAAAAAAAAA
AAAAAAAAAAAAAAAAAAAA00000000AAAAAAAAAAAAAAAAAAAA
AAAAAAAAAAAAAAAAAAAA00000000AAAAAAAAAAAAAAAAAAAA
AAAAAAAAAAAAAAAAAAAA00000000AAAAAAAAAAAAAAAAAAAA
AAAAAAAAAAAAAAAAAAAAAAAAAAAAAAAAAAAAAAAAAAAAAAAA
AAAAAAAAAAAAAAAAAAAAAAAAAAAAAAAAAAAAAAAAAAAAAAAA
AAAAAAAAAAAAAAAAAAAAAAAAAAAAAAAAAAAAAAAAAAAAAAAA
AAAAAAAAAAAAAAAAAAAAAAAAAAAAAAAAAAAAAAAAAAAAAAAA
AAAAAAAAAAAAAAAAAAAAAAAAAAAAAAAAAAAAAAAAAAAAAAAA
AAAAAAAAAAAAAAAAAAAAAAAAAAAAAAAAAAAAAAAAAAAAAAAA
AAAAAAAAAAAAAAAAAAAAAAAAAAAAAAAAAAAAAAAAAAAAAAAA
AAAAAAAAAAAAAAAAAAAAAAAAAAAAAAAAAAAAAAAAAAAAAAAA
AAAAAAAAAAAAAAAAAAAAAAAAAAAAAAAAAAAAAAAAAAAAAAAA
AAAAAAAAAAAAAAAAAAAAAAAAAAAAAAAAAAAAAAAAAAAAAAAA
AAAAAAAAAAAAAAAAAAAAAAAAAAAAAAAAAAAAAAAAAAAAAAAA
AAAAAAAAAAAAAAAAAAAAAAAAAAAAAAAAAAAAAAAAAAAAAAAA
AAAAAAAAAAAAAAAAAAAAAAAAAAAAAAAAAAAAAAAAAAAAAAAA
AAAAAAAAAAAAAAAAAAAAAAAAAAAAAAAAAAAAAAAAAAAAAAAA
AAAAAAAAAAAAAAAAAAAAAAAAAAAAAAAAAAAAAAAAAAAAAAAA
AAAAAAAAAAAAAAAAAAAAAAAAAAAAAAAAAAAAAAAAAAAAAAAA
AAAAAAAAAAAAAAAAAAAAAAAAAAAAAAAAAAAAAAAAAAAAAAAA
AAAAAAAAAAAAAAAAAAAAAAAAAAAAAAAAAAAAAAAAAAAAAAAA
AAAAAAAAAAAAAAAAAAAAAAAAAAAAAAAAAAAAAAAAAAAAAAAA
AAAAAAAAAAAAAAAAAAAAAAAAAAAAAAAAAAAAAAAAAAAAAAAA
```

Filename: test_mpel6080_2step.inp

Note that the material code lines beginning with "7." are longer than the line space, and therefore, are continued on the next line. Each of those lines ends with "3.3000000E-001."

```
Test Problem, multipoint elastic 60%-80% case
0.287913 2.34594e+06       1
      27
      1.  0.3700000E+006  1.3909800E+005  0.0000000E+000  0.0000000E+000  0.0000000E+000
      7.  2.0899636E+004  5.6485503E-002  3.1349454E+004  8.4728254E-002  4.1799272E+004  1.1297101E-001  6.2698908E+004  1.6945651E-001
3.7000000E+005  1.0000000E+000  3.3000000E-001
      7.  2.0605091E+004  5.5689435E-002  3.0907637E+004  8.3534153E-002  4.1210182E+004  1.1137887E-001  6.1815273E+004  1.6706831E-001
3.7000000E+005  1.0000000E+000  3.3000000E-001
      7.  1.9132364E+004  5.1709092E-002  2.8698546E+004  7.7563638E-002  3.8264728E+004  1.0341818E-001  5.7397092E+004  1.5512728E-001
3.7000000E+005  1.0000000E+000  3.3000000E-001
      7.  1.8837818E+004  5.0913022E-002  2.8256727E+004  7.6369532E-002  3.7675636E+004  1.0182604E-001  5.6513454E+004  1.5273906E-001
3.7000000E+005  1.0000000E+000  3.3000000E-001
      7.  1.7365091E+004  4.6932678E-002  2.6047637E+004  7.0399018E-002  3.4730182E+004  9.3865357E-002  5.2095273E+004  1.4079804E-001
3.7000000E+005  1.0000000E+000  3.3000000E-001
      7.  1.7070545E+004  4.6136608E-002  2.5605818E+004  6.9204912E-002  3.4141090E+004  9.2273216E-002  5.1211635E+004  1.3840982E-001
3.7000000E+005  1.0000000E+000  3.3000000E-001
      7.  1.5597818E+004  4.2156265E-002  2.3396727E+004  6.3234397E-002  3.1195636E+004  8.4312530E-002  4.6793454E+004  1.2646879E-001
3.7000000E+005  1.0000000E+000  3.3000000E-001
      7.  1.5303273E+004  4.1360197E-002  2.2954910E+004  6.2040296E-002  3.0606546E+004  8.2720395E-002  4.5909819E+004  1.2408059E-001
3.7000000E+005  1.0000000E+000  3.3000000E-001
      7.  1.3830545E+004  3.7379851E-002  2.0745818E+004  5.6069777E-002  2.7661090E+004  7.4759703E-002  4.1491635E+004  1.1213955E-001
3.7000000E+005  1.0000000E+000  3.3000000E-001
      7.  1.3536000E+004  3.6583784E-002  2.0304000E+004  5.4875676E-002  2.7072000E+004  7.3167568E-002  4.0608000E+004  1.0975135E-001
3.7000000E+005  1.0000000E+000  3.3000000E-001
      7.  1.2063273E+004  3.2603441E-002  1.8094910E+004  4.8905161E-002  2.4126546E+004  6.5206881E-002  3.6189819E+004  9.7810322E-002
3.7000000E+005  1.0000000E+000  3.3000000E-001
      7.  1.1768727E+004  3.1807370E-002  1.7653091E+004  4.7711055E-002  2.3537454E+004  6.3614741E-002  3.5306181E+004  9.5422111E-002
3.7000000E+005  1.0000000E+000  3.3000000E-001
      7.  1.0296000E+004  2.7827027E-002  1.5444000E+004  4.1740541E-002  2.0592000E+004  5.5654054E-002  3.0888000E+004  8.3481081E-002
3.7000000E+005  1.0000000E+000  3.3000000E-001
      7.  1.0001455E+004  2.7030959E-002  1.5002183E+004  4.0546439E-002  2.0002910E+004  5.4061919E-002  3.0004365E+004  8.1092878E-002
3.7000000E+005  1.0000000E+000  3.3000000E-001
      7.  8.5287273E+003  2.3050614E-002  1.2793091E+004  3.4575921E-002  1.7057455E+004  4.6101229E-002  2.5586182E+004  6.9151843E-002
3.7000000E+005  1.0000000E+000  3.3000000E-001
      7.  1.0001455E+004  2.7030959E-002  1.5002183E+004  4.0546439E-002  2.0002910E+004  5.4061919E-002  3.0004365E+004  8.1092878E-002
3.7000000E+005  1.0000000E+000  3.3000000E-001
      7.  6.7614545E+003  1.8274201E-002  1.0142182E+004  2.7411302E-002  1.3522909E+004  3.6548403E-002  2.0284364E+004  5.4822604E-002
3.7000000E+005  1.0000000E+000  3.3000000E-001
      7.  6.4669091E+003  1.7478133E-002  9.7003637E+003  2.6217199E-002  1.2933818E+004  3.4956265E-002  1.9400727E+004  5.2434398E-002
3.7000000E+005  1.0000000E+000  3.3000000E-001
      7.  4.9941818E+003  1.3497789E-002  7.4912727E+003  2.0246683E-002  9.9883636E+003  2.6995577E-002  1.4982545E+004  4.0493366E-002
3.7000000E+005  1.0000000E+000  3.3000000E-001
      7.  4.6996364E+003  1.2701720E-002  7.0494546E+003  1.9052580E-002  9.3992728E+003  2.5403440E-002  1.4098909E+004  3.8105160E-002
3.7000000E+005  1.0000000E+000  3.3000000E-001
      7.  3.2269091E+003  1.0901720E-002  4.8403637E+003  1.6352580E-002  6.4538182E+003  2.1803440E-002  9.6807273E+003  3.2705160E-002
2.9600000E+005  1.0000000E+000  3.3000000E-001
      7.  2.9323636E+003  9.9066338E-003  4.3985454E+003  1.4859951E-002  5.8647272E+003  1.9813268E-002  8.7970908E+003  2.9719901E-002
2.9600000E+005  1.0000000E+000  3.3000000E-001
      7.  1.4596364E+003  6.5749387E-003  2.1894546E+003  9.8624081E-003  2.9192728E+003  1.3149877E-002  4.3789092E+003  1.9724816E-002
2.2200000E+005  1.0000000E+000  3.3000000E-001
      7.  1.1650909E+003  5.2481572E-003  1.7476364E+003  7.8722358E-003  2.3301818E+003  1.0496314E-002  3.4952727E+003  1.5744472E-002
2.2200000E+005  1.0000000E+000  3.3000000E-001
      5.  0.1000000E+003  0.2302920E+006  0.4000000E+004  0.1000000E+001  0.3300000E+000
      5.  0.1000000E+003  0.2158980E+006  0.4000000E+004  0.1000000E+001  0.3300000E+000
     0.00000  0.03786010     0.00000  0.00000000     0.00000  0.00000000     0.00000  0.03786010     0.00000  0.00000000     0.00000
0.09363830
  600.00      48      48               0      21      28      21      28
     0.0     0.0 -27042.   132.0
 1.00000 0.00000 0.00000 0.00000 1.00000 0.00000 0.00000 0.00000 1.00000
1.350000 1.000000000    3000                                  1       2
BDFHJLNPRTVX11XVTRPNNPRTVX11XVTRPNLJHFDB
BDFHJLNPRTVX11XVTRPNNPRTVX11XVTRPNLJHFDB
BDFHJLNPRTVX11XVTRPNNPRTVX11XVTRPNLJHFDB
BDFHJLNPRTVX11XVTRPNNPRTVX11XVTRPNLJHFDB
BDFHJLNPRTVX11XVTRPNNPRTVX11XVTRPNLJHFDB
BDFHJLNPRTVX11XVTRPNNPRTVX11XVTRPNLJHFDB
BDFHJLNPRTVX11XVTRPOOPRTVX11XVTRPNLJHFDB
BDFHJLNPRTVX11XVTRQPPQRTVX11XVTRPNLJHFDB
BDFHJLNPRTVX11XVTSRRRRSTVX11XVTRPNLJHFDB
BDFHJLNPRTVX11XVUTTTTTTUVX11XVTRPNLJHFDB
BDFHJLNPRTVX11XWVVVVVVVVWX11XVTRPNLJHFDB
BDFHJLNPRTVX11YXXXXXXXXXXY11XVTRPNLJHFDB
BDFHJLNPRTVX1111111111111111XVTRPNLJHFDB
BDFHJLNPRTVX1111111111111111XVTRPNLJHFDB
BDFHJLNPRTVX11YXXXXXXXXXXY11XVTRPNLJHFDB
BDFHJLNPRTVX11XWVVVVVVVVWX11XVTRPNLJHFDB
BDFHJLNPRTVX11XVUTTTTTTUVX11XVTRPNLJHFDB
BDFHJLNPRTVX11XVTSRRRRSTVX11XVTRPNLJHFDB
BDFHJLNPRTVX11XVTRQPPQRTVX11XVTRPNLJHFDB
BDFHJLNPRTVX11XVTRPOOPRTVX11XVTRPNLJHFDB
BDFHJLNPRTVX11XVTRPOOPRTVX11XVTRPNLJHFDB
BDFHJLNPRTVX11XVTRQPPQRTVX11XVTRPNLJHFDB
```

```
BDFHJLNPRTVX11XVTSRRRRSTVX11XVTRPNLJHFDB
BDFHJLNPRTVX11XVUTTTTTTUVX11XVTRPNLJHFDB
BDFHJLNPRTVX11XWVVVVVVVVWX11XVTRPNLJHFDB
BDFHJLNPRTVX11YXXXXXXXXXXY11XVTRPNLJHFDB
BDFHJLNPRTVX1111111111111111XVTRPNLJHFDB
BDFHJLNPRTVX1111111111111111XVTRPNLJHFDB
BDFHJLNPRTVX11YXXXXXXXXXXY11XVTRPNLJHFDB
BDFHJLNPRTVX11XWVVVVVVVVWX11XVTRPNLJHFDB
BDFHJLNPRTVX11XVUTTTTTTUVX11XVTRPNLJHFDB
BDFHJLNPRTVX11XVTSRRRRSTVX11XVTRPNLJHFDB
BDFHJLNPRTVX11XVTRQPPQRTVX11XVTRPNLJHFDB
BDFHJLNPRTVX11XVTRPOOPRTVX11XVTRPNLJHFDB
BDFHJLNPRTVX11XVTRPNNPRTVX11XVTRPNLJHFDB
BDFHJLNPRTVX11XVTRPNNPRTVX11XVTRPNLJHFDB
BDFHJLNPRTVX11XVTRPNNPRTVX11XVTRPNLJHFDB
BDFHJLNPRTVX11XVTRPNNPRTVX11XVTRPNLJHFDB
BDFHJLNPRTVX11XVTRPNNPRTVX11XVTRPNLJHFDB
BDFHJLNPRTVX11XVTRPNNPRTVX11XVTRPNLJHFDB
AAAAAAAAAAAAAAAAAAAAAAAAAAAAAAAAAAAAAAAAAAAAAAAA
AAAAAAAAAAAAAAAAAAAAAAAAAAAAAAAAAAAAAAAAAAAAAAAA
AAAAAAAAAAAAAAAAAAAAAAAAAAAAAAAAAAAAAAAAAAAAAAAA
AAAAAAAAAAAAAAAAAAAAAAAAAAAAAAAAAAAAAAAAAAAAAAAA
AAAAAAAAAAAAAAAAAAAAAAAAAAAAAAAAAAAAAAAAAAAAAAAA
AAAAAAAAAAAAAAAAAAAAAAAAAAAAAAAAAAAAAAAAAAAAAAAA
AAAAAAAAAAAAAAAAAAAAAAAAAAAAAAAAAAAAAAAAAAAAAAAA
AAAAAAAAAAAAAAAAAAAAAAAAAAAAAAAAAAAAAAAAAAAAAAAA
AAAAAAAAAAAAAAAAAAAAAAAAAAAAAAAAAAAAAAAAAAAAAAAA
AAAAAAAAAAAAAAAAAAAAAAAAAAAAAAAAAAAAAAAAAAAAAAAA
AAAAAAAAAAAAAAAAAAAAAAAAAAAAAAAAAAAAAAAAAAAAAAAA
AAAAAAAAAAAAAAAAAAAAAAAAAAAAAAAAAAAAAAAAAAAAAAAA
AAAAAAAAAAAAAAAAAAAAAAAAAAAAAAAAAAAAAAAAAAAAAAAA
AAAAAAAAAAAAAAAAAAAAAAAAAAAAAAAAAAAAAAAAAAAAAAAA
AAAAAAAAAAAAAAAAAAAAAAAAAAAAAAAAAAAAAAAAAAAAAAAA
AAAAAAAAAAAAAAAAAAAAAAAAAAAAAAAAAAAAAAAAAAAAAAAA
AAAAAAAAAAAAAAAAAAAAAAAAAAAAAAAAAAAAAAAAAAAAAAAA
AAAAAAAAAAAAAAAAAAAAAAAAAAAAAAAAAAAAAAAAAAAAAAAA
AAAAAAAAAAAAAAAAAAAAAAAAAAAAAAAAAAAAAAAAAAAAAAAA
AAAAAAAAAAAAAAAAAAAAAAAAAAAAAAAAAAAAAAAAAAAAAAAA
AAAAAAAAAAAAAAAAAAAA00000000AAAAAAAAAAAAAAAAAAAA
AAAAAAAAAAAAAAAAAAAA00000000AAAAAAAAAAAAAAAAAAAA
AAAAAAAAAAAAAAAAAAAA00000000AAAAAAAAAAAAAAAAAAAA
AAAAAAAAAAAAAAAAAAAA00000000AAAAAAAAAAAAAAAAAAAA
AAAAAAAAAAAAAAAAAAAA00000000AAAAAAAAAAAAAAAAAAAA
AAAAAAAAAAAAAAAAAAAA00000000AAAAAAAAAAAAAAAAAAAA
AAAAAAAAAAAAAAAAAAAA00000000AAAAAAAAAAAAAAAAAAAA
AAAAAAAAAAAAAAAAAAAA00000000AAAAAAAAAAAAAAAAAAAA
AAAAAAAAAAAAAAAAAAAAAAAAAAAAAAAAAAAAAAAAAAAAAAAA
AAAAAAAAAAAAAAAAAAAAAAAAAAAAAAAAAAAAAAAAAAAAAAAA
AAAAAAAAAAAAAAAAAAAAAAAAAAAAAAAAAAAAAAAAAAAAAAAA
AAAAAAAAAAAAAAAAAAAAAAAAAAAAAAAAAAAAAAAAAAAAAAAA
AAAAAAAAAAAAAAAAAAAAAAAAAAAAAAAAAAAAAAAAAAAAAAAA
AAAAAAAAAAAAAAAAAAAAAAAAAAAAAAAAAAAAAAAAAAAAAAAA
AAAAAAAAAAAAAAAAAAAAAAAAAAAAAAAAAAAAAAAAAAAAAAAA
AAAAAAAAAAAAAAAAAAAAAAAAAAAAAAAAAAAAAAAAAAAAAAAA
AAAAAAAAAAAAAAAAAAAAAAAAAAAAAAAAAAAAAAAAAAAAAAAA
AAAAAAAAAAAAAAAAAAAAAAAAAAAAAAAAAAAAAAAAAAAAAAAA
AAAAAAAAAAAAAAAAAAAAAAAAAAAAAAAAAAAAAAAAAAAAAAAA
AAAAAAAAAAAAAAAAAAAAAAAAAAAAAAAAAAAAAAAAAAAAAAAA
AAAAAAAAAAAAAAAAAAAAAAAAAAAAAAAAAAAAAAAAAAAAAAAA
AAAAAAAAAAAAAAAAAAAAAAAAAAAAAAAAAAAAAAAAAAAAAAAA
AAAAAAAAAAAAAAAAAAAAAAAAAAAAAAAAAAAAAAAAAAAAAAAA
AAAAAAAAAAAAAAAAAAAAAAAAAAAAAAAAAAAAAAAAAAAAAAAA
AAAAAAAAAAAAAAAAAAAAAAAAAAAAAAAAAAAAAAAAAAAAAAAA
AAAAAAAAAAAAAAAAAAAAAAAAAAAAAAAAAAAAAAAAAAAAAAAA
AAAAAAAAAAAAAAAAAAAAAAAAAAAAAAAAAAAAAAAAAAAAAAAA
AAAAAAAAAAAAAAAAAAAAAAAAAAAAAAAAAAAAAAAAAAAAAAAA
BDFHJLNPRTVX11XVTRPNNPRTVX11XVTRPNLJHFDB
BDFHJLNPRTVX11XVTRPNNPRTVX11XVTRPNLJHFDB
BDFHJLNPRTVX11XVTRPNNPRTVX11XVTRPNLJHFDB
BDFHJLNPRTVX11XVTRPNNPRTVX11XVTRPNLJHFDB
BDFHJLNPRTVX11XVTRPNNPRTVX11XVTRPNLJHFDB
BDFHJLNPRTVX11XVTRPNNPRTVX11XVTRPNLJHFDB
BDFHJLNPRTVX11XVTRPOOPRTVX11XVTRPNLJHFDB
BDFHJLNPRTVX11XVTRQPPQRTVX11XVTRPNLJHFDB
BDFHJLNPRTVX11XVTSRRRRSTVX11XVTRPNLJHFDB
BDFHJLNPRTVX11XVUTTTTTTUVX11XVTRPNLJHFDB
BDFHJLNPRTVX11XWVVVVVVVVWX11XVTRPNLJHFDB
BDFHJLNPRTVX11YXXXXXXXXXXY11XVTRPNLJHFDB
BDFHJLNPRTVXZZZZZZZZZZZZZZZZXVTRPNLJHFDB
BDFHJLNPRTVXZZZZZZZZZZZZZZZZXVTRPNLJHFDB
BDFHJLNPRTVXZZZZZZZZZZZZZZZZXVTRPNLJHFDB
BDFHJLNPRTVXZZZZZZZZZZZZZZZZXVTRPNLJHFDB
BDFHJLNPRTVXZZZZZZZZZZZZZZZZXVTRPNLJHFDB
BDFHJLNPRTVXZZZZZZZZZZZZZZZZXVTRPNLJHFDB
BDFHJLNPRTVXZZZZZZZZZZZZZZZZXVTRPNLJHFDB
BDFHJLNPRTVXZZZZZZZZZZZZZZZZXVTRPNLJHFDB
BDFHJLNPRTVXZZZZZZZZZZZZZZZZXVTRPNLJHFDB
BDFHJLNPRTVXZZZZZZZZZZZZZZZZXVTRPNLJHFDB
BDFHJLNPRTVXZZZZZZZZZZZZZZZZXVTRPNLJHFDB
BDFHJLNPRTVXZZZZZZZZZZZZZZZZXVTRPNLJHFDB
BDFHJLNPRTVXZZZZZZZZZZZZZZZZXVTRPNLJHFDB
BDFHJLNPRTVXZZZZZZZZZZZZZZZZXVTRPNLJHFDB
```

```
BDFHJLNPRTVXZZZZZZZZZZZZZZZZXVTRPNLJHFDB
BDFHJLNPRTVXZZZZZZZZZZZZZZZZXVTRPNLJHFDB
BDFHJLNPRTVX11YXXXXXXXXXXY11XVTRPNLJHFDB
BDFHJLNPRTVX11XWVVVVVVVVWX11XVTRPNLJHFDB
BDFHJLNPRTVX11XVUTTTTTTUVX11XVTRPNLJHFDB
BDFHJLNPRTVX11XVTSRRRRSTVX11XVTRPNLJHFDB
BDFHJLNPRTVX11XVTRQPPQRTVX11XVTRPNLJHFDB
BDFHJLNPRTVX11XVTRPOOPRTVX11XVTRPNLJHFDB
BDFHJLNPRTVX11XVTRPNNPRTVX11XVTRPNLJHFDB
BDFHJLNPRTVX11XVTRPNNPRTVX11XVTRPNLJHFDB
BDFHJLNPRTVX11XVTRPNNPRTVX11XVTRPNLJHFDB
BDFHJLNPRTVX11XVTRPNNPRTVX11XVTRPNLJHFDB
BDFHJLNPRTVX11XVTRPNNPRTVX11XVTRPNLJHFDB
BDFHJLNPRTVX11XVTRPNNPRTVX11XVTRPNLJHFDB
AAAAAAAAAAAAAAAAAAAAAAAAAAAAAAAAAAAAAAAAAAAAAAAA
AAAAAAAAAAAAAAAAAAAAAAAAAAAAAAAAAAAAAAAAAAAAAAAA
AAAAAAAAAAAAAAAAAAAAAAAAAAAAAAAAAAAAAAAAAAAAAAAA
AAAAAAAAAAAAAAAAAAAAAAAAAAAAAAAAAAAAAAAAAAAAAAAA
AAAAAAAAAAAAAAAAAAAAAAAAAAAAAAAAAAAAAAAAAAAAAAAA
AAAAAAAAAAAAAAAAAAAAAAAAAAAAAAAAAAAAAAAAAAAAAAAA
AAAAAAAAAAAAAAAAAAAAAAAAAAAAAAAAAAAAAAAAAAAAAAAA
AAAAAAAAAAAAAAAAAAAAAAAAAAAAAAAAAAAAAAAAAAAAAAAA
AAAAAAAAAAAAAAAAAAAAAAAAAAAAAAAAAAAAAAAAAAAAAAAA
AAAAAAAAAAAAAAAAAAAAAAAAAAAAAAAAAAAAAAAAAAAAAAAA
AAAAAAAAAAAAAAAAAAAAAAAAAAAAAAAAAAAAAAAAAAAAAAAA
AAAAAAAAAAAAAAAAAAAAAAAAAAAAAAAAAAAAAAAAAAAAAAAA
AAAAAAAAAAAAAAAAAAAAAAAAAAAAAAAAAAAAAAAAAAAAAAAA
AAAAAAAAAAAAAAAAAAAAAAAAAAAAAAAAAAAAAAAAAAAAAAAA
AAAAAAAAAAAAAAAAAAAAAAAAAAAAAAAAAAAAAAAAAAAAAAAA
AAAAAAAAAAAAAAAAAAAAAAAAAAAAAAAAAAAAAAAAAAAAAAAA
AAAAAAAAAAAAAAAAAAAAAAAAAAAAAAAAAAAAAAAAAAAAAAAA
AAAAAAAAAAAAAAAAAAAAAAAAAAAAAAAAAAAAAAAAAAAAAAAA
AAAAAAAAAAAAAAAAAAAAAAAAAAAAAAAAAAAAAAAAAAAAAAAA
AAAAAAAAAAAAAAAAAAAAAAAAAAAAAAAAAAAAAAAAAAAAAAAA
AAAAAAAAAAAAAAAAAAAA00000000AAAAAAAAAAAAAAAAAAAA
AAAAAAAAAAAAAAAAAAAA00000000AAAAAAAAAAAAAAAAAAAA
AAAAAAAAAAAAAAAAAAAA00000000AAAAAAAAAAAAAAAAAAAA
AAAAAAAAAAAAAAAAAAAA00000000AAAAAAAAAAAAAAAAAAAA
AAAAAAAAAAAAAAAAAAAA00000000AAAAAAAAAAAAAAAAAAAA
AAAAAAAAAAAAAAAAAAAA00000000AAAAAAAAAAAAAAAAAAAA
AAAAAAAAAAAAAAAAAAAA00000000AAAAAAAAAAAAAAAAAAAA
AAAAAAAAAAAAAAAAAAAA00000000AAAAAAAAAAAAAAAAAAAA
AAAAAAAAAAAAAAAAAAAAAAAAAAAAAAAAAAAAAAAAAAAAAAAA
AAAAAAAAAAAAAAAAAAAAAAAAAAAAAAAAAAAAAAAAAAAAAAAA
AAAAAAAAAAAAAAAAAAAAAAAAAAAAAAAAAAAAAAAAAAAAAAAA
AAAAAAAAAAAAAAAAAAAAAAAAAAAAAAAAAAAAAAAAAAAAAAAA
AAAAAAAAAAAAAAAAAAAAAAAAAAAAAAAAAAAAAAAAAAAAAAAA
AAAAAAAAAAAAAAAAAAAAAAAAAAAAAAAAAAAAAAAAAAAAAAAA
AAAAAAAAAAAAAAAAAAAAAAAAAAAAAAAAAAAAAAAAAAAAAAAA
AAAAAAAAAAAAAAAAAAAAAAAAAAAAAAAAAAAAAAAAAAAAAAAA
AAAAAAAAAAAAAAAAAAAAAAAAAAAAAAAAAAAAAAAAAAAAAAAA
AAAAAAAAAAAAAAAAAAAAAAAAAAAAAAAAAAAAAAAAAAAAAAAA
AAAAAAAAAAAAAAAAAAAAAAAAAAAAAAAAAAAAAAAAAAAAAAAA
AAAAAAAAAAAAAAAAAAAAAAAAAAAAAAAAAAAAAAAAAAAAAAAA
AAAAAAAAAAAAAAAAAAAAAAAAAAAAAAAAAAAAAAAAAAAAAAAA
AAAAAAAAAAAAAAAAAAAAAAAAAAAAAAAAAAAAAAAAAAAAAAAA
AAAAAAAAAAAAAAAAAAAAAAAAAAAAAAAAAAAAAAAAAAAAAAAA
AAAAAAAAAAAAAAAAAAAAAAAAAAAAAAAAAAAAAAAAAAAAAAAA
AAAAAAAAAAAAAAAAAAAAAAAAAAAAAAAAAAAAAAAAAAAAAAAA
AAAAAAAAAAAAAAAAAAAAAAAAAAAAAAAAAAAAAAAAAAAAAAAA
AAAAAAAAAAAAAAAAAAAAAAAAAAAAAAAAAAAAAAAAAAAAAAAA
AAAAAAAAAAAAAAAAAAAAAAAAAAAAAAAAAAAAAAAAAAAAAAAA
```

Mark-Bieniawski Softening Problem Using Softening Law

Filename: test_MB900sftn_2step.inp

```
Test Problem, Mark-Bieniawski 900-psi coal, 2 mining steps
0.287913 2.34594e+06       1
      27
      1.  0.3700000E+006  1.3909800E+005  0.0000000E+000  0.0000000E+000  0.0000000E+000
      2.  2.0899636E+004  5.6485504E-002  2.2352322E+004  1.1297101E-001  3.3000000E-001
      2.  2.0605091E+004  5.5689435E-002  2.2037303E+004  1.1137887E-001  3.3000000E-001
      2.  1.9132364E+004  5.1709091E-002  2.0069900E+004  1.0341818E-001  3.3000000E-001
      2.  1.8837818E+004  5.0913022E-002  1.9760921E+004  1.0182604E-001  3.3000000E-001
      2.  1.7365091E+004  4.6932678E-002  1.7824291E+004  9.3865356E-002  3.3000000E-001
      2.  1.7070545E+004  4.6136609E-002  1.7521956E+004  9.2273219E-002  3.3000000E-001
      2.  1.5597818E+004  4.2156265E-002  1.5619243E+004  8.4312531E-002  3.3000000E-001
      2.  1.5303273E+004  4.1360197E-002  1.5324293E+004  8.2720393E-002  3.3000000E-001
      2.  1.3830545E+004  3.7379853E-002  1.3459359E+004  7.4759705E-002  3.3000000E-001
      2.  1.3536000E+004  3.6583784E-002  1.3172718E+004  7.3167568E-002  3.3000000E-001
      2.  1.2063273E+004  3.2603440E-002  1.1350416E+004  6.5206880E-002  3.3000000E-001
      2.  1.1768727E+004  3.1807371E-002  1.1073277E+004  6.3614742E-002  3.3000000E-001
      2.  1.0296000E+004  2.7827027E-002  9.2998919E+003  5.5654054E-002  3.3000000E-001
      2.  1.0001455E+004  2.7030958E-002  9.0338428E+003  5.4061916E-002  3.3000000E-001
      2.  8.5287273E+003  2.3050614E-002  7.3178333E+003  4.6101229E-002  3.3000000E-001
      2.  8.2341818E+003  2.2254545E-002  7.0651069E+003  4.4509091E-002  3.3000000E-001
      2.  6.7614545E+003  1.8274201E-002  5.4184637E+003  3.6548403E-002  3.3000000E-001
      2.  6.4669091E+003  1.7478133E-002  5.1824222E+003  3.4956265E-002  3.3000000E-001
      2.  4.9941818E+003  1.3497789E-002  3.6234518E+003  2.6995577E-002  3.3000000E-001
      2.  4.6996364E+003  1.2701720E-002  3.4097488E+003  2.5403440E-002  3.3000000E-001
      2.  3.2269091E+003  8.7213759E-003  1.9696876E+003  1.7442752E-002  3.3000000E-001
      2.  2.9323636E+003  7.9253071E-003  1.7898987E+003  1.5850614E-002  3.3000000E-001
      2.  1.4596364E+003  3.9449631E-003  5.2950835E+002  7.8899263E-003  3.3000000E-001
      2.  1.1650909E+003  3.1488943E-003  4.2265689E+002  6.2977887E-003  3.3000000E-001
      5.  0.1000000E+003  0.2302920E+006  0.4000000E+004  0.1000000E+001  0.3300000E+000
      5.  0.1000000E+003  0.2158980E+006  0.4000000E+004  0.1000000E+001  0.3300000E+000
    0.00000  0.03786010     0.00000  0.00000000     0.00000  0.00000000     0.00000  0.03786010     0.00000  0.00000000     0.00000
0.09363830
  600.00      48      48               0      21      28      21      28
    0.0     0.0 -27042.   132.0
 1.00000 0.00000 0.00000 0.00000 1.00000 0.00000 0.00000 0.00000 1.00000
1.350000 1.000000000    3000                                1       2
BDFHJLNPRTVX11XVTRPNNPRTVX11XVTRPNLJHFDB
BDFHJLNPRTVX11XVTRPNNPRTVX11XVTRPNLJHFDB
BDFHJLNPRTVX11XVTRPNNPRTVX11XVTRPNLJHFDB
BDFHJLNPRTVX11XVTRPNNPRTVX11XVTRPNLJHFDB
BDFHJLNPRTVX11XVTRPNNPRTVX11XVTRPNLJHFDB
BDFHJLNPRTVX11XVTRPNNPRTVX11XVTRPNLJHFDB
BDFHJLNPRTVX11XVTRPOOPRTVX11XVTRPNLJHFDB
BDFHJLNPRTVX11XVTRQPPQRTVX11XVTRPNLJHFDB
BDFHJLNPRTVX11XVTSRRRRSTVX11XVTRPNLJHFDB
BDFHJLNPRTVX11XVUTTTTTTUVX11XVTRPNLJHFDB
BDFHJLNPRTVX11XWVVVVVVVVWX11XVTRPNLJHFDB
BDFHJLNPRTVX11YXXXXXXXXXXY11XVTRPNLJHFDB
BDFHJLNPRTVX11111111111111111XVTRPNLJHFDB
BDFHJLNPRTVX11111111111111111XVTRPNLJHFDB
BDFHJLNPRTVX11YXXXXXXXXXXY11XVTRPNLJHFDB
BDFHJLNPRTVX11XWVVVVVVVVWX11XVTRPNLJHFDB
BDFHJLNPRTVX11XVUTTTTTTUVX11XVTRPNLJHFDB
BDFHJLNPRTVX11XVTSRRRRSTVX11XVTRPNLJHFDB
BDFHJLNPRTVX11XVTRQPPQRTVX11XVTRPNLJHFDB
BDFHJLNPRTVX11XVTRPOOPRTVX11XVTRPNLJHFDB
BDFHJLNPRTVX11XVTRPOOPRTVX11XVTRPNLJHFDB
BDFHJLNPRTVX11XVTRQPPQRTVX11XVTRPNLJHFDB
BDFHJLNPRTVX11XVTSRRRRSTVX11XVTRPNLJHFDB
BDFHJLNPRTVX11XVUTTTTTTUVX11XVTRPNLJHFDB
BDFHJLNPRTVX11XWVVVVVVVVWX11XVTRPNLJHFDB
BDFHJLNPRTVX11YXXXXXXXXXXY11XVTRPNLJHFDB
BDFHJLNPRTVX11111111111111111XVTRPNLJHFDB
BDFHJLNPRTVX11111111111111111XVTRPNLJHFDB
BDFHJLNPRTVX11YXXXXXXXXXXY11XVTRPNLJHFDB
BDFHJLNPRTVX11XWVVVVVVVVWX11XVTRPNLJHFDB
BDFHJLNPRTVX11XVUTTTTTTUVX11XVTRPNLJHFDB
BDFHJLNPRTVX11XVTSRRRRSTVX11XVTRPNLJHFDB
BDFHJLNPRTVX11XVTRQPPQRTVX11XVTRPNLJHFDB
BDFHJLNPRTVX11XVTRPOOPRTVX11XVTRPNLJHFDB
BDFHJLNPRTVX11XVTRPNNPRTVX11XVTRPNLJHFDB
BDFHJLNPRTVX11XVTRPNNPRTVX11XVTRPNLJHFDB
BDFHJLNPRTVX11XVTRPNNPRTVX11XVTRPNLJHFDB
BDFHJLNPRTVX11XVTRPNNPRTVX11XVTRPNLJHFDB
BDFHJLNPRTVX11XVTRPNNPRTVX11XVTRPNLJHFDB
BDFHJLNPRTVX11XVTRPNNPRTVX11XVTRPNLJHFDB
AAAAAAAAAAAAAAAAAAAAAAAAAAAAAAAAAAAAAAAAAAAAAAAAAAAAAAAA
AAAAAAAAAAAAAAAAAAAAAAAAAAAAAAAAAAAAAAAAAAAAAAAAAAAAAAAA
AAAAAAAAAAAAAAAAAAAAAAAAAAAAAAAAAAAAAAAAAAAAAAAAAAAAAAAA
AAAAAAAAAAAAAAAAAAAAAAAAAAAAAAAAAAAAAAAAAAAAAAAAAAAAAAAA
AAAAAAAAAAAAAAAAAAAAAAAAAAAAAAAAAAAAAAAAAAAAAAAAAAAAAAAA
AAAAAAAAAAAAAAAAAAAAAAAAAAAAAAAAAAAAAAAAAAAAAAAAAAAAAAAA
AAAAAAAAAAAAAAAAAAAAAAAAAAAAAAAAAAAAAAAAAAAAAAAAAAAAAAAA
AAAAAAAAAAAAAAAAAAAAAAAAAAAAAAAAAAAAAAAAAAAAAAAAAAAAAAAA
```

```
AAAAAAAAAAAAAAAAAAAAAAAAAAAAAAAAAAAAAAAAAAAAAAAA
AAAAAAAAAAAAAAAAAAAAAAAAAAAAAAAAAAAAAAAAAAAAAAAA
AAAAAAAAAAAAAAAAAAAAAAAAAAAAAAAAAAAAAAAAAAAAAAAA
AAAAAAAAAAAAAAAAAAAAAAAAAAAAAAAAAAAAAAAAAAAAAAAA
AAAAAAAAAAAAAAAAAAAAAAAAAAAAAAAAAAAAAAAAAAAAAAAA
AAAAAAAAAAAAAAAAAAAAAAAAAAAAAAAAAAAAAAAAAAAAAAAA
AAAAAAAAAAAAAAAAAAAAAAAAAAAAAAAAAAAAAAAAAAAAAAAA
AAAAAAAAAAAAAAAAAAAAAAAAAAAAAAAAAAAAAAAAAAAAAAAA
AAAAAAAAAAAAAAAAAAAAAAAAAAAAAAAAAAAAAAAAAAAAAAAA
AAAAAAAAAAAAAAAAAAAAAAAAAAAAAAAAAAAAAAAAAAAAAAAA
AAAAAAAAAAAAAAAAAAAAAAAAAAAAAAAAAAAAAAAAAAAAAAAA
AAAAAAAAAAAAAAAAAAAAAAAAAAAAAAAAAAAAAAAAAAAAAAAA
AAAAAAAAAAAAAAAAAAAA00000000AAAAAAAAAAAAAAAAAAAA
AAAAAAAAAAAAAAAAAAAA00000000AAAAAAAAAAAAAAAAAAAA
AAAAAAAAAAAAAAAAAAAA00000000AAAAAAAAAAAAAAAAAAAA
AAAAAAAAAAAAAAAAAAAA00000000AAAAAAAAAAAAAAAAAAAA
AAAAAAAAAAAAAAAAAAAA00000000AAAAAAAAAAAAAAAAAAAA
AAAAAAAAAAAAAAAAAAAA00000000AAAAAAAAAAAAAAAAAAAA
AAAAAAAAAAAAAAAAAAAA00000000AAAAAAAAAAAAAAAAAAAA
AAAAAAAAAAAAAAAAAAAA00000000AAAAAAAAAAAAAAAAAAAA
AAAAAAAAAAAAAAAAAAAAAAAAAAAAAAAAAAAAAAAAAAAAAAAA
AAAAAAAAAAAAAAAAAAAAAAAAAAAAAAAAAAAAAAAAAAAAAAAA
AAAAAAAAAAAAAAAAAAAAAAAAAAAAAAAAAAAAAAAAAAAAAAAA
AAAAAAAAAAAAAAAAAAAAAAAAAAAAAAAAAAAAAAAAAAAAAAAA
AAAAAAAAAAAAAAAAAAAAAAAAAAAAAAAAAAAAAAAAAAAAAAAA
AAAAAAAAAAAAAAAAAAAAAAAAAAAAAAAAAAAAAAAAAAAAAAAA
AAAAAAAAAAAAAAAAAAAAAAAAAAAAAAAAAAAAAAAAAAAAAAAA
AAAAAAAAAAAAAAAAAAAAAAAAAAAAAAAAAAAAAAAAAAAAAAAA
AAAAAAAAAAAAAAAAAAAAAAAAAAAAAAAAAAAAAAAAAAAAAAAA
AAAAAAAAAAAAAAAAAAAAAAAAAAAAAAAAAAAAAAAAAAAAAAAA
AAAAAAAAAAAAAAAAAAAAAAAAAAAAAAAAAAAAAAAAAAAAAAAA
AAAAAAAAAAAAAAAAAAAAAAAAAAAAAAAAAAAAAAAAAAAAAAAA
AAAAAAAAAAAAAAAAAAAAAAAAAAAAAAAAAAAAAAAAAAAAAAAA
AAAAAAAAAAAAAAAAAAAAAAAAAAAAAAAAAAAAAAAAAAAAAAAA
AAAAAAAAAAAAAAAAAAAAAAAAAAAAAAAAAAAAAAAAAAAAAAAA
AAAAAAAAAAAAAAAAAAAAAAAAAAAAAAAAAAAAAAAAAAAAAAAA
AAAAAAAAAAAAAAAAAAAAAAAAAAAAAAAAAAAAAAAAAAAAAAAA
AAAAAAAAAAAAAAAAAAAAAAAAAAAAAAAAAAAAAAAAAAAAAAAA
AAAAAAAAAAAAAAAAAAAAAAAAAAAAAAAAAAAAAAAAAAAAAAAA
AAAAAAAAAAAAAAAAAAAAAAAAAAAAAAAAAAAAAAAAAAAAAAAA
BDFHJLNPRTVX11XVTRPNNPRTVX11XVTRPNLJHFDB
BDFHJLNPRTVX11XVTRPNNPRTVX11XVTRPNLJHFDB
BDFHJLNPRTVX11XVTRPNNPRTVX11XVTRPNLJHFDB
BDFHJLNPRTVX11XVTRPNNPRTVX11XVTRPNLJHFDB
BDFHJLNPRTVX11XVTRPNNPRTVX11XVTRPNLJHFDB
BDFHJLNPRTVX11XVTRPNNPRTVX11XVTRPNLJHFDB
BDFHJLNPRTVX11XVTRPOOPRTVX11XVTRPNLJHFDB
BDFHJLNPRTVX11XVTRQPPQRTVX11XVTRPNLJHFDB
BDFHJLNPRTVX11XVTSRRRRSTVX11XVTRPNLJHFDB
BDFHJLNPRTVX11XVUTTTTTTUVX11XVTRPNLJHFDB
BDFHJLNPRTVX11XWVVVVVVVVWX11XVTRPNLJHFDB
BDFHJLNPRTVX11YXXXXXXXXXXY11XVTRPNLJHFDB
BDFHJLNPRTVXZZZZZZZZZZZZZZZZXVTRPNLJHFDB
BDFHJLNPRTVXZZZZZZZZZZZZZZZZXVTRPNLJHFDB
BDFHJLNPRTVXZZZZZZZZZZZZZZZZXVTRPNLJHFDB
BDFHJLNPRTVXZZZZZZZZZZZZZZZZXVTRPNLJHFDB
BDFHJLNPRTVXZZZZZZZZZZZZZZZZXVTRPNLJHFDB
BDFHJLNPRTVXZZZZZZZZZZZZZZZZXVTRPNLJHFDB
BDFHJLNPRTVXZZZZZZZZZZZZZZZZXVTRPNLJHFDB
BDFHJLNPRTVXZZZZZZZZZZZZZZZZXVTRPNLJHFDB
BDFHJLNPRTVXZZZZZZZZZZZZZZZZXVTRPNLJHFDB
BDFHJLNPRTVXZZZZZZZZZZZZZZZZXVTRPNLJHFDB
BDFHJLNPRTVXZZZZZZZZZZZZZZZZXVTRPNLJHFDB
BDFHJLNPRTVXZZZZZZZZZZZZZZZZXVTRPNLJHFDB
BDFHJLNPRTVXZZZZZZZZZZZZZZZZXVTRPNLJHFDB
BDFHJLNPRTVXZZZZZZZZZZZZZZZZXVTRPNLJHFDB
BDFHJLNPRTVXZZZZZZZZZZZZZZZZXVTRPNLJHFDB
BDFHJLNPRTVXZZZZZZZZZZZZZZZZXVTRPNLJHFDB
BDFHJLNPRTVX11YXXXXXXXXXXY11XVTRPNLJHFDB
BDFHJLNPRTVX11XWVVVVVVVVWX11XVTRPNLJHFDB
BDFHJLNPRTVX11XVUTTTTTTUVX11XVTRPNLJHFDB
BDFHJLNPRTVX11XVTSRRRRSTVX11XVTRPNLJHFDB
BDFHJLNPRTVX11XVTRQPPQRTVX11XVTRPNLJHFDB
BDFHJLNPRTVX11XVTRPOOPRTVX11XVTRPNLJHFDB
BDFHJLNPRTVX11XVTRPNNPRTVX11XVTRPNLJHFDB
BDFHJLNPRTVX11XVTRPNNPRTVX11XVTRPNLJHFDB
BDFHJLNPRTVX11XVTRPNNPRTVX11XVTRPNLJHFDB
BDFHJLNPRTVX11XVTRPNNPRTVX11XVTRPNLJHFDB
BDFHJLNPRTVX11XVTRPNNPRTVX11XVTRPNLJHFDB
BDFHJLNPRTVX11XVTRPNNPRTVX11XVTRPNLJHFDB
AAAAAAAAAAAAAAAAAAAAAAAAAAAAAAAAAAAAAAAAAAAAAAAA
AAAAAAAAAAAAAAAAAAAAAAAAAAAAAAAAAAAAAAAAAAAAAAAA
AAAAAAAAAAAAAAAAAAAAAAAAAAAAAAAAAAAAAAAAAAAAAAAA
AAAAAAAAAAAAAAAAAAAAAAAAAAAAAAAAAAAAAAAAAAAAAAAA
AAAAAAAAAAAAAAAAAAAAAAAAAAAAAAAAAAAAAAAAAAAAAAAA
AAAAAAAAAAAAAAAAAAAAAAAAAAAAAAAAAAAAAAAAAAAAAAAA
AAAAAAAAAAAAAAAAAAAAAAAAAAAAAAAAAAAAAAAAAAAAAAAA
AAAAAAAAAAAAAAAAAAAAAAAAAAAAAAAAAAAAAAAAAAAAAAAA
AAAAAAAAAAAAAAAAAAAAAAAAAAAAAAAAAAAAAAAAAAAAAAAA
AAAAAAAAAAAAAAAAAAAAAAAAAAAAAAAAAAAAAAAAAAAAAAAA
AAAAAAAAAAAAAAAAAAAAAAAAAAAAAAAAAAAAAAAAAAAAAAAA
AAAAAAAAAAAAAAAAAAAAAAAAAAAAAAAAAAAAAAAAAAAAAAAA
```

```
AAAAAAAAAAAAAAAAAAAAAAAAAAAAAAAAAAAAAAAAAAAAAAAA
AAAAAAAAAAAAAAAAAAAAAAAAAAAAAAAAAAAAAAAAAAAAAAAA
AAAAAAAAAAAAAAAAAAAAAAAAAAAAAAAAAAAAAAAAAAAAAAAA
AAAAAAAAAAAAAAAAAAAAAAAAAAAAAAAAAAAAAAAAAAAAAAAA
AAAAAAAAAAAAAAAAAAAAAAAAAAAAAAAAAAAAAAAAAAAAAAAA
AAAAAAAAAAAAAAAAAAAAAAAAAAAAAAAAAAAAAAAAAAAAAAAA
AAAAAAAAAAAAAAAAAAAAAAAAAAAAAAAAAAAAAAAAAAAAAAAA
AAAAAAAAAAAAAAAAAAAAAAAAAAAAAAAAAAAAAAAAAAAAAAAA
AAAAAAAAAAAAAAAAAAAA00000000AAAAAAAAAAAAAAAAAAAA
AAAAAAAAAAAAAAAAAAAA00000000AAAAAAAAAAAAAAAAAAAA
AAAAAAAAAAAAAAAAAAAA00000000AAAAAAAAAAAAAAAAAAAA
AAAAAAAAAAAAAAAAAAAA00000000AAAAAAAAAAAAAAAAAAAA
AAAAAAAAAAAAAAAAAAAA00000000AAAAAAAAAAAAAAAAAAAA
AAAAAAAAAAAAAAAAAAAA00000000AAAAAAAAAAAAAAAAAAAA
AAAAAAAAAAAAAAAAAAAA00000000AAAAAAAAAAAAAAAAAAAA
AAAAAAAAAAAAAAAAAAAA00000000AAAAAAAAAAAAAAAAAAAA
AAAAAAAAAAAAAAAAAAAAAAAAAAAAAAAAAAAAAAAAAAAAAAAA
AAAAAAAAAAAAAAAAAAAAAAAAAAAAAAAAAAAAAAAAAAAAAAAA
AAAAAAAAAAAAAAAAAAAAAAAAAAAAAAAAAAAAAAAAAAAAAAAA
AAAAAAAAAAAAAAAAAAAAAAAAAAAAAAAAAAAAAAAAAAAAAAAA
AAAAAAAAAAAAAAAAAAAAAAAAAAAAAAAAAAAAAAAAAAAAAAAA
AAAAAAAAAAAAAAAAAAAAAAAAAAAAAAAAAAAAAAAAAAAAAAAA
AAAAAAAAAAAAAAAAAAAAAAAAAAAAAAAAAAAAAAAAAAAAAAAA
AAAAAAAAAAAAAAAAAAAAAAAAAAAAAAAAAAAAAAAAAAAAAAAA
AAAAAAAAAAAAAAAAAAAAAAAAAAAAAAAAAAAAAAAAAAAAAAAA
AAAAAAAAAAAAAAAAAAAAAAAAAAAAAAAAAAAAAAAAAAAAAAAA
AAAAAAAAAAAAAAAAAAAAAAAAAAAAAAAAAAAAAAAAAAAAAAAA
AAAAAAAAAAAAAAAAAAAAAAAAAAAAAAAAAAAAAAAAAAAAAAAA
AAAAAAAAAAAAAAAAAAAAAAAAAAAAAAAAAAAAAAAAAAAAAAAA
AAAAAAAAAAAAAAAAAAAAAAAAAAAAAAAAAAAAAAAAAAAAAAAA
AAAAAAAAAAAAAAAAAAAAAAAAAAAAAAAAAAAAAAAAAAAAAAAA
AAAAAAAAAAAAAAAAAAAAAAAAAAAAAAAAAAAAAAAAAAAAAAAA
AAAAAAAAAAAAAAAAAAAAAAAAAAAAAAAAAAAAAAAAAAAAAAAA
AAAAAAAAAAAAAAAAAAAAAAAAAAAAAAAAAAAAAAAAAAAAAAAA
AAAAAAAAAAAAAAAAAAAAAAAAAAAAAAAAAAAAAAAAAAAAAAAA
AAAAAAAAAAAAAAAAAAAAAAAAAAAAAAAAAAAAAAAAAAAAAAAA
```

Filename: test_mpMB900sftn_2step.inp

Note that the material code lines beginning with "7." are longer than the line space, and therefore, are continued on the next line. Each of those lines ends with "3.3000000E-001."

```
Test Problem, multipoint Mark-Bieniawski with softening case
0.287913 2.34594e+06       1
      27
      1.  0.3700000E+006  1.3909800E+005  0.0000000E+000  0.0000000E+000  0.0000000E+000
      7.  2.0899636E+004  5.6485504E-002  2.2352322E+004  1.1297101E-001  2.2352322E+004  2.0000000E-001  2.2352322E+004  3.0000000E-001
2.2352322E+004  4.0000000E-001  3.3000000E-001
      7.  2.0605091E+004  5.5689435E-002  2.2037303E+004  1.1137887E-001  2.2037303E+004  2.0000000E-001  2.2037303E+004  3.0000000E-001
2.2037303E+004  4.0000000E-001  3.3000000E-001
      7.  1.9132364E+004  5.1709091E-002  2.0069900E+004  1.0341818E-001  2.0069900E+004  2.0000000E-001  2.0069900E+004  3.0000000E-001
2.0069900E+004  4.0000000E-001  3.3000000E-001
      7.  1.8837818E+004  5.0913022E-002  1.9760921E+004  1.0182604E-001  1.9760921E+004  2.0000000E-001  1.9760921E+004  3.0000000E-001
1.9760921E+004  4.0000000E-001  3.3000000E-001
      7.  1.7365091E+004  4.6932678E-002  1.7824291E+004  9.3865356E-002  1.7824291E+004  2.0000000E-001  1.7824291E+004  3.0000000E-001
1.7824291E+004  4.0000000E-001  3.3000000E-001
      7.  1.7070545E+004  4.6136609E-002  1.7521956E+004  9.2273219E-002  1.7521956E+004  2.0000000E-001  1.7521956E+004  3.0000000E-001
1.7521956E+004  4.0000000E-001  3.3000000E-001
      7.  1.5597818E+004  4.2156265E-002  1.5619243E+004  8.4312531E-002  1.5619243E+004  2.0000000E-001  1.5619243E+004  3.0000000E-001
1.5619243E+004  4.0000000E-001  3.3000000E-001
      7.  1.5303273E+004  4.1360197E-002  1.5324293E+004  8.2720393E-002  1.5324293E+004  2.0000000E-001  1.5324293E+004  3.0000000E-001
1.5324293E+004  4.0000000E-001  3.3000000E-001
      7.  1.3830545E+004  3.7379853E-002  1.3459359E+004  7.4759705E-002  1.3459359E+004  2.0000000E-001  1.3459359E+004  3.0000000E-001
1.3459359E+004  4.0000000E-001  3.3000000E-001
      7.  1.3536000E+004  3.6583784E-002  1.3172718E+004  7.3167568E-002  1.3172718E+004  2.0000000E-001  1.3172718E+004  3.0000000E-001
1.3172718E+004  4.0000000E-001  3.3000000E-001
      7.  1.2063273E+004  3.2603440E-002  1.1350416E+004  6.5206880E-002  1.1350416E+004  2.0000000E-001  1.1350416E+004  3.0000000E-001
1.1350416E+004  4.0000000E-001  3.3000000E-001
      7.  1.1768727E+004  3.1807371E-002  1.1073277E+004  6.3614742E-002  1.1073277E+004  2.0000000E-001  1.1073277E+004  3.0000000E-001
1.1073277E+004  4.0000000E-001  3.3000000E-001
      7.  1.0296000E+004  2.7827027E-002  9.2998919E+003  5.5654054E-002  9.2998919E+003  2.0000000E-001  9.2998919E+003  3.0000000E-001
9.2998919E+003  4.0000000E-001  3.3000000E-001
      7.  1.0001455E+004  2.7030958E-002  9.0338428E+003  5.4061916E-002  9.0338428E+003  2.0000000E-001  9.0338428E+003  3.0000000E-001
9.0338428E+003  4.0000000E-001  3.3000000E-001
      7.  8.5287273E+003  2.3050614E-002  7.3178333E+003  4.6101229E-002  7.3178333E+003  2.0000000E-001  7.3178333E+003  3.0000000E-001
7.3178333E+003  4.0000000E-001  3.3000000E-001
      7.  8.2341818E+003  2.2254545E-002  7.0651069E+003  4.4509091E-002  7.0651069E+003  2.0000000E-001  7.0651069E+003  3.0000000E-001
7.0651069E+003  4.0000000E-001  3.3000000E-001
      7.  6.7614545E+003  1.8274201E-002  5.4184637E+003  3.6548403E-002  5.4184637E+003  2.0000000E-001  5.4184637E+003  3.0000000E-001
5.4184637E+003  4.0000000E-001  3.3000000E-001
      7.  6.4669091E+003  1.7478133E-002  5.1824222E+003  3.4956265E-002  5.1824222E+003  2.0000000E-001  5.1824222E+003  3.0000000E-001
5.1824222E+003  4.0000000E-001  3.3000000E-001
      7.  4.9941818E+003  1.3497789E-002  3.6234518E+003  2.6995577E-002  3.6234518E+003  2.0000000E-001  3.6234518E+003  3.0000000E-001
3.6234518E+003  4.0000000E-001  3.3000000E-001
      7.  4.6996364E+003  1.2701720E-002  3.4097488E+003  2.5403440E-002  3.4097488E+003  2.0000000E-001  3.4097488E+003  3.0000000E-001
3.4097488E+003  4.0000000E-001  3.3000000E-001
      7.  3.2269091E+003  8.7213759E-003  1.9696876E+003  1.7442752E-002  1.9696876E+003  2.0000000E-001  1.9696876E+003  3.0000000E-001
1.9696876E+003  4.0000000E-001  3.3000000E-001
      7.  2.9323636E+003  7.9253071E-003  1.7898987E+003  1.5850614E-002  1.7898987E+003  2.0000000E-001  1.7898987E+003  3.0000000E-001
1.7898987E+003  4.0000000E-001  3.3000000E-001
      7.  1.4596364E+003  3.9449631E-003  5.2950835E+002  7.8899263E-003  5.2950835E+002  2.0000000E-001  5.2950835E+002  3.0000000E-001
5.2950835E+002  4.0000000E-001  3.3000000E-001
      7.  1.1650909E+003  3.1488943E-003  4.2265689E+002  6.2977887E-003  4.2265689E+002  2.0000000E-001  4.2265689E+002  3.0000000E-001
4.2265689E+002  4.0000000E-001  3.3000000E-001
      5.  0.1000000E+003  0.2302920E+006  0.4000000E+004  0.1000000E+001  0.3300000E+000
      5.  0.1000000E+003  0.2158980E+006  0.4000000E+004  0.1000000E+001  0.3300000E+000
     0.00000  0.03786010     0.00000  0.00000000     0.00000  0.00000000     0.00000  0.03786010     0.00000  0.00000000     0.00000
0.09363830
  600.00      48      48               0      21      28      21      28
     0.0     0.0 -27042.   132.0
 1.00000 0.00000 0.00000 0.00000 1.00000 0.00000 0.00000 0.00000 1.00000
1.350000 1.000000000    3000                                1       2
BDFHJLNPRTVX11XVTRPNNPRTVX11XVTRPNLJHFDB
BDFHJLNPRTVX11XVTRPNNPRTVX11XVTRPNLJHFDB
BDFHJLNPRTVX11XVTRPNNPRTVX11XVTRPNLJHFDB
BDFHJLNPRTVX11XVTRPNNPRTVX11XVTRPNLJHFDB
BDFHJLNPRTVX11XVTRPNNPRTVX11XVTRPNLJHFDB
BDFHJLNPRTVX11XVTRPNNPRTVX11XVTRPNLJHFDB
BDFHJLNPRTVX11XVTRPOOPRTVX11XVTRPNLJHFDB
BDFHJLNPRTVX11XVTRQPPQRTVX11XVTRPNLJHFDB
BDFHJLNPRTVX11XVTSRRRRSTVX11XVTRPNLJHFDB
BDFHJLNPRTVX11XVUTTTTTTUVX11XVTRPNLJHFDB
BDFHJLNPRTVX11XWVVVVVVVVVWX11XVTRPNLJHFDB
BDFHJLNPRTVX11YXXXXXXXXXXY11XVTRPNLJHFDB
BDFHJLNPRTVX11111111111111111XVTRPNLJHFDB
BDFHJLNPRTVX11111111111111111XVTRPNLJHFDB
BDFHJLNPRTVX11YXXXXXXXXXXY11XVTRPNLJHFDB
BDFHJLNPRTVX11XWVVVVVVVVVWX11XVTRPNLJHFDB
BDFHJLNPRTVX11XVUTTTTTTUVX11XVTRPNLJHFDB
BDFHJLNPRTVX11XVTSRRRRSTVX11XVTRPNLJHFDB
BDFHJLNPRTVX11XVTRQPPQRTVX11XVTRPNLJHFDB
BDFHJLNPRTVX11XVTRPOOPRTVX11XVTRPNLJHFDB
BDFHJLNPRTVX11XVTRPOOPRTVX11XVTRPNLJHFDB
```

```
BDFHJLNPRTVX11XVTRQPPQRTVX11XVTRPNLJHFDB
BDFHJLNPRTVX11XVTSRRRRSTVX11XVTRPNLJHFDB
BDFHJLNPRTVX11XVUTTTTTTUVX11XVTRPNLJHFDB
BDFHJLNPRTVX11XWVVVVVVVVWX11XVTRPNLJHFDB
BDFHJLNPRTVX11YXXXXXXXXXXY11XVTRPNLJHFDB
BDFHJLNPRTVX1111111111111111XVTRPNLJHFDB
BDFHJLNPRTVX1111111111111111XVTRPNLJHFDB
BDFHJLNPRTVX11YXXXXXXXXXXY11XVTRPNLJHFDB
BDFHJLNPRTVX11XWVVVVVVVVWX11XVTRPNLJHFDB
BDFHJLNPRTVX11XVUTTTTTTUVX11XVTRPNLJHFDB
BDFHJLNPRTVX11XVTSRRRRSTVX11XVTRPNLJHFDB
BDFHJLNPRTVX11XVTRQPPQRTVX11XVTRPNLJHFDB
BDFHJLNPRTVX11XVTRPOOPRTVX11XVTRPNLJHFDB
BDFHJLNPRTVX11XVTRPNNPRTVX11XVTRPNLJHFDB
BDFHJLNPRTVX11XVTRPNNPRTVX11XVTRPNLJHFDB
BDFHJLNPRTVX11XVTRPNNPRTVX11XVTRPNLJHFDB
BDFHJLNPRTVX11XVTRPNNPRTVX11XVTRPNLJHFDB
BDFHJLNPRTVX11XVTRPNNPRTVX11XVTRPNLJHFDB
BDFHJLNPRTVX11XVTRPNNPRTVX11XVTRPNLJHFDB
AAAAAAAAAAAAAAAAAAAAAAAAAAAAAAAAAAAAAAAAAAAAAAAA
AAAAAAAAAAAAAAAAAAAAAAAAAAAAAAAAAAAAAAAAAAAAAAAA
AAAAAAAAAAAAAAAAAAAAAAAAAAAAAAAAAAAAAAAAAAAAAAAA
AAAAAAAAAAAAAAAAAAAAAAAAAAAAAAAAAAAAAAAAAAAAAAAA
AAAAAAAAAAAAAAAAAAAAAAAAAAAAAAAAAAAAAAAAAAAAAAAA
AAAAAAAAAAAAAAAAAAAAAAAAAAAAAAAAAAAAAAAAAAAAAAAA
AAAAAAAAAAAAAAAAAAAAAAAAAAAAAAAAAAAAAAAAAAAAAAAA
AAAAAAAAAAAAAAAAAAAAAAAAAAAAAAAAAAAAAAAAAAAAAAAA
AAAAAAAAAAAAAAAAAAAAAAAAAAAAAAAAAAAAAAAAAAAAAAAA
AAAAAAAAAAAAAAAAAAAAAAAAAAAAAAAAAAAAAAAAAAAAAAAA
AAAAAAAAAAAAAAAAAAAAAAAAAAAAAAAAAAAAAAAAAAAAAAAA
AAAAAAAAAAAAAAAAAAAAAAAAAAAAAAAAAAAAAAAAAAAAAAAA
AAAAAAAAAAAAAAAAAAAAAAAAAAAAAAAAAAAAAAAAAAAAAAAA
AAAAAAAAAAAAAAAAAAAAAAAAAAAAAAAAAAAAAAAAAAAAAAAA
AAAAAAAAAAAAAAAAAAAAAAAAAAAAAAAAAAAAAAAAAAAAAAAA
AAAAAAAAAAAAAAAAAAAAAAAAAAAAAAAAAAAAAAAAAAAAAAAA
AAAAAAAAAAAAAAAAAAAAAAAAAAAAAAAAAAAAAAAAAAAAAAAA
AAAAAAAAAAAAAAAAAAAAAAAAAAAAAAAAAAAAAAAAAAAAAAAA
AAAAAAAAAAAAAAAAAAAAAAAAAAAAAAAAAAAAAAAAAAAAAAAA
AAAAAAAAAAAAAAAAAAAAAAAAAAAAAAAAAAAAAAAAAAAAAAAA
AAAAAAAAAAAAAAAAAAAA00000000AAAAAAAAAAAAAAAAAAAA
AAAAAAAAAAAAAAAAAAAA00000000AAAAAAAAAAAAAAAAAAAA
AAAAAAAAAAAAAAAAAAAA00000000AAAAAAAAAAAAAAAAAAAA
AAAAAAAAAAAAAAAAAAAA00000000AAAAAAAAAAAAAAAAAAAA
AAAAAAAAAAAAAAAAAAAA00000000AAAAAAAAAAAAAAAAAAAA
AAAAAAAAAAAAAAAAAAAA00000000AAAAAAAAAAAAAAAAAAAA
AAAAAAAAAAAAAAAAAAAA00000000AAAAAAAAAAAAAAAAAAAA
AAAAAAAAAAAAAAAAAAAA00000000AAAAAAAAAAAAAAAAAAAA
AAAAAAAAAAAAAAAAAAAAAAAAAAAAAAAAAAAAAAAAAAAAAAAA
AAAAAAAAAAAAAAAAAAAAAAAAAAAAAAAAAAAAAAAAAAAAAAAA
AAAAAAAAAAAAAAAAAAAAAAAAAAAAAAAAAAAAAAAAAAAAAAAA
AAAAAAAAAAAAAAAAAAAAAAAAAAAAAAAAAAAAAAAAAAAAAAAA
AAAAAAAAAAAAAAAAAAAAAAAAAAAAAAAAAAAAAAAAAAAAAAAA
AAAAAAAAAAAAAAAAAAAAAAAAAAAAAAAAAAAAAAAAAAAAAAAA
AAAAAAAAAAAAAAAAAAAAAAAAAAAAAAAAAAAAAAAAAAAAAAAA
AAAAAAAAAAAAAAAAAAAAAAAAAAAAAAAAAAAAAAAAAAAAAAAA
AAAAAAAAAAAAAAAAAAAAAAAAAAAAAAAAAAAAAAAAAAAAAAAA
AAAAAAAAAAAAAAAAAAAAAAAAAAAAAAAAAAAAAAAAAAAAAAAA
AAAAAAAAAAAAAAAAAAAAAAAAAAAAAAAAAAAAAAAAAAAAAAAA
AAAAAAAAAAAAAAAAAAAAAAAAAAAAAAAAAAAAAAAAAAAAAAAA
AAAAAAAAAAAAAAAAAAAAAAAAAAAAAAAAAAAAAAAAAAAAAAAA
AAAAAAAAAAAAAAAAAAAAAAAAAAAAAAAAAAAAAAAAAAAAAAAA
AAAAAAAAAAAAAAAAAAAAAAAAAAAAAAAAAAAAAAAAAAAAAAAA
AAAAAAAAAAAAAAAAAAAAAAAAAAAAAAAAAAAAAAAAAAAAAAAA
AAAAAAAAAAAAAAAAAAAAAAAAAAAAAAAAAAAAAAAAAAAAAAAA
AAAAAAAAAAAAAAAAAAAAAAAAAAAAAAAAAAAAAAAAAAAAAAAA
AAAAAAAAAAAAAAAAAAAAAAAAAAAAAAAAAAAAAAAAAAAAAAAA
AAAAAAAAAAAAAAAAAAAAAAAAAAAAAAAAAAAAAAAAAAAAAAAA
BDFHJLNPRTVX11XVTRPNNPRTVX11XVTRPNLJHFDB
BDFHJLNPRTVX11XVTRPNNPRTVX11XVTRPNLJHFDB
BDFHJLNPRTVX11XVTRPNNPRTVX11XVTRPNLJHFDB
BDFHJLNPRTVX11XVTRPNNPRTVX11XVTRPNLJHFDB
BDFHJLNPRTVX11XVTRPNNPRTVX11XVTRPNLJHFDB
BDFHJLNPRTVX11XVTRPNNPRTVX11XVTRPNLJHFDB
BDFHJLNPRTVX11XVTRPOOPRTVX11XVTRPNLJHFDB
BDFHJLNPRTVX11XVTRQPPQRTVX11XVTRPNLJHFDB
BDFHJLNPRTVX11XVTSRRRRSTVX11XVTRPNLJHFDB
BDFHJLNPRTVX11XVUTTTTTTUVX11XVTRPNLJHFDB
BDFHJLNPRTVX11XWVVVVVVVVWX11XVTRPNLJHFDB
BDFHJLNPRTVX11YXXXXXXXXXXY11XVTRPNLJHFDB
BDFHJLNPRTVXZZZZZZZZZZZZZZZZXVTRPNLJHFDB
BDFHJLNPRTVXZZZZZZZZZZZZZZZZXVTRPNLJHFDB
BDFHJLNPRTVXZZZZZZZZZZZZZZZZXVTRPNLJHFDB
BDFHJLNPRTVXZZZZZZZZZZZZZZZZXVTRPNLJHFDB
BDFHJLNPRTVXZZZZZZZZZZZZZZZZXVTRPNLJHFDB
BDFHJLNPRTVXZZZZZZZZZZZZZZZZXVTRPNLJHFDB
BDFHJLNPRTVXZZZZZZZZZZZZZZZZXVTRPNLJHFDB
BDFHJLNPRTVXZZZZZZZZZZZZZZZZXVTRPNLJHFDB
BDFHJLNPRTVXZZZZZZZZZZZZZZZZXVTRPNLJHFDB
BDFHJLNPRTVXZZZZZZZZZZZZZZZZXVTRPNLJHFDB
BDFHJLNPRTVXZZZZZZZZZZZZZZZZXVTRPNLJHFDB
BDFHJLNPRTVXZZZZZZZZZZZZZZZZXVTRPNLJHFDB
BDFHJLNPRTVXZZZZZZZZZZZZZZZZXVTRPNLJHFDB
```

```
BDFHJLNPRTVXZZZZZZZZZZZZZZZZXVTRPNLJHFDB
BDFHJLNPRTVXZZZZZZZZZZZZZZZZXVTRPNLJHFDB
BDFHJLNPRTVXZZZZZZZZZZZZZZZZXVTRPNLJHFDB
BDFHJLNPRTVX11YXXXXXXXXXXY11XVTRPNLJHFDB
BDFHJLNPRTVX11XWVVVVVVVVWX11XVTRPNLJHFDB
BDFHJLNPRTVX11XVUTTTTTTUVX11XVTRPNLJHFDB
BDFHJLNPRTVX11XVTSRRRRSTVX11XVTRPNLJHFDB
BDFHJLNPRTVX11XVTRQPPQRTVX11XVTRPNLJHFDB
BDFHJLNPRTVX11XVTRPOOPRTVX11XVTRPNLJHFDB
BDFHJLNPRTVX11XVTRPNNPRTVX11XVTRPNLJHFDB
BDFHJLNPRTVX11XVTRPNNPRTVX11XVTRPNLJHFDB
BDFHJLNPRTVX11XVTRPNNPRTVX11XVTRPNLJHFDB
BDFHJLNPRTVX11XVTRPNNPRTVX11XVTRPNLJHFDB
BDFHJLNPRTVX11XVTRPNNPRTVX11XVTRPNLJHFDB
BDFHJLNPRTVX11XVTRPNNPRTVX11XVTRPNLJHFDB
AAAAAAAAAAAAAAAAAAAAAAAAAAAAAAAAAAAAAAAAAAAAAAAA
AAAAAAAAAAAAAAAAAAAAAAAAAAAAAAAAAAAAAAAAAAAAAAAA
AAAAAAAAAAAAAAAAAAAAAAAAAAAAAAAAAAAAAAAAAAAAAAAA
AAAAAAAAAAAAAAAAAAAAAAAAAAAAAAAAAAAAAAAAAAAAAAAA
AAAAAAAAAAAAAAAAAAAAAAAAAAAAAAAAAAAAAAAAAAAAAAAA
AAAAAAAAAAAAAAAAAAAAAAAAAAAAAAAAAAAAAAAAAAAAAAAA
AAAAAAAAAAAAAAAAAAAAAAAAAAAAAAAAAAAAAAAAAAAAAAAA
AAAAAAAAAAAAAAAAAAAAAAAAAAAAAAAAAAAAAAAAAAAAAAAA
AAAAAAAAAAAAAAAAAAAAAAAAAAAAAAAAAAAAAAAAAAAAAAAA
AAAAAAAAAAAAAAAAAAAAAAAAAAAAAAAAAAAAAAAAAAAAAAAA
AAAAAAAAAAAAAAAAAAAAAAAAAAAAAAAAAAAAAAAAAAAAAAAA
AAAAAAAAAAAAAAAAAAAAAAAAAAAAAAAAAAAAAAAAAAAAAAAA
AAAAAAAAAAAAAAAAAAAAAAAAAAAAAAAAAAAAAAAAAAAAAAAA
AAAAAAAAAAAAAAAAAAAAAAAAAAAAAAAAAAAAAAAAAAAAAAAA
AAAAAAAAAAAAAAAAAAAAAAAAAAAAAAAAAAAAAAAAAAAAAAAA
AAAAAAAAAAAAAAAAAAAAAAAAAAAAAAAAAAAAAAAAAAAAAAAA
AAAAAAAAAAAAAAAAAAAAAAAAAAAAAAAAAAAAAAAAAAAAAAAA
AAAAAAAAAAAAAAAAAAAAAAAAAAAAAAAAAAAAAAAAAAAAAAAA
AAAAAAAAAAAAAAAAAAAAAAAAAAAAAAAAAAAAAAAAAAAAAAAA
AAAAAAAAAAAAAAAAAAAAAAAAAAAAAAAAAAAAAAAAAAAAAAAA
AAAAAAAAAAAAAAAAAAAA00000000AAAAAAAAAAAAAAAAAAAA
AAAAAAAAAAAAAAAAAAAA00000000AAAAAAAAAAAAAAAAAAAA
AAAAAAAAAAAAAAAAAAAA00000000AAAAAAAAAAAAAAAAAAAA
AAAAAAAAAAAAAAAAAAAA00000000AAAAAAAAAAAAAAAAAAAA
AAAAAAAAAAAAAAAAAAAA00000000AAAAAAAAAAAAAAAAAAAA
AAAAAAAAAAAAAAAAAAAA00000000AAAAAAAAAAAAAAAAAAAA
AAAAAAAAAAAAAAAAAAAA00000000AAAAAAAAAAAAAAAAAAAA
AAAAAAAAAAAAAAAAAAAA00000000AAAAAAAAAAAAAAAAAAAA
AAAAAAAAAAAAAAAAAAAAAAAAAAAAAAAAAAAAAAAAAAAAAAAA
AAAAAAAAAAAAAAAAAAAAAAAAAAAAAAAAAAAAAAAAAAAAAAAA
AAAAAAAAAAAAAAAAAAAAAAAAAAAAAAAAAAAAAAAAAAAAAAAA
AAAAAAAAAAAAAAAAAAAAAAAAAAAAAAAAAAAAAAAAAAAAAAAA
AAAAAAAAAAAAAAAAAAAAAAAAAAAAAAAAAAAAAAAAAAAAAAAA
AAAAAAAAAAAAAAAAAAAAAAAAAAAAAAAAAAAAAAAAAAAAAAAA
AAAAAAAAAAAAAAAAAAAAAAAAAAAAAAAAAAAAAAAAAAAAAAAA
AAAAAAAAAAAAAAAAAAAAAAAAAAAAAAAAAAAAAAAAAAAAAAAA
AAAAAAAAAAAAAAAAAAAAAAAAAAAAAAAAAAAAAAAAAAAAAAAA
AAAAAAAAAAAAAAAAAAAAAAAAAAAAAAAAAAAAAAAAAAAAAAAA
AAAAAAAAAAAAAAAAAAAAAAAAAAAAAAAAAAAAAAAAAAAAAAAA
AAAAAAAAAAAAAAAAAAAAAAAAAAAAAAAAAAAAAAAAAAAAAAAA
AAAAAAAAAAAAAAAAAAAAAAAAAAAAAAAAAAAAAAAAAAAAAAAA
AAAAAAAAAAAAAAAAAAAAAAAAAAAAAAAAAAAAAAAAAAAAAAAA
AAAAAAAAAAAAAAAAAAAAAAAAAAAAAAAAAAAAAAAAAAAAAAAA
AAAAAAAAAAAAAAAAAAAAAAAAAAAAAAAAAAAAAAAAAAAAAAAA
AAAAAAAAAAAAAAAAAAAAAAAAAAAAAAAAAAAAAAAAAAAAAAAA
AAAAAAAAAAAAAAAAAAAAAAAAAAAAAAAAAAAAAAAAAAAAAAAA
AAAAAAAAAAAAAAAAAAAAAAAAAAAAAAAAAAAAAAAAAAAAAAAA
AAAAAAAAAAAAAAAAAAAAAAAAAAAAAAAAAAAAAAAAAAAAAAAA
```

Promoting productive workplaces through safety and health research

DHHS (NIOSH) Publication No. 2020-104

DOI: https://doi.org/10.26616/NIOSHPUB2020104